Year : 2013

SEDIMENTOLOGY, GEOCHEMISTRY AND MINERALOGY OF THE PALEOCENE-EOCENE THERMAL MAXIMUM (PETM): SEDIMENT RECORDS FROM EGYPT, INDIA AND SPAIN

SALEH HASSAN KHOZYEM

UNIL | Université de Lausanne

Faculté des Géosciences et de l'environnement

Institut des Sciences de la Terre

SEDIMENTOLOGY, GEOCHEMISTRY AND MINERALOGY OF THE PALEOCENE-EOCENE THERMAL MAXIMUM (PETM): SEDIMENT RECORDS FROM EGYPT, INDIA AND SPAIN

THÈSE DE DOCTORAT

Présentée à la
Faculté des Géosciences et de l'Environnement de l'Université de Lausanne
Pour l'obtention du grade de
Docteur ès Sciences

Par

Hassan Mohamed Ahmed Khozyem SALEH

Jury

Prof. Dr. Verrecchia Eric, Université de Lausanne (Président du Jury)
Dr. Thierry Adatte, Université de Lausanne (Directeur de thèse)
Prof. Dr. Karl B. Föllmi, Université de Lausanne (Expert interne, rapporteur de thèse)
Prof. Dr. Gerta Keller, Université de Princeton (Expert externe)
Dr. Jorge E. Spangenberg, Université de Lausanne (Expert interne)
Prof. Dr. Nicolas P. Tribovillard, Université de Lille (Expert externe)

LAUSANNE 2013

UNIL | Université de Lausanne

Faculté des Géosciences et de l'environnement

Institut des Sciences de la Terre

SEDIMENTOLOGY, GEOCHEMISTRY AND MINERALOGY OF THE PALEOCENE-EOCENE THERMAL MAXIMUM (PETM): SEDIMENT RECORDS FROM EGYPT, INDIA AND SPAIN

Par

Hassan Mohamed Ahmed Khozyem SALEH

Titulaire d'un Master en Géologie

Faculté des Sciences Assouan

LAUSANNE 2013

UNIL | Université de Lausanne
Décanat Géosciences et de l'Environnement
bâtiment Géopolis
CH-1015 Lausanne

IMPRIMATUR

Vu le rapport présenté par le jury d'examen, composé de

Président de la séance publique :	M. le Professeur Eric Verrecchia
Président du colloque :	M. le Professeur Eric Verrecchia
Directeur de thèse :	M. le Docteur Thierry Adatte
Rapporteur :	M. le Professeur Karl Föllmi
Experte externe :	Mme la Professeure Gerta Keller
Expert externe :	M. le Professeur Nicolas Tribovillard
Expert interne :	M. le Docteur Jorge Spangenberg

Le Doyen de la Faculté des géosciences et de l'environnement autorise l'impression de la thèse de

Monsieur Hassan Mohamed Ahmed Khozyem SALEH

Titulaire d'un
Master en géologie
South Valley University, Aswan, Egypte

intitulée

SEDIMENTOLOGY, GEOCHEMISTRY AND MINERALOGY OF THE PALEOCENE EOCENE THERMAL MAXIMUM (PETM) : SEDIMENT RECORDS FROM EGYPT, INDIA, AND SPAIN

Lausanne, le 3 décembre 2013

Pour le Doyen de la Faculté des géosciences et de l'environnement

Professeur Eric Verrecchia, Vice-doyen

«WHAT WE KNOW IS A DROP.
WHAT WE DON'T KNOW IS AN OCEAN.»

- ISAAC NEWTON

ACKNOWLEDGEMENTS

This dissertation never would have happened without guidance and assistance from a vast number of people. You have made this dissertation far better than if I had worked alone.

Thank you for your effort and encouragement.

First of all, I would like to express my gratitude to the Geology Department, Faculty of Science, Aswan University, Egypt for nominated me and giving me the opportunity to pursue my science career to PhD level.

Secondly, I would like to thank Dr. Thierry Adatte, my thesis advisor, who constantly encouraged and supported me with his enthusiasm for science; his belief in my abilities gave me confidence to reach higher improved my scientific affinities and analytical abilities. The tremendous amount of time he devoted to sharpen my scientific and language skills, attending scientific meetings handed my presentation skills. Fieldwork with Thierry was always a great adventure. He also opened a door into my knowledge of the scientific innovative world.

I also cordially thank Prof. Gerta Keller for all her personal and scientific support and the fruitful discussions we had, along the long going to achieve this work. Her precious advise I will keep them as a treasure for the future. For Dr. Thierry ADATTE and Prof. Gerta KELLER, no words can express my feelings of appreciation and acknowledge working with you both have given me.

A special thank to Dr. Jorge. E. Spangenberg for his patient and constructive discussions while carrying out the analysis and spending hours explaining, discussing and improving my knowledge on different issues. I am very grateful to Prof. Karl Föllmi for his fruitful discussion and his kind advice during the coms of work. I appreciate and acknowledge Prof. Dr. Nicolas P. Tribovillard for his participation in the Jury committee for my PhD thesis.

I want to acknowledge numerous scientific collaborators, who took an integral part in various projects presented in this PhD thesis. I am grateful to Prof. Abdel Aziz Tantawy, at Aswan University, who was an effective and invaluable collaborator during fieldwork and in biostratigraphic studies. I thank Dr. Samanta Bandana from the Postgraduate Department of Geology, Nagpur University, India for providing the palynology for the studied Indian sections. I am grateful to Prof. Suresh Mathur, Jai Narain Vyas University, Jodhpur, Prof. Sunil Bajpai, and Dr. N. Saravanan Indian Institute of Technology Roorkee for their field assistance and discussion during the fieldwork in India.

I thank Tiffany Monnier, Jean Claude Lavanchy, Dr. Pierre Vonlanthen, and Dr. Alexey Ulianov for their kind help carrying out different types of analysis.

Among my fellow gratitude I would like to thank Chloé Morales, Lucie Bonvallet, Brahimsamba Bomou, Stephan Westermann, Melody Stein, Alex Godet, Brian Gertsch and many others that helped me adapt and encouraged in their own ways provided many good times during my stay at Lausanne University.

I warmly thank the administration staff particularly Anne-Marie, Nadia and Krystel

who with their smiles facilitated my graduate life inside Unil. The period I spent in Lausanne was really special. For that, I thank all people I met during that time and who made that period so pleasant.

Finally behind every success, there are some hidden persons encouraging, helping, and providing indispensably emotional support for a happy and confortable life during PhD study. In my life, they were my wife FATMA and my children MARIAM and YAHYA. They endured a lot during the last five years of my PhD studies and still extended patience, endless support, generous encouragements and there are no words that can express my gratitude to them.

ABSTRACT

A gradual increase in Earth`s surface temperatures marking the transition from the late Paleocene to early Eocene (55.8±0.2Ma), represents an extraordinary warming event known as Paleocene-Eocene Thermal Maximum (PETM). Both marine and continental sedimentary records during this period reveal evidences for the massive injection of isotopically light carbon. The carbon dioxide injection from multiple potential sources may have triggered the global warming. The importance of the PETM studies is due to the fact that the PETM bears some striking resemblances to the human-caused climate change unfolding today. Most notably, the culprit behind it was a massive injection of heat-trapping greenhouse gases into the atmosphere and oceans, comparable in volume to what our persistent burning of fossil fuels could deliver in coming centuries. The exact knowledge of what went on during the PETM could help us to foresee the future climate change.

The response of the oceanic and continental environments to the PETM is different. Many factors might control the response of the environments to the PETM such as paleogeography, paleotopography, paleoenvironment, and paleodepth.

To better understand the mechanisms triggering PETM events, two different environments were studied: 1) shallow marine to inner shelf environment (Wadi Nukhul, Sinai; and the Dababiya GSSP, Luxor, Egypt), and 2) terrestrial environments (northwestern India lignite mines) representing wetland, and fluvial environments (Esplugafreda, Spain) both highlighting the climatic changes observed in continental conditions.

In the marine realm, the PETM is characterized by negative $\boldsymbol{\delta}^{13}C_{car}$ and $\boldsymbol{\delta}^{13}C_{org}$ excursions and shifts in $\boldsymbol{\delta}^{15}N$ to ~0‰ values above the P/E boundary and persisting along the interval suggesting a bloom and high production of atmospheric N_2-fixers. Decrease in carbonate contents could be due to dissolution and/or dilution by increasing detrital input. High Ti, K and Zr and decreased Si contents at the P/E boundary indicate high weathering index (CIA), which coincides with significant kaolinite input and suggests intense chemical weathering under humid conditions at the beginning of the PETM. Two anoxic intervals are observed along the PETM. The lower one may be linked to methane released from the continental shelf with no change in the redox proxies, where the upper anoxic to euxinic conditions are revealed by increasing U, Mo, V, Fe and the presence of small size pyrite framboids (2-5**µ**m). Productivity sensitive elements (Cu, Ni, and Cd) show their maximum concentrated within the upper anoxic interval suggesting high productivity in surface water. The obtained data highlight that intense weathering and subsequent nutrient inputs are crucial parameters in the chain of the PETM events, triggering productivity during the recovery phase.

In the terrestrial environments, the establishment of wetland conditions and consequence continental climatic shift towards more humid conditions led to migration of modern mammals northward following the extension of the tropical belts. Relative ages of this mammal event based on bio-chemo- and paleomagnetic stratigraphy support a migration path originating from Asia into Europe and North America, followed by later

migration from Asia into India and suggests a barrier to migration that is likely linked to the timing of the India-Asia collision. In contrast, at Esplugafereda, northeastern Spain, the terrestrial environment reacted differently. Two significant $\delta^{13}C$ shifts with the lower one linked to the PETM and the upper corresponding to the Early Eocene Thermal Maximum (ETM2); $^{18}O/^{16}O$ paleothermometry performed on two different soil carbonate nodule reveal a temperature increase of around 8°C during the PETM. The prominent increase in kaolinite content within the PETM is linked to increased runoff and/or weathering of adjacent and coeval soils. These results demonstrate that the PETM coincides globally with extreme climatic fluctuations and that terrestrial environments are very likely to record such climatic changes.

RESUME

La transition Paléocène-Eocène (55,8±0,2 Ma) est marquée par un réchauffement extraordinaire communément appelé « Paleocene-Eocene Thermal Maximum » (PETM).

Les données géochimiques caractérisant les sédiments marins et continentaux de cette période indiquent que ce réchauffement a été déclenché par une augmentation massive de CO_2 lié à la déstabilisation des hydrates de méthane stockés le long des marges océaniques. L'étude des événements PETM constitue donc un bon analogue avec le réchauffement actuel. Le volume de CO_2 émis durant le PETM est comparable avec le CO_2 lié à l'activité actuelle humaine. La compréhension des causes du réchauffement du PETM peut être cruciale pour prévoir et évaluer les conséquences du réchauffement anthropogénique, en particulier les répercussions d'un tel réchauffement sur les domaines continentaux et océaniques. De nombreux facteurs entrent en ligne de compte dans le cas du PETM, tels que la paléogéographie, la paléotopographie et les paléoenvironnement. Pour mieux comprendre les réponses environnementales aux événements du PETM, 2 types d'environnements ont été choisis : (1) le domaine marin ouvert mais relativement peu profond (Wadi Nukhul. Sinai, Dababiya, Luxor, Egypte), (2) le milieu continental marécageux humide (mines de lignite, Inde) et fluviatile, semi-aride (Esplugafreda, Pyrénées espagnoles).

Dans le domaine marin, le PETM est caractérisé par des excursions négatives du $\delta^{13}C_{car}$ et $\delta^{13}C_{org}$ et un shift persistant des valeurs de $\delta^{15}N$ à ~ 0 ‰ indiquant une forte activité des organismes (bactéries) fixant l'azote. La diminution des carbonates observée durant le PETM peut-être due à des phénomènes de dissolution ou une augmentation des apports terrigènes. Des taux élevés en Ti, K et Zr et une diminution des montants de Si, reflétés par des valeurs des indices d'altération (CIA) qui coïncident avec une augmentation significative des apports de kaolinite impliquent une altération chimique accrue, du fait de conditions plus humides au début du PETM. Deux évènements anoxiques globaux ont été mis en évidence durant le PETM. Le premier, situé dans la partie inférieur du PETM, serait lié à la libération des hydrates de méthane stockés le long des talus continentaux et ne correspond pas à des variations significatives des éléments sensibles aux changements de conditions redox. Le second est caractérisé par une augmentation des éléments U, Mo, V et Fe et la présence de petit framboids de pyrite dont la taille varie entre 2 et 5µm. Le second épisode anoxique est caractérisé par une forte augmentation des éléments sensibles aux changements de la productivité (Cu, Ni et Co), indiquant une augmentation de la productivité dans les eaux de surface. Les données obtenues mettent en évidence le rôle crucial joué par l'altération et les apports en nutriments qui en découlent. Ces paramètres sont cruciaux pour la succession des évènements qui ont conduit au PETM, et plus particulièrement l'augmentation de la productivité dans la phase de récupération.

Durant le PETM, le milieu continental est caractérisé par l'établissement de conditions humides qui ont facilité voir provoqué la migration des mammifères modernes qui ont suivi le déplacement de ces ceintures climatiques. L'âge de cette migration est basé sur des arguments chimiostratigraphiques (isotopes stables), biostratigraphiques et

paléomagnétiques. Les données bibliographiques ainsi que celles que nous avons récoltées en Inde, montrent que les mammifères modernes ont d'abord migré depuis l'Asie vers l'Europe, puis dans le continent Nord américain. Ces derniers ne sont arrivés en Inde que plus tardivement, suggérant que le temps de leur migration est lié à la collision Inde-Asie. Dans le Nord-Est de l'Espagne (Esplugafreda), la réponse du milieu continental aux événements PETM est assez différente. Comme en Inde, deux excursions signicatives en $\delta^{13}C$ ont été observées. La première correspond au PETM et la seconde est corrélée avec l'optimum thermique de l'Eocène précoce (ETM2). Les isotopes stables de l'oxygène mesurés 2 différents types de nodules calcaires provenant de paléosols suggère une augmentation de 10°C pendant le PETM. Une augmentation simultanée des taux de kaolinite indique une intensification de l'altération chimique et/ou de l'érosion de sols adjacents. Ces résultats démontrent que le PETM coïncide globalement avec des variations climatiques extrêmes qui sont très aisément reconnaissables dans les dépôts continentaux.

Dedicated To My Wife
You Complete Me

TABLE OF CONTENTS

CHAPTER I

INTRODUCTION

INTRODUCTION

1. THE PALEOCENE-EOCENE EVENTS: GENERAL OVERVIEW

During the last 65 million years, the Earth has undergone many episodes of natural global warming and cooling due to various causes. The sedimentary rocks hold a good record of the environmental changes during this part of Earth`s history. Most of these environmental changes are linked to carbon cycle perturbations that resulted in the increase or decrease in Earth`s temperature linked to variations between extremes of expansive warmth with ice-free poles to extremes of cold with massive continental ice-sheets and polar ice caps. Such extreme climatic changes are controlled on a global scale by Earth's orbital geometry and/or plate tectonics (Zachos et al., 2001).

The Eocene (55.8±0.2 to 33.9±0.1Ma. Gradstein at al., 2012), is a period in Earth history characterized by climatic extremes varying from greenhouse to icehouse conditions. The warmest period of the Cenozoic era coincides with an extreme warming event at the Paleocene-Eocene transition known as Paleocene-Eocene Thermal Maximum (ETM1 or PETM) (Katz et al., 1999). Climate warmed steadily until the Early Eocene Climatic Optimum (EECO) ~53.5 Ma when temperatures and greenhouse gas concentrations peaked at their maxima for ~1.5 myr (Zachos et al. 2008). These two major events are followed by several abrupt and short hyperthermal events including H2 (53.6 Ma), I1 (53.3 Ma), I2 (53.2 Ma) and ETM-3 (52.8 Ma) (Zachos et al., 2008, Cramer et al. 2009). A major negative $\delta^{13}C_{org}$ excursion marks each of these hyperthermal events (Fig. 1)

The most recognizable amongst these warming events is the Paleocene-Eocene Thermal Maximum (PETM), which was first recognized by Kennet and Stott (1991) in the Ocean Drilling Program (ODP) site 690B cores, and associated with a temperature rise of 5–9°C over about 10,000 years (Fig.1). Subsequently, this thermal maximum was shown to gradually decrease to pre-excursion $\delta^{13}C_{org}$ values over about 150,000 to 220,000 years (Westerhold et al., 2009; McInerney at al., 2011). The PETM is characterized by a decline in oxygen isotope ratios indicating a warming of 3-4C^{o} of surface water and 6C^{o} in deep water. This increase in temperature is associated by a negative shift in carbon isotope of nearly -2 ‰ for the benthic foraminifera and -4‰ for planktic foraminifera. The PETM events, led to major species extinctions in deep marine benthic foraminifera (Thomas 1989; Speijer et al., 2002; Alegret et al., 2009) but diversification in planktic foraminifera with subtropical affinities (Kelly et al., 1996; Lu et al., 1998; Luciani et al., 2007). Mineralogically, the PETM is marked by increased detrital input and kaolinite contents due to intense on-land weathering during the hot humid climate (Bolle et al., 2000; 2001). In the terrestrial realm, it led to the diversification of modern mammal species and their migration across the northern continents (Bowen et al., 2004; 2002; Wing et al., 2005, Krause and Maas 1990, Rodríguez, 1999; Rana et al., 2008; Bajpai et al., 2008), many of which immigrated to the North American continent during the greenhouse warming (Wing et al. 1995). Moreover, Smith et al. (2007) hypothesized that the temperature and precipitation changes associated with the PETM stimulated rapid shifts in plant community composition.

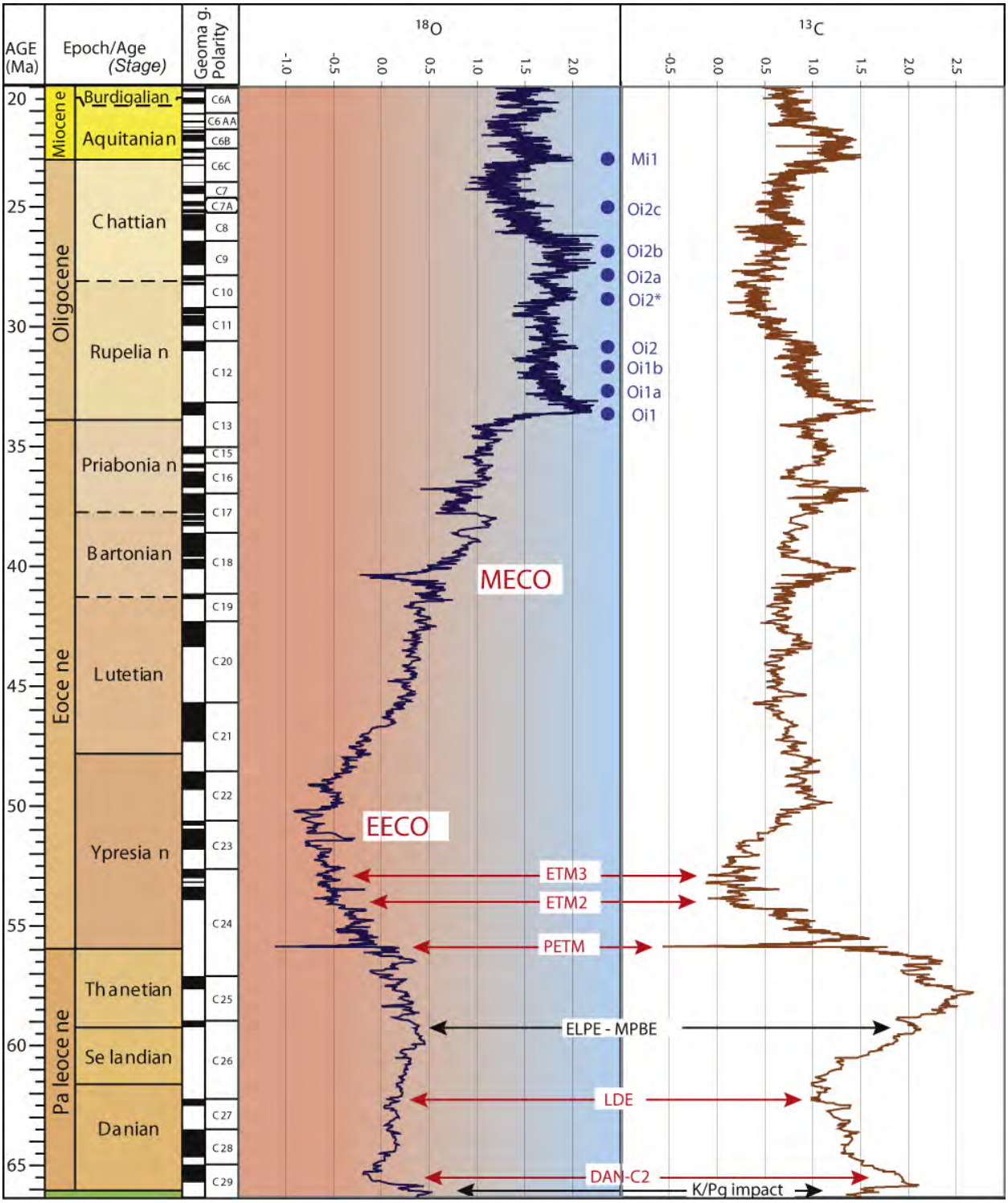

***Figure 1**. Position of main Paleogene climatic events against the generalized oxygen and carbon isotope curves for the Paleogene (Cramer et al. 2009).*

2- PROPOSED SCENARIO TO EXPLAIN THE PETM EVENTS

The PETM is marked by a large negative carbon isotope excursion (CIE) in terrestrial and marine carbonates and organic matter (Kennett and Stott, 1991; Koch et al., 1992, 1995; Magioncalda et al., 2004; Wing et al., 2005), reflecting a rapid release of ^{13}C-depleted carbon into the ocean–atmosphere system due to injection of huge amount of CO_2 into the atmosphere

estimated to reach about 2000 to 2600Gt over 10 ka (Zachos et al. 2001; 2005). There are many potential sources of CO_2 during the PETM and many scenarios have been proposed to explain the injection of high amounts of CO_2 (about 2000Gt, Zachos et al., 2001) in both marine and atmospheric ecosystems leading subsequently to the perturbation of the carbon cycle from the latest of Paleocene into the earliest Eocene. More than twenty-five years and hundreds of studies of both surface and subsurface sections covering the PETM interval yielded five main hypotheses summarized by McInerney and Wing (2011).

1- Wildfires: Burning of the extensive peat and coal deposited during the Paleocene ($\delta^{13}C$ of ~−22‰) could have resulted from increasing atmospheric O_2, dryer climate, and/or uplift of coal basins (Kurtz et al. 2003). However, no increase in combustion byproducts was observed in cores from neither the Atlantic nor Pacific (Moore and Kurtz 2008).

2- Thermogenic methane: Injection of magma into organic-rich sediments could have caused the explosive release of thermogenic methane ($\delta^{13}C$ of~−30‰) from Cretaceous-Paleocene mudstones in the North Atlantic (Fig. 2) (Svensen et al. 2004, 2010; Westerhold et al. 2009).

3- Drying epicontinental seas: Tectonically driven isolation of an epicontinental seaway could have led to rapid (<20 ka) desiccation and oxidation of organic matter ($\delta^{13}C$ of ~−22‰) (Higgins and Schrag 2006). However, shallow seaways of the Paleocene-Eocene covered vast areas of central Asia and none are known to have dried up coincident with the PETM (Gavrilov et al., 2003).

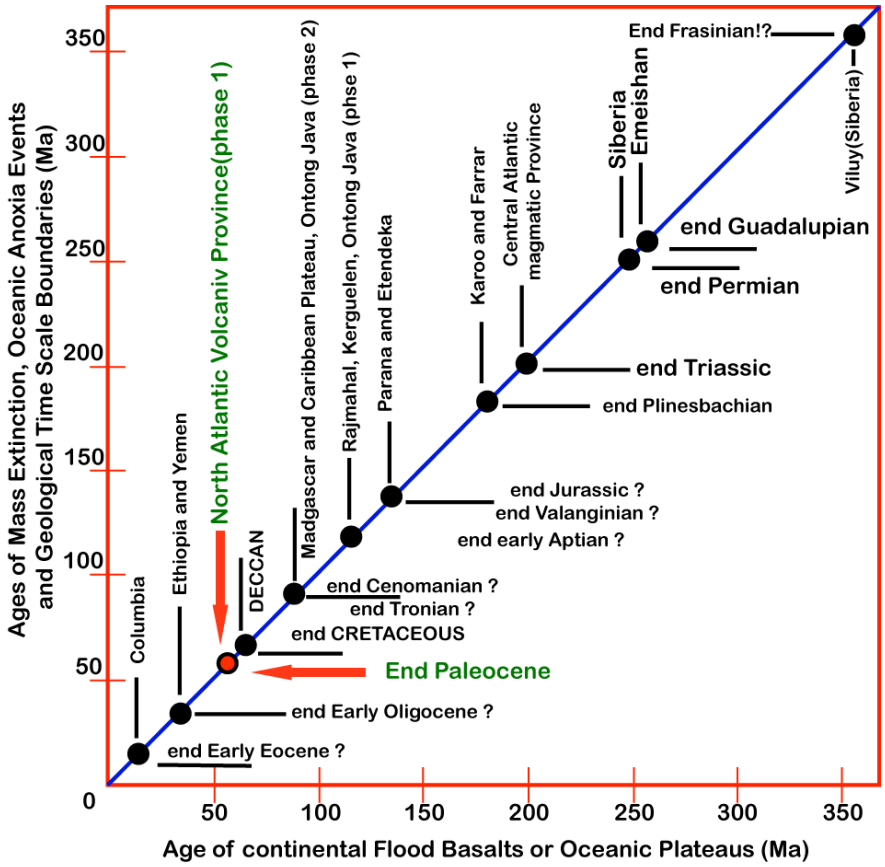

***Figure. 2**. Major volcanic events in the Phanerozoic compared to mass extinction, bio-events, and geological time, modified after (Courtillot and Renne, 2003).*

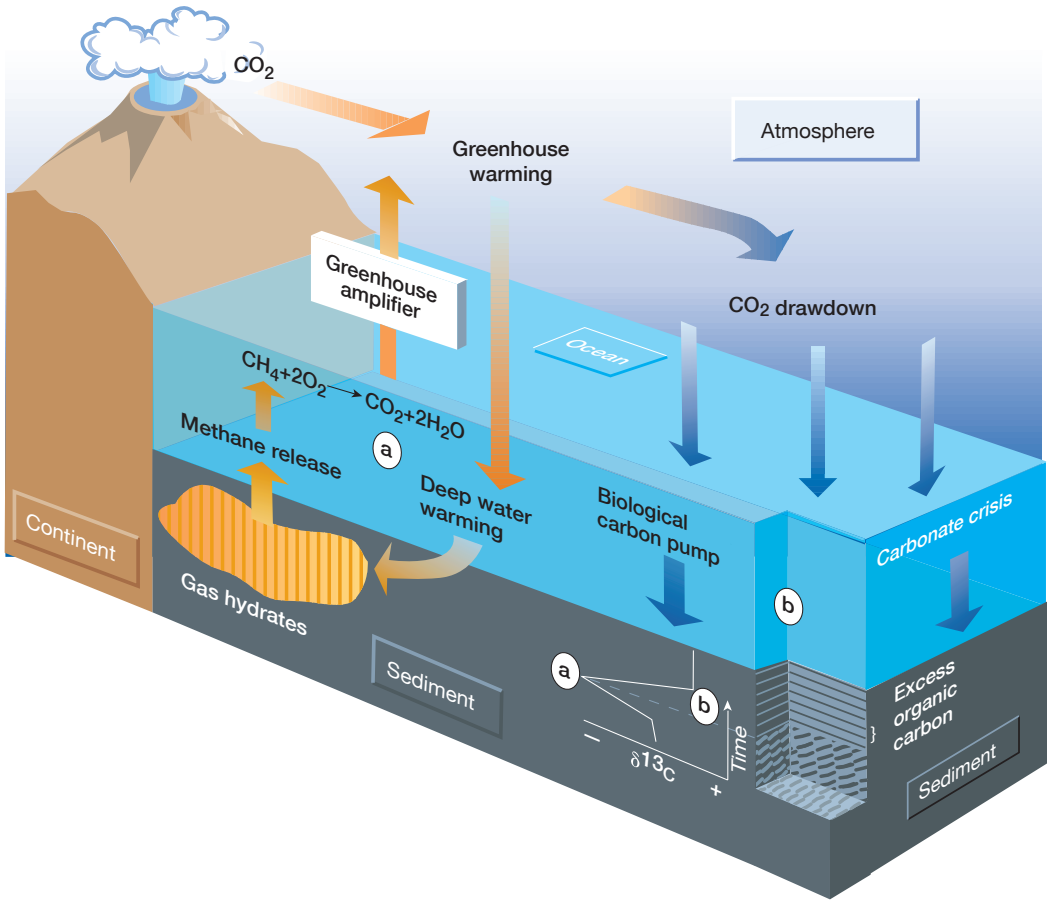

***Figure 3**. Mechanism of positive and negative feedbacks during extreme warming events (Weissert 2000). In the past, episodes of greenhouse warming may have caused the sudden release of methane from gas hydrates in ocean sediments, as recorded in a negative carbon isotope anomaly. Methane-derived CO_2 led to the amplification of the greenhouse climate. The biosphere responded to the higher CO_2 levels with accelerated burial of organic carbon on the ocean floor, and with crises in carbonate production, as recorded in positive carbon-isotope anomalies. Both processes contributed to a lowering of atmospheric CO_2 levels. However, the most likely mechanism for atmospheric CO_2 removal appears to be increased silicate weathering.*

4- Permafrost: During the Paleogene, Antarctica did not support a large ice cap and may have stored huge quantities of carbon as permafrost and peat that could have been rapidly defrosted and oxidized, releasing carbon ($\boldsymbol{\delta}^{13}C$ of ~−30‰) (DeConto et al. 2010).

5- Catastrophic methane release: the most recognized scenario explaining the PETM event is the catastrophic methane release from hydrates (clathrates) (Dickens et al., 1995; Kennett et al., 2002).

This scenario invokes methane released from the continental margin that could have led to carbon dioxide input estimated at $2000x10^9$ metric tons over 10,000 years (Zachos et al., 2005), which was suggested as potentially the main cause for the PETM (Katz et al 2001; Dickens, 2011). Clathrates are stable in deep-sea sediments, but can be destabilized by increasing temperature caused by changes in ocean circulation (Dickens et al. 1995, 1997), by decreasing pressure resulting from slope failure (Katz et al. 1999) or sea level changes. Clathrate release could also result from late Paleocene volcanic activities linked to the opening of the North

Atlantic Ocean. (Bowen and Zachos 2010; Courtillot and Renne 2003, Fig. 2). Whatever the source of CO_2 released during the PETM, global temperature increased about 5–9◦C during a period of about 200 ka (Sluijs et al., 2006; Zachos et al., 2006; Weijers et al., 2007; Handley et al., 2008).

The termination of the PETM was a response to an increase in the intensity of the marine biological pump (productivity feedback) resulting in the drawdown of atmospheric CO_2 and subsequent carbon sequestration in the ocean (Torfstein et al., 2010; Bains et al., 2000; Weissert 2000, Fig.3). The export production did not facilitate rapid removal of excess carbon from the atmosphere (Torfstein et al., 2010). Thus, the most likely mechanism for atmospheric CO_2 removal appears to be increased silicate weathering, which occurred at much faster rates than previously assumed (Kelly et al., 2005, 2010).

3- CHARACTERISTICS AND TIMING

In 2003 the International Commission for Stratigraphy (ICS) designated the Dababiya Quarry in southern Egypt (Dababiya village, Luxor) as the Global Stratigraphic Section and Point (GSSP) for the Paleocene-Eocene (PE) boundary as marked by the PETM event. The PE boundary is placed in the basal part of the Esna Formation (Dupuis et al., 2003; Aubry et al., 2007) based on the following criteria: (1) the negative organic carbon isotope excursion (CIE), (2) the extinction of deep water benthic foraminifera (*Stensioina beccariiformis*), (3) the transient occurrence of planktonic foraminifera (*Acarinina africana, A.sibaiyaensis, Morozovella allisonensis*) during the $\delta^{13}C$ excursion, (4) the transient occurrence of the *Rhomboaster* spp. – *Discoaster araneus* (RD) nannofossils assemblage, and (5) an acme of the dinoflagellate *Apectodiniu.* Based on these criteria the Dababiya section was considered as one of the most complete and expanded Upper Paleocene to Lower Eocene sequences and representative of this boundary event globally (Dupuis et al., 2003; Aubry et al., 2007). The age estimate of the CIE onset has been recently determined to be 56.011 Ma using radiometric data obtained from a marine ash layer (Westerhold et al. 2009), whereas dating based on the zircon crystals collected in a bentonite located in the upper part of the CIE gave age of 56.09 ± 0.03 Ma (Jaramillo et al. 2010). Astronomically calibrated cyclostratigraphy timescale indicates a duration of 150 – 220 ka for the CIE (Aziz et al. 2008; Röhl et al. 2007), whereas calculations based on the extra-terrestrial ^{3}He fluxes suggest a duration between 120 -220 ka (Murphy et al. 2010). The time interval between the pre-CIE $\delta^{13}C$ value and the CIE-minimum has been estimated to be 10 to 25 ka (Zachos et al. 2005; Khozyem et al., 2013) the accuracy of this determination depends on the presence of the uppermost Paleocene dissolution levels.

4- WHY TO STUDY THE PETM?

The importance of the PETM studies is due to the fact that this event bears some striking resemblances to the human-caused climate change unfolding today. Most notably, the culprit behind the PETM was a massive injection of heat-trapping greenhouse gases into the atmosphere and oceans, comparable in volume to today's persistent burning of fossil fuels. Knowledge causes and mechanisms of the PETM could help us foresee the climate warming in our near future and design possible ways to mitigate its potentially adverse impact. The PETM is believed to have been caused by greenhouse gas emissions, similarly to today's anthropogenic warming and therefore can serve as analogue to the actual warming. However, the current warming is estimated to be 10 times faster than the PETM (Fig. 4).

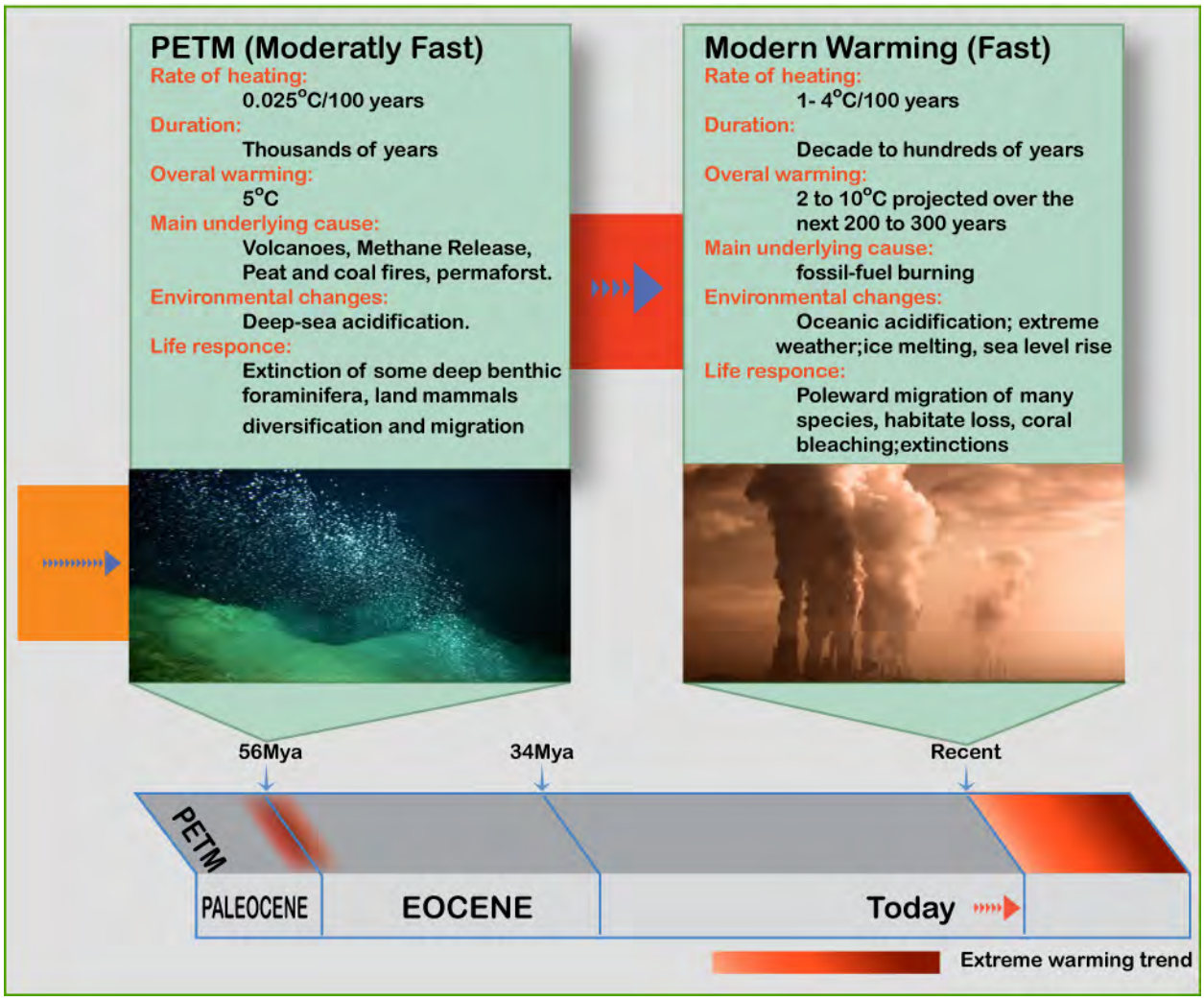

Figure 4. *Comparison between the PETM and the current warming, that reflect the importance of the PETM study, and how it can help to understand the future climatic changes and the effect of the temperature increase on various environments.*

5- AIMS OF THE PRESENT STUDY

The present work is delineating the climatic and environmental changes that prevailed before, during and after the early Eocene hyperthermal events with a special focus on the Paleocene Eocene Thermal Maximum (PETM) and Early Eocene climatic optimum (ETM2), and the environmental response to these hyperthermal events.

To achieve the objectives of this study three main areas representing two different environments were chosen: (1) marine environments including inner shelf and shallow marine conditions in two different localities in Egypt (Wadi Nukhul, Sinai, and Dababiya GSSP, Louxor), and India (Kutch section, Gujarat); (2) Wetland environments (Swamps) represented by the northeastern Indian lignite mines (Giral mine, Rajasthan; Vastan mine, Tadkeshwar mine, Panandhor mine, and Bhavnagar mine, Gujarat, India); and (3) fluvial plain environments of Spain (Esplugafreda area); (Fig.5).

6- MATERIALS AND METHODS

To achieve the stated objectives we use a multidisciplinary approach including carbon and oxygen isotopes, organic carbon and nitrogen isotopes, total organic carbon contents, bulk and

clay mineralogy, major, trace, rare earth elements, total phosphorus analysis, biostratigraphy (benthic, planktonic foraminifera and nannofosils, palynology) and scanning electron microscope analysis.

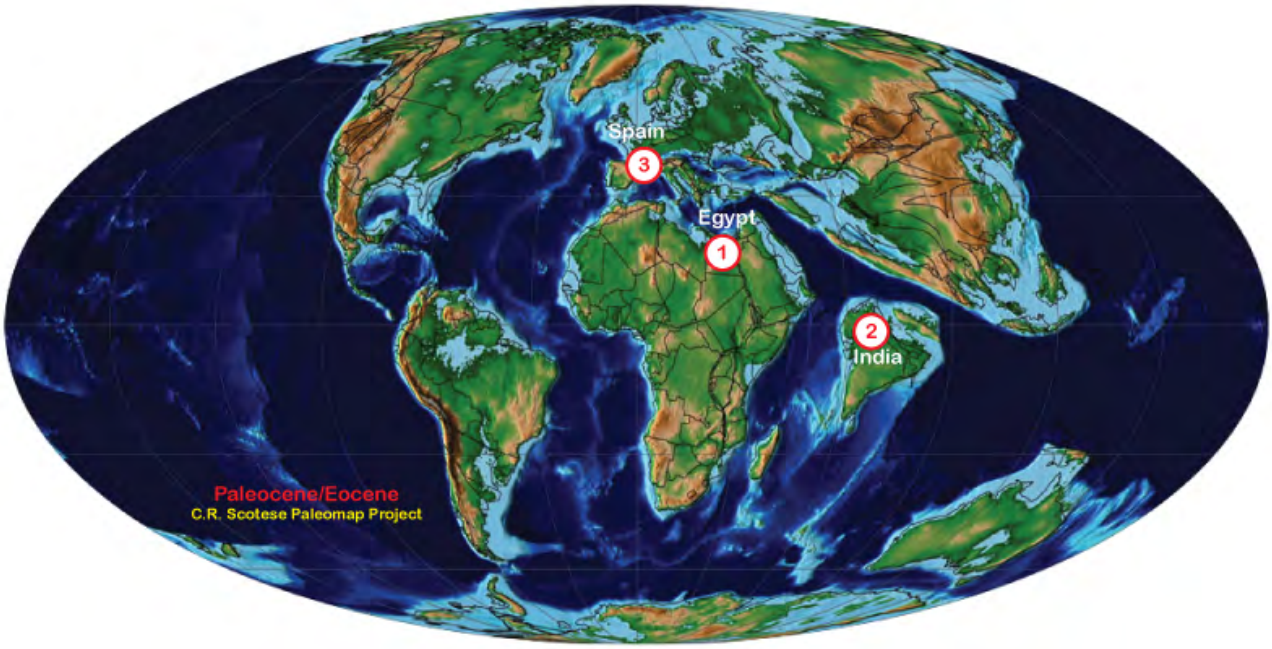

Figure 5. *Paleogeographic reconstruction of the Paleocene Eocene Thermal Maximum (56Ma, C.R. Scotese paleomap project). Paleoposition of the studied section: 1- Egypt, 2- India, and 3- Spain*

6.1- Samples preparation

25gm of each sample was powdered using a mechanical agate mortar, avoiding gypsum veinlets, altered zones and calcite recrystallizations features. The length of time to powder samples depends on the rock type and ranges between 60 seconds to 2 minutes. The obtained powder is subjected to different analytical procedures.

6.2- Organic-matter contents

The content and type of the organic matter were determined using Rock Eval pyrolysis (Rock-EvalTM6, Behar et al., 2001). Total organic carbon contents (TOC, in weight %) were obtained using the standard temperature cycle. Samples were calibrated with both IFP160000 and an internal standard with an instrumental precision of <0.2% (Espitalié et al., 1985).

6.3- Bulk-rock analyses

Bulk-rock analyses were performed at the Lausanne University Institute of Earth Science and Environments (ISTE) using a X-TRA Thermo-ARL Diffractometer, following the procedure described in Klug and Alexander (1974), Kübler (1983) and Adatte et al. (1996). This method for semi-quantitative analysis of the bulk rock mineralogy (obtained by XRD patterns of random powder samples) uses external standards with error margins varying between 5 and 10% for the phyllosilicate and 5% for grain minerals.

6.4- Clay mineral analyses

Clay mineral analyses were performed at the University of Lausanne using a X-TRA Thermo-ARL Diffractometer, following the procedure described in Kübler (1987) and Adatte et al. (1996). Samples are introduced into glass containers with deionized water. They are then decarbonized by HCl 10% (1.25 N) during 20 minutes and regularly agitated. Dissolution is helped by 3 minutes of ultrasonic disaggregation for each sample. The insoluble residues are washed by centrifugation and repeated until a neutral solution (pH 7) is obtained. Following the Stockes law, two granulometric fractions (<2µm and 2-16µm) are pipetted and deposited on a glass plate. After air-drying, samples are analyzed by XRD. Subsequently, the <2µm fraction samples are saturated with ethylen-glycol and re-measured in order to check for swelling minerals. This method allows the semi-quantification of the proportion of clay minerals with a precision better than 5%.

6.5- Stable Isotopes

Carbon and oxygen isotopes were performed using procedures described by (Revesz et al., 2001). Analyses of aliquots of all samples were performed using a Thermo Fisher Scientific (formerly ThermoQuest/ Finnigan, Bremen, Germany) GasBench II preparation device interfaced to a Thermo Fisher Scientific Delta Plus XL continuous flow isotope ratio mass spectrometer (IRMS) (Revesz et al., 2001). The CO_2 extraction was done at 90°C. The stable carbon and oxygen isotope ratios are reported in the delta (δ) notation as the per mil (‰) deviation relative to the Vienna–Pee Dee belemnite standard (VPDB). Analytical uncertainty (2σ), monitored by replicate analyses of the international calcite standard NBS-19 and the laboratory standards Carrara Marble and Binn Dolomite are not greater than ±0.05‰ for $\delta^{13}C$ and ±0.1‰ for $\delta^{18}O$.

The kerogen was isolated from powdered samples by HCl treatment. The carbon and nitrogen isotope composition of the kerogens were determined by flash combustion on a Carlo Erba 1108 elemental analyzer (EA) connected to a Thermo Fisher Scientific Delta S isotope ratio mass spectrometer (IRMS) that was operated in the continuous helium flow mode via a Conflo III split interface (EA– IRMS). An aliquot of the sample was wrapped in a tin capsule and combustion was done in an O_2 atmosphere in a quartz reactor at 1020 °C packed with Cr_2O_3 and (Co_3O_4) Ag to form CO_2, N_2, NOx and H_2O. The gases were then passed through a reduction reactor containing elemental copper and copper oxide at 640 °C to remove excess of oxygen and to reduce the non-stoichiometric nitrous products (NOx) to N_2. Water was subsequently removed by anhydrous Mg $(ClO_4)_2$. N_2 and CO_2 were then separated in a gas chromatograph fitted with a packed column (Pora-PLOT Q, 5 m length, 1/4 in. i.d.) at 70 °C, and analyzed for their isotopic composition on the IRMS. Pure N_2 and CO_2 gases were inserted in the He carrier flow as pulses of standard gases. The $\delta^{13}C$ and $\delta^{15}N$ values are reported relative to VPDB and air–N_2, respectively. The calibration and assessment of the reproducibility and accuracy of the isotopic analysis were based on replicate analyses of laboratory standard materials and international reference materials. The reproducibility was better than 0.1‰ (1σ) for both carbon and nitrogen.

6.6- Major (MEs), trace (TEs), and Rare Earth Elements (REEs)

Elemental analysis was carried out at the Institute of Mineralogy and Geochemistry of the Lausanne University, Switzerland, with a FRX Philips PW2400 X-ray fluorescence spectrometer using lithium tetraborate fused pellets for major elements (ME). For the (TEs), the XRF analyses

were conducted on powder tablets obtained by pressing 10 g of the sample on a support of polyvinyl alcohol (2%) at over 5000 kg/cm2 (Mori et al., 1999). The detection limits are 0.01% for MEs and 1 to 4 ppm for TEs. The accuracies of the analyses were assessed by analyses of standard reference materials. The accuracies of the analyses were assessed by analyses of standard reference materials (NIM-G; SDC; BHVO; QLO).

The REEs were measured by inductively coupled plasma–mass spectrometry (ICP-MS) (ELAN 6100 DRC ICP–MS), calibrated using standard SRM 612. The detection limit for major elements is better than 0.01 wt.%, for trace elements is generally 1 to 4 ppm, and 0.02 to 0.15 ppm for the REE. Total phosphorus (P_{tot}) analyses were performed for all samples using the ascorbic acid method (Mort et al., 2007b). Replicate analyses of indicated a precision better than 5%.

6.7- Biostratigraphy

For foraminiferal analysis, about 100gr. sediment was processed per sample by standard methods and washed through 63 mm and 38 mm screens to preserve small species (Keller et al., 1995). In carbonate-rich intervals preservation is excellent and shells are not recrystallized. However, in Dababiya GSSP the PETM excursion interval the basal part of the $\delta^{13}C_{Carb}$ excursion is barren and the upper part preceding $\delta^{13}C_{Carb}$ recovery contains intermittent poorly preserved specimens of the transient PETM fauna. Biostratigraphic analysis was performed on >63 mm and 38-63 mm size fractions. Quantitative counts of ~300 specimens were picked from the >63 mm size fraction, mounted on cardboard slides for a permanent record and identified to obtain relative species abundance data. The remaining sample residue for each sample was searched for rare and zone-defining index species (analytical work done by G. Keller at the Department of Geosciences, Princeton University, USA).

For calcareous nannofossil, samples were processed in Aswan Faculty of Science, Aswan, Egypt, and analyzed by A.A. Tantawy by smear slide preparation from raw sediment samples as described by Perch-Nielsen (1985). The calcareous nannofossils were observed in the light microscope at a magnification of 1000×. The taxonomy used is described in Aubry (1984, 1988, 1989, 1990, 1999) and Perch-Nielsen (1985).

For palynomorph extraction, samples were treated with HCl, HF and HNO_3 followed by 5% solution of KOH. The sample residue was washed with water through a 15µm screen. The slides were prepared in polyvinyl alcohol and mounted in Canada balsam. A Leitz Laborlux-S and Olympus BX51 microscope were used for their study and photomicrography (RTM Nagpur University, Nagpur, India, (analytical work done by Bandana Sament).

Scanning electron microscopy (SEM; Tescan Mira/LMU) of gold and carbon coated samples was used to assess different features (e.g., foraminifera and structures of extracellular polymeric substances framboidal pyrite etc.).

REFERENCES

Adatte, T., Stinnesback, W., and Keller, G., 1996, Lithostratigraphic and mineralogic correlations near K/T boundary clastc sediments in northern Mexico: Implication for origin and nature of deposition. Geological Society of America, special paper, v.307, pp.211-226.

Alegret, L., Ortiz, S., and Molina, E., 2009, Extinction and recovery of benthic foraminifera across the Paleocene–Eocene Thermal Maximum at the Alamedilla section (Southern Spain). Palaeogeography, Palaeoclimatology, Palaeoecology, v.279, pp.186–200.

Aubry, M.-P., 1984, Handbook of Cenozoic calcareous nannoplankton, book 1, Ortholithae (Discoaster). Micropaleontology Press, American Museum of Natural History. New York. 263 pp.

Aubry, M.-P., 1988, Handbook of Cenozoic calcareous nannoplankton, book 2, Ortholithae (Holococcoliths, Ceratoliths, Ortholiths and other). Micropaleontology Press, American Museum of Natural History. New York. 279 pp.

Aubry, M.-P., 1989, Handbook of Cenozoic calcareous nannoplankton, book 3, Ortholithae (Pentaliths and other), Heliolithae (Fasciculiths, Sphenoliths and others). Micropaleontology Press, American Museum of Natural History, New York, 279 pp.

Aubry, M.-P., 1990, Handbook of Cenozoic calcareous nannoplankton, book 4, Heliolithae (Helicoliths, Cribriliths, Lopadoliths and other). Micropaleontology Press, American Museum of Natural History, New York 381 pp.

Aubry, M.-P., Berggren, W. A., Cramer, B., Dupuis, C., Kent, D. V., Ouda, K., Schmitz, B., and Steurbaut, E., 1999, Paleocene/Eocene Boundary Sections in Egypt. In Ouda, K., Ed., Late Paleocene-Early Eocene Events from North Africa to the Middle East, Symposium. First International Conference on the Geology of North Africa, pp. 1-11.

Aubry, M.-P., Ouda, K., Dupuis, C., Berggren, W.A., Van Couvering, J.A., Members of the Working Group on the Paleocene/Eocene Boundary, 2007, The Global Standard Stratotype-section and Point (GSSP) for the base of the Eocene Series in the Dababiya section (Egypt). Episodes, v.30 no.4, pp. 271–286.

Aziz, H.A., Hilgen, F.J., Luijk, G.M., Sluijs, A., and Kraus, M.J., 2008, Astronomical climate control on paleosol stacking patterns in the upper Paleocene-lower EoceneWillwood Formation, Bighorn Basin, Wyoming. Geology, v. 36, pp. 531–534.

Bains, S., Norris, R.D., Corfield, R.M., Faul, K.L., 2000, Termination of global warmth at the Palaeocene/Eocene boundary through productivity feedback. Nature, v.407, pp.171–174.

Bajpai, S., Kay, R.F., Williams, B.A., Das, D.P., Kapur, V.V., and Tiwari, B.N., 2008, The oldest Asian record of Anthropoidea: National Academy of Sciences Proceedings, v.105, no.11, pp. 093–098.

Behar, F., Beaumont, V., Penteado, H.L.D., 2001. Rock-Eval 6 technology: performances and developments. Oil and Gas Science and Technology, v. 56, pp. 111–134.

Bolle, M.P., and Adatte, T., 2001, Paleocene–Early Eocene climatic evolution in the Tethyan realm: clay mineral evidence. Clay Mineralogy, v. 36, pp. 249–261.

Bolle, M.-P., Tantawy, A.A., Pardo, A., Adatte, T., Burns, S.J., and Kassab, A., 2000, Climatic and environmental changes documented in the upper Paleocene to lower Eocene of Egypt. Eclogae Geologicae Helvetiae, v. 93, pp. 33–51.

Bowen, G.J., and Zachos, J.C., 2010, Rapid carbon sequestration at the termination of the Palaeocene-Eocene Thermal Maximum. Nature Geosciences, v. 3, pp. 866–869

Bowen, G. J., Beerling, D. J., Koch, P. L., Zachos, J. C., and Quattlebaum, T., 2004, A humid climate state during the Paleocene–Eocene Thermal Maximum. Nature, v. 432, pp. 495–499.

Bowen, G.J., Clyde, W.C., Koch, P.L., Ting, S., Alroy, J., Tsubamoto, T., Wang, Y., and Wang, Y., 2002, Mammalian dispersal at the Paleocene/Eocene boundary, Science, v. 295, pp. 2062–2065.

Courtillot, V., and Renne, P., 2003, On the ages of flood basalt events. Comp. Rendus Geosciences, v.335, pp.113–140.

DeConto, R., Galeotti. S., Pagani, M., Tracy, D.M., Pollard, D., Beerling, D.J., 2010, Hyperthermals and orbitally paced permafrost soil organic carbon dynamics. Presented at AGU Fall Meet. Dec. 13–17, San Francisco (Abstr. PP21E-08).

Dickens, G.R., Castillo, M.M., Walker, J.C.G., 1997, A blast of gas in the latest Paleocene: simulating first-order effects of massive dissociation of oceanic methane hydrate. Geology, v. 25, pp. 259–262.

Dickens, G. R., O'Neil, J. R., Rea, D. K., and Owen, R. M., 1995, Dissociation of oceanic methane hydrate as a cause of the carbon isotope excursion at the end of the Paleocene, Paleoceanography, v. 10, pp. 965-971.

Dickens, G., 2011, Down the Rabbit Hole: toward appropriate discussion of methane release from gas hydrate systems during the Paleocene-Eocene thermal maximum and other past hyperthermal events. Climate of the Past, v.7, pp.831–846.

Dupuis, C., Aubry, M.-P., Steurbaut, E., Berggren, W.A., Ouda, K., Magioncalda, R., Cramer, B.S., Kent, D.V., Speijer, R.P., and Heilmann-Clausen, C., 2003, The Dababiya Quarry section: lithostratigraphy, clay mineralogy, geochemistry and paleontology. In: Ouda, K., Aubry, M.-P. (Eds.), The Upper Paleocene–Lower Eocene of the Upper Nile Valley: Part 1.Stratigraphy: Micropaleontology, v. 49, pp. 41–59.

Espitalié, J., Deroo, G., and Marquis, F., 1985, La pyrolyse Rock-Eval et ses applications.Revue de l`Institute francais de Pérole, v. 40, pp. 563-579.

Gavrilov, Y.O., Shcherbinina, E.A., and Oberhänsli, H., 2003, Paleocene-Eocene boundary events in the northeastern Peri-Tethys. Geological Society of America, Special Paper, v. 369, pp.147–168.

Gradstein, M.F., Ogg, J.G., Schmitz M.D., and Ogg., G.M., 2012, The Geologic Time Scale 2012. Elsevier, v.1, 1144 pp.

Hansen, J., Mki. Sato, P. Kharecha, D. Beerling, R. Berner, V. Masson-Delmotte, M. Pagani, M. Raymo, D.L. Royer, and J.C. Zachos., 2008, Target atmospheric CO2: Where should humanity aim? Open Atmospheric Science Journal, v. 2, pp. 217-231.

Higgins, J.A., and Schrag, D.P., 2006, Beyond methane: towards a theory for the Paleocene-Eocene Thermal Maximum. Earth Planetary Science Letter, v. 245, pp. 523–537

Jaramillo, C.A., Ochoa, D., Contreras, L., Pagani, M., Carvajal-Ortiz, H., et al., 2010, Effects of rapid global warming at the Paleocene-Eocene boundary on Neotropical vegetation. Science, v. 330, pp.957–961

Katz, M., Cramer, B., Mountain, G., Katz S., and Miller, K., 2001, Uncorking The Bottle: What Triggered The Paleocene/Eocene Thermal Maximum Methane Release? Paleoceanography, v.16, no. 6, pp. 549–562

Katz, M.E., Pak, D.K., Dickens, G.R., and Miller, K.G., 1999, The source and fate of massive carbon input during the Latest Paleocene Thermal Maximum. Science, v. 286, pp. 1531–1533.

Keller, G., Li, L., and Macleod, N., l995, The Cretaceous/Tertiary boundary stratotype section at El Kef, Tunisia: How catastrophic was the mass extinction? Palaeogeography, Palaeoclimatology, Palaeoecology, v. 119, pp. 221-254.

Kelly, D.C., Bralower, T.J., Zachos, J.C., Premoli-Silva, I., and Thomas, E., 1996, Rapid diversification of planktonic foraminifera in the tropical Pacific (ODP Site 865) during the late Paleocene Thermal Maximum. Geology, v. 24, p. 423–426.

Kelly, D.C., Nielsen, T., McCarren, H., Zachos, J.C., and Rohl, U., 2010, Spatiotemporal patterns of carbonate sedimentation in the South Atlantic: implications for carbon cycling during the Paleocene-Eocene Thermal Maximum. Palaeogeography, Palaeoclimatology, Palaeoecology, v. 293, pp.30–40

Kelly, D.C., Zachos, J.C., Bralower, T.J., and Schellenberg, S.A., 2005, Enhanced terrestrial weathering/runoff and surface ocean carbonate production during the recovery stages of the Paleocene Eocene Thermal Maximum. Paleoceanography, v. 20, pp. 4023

Kennett, J.P., and Stott, L.D., 1991, Abrupt deep-sea warming, palaeoceanographic changes and

benthic extinctions at the end of the Palaeocene. Nature, v. 353, pp. 225–229.

Kennett, J. P., Cannariato, K. G., Hendy, I. L., and Behl R. J., 2002, Methane Hydrates in Quaternary Climate Change: The Clathrate Gun Hypothesis, Special Publication, v. 54, 224 pp., AGU, Washington, D. C.

Khozyem, H., Adatte, T., Spangenberg, E.J., Tantawy, A, and Gerta Keller, K., 2013, Paleoenvironmental and climatic changes during the Paleocene-Eocene Thermal Maximum (PETM) at the Wadi Nukhul Section, Sinai, Egypt. Journal of the Geological Society, London, v.170, pp. 341–352.

Klug, H.P., and Alexander, L.E., 1974, X-ray Difiaction Procedures for Polycrystalline and Amorphous Materials. 2nd Edition, Wiley-VCH, pp. 992

Koch, P. L., Zachos, J. C., and Dettman, D. L., 1995, Stable isotope stratigraphy and paleoclimatology of the Paleogene Bighom Basin (Wyoming, USA). Palaeogeography. Palaeoclimatology. Palaeoecology, v.115, pp.61-89.

Koch, P. L., Zachos, J. C., and Gingerich, P., D., 1992, Correlation between isotope records in marine and continental carbon reservoirs near the Paleocene- Eocene boundary. Nature v.358, p.319-322.

Kübler, B., 1983, Dosage quantitatif des minéraux majeurs des roches sédimentaires par diffraction X. Cahier de l'Institut de Géologie de Neuchâtel,Série AX N°1.1 &1.2

Kübler, B., 1987, Cristallinité de l'illite: méthode normalisées de préparation de mesure, méthode automatique normalisées de mesure. Cahiers de l'Institut de Géologie, Series AX n°3.1 and 3.2.

Kurtz, A.C., Kump, L.R., Arthur, M.A., Zachos, J.C., Paytan, A., 2003, Early Cenozoic decoupling of the global carbon and sulfur cycles. Paleoceanography, v.18, 1090 pp.

Lu, G., Adatte, T., Keller, G., and Ortiz, N., 1998, Abrupt climatic, oceanographic and ecologic changes near the Paleocene-Eocene transition in the deep Tethys basin: The Alamedilla section, southern Spain. Ecologica Geologica Helvatica, v. 91, pp. 293-306.

Luciani, V., Giusberti, L., Agnini, C., Backman, J., Fornaciari, E., and Rio, D., 2007, Paleocene–Eocene Thermal Maximum as recorded by Tethyan planktonic foraminifera in the Forada section (northern Italy). Marine Micropaleontology, v.64, pp.189-214.

Magioncalda, R., Dupuis, C., Smith, T., Steurbaut, E., Gingerich, P.D., 2004, Paleocene-Eocene carbon isotope excursion in organic carbon and pedogenic carbonate: direct comparison in a continental stratigraphic section. Geology, v. 32 pp.553–556.

McInerney, F. A., and Wing, S. L., 2011, The Paleocene–Eocene Thermal Maximum: A perturbation of carbon cycle, climate, and biosphere with implications for the future. Annual Review in Earth Planetary Science, v.39, p.489–516.

Moore, E.A., and Kurtz, A.C., 2008, Black carbon in Paleocene-Eocene boundary sediments: a test of biomass combustion as the PETM trigger. Palaeogeography, Palaeoclimatology, Palaeoecology, v. 267, pp.147–52

Mori, P.E., Reeves, S., Correia, C.T., and Haukka, M., 1999, Development of afused glass disc XRF facility and comparison with the pressed powder pellet technique at instituto de geociencias, Sao Paulo University. Revista Brasileira de Geociencias, v. 29, no. 3, pp. 441-446.

Mort, H.P., Adatte, T., Föllmi, K.B., Keller, G., Steinmann, P., Matera, V., Berner, Z. and Stüben, D., 2007, Phosphorus and the roles of productivity and nutrient recycling during oceanic anoxic event 2. Geology, v. 35, pp. 483-486.

Murphy, B.H., Farley, K.A., Zachos, J.C., 2010, An extraterrestrial ^{3}He-based timescale for the Paleocene-Eocene ThermalMaximum (PETM) fromWalvis Ridge, IODP Site 1266. Geochimecal Cosmochimecal Acta, v. 74, pp.5098–1508

Perch-Nielsen. K., 1985, Mesozoic calcareous nannofossils. in H. H. Bolli, J. B. Saunders, and K. Perch-Nielsen, eds., Plankton Stratigraphy. Cambridge University Press, pp. 329-426.

Rana, R.S., et al., 2008, An ailuravine rodent from the Lower Eocene Cambay Formation at Vastan, western India, its palaeobiogeographic implications: Acta Palaeontolgica Polinica, v.53, pp. 1–14.

Revesz, K.M., Landwehr, J.M., and Keybl, J., 2001, Measurement of $\delta^{13}C$ and $\delta^{18}O$ isotope ratios of $CaCO_3$ using a Thermoquest Finnigan GasBench II Delta Plus XL Continuous Flow Isotope Ratio Mass Spectrometer with application to Devils Hole Core DH-11 Calcite. U.S. Geological Survey Open-File-Report 01-257, 17 pp.

Rodríguez, J., 1999, Use of cenograms in mammalian palaeoecology. A critical review. Lethaia, v. 32, pp. 331–347.

Röhl, U., Westerhold, T., Bralower, T.J., and Zachos, J.C., 2007, On the duration of the Paleocene-Eocene Thermal Maximum (PETM). Geochemical, Geophysical, and Geosysteme, v. 8, Q12002 pp.

Sluijs, A., Schouten, S., Pagani, M., Woltering, M., Brinkhuis, H., Sinninghe Damsté, J.S., Dickens, G.R., Huber, M., Reichart, G.J., and Stein, R., 2006., Subtropical Arctic Ocean temperatures during the Palaeocene/Eocene thermal maximum. Nature, v. 441, pp. 610–613.

Smith, T., Rana, R.S., Missiaen, P., Rose, K.D., Sahni, A., Singh, H., and Singh, L., 2007, Highest diversity of earliest bats in the Early Eocene of India. Naturwissenscehaften, v.94, pp.1003–1009.

Speijer, R., and Wagner, T., 2002, Sea-level changes and black shales associated with the late Paleocene thermal maximum: Organic-geochemical and micropaleontologic evidence from the southern Tethyan margin (Egypt-Israel): Geological Society of America Special Paper, v. 356, pp. 533–549.

Svensen, H., Planke, S., and Corfu, F., 2010, Zircon dating ties NE Atlantic sill emplacement to initial Eocene global warming. Journal of the Geological Society, London, v.167, pp. 433–436.

Svensen, H., Planke, S., Malthe-Sorenssen, A., Jamtveit, B., Myklebust, R., et al., 2004, Release of methane from a volcanic basin as a mechanism for initial Eocene global warming. Nature, v. 429, pp. 542–545.

Thomas, E., 1989, Development of Cenozoic deep-sea benthic foraminiferal faunas in Antarctic waters. Journal of the Geological Society, London. Special Publication, v.47, pp.283–296

Torfstein, A., Winckler, G., and Tripati, A., 2010, Productivity feedback did not terminate the Paleocene Eocene Thermal Maximum (PETM). Climateof the Past, v. 5, pp. 2391–2410.

Weijers, J.W.H., Schouten, S., Sluijs, A., Brinkhuis, H., and Sinninghe Damsté, J.S., 2007, Warm arctic continents during the Palaeocene–Eocene thermal maximum. Earth Planet Science Letter, v. 261, pp. 230–238.

Westerhold, T., Röhl, U., McCarren, H., and Zachos, J., 2009, Latest on the absolute age of the Paleocene–Eocene Thermal Maximum (PETM): New insights from exact stratigraphic position of key ash layers + 19 and – 17. Earth and Planetary Science Letters, v. 287, no. 3–4, pp. 412–419

Wing, S.L., Alroy, J., and Hickey, L.J., 1995, Plant and mammal diversity in the Paleocene to early Eocene of the Bighorn Basin. Palaeogeography, Palaeoclimatology, and Palaeoecology, v. 115, pp.117–155

Wing, S.L., Harrington, G.J., Smith, F.A., Bloch, J.I., Boyer, D.M., and Freeman, K.H., 2005, Transient floral change and rapid global warming at the Paleocene–Eocene boundary. Science v. 310, p. 993–996.

Zachos, J.C., Röhl, U., Schellenberg, S.A., Sluijs, A., Hodell, D.A., Kelly, D.C., Thomas, E., Nicolo, M., Raffi, I., Lourens, L.J., McCarren, H., and Kroon, D., 2005, Rapid acidification of the ocean during the Paleocene–Eocene Thermal Maximum. Science, v. 308, pp.1161–1611.

Zachos, J. C., Dickens, G. R., and Zeebe, R. E., 2008, An early Cenozoic perspective on greenhouse warming and carbon cycle dynamics. Nature, v. 451, p. 279–283

Zachos, J., Pagani, M., Sloan, L., Thomas, E., and Billups, K., 2001, Trends, rhythms, and aberrations in global climate 65 Ma to present. Science, v. 292, pp. 686–693.

Zachos, J.C., Schouten, S., Bohaty, S., Quattlebaum, T., Sluijs, A., Brinkhuis, H., Gibbs, S.J., and Bralower, T.J., 2006, Extreme warming of mid-latitude coastal ocean during the Paleocene–Eocene Thermal Maximum: inferences from TEX86 and isotope data. Geology, v. 34, pp. 737–740.

CHAPTER II

PALEOENVIRONMENTAL AND CLIMATIC CHANGES DURING THE PALEOCENE-EOCENE THERMAL MAXIMUM (PETM) AT THE WADI NUKHUL SECTION, SINAI, EGYPT

HASSAN KHOZYEM[1,2] *, THIERRY ADATTE[1] , JORGE E. SPANGENBERG[1] , ABDEL AZIZ TANTAWY[2]& GERTA KELLER[3]

[1]Institut de Science de la Terre (ISTE), Université de Lausanne, Switzerland

[2]Department of Geology, Aswan University, 81528, Aswan, Egypt

[3]Department of Geosciences, Princeton University, Guyot Hall, Princeton, NJ 08544, USA

**Corresponding author (e-mail: HassanMohamed.Saleh@unil.ch)*

Journal of the Geological Society, London, Vol. 170, 2013, pp. 341 –352. doi: 10.1144/jgs2012-046.

PALEOENVIRONMENTAL AND CLIMATIC CHANGES DURING THE PALEOCENE-EOCENE THERMAL MAXIMUM (PETM) AT THE WADI NUKHUL SECTION, SINAI, EGYPT[1]

Abstract. The Paleocene-Eocene Thermal Maximum (PETM) interval at the Wadi Nukhul section (Sinai, Egypt) is represented by a 10 cm thick condensed clay-rich layer corresponding to the NP9a/NP9b nannofossil subzone boundary. The Wadi Nukhul Paleocene-Eocene boundary (PEB) is characterized by: (1) an abrupt negative excursion in carbonate and organic carbon isotope ratios (–6‰ in $\delta^{13}C_{carb}$ and –2‰ $\delta^{13}C_{org}$), (2) an abrupt persistent negative shift in organic nitrogen isotope values ($\delta^{15}N_{org}$), (3) a significant increase in phosphorous concentrations just above the carbon isotope excursion, (4) a decrease in carbonate content and significant increase in kaolinite and (5) high vanadium and low manganese contents coincident with the occurrence of framboidal pyrite. The abrupt correlative isotopic excursions of $\delta^{13}C_{carb}$, $\delta^{13}C_{org}$ and $\delta^{15}N$ suggest that the lowermost part of the PETM is missing. The decrease in carbonate content indicates dilution by high detrital input triggered by acid weathering and carbonate dissolution in response to increased atmospheric CO_2 resulting from the oxidation of methane. The sudden increase in kaolinite content reflects a short-lived change to humid conditions. The $\delta^{15}N$ values close to 0‰ above the PEB suggest a bloom of N_2-fixing cyanobacteria. Increased bacterial activity may be either the cause or the result of the anoxia locally associated with the PETM.

1. INTRODUCTION

The Paleocene–Eocene boundary (PEB), 55.8 Ma ago (Westerhold et al 2009) is a critical time interval in environmental changes and subsequent biotic changes. The global warming that started in the late Paleocene and continued during the early Eocene known as the Paleocene Eocene Thermal Maximum (PETM), where the PEB transition interval shows exceptional global conditions, including rising temperatures to at least 8°C at the poles and 5°C in the tropics for several tens of thousands of years (Sluijs et al., 2006; Zachos et al., 2006; Weijers et al., 2007; Handley et al., 2008). These climatic changes coincide with a negative carbon isotope excursion (CIE) of -2 to -6‰ in marine organic carbon (Sluijs et al., 2006) and bulk marine carbonate (Zachos et al., 2005) respectively, and severe extinctions in benthic foraminifers (35–50%) (Alegret et al., 2009). Moreover, the widespread abundance of kaolinite in marine sediments during the PETM interval throughout the Tethys region points to a warm and humid late Paleocene–early Eocene climate with high rainfall (Bolle et al., 2000, Bolle & Adatte 2001).

Catastrophic methane release from hydrates (clathrates) could be responsible for the rapid climatic change (Dickens et al., 1995; Kennett et al., 2002). Methane is stored along the

[1] ***Hassan Khozyem, Thierry Adatte, Jorge E. Spangenberg, Abdel Aziz Tantawy, Gerta Keller, 2013, Paleoenvironmental And Climatic Changes During The Paleocene-Eocene Thermal Maximum (Petm) At The Wadi Nukhul Section, Sinai, Egypt.*** ***Journal of Geological Society. London. Vol. 170, 2013, pp. 341 –352.***

continental margin where its stabilization as methane hydrate requires high pressure and relatively low temperature but may become unstable if the ocean warms rapidly (Dickens 2001). This could lead to the release of carbon estimated at $2000x10^9$ metric tons over 10,000 years (Zachos et al., 2005), which is commonly believed to be the main cause for the PETM (Katz et al 2001; Dickens, 2011).

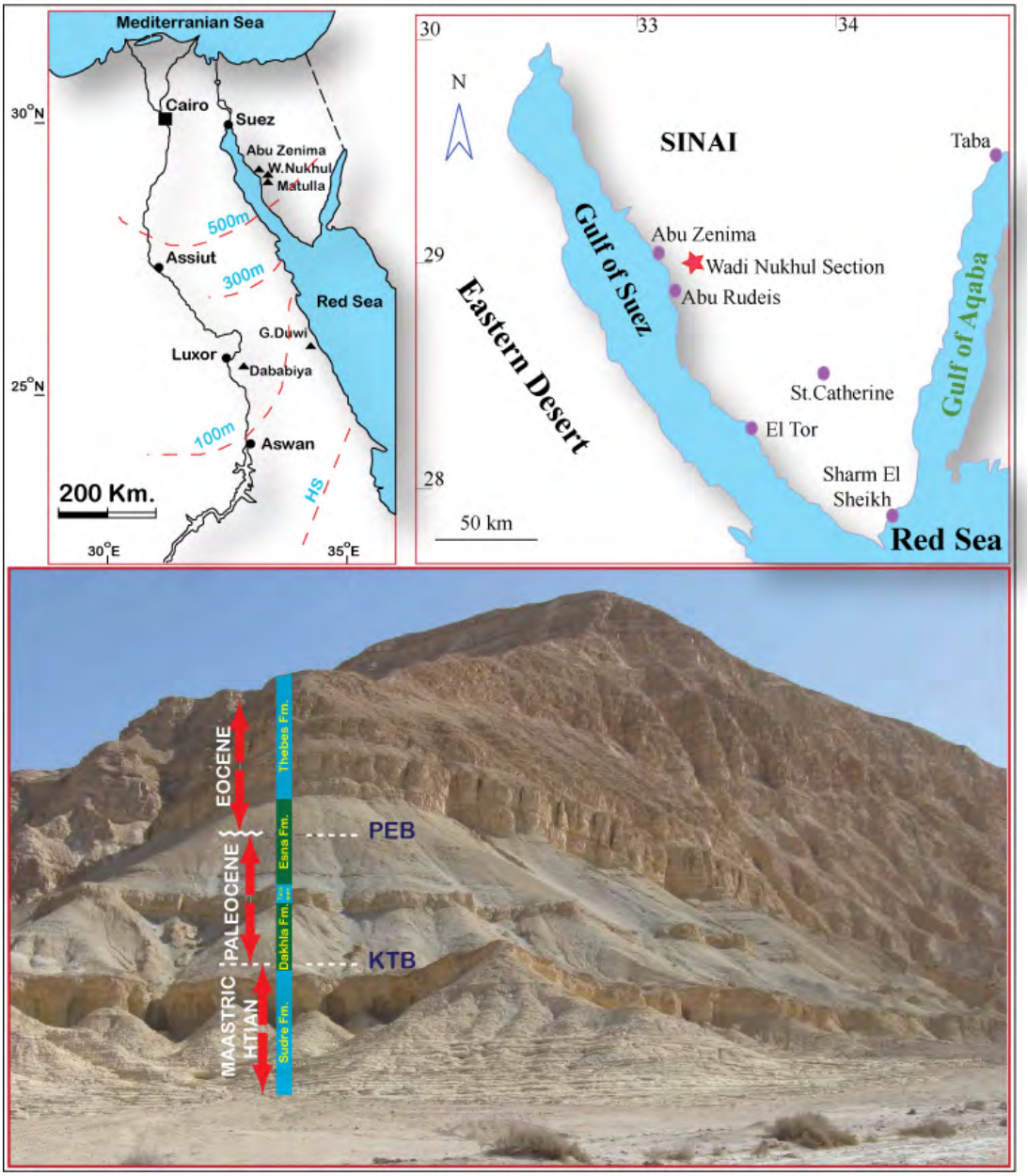

***Figure 1**. Location map of the Wadi Nukhul section (Sinai, Egypt) and photograph of the outcrop showing the Maastrichtian to Eocene sequence with the Cretaceous-Tertiary boundary (KTB) and Paleocene-Eocene boundary (PEB) locations.*

Moreover many other hypothesis have been recently proposed by several authors to explain that increase in atmospheric CO_2, amongst them: (1) Kurtz et al., (2003), suggested the extensive burning of peat and coal deposits of Paleocene linked with the arid period which prevailed during the uppermost Paleocene; but in their recent study, Moore & Kurtz (2008) did not find any indications of such process in cores from either the Atlantic or Pacific, (2) thermogenic methane linked to hydrothermal injection in organic rich sediments would led to the explosive

release of methane from Cretaceous–Paleocene mudstones in the North Atlantic (Westerhold et al. 2009), which is unlikely for the Tethys area that was tectonically stable during this period, (3) the drying of isolated epicontinental seas which led to rapid oxidation of organic matter, (4) melting of the methane-rich permafrost (DeConto et al., 2010).

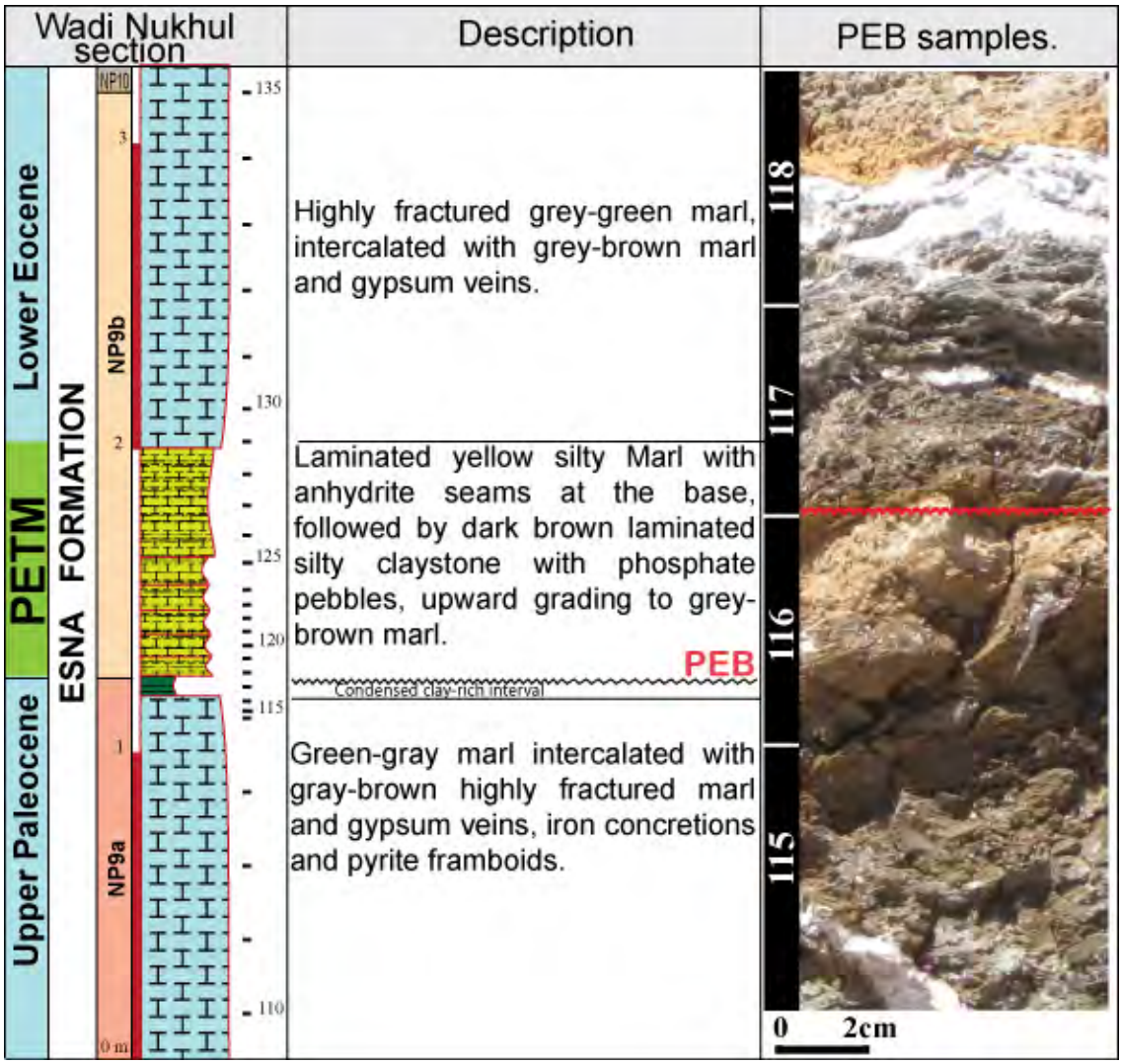

Figure 2. *Lithology of the Wadi Nukhul section with major sedimentary features, outcrop photographs and samples distribution across uppermost Paleocene-lowermost Eocene interval*

In Egypt, the base of the PETM is also characterized by minimal phosphorus accumulation rates, low biological productivity, a sea level fall and increase in detrital content followed by a rapid increase in primary production and accelerated phosphorus accumulation (Bolle et al., 2000) coincident with increased humidity recorded by high kaolinite content.

This study examines the PETM interval in the Wadi Nukhul, Sinai, Egypt, focusing on climatic and paleoenvironmental changes before, during and after the PETM spanning an interval of about 3.5 m. This interval is part of a 38 m thick succession of upper Maastrichtian to lower Eocene pelagic sediments exposed at Wadi Nukhul in the southwestern part of the Sinai (29^{o} 02`06``N and $33^{o}$ 11` 47``E) about 9 km east of Abu Zenima City (Fig. 1). Sediment deposition during the PETM interval occurred at about 500 to 600 m water depth, in an upper bathyal environment (Speijer et al., 1997).

2. MATERIAL AND METHODS

A total of 25 samples covering the Upper Paleocene Lower Eocene interval were examined for bulk and clay mineralogy, major and trace elements, total phosphorous (P_{tot}), and stableisotopes ($\delta^{13}C_{car}$, $\delta^{13}C_{org}$, $\delta^{15}N_{org}$). Carbon isotope analyses of aliquots of all samples were performed using a Thermo Fisher Scientific (Bremen, Germany) GasBench II preparation device interfaced to a Thermo Fisher Scientific Delta Plus XL continuous flow isotope ratio mass spectrometer (IRMS). Analytical uncertainty (2σ) monitored by replicate analyses of the international calcite standard NBS-19 and the laboratory standards Carrara Marble and Binn Dolomite is no greater than±0.05‰ for $\delta^{13}C_{carb}$.

Organic carbon and nitrogen isotope analyses were performed on decarbonated and oven-dried bulk sediment samples by flash combustion on a Carlo Erba 1108 elemental analyser connected to a Thermo Fisher Scientific Delta V isotope ratio mass spectrometer that was operated in the continuous helium flow. The $\delta^{13}C_{org}$ and $\delta^{15}N_{org}$ values are reported relative to VPDB and air–N_2, respectively. The reproducibility was better than 0.1‰ (1σ) for both carbon and nitrogen.

Bulk rock and clay mineralogy was determined by XRD based on method described by Kübler (1987) and Adatte et al. (1996) using Thermo-Xtra. Elemental analyses were performed with a FRX Philips PW2400 X-ray fluorescence spectrometer using lithium tetraborate fussed pellets for major elements (MEs) and pressed powder pellets for trace elements (TEs). The detection limits are 0.01% for MEs and 1 to 4 ppm for TEs. The accuracies of the analyses were assessed by analyses of standard reference materials.

Scanning electron microscopy (SEM; Tescan Mira/LMU) of gold and carbon coated PEB samples were used to assess the PEB interval for the presence of bacterially induced sedimentary structures (e.g., structures of extracellular polymeric substances framboidal pyrite).

Total phosphorus (P_{tot}) analyses were performed for all Wadi Nukhul samples using the ascorbic acid method (Mort et al., 2007b). Replicate analyses of indicated a precision better than 5%. In addition P_{tot} analysis were performed on several other sections from the central eastern desert of Egypt (e.g., Gebel Duwi, Bolle et al. (2000), Dababiya GSSP, Dupuis et al., 2003) and from central Sinai (Abu Zenima and Gebel Matulla, Bolle et al., 2000).

Biostratigraphy is based on calcareous nannofossils, which were analysed from smear-slides using a light microscope and 1000X magnification (Aswan University, Egypt).

3. RESULTS

At Wadi Nukhul, the PETM is part of the Esna Formation (5m above the Tarawan Formation). The studied interval can be divided into three parts from the base to the top: (1) the 1.10 m thick grey-green marls of the uppermost-Paleocene, (2) the 80 cm thick alternating brown to grey marl with gypsum veins and anhydrite, starting at the base with 10 cm thick condensed clay-rich interval including the PETM, and (3) the 1.4 m thick grey-green marl of lower Eocene age. Following the recommendation of the International Commission of Stratigraphy (ICS), the PEB is defined by the basal inflection of the carbon isotopic excursion ($\delta^{13}C_{carb}$). At Wadi Nukhul, the PEB is thus placed at the minimum of the $\delta^{13}C_{carb}$ excursions located at the base of the brown clay layer (sample 117, Fig. 2).

3.1. **Stable isotopes: $\delta^{13}C_{carb}$, $\delta^{13}C_{org}$ and $\delta^{15}N_{org}$**

Wadi Nukhul carbon isotopes show similar trends in $\delta^{13}C_{carb}$ and $\delta^{13}C_{org}$ values. Below the PETM (samples 110-116) $\delta^{13}C_{carb}$ and $\delta^{13}C_{org}$ values average 1.1 ‰ and 9.4‰, respectively (Fig. 4). At the condensed clay-rich interval, the $\delta^{13}C_{carb}$ values decrease abruptly (~ -4‰) followed by a similar but delayed (5 cm upwards) shift in $\delta^{13}C_{org}$ (~ -28 ‰). Above condensed clay-rich interval (samples 119 to 129) $\delta^{13}C_{carb}$ values increase gradually to the background values observed below the PETM, whereas low $\delta^{13}C_{org}$ values persist up to the end of the PETM interval. Above the PETM interval $\delta^{13}C_{carb}$ returns to pre-PETM values, whereas $\delta^{13}C_{org}$ shows strong fluctuations (Fig. 4). A similar pattern is observed in $\delta^{15}N_{org}$ values, although with increasing values below the PETM, followed by an abrupt decrease in $\delta^{15}N_{org}$ values persist through the PETM interval. Above this interval the $\delta^{15}N_{org}$ values are more depleted though fluctuating, similar to $\delta^{13}C_{org}$ (Fig. 4).

3.2. **Biostratigraphy**

For the calcareous nannofossil biostratigraphy the modified standard zonal scheme of Romein (1979) was used. The Paleocene/Eocene interval is identified based on *Discoaster multiradiatus*, which defines zone NP9a and NP9b spans the studied interval. Bybell and Self-Trail (1997) divided zone NP9 into a and b subzones based on the extinction of *Fasciculithus* species, such as *F. hayi, F. clinatus,is F. lillianae, F.bobii F. alanii* and *F. mitreus.* In the Wadi Nukhul section, these species disappear in the middle part of NP9 in a 10 cm thick condensed clay-rich interval that may be due to the dissolution of carbonate sediments and coincident with a sharp decrease in *Toweius* spp., *Coccolithus pelagicus/Ericsonia subpertusa* (NP9a) and the carbon isotope excursion (Fig. 3). Subzone NP9b is marked by persistence of *Toweius spp,* blooms of *Coccolithus pelagicus/Ericsonia subpertusa* and the first appearance of short-lived *Rhomboaster spp.* and *Discoaster araneus,* or *RD* assemblage (Fig. 3). Above the condensed clay-rich interval (sample 118), *Toweius* spp. gradually increases with a notable decrease in *Coccolithus pelagicus/subpertusa* marking a gradual return to pre-PETM environmental conditions.

3.3. **Mineralogy**

The PETM interval (sample Nu-117 to 129) shows a 10 cm condensed clay-rich interval at the base with a rapid decrease in carbonate content to 5.14% with no change in the other bulk rock components, except anhydrite which reaches maximum contents (17.08%) within the PEB, both rich interval (39.7% and 9.7% respectively) still coinciding with low calcite content. At the top of the condensed clay-rich interval, Ca-apatite suddenly increases to (17.22%). Above this condensed interval, clays grade into marls as calcite increases (mean value 61.81%) and phyllosilicates decrease (6.87%). phyllosilicates and quartz reaching their maximum contents in the middle of the condensed clay- Anhydrite disappears in the middle of the PETM interval. Above the PETM interval (samples Nu-130 -135) sediments getting more marly and all mineral components return to normal pre-PETM values (Fig. 5). In addition, microscopic observations indicate clear sedimentary structures of bacterial activities with characteristic shapes for cyanobacteria and sulphur reducing bacteria associated with framboidal pyrite less than 5 μm in diameter (Fig. 7) within and close to the PEB samples (Nu-117, Nu-118 and Nu-119).

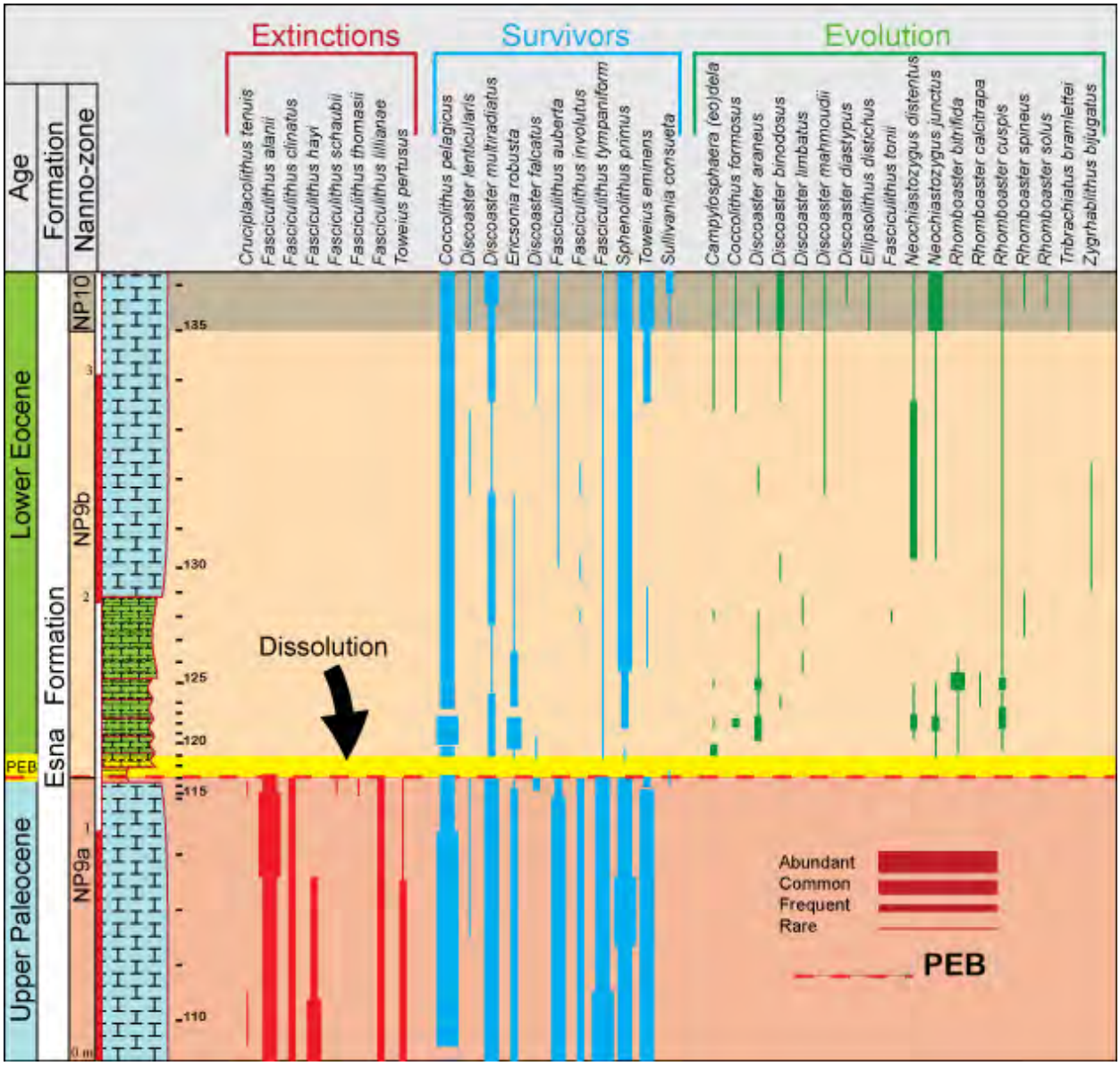

Figure 3*. Nannofossil biostratigraphy showing the faunal changes across the PETM event at Wadi Nukhul. Note the sharp faunal change coincides with the carbonate dissolution interval and represent a hiatus. (Condensed clay-rich layer)*

Clay minerals detected at Wadi Nukhul are kaolinite, smectite, illite, sepiolite and palygorskite. Kaolinite shows a gradual increase below the PETM (mean values 8.3%), rapidly increases to 50% just above the $\delta^{13}C_{carb}$ excursion and returns to pre-PETM values (Fig. 5). Smectite sharply decreases (11.7%) below the PETM and remains low into the condensed clay-rich interval, followed by a gradual increase to values (up to 80%) that are commonly observed below and above the PETM in several sections located in Sinai (e.g. Mattula, Bolle et al., 2000). As palygorskite and sepiolite have the same origin and indicate the same environment, we cumulate their values, they are present just below the PEB in high amounts (72.3%) but decrease during the PETM and gradually disappear above it (Fig. 5). The kaolinite/smectite ratio is close to zero below and above the PEB, but shows an abrupt increase, up to 2.1, at the middle of the condensed clay-rich interval. The kaolinite/(sepiolite+palygorskite) ratio shows the same trend

through the PEB but returns more gradually to background values above the PETM interval (sample 129).

3.4. Major and trace elements

Major and trace elements (MEs, TEs) are normalized to aluminium (Tribovillard et al., 2006). The palaeo-depositional environment during the PETM is evaluated based on (a) elements indicative of detrital input rates (Si/Al, Ti/Al, Zr/Al and K/Al), (b) productivity sensitive elements (P_{tot}, Ni/Al, Zn/Al and Cu/Al) and (c) redox sensitive parameters (Mn*, V/Al, and V/Cr ratio) where Mn* is calculated as Log ((Mn_{Sample}/Mn_{PAAS})/(Fe_{Sample}/Fe_{PAAS})) (Cullers. R., 2002). The variations of different weathering indexes were examined.

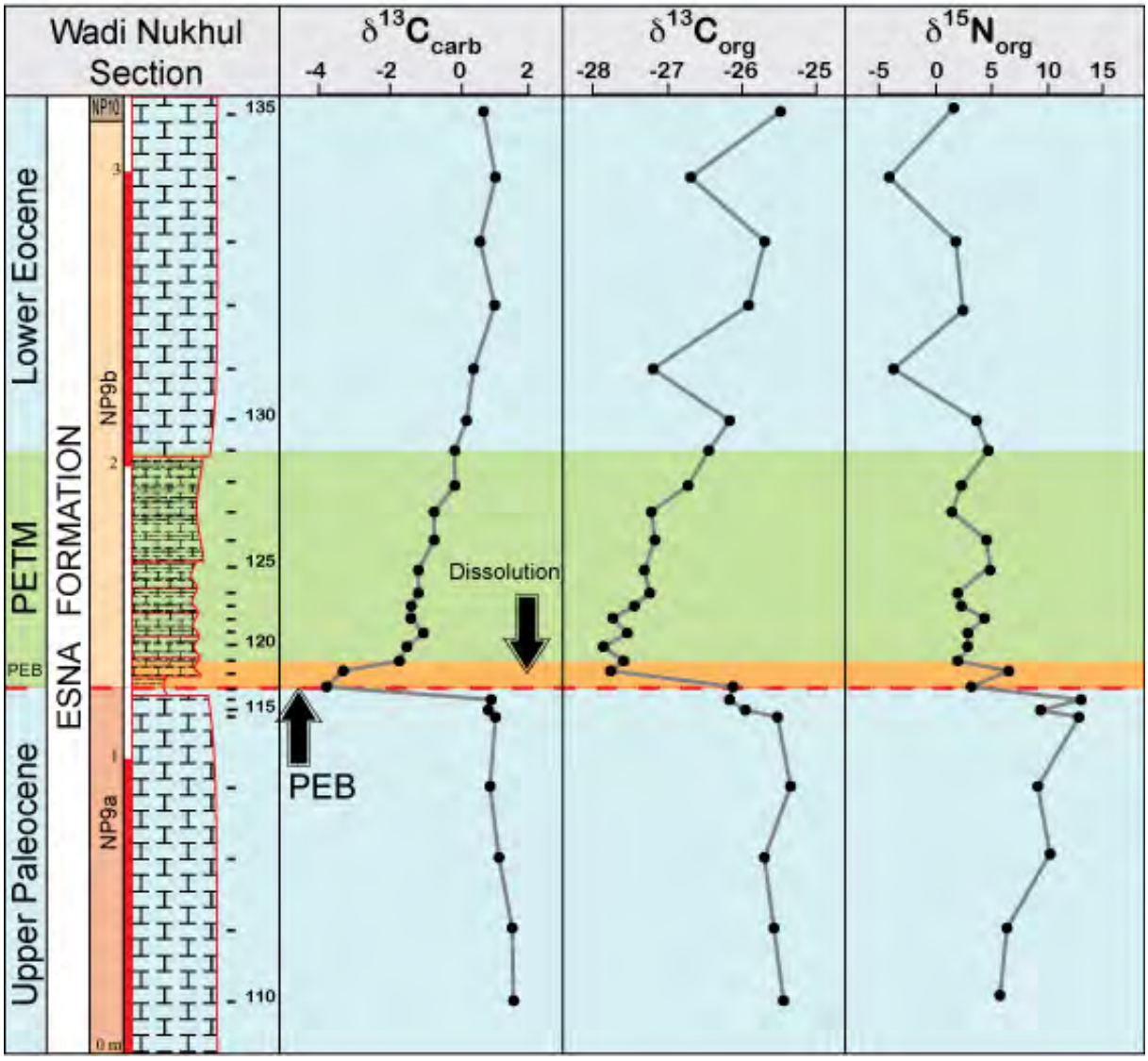

Figure 4. *Isotopic records ($\delta^{13}C_{car}$, $\delta^{13}C_{org}$ and $\delta^{15}N_{org}$) of the Wadi Nukhul across the uppermost Paleocene, PETM and lowermost Eocene. Note the negative excursion in both $\delta^{13}C_{car}$ and $\delta^{13}C_{org}$, and the persistent negative $\delta^{15}N_{org}$ values in the PETM interval.*

Below the PETM, Ti/Al, K/Al and Zr/Al ratios increase slightly from the base towards the PEB with average values of 0.084, 0.25 and 0.0037 respectively, whereas Si/Al contents decrease to 3.15 just below the PEB (Fig. 6). At the PEB, both Ti/Al and Zr/Al reach maxima (0.11 and 0.0045) and Si/Al and K/Al show minimum values (2.51 and 0.14).

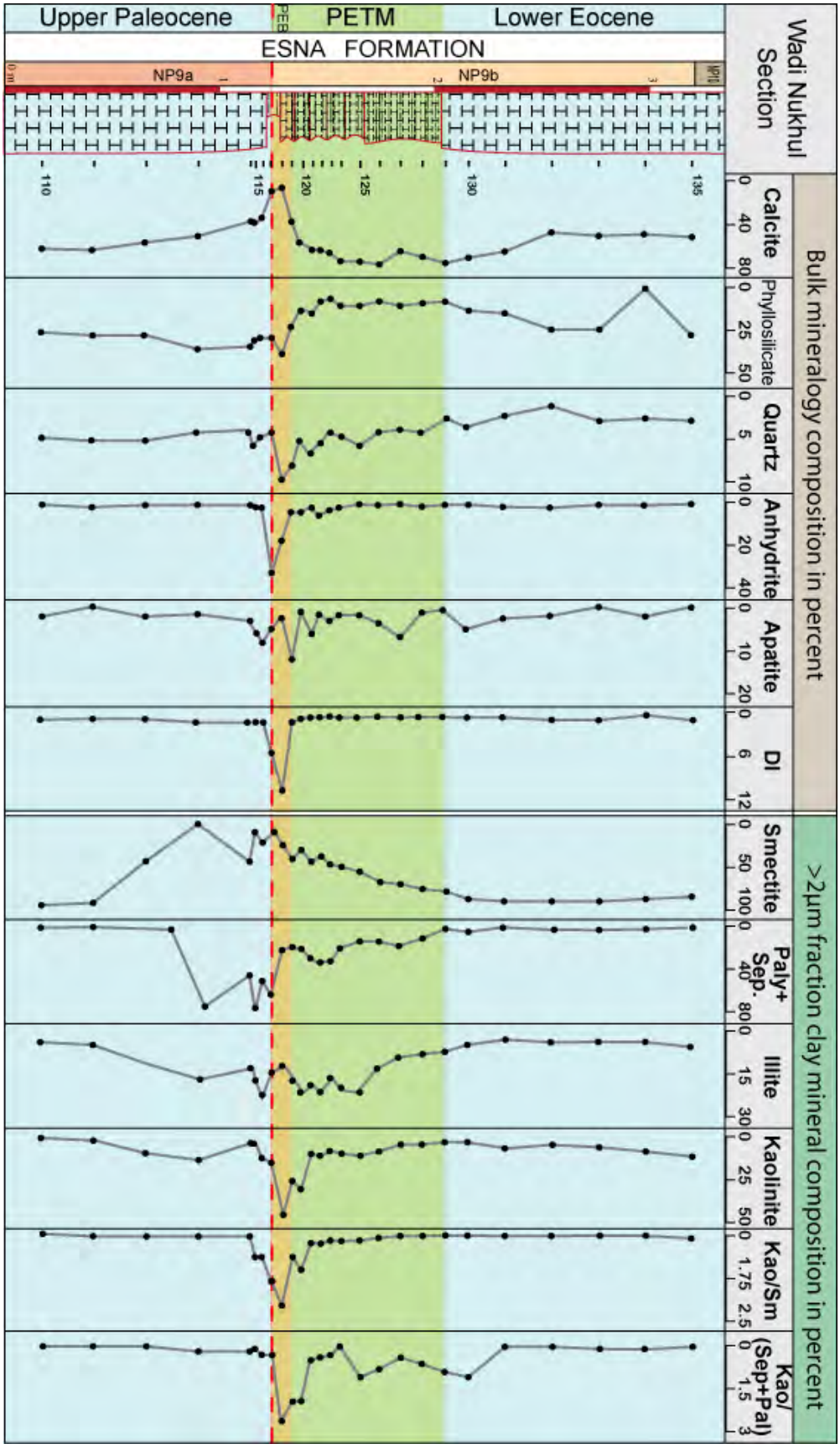

Figure 5. *Bulk rock and clay minerals composition in relative percentage and their ratios across the PETM interval at Wadi Nukhul. DI is the detrital input determined as DI=Quartz+Feldspare /Calcite*

A notable increase in Si/Al, Ti/Al and K/Al is observed just above the PEB with maximum values in the middle PETM (6.24, 0.10 and 0.55 respectively), coeval with a drop in Zr/Al to zero. Above the PETM interval these elements recovered to pre-PETM values (Fig. 6). The weathering index (WI) depends mainly on the mobility of major elements and their behaviour during the weathering process of the parent rock, some may increase with the progress of weathering whereas other decrease. For this reason we use three different WI to emphasize the role of weathering during the PETM event: (1) the Weathering Index of Parker (WIP; WIP = (100)[(2Na_2O/0.35)+(MgO/0.7)+(2K_2O/0.25)(CaO/0.7)]), which can be applied to weathered material that was derived from acidic, intermediate and basic igneous rocks taking into account the Al mobility (Parker, 1970, Price & Velbel., 2003).

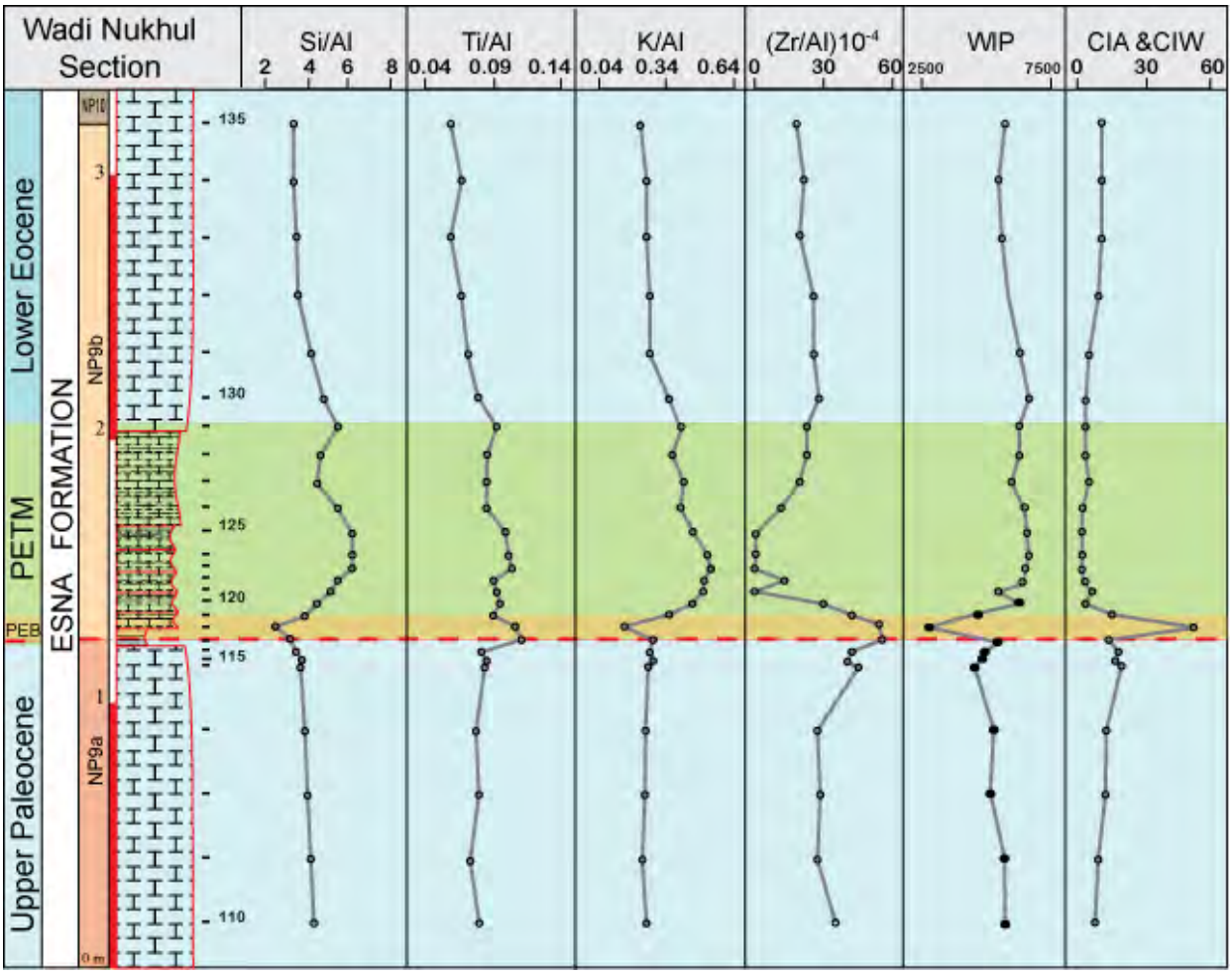

***Figure 6**. Plot of elements indicative of detrital input at PETM interval in Wadi Nukhul compared with different weathering indexes (WIP, CIA, CIW). See text for explanation.*

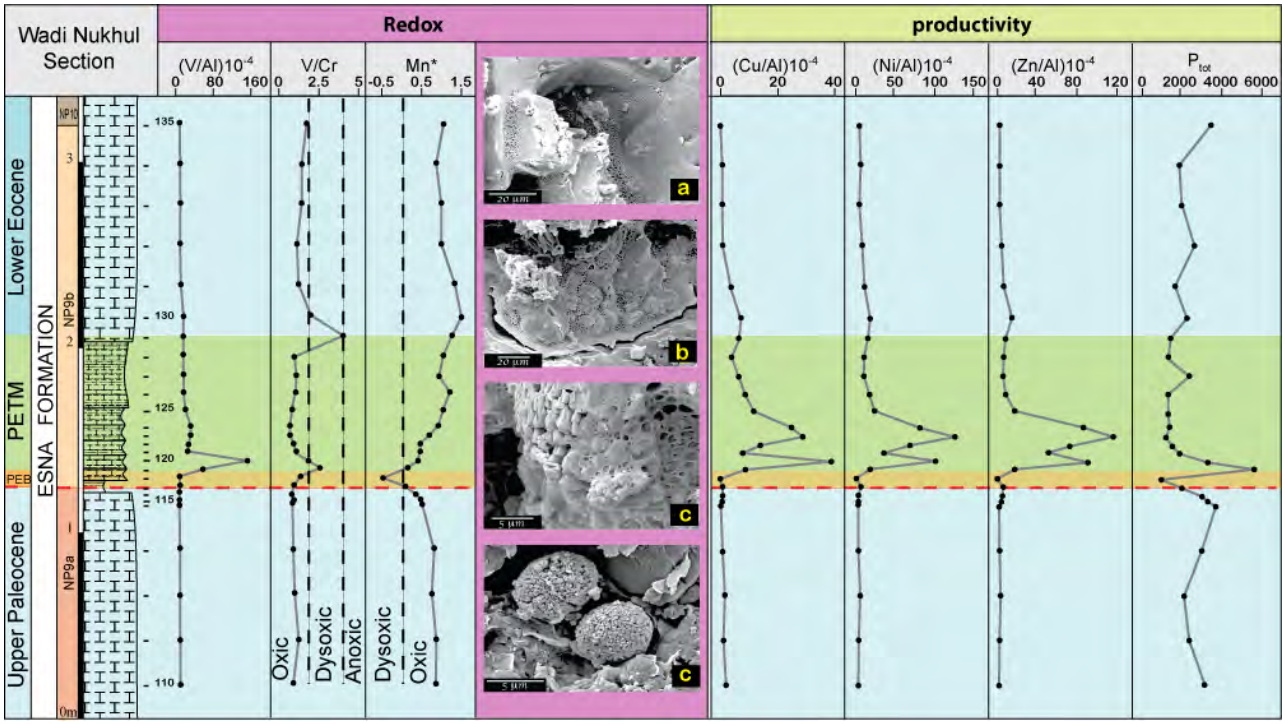

Figure 7*. Plot of redox sensitive elements across the PETM interval at Wadi Nukhul section, reveals the establishment of the dysoxic conditions across the PEB, a, b and c SEM pictures showing the abundant EPS-like within the PEB (sample Nu-118), d) SEM picture indicate the presence of the pyrite framboids (<5μm) and Plot of elements indicating productivity during the PETM interval at Wadi Nukhul show the accumulation of P_{tot} just above the PEB associated with increase in productivity sensitive trace elements Cu/Al, Ni/Al, and Zn/Al.*

WIP values show a strong negative shift (2852) from mean values below and above the PEB (~6000) at Wadi Nukhul. (2) The Chemical Index of Alteration (CIA; CIA = (100)[Al_2O_3/(Al_2O_3+CaO*+Na_2O+K_2O)]) measures feldspar conversion to clay minerals such as kaolinite, which explains the migration of climatic zones (Nesbit & Young, 1984, 1989; Price & Velbel, 2003). CIA values are high (53) across the PEB at Wadi Nukhul, which suggests intense chemical weathering. (3) The Chemical index of Weathering (CIW; CIW = (100)[Al_2O_3/(Al_2O_3+CaO*+Na_2O)]; Harnois 1988) is similar to CIA by eliminating K_2O from the equation and reflects the progressive conversion of feldspar to clay. CIW and CIA have identical values across the PEB at Wadi Nukhul, solely exceeding the background values at the PEB (Fig. 6).

V/Al, V/Cr and Mn* show similar behaviour before and after the PETM. Below the PEB, their ratios are very low with average 1.8 (10^{-4}), 0.81 and 0.61. Mn* reaches minimum values (-0.49) at the base of Eocene (sample 118, Fig. 7). V/Al shows the highest values at samples Nu-119 (52.6x10^{-4}) and Nu-120 (155x10^{-4}). V/Cr also reaches maximum values at the same level (Nu-119= 1.21, Nu-120= 2.54), and gradually return to the background value (Fig. 7).

The productivity parameters in this study are based on four different element concentration ratios (Cu/Al, Ni/Al, Zn/Al and P_{tot}), which are strongly related to organic matter. Below the PETM, all elements, except Ba, show low concentrations with mean values of Zn/Al (1083x 10^{-4}), Cu/Al (22x 10^{-4}), Ni/Al (95x 10^{-4}), and P tot (2790 ppm) slightly increasing up to the top of the Paleocene (Fig. 7). At the PEB all parameters show sudden depletion to minimum values. Above

the PEB to the middle PETM interval (samples from 119 to 124) all productivity sensitive TEs and P_{tot} reach maximum values (Cu/Al: 231x10^{-4}, Ni/Al: 923x10^{-4} and P_{tot}: 5498 ppm). Above this interval all elements return to the Paleocene background concentrations (Fig. 7).

4. DISCUSSION

4.1. Completeness of the PETM at Wadi Nukhul

Whether a sedimentation record is continuous or partly missing due to a hiatus can be assessed by the abruptness of geochemical changes. At Wadi Nukhul, the negative $\delta^{13}C_{org}$ and $\delta^{13}C_{carb}$ excursions are very abrupt (from -25.5 to -28‰ and from 1 to -4‰, respectively). Similar sharp negative excursions are observed in $\delta^{15}N_{org}$ values (Fig. 4). Such abrupt shifts suggest the presence of a hiatus. Lithologically, the base of Eocene at Wadi Nukhul shows a sudden change from marl to a condensed clay-rich layer that is characterized by an abrupt decrease in calcite content from 32.4% to 7.6% coinciding with a sharp increase in detrital components (phyllosilicates and quartz). At the same level, the absence of benthic foraminifera (Speijer and Wagner, 2002) could be due to carbonate dissolution and/or dilution by increased detrital input. All these criteria together with the abrupt shift in $\delta^{13}C_{carb}$ supports the presence of a hiatus, which is also observed in other sections from Egypt (e.g., Gebel Duwi and Gebel Aweina sections; Speijer et al., 2000, 2002), Italy (Forada section; Agnini et al., 2007), Spain (Zumaya section; Schmitz et al., 1997), Uzbekistan (Aktumsuk section; Bolle et al., 2000), ODP sites 690, 685, 248 689, 865, 1051, 1263, 1260B and 1172D (Katz et al., 2003; Mutterlose et al., 2007) and DSDP site 401 (Pardo et al., 1997). A gradual decrease in carbon isotope ratios 1-2 m below the PEB (estimated to represent 120 kyr,) was observed at Alamedilla, Spain (Alegret et al., 2009), Aktumsuk, Uzbekistan (Bolle et al., 2001) and Dababiya, Egypt (Aubry et al., 2007) (Fig. 8).

Comparison of the carbon isotope result of the Wadi Nukhul section with the already published record of the Dababiya GSSP (Dupuis et al., 2003, Aubry et al., 2007) suggest that the lowermost Eocene sediments are missing from Wadi Nukhul (bed-1 to middle of bed-3 in the Dababiya GSSP and ODP 690B in the south Atlantic). This missing part of the section spans about 50.6 k.y of time (Figs. 2, 4 and 5) and corresponds a third order sea level fall overlain by the next transgressive system tract (TST) coincident with the PETM (Ernst et al., 2006). This may also explain the absence of lowermost Eocene sediments from Wadi Nukhul section.

4.2. Bulk rock proxies

Bulk rock composition of the Paleocene-Eocene interval at Wadi Nukhul reflect changes in the source and proximity of sediments from terrigenous areas and the intensity of erosion transportation in response to sea level and climatic changes. Below the PETM, most of the minerals analysed show normal background concentrations, except phyllosilicates, which increase slightly to the detriment of calcite (Fig. 5). This may be linked to a low sea level and proximity to a detrital source. The onset of the PETM is marked by an abrupt decrease in calcite coincident with a sharp increase in phyllosilicates and quartz (see DI, Fig. 5). This increased detrital input reflects significant reworking linked to the early Transgressive System Tract (TST) and/or intense dissolution due increased acidity (Zachos et al, 2005).

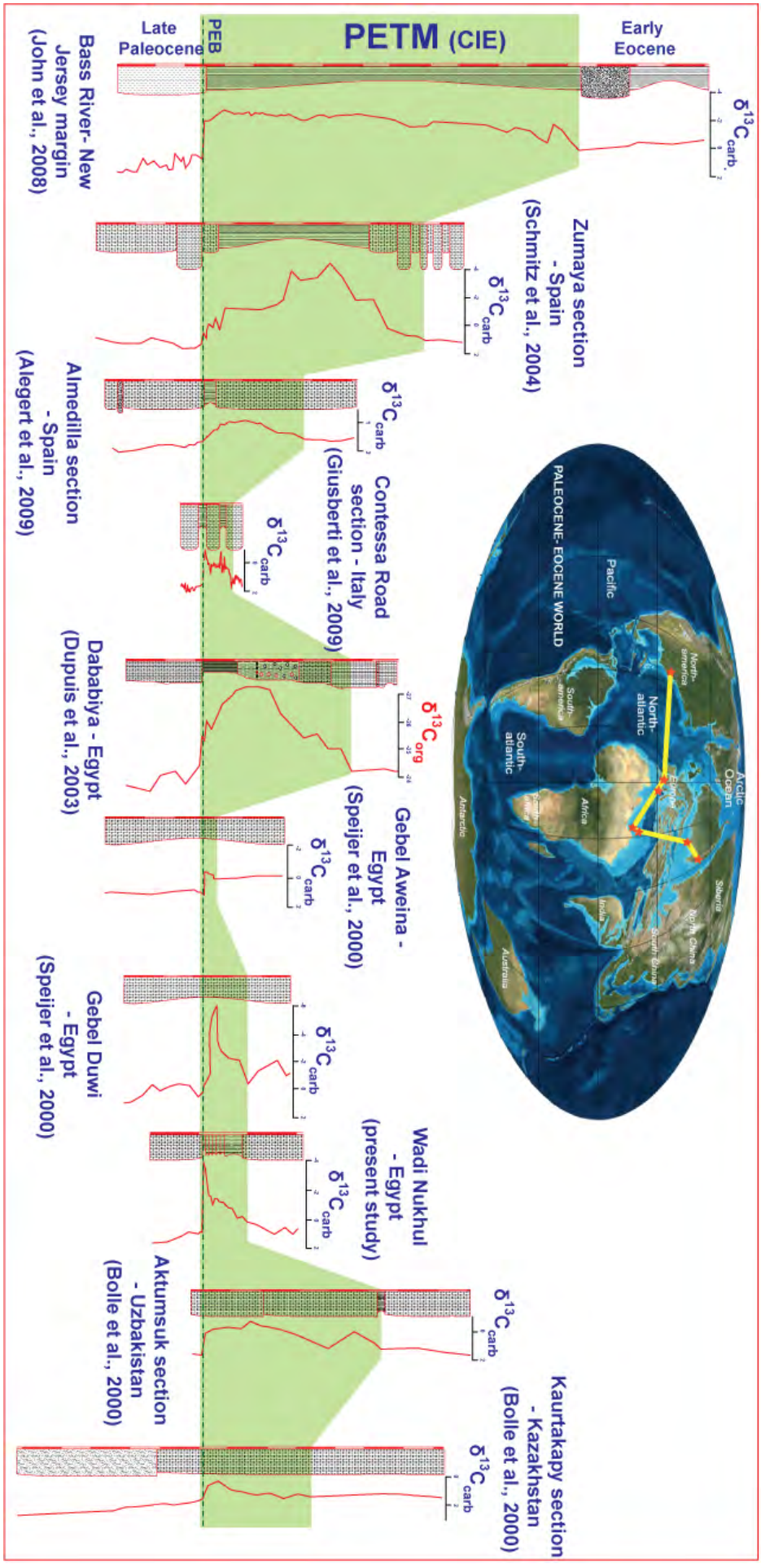

Figure 8. *Local and global correlation of the PETM interval with the Wadi Nukhul section based on correlation of the organic and inorganic carbon isotope shifts.*

Moreover, low calcite is associated with increased Ca-apatite linked to increased biomass productivity, as indicated by Cu, Ni and Ba coeval enrichments. The presence of a single anhydrite layer at the same level remains difficult to explain but may be linked to methane hydrate release through complex redox cycles led to sulphide oxidation (Arthur et al., 1988). Further investigations are needed to evaluate this process. Calcite content gradually returns to high values (70%) about 10 cm above the PEB and detrital input gradually decreases to normal background values. This reflects normal rate of carbonate productivity and termination of the PETM event.

4.3. **Clay minerals as palaeoclimatic indicators**

Clay minerals and their relative abundance in marine sediments may record information on climate, eustasy, diagenesis, or reworking (Chamley, 1989). In order to interpret clay mineral associations, the relative role of detritus and authigenesis must be distinguished. Smectite can be locally formed in the marine realm from early diagenesis, halmolysis (Karpoff et al., 1989), or hydrothermal weathering of volcanic rocks (Chamley, 1998). Smectite may also be derived from alteration of ash layers. Finally, palygorskite and sepiolite are fibrous clay minerals that can be formed in situ as a result of hydrothermal processes as well as low-temperature alteration of Mg-bearing rocks (Karpoff et al., 1989).

Most of the mechanisms explaining the authigenesis of palygorskite, sepiolite, and smectite occur in hydrothermal environments such as mid-ocean ridges (e.g., Karpoff et al., 1989). However, the Wadi Nulkhul section is located in an upper bathyal setting (500-600 m depth, Speijer et al., 1997) and no evidence of such processes could be found. More commonly, clay minerals are of detrital origin and represent the end product of continental weathering and transport into marine basins.

The nature of the clay depends mainly on the climatic conditions and the nature of the rock being weathered. Clay mineral assemblages therefore reflect continental morphology and tectonic activity, as well as climate evolution and associated sea-level fluctuations (Chamley, 1989; Weaver, 1989). Illite and chlorite are considered common by-products of weathering reactions with low hydrolysis typical of cool to temperate and/or dry climate. Smectite formed in soils developed under a warm arid to temperate climate characterized by alternating humid and dry seasons (Chamley, 1998). Palygorskite and, to a lesser extent, sepiolite are continental products frequently found in a lacustrine environment and calcrete soils in arid to semi arid climatic zones. Nevertheless, palygorskite preferentially forms in perimarine environments where continental alkaline waters are concentrated by evaporation. This latter process is accelerated in higher temperature zones (Callen, 1984; Robert & Chamley, 1991). Since each of the mechanisms for palygorskite formation requires warm and arid climatic conditions, its occurrence is considered as indicator of continental aridity (Chamley, 1989; Adatte et al., 2002). Kaolinite is generally a by-product of highly hydrolytic weathering reactions in perennially warm humid climates.

The Wadi Nukhul sediments just below the PEB are enriched in palygorskite and sepiolite (15.8% and 56.5%, respectively) coinciding with high illite, which indicates that arid to semi arid climate conditions prevailed just before the PETM (Bolle et al., 2000). The palygorskite and sepiolite amounts gradually decrease during the PETM and disappear in the Early Eocene samples (Fig. 5), where smectite content increases, indicating a more contrasted seasonal

climate. The sharp increase in kaolinite observed in the lowermost PETM samples suggests a short period of warm humid condition. The calculated kaolinite/smectite and kaolinite/(sepiolite+palygorskite) can be used as a signal of climatic change during the PETM interval. Both ratios reach their maximum during the PEB followed by a gradual decrease in the kaolinite/(sepiolite+palygorskite) ratio, which indicates a wet hot climate at the PEB followed by a gradual re-establishment of the semi arid to arid condition during the PETM.

Above the PETM, kaolinite/smectite and kaolinite/(sepiolite+palygorskite) values are close to zero reflecting prevalence of an arid climate after the PETM (Fig. 5). A similar kaolinite increase during the PETM indicative of warm and humid conditions has previously been observed in the Sinai (Bolle et al., 2000), Spain (Lu et al., 1998), and Uzbekistan (Bolle and Adatte, 2001). Dupuis al al. (2003) and Ernst et al. (2006) did not report the presence of palygorskite and sepiolite in the Dababya GSSP section, whereas Bolle et al., (2000) found only low amounts of palygorskite (up to 10%) in the nearby coeval sections of Abu Zenima and Gebel Matulla sections. These differences are probably due to the use of more accurate deconvolution software to discriminate the smectite and illite peaks from the palygorskite and sepiolite reflexions.

4.4. **Palaeoenvironmental geochemical proxies**

The removal of dissolved major and trace elements from the water column and their incorporation into sediments depends on biotic and abiotic processes (Tribovillard et al., 2006). In oxic environments TE enrichments are related to abiotic processes. In dysoxic-anoxic conditions, they are linked with diffusion and remobilization processes at the sediment-water interface through redox cycles in the sediments and microbial activity (Tribovillard et al., 2006), and more particularly with redox cycling of Mn and Fe (Lyons et al., 2003; Sageman & Lyons 2003; Algeo and Maynard, 2004; Riquier et al., 2006). MEs and TEs can thus provide insights into the palaeo-depositional environment of the PETM. For example, Al-normalized elements, such as Si, Ti K and Zr reflect enhanced delivery of detritus from different sources including riverine, aeolian or volcanic (Bertrand et al., 1996; Murphy et al., 2000b; Pujol et al., 2006). High Ti/Al ratios may reflect enhanced detrital supply from rivers where Ti is associated with heavy mineral grains that require high transport energy from the source area and may therefore also indicate a sea level fall. However, in some cases increased Ti correlates with a sea level rise and thus reflects volcanic input, especially when high Ti input correlates with high Zr/Al ratios. In contrast, a uniform stratigraphic distribution of the K/Al, Fe/Al and Si/Al suggests a homogeneous detrital supply (Riquier et al., 2006).

At Wadi Nukhul, high Ti/Al and Zr/Al ratios coincide with high weathering indexes, such as WIP, CIA and CIW (Fig. 5, 6). Increased weathering at the PEB may result in concentration of these elements due to the removal of alkaline elements during weathering of the parent rock. The slight decrease in authigenic and/or biogenic Si at the PEB may be due to an increase in detrital input (Tribovillard et al., 2006), as commonly observed in TST deposits.

Fluctuations of the bottom water oxygenation during depositional processes can be deciphered by using different elemental ratios (e.g., V/Cr, Ni/Co, U/Th, etc.) and Al-normalized contents of redox sensitive or chalcophile elements (e.g., Fe, Mn, U, V, Zn, Pb, Cu, Ni) (Joachimski et al., 2001; Algeo & Maynard, 2004; Cruse & Lyons, 2004; Pujol et al., 2006). However, some of these elements are typically associated with hydrothermal activity (e.g., Pb,

Zn, Cu, Co, Ag, Mo) and the cause of their enrichment remains often ambiguous (Cruse & Lyons, 2004). Since the Wadi Nukhul area was part of the southern Tethys margin (with palaeodepth about 500-600m), which was tectonically stable during the late Paleocene early Eocene, these elemental ratios can be also used to constrain the water column oxygenation during the deposition of the PETM sediments. The Mn* parameter is an indicator of redox conditions in depositional environments (Cullers 2002). In this study the use of V/Cr was additionally used in combination with Al-normalized V and Mn* calcophiles as redox sensitive to bottom water oxygenation (Fig. 7) in association with pyrite framboids. The calculated Mn* is the best way to represent the Mn part linked to redox conditions. We use this parameter because during diagenesis of Ca-rich sediments Mn(II) can replace Ca and form Mn-bearing carbonates.

Vanadium in oxic waters is present as V(IV) and V(V) ions, which are tightly coupled with the redox cycle of Mn. Vanadate readily adsorbs onto Mn-and Fe-oxyhydroxides and possibly kaolinite (Tribovillard et al., 2006). Vanadium can also be derived from sedimentary biomass, where occurs in the active sites of some enzymes in nitrogen-fixing bacteria (Anbar, 2004; Grosjean et al., 2004; Tribovillard et al., 2006). According to Hoffman et al. (1998), a V/Cr ratio of 5 corresponds to the limit between dysoxic and anoxic conditions, whereas lower V/Cr ratios generally indicate oxic/dysoxic conditions (Pujol et al., 2006).

At Wadi Nukhul, the vertical distribution of both V/Al and V/Cr values suggests oxic conditions, except in the 5 cm interval just above the PEB (Fig. 7), characterized by the highest values in V/Al and V/Cr, but still in the range of oxic/dysoxic conditions (V/Cr = 3.6) though slightly dysoxic. This is consistent with the vertical distributions of Mn and Fe with very low values in the interval of dysoxic conditions (5 cm above the P/E boundary) and increasing upward to the top of the PETM. This may reflect an increase in water column oxygenation in the upper PETM. The positive Mn* above and below the PEB suggest oxidizing conditions in contrast to the negative Mn* value recorded within the PEB level (-0.4), which can be linked to increased anoxia. Most of the iron tends to be incorporated in sulfides under reducing conditions explaining presence of small pyrite framboids (less than 5 μm in diameter, Riquier et al., 2006) at the PEB (sample 117 and 119) and their small size reflects slightly anoxic conditions in the water column. This is also supported by the presence of different bacterial communities that remove oxygen and reduced sulfated for precipitation of small pyrite framboids (Fig. 7). Their presence is in apparent contradiction with the observed V/Cr and Mn* ratios indicative of dysoxic to slightly anoxic conditions as also observed by Speijer et al. (1997) using lithologic and biotic criteria. This discrepancy could be explained by the removal of these redox sensitive elements by oxidation due to recent weathering processes.

Phosphorus (P) is the most important element used by all living organisms for their metabolism. In marine environments, P controls primary production over the long timescale (Tyrell 1999). Phosphorus content in sediments is strongly linked with organic matter (OM) content and reflects high productivity (Tribovillard, 2006). Phosphorus accumulation in sediments derives from different sources, including phytoplankton, fish scales, bones or detrital reworked P grains. In general, P is released as PO_4^{-3} from decaying organic matter during oxic, suboxic and anoxic bacterial degradation below the sediment–water interface (Tribovillard et al., 2006). But under anoxic conditions, P is less retained in the sediment and generally diffuses upward from the sediment and returns to the water column (Mort et al., 2008). Phosphorus enrichment may result from high OM supply in highly productive marine environments such as

upwelling areas. In low-productivity areas P enrichment can be triggered through redox cycling of iron, with P adsorption onto iron-oxyhydroxide coatings and Fe–P co-precipitation (e.g., Jarvis et al., 1994; Piper & Perkins, 2004). An alternative mechanism for P retention may be uptake by bacterially precipitated polyphosphates. The degree to which remineralized organic P is retained as a reactive fraction in sediments depends on the redox conditions of the depositional system. In environments with at least intermittently oxic bottom waters, redox cycling of Fe in the sediments limits the diffusive flux of demineralized P to the overlying water column (Tribovillard et al., 2006; Mort et al., 2008).

At Wadi Nukhul, increasing relative abundances of *Discoaster*, *Fasciculithus tympaniform*, and *Sphenolithus primus* have been interpreted to represent more oligotrophic, but also warmer environments as noted at sites 690 and 1209 by Bralower (2002) and Gibbs et al. (2006). *RD* taxa are interpreted as proxies for warm surface waters and/or increased salinity with possibly low pH and increasing acidity (Tantawy, 2006). Within the PETM an increase of both eutrophic *Coccolithus* and *Ericsonia* associated with decrease of *Sphenolithus* interpreted by Agnini et al (2007) as a response to nutrient enhanced conditions induced by increase in weathering.

Above the CIE-PETM, the abundance shifts of nannofossil taxa that are considered indicator of cold-water conditions and/or which were adapted to mesotrophic–eutrophic environments such as *Toweius* could indicate the termination of the PETM climatic changes. Thus the P_{tot} fluctuations can be divided into four parts: (1) in the latest Paleocene P_{tot} increases to exceed the mean value in normal oxic conditions; (2) at the PEB, P_{tot} depletion is at its maximum and coincides with anoxic oligotrophic conditions; (3) the highest concentrations at 10 cm above the PEB is possibly due to increasing of eutrophic conditions and primary productivity and/or deposition of fish remains and coprolites within the laminated marl (Speijer and Wanger 2002; Soliman et al., 2006) and (4) the decrease to the normal background above the lower PETM, due to the mesotrophic–eutrophic conditions prevailed. Such fish remains and coprolite accumulations typify condensed intervals characterizing the TST.

Similar sequences of P_{tot} depletion and enrichments characterize the PETM interval in several sections in Egypt (Dababiya, Abu Zenima, Gebel Mattula and Duwi sections, Fig. 9). In all these sections, a significant decrease in P_{tot} contents coincides with the PEB linked to anoxia prevailed during eutrophic conditions, and followed by a sharp increase reflecting rising primary productivity and /or deposition of condensed layers enriched in coprolite and fish remains. The correlation of these sections (Fig. 9) shows that the thickness of the P_{tot} enriched interval and the P_{tot} contents are decreasing from proximal (Duwi and Dababiya) to more distal environments (Mutalla, Abou Zenima and Wadi Nukhul), this can be explained by reduced sedimentation in the deeper sections during the transgressive interval and/or higher P_{tot} input in shallower environments. In oxic marine environments Ni, Zn and Cu act as nutrients and may be present as soluble Ni(II), Zn(II) and Cu(II) cations or chlorides. Ni is present as a soluble Ni-carbonate (NiCO3), or associated with Zn and Cu adsorbed into organic matter (Calvert and Pedersen, 1996; Algeo and Maynard, 2004; Tribovillard et al., 2006). They may also be adsorbed onto particulate Fe–Mn-oxyhydroxides. The formation of Ni, Zn, and Cu complex compounds with OM accelerates removal from the water column and enriching sediments (Piper & Perkins, 2004). At Wadi Nukhul, these elements show the same enrichment trends with high values 10 cm above the PEB (Fig. 7), coeval with increasing phosphorus and carbonate contents.

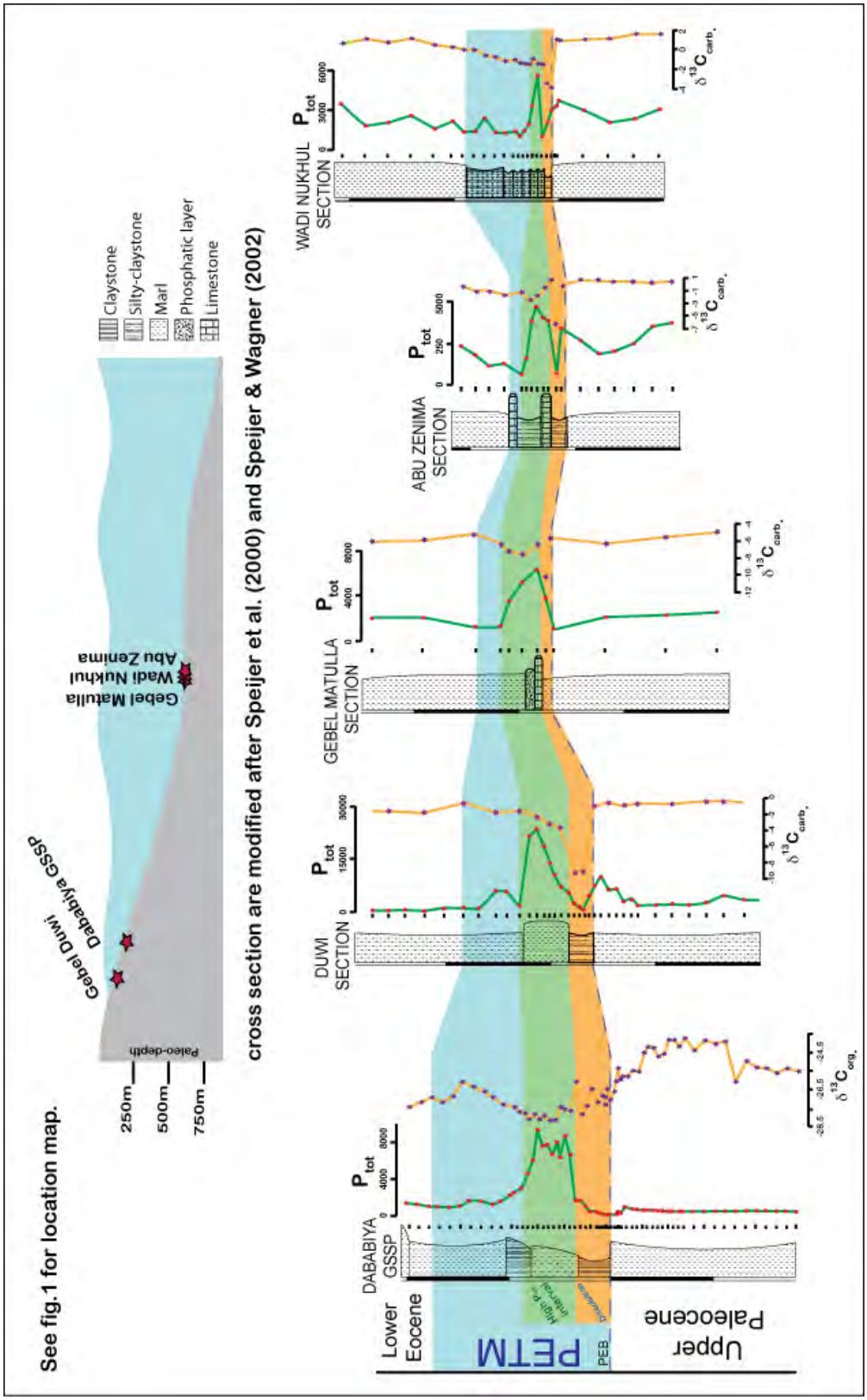

***Figure 9**. Correlation of Wadi Nukhul with Dababiya GSSP, Gebel Duwi section Abu Zenima section and Gebel Matulla section based on both $\delta^{13}C_{car}$ and P_{tot} contents. Note decrease in thickness and P_{tot} content toward the distal environment.*

Moreover, elevated Ni/Al, Zn/Al and Cu/Al ratios suggest high organic matter content, although organic matter is largely oxidized/removed due to strong weathering (Speijer & Wagner, 2002). However, increased productivity is apparent above the $\delta^{13}C_{org}$ negative excursion, reflecting a gradual recovery.

5. CONCLUSIONS

Detailed geochemical analyses of the Wadi Nukhul section in the SW Sinai and comparison with other sections in Egypt reveals the climatic and environmental changes across the P/E transition and PETM interval. The PEB at the Wadi Nukhul section shows: (1) an abrupt negative shift in $\delta^{13}C_{carb}$ followed by $\delta^{13}C_{org}$ shift (–6‰ and –2‰ respectively) which suggests a hiatus including the earliest Eocene, this short hiatus is observed in the basal part of the PETM at Wadi Nukhul and also in most of the PETM section in Egypt except in the Dababiya GSSP (2) a strong and persistent decrease in $\delta^{15}N_{org}$ to ~0‰, reflecting significant bacterial activity such as sulfur reducing and cyanobacteria activities as indicated by low N isotope and the presence of EPS-like structures within the PETM interval; (3) a significant increase in P_{tot} content just above the negative isotopes excursion, indicates increased primary productivity induced by increasing nutrient input linked with intense weathering period and prevailing of oligotrophic conditions, (4) a decrease in carbonate content which may be linked to the dissolution and/or the dilution of carbonate due to high detrital input, (5) the presence of small framboidal pyrite (less than 5μm) coincident with high V content and negative Mn*; all are strong evidences of rising dysoxic to suboxic conditions (6) The topmost Paleocene experienced a period of aridity as indicated by the presence of both sepiolite and palygorskite followed by significant increase in kaolinite contents triggered by humid climatic conditions; then returning to semi-arid conditions in the topmost CIE of the PETM interval.

ACKNOWLEDGEMENTS: We thank T. Monnier and J. C. Lavanchy for technical support and carrying out different types of analyses (phosphorus and XRF analyses). Also, we thank P. Vonlanthen for his help during SEM analyses and A. Villars, for the preparation of thin sections. We deeply thank M. P. Bolle, for providing us samples of Gebel Mattula Abu Zenima and Duwi. We warmly thank B. Bomou, for his precious help with fieldwork. We gratefully acknowledge Prof. K. Föllmi for stimulating discussion during the preparation of this manuscript. We thank R. Speijer and an anonymous reviewer for their constructive and thorough comments. Work funded by the Egyptian Ministry of Higher Education (Mission No.001/013/104).

REFERENCES

Adatte, T., Stinnesback, W. & Keller, G. 1996. Lithostratigraphic and mineralogic correlations near K/T boundary clastc sediments in northern Mexico: Implication for origin and nature of deposition. *Geological Society of America*, special paper, v. 307, pp. 211-226.

Adatte, T., Keller G. & Stinnesbeck, W. 2002. Late Cretaceousto Early Paleocene climate and sea-level fluctuations, in Remane, J., et al., eds., Cretaceous-Paleogene transition in Tunisia. *Palaeogeography, Palaeoclimatology, Palaeoecology*, Special issue, v. 178, pp.165–196.

Agnini, C., Fornaciari, E., Rio, D., Tateo, F., Backman, J. & Giusberti, L. 2007. Responses of calcareous nannofossil assemblages, mineralogy and geochemistry to the environmental perturbations across the Paleocene/Eocene boundary in the Venetian Pre-Alps. *Marine Micropaleontology*, v. 63, pp.19–38.

Alegret, L., Ortiz, S. & Molina E., 2009. Extinction and recovery of benthic foraminifera across the Paleocene–Eocene Thermal Maximum at the Alamedilla section (Southern Spain). *Palaeogeography, Palaeoclimatology, Palaeoecology,* v.279, pp.186–200.

Algeo, T.J. & Maynard, J.B., 2004. Trace-element behavior and redox facies in core shales of Upper Pennsylvanian Kansas-type cyclothems. *Chemical Geology,* 206, 289–318.

Anbar, A.D., 2004. Molybdenum stable isotopes: observations interpretations and directions. *Review in Mineralogy and. Geochemistry,* v. 55, pp. 429–454.

Arthur M.A., Dean W. E & Pratt L. M., 1988. Geochemical and climatic effects of increased marine organic carbon burial at the Cenomanian-Turonian coundary. *Nature,* v. 335, pp.714-717.

Aubry, M.P., Ouda, K., Dupuis, Ch., Berggren, W.A., Van Couvering, J.A., & The Members Of The Working Group On The Paleocene/Eocene Boundary, 2007, The Global Standard Stratotype-Section and Point (GSSP) for the base of the Eocene Series in the Dababiya section (Egypt). *Episodes*, v. 30, pp. 271–286.

Bertrand, P., Shimmield, G., Martinez, P., Grousset, F., Jorissen, F., Paterne, M., Pujol, C., Bouloubassi, I., Buat Menard, P., Peypouquet, J.-P., Beaufort, L., Sicre, M.-A., Lallier- Verges, E., Foster, J.M., Ternois, Y. and other participants of the Sedorqua Program, 1996. The glacial ocean productivity hypothesis: the importance of regional temporal and spatial studies. *Marine Geology*, v. 130, pp. 1–9.

Bolle, M.P. & Adatte, T., 2001. Paleocene–Early Eocene climatic evolution in the Tethyan realm: clay mineral evidence. *Clay Mineralogy*, v. 36, pp. 249–261.

Bolle, M.-P., Tantawy, A.A., Pardo, A., Adatte, T., Burns, S.J. & Kassab, A., 2000. Climatic and environmental changes documented in the upper Paleocene to lower Eocene of Egypt. *Eclogae Geologicae Helvetiae*, v. 93, pp. 33–51.

Bralower, T.J., 2002. Evidence of surfacewater oligotrophy during the Paleocene–Eocene thermal maximum: nannofossil assemblage data from Ocean Drilling Program Site 690, Maud Rise, Weddel Sea. *Paleoceanography*, v.17, no. 2, pp. 1029–1042.

Bybell, L.M. & Self-Trail, J.M., 1997. Late Paleocene and early Eocene calcareous nannofossils from three boreholes in an onshore–offshore transect from New Jersey to the Atlantic continental rise. In: Miller, K.G., Snyder, S.W. (Eds.), Proc. Ocean Drill. Prog., Sci. Results, *vol. 150X. Ocean Drilling Program*, College Station, TX, pp.91

Callen, R.A. 1984. Clays of the palygorskite-sepiolite group: Depositional environment, age and distribution, in Singer, A., and Calan, E., eds. Palygorskite-Sepiolite: Occurences, genesis and uses. *Developments in Sedimentology,* v.37, pp. 1-37.

Calvert, S.E. & Pedersen, T.F., 1996. Sedimentary geochemistry of manganese: implications for the environment of formation of manganiferous black shales. *Economic Geology*, 91, 36–47.

Chamley, H. 1989. Clay sedimentology, 623 pp. (*Springer-Verlag, Berlin*).

Chamley, H. 1998, Clay mineral sedimentation in the Ocean in Paquet, H., and Clauer, N., eds., *Soils and sediments (mineralogy and geochemistry)*. Berlin, Springer-Verlag, pp. 269–302.

Cruse, A.M. & Lyons, T.W., 2004. Trace metal records of regional paleoenvironmental variability in Pennsylvanian (Upper Carbonaferous) black shales. *Chemical Geology*, v. 206, pp. 319–345.

Cullers, R. L., 2002. Implications of elemental concentrations for provenance, redox conditions, and metamorphic studies of shales and limestones near Pueblo, CO, USA. *Chemical Geology*, v.191, pp. 305-327.

DeConto R, Galeotti S, Pagani M, Tracy DM, Pollard D, Beerling DJ. 2010. Hyperthermals and orbitally paced permafrost soil organic carbon dynamics. *Presented at AGU Fall Meet., Dec. 13–17*, San Francisco (Abstr. PP21E-08)

Dickens, G., 2001. Carbon addition and removal during the Late Palaeocene Thermal Maximum: basic theory with a preliminary treatment of the isotope record at ODP Site 1051, Blake Nose, in: D. Kroon, R.D. Norris, A. Klaus (Eds.), Western North Atlantic Palaeogene and Cretaceous Palaeoceanography, *Geological Society of London.* Special Pub, v.183, pp. 293–305.

Dickens, G. R., O'Neil, J. R., Rea, D. K. & Owen, R. M., 1995. Dissociation of oceanic methane hydrate as a cause of the carbon isotope excursion at the end of the Paleocene, *Paleoceanography*, v.10, pp. 965-971.

Dickens G. 2011. Down the Rabbit Hole: toward appropriate discussion of methane release from gas hydrate systems during the Paleocene-Eocene thermal maximum and other past hyperthermal events. *Climate of the Past*, v.7, pp. 831–846.

Dupuis, C., Aubry, M.-P., Steurbaut, E., Berggren, W.A., Ouda, K., Magioncalda, R., Cramer, B.S., Kent, D.V., Speijer, R.P., Heilmann-Clausen, C., 2003. The Dababiya Quarry section: lithostratigraphy, clay mineralogy, geochemistry and paleontology. In: Ouda, K., Aubry, M.-P. (Eds.), The Upper Paleocene–Lower Eocene of the Upper Nile Valley: Part 1.Stratigraphy: *Micropaleontology*, v. 49, pp. 41–59.

Ernst, S.R., Guasti, E., Dupuis, C. & Speijer, R.P., 2006. Environmental perturbation in the southern Tethys across the Paleocene/Eocene boundary (Dababiya, Egypt): foraminiferal and clay mineral records. *Marine Micropaleontology*, v. 60, no.1, pp. 89–111.

Gibbs, S.J., Bralower, T.J., Bown, P.R., Zachos, J.C.& Bybell, L.M., 2006. Shelf and open-ocean calcareous phytoplankton assemblages across the Paleocene–Eocene thermal maximum: implication for global productivity gradients. *Geology*, v. 34, no. 4, pp. 233–236.

Grosjean, E., Adam, P., Connan, P. & Albrecht, P. 2004. Effects of weathering on nickel and vanadyl porphyrins of Lower Toarcian shale of the Paris basin. *Geochemical Cosmochemical Acta*, v.68, pp. 789–804.

Handley, L., Pearson, P., McMillan, I.K. & Pancost, R.D. 2008. Large terrestrial and marine carbon and hydrogen isotope excursions in a new Paleocene/Eocene boundary section from Tanzania. *Earth and Planetary Science*, v. 275, pp. 17–25.

Harnois, L., 1988, The CIW index: a new Chemical Index of Weathering. *Sedimentary Geology, v.*55, pp. 319-322.

Hoffman, P.F., Kaufman, A.J., Halverson, G.P. & Shrag, D.P. 1998. A Neoproterozoic snowball earth. *Science*, v. 281, pp. 1342–1346.

Jarvis, I., Burnett, W.C., Nathan, Y., Almbaydin, F.S.M., Attia, A.K. M., Castro, L.N., Flicoteaux, R., Hilmy, M.E., Husain, V.,Qutawnnah, A.A., Serjani, A. & Zanin, Y.N., 1994. Phosphorite geochemistry: state of the art and environmental concerns. *Eclogae Geologica Helvetica, v.*87, pp. 643–700.

Joachimski, M.M., Pancost, R.D., Freeman, K.H., Ostertag-Henning, C. & Buggisch, W. 2002. Carbon isotope geochemistry of the Frasnian–Famennian transition. *Palaeogeography, Palaeoclimatology, Palaeoecology*, v.181, pp. 91–109.

John, C. M., Bohaty, S. M., Zachos, J. C., Gibbs, S., Brinkhuis, H., Sluijs, A. & Bralower, T., 2008, Impact of the Paleocene-Eocene thermal maximum on continental margins and implications for the carbon cycle in near-shore environments: *Paleoceanography*, v. 23, p. PA2217.

Karpoff, A.M., Lagabrielle, Y., Boillot, G. & Girardeau, J. 1989. L'authigenèse océanique de palygorskite par halmyrolyse de péridotites serpentinisées (Marge de Galice); ses implications geéodynamiques, Comptes Rendus de l'Académie des Sciences, Série 2, Mécanique, Physique, Chimie, Sciences de l'Univers: Montrouge, France, Gauthier-Villars, *Sciences de la Terre*, v.308, no. 7, pp. 647–654.

Katz, M., Cramer, B., Mountain, G., Katz S. & Miller, K. 2001. Uncorking The Bottle: What Triggered The Paleocene/Eocene Thermal Maximum Methane Release? *Paleoceanography*, v.16, no.6, pp.549–562

Katz, M. E., D. R. Katz, J. D. Wright, K. G. Miller, D. K. Pak, N. J. Shackleton, & E. Thomas (2003), Early Cenozoic benthic foraminiferal isotopes: Species reliability and interspecies correction factors, *Paleoceanography*, v.18, no. 2, p.1024.

Kennett, J. P., Cannariato, K. G., Hendy, I. L. & Behl R. J. 2002. Methane Hydrates in Qua- ternary Climate Change: *The Clathrate Gun Hypothesis*, Special Publication,. 54, 224 pp., AGU, Washington, D. C.

Kurtz AC, Kump LR, Arthur MA, Zachos JC, Paytan A. 2003. Early Cenozoic decoupling of the global carbon and sulfur cycles. *Paleoceanography*, v.18, p.1090

Kübler, B., 1987. Cristallinité de l'illite: méthode normalisées de préparation de mesure, méthode automatique normalisées de mesure. *Cahiers de l'Institut de Géologie*, Series AX n°3.1 and 3.2.

Lu G., Adatte T., Keller G. & Ortiz N.1998. Abrupt climatic, oceanographic and ecologic changes near the Paleocene-Eocene transition in the deep Tethys basin: The Alamedilla section, southern Spain. *Ecologica Geologica Helvatica*, v.91, pp. 293 306.

Lyons, T.W., Werne, J.P., Hollander, D.J.& Murray, R.W. 2003. Contrasting sulfur geochemistry and Fe/Al and Mo/Al ratios across the last oxic-to-anoxic transition in the Cariaco Basin, Venezuela. *Chemical Geology*, v.195, pp.131–157.

Moore E.A. & Kurtz A.C. 2008. Black carbon in Paleocene-Eocene boundary sediments: a test of biomass combustion as the PETM trigger. *Palaeogeography, Palaeoclimatology, Palaeoecology*, v.267, pp.147–52

Mort, H.P., Adatte, T., Föllmi, K.B., Keller, G., Steinmann, P., Matera, V., Berner, Z. & Stüben, D. 2007b. Phosphorus and the roles of productivity and nutrient recycling during oceanic anoxic event 2. *Geology*, v. 35, pp. 483-486.

Mort, H., Adatte, T., Keller, G., Bartels, D., Föllmi, K., Steinmann, P., Berner, Z. & Chellai, E.H. 2008. Organic carbon deposition and phosphorus accumulation during Oceanic Anoxic Event 2 in Tarfaya, Morocco. *Cretaceous Research*, v.29, pp.1008-1023.

Murphy, A.E., Sageman, B.B., Hollander, D.J., Lyons, T.W. & Brett, C. E. 2000b. Black shale deposition and faunal overturn in Devonian Appalachian basin: clastic starvation, seasonal water-column mixing, and efficient biolimiting nutrient recycling. *Paleoceanography*, v.15, pp. 280–291.

Mutterlose, J., Linnert, Ch. & Norris, R., 2007. Calcareous nannofossils from the Paleocene– Eocene Thermal Maximum of the equatorial Atlantic (ODP Site 1260B): evidence for tropical warming. *Marine Micropaleontology*, v.65 no.1–2, pp.13–31.

Nesbitt, H.W. & Young, G.M., 1984. Prediction of some weathering trends of plutonic and volcanic rocks based on thermodynamic and kinetic considerations. *Geochemica et Cosmochemica Acta*, v. 48, pp. 1523-1534.

Nesbitt H.W.& Young G.M. 1989. Formation and diagenesis of weathering profiles. *Journal of Geology*, v.97, pp.129-147.

Pardo, A., Keller, G., Molina, E. & Canudo, J. 1997. Planktic foraminiferal turnover across the Paleocene-Eocene transition at DSDP Site 401, Bay of Biscay, North Atlantic. *Marine Micropaleontology*, v.29, no.2, pp.129-158.

Parker, A., 1970, An index of weathering for silicate rocks. *Geological Magazine*, v.107, pp. 501–504.

Piper, D.Z. & Perkins, R.B. 2004. A modern vs. Permian black shale— the hydrography, primary productivity, and water-column chemistry of deposition. *Chemical Geology*, v. 206, pp. 177–197.

Price, J.R. & Velbel, M.A. 2003. Chemical weathering indices applied to weathering profiles developed on heterogeneous felsic metamorphic parent rocks. *Chemical Geology*, v. 202, pp. 397–416.

Pujol, F., Berner, Z. & Stüben, D. 2006. Chemostratigraphy of some European Frasnian- Famennian boundary key sections. *Palaeogeography, Palaeoclimatology, Palaeoecology*, v.240, pp. 120–145.

Riquier, L., Tribovillard, N., Averbuch, O., Devleeschouwer, X. & Riboulleau, A. 2006. The Late Frasnian Kellwasser horizons of the Harz Mountains (Germany): two oxygen-deficient periods resulting from contrasting mechanisms. *Chemical Geology v. 233, pp.137-155*.

Robert, C. & Chamley, H., 1991. Development of Early Eocene warm climates, as inferred from clay mineral variations in oceanic sediments. *Palaeogeography, Palaeoclimatology, Palaeoecology*, v.89, pp. 315–331.

Romein, A. J. T., 1979. Lineages in early Paleogene calcareous nannoplankton. *Utrecht Micropaleontology Bulletin*, v.22, p.231.

Sageman, B.B. & Lyons, T.W. 2003. Geochemistry of fine-grained sediments and sedimentary rocks, in Holland, H.D., and Turekian, K.K., eds., *Treatise on Geochemistry*: Amsterdam, Elsevier, Chapter 7.06.

Schmitz, B., Asaro, F., Molina, E., Monechi, S., von Salis, K. and Speijer, R. P., 1997a. High-resolution iridium, δ13C, δ18O, foraminifera and nannofossil profiles across the latest Paleocene benthic extinction event at Zumaya, Spain. *Palaeogeography, Palaeoclimatology, Palaeoecology*, v. 133, pp. 49-68.

Sluijs, A., Schouten, S., Pagani, M., Woltering, M., Brinkhuis, H., Sinninghe Damsté, J.S., Dickens, G.R., Huber, M., Reichart, G.J. & Stein, R. 2006. Subtropical Arctic Ocean temperatures during the Palaeocene/Eocene thermal maximum. *Nature,* v.441, pp. 610–613.

Soliman, M.F., Ahmed, E., Kurzweil, H., 2006. Geochemistry and mineralogy of the Paleocene/Eocene boundary at Gabal Dababiya (GSSP) and Gabal Owaina sections, Nile Valley, Egypt. *Stratigraphy, v.3*, pp. 31–52.

Speijer, R.P., Schmitz, B. & Luger, P. 2000. Stratigraphy of late Palaeocene events in the Middle East: Implications for low to middle-latitude successions and correlations. *Journal of the Geological Society,* London, v. 157, pp. 37-47.

Speijer, R., & Wagner, T., 2002, Sea-level changes and black shales associated with the late Paleocene thermal maximum: Organic-geochemical and micropaleontologic evidence from the southern Tethyan margin (Egypt-Israel): *Geological Society of America* Special Paper, v. 356, pp. 533–549.

Tantawy, Abdel Aziz A.M., 2006. Calcareous nannofossils of the Paleocene-Eocene transition at Qena Region, Central Nile Valley, Egypt. *Micropaleontology*, v. 52, no. 3, pp.193-222.

Tribovillard, N., Algeo, J., Lyons, T. & Riboulleau, A. 2006. Trace metals as palaeoredox and palaeoproductivity proxies: An update. *Chemical Geology,* v.232, pp.12–32.

Tyrell, T. 1999. The relative influences of nitrogen and phosphorus on oceanic primary production. *Nature, v.*400, pp. 525–531.

Weaver, C.E. 1989. Clays, muds, and shales. *Developments in sedimentology*, v. 44, 819 p.

Weijers, J.W.H., Schouten, S., Sluijs, A., Brinkhuis, H. & Sinninghe Damsté, J.S. 2007. Warm arctic continents during the Palaeocene–Eocene thermal maximum. *Earth Planet Science Letter,* v.261, pp. 230–238.

Westerhold T., Röhl U., McCarren H. & Zachos J. 2009. Latest on the absolute age of the Paleocene–Eocene Thermal Maximum (PETM): New insights from exact stratigraphic position of key ash layers + 19 and – 17. *Earth and Planetary Science Letters*, v.287, no. 3–4, pp. 412–419.

Zachos, J.C., Röhl, U., Schellenberg, S.A., Sluijs, A., Hodell, D.A., Kelly, D.C., Thomas, E., Nicolo, M., Raffi, I., Lourens, L.J., McCarren, H. & Kroon, D., 2005. Rapid acidification of the ocean during the Paleocene–Eocene Thermal Maximum. *Science, v.* 308, pp. 161–1611.

Zachos, J.C., Schouten, S., Bohaty, S., Quattlebaum, T., Sluijs, A., Brinkhuis, H., Gibbs, S.J.& Bralower, T.J. 2006. Extreme warming of mid-latitude coastal ocean during the Paleocene–Eocene Thermal Maximum: inferences from TEX86 and isotope data. *Geology*, v.34, pp.737–740.

CHAPTER III

A. THE PALEOCENE-EOCENE GSSP AT DABABIYA, EGYPT - REVISITED

HASSAN KHOZYEM[1,3], THIERRY ADATTE[1], GERTA KELLER[2], , ABDEL AZIZ TANTAWY[3] AND JORGE E. SPANGENBERG[1]

[1]Institut de Science de la Terre (ISTE), Université de Lausanne, Switzerland

[2]Department of Geosciences, Princeton University, Guyot Hall, Princeton, NJ 08544, USA

[3]Departement of Geology Faculty of science, Aswan University, Aswan, Egypt.

B. NEW GEOCHEMICAL CONSTRAINTS ON THE PALEOCENE-EOCENE THERMAL MAXIMUM: DABABIYA GSSP, EGYPT

HASSAN KHOZYEM[1,3], THIERRY ADATTE[1], GERTA KELLER[2], , ABDEL AZIZ TANTAWY[3], JORGE E. SPANGENBERG[1] AND ALEXY ULIANOVE

[1]Institut de Science de la Terre (ISTE), Université de Lausanne, Switzerland

[2]Department of Geosciences, Princeton University, Guyot Hall, Princeton, NJ 08544, USA

[3]Departement of Geology Faculty of science, Aswan University, Aswan, Egypt.

A. THE PALEOCENE-EOCENE GSSP AT DABABIYA, EGYPT - REVISITED[1]

Abstract. We investigated the Paleocene-Eocene boundary GSSP (Dababiya quarry) near Luxor, Egypt, in two nearby (25m and 50m) successions based on high-resolution biostratigraphy, lithostratigrapy, mineralogy and geochemistry. Results confirm the many positive aspects of the Dababiya GSSP but also show potentially serious and limiting factors: 1) the GSSP is located in the deepest part of a ~200 m wide submarine channel, which limits its use as global type section. 2) Some lithologic units identified at the GSSP are absent or thin out and disappear within the channel and beyond. 3) The P-E boundary is placed at the base of a clay layer above an erosion surface with variable erosion of latest Paleocene and earliest Eocene sediments. 4) The current definition of the P-E boundary as marked by the abrupt onset of the carbon isotope excursion at the base of a clay layer is not supported at the GSSP because 50m to the left the excursion begins gradually 60cm below the P-E boundary and reaches minimum values in the boundary clay. With awareness of these limiting factors and recognition of the gradual onset of the PETM excursion the GSSP can contribute significantly to a more complete understanding of this global warm event.

1. INTRODUCTION

The Paleocene-Eocene Thermal Maximum (PETM) at ~55.9 Ma is one of the most important climatic event of the Cenozoic accompanied by a major $d^{13}C$ shift, sudden increase in temperature, diversification in planktic foraminifera and extinction in benthic foraminifera, followed by diversification and migration of modern mammals (e.g., Kennett and Stott, 1991; Zachos et al., 2001, 2003, 2005; Westerhold et al 2009; Alegret at al., 2005; Alegret and Ortiz 2007; Berggren and Ouda 2005; Lu and Keller 1995 and Pardo et al., 1999). McInerney and Wing (2011) summarized the scenarios proposed to explain the PETM including wildfires as a result of burning peat and exposed coal deposits in a dry climate of the Paleocene. Others proposed injection of hydrothermal bodies into organic-rich mudstones of Cretaceous-Paleocene age in the North Atlantic resulting in thermogenic methane release (Svensen et al., 2010; Westerhold et al. 2009), or melting of methane-rich permafrost (DeConto et al. 2010).

Methane release from clathrates is currently the most commonly cited scenario for the PETM event. Methane clathrates are stored along the continental margin under stable conditions high pressure and relatively low temperatures. Any change in the physico-chemical conditions of the oceans can result in methane release, including changes in ocean circulation (Dickens et al. 1995), decreased pressure resulting from slope failure (Katz et al. 1999), and change in bottom water temperature due to changes in thermohaline circulation (Bice and Marotzke 2002). On a global scale most studies show an abrupt negative $\delta^{13}C$ shift linked to an abrupt increase in temperature as result of a massive input of greenhouse gases upsetting the carbon cycle in marine and terrestrial ecosystems (Zachos et al., 2001, 2005; Dickens et al., 1995, 2001; Kennett

[1] ***Hassan Khozyem, Thierry Adatte, Gerta Keller, Abdel Aziz Tantawy and J.E. Spangenberg, 2013, The Paleocene-Eocene Gssp at Dababiya, Egypt – Revisited. Submitted to Episodes***

and Stott, 1991; Ernst et al., 2006; John et al., 2008).

In 2003 the International Commission for Stratigraphy (ICS) designated the Dababiya Quarry, located near the Dababiya village, Luxor, Egypt, as the Global Stratotype Section and Point (GSSP) for the Paleocene-Eocene (PE) boundary, which is also marked by the PETM event. The golden spike for the PE boundary was placed in the basal part of the Esna Formation (Dupuis et al., 2003; Aubry, et al., 2007) based on the following criteria: (1) the abrupt organic carbon isotope excursion (CIE), (2) extinction of deep-water benthic foraminifera (including *Stensioina beccariiformis*), (3) the transient occurrence of planktonic foraminifera (*Acarinina africana, A.sibaiyaensis, Morozovella allisonensis*) during the $\delta^{13}C$ excursion, (4) the transient occurrence of the *Rhomboaster* spp. – *Discoaster araneus* (RD) nannofossils assemblage, and (5) an acme of the dinoflagellate *Apectodinium.*

Based on these criteria the Dababiya section was considered the most complete and expanded Upper Paleocene to Lower Eocene sequence and representative of this boundary event globally (Dupuis et al., 2003; Aubry et al., 2007). A lithologic sequence of five distinct beds was identified and believed to be traceable throughout the area and possibly into neighboring countries (Speijer et al., 2000). Subsequently, it was recognized that the basal beds of the GSSP were deposited in a submarine channel with river discharge (Schulte et al., 2011, this study) placing some doubt on the completeness of this section and its value as a global stratotype. This study further evaluates this stratotype section based on (1) the nature and completeness of the sedimentary record, depositional environment and high-resolution biostratigraphy, (2) the nature of the $\delta^{13}C_{Carb}$ and $\delta^{13}C_{org}$ records, and (3) the climate changes before, during and after the PETM event.

2. METHODS

The designated Dababiya GSSP outcrop, which has the most expanded sedimentary record, is not available for sampling because of its limited lateral exposure to a just a few tens of meters. Permission was granted to sample two sections at 50m to left (LSS) and 25m to the right (RSS) of the GSSP (Fig. 1). A total of 102 samples were collected at 2cm, 5cm, and 10cm sample spacing spanning the Upper Paleocene to Lower Eocene interval.

Biostratigraphy: For foraminiferal analysis about 100gr sediment (from the left side section) was processed per sample by standard methods (Keller et al., 1995). Shell preservation is excellent in carbonate-rich intervals but poor to absent in the PETM excursion interval. Biostratigraphic analysis was performed on >63 mm and 38-63 mm size fractions with quantitative counts of ~300 specimens picked and mounted on cardboard slides for a permanent record and the remaining sample residue searched for rare and zone-defining index species. *For calcareous nannofossils s*amples were processed by smear slide preparation from raw sediment samples as described by Perch-Nielsen (1985). The calcareous nannofossils were observed with the light microscope at a magnification of 1000×. The taxonomy used is described in Aubry (e.g. 1999) and Perch-Nielsen (1985).

Geochemical and mineralogical analyses: For each sample 25gr of sediment was cleaned and powdered in an agate mortar. After each sample the agate mortar was cleaned three times with deionised water and once with ethanol, and then air-dried to avoid sample contamination. Powdered samples were analysed for bulk rock mineralogy and stable isotopes ($\delta^{13}C_{car}$, $\delta^{13}C_{org}$) at the Institute of Earth Sciences and Environments (ISTE) at Lausanne University, Switzerland.

For XRD mineralogy, whole rock and clay mineral analyses, samples were prepared following the procedures of Kübler (1987) and Adatte et al. (1996).

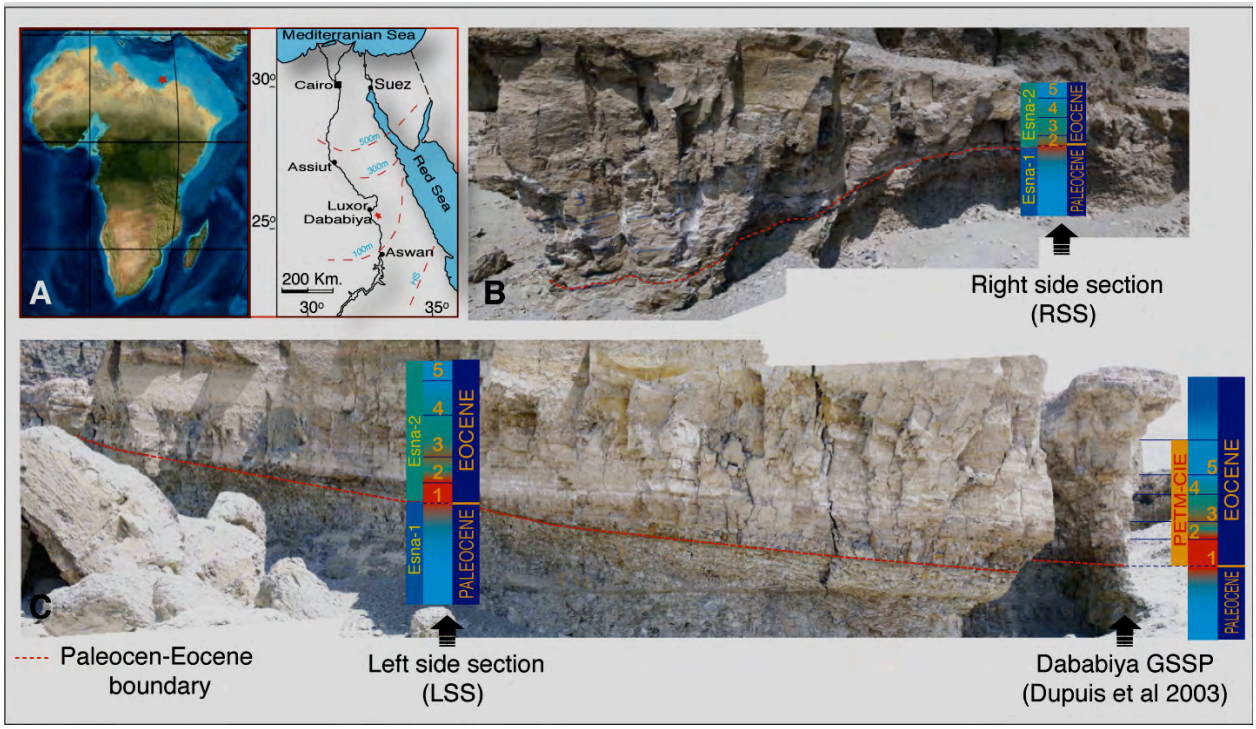

Figure 1. *A: Location of the Dababiya GSSP. B&C: Field photographs show the lithology across the 25 m from the GSSP to the right side section (RSS) and the 50 m to the left side section (LSS). Note the sharp thinning out of the sedimentary units to the right and more gradual thinning out to the left of the GSSP marks a channel deposit.*

The semi-quantification of whole-rock mineralogy is based on XRD patterns of random powdered samples by using external standards with an error margin between 5 and 10% for the phyllosilicates and 5% for grain minerals.

3. GEOLOGIC SETTING and LITHOSTRATIGRAPHY

The Dababiya GSSP section is located on the eastern side of the upper Nile Valley 35 km southeast of Luxor City (25° 30` N, 32°31` Fig.1). Four lithostratigraphic formations (Fm) are exposed in the area: the Dakhla Fm. at the base is a greenish calcareous shale, above is the marly limestone to chalk of the Tarawan Fm., followed by the green-gray to dark-gray shale of the Esna Fm. and ending at the top with the limestones or flint of the Thebes Fm. Dupuis et al. (2003) subdivided the Esna Fm. into three main units (Esna-1, Esna-2, and Esna-3) based on carbonate contents. Only Esna-1 and Esna-2 are exposed at the GSSP (Figs. 2, 3). The P/E boundary is placed in the lower part of the Esna Fm. between Esna-1 and Esna-2, about 7m above the Tarawan Formation. Five distinct beds in Esna-2 mark the GSSP PETM interval (Dupuis et al., 2003). At the base of Esna-2, Bed-1 consists of 0.63m of dark laminated, non-calcareous clay with a few phosphatic coprolites at the base. The overlying Bed-2 consists of 0.5m of brown shale with coprolites and low carbonate content. Bed-3 is a 0.84m-thick shale, cream-colored, laminated and phosphatic. Bed-4 is a 0.71m-thick gray shale with high carbonate content, and Bed-5 consists of 1m-thick grey marl to marly limestone (Fig. 2).

At 50m to the left of the GSSP the Dababiya left side section (LSS) was sampled. The section consists of the late Paleocene marl to marly shale of Esna-1, a well-defined sequence boundary (SB) and the overlying early Eocene Esna-2 units (Figs. 2, 3B). Esna-2 units are significantly reduced to the left and right sides from the GSSP location reflecting the submarine channel morphology. Following Dupuis et al. (2003) we divide Esna-2 into five beds with the following thicknesses and lithological characteristics: Bed-1 (0.32m) and Bed-2 (0.48m) consist of slity claystone with anhydrite layers. Bed-3 (0.24m) is a silty marl with phosphatic nodules and anhydrite. Bed-4 (1.0m) consists of marl to marly limestone (Fig. 2). Only the basal 5cm was recovered from Bed-5.

At 25m to the right of the GSSP the Dababiya right side section (RSS) was sampled with the same lithologies as at the LSS, except that Bed-1 is absent and possibly also the lower part of Bed-2, which is only 0.24m thick (Fig. 3B), as also suggested by mineralogic data including the absence of one of the four anhydrite layers present in LSS (Fig. 2, discussed below). Bed-3 (0.4m) consists of silty clay with phosphatic nodules, Bed-4 (0.6m) is marl and Bed-5 consists of a 0.4m thick marly limestone (Fig. 2).

4. RESULTS

4.1. Bulk rock mineralogy

At Dababiya LSS, bulk rock components in the interval below the PETM (samples 1 to 27) indicate marls with a low detrital index (DI 1.15) and average 42.70% calcite, 40.65% phyllosilicates, 6.93% quartz, 0.37% anhydrite (Ca-apatite is absent, Fig. 2). The sequence boundary (SB) marks the base of the PETM and a sharp decrease in calcite (5.44%) coincides with increased phyllosilicate (57.74%), quartz (8.21%), anhydrite (7.09%), and Ca-apatite (7.48%). The detrital index is relatively high (DI 13). Also present are goethite (1.64%), K (1.76%) and Na feldspar (3.04%).

In Esna-2 three distinct intervals mark Beds 2-5. Bed-1 to base Bed-2 (samples 29-39) shows an abrupt increase in phyllosilicate (64.77%), quartz (16.75%), goethite (1.26%), and anhydrite (11.7%) (Fig. 2). In contrast, K- and Na- feldspar are low and calcite nearly zero (0.82%). Low Ca-apatite (0.56) may be reworked from the underlying sediments. In the middle of Bed-2 (samples 40-42), sharply increased calcite (34.48%) correlates with decreased other bulk rock contents and disappearance of Ca- apatite.

Upper Bed-2 and Bed-3 (samples 43-50) contain maximum Ca-apatite (25.56%) coincident with increasing anhydrite and decreasing other minerals, though calcite remains relatively high (24.27%). Bed-4 shows the return to marl composition (average: calcite 49.93%, phyllosilicate 33.2%, Ca-apatite 5.81%, quartz 5.54%, anhydrite 1.08%).

RSS is similar to LSS except that Bed-1 and the lower part of Bed-2 are missing (Fig. 2). Below the P/E boundary marls contain relatively high phyllosilicate (38.76), and calcite (49.74%) and low quartz (5.34%). An abrupt change at the P/E boundary (Bed-2, sample 21) shows increased phyllosilicate (57.09%) and quartz (17.35%), and sharply decreased calcite (1.64%). From the upper Bed-2 into the middle of Bed-3 (samples 22-31) calcite increases to 35.27% and phyllosilicate and quartz decrease to 25.13% and 9.33%, respectively. In Beds 4 and 5 (samples 32-42, Fig. 2), all bulk rock components return to the marl composition observed below the P/E boundary.

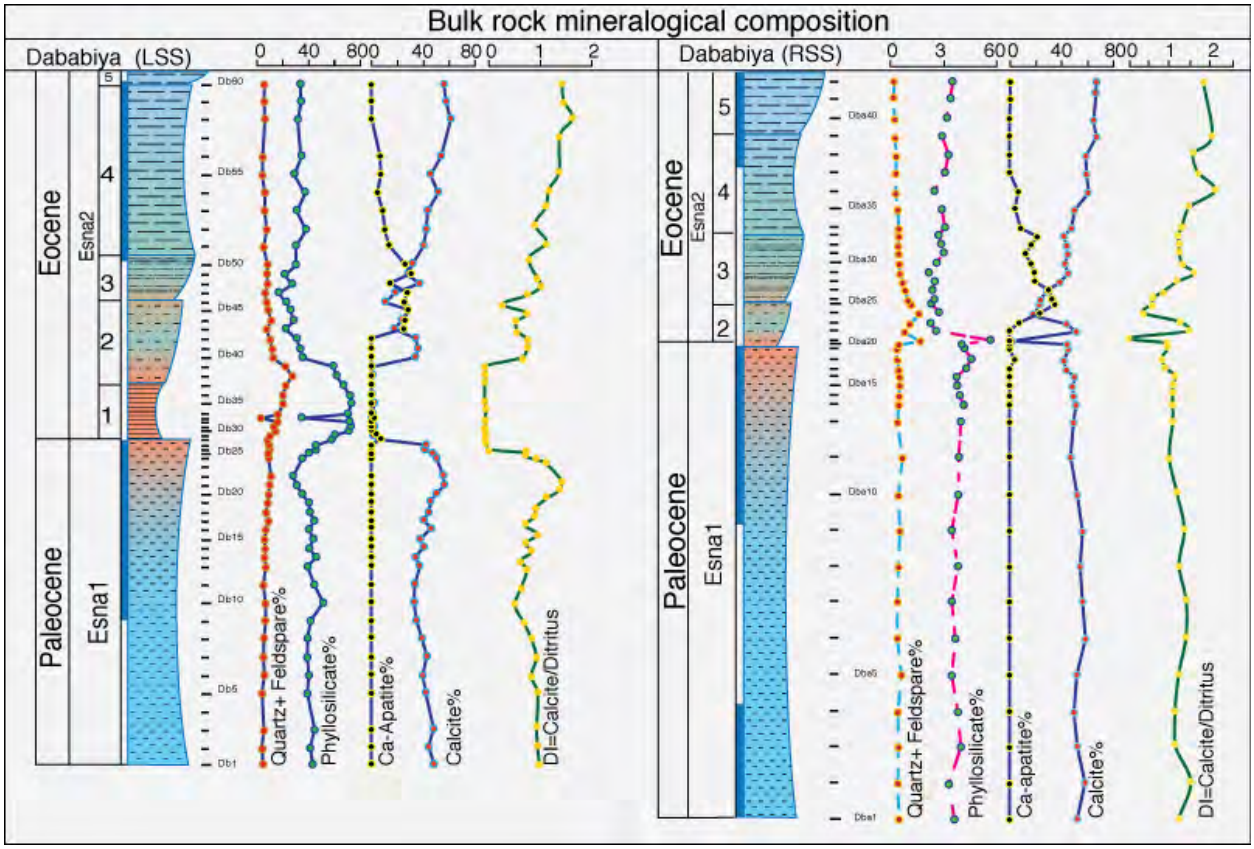

Figure 2. *Vertical distribution of bulk rock mineralogical data in the sections to the left (LSS) and right (RSS) of the GSSP. Note the differences in bulk rock compositions in these channel deposits reflect the absence of the lowermost Eocene sediments from the RSS.*

4.2. **Isotopes**

The Dababiya LSS and RSS were measured for bulk rock carbonate isotopes ($\delta^{13}C_{carb}$) and organic carbon isotopes ($\delta^{13}C_{org}$) and compared with the $\delta^{13}C_{carb}$ of the GSSP section (Dupuis et al., 2003). At LSS the upper Paleocene (samples 1-15) shows relatively steady $\delta^{13}C_{carb}$ values around 1‰ (except for a single point of 2.2‰, Fig. 3A). In the 50cm below the PE boundary (samples 16-27) $\delta^{13}C_{carb}$ values gradually decrease to -3.5‰. The PETM corresponding to Bed-1 and base of Bed-2 is carbonate poor yielding no $\delta^{13}C_{carb}$ data. From Bed-2 to the middle of Bed-3 $\delta^{13}C_{carb}$ values remain low at around -2‰, then rapidly increase to about 0‰ near the base of Bed-4 and reaching 0.39‰ at the top of the section (Fig. 3A).

Organic carbon isotopes show similar trends. In the lower part of Esna-1 $\delta^{13}C_{org}$ values are around -25.8‰, then increase to -23.8‰ (sample 8) and gradually decrease to the minimum values between -27 ‰ and -28 ‰ in the PETM interval (Beds-1 and 2). A gradual increase in Bed-3 reaches maximum values of -26.1‰ in the middle of Bed-4 (sample 55) then gradually decreases at the top of the section.

Dababiya RSS differs significantly from the LSS section due to the erosional disconformity that marks the P/E boundary (Fig. 3A). Paleocene values of both $\delta^{13}C_{org}$ and $\delta^{13}C_{carb}$ are steady through Esna-1 with a sharp negative excursion at the P/E boundary. This indicates that the gradual decrease observed in the LSS section is missing due to erosion as also indicated by the missing Bed-1 of the basal Paleocene. The $\delta^{13}C_{org}$ and $\delta^{13}C_{carb}$ values average of -28 and -2.41‰, respectively, above the erosion surface in Beds-2 and 3 (samples 20-31) and are similar

to the equivalent interval in the LSS. In Beds 4 and 5 $\delta^{13}C_{org}$ (-26.7) and $\delta^{13}C_{carb}$ (0.05‰) values return to nearly pre-P/E boundary values (-25.3 and 0.89‰).

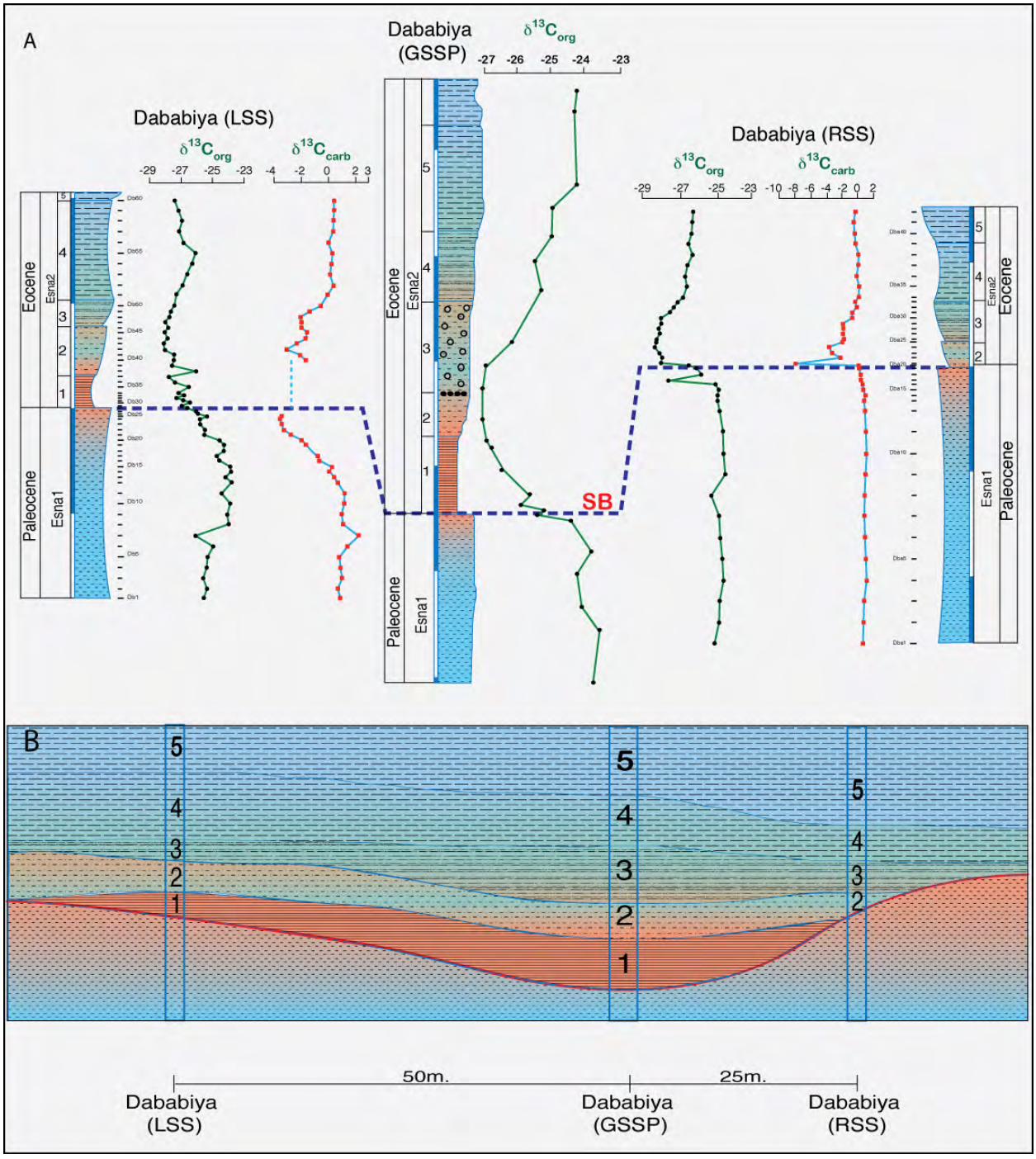

Figure 3: *A. Correlation of the LSS and the RSS with the published Dababiya GSSP (Dupuis et al., 2003) based on both organic Carbon isotopes, and new data obtained for inorganic carbon isotopes. Both $\delta^{13}C_{Carb}$ and $\delta^{13}C_{org}$ in the LSS show gradual decreases starting 60cm below the SB. The $\delta^{13}C_{Carb}$ CIA-minimum coincides with the SB whereas the $\delta^{13}C_{org}$ CIA-minimum is in the upper third of bed-2. B. Diagram illustrating the lateral disappearance of beds 1 and 2 on either sides of the main GSSP marks deposition in asymmetric channel. See photo illustration in Fig. 1B,C.*

4.3. **Biostratigraphy**

Planktic foraminiferal and calcareous nannofossil biostratigraphy of the more complete Dababiya LSS shows major turnovers across the PETM interval (Fig. 4). Planktic foraminifera span biozones P4c, P5, E1 and E2 with an estimated time span of 2 m.y. (54.5-56.5Ma, Olsson et al., 1999; Pearson et al., 2006). Zone P4c marks the base of the section (samples 1-12) as indicated by the disappearance of the index species *Globanomalina pseudomenardii*. This assemblage is dominated by *Igorina tadjjikistanensis, Acarinina soldadoensis, Subbotina hornibrooki, Morozovella acuta and M. aequa*.

The interval from the extinction of *Gl. pseudomenardii* to the first appearance of *Acarinina sibaiyaensis* marks zone P5 and the top of the Paleocene. At Dababiya LSS this 62cm thick interval corresponds to the gradual decrease in δ^{13}Corg and δ^{13}Ccarb values, and experienced a 40% increase in species diversity (from 21 to 35 species) and decreased abundance of the dominant zone P5 species. Most common among the newly appearing species are *Igorina broedermanni, I. lodoensis, Globanomalina luxorensis, Gl. australiformis, Gl. chapmani, Gl. planoconica,* and *Morozoevella gracilis.*

Acarinina sibaiyaensis, which marks the base of zone E1, first appears just below the 42 cm thick barren clay interval of Bed-1 (samples 25-26). A good assemblage of the transient PETM fauna dominated by *A. sibaiyaensis* and *A. Africana* and the first appearances of *A. africana, Morozovella allisonensis,* and the zone E2 index species *Pseudohastigerina wilcoxensis* occurs in a 5 cm interval between the barren clay below and the slightly calcareous clay above (Fig. 4). The upper clay (35cm, upper Bed-2 and Bed-3 corresponds to the upper part of the PETM. Bed-4 contains a diverse and well-preserved zone E2 assemblage (*P. wilcoxensis* and *M. velascoensis*) dominated by *Planorotalites pseudoscitula, Morozovella acuta, I. lodoensis, I broedermanni, A. esnaensis, A. eshnehensis).* The return of this thriving assemblage coincides with the recovery of the $\delta^{13}C_{org}$ and $\delta^{13}C_{carb}$ values after the PETM.

The calcareous nannofossil assemblage is moderately diversified, and the preservation varies from poor to moderate, except for the dissolution interval (devoid of nannofossils) that spans Bed-1 and the lower part of Bed-2. Below the barren interval, nannofossil diversity averages about 16 species, whereas above it both abundance and diversity sharply decrease to about 8 species and dissolution resistant taxa dominate (e.g. *Discoaster, Coccolithus pelagicus*) along with reworked forms. Nannofossil Diversity increases gradually parallel to the CIE and reaches a maximum of 20 species at the base of Bed-5 (Fig. 4).

The calcareous nannofossil turnover spans subzones NP9a and NP9b (e.g., Martini, 1971; Okada and Bukry, 1980). The first appearance of *Discoaster multiradiatus* defines the base of Zones NP9 of Martini (1971) whereas *Fasciculithus bobbi* disappears consistently near the middle of subzone NP9a (sample 9) and *F. alanii* near the top (Fig. 4, Perch-Nielsen, 1985; Aubry, 1999). The diversity and abundance of representatives of the genus *Fasciculithus* decrease abruptly towards the PETM, become rare and disappear in the lowermost Eocene (NP9b). *Fasciculithus tonii* last occurs in the upper Bed-4 (sample Db57) and *F. tympaniformis* at the base of Bed-5 (sample 60), as also observed in the Atlantic, Pacific and Tethys oceans (Monechi et al., 2000; Raffi et al., 2005; Tantawy, 2006; Agnini et al., 2007).

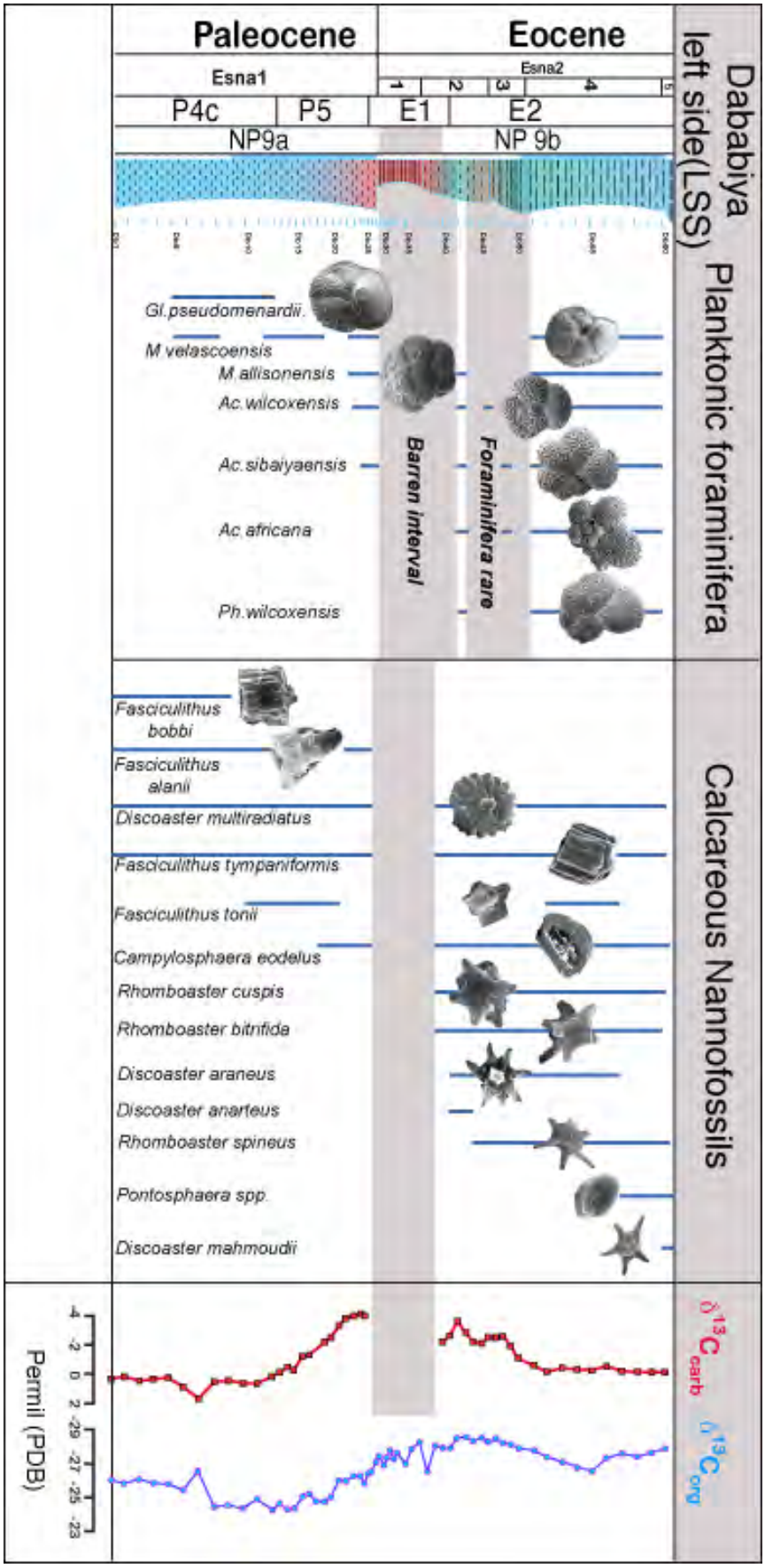

Figure 4. *Carbon isotopes ($\delta^{13}C_{org}$ and $\delta^{13}C_{carb}$) and selected species ranges of planktic foraminifera and calcareous nannofossil species at 50 m to the left of the Dababiya GSSP. Note that a reduction in species richness in the late Paleocene is offset by a few new species during the gradual decrease in carbon isotopes and this evolutionary trend increased during the gradual recovery in carbon isotopes in the early Eocene.*

The base of Subzone NP9b was defined based on the first appearances of *Campylosphaera eodelus* and *Rhomboaster* (Okada and Bukry, 1980), or alternatively the simultaneous first appearances of *R. calcitrapa*, *R. spineus*, *D. araneus* and *D. anartios* (Aubry et al., 2003).

At Dababiya the NP9a/NP9b transition coincides with the PETM dissolution interval, which is followed by the first appearance of *Rhomboaster cuspis* and *R. bitrifida* (sample 40), *D. araneus* and *D. anarteus* (sample 41), whereas *C. eodelus* appears earlier in NP9a (sample 18) and *R. spineus* later in NP9b (Fig. 4) as also observed in the southeast Atlantic (Agnini et al., 2007) and Kharga Oasis, Western Desert, Egypt (Tantawy 2006). Other taxa first appear above the dissolution interval, including poorly preserved *Pontosphaera plana* in the upper part of Bed-4 (sample 58) and *Discoaster mahmoudii* at the base of Bed-5 (sample 60, Fig. 4).

5. DISCUSSION & CONCLUSIONS

The most important criterion for any GSSP is a continuous sedimentation record. In the primary analysis leading to the designation of the Dababiya section as GSSP, the sedimentation record was considered expanded and complete (Dupuis et al., 2003; Ouda, 2003; Aubry et al., 2007). This conclusion was supported by an expanded and gradually changing carbon isotope curve across the PETM. Subsequently, Schulte et al. (2011) observed that deposition of the GSSP occurred in a submarine channel, which introduced some doubts as to the viability of Dababiya as a global representative of the PE boundary event. Our study confirms deposition in a submarine channel, but also determined significant lateral variations in lithology and mineralogy within 25m and 50m of either side of the GSSP suggesting erosion and/or non-deposition. We discuss these observations and their implications for the viability of Dababiya as GSSP.

5.1. How complete is the GSSP?

5.1.1. Lithostratigraphy

The Paleocene-Eocene boundary at the Dababiya GSSP is placed at a sequence boundary (SB) that marks a change in lithology from hemipelagic marine to sediments enriched in fluvial discharge (Schulte et al., 2011). This lithologic change is characterized by: (1) increased detrital components (quartz, phyllosilicates and feldspar) and decreased carbonate content. The latter may be linked to carbonate dissolution and/or dilution due to increased detrital input (Fig. 2). (2) The thickness of Bed-1 is variable: at the maximum in the main GSSP outcrop, reduced to half the thickness at 50m to the left (LSS) and absent at 25m to the right (RSS). (3) Above the sequence boundary, the change in the vertical distribution of the bulk rock compositions from the LSS to the RSS outcrops shows persistent increases in phyllosilicates and quartz, the presence of feldspar and minimum values in calcite (Fig. 2). The bulk rock composition at the RSS outcrop shows abrupt changes at the P/E boundary as quartz, feldspar, and phyllosilicates increase and calcite decreases within a 5cm thick interval above the SB. This abrupt change in the bulk rock composition marks the absence of lowermost Eocene sediments from the RSS outcrop due to erosion linked to the existing paleorelief. (4) Variation in Ca-apatite is another indicator of erosion and/or variable sedimentation. In the LSS outcrop Ca-apatite increased 60cm above the SB whereas in the RSS outcrop this increase is observed just above the SB. This suggests that at least 60cm is missing at the RSS compared with the LSS outcrop and about 80cm missing compared with the GSSP (including Bed-1 and part of Bed-2, Fig. 3, 3B).

Based on field observations and variations in bulk rock compositions, we conclude that the lower part of the Dababiya GSSP section (Bed-1 and Part of Bed-2) was deposited in a submarine channel. This channel extended at least 25m to right of the GSSP and about 150m to the left with maximum width of about 200m. The sequence boundary (SB) marks erosion and/or condensed sedimentation, which varies in the three outcrops as evident in the presence or absence of lithologic units particularly early Eocene Beds-1 and 2. The maximum depth of this channel-fill above the SB at the main GSSP outcrop is about 0.88m (Bed-1 to middle part of Bed-2) and missing at RSS, as also indicated by the absence of the 0.60m thick Ca-apatite rich interval of the LLS outcrop. In contrast, the LSS outcrop is more complete though condensed compared with the GSSP (Fig. 2).

5.1.2. **Isotope stratigraphy**

At Dababiya the carbon isotope records of three closely spaced sections over a distance of just 75m yield further confirmation of the variable erosion pattern at the GSSP location. Dupuis et al.'s (2003) $\delta^{13}C_{org}$ values for the Dabbabiya GSSP can be divided into three main parts: (1) a rapid decrease 10 cm below Bed-1 and the SB where the P/E boundary is placed followed by gradually decreasing values through Bed-1; (2) minimum values persist through Bed-2 into the lower 1/3 of Bed-3; (3) a gradual increase in Bed-3 to the middle of Bed-5 reaching background values (Fig. 3).

The two sections analyzed to the right and left of the GSSP show similarities and differences. The most comparable is the LSS outcrop where carbon isotope analysis permits the same subdivisions as the GSSP but with important differences. Most important is the gradual decrease in $\delta^{13}C_{Carb}$ and $\delta^{13}C_{org}$ in the uppermost Palaeocene spanning about 60cm below the SB (Fig. 3A). This latest Paleocene interval is not present at the GSSP or the RSS outcrops where both $\delta^{13}C_{org}$ and $\delta^{13}C_{Carb}$ curves shift abruptly at the SB. This suggests that a minimum 60 cm is missing at the top of the Paleocene at the GSSP and probably more at the RSS outcrop. Isotope stratigraphy also confirms the absence of the basal Eocene (Bed-1 and half of Bed-2) at the RSS outcrop. This is evident in the $\delta^{13}C_{Carb}$ values of the upper Bed-2 at LSS that mirror similar values in the upper Bed-2 directly overlying the SB horizon at the RSS outcrop. In the early Eocene $\delta^{13}C_{org}$ curves at LSS and GSSP are very similar with minor differences due to the lower sediment accumulation rate and higher sample resolution at LSS compared with the GSSP.

5.1.3. **Implications for the GSSP**

The idea of the GSSP record is to have a single locality and section were all the best characteristics of a given boundary event can be observed and taken as representative of coeval sequences worldwide. Ideally the GSSP should have a continuous sedimentation record with no discernable interruptions due to current erosion or tectonic disturbance, the fossil content should be abundant and well preserved and the lithology should have characteristic features that permit easy identification in the field at the GSSP as well as in coeval sequences globally. The Dababiya GSSP satisfies these qualifications in most parts, including excellent outcrops, well-preserved fossil records (except for the PETM clay layer), easily identifiable lithostratigraphic units (at least for the area), characteristic mineralogical and geochemical contents, and globally representative carbon isotope signals (Dupuis et al., 2003; Zachos et al., 2001). Based on all these characteristics, the Dababiya section was deemed to be the best choice for the Paleocene-Eocene boundary event and designated the GSSP (Aubry et al., 2007).

No GSSP is perfect and no single locality can be representative of all coeval sedimentary sequences globally. Some adjustments have to be made for local characteristics whether at the GSSP locality or elsewhere. The Dababiya GSSP is no exception. Our research based on lithostratigraphy, stable isotope stratigraphy and biostratigraphy demonstrates a few problems: a) the chosen GSSP is located in a submarine channel that is asymmetric and about 200m wide. b) The P/E boundary placed at the base of the clay layer is a sequence boundary that marks the channel along with variable erosion. c) The critical PETM Beds-1 to 4 are of varying thickness and/or absence due to erosion, including absence of the latest Paleocene at the GSSP and RSS outcrops and early Eocene erosion at RSS (Bed-1 to middle Bed-2. Fig. 3A) making long-distance correlation problematic even within the area let alone globally.

All these factors present some problems for the Dababiya GSSP, but how serious are they? When the two new sections (RSS, LSS) plus the GSSP are viewed in their lateral positions in the submarine channel (Fig. 3A, B), erosion at the sequence boundary is greatest (total of 1.2m) at the RSS outcrop encompassing both latest Paleocene and earliest Eocene. At the GSSP outcrop just 25m to the left erosion primarily affects the latest Paleocene (total of about 0.60m). At LSS just 50 m further to the left of the GSSP, erosion appears to be minimal as observed by the gradual change of the carbon isotope curves. However, the overall rate of sediment accumulation is highest at the GSSP, as would be expected with its location in the deepest part of an asymmetric submarine channel.

Erosion at the P/E sequence boundary is thus the most negative aspect of the GSSP. On the positive side erosion appears limited in some sections and the overall shape of the carbon isotope curves (both $\delta^{13}C_{Carb}$ and $\delta^{13}C_{org}$) show gradual changes approaching the P/E sequence boundary with minimum values reached in the clay layer and followed by a gradual increase to pre-PETM values. How common are these gradual $\delta^{13}C$ changes across the PETM? Although most PETM records show abrupt changes, more gradual long-term decreases in $\delta^{13}C_{Carb}$ and $\delta^{13}C_{org}$ were observed at ODP site 690 (Bains et al., 1999) and in pedogenic carbonate from Polecat Bench, Wyoming (Bowen et al., 2001). This suggests that the Dababiya GSSP may indeed be among the more complete and expanded records despite the SB erosion and can serve as reference section for the global record.

ACKNOWLEDGEMENTS

We are grateful to the Egyptian ministry of state for environmental affairs and the president of the International Committee of Stratigraphy (ICS) for providing the necessary permission and official access to the GSSP site for sampling. This study was conducted at the University of Lausanne. Funding was provided to HK by the Egyptian ministry of higher education (mission No.001/013/104). Partial support was received from the University of Lausanne and the US National Science Foundation NSF OISE-0912144.

REFERENCES

Adatte, T., Stinnesbeck, W., and Keller, G., 1996, Lithostratigraphic and mineralogic correlations near K/T boundary clastic sediments in northern Mexico: Implication for origin and nature of deposition: Geological Society of America, Special Papers, v. 307, pp. 211–226

Agnini, C., Fornaciari, E., Rio, D., Tateo, F., Backman, J., and Giusberti, L., 2007, Responses of calcareous nannofossil assemblages, mineralogy and geochemistry to the environmental perturbations across the Paleocene/Eocene boundary in the Venetian Pre- Alps: Marine Micropaleontology, v.63,

pp. 19–38.

Alegret, L., and Ortiz, S., 2007, Global extinction event in benthic foraminifera across the Paleocene/Eocene boundary at the Dababiya Stratotype section: Micropaleontology, v. 52, no. 5, pp. 433-447.

Alegret, L., Ortiz, S., Arenillas, I., and Molina, E., 2005, Palaeoenvironmental turnover across the Palaeocene/Eocene boundary at the Stratotype section in Dababiya (Egypt) based on benthic foraminifera: Terra Nova, v. 17, no. 6, pp. 526–536.

Aubry, M.-P., Berggren, W.A., Van Couvering, J.A. , Ali, J., Brinkhuis, H., Cramer, B., Kent, D.V., Swisher, III, C.C., Gingerich, P.R., Heilmann- Clausen, C., Knox, R.W.O'B., Laga, P., Steurbaut, E., Stott, L.D., and Thiry, M, 2003, Chronostratigraphic Terminology at the Paleocene/Eocene Boundary: In Wing, S.L., Gingerich, P.D., Schmitz, B., and Thomas, E., eds., Causes and Consequences of Globally Warm Climates in the Early Paleogene: Boulder, Colorado, GSA Special Paper 369, Chapter 35, pp. 551–566.

Aubry, M.-P., Berggren, W. A., Cramer, B., Dupuis, C., Kent, D. V., Ouda, K., Schmitz, B., And Steurbaut, E., 1999, Paleocene/Eocene Boundary Sections in Egypt. In Ouda, K., Ed., Late Paleocene-Early Eocene Events from North Africa to the Middle East, Symposium. First International Conference on the Geology of North Africa, pp.1-11.

Aubry, M.-P., Ouda, K., Dupuis, C., Berggren, W.A., Van Couvering, J.A., Members of the Working Group on the Paleocene/Eocene Boundary, 2007, The Global Standard Stratotype-section and Point (GSSP) for the base of the Eocene Series in the Dababiya section (Egypt): Episodes, v.30 no.4, pp. 271–286.

Bains, S., Corfield, R. M., and Norris, R. D., 1999, Mechanisms of climate warming at the end of the Paleocene: Science, v. 285, pp. 724-727.

Berggren, W., and Ouda, K., 2005. Upper Paleocene-lower Eocene planktonic foraminiferal biostratigraphy of the Dababiya section, Upper Nile Valley (Egypt): Micropaleontology, v. 49, pp. 61-92.

Bice, K. L., and Marotzke, J., 2002, Could changing ocean circulation have destabilized methane hydrate at the Paleocene/Eocene boundary?: Paleoceanography, v.17, no. 2, pp.1018

Bowen, G.J., Koch, P.L., Gingerich, P.D., Norris, R.D., Bains, S., Corfield, R.M., 2001. Refined isotope stratigraphy across the continental Paleocene-Eocene boundary at Polecat Bench in the northern Bighorn Basin: University of Michigan: Papers on Paleontology, v.33, 73-88.

DeConto, R., Galeotti, S., Pagani, M., Tracy, D.M., Pollard, D. and Beerling, D.J., 2010, Hyperthermals and orbitally paced permafrost soil organic carbon dynamics: Presented at AGU Fall Meet., Dec. 13–17, San Francisco (Abstr. PP21E-08)

Dickens, G. R., O'Neil, J. R., Rea, D. K., and Owen, R. M., 1995, Dissociation of oceanic methane hydrate as a cause of the carbon isotope excursion at the end of the Paleocene: Paleoceanography, v.10, pp. 965-971.

Dickens, G., 2001, Carbon addition and removal during the Late Palaeocene Thermal Maximum: basic theory with a preliminary treatment of the isotope record at ODP Site 1051, Blake Nose, in: D. Kroon, R.D. Norris, A. Klaus (Eds.), Western North Atlantic Palaeogene and Cretaceous Palaeoceanography: Geological Society of London. Special Publication, v.183, pp. 293–305.

Dupuis, C., Aubry, M.-P., Steurbaut, E., Berggren, W.A., Ouda, K., Magioncalda, R., Cramer, B.S., Kent, D.V., Speijer, R.P., and Heilmann-Clausen, C., 2003, The Dababiya Quarry section: lithostratigraphy, clay mineralogy, geochemistry and paleontology. In: Ouda, K., Aubry, M.-P. (Eds.), The Upper Paleocene–Lower Eocene of the Upper Nile Valley: Part 1.Stratigraphy: Micropaleontology, v. 49, pp. 41–59.

Ernst, S.R., Guasti, E., Dupuis, C., and Speijer, R.P., 2006, Environmental perturbation in the southern Tethys across the Paleocene/Eocene boundary (Dababiya, Egypt): foraminiferal and clay mineral records: Marine Micropaleontology, v. 60, no.1, pp.89–111.

Gavrilov, Y.O., Shcherbinina, E.A., and Oberhänsli, H., 2003, Paleocene-Eocene boundary events in the northeastern Peri-Tethys: Geological Society of America, Special Publication, v. 369, pp.147–68

John, C. M., Bohaty, S. M., Zachos, J. C., Gibbs, S., Brinkhuis, H., Sluijs, A., and Bralower, T., 2008, Impact of the Paleocene-Eocene thermal maximum on continental margins and implications for the carbon cycle in near-shore environments: Paleoceanography, v. 23, p. PA2217.

Katz, M.E., Pak, D.K., Dickens, G.R., and Miller, K.G., 1999, The source and fate of massive carbon input during the Latest Paleocene Thermal Maximum: Science, v. 286, pp.1531–33

Keller, G., Li, L., and Macleod, N., l995, The Cretaceous/Tertiary boundary stratotype section at El Kef, Tunisia: How catastrophic was the mass extinction?: Palaeogeography, Palaeoclimatology, Palaeoecology, v. 119, pp. 221-254.

Kennett, J.P., and Stott, L.D., 1991, Abrupt deep-sea warming, palaeoceanographic changes and benthic extinctions at the end of the Paleocene: Nature, v. 353, pp.225–229

Kübler, B., 1987, Cristallinité de l'illite: méthode normalisées de préparation de mesure, méthode automatique normalisées de mesure: Cahiers de l'Institut de Géologie, Series AX no. 3.1 and 3.2.

Lu, G.Y., and Keller, G., 1995, Planktic foraminiferal faunal turnovers in the subtropical Pacific during the Late Paleocene to Early Eocene: Journal of Foraminifera. Research, v. 25, pp. 97–116.

Martini, E., 1971. Standard Tertiary and Quaternary calcareous nannoplankton zonation, in FARINACCI, A. (ed.), Proceedings of the Second Planktonic Conference. Roma, Italy, Tecnoscienza, p. 739-785.

McInerney, F. A., and Wing, S. L., 2011, The Paleocene–Eocene Thermal Maximum: A perturbation of carbon cycle, climate, and biosphere with implications for the future: Annual Review in Earth Planetary Science, v. 39, pp. 489–516.

Monechi, S., Angori, E., and Speijer, R.P., 2000, Upper Paleocene biostratigraphy in the Mediterranean region: Zonal markers, diachronism, and preservational problems. GFF. Geologiska Föreningens, Stockholm Förhandligar, v.122, pp.108-110.

Okada, H., and Bukry, D., 1980., Supplementary modification and introduction of code numbers to the low-latitude coccolith biostratigraphic zonation (Bukry, 1973; 1975): Marine Micropaleontology, v. 5, pp. 321–325

Olsson, R.K., Berggren, W.A., Hemleben, C., and Huber, B.T., 1999, Atlas of Paleocene planktonic foraminifera - online version. , Smithsonian Contributions to Paleobiology, v. 85, pp. 1-252

Ouda, K., and Berggren, W.A, 2003, Biostratigraphic correlation of the Upper Paleocene–Lower Eocene succession in the Upper Nile Valley: a synthesis: Micropaleontology, v. 49, pp. 179–212.

Pardo, A., Keller, G., and Oberhänsli, H., 1999, Paleoecologic and paleoceanographic evolution of the Tethyan Realm during the Paleocene-Eocene transition: Journal of Foraminifera research, v. 29, pp.37–57.

Pearson, P.N., Olsson, R.K., Huber, B.T., Hemleben, C., and Berggren W.A., (eds), 2006, Atlas of Eocene planktonic foraminifera. Cushman Foundation Special Publication, v. 41, pp. 1-513.

Perch-Nielsen, K., 1985, Mesozoic calcareous nannofossils in H. H. Bolli, J. B. Saunders, and K. Perch-Nielsen, eds. Plankton Stratigraphy. Cambridge University Press, pp. 329-426.

Raffi, I., Backman, J., Pälike, H., 2005, Changes in calcareous nannofossil assemblage across the Paleocene/Eocene transition from the paleo-equatorial Pacific Ocean: Paleogeography, Paleoclimatology, Paleoecology, v. 226, pp. 93–126.

Schulte, P., Scheibner, C., and Speijer, R., 2011, Fluvial discharge and sea-level changes controlling black shale deposition during the Paleocene–Eocene Thermal Maximum in the Dababiya Quarry section, Egypt: Chemical Geology, v. 285, pp. 167-183.

Speijer, R.P., Schmitz, B., and Luger, P., 2000, Stratigraphy of late Palaeocene events in the Middle East: Implications for low to middle-latitude successions and correlations: Journal of the Geological Society, London, v.157, pp.37-47.

Svensen, H., Planke, S., and Corfu, F., 2010, Zircon dating ties NE Atlantic sill emplacement to initial Eocene global warming: Journal of the Geological Society, London, v. 167, pp.433–36.

Tantawy, A. A., 2006, Calcareous nannofossils of the Paleocene-Eocene transition at Qena Region, Central Nile Valley, Egypt: Micropaleontology, v. 52, no. 3, pp.193-222.

Westerhold, T., Röhl, U., McCarren, H., and Zachos J., 2009, Latest on the absolute age of the Paleocene–Eocene Thermal Maximum (PETM): New insights from exact stratigraphic position of key ash layers + 19 and – 17: Earth and Planetary Science Letters, v.287, no. 3–4, pp. 412–419.

Zachos, J., Pagani, M., Sloan, L., Thomas, E., and Billups, K., 2001, Trends, rhythms, and aberrations in global climate 65 Ma to present: Science, v. 292, pp. 686–693.

Zachos, J.C., Röhl, U., Schellenberg, S.A., Sluijs, A., Hodell, D.A., Kelly, D.C., Thomas, E., Nicolo, M., Raffi, I., Lourens, L.J., McCarren, H., and Kroon, D., 2005, Rapid acidification of the ocean during the Paleocene–Eocene Thermal Maximum: Science, v.308, pp.161–1611.

B. NEW GEOCHEMICAL CONSTRAINTS ON THE PALEOCENE-EOCENE THERMAL MAXIMUM: DABABIYA GSSP, EGYPT[1].

Abstract. The Paleocene Eocene thermal maximum (55.8 million years) shows an extraordinary drop in both $\delta^{13}C_{carb}$ and $\delta^{13}C_{org}$ values, suggesting that a massive amount of ^{12}C-rich carbon dioxide was released into the atmosphere in a very short time (of the order of few hundred ky). The most likely source would have been methane from ocean sediments or continental areas. The emitted CO_2 is removed from the atmosphere by carbonate precipitation, photosynthesis and silicate rock weathering reactions. This balance is thought to have stabilized greenhouse conditions. The Dababiya GSSP (Luxor, Egypt) is thought to be the most complete known PETM section. Detailed geochemical and mineralogical studies were performed on 106 samples spanning the PETM interval to evaluate the rate of weathering and it's feedback. The base of the Eocene is marked by unconformity overlain by silty clays deposited during low sea level (Bed 1) and followed by marly shales reflecting a progressive sea-level rise (Beds 2-5). Both organic and carbonate isotopes show a long-term decrease starting 0.6 m below the P-E boundary. The persistent shift of $\delta^{15}N_{org}$ values to nearly zero reflects the gradual increased in bacterial activity. High Ti, K and Zr and low Si contents at the P/E boundary coincide with significant kaolinite contents. This suggests intense chemical weathering under humid conditions at the beginning of the PETM. Negative Ce/Ce* anomaly intervals reflect two different anoxic conditions during the lower and middle PETM (Bed 2). High U, Mo, V, Fe and abundant small sized (2–5 μm) pyrite framboids confirm anoxic to euxinic conditions in the water column. At the same time interval, productivity sensitive elements (Cu, Ni, and Cd) show maximum concentration ratios suggesting high productivity in surface water. Above, phosphorus and barium tend to precipitate, as oxic conditions were re-installed. In the upper PETM (Bed 3) high P and Ba contents suggest oxygenated conditions. This new data highlights that intense weathering is one crucial parameter of the PETM events, especially during the recovery phase. The result reveals the deposition of Dababiya GSSP in a submarine channel that extended laterally about 200 m with deepest part of 0.8 m at the main GSSP section.

1. INTRODUCTION

The Paleocene-Eocene Thermal Maximum events (PETM) took place ca. 55.8 Ma ago (Westerhold et al 2009), and were associated with an abrupt negative shift in $\delta^{13}C$ and a sudden increase in earth's temperature due to huge input of greenhouse gas that led to perturbation of the carbon cycle in both marine and terrestrial ecosystem. The nature and tempo of the resulting stable isotopic excursions are recorded from both marine and terrestrially derived organic matter (e.g. Kennett and Stott, 1991; Sluijs et al., 2007a; Zachos et al., 2001, 2003, 2005, 2006; John et al., 2008; Magioncalda et al., 2004; Dickens et al., 1995; Kennett et al., 2002).

The most accepted cause of this event is a catastrophic destabilization of gas hydrates

[1] ***Hassan Khozyem, Thierry Adatte, Jorge E. Spangenberg, Abdel Aziz Tantawy, and Alexi Ulyanov, 2013, new geochemical constraints on the Paleocene-Eocene Thermal Maximum: Dababiya Gssp, Egypt. In preparation***

(clathrates) from the continental margin (Dickens et al., 1995; Dickens, 2011; Katz et al 2001; Kennett et al., 2002); the released methane lead to the input of ca. $2000x10^9$ metric tons CO_2 over 10,000 years (Zachos et al., 2005). Clathrates are stable in deep-sea sediments, but it can be destabilized by a temperature increase caused by changes in ocean circulation (Dickens et al. 1995, 1997) or by decreasing drop due to slope failure (Katz et al. 1999) or sea level changes. Other authors argued that release of methane alone would not be sufficient to explain the huge input of CO_2 in both ocean and atmosphere (Zachose et al., 2004, Dickens et al., 1995). Pore fluids venting and oxidation of organic matter-rich terrigenous sediments, probably associated with gas hydrates dissociation, would increase the quantity of released greenhouse gases, but remain insufficient to raise global temperature (DeConto et al. 2010). Higgins and Schrag (2006) proposed that the oxidation of ca. 5000 Gt. of organic carbon could most likely explain the geochemical and climatic changes during the PETM. The interaction of hydrothermal fluid with organic-rich Cretaceous-Paleocene sediments of the North Atlantic could produce significant amount of thermogenic methane (Svensen et al. 2004, 2010; Westerhold et al. 2009). Desiccation and oxidation of organic matter in vast areas of dried epicontinental seas would have contributed important CO_2 to the atmosphere (Higgins and Schrag, 2006; Gavrilov et al., 2003). Whatever the source, the high quantity of atmospheric CO_2 triggered the global temperature rise of 5–9°C during a period of about 200 ka (Sluijs et al., 2006; Zachos et al., 2006; Weijers et al., 2007; Handley et al., 2008). This environmental perturbation was the main reason for the severe (35–50%) benthic foraminiferal extinction and diversification in both marine plankton and terrestrial mammals (e.g. Alegret et al., 2009). An increase in the intensity of the marine biological productivity resulted in drawdown of atmospheric CO_2 that induced the termination of the PETM crisis (Torfstein et al., 2010; Bains et al., 2000). A further likely mechanism for atmospheric CO_2 removal was silicate weathering, which operated at much lower rates than previously supposed (Kelly et al., 2005, 2010). The PETM Global Stratigraphic Section and Point (GSSP) has been carefully selected by the International Commission for Stratigraphy (ICS), at the Dababiya Quarry south-eastern Egypt (Dababiya Village, Luxor). The golden spike of the Paleocene Eocene boundary had been placed at the base of the Esna Formation (Aubry, et al., 2007). This selection followed several criteria: (1) the organic carbon isotope excursion (CIE) located at the base of bed-1, (2) the disappearance of the deep benthic foraminifer *Stensioina beccariiformis*, (3) the transient occurrence of taxa among the planktonic foraminifera (*Acarinina africana, A.sibaiyaensis, Morozovella allisonensis)* during the $\delta^{13}C$ excursion, (4) the transient occurrence of the *Rhomboaster spp. – Discoaster araneus* (RD) assemblage and (5) an acme of the dinoflagellate *Apectodinium.* Based on these criteria, the Dababiya Section is thought to be one of the world's most complete and most expanded Upper Paleocene to Lower Eocene sequences (Dupuis et al., 2003). Speijer et al. (2000) concluded that the PETM event at Dababiya Quarry Beds are represented by five distinct beds that can be traced throughout a large area in Egypt and probably neighboring countries. Schulte, et al., (2011, 2013) observed that the basal GSSP bed was deposited in a submarine channel with river discharge

The completeness of the PETM section is imperative to understand the nature and tempo of this event. Some petrographic and geochemical studies have been conducted on the most complete PETM section in Dababiya (Soliman et al., 2006, 2011; Schulte et al., 2011, 2013). We performed a detailed geochemical and mineralogical study of the Dababiya GSSP, Luxor, Egypt, focused on the paleoenvironmental and climatic changes through the PETM.

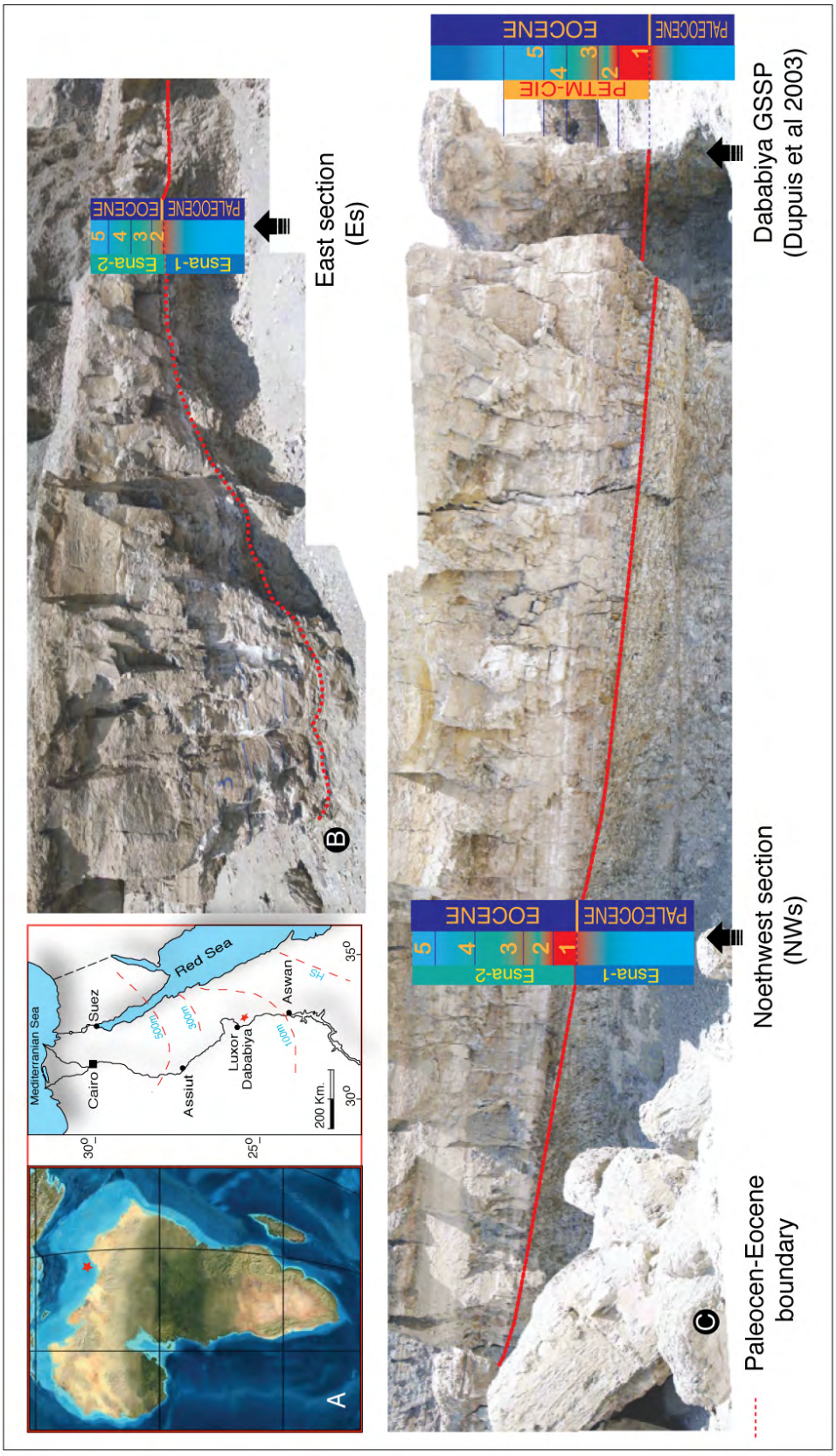

Figure 1: (a) *Location of the Dababiya GSSP.* ***b&c*** *show field photographs marking the relative distance of the NW and E sections from the main GSSP outcrop.*

2. LITHOLOGY

The Dababiya section (GSSP) is located at the eastern side of the upper Nile Valley 35 km southeast of Luxor City (25° 30` N, 32°31` Fig.1). Two stratigraphic successions were recovered to the northwest (hereafter refer to NWs) and the east (Es) of the main GSSP section (Fig.1; Dupuis et al., 2003). However, the main GSSP section was never sampled in detail due to various problems associated with limited exposure accessibility, the likely annihilation of the rock exposure due to oversampling, and others political complications.

Four lithostratigraphic formations were exposed in the area from older to younger: Dakhla shale Formation (greenish calcareous shale), Tarawan Formation (marly limestone to chalk), Esna shale (greenish gray to dark gray shale), and the Thebes Formation (limestone and flint). The Esna shale Formation was divided into three main units (Esna-1, Esna-2, and Esna-3) based on carbonate contents (Dupuis et al., 2003). Only Esna-1 and Esna-2 are exposed at the GSSP (Fig. 2).

The P/E boundary is placed at the lower part of the Esna shale Formation between units Esna-1 and Esna-2.

The PETM interval is marked by 5 distinctive beds forming unit Esna-2. At the base of Esna-2 and directly overlying unit Esna-1 separated by a distinctive sequence boundary surface, Bed-1 consists of 0.63 m of dark laminated non-calcareous clay with a few phosphatic coprolites at the base. The overlying Bed-2 consisted of 0.5 m of brown shale with coprolites and low carbonate content. Bed-3 consists of 0.84m of cream-colored, laminated phosphatic shale, Bed-4 is a 0.71m thick gray shale with high carbonate content, and Bed-5 is a 1m thick grey marl to marly calcarenitic limestone (Dupui et al., 2003).

The Dababiya NWs, located 50m to the left of the Dababiya GSSP exposure, comprises sediments of the late Paleocene Esna-1 and early Eocene Esna-2 units (Fig. 2). Esna-1 consists of marl to marly shale. A well-defined sequence boundary (SB) separates Esna-1 and Esna-2 units (Fig. 2). Esna-2 was divided into five beds with the following thicknesses and lithologies (Depuis et al., 2003): Beds 1 and 2 are 0.32m and 0.48m thick, respectively, and consist of silty claystone with anhydrite layers. Bed 3 consist of 0.24m of silty marl with phosphatic nodules and anhydrite, and bed 4is a 1m thick of marl to marly limestone. Only 5 cm could be sampled from the base of bed 5. *The Dababiya Es* was collected 25m to the right of the Dababiya GSSP and contains similar rocks as the NW section, but bed 1 is missing and the lower part of Bed-2 is only 24 cm thick (Figs.3). The absence of bed 1 was confirmed by mineralogical analysis, particularly the high phyllosilicate, quartz, feldspar, and Ca-apatite contents followed by high calcite and only three of the four-anhydrite layers observed at the NW section. Bed 3 consists of 0.4m thick silt-clay layer with phosphatic nodules. Bed 4 consists of a 0.6 m thick marl and bed 5 of a 0.4 m thick marly limestone (Fig. 3).

3. MATERIAL AND METHODS

Both NWs and Es sequences of the Dababiya GSSP section (50m to NW and 25m to E; Fig. 1) were sampled at high resolution (2, 5, and 10cm, total of 102 samples) through the Upper Paleocene to Lower Eocene interval. The surfaces of the samples were carefully cleaned and all the weathered material was removes. An aliquot of ca. 25 g was powdered in an agate mortar previosly washed three times with deionised water, rinsed with ethanol, and air-dried to avoid any possibilty of cross-contaminations between samples.

The samples were subjected to extensive mineralogical and geochemical studies, including bulk and clay mineralogy, major (MEs), trace elements (TEs), rare earth elements (REEs), total P, and TOC contents, and stable isotopes at the Institute of Earth Sciences of the University of Lausanne (ISTE-UNIL).

Stable carbon and oxygen isotope analyses of aliquots of whole rock samples were performed using a Thermo Fisher Scientific Gas Bench II carbonate preparation device connected to a Delta Plus XL isotope ratio mass spectrometer (Spangenberg and Herlec, 2006). The CO_2 extraction was done by reaction with anhydrous phosphoric acid at 90°C. The stable carbon and oxygen isotope ratios are reported in the delta (δ) notation as the per mil (‰) deviation relative to the Vienna Pee Dee belemnite standard (VPDB). The standardization of the $\delta^{13}C$ and $\delta^{18}O$ values relative to the international VPDB scale was done by calibration of the reference gases and working standards with IAEA standards. Analytical uncertainty (2 s), monitored by replicate analyses of the international calcite standard NBS-19 and the laboratory standards Carrara Marble was not greater than ±0.1‰ for $\delta^{13}C$ and ±0.2‰ for $\delta^{18}O$.

The kerogen was separated from the samples by HCl treatment, dried (40°C, 16 h), and submitted to carbon and nitrogen isotope analysis by flash combustion on a Carlo Erba 1108 elemental analyzer (EA) connected to a Thermo Fisher Scientific Delta S isotope ratio mass spectrometer (IRMS) that was operated in the continuous helium flow mode via a Conflo III split interface (EA–IRMS). The $\delta^{13}C$ and $\delta^{15}N$ values were reported relative to VPDB and air–N_2, respectively. The calibration and assessment of the reproducibility and accuracy of the isotopic analysis were based on replicate analyses of laboratory standard materials and international reference materials. The reproducibility was better than 0.1‰ (1σ) for both carbon and nitrogen.

XRD analyses of the whole rock will be carried out for all the samples at the Geological Institute of the University of Lausanne, Switzerland. The samples will be prepared following the procedure of Kübler (1987). Random powder of the bulk sample is used for characterization of the whole rock mineralogy. Nearly 20 gr of each rock sample was ground with a "jaw" crusher to obtain small chips (1 to 5 mm) of rock. Approximately 5 grams were dried at a temperature of 60 °C and then ground again to a homogenous powder with particle sizes <40μm. 800 mg of this powder were pressed (20 bars) in a powder holder covered with a blotting paper and analyzed by XRD. Whole rock composition was determined by XRD (Xtra Diffractometer, Thermo, Ecublens, Switzerland) based on methods described by Ferrero (1965, 1966), Klug and Alexander (1974) Kübler (1983) and Rolli (1990). This method for semi-quantitative analysis of the bulk rock mineralogy (obtained by XRD patterns of random powder samples) used external standards. The Calcite/Detritism ratio (C/D=Calcite/(Quartz+Phyllosilicates+Plagioclases+K-Feldspars), an index of detritism, was calculated based on bulk-rock mineralogy to evaluate the variations in detrital input

Clay mineral analyses were based on methods by Kübler (1987). Ground chips were mixed with de-ionized water (pH 7-8) and agitated. The carbonate fraction was removed with the addition of HCl 10% (1.25 N) at room temperature for 20 minutes, or more until all the carbonate was dissolved. Ultrasonic desagregation was accomplished during 3 minutes intervals. The insoluble residue was washed and centrifuged (5-6 times) until a neutral suspension was obtained (pH 7-8). Separation of different grain size fractions (< 2μm and 2-16 μm) was obtained by the timed settling method based on Stokes law. The selected fraction was then

pipetted onto a glass plate and air-dried at room temperature. XRD analyses of oriented clay samples were made after air-drying at room temperature and ethylen-glycol solvated conditions. The intensities of selected XRD peaks characterizing each clay mineral present in the size fraction (e.g. chlorite, mica, kaolinite, palygorskite, sepiolite, smectite and illite-smectite mixed-layers) were measured for a semi-quantitative estimate of the proportion of clay minerals present in the size-fractions <2μm and 2-16μm. Therefore, clay minerals are given in relative percent abundance without correction factors. Content in swelling (% smectite) is estimated by using the method of Moore and Reynolds (1989).

For major (MEs) and trace elements (TEs), the analyses were done on pressed powder after mixing the samples with the Mowiol II polyvinyl alcohol and pressed to pellets of 4 cm in diameter (measurement of TEs) and the samples have been measured for (MEs) after fusion with tetra borate melted pellets using the FRX Philips PW2400 X-ray fluorescence spectrometer, which is a good compromise for MEs and TEs. The detection limits are approx. 0.01% for MEs and 1 to 4 ppm for TEs. The accuracies of the analyses were assessed by analyses of standard reference materials.

The REEs were measured by inductively coupled plasma–mass spectrometry (ICP-MS) (ELAN 6100 DRC ICP–MS), calibrated using standard SRM 612. The detection limit for major elements is better than 0.01 wt.%, for trace elements is generally 1 to 4 ppm, and 0.02 to 0.15 ppm for the REE.

Selected samples close to the PETM interval were studied by scanning electron microscopy (SEM; Tescan Mira LMU) after gold-carbon coating.

Total phosphorus analyses were performed on bulk rock samples, using the ascorbic acid method of Eaton et al. (1995). Samples were analysed in triplicate; in the case of high P content the samples were diluted to x100 and x200.

The organic matter contents were determined using Rock Eval pyrolysis (Rock-EvalTM6 Behar et al., 2001). Total organic carbon contents (TOC) were obtained using the standard temperature cycle. Samples were calibrated with both IFP160000 and an internal standard with an instrumental precision of <2% (Espitalié et al., 1985).

4. RESULTS

4.1. Whole rock and clay mineralogy

The whole rock mineralogy of the samples (No. 1 to 27) of the NW sequence below the PETM interval is characteristic for a marl with mean value 42.7% calcite, 40.7% phyllosilicates, 7% quartz, and 0.4% anhydrite, and absence of Ca-apatite. These samples have low values for the detrital index (1.15) (Fig.2). At the onset of the CIE, a sharp decrease in calcite content (5.4%) coincides with increasing phyllosilicate, quartz, anhydrite and Ca-apatite contents (57.7%, 8.2%, 7.1%, and 7.5%) respectively and DI value (to 13) with the presence of goethite, K and Na feldspar (1.64 %, 1.76%, and 3.04%). The interval up to 110 cm above the CIE-onset (sample 51) can be divided into three main groups based on the whole rock compositions: samples 29 to 39 show an abrupt change in the mean bulk rock composition an increase in phyllosilicate, quartz, goethite and anhydrite contents to maximum mean values 64.8%, 16.8%, 1.26%, 11.7%, respectively, and DI to 2.15, with low amounts of K and Na feldspar and calcite contents near zero (0.82%).

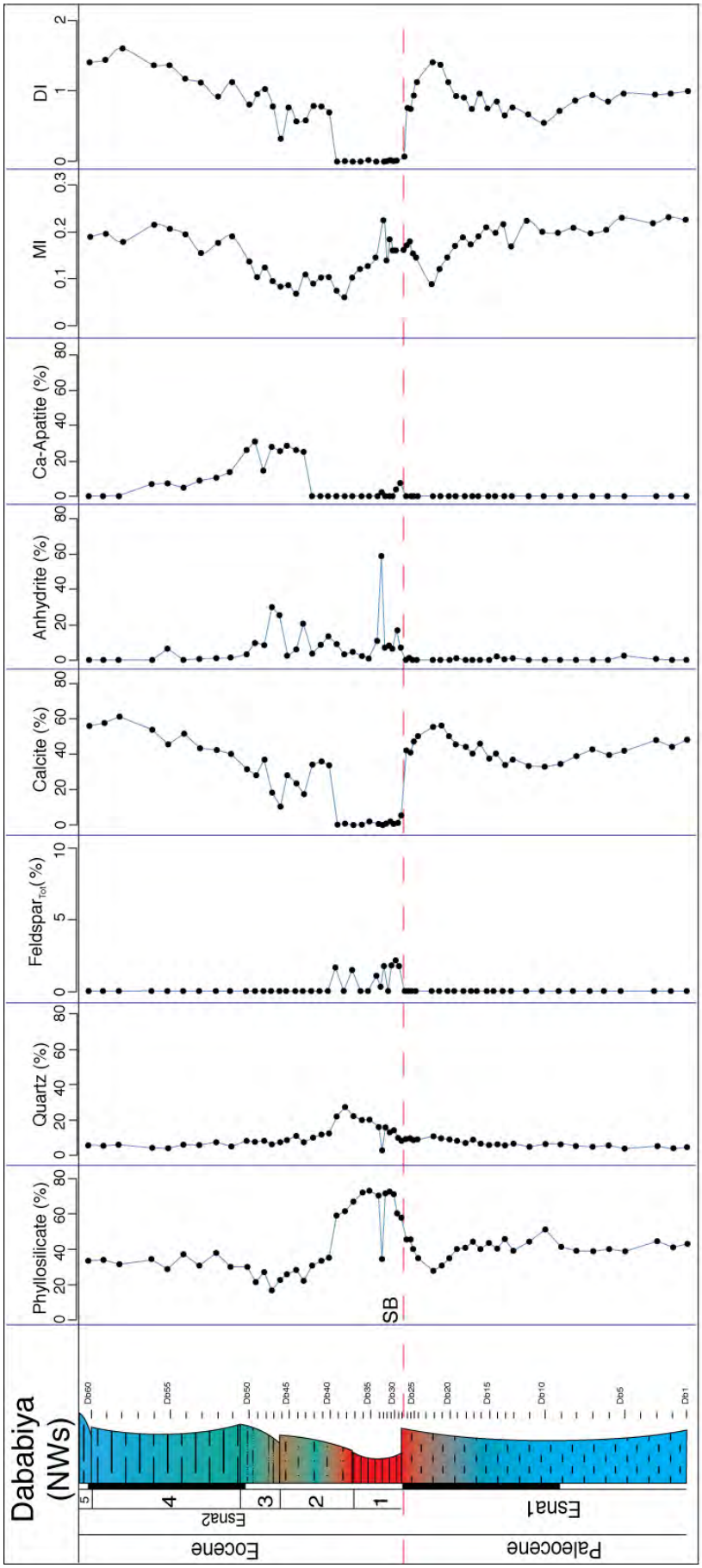

Figure 2: *Relative percent of the whole rock mineralogical data in the NW section.*

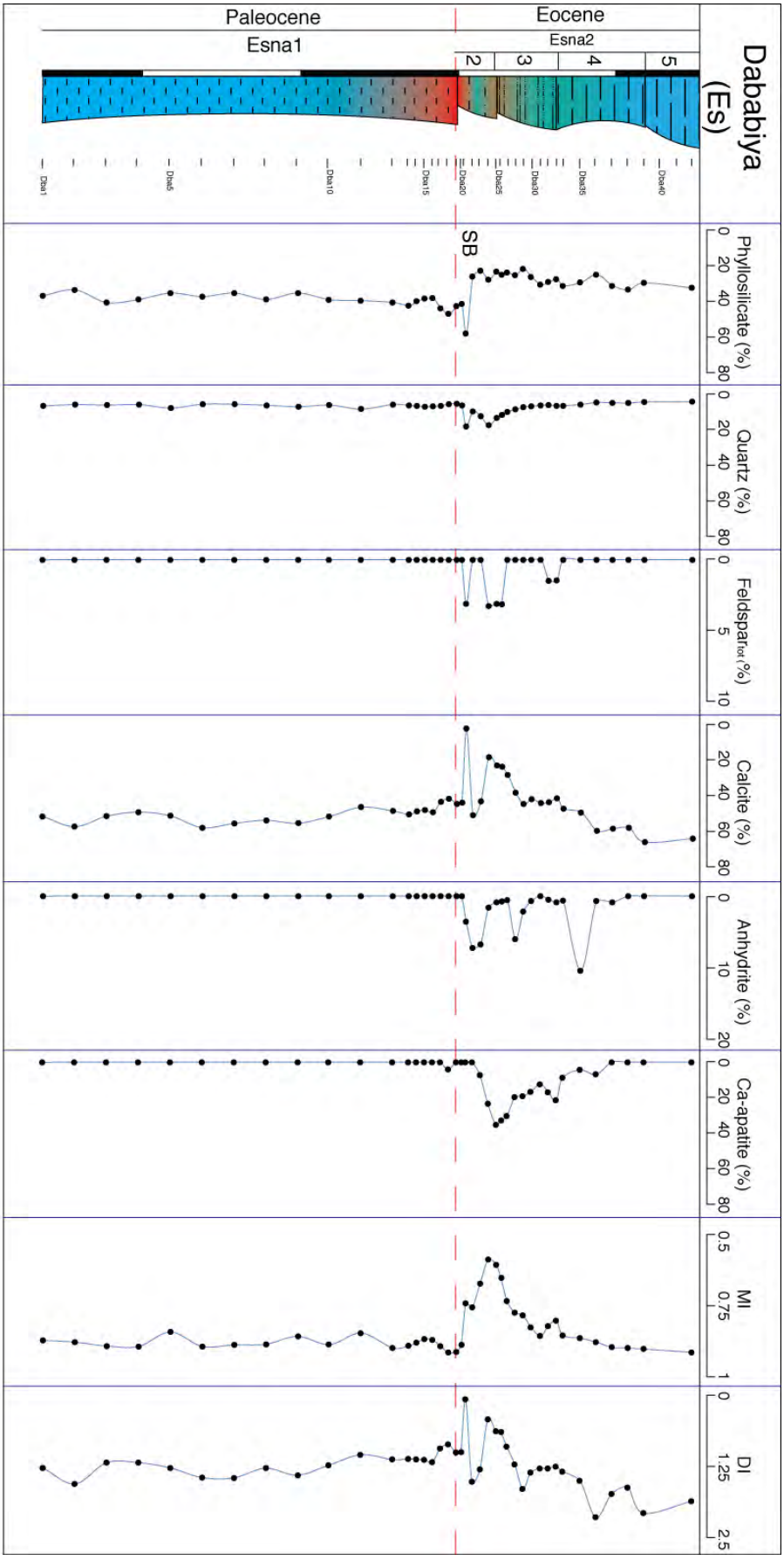

Figure 3: *relative percent of abundant whole rock mineralogical data in the E section.*

Low Ca-apatite (0.56%) content probably originated from reworking of the underlying sediments. Samples from 40 to 42 show a sharp increase in calcite content (34.5%) that coincides with a decrease in the rest of the bulk rock contents, disappearance of Ca-apatite and decrease of the DI to 1.32. The third group of samples (from 43 to50) marks a notable increase in Ca-apatite up 25.6% coincident with a relative increase in anhydrite. Above sample 50 up to the top of the section the bulk rock components return to marl composition with mean values for calcite (49.93%), phyllosilicate (33.2%), Ca-apatite (5.81%) quartz (5.54%), anhydrite (1.08%) and detrital index of 0.79 (Fig.2).

At the E sequence, below the P/E boundary, the marl bulk rock show mean components show a mean composition typical for marls with 38.76% phyllosilicate, 5.34% quartz, and 49.74% of calcite. This composition abruptly changed at the P/E boundary (sample 21) with increased phyllosilicate (57.09%) and quartz (17.35%), a sharp decrease in calcite content to 1.64%. During the PETM CIE (samples 22 to 31), the bulk rock composition increased in both quartz and phyllosilicate to mean contents ogf 25.13% and 9.33% respectively, with calcite increasing to 35.27%. Above sample 31, all bulk rock components return to the background values observed below the P/E boundary (Fig. 3).

The clay fractions of the NWs samples show abundant smectite, Illite, kaolinite, chlorite, illite-smectite and palygorskite. Smectite is the major component below the SB (mean value 68%), followed by 14% of illite, 6.5% illite-smectite, 3.9% palygorskite, 3.5 % kaolinite, and 3.25% chlorite. At the SB, smectite content increased (mean 75%, samples from 28 to 38) with almost no change in the other components (Fig. 4). From samples 39 to 44 (middle of Bed 2), a sudden decrease in smectite (45%) is concomitant with a sharp increase in kaolinite (maximum 10%) and gradual increase in illite (18.5%), chlorite (12%), illite-smectite (10.8%) and palygorskite (8.8%). Above sample 44, the clay mineralogy returns to the mean composition observed below the SB (Fig. 4).

4.2 **Isotopes**

The isotopic composition of whole rock carbonates ($\delta^{13}C_{carb}$) and associated organic matter ($\delta^{13}C_{org}$, $\delta^{15}N$) isotopes for both studied sections can be summarized as follows.

4.2.1. Northwest section (NWs)

The P/E boundary is placed at the erosional surface between the uppermost Paleocene and the lowermost Eocene represented by abrupt changes in bulk rock mineralogy. The $\delta^{13}C_{carb}$ values in the uppermost part of Plaeocene (Esna-1 bed, samples 1-15) range from 0.04 to 2.2‰. From samples 16 to 27 values gradually decrease to a mean value of -1.57 ‰. In samples 28-39, $\delta^{13}C_{carb}$ values are corrupted probably due to the very low carbonate content and increased weathering. From samples 44 upwards, the $\delta^{13}C_{carb}$ values gradually increase and reach 0.39‰ at the top of the section (Fig. 5). The $\delta^{13}C_{org}$ values show a similar pattern as the $\delta^{13}C_{carb}$ data. In the uppermost Paleocene samples, $\delta^{13}C_{org}$ values vary between -25.8 and -23.8‰, and are followed by a gradual decrease to the more negative value (ca. -27‰) at sample 29 and the PETM interval. The $\delta^{15}N$ values range from 2.3 to 23.4‰, and show a similar stratigraphic trend as observed for $\delta^{13}C$ and $\delta^{13}C_{org}$. The highest values are observed (sample 3) at the base of the section where the lowest value is in sample 41. The negative shift begins at the CIE onset. The $\delta^{15}N$ values reach 6‰ at sample 29 and persist to the top of the PETM interval (sample 54) with a mean value of 5.2 ‰ then drop back to values observed below the PETM (ca. 18.8‰; Fig. 5).

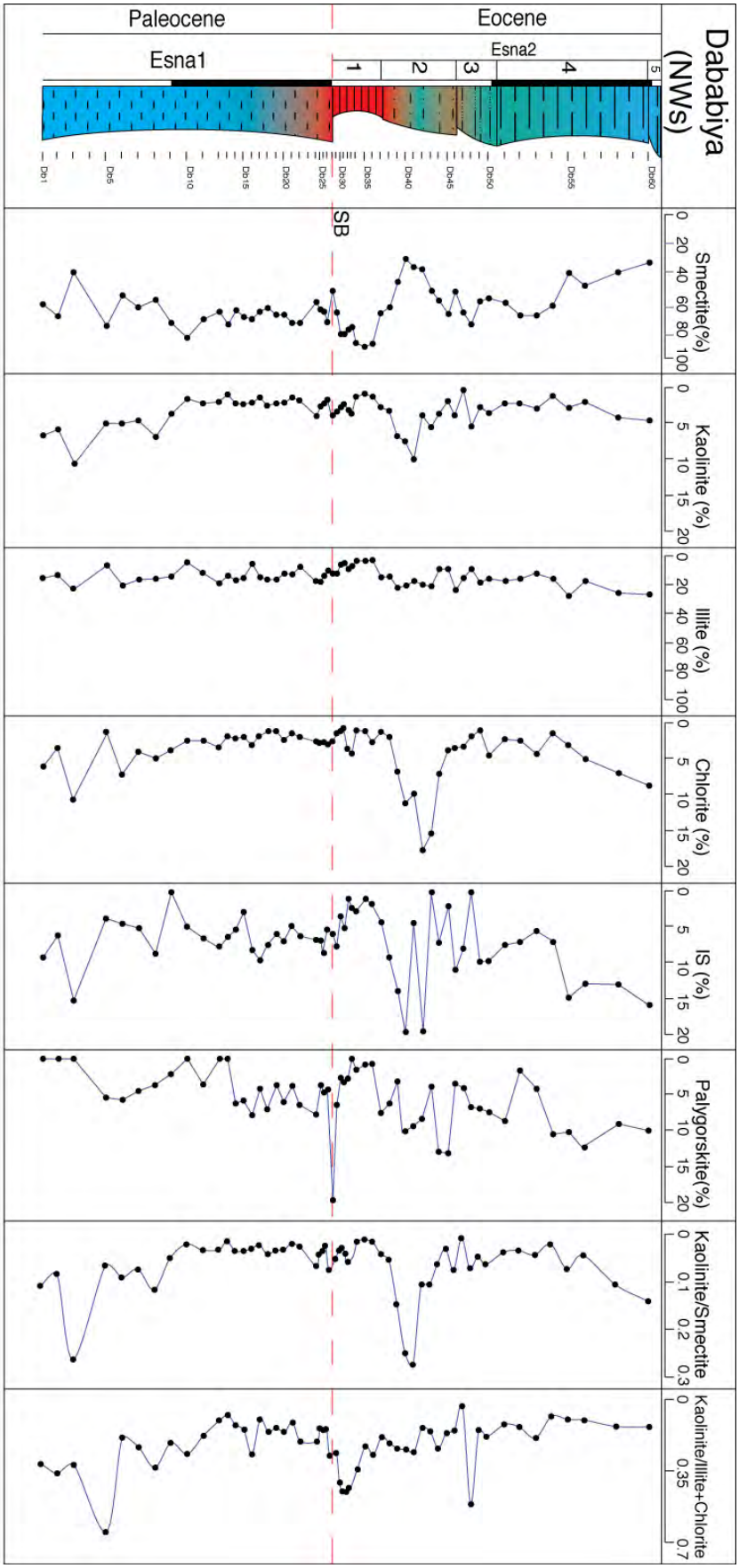

Figure 4: *Relative percentage and ratios (Kaolinite/smectite; kaolinite/illite+chlorite) of clay mineral compositions of the NW section*

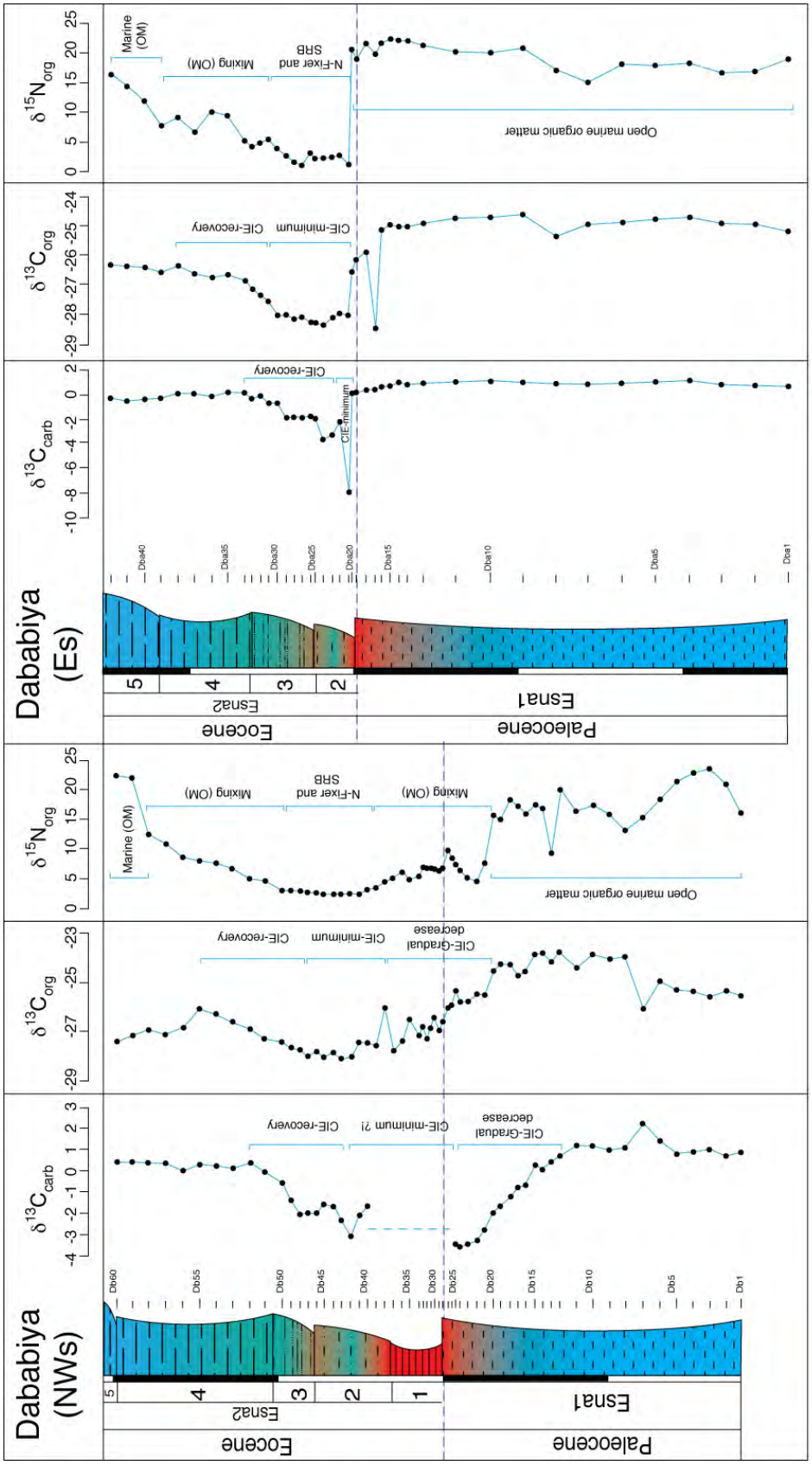

Figure 5: *The $\delta^{13}C_{Carb}$, $\delta^{13}C_{org}$ and $\delta^{15}N$ patterns of NW and E sections. Note the gradual decrease in carbon isotopic compositions of both $\delta^{13}C_{Carb}$ and $\delta^{13}C_{org}$ at the NW and abrupt shifts at the E sections.*

4.2.2. East section (Es)

The P/E boundary is placed at the erosional surface between the uppermost Paleocene (Esna 1) and the lowermost Eocene (Esna 2, bed 2) with bed1 and part of bed 2 missing. A sharp negative shift marks the erosional surface in both organic and inorganic $\delta^{13}C$ (-2.5‰ and -2.3‰, respectively). In Bed 3 $\delta^{13}C_{org}$ and $\delta^{13}C_{carb}$ gradually return to pre-excursion values (sample 31) with means of -28 and -2.41‰ respectively. Above sample 31 both $\delta^{13}C_{org}$ and $\delta^{13}C_{carb}$ return to the normal values (-26.7‰ $\delta^{13}C_{org}$ and 0.05‰ $\delta^{13}C_{carb}$) comparable to values observed below the P/E boundary (-25.3‰ $\delta^{13}C_{org}$ and 0.89‰ $\delta^{13}C_{carb}$).

A sharp and persistence shift in $\delta^{15}N$ to nearly 0‰ during the PETM interval (sample from 21 to 31) is associated with the organic and inorganic carbon isotope shifts (Fig. 5).

4.3. **Elemental Geochemistry**

4.3.1 Major element abundances

Major element (MEs) abundances vary significantly within the Dababiya northwest section (NWs) due to dilution effect of the clay contents in the sediments.

From the base of the section up to 60cm below the sequence boundary, the MEs show no changes below the sequence boundary (samples 1 to 12, Fig. 6). From 60 cm to the SB (samples 13 to 27) the SiO_2, Al_2O_3, TiO_2, Fe_2O_3, Na_2O_3 and K_2O concentrations gradually decreased toward the SB (mean values of 33%, 9.12%, 0.36%, 3.1%, 2%, and 0.27% respectively) and the CaO increased (mean value of 22.56%). At the same interval there are no notable changes in MgO, MnO and P_2O_5 concentrations. Abrupt changes have been observed in all the MEs components, with recorded mean values 52.5% SiO_2, 13% Al_2O_3, 0.75 %TiO_2, 4.52% Fe_2O_3, 2.76% MgO, 3.37% Na_2O_3 and 1.02% K_2O. No changes have been observed in P_2O_5, but a significant decrease is observed in both MnO and CaO to 0.01 and 4.28%, respectively. Above this interval all the MEs gradually return to the mean values observed below the SB except for P_2O_5, which shows a strong accumulation with a mean value of 6.05% between samples 41 and 51 (Fig. 6).

4.3.2. Trace element abundances

The normalization of trace element (TE) concentrations in marine sediments by the Al-content is commonly used to estimate the enrichment in the elements relative to reference materials. The TE trends show a distinctive behaviour above the SB (Fig. 7). The Al-normalized V, U, Mo, Cd, Ni, and Zn represent sharp enrichments at the middle part of Bed 2 (samples 38 to 42) where the mean values increased from 120×10^{-4} to 175×10^{-4} for V/Al, 2×10^{-4} to 11×10^{-4} for U/Al, 9×10^{-4} to 276×10^{-4} for Mo/Al, 0.8×10^{-4} to 4×10^{-4} for Cd/Al, 58×10^{-4} to 120×10^{-4} for Ni/Al, and 40×10^{-4} to 235×10^{-4} for Zn/Al. these elements return to the mean values above sample 42 (Fig. 7). Below the P/E, and above sample 42, values of Al-normalized Cu, Zr and Pb are 8×10^{-4}, 17×10^{-4}, and 0.6×10^{-4} respectively. A clear enrichment trend in these elements is observed from the P/E interval to the middle pat of Bed 2 (samples 27 to 42) with mean values of 36×10^{-4} for Cu/Al, 26×10^{-4} for Zr/Al and 2×10^{-4} Pb/Al. At this level, Co/Al and Ba/Al are low (minimum value of 1.5×10^{-4} and 51×10^{-4} respectively). Cr concentrations is uniform in this interval and higher between samples 38 to 51.

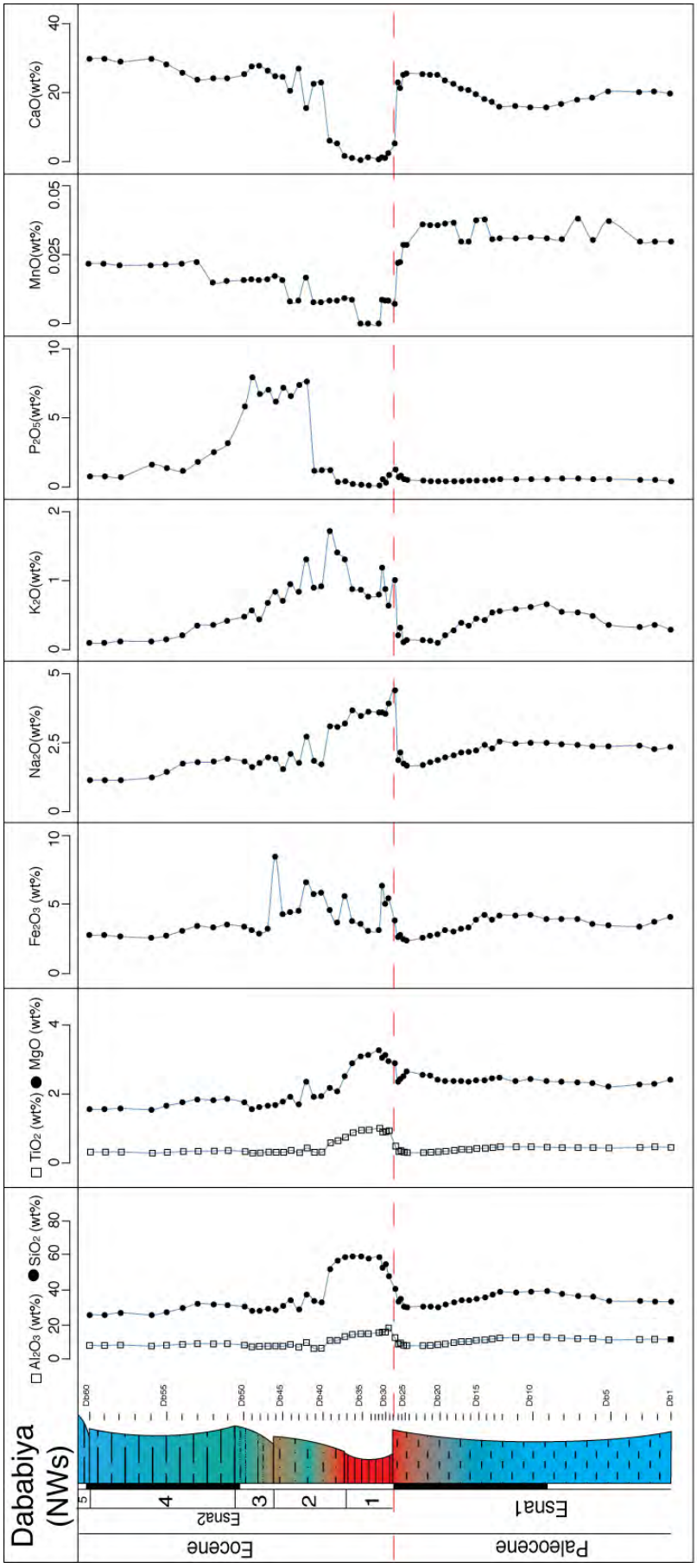

Figure 6: *Major element distributions of the Dababiya NW section.*

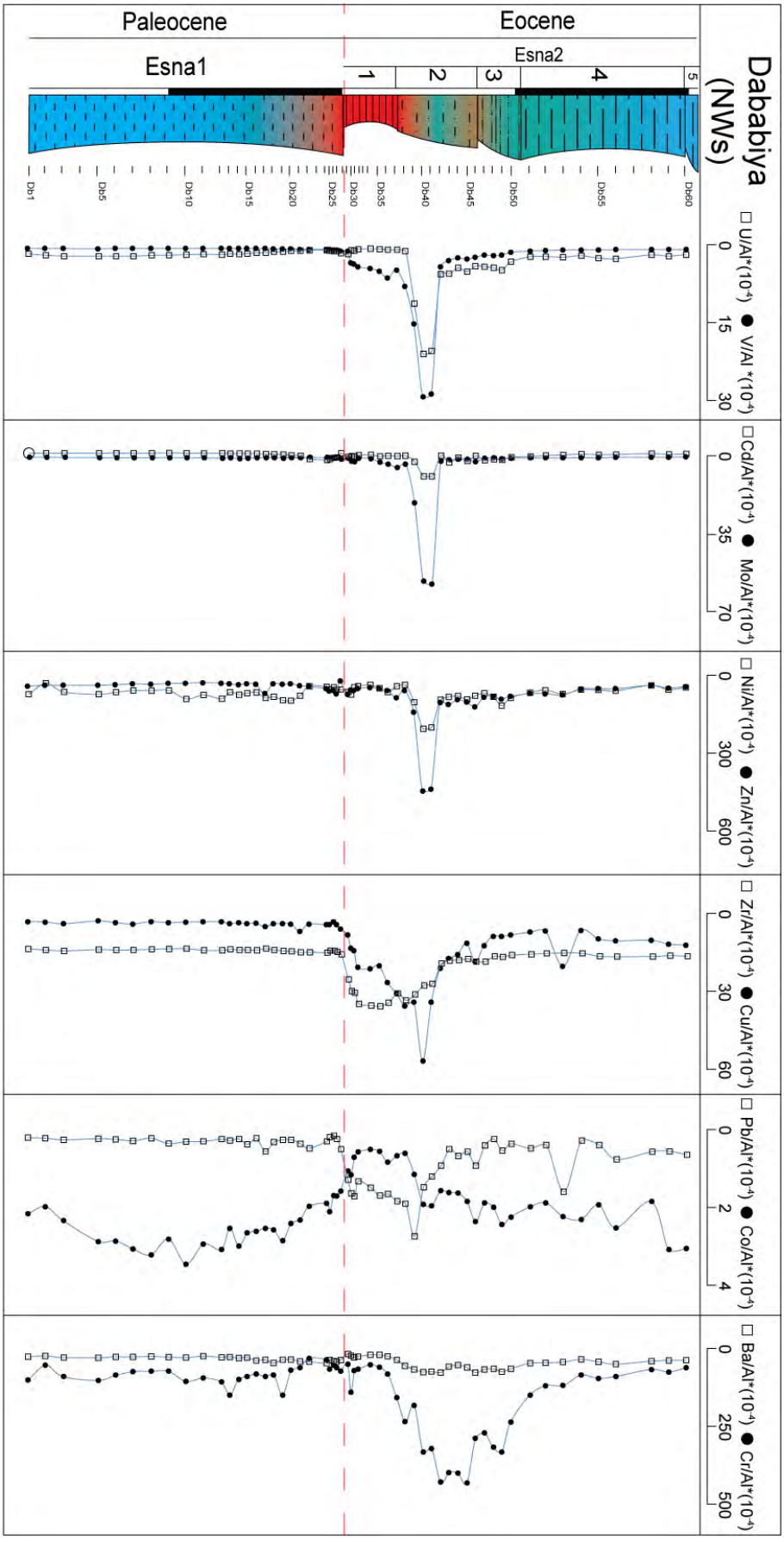

Figure 7: *Al- normalized trace elements plotted against the litho-log of the Dababiya NW section.*

4.3.3. Rare Earth Elements

The stratigraphic evolution of ΣREE, light REE (LREE), heavy REE (HREE) contents and La/Yb ratios are shown in Fig. 8 together with the REE patterns normalized to Post-Archaean Average Shale (PAAS; Taylor and McLennan, 1985). The ΣREE contents reach a maximum value in the basal part of the section (samples 1 to 12) with a mean value of 146.5 ppm, 111.7 ppm in LREEs and 7.9 ppm in HREE. The La/Yb ratio is 11.8, indicating higher LREEs than HREE contents. The ΣREE content gradually decreases toward the SB with mean values of 116.35ppm (88.2 LREEs, 6.7 HREEs) and similar La/Yb ratio (11.2). An abrupt increase in ΣREE (to 169.3 ppm; 123.5 ppm LREE and 14.44ppm HREE) and a decrease in the La/Yb ratio to 7.35 are observed in sample 28. A persistent decrease in ΣREE spans the interval from sample 28 to 38 (96.52 ppm mean value, 68.9 LREEs and 8.7ppm HREE) with almost no change in the La/Yb ratio. From sample 39 to the top of the studied section the ΣREEs gradually increase to the mean value observed in the lower part of the section (113ppm, 83.3ppm LREE and 8.4ppm HREE).

5. DISCUSSION

5.1. Carbon isotope variations

The Dabbabiya GSSP carbon isotope curve of Dupuis et al., (2003) can be divided into three main parts: 1) a gradual decrease from the sequence boundary (SB) where the P/E is placed up to 10 cm below the top of Bed 1; 2) a persistent CIE-minimum from 10 cm below the Bed 2 to middle of Bed 3; and 3) gradual increase in $\delta^{13}C_{org}$ in the middle part of Bed 5 to values similar of those below the PETM.

The carbon isotope curve of the NW section shows generally similar trends as the Dababiya GSSP, with some clear differences. The main differences are: a) the long-term decrease in $\delta^{13}C$ values recorded in the NWs for both $\delta^{13}C_{car}$ and $\delta^{13}C_{org}$ in uppermost Palaeocene sediments beginning about 60 cm below the P/E, and b) the abrupt negative $\delta^{13}C$ excursion in the Es as a result of erosion of the basal Eocene Bed 1 and part of Bed 2 (Fig. 2, 5).

The long-term decrease in both $\delta^{13}C_{carb}$ and $\delta^{13}C_{org}$ may be an inherited signal of a gradual increase in both marine and atmospheric CO_2 associated with North Atlantic volcanism (Bowen and Zachos., 2010). The maximum volcanic activity phase probably resulted in changes in ocean circulation, chemistry and heat transport (Renssen et al., 2004; Kennett et al., 1999). Which may have destabilized the methane hydrate stored in the continental shelf, releasing large quantities of methane into the water column and atmosphere.

The oxidation of this methane produced strongly ^{13}C-depleted CO_2 which precipitated carbonates of low $\delta^{13}C$ values, inducing full expression of the CIE-minimum in $\delta^{13}C_{carb}$ at the P/E boundary well before that of $\delta^{13}C_{org}$ values. The CIE-minimum in $\delta^{13}C_{org}$ is within the onset of the "recovery phase" of the PETM in the upper part of Bed 2, which is characterized by a significant increase of Ca-apatite. A possible explanation for this delay of the CIE-minimum in organic carbon is that the isotopically light carbon released from methane oxidation could have drawn by different processes, including: i) increased continental silicate weathering (Bowen and Zachos 2010; Kelly et al., 2005; 2010), ii) photosynthetic fixation of the excess atmospheric CO_2 mostly by terrestrial plants that developed during the hot humid climate with formation of floodplain wetlands (Beerling 2000, Zeebe et al., 2009; Bains et al., 2000; Dickens, et al., 1997)), and iii) increase of the ocean primary productivity (Torfstein at al., 2010).

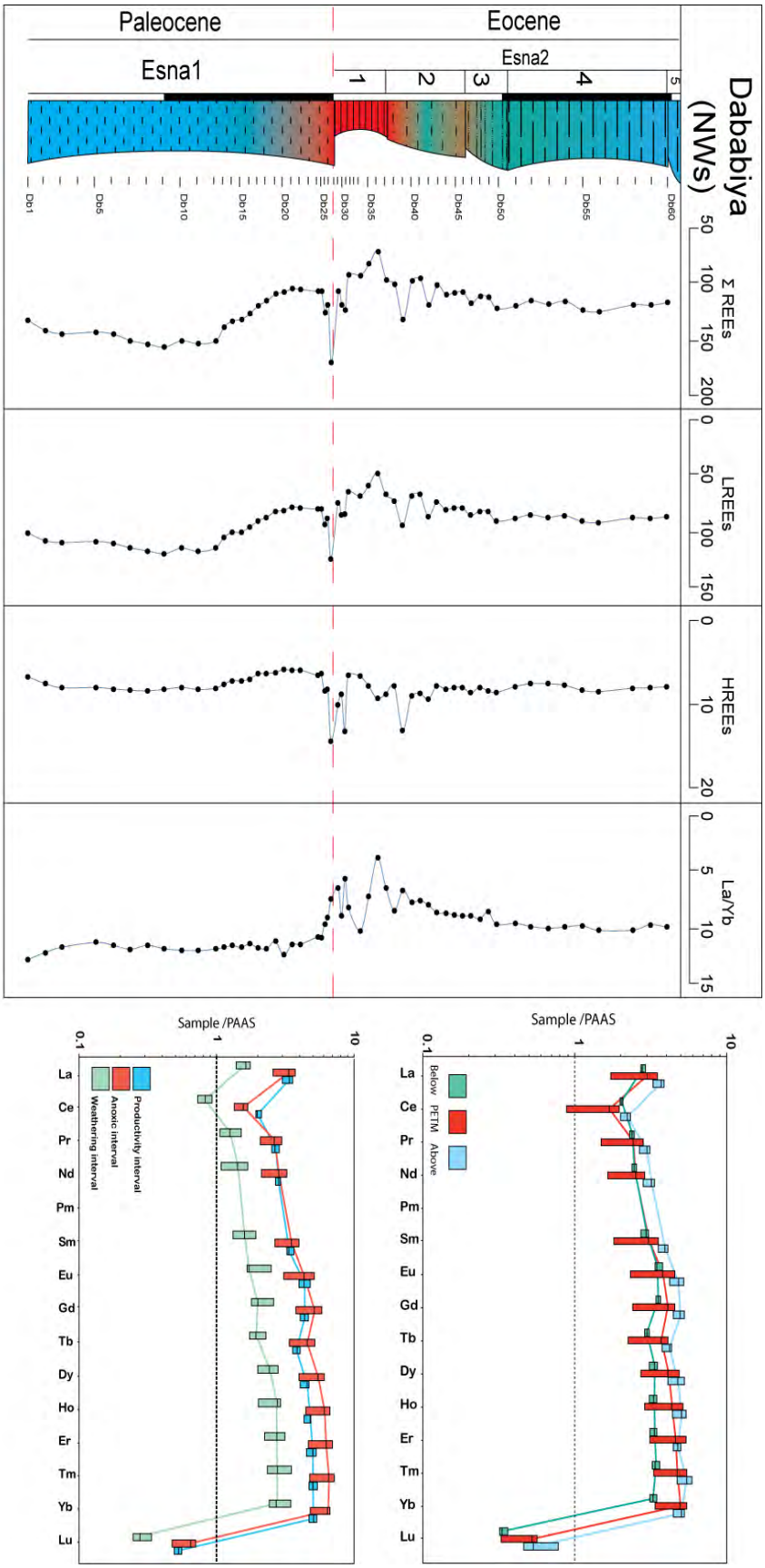

Figure 8: *Plots of the ΣREE, LREE, HREE, the ratios between LREE, HREE (La/Yb) and the PAAS normalized REE pattern for the different recognized intervals at the Dababiya NW section.*

The CIE-minimum in $\delta^{13}C_{org}$ values coincides with the maximum content of organic matter, which appears to be of terrestrial origin, and thus reflects the delayed response of the continental environment to the huge input of light carbon to the atmosphere. Based on that behaviour of the $\delta^{13}C_{org}$ that is also noted in other PETM section in Egypt (Khozyem et al., 2013), the $\delta^{13}C_{org}$ minimum could be limited to the onset of the recovery phase, rather than the P/E boundary and more particularly with presence of high apatite and calcite contents.

5.2. **Completeness of the GSSP**

The Paleocene-Eocene boundary (P/E) global strato-type section and point (GSSP) was defined by Aubry and Ouda (2003) and Gradstein et al. (2004) and placed at the base of the clay layer coinciding with the steepest slope of the negative CIE in the Gebel Dababiya section (Egypt). As a consequence, the base of the CIE has been used as global reference to pinpoint the P/E boundary. In most of the studied section for the PETM events both $\delta^{13}C_{org}$ and $\delta^{13}C_{car}$ values show sharp abrupt negative excursions. Similar, but less prominent, excursions characterize the $\delta^{18}O$ and $\delta^{15}N_{org}$ values. Such abrupt isotopic changes probably record a hiatus at the base of the PETM, as observed worldwide: Egypt (Gebel Duwi, Gebel Aweina; Speijer et al 2000, 2002; Wadi Nukhul; Khozyem et al., 2013) Italy (Forada section; Agnini et al., 2007), Spain (Zumaya section; Schmitz et al., 1998), Uzbekistan (Trabakua section; Bolle et al., 2000), ODP sites 690, 685, 689, 865, 1051, 1263, 1260B and 1172D (Katz et al., 2003; Sluijs et al., 2008; Mutterlose et al., 2007) and DSDP sites 401.

However, gradual decreases in the stable isotope ratios have been observed 1-2 m below the PEB, corresponding to duration of 120 kys (Speijer et al., 2000) in several marine and terrestrial sections, including Alamedilla in Spain (Lu et al., 1996), Aktumsuk in Uzbekistan (Bolle et al., 2000), Dababiya in Egypt (Aubry et al., 2007), ODP site 690 (Bains et al., 1999) and in pedogenic carbonate from Polecat Bench, Wyoming (Bowen et al., 2001).

The P/E boundary in Dababiya GSSP is placed at the sequence boundary represent a change in lithology from marine hemiplegic to more coarser sediments linked to increased fluvial discharge from shallower environment (Schulte et al., 2011), characterized by an increase in detrital components (e.g., quartz, phyllosilicates, feldspars) and an abrupt decrease in carbonate contents. The decrease in $CaCO_3$ contents could be explained by carbonate dissolution and/or dilution due to increasing detrital input (Figs. 2, 9a,b). The thickness of Bed 1 reaches its maximum at the main GSSP outcrop. The lateral variation is evidenced by comparison with the NW and E sections. At the NWs only 50 m from the GSSP, the thickness of bed 1 decreased to almost half. At the E section only 25cm from Bed 2, and bed 1 is absent. Schulte et al. (2011) also noted the geometric and grain size differences of Bed 1 and suggested deposition occurred in a submarine channel. The change in the whole rock compositions from the NW and E sections further support this observation. The NWs represent an abrupt change in whole rock composition that persists for 58 cm above the SB with increased phyllosilicate, quartz, and feldspar contents, and no change in Ca-apatite. At the Es the whole rock composition changes sharply at the P/E boundary, with notable increases in quartz, feldspar, and phyllosilicate and an abrupt decrease in calcite content. All these changes are observed 5 cm above the SB. The abrupt changes in the whole rock composition could be linked to the absence of the lowermost Eocene sediments from the Es and/or erosion and weathering of these rocks due to the paleogeography.

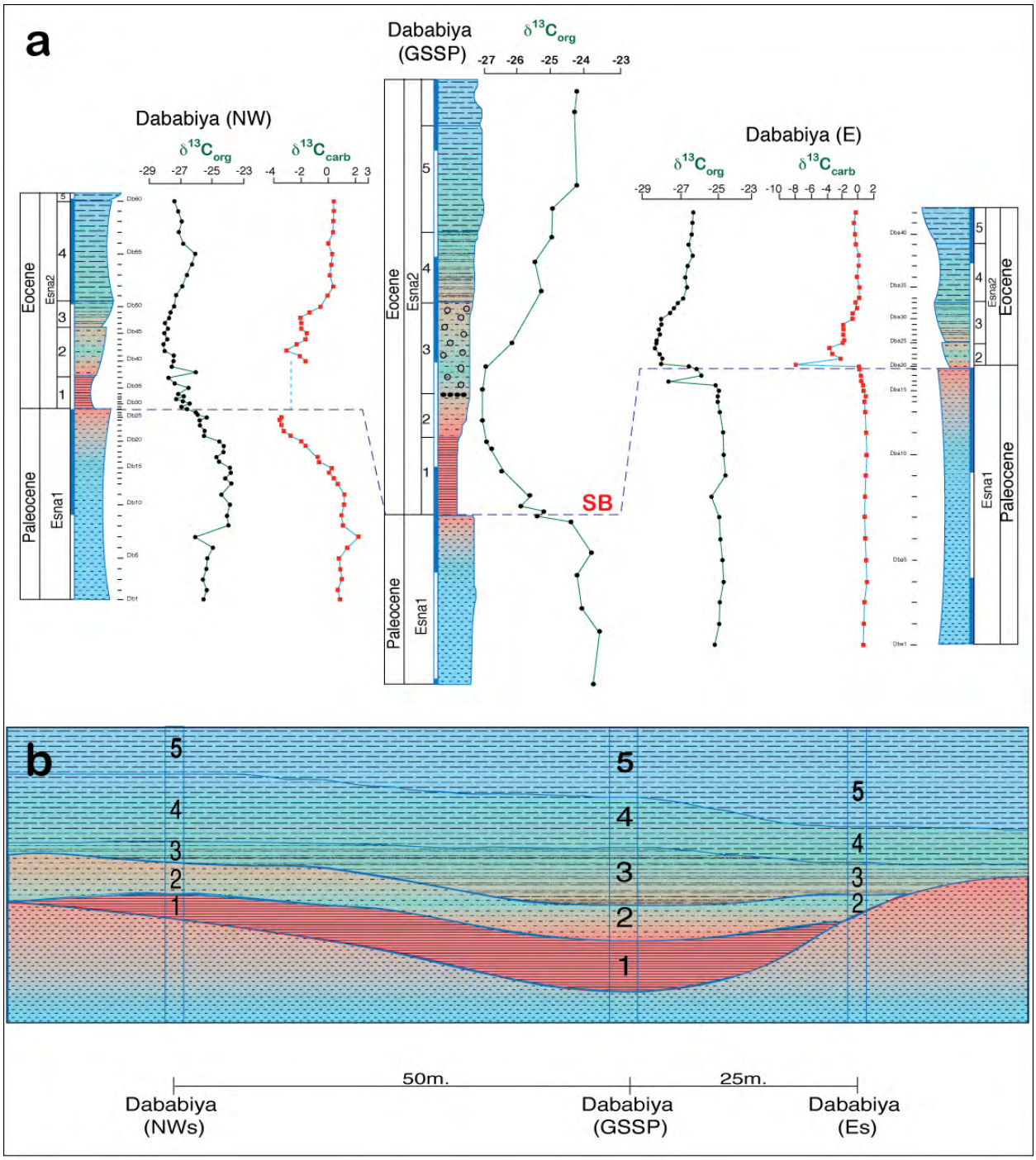

Figure 9: (a) *Correlation of the NWs and the Es with the published Dababiya GSSP (Dupuis et al., 2003) based on both organic Carbon isotopes, and new data obtained from inorganic carbon isotope. Both* $\delta^{13}C_{Carb}$ *and* $\delta^{13}C_{org}$ *in the LSS show gradual decreases beginning 60cm below the SB and reaching the CIA-minimum for* $\delta^{13}C_{Carb}$ *at the SB, whereas the* $\delta^{13}C_{org}$ *CIA-minimum is reached in the upper third of Bed 2.* ***(b)*** *Schematic diagram showing the benching out of Bed 1 and Bed 2 to the NW and E sides of the main GSSP, marking the deposition in an asymmetrical submarine channel.*

The gradual decrease in the $\delta^{13}C_{org}$ and $\delta^{13}C_{carb}$ values at Dababiya (NWs) may be linked to the gradual increase in temperature at the end of the Paleocene (Bowen and Zachos, 2010). The correlation between NW, E and the GSSP sections indicates that the PETM is at the maximum thickness in the middle part and thinning towards the NW and E sections. At the NWs, the PETM interval minus by about 30% compared with the GSSP. At the Es, the absence of the basal $\delta^{13}C_{org}$ and $\delta^{13}C_{carb}$ variations reflects the absence of lowermost Eocene sediments of that section (Bed1 and part of Bed 2, Fig. 9a,b). The correlation between the studied sections and the GSSP studied by Depuis et al. (2003), including the field observation, the lithostartigraphic records, and the whole rock mineralogy suggest that the Dababiya GSSP deposition occurred along channel banks (Schulte et al 2011; Khozyem at al., *submitted*). The new data, confirms that the lower part of the Dababiya GSSP section (Bed 1 and Part of Bed 2) was deposited in an asymmetric submarine channel that extended 25m eastward and about 150 m to northwest with maximum width of about 200 m and maximum depth of 0.88 m.

5.3. **Mineralogical proxies: paleoenvironmental implications**

The whole rock and clay minerals and their ratios, such as Detrital Index (DI: calcite/quartz+phyllosilicate+feldspar), kaolinite/smectite, and kaolinite/illite+chlorite are good proxies for paleoclimatic changes (Adatte et al., 2002, Shamly et al., 1989)

At Dababiya NWs, the weathered interval spans about 0.5 m above the SB. The abrupt change in whole rock composition at the SB is linked to the enrichment in phyllosilicate quartz and feldspar that represents the high detrital input as also noted by the decreasing detrital index (DI=calcite/quartz+Phyllosilicate+feldspar). At the SB, the increased detrital input negatively affects the calcite content resulting in minimum values that could be due to leaching of the carbonate contents under acid conditions and/or dilution by increasing detrital input. This changes in the whole rock composition at the SB is due to the high input of terrigenous sediments, associated with increased erosion and transport of detrital material in response to climatic and see level changes (Khozyem et al., 2013). Schulte et al., (2011) discussed the nature and origin of the weathering process suggesting that the increase in detrital input and the abrupt higher content in phyllosilicate were due to fluvial input during a period of low or rising sea level. Speijer and Wagner (2002) explained the increase in detrital input as a result of reworking linked to the transgressive system tract (TST) during a period of high silicate weathering. Based on these two explanations and the architecture of the depositional basins, we interpret the weathered interval at Dababiya GSSP as a submarine channel filled by detrital sediments reflecting increased fluvial discharge during a period of TST (Fig. 2).

The increase in Ca-apatite was contemporaneous with a gradual increase in calcite; this could be interpreted as an increase in surface productivity and the onset of a recovery period (Torfstein et al., 2010). The Ca-apatite enrichment could also be explained by remobilization of phosphate from detrital material (Fig. 2) and the termination of anoxic conditions. The diagenetic overprint on the clay minerals usually occurs at burial depth exceeding 2 km (Chamly, 1998). The sediments from NWs show no sign of burial diagensis as indicated by the variable presence of smectite and low contents of mixed layer illite-smectite (e.g., Bolle and Adatte, 2000). The detrital input is responsible for the clay mineral distribution in marine sediments (Millot, 1970). The weathering interval at Dababiya NWs is most enriched in phyllosilicates (Fig. 4), which permits us to distinguish two horizons: one rich in smectite and no change in the

kaolinite/smectite ratio from the SB to top of Bed 1, and the second low in smectite, a relatively high kaolinite/smectite ratio and higher content in favor of kaolinite, chlorite, illite-smectite and palygorskite. The first horizon suggests two possible scenarios: a) no significant climatic control (e.g, chemical weathering) associated with increased riverine input of detrital material, and/or b) an increase in physically weathered material reaching this site masking the impact of chemical weathering.

Millot (1970) and Chamley (1998) discussed the origin of clay minerals and refer to the possible formation of illite, chlorite, smectite-illite in area of steep relief with active mechanical erosion during a period of enhanced tectonic activity. The alternative process they proposed is the formation of these minerals in cold or desert regions under low temperature and/or low precipitation rate, which would reduce the chemical weathering. This suggests a scenario of a tectonic stable southern Tethys during the Paleocene-Eocene interval with low chemical weathering, and formation of illite, chlorite, and illite-smectite transported into the depositional basin by seasonal riverine input (Fig.4).

High kaolinite content is generally interpreted as an indicator of tropical weathering (Srodon, 1999). In Dababiya NWs, the kaolinite content is low, except in the middle of Bed 2, the top of the weathering interval. This high kaolinite content observed in that interval most probably most probably originated from chemical weathering of silicate rocks.

The mineralogy of the two horizons marked by increased weathering conditions helped to explain the nature of weathering processes which began at the sequence boundary with intensive physical weathering associated with rainfall triggering the transport of eroded material into submarine channel. Decreased rainfall and/or seasonal tropical changes in the climate altered the weathering regime. The mechanically disintegrated materials were submitted to prolonged chemical weathering resulting in the accumulation of kaolinite at the top of bed 2 and the disappearance of feldspars. Above, the climate gradually changed to seasonal and/or arid conditions as observed by the gradual return of the phyllosilicates to its values observed below the SB.

5.4. **Nitrogen isotope variations: ocean eutrophication**

The stable isotope ratio of nitrogen may be a promising proxy for delineating the eutrophication in the ocean during the PETM, because nitrogen is a main nutrient in the ocean. Furthermore, the nitrogen isotope fractionation of sedimentary organic matter helps tracing the processes of nitrification in aquatic environments including biological nitrogen fixation, heterotrophic denitrification and anaerobic ammonia oxidation (references in Spangenberg et al., 2013). This provides important clues on the trophication level in the aquatic ecosystem. The marine N cycle during the PETM was similar to today. In the modern ocean, N_2 fixation is mainly associated with areas of low productivity and low accumulation of sedimentary organic carbon (Kuypers et al., 2004). The conversion of nutrient N to N_2 predominantly occurs in the oxygen-depleted waters and sediments underlying upwelling zones characterized by high productivity and high rates of organic carbon accumulation. The nitrogen depletion is a phenomenon linked to the high ocean surface production and intense oxygen minima as observed in the present day ocean (Ohkouchi et al., 1997, 2006; Farrimond et al., 2004; Kuypers et al., 2004; Dumitrescu and Brassell, 2006; Jenkyns 2010).

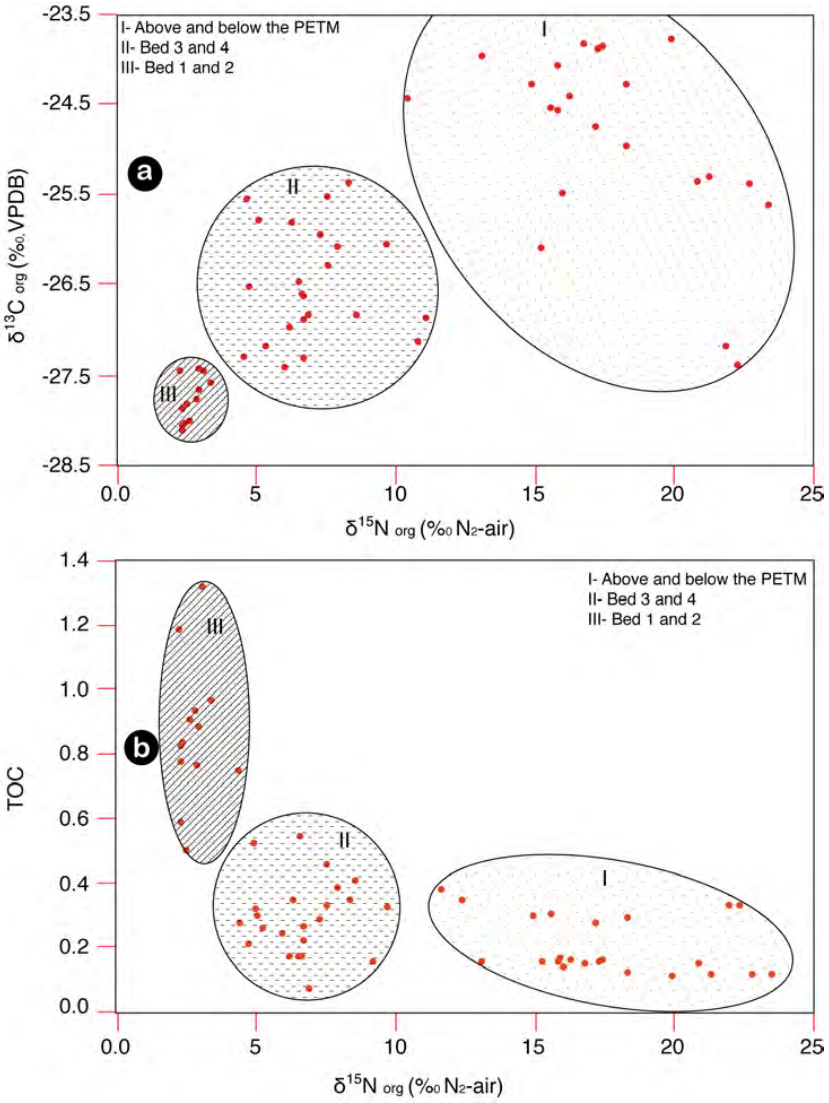

Figure 10: a) *Cross plot of* $\delta^{13}C_{org}$ *vs.* $\delta^{15}N$ *and* ***b)*** *TOC vs.* $\delta^{15}N$ *showing differences in organic matter types above and below the PETM and at the interval marked by increased weathering.*

The nitrogen isotopes composition of the kerogens covers a broad range of almost 23‰ indicating the compositional variability of organic matter where value >7‰ marine to open marine organic matter and those <7‰ reflects terrestrial and mixed organic matter contents (Peters et al., 1978).

The relatively low $\delta^{15}N$ values, close to that of the modern atmospheric N_2 ($\delta^{15}N \approx 0‰$), may result from primary contribution of microbial N_2 fixers as oxygenic photosynthetic cyanobacteria and/or input of nitrogen-fixing terrestrial plant debris into the marine sediments (e.g., Fio et al., 2010). The cross plot $\delta^{15}N$- $\delta^{13}C_{org}$ helps unravel the nature of the sedimentary organic matter and the deposition conditions at Dababiya NWs (Fig. 5, 10a). Analytical data fall into three distinctive fields: i) open marine organic matter supply (>+10‰ $\delta^{15}N_{org}$ and -27.5 to -23.5‰ $\delta^{13}C_{org}$) for the group of samples representing the late Paleocene and above the PETM level; and ii) mixed organic sources (≈ +4 to +10‰ $\delta^{15}N_{org}$ and t-27.5‰ to -25.2 $\delta^{13}C_{org}$) the PETM excluding the weathered interval and the anoxic levels; and (iii) bacterial derived organic matter (<3‰ $\delta^{15}N$ and -27.5 to -28.5‰ $\delta^{13}C_{org.}$) characterizing the interval including the anoxia levels.

As noted in the middle part of Bed 2 at NWs, the $\delta^{15}N$ reached minimum values at the same time as the maximum of TOC concentration (Fig. 10b). This suggests mainly cyanobacterial

contribution, probably due to the introduction of soil microbial biomass from river waters into the shallow-shelf system (e.g., Fio et al., 2010). Cyanobacteria are known to be capable of surviving in high-stress environments (e.g., Roszak and Colwell, 1987; Ben-Jacob et al., 2000; Cao et al., 2009) and also may be responsible for increasing oxygen content in the water column and nitrification. This could be associated with bacterial activities (sulphur reducing bacteria and N-fixers) near the onset of the PETM recovery phase. Similarly, the N_2 fixation was the source of nutrient N in vast areas of the Mesozoic oceans characterized by strong oxygen depletion, high nutrient N loss, and high rates of organic carbon accumulation under anoxic conditions (Meyers et al., 2006, Knies, et al., 2008) (Fig. 10).

5.5. Proxies from element associations and element ratios

A cluster analysis (using Minitab 11 software) performed on major and trace element concentrations defined three main groups of samples with characteristic enrichments/depletion, reflecting successive climatic and environmental changes during the PETM. The three groups represent: (a) the detrital input and weathering indexes, (b) redox conditions and (c) productivity sensitive trace elements. The interpretation of these geochemical groups was further supported by the stratigraphic variations of element ratios commonly used as proxies for redox conditions, detrital input, weathering rates and productivity. These included an Eu anomaly (Eu/Eu*=(3Eun/[2 Sm_n+Tb_n], Zang et al., 2008), Ce anomaly (Ce/Ce*=(Ce_n/[(La_n+Pr_n)/2]), chemical index of alteration (CIA = [Al2O3|(Al2O3+CaO*+K2O+Na2O)]×100, Nesbitt & Young 1984, 1989; Price & Velbel 2003), the La_n/Yb_n ratio and such as Mn*= log [(Mn_{sample}/Mn_{PAAS})/Fe_{sample}/Fe_{PAAS})], V/Cr, and V/(V+Ni), P/Ti, Ba/Ti, Cd/Ti, Mo/Ti as well as the TOC contents (Cullers 2002; Brumsak et al., 2006; Riquier et al, 2006; Tribovillard et al., 2006; Kraal et al., 2010).

The first group of elements indicate the detrital input and weathering rate including: Si/Al, Ti/Al, K/Al, Zr/Al, La/Yb, Eu/Eu*, and CIA show that abrupt changes occurred at the sequence boundary up to the middle part of Bed 2. Below the SB (sample 1 to 27, Fig.11) the recorded mean values are 3.1 for Si/Al, 0.04 for Ti/Al, 0.3 for K/Al, 13 $X10^{-4}$ for Zr/Al, La/Yb around 11.46, 1.2 for the Eu/Eu*, and 30.86 for CIA. At the SB, a persistent change from sample 28 to 42 records mean values of 3.7, 0.06, 0.4, $28X10^{-4}$, 7.3, 1.1, and 56.92, respectively, and all Al-normalized elements and their ratios are enriched comparable to the PAAS (Fig. 11). Above sample 42 all the Al- normalized elements and the ratios used as detrital input indicator return to the mean values observed below the SB.

The second cluster of the elements includes the redox sensitive elements and ratios. The Ce/Ce* show a notable decrease from the mean 0.78 to 0.59 at the SB this interval spans samples 28 to 42. Above sample 42 to the top of the section Ce/Ce* increased to 0.67 (Fig. 12). Low Ce/Ce* values were found at the base of Bed 1 (samples 29 to 34) and at the middle part of Bed 2 (samples 39 to 42). These negative Ce/Ce* ratios are associated with sharp peaks of V/Cr (Fig. 12). Above the P/E a sharp increase in the V/(V+Ni) ratio spans from the SB to sample 42, where minimum Mn* values are reached at 10 cm above the P/E (Fig. 12). The third element association includes phosphorous (P_{tot}) and productivity sensitive trace elements (Mo, Cd, Ba, and P), which show high concentrations in the NWs at the second anoxia, generally associated

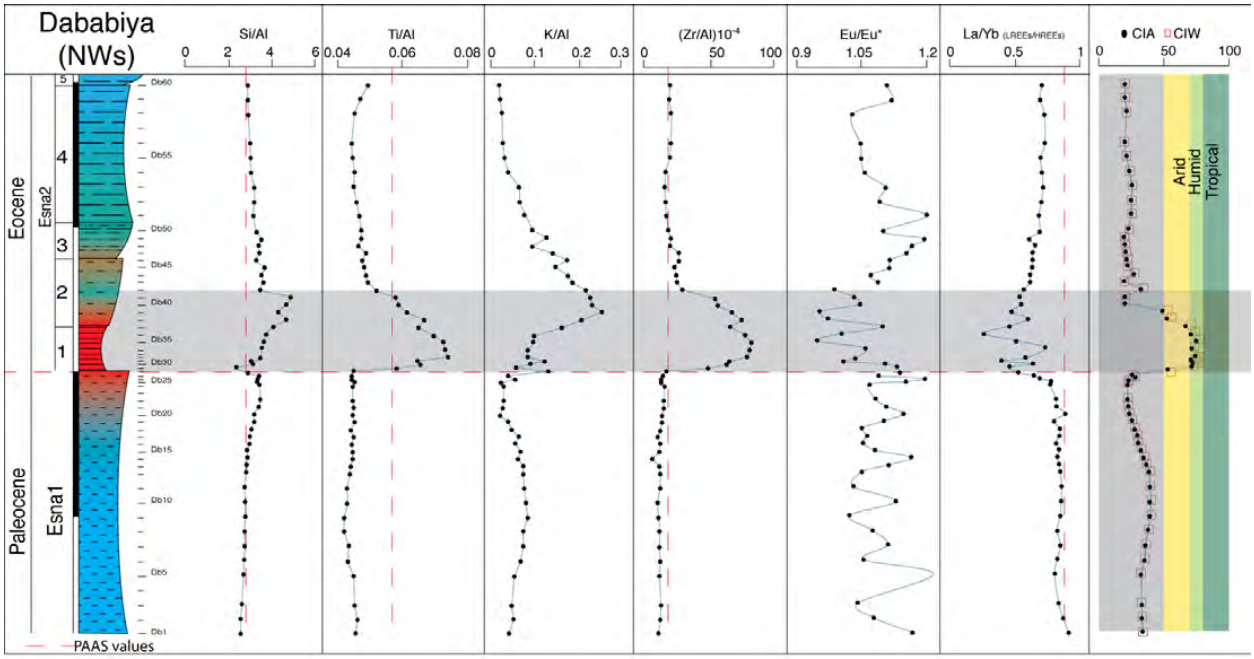

Figure 11: *Detrital input proxies together with Eu-anomaly, La/Yb ratio and weathering index (CIA and CIW).*

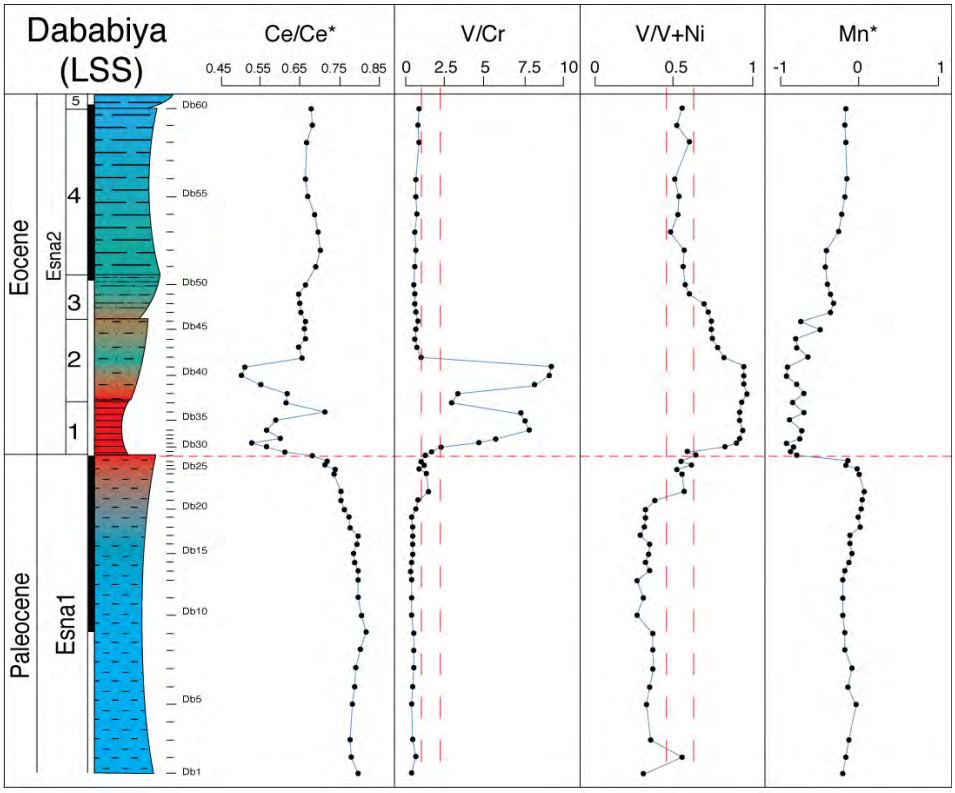

Figure 12: *Ce-anomaly and redox parameters (V/Cr, V/V+Ni, and Mn*) showing the different anoxic intervals recorded at the Dababiya NW section.*

with high TOC contents. B and P_{tot} show a sharp increase at the middle part of Bed 2 (sample 40), which persists up to the top of the PETM interval. The high nutrient content at the base of this interval is suggested by trace element (Mo, Cd, Ni, Zn and Cu) concentrations associated with the second Ce/Ce* negative peak (Fig. 7, 12).

Removal of the dissolved major, trace and rare earth elements from the water column and their incorporation in sediments depends on biotic and abiotic processes and redox conditions in the water column and the water-sediment interface (e.g., Tribovillard et al., 2006). In oxic environments trace elements are scavenged by precipitating Fe-Mn oxyhydroxides, whereas in dysoxic and anoxic environments the TE enrichments are linked to redox cycles in the sediments-water interface and associated microbial activities (Lyons et al., 2003; Sageman & Lyons 2003; Algeo and Maynard, 2004; Tribovillard et al., 2006; Riquier et al., 2006). Therefore the ME and TE can provide insights into the paleo-depositional environments at the PETM.

The Al-normalized Si, Ti, K, and Zr contents, combined with the La/Yb, and Eu/Eu* ratios can be use to distinguish detrital material from different sources with a riverine origin as the most recognizable source (Bertrand et al., 1996; Murphy et al., 2000b; Pujol et al., 2006, Khozyem et al., 2013). At the weathering interval of Dababiya NWs, a strong period of fluvial discharge was the main source of weathered material into the ocean (e.g., Schulte et al., 2011), as indicated by high Ti/Al, and Zr/Al ratios. The source of the detritus in the NW section appears to be a homogenous as indicated by the uniform stratigraphic distribution of both Si/Al and K/Al (Riquier et al., 2006). The gradual increase in authigenic and/or biogenic silica in the lower part of the weathering zone may be due to a progressive increase in detrital input (Tribovillard et al., 2006) as commonly observed in the transgressive system tract (TST; Speijer et al., 2000).

Changes in bottom water conditions can be interpreted based on different element ratios (e.g., V/Sc, V/Cr, Ni/Co, U/Th, V/V+Ni etc.) and Al-normalized contents of redox sensitive and chalcophile elements (e.g., Fe, Mn, U, V, Zn, Pb, Cu, Ni) (Joachimski et al., 2001; Rimmer, 2004; Algeo and Maynard, 2004; Cruse & Lyons, 2004; Pujol et al., 2006). However, some of these elements are typically associated with hydrothermal activity (e.g., Pb, Zn, Cu, Co, Ag, Mo) and the cause of their enrichment remains often ambiguous (Cruse & Lyons, 2004). The Ce-anomaly is one of the strongest indicators for water column oxygenation during the major events. Seawater contains low concentration of Ce because it can be easily oxidized to the 4^{+} insoluble state under oxic conditions (Holser, 1997; Shields and Stille, 2001); the Ce^{4+} tend to be lost from the sediments under reducing conditions, similar process leads to Mn enrichment in sediments deposited under oxic condition (Clavert and Pedersen, 1993). Mn* (Cullers, 2002) is the best presentation of the Mn concentrations linked to redox conditions, where Mn^{2+} replaces Ca in Ca-rich sediments during the diagenetic processes and forming Mn-bearing carbonate. Vanadium is strongly coupled with the redox cycle of both Mn and Fe-oxyhydroxides and could be incorporated into Mn-Fe bearing minerals (Tribovillard et al., 2006). Another source of V is the sedimentary biomass from nitrogen fixing bacteria (Anbar, 2004; Grosjean et al., 2004). Low Mn contents can be indicative of dysoxic bottom water conditions given that under reducing conditions at the sediment/water interface, soluble Mn^{2+} diffuses from the sediments into the oxygen-depleted bottom waters (Landing and Bruland, 1980; Bruland, 1983; Landing and Bruland, 1987).

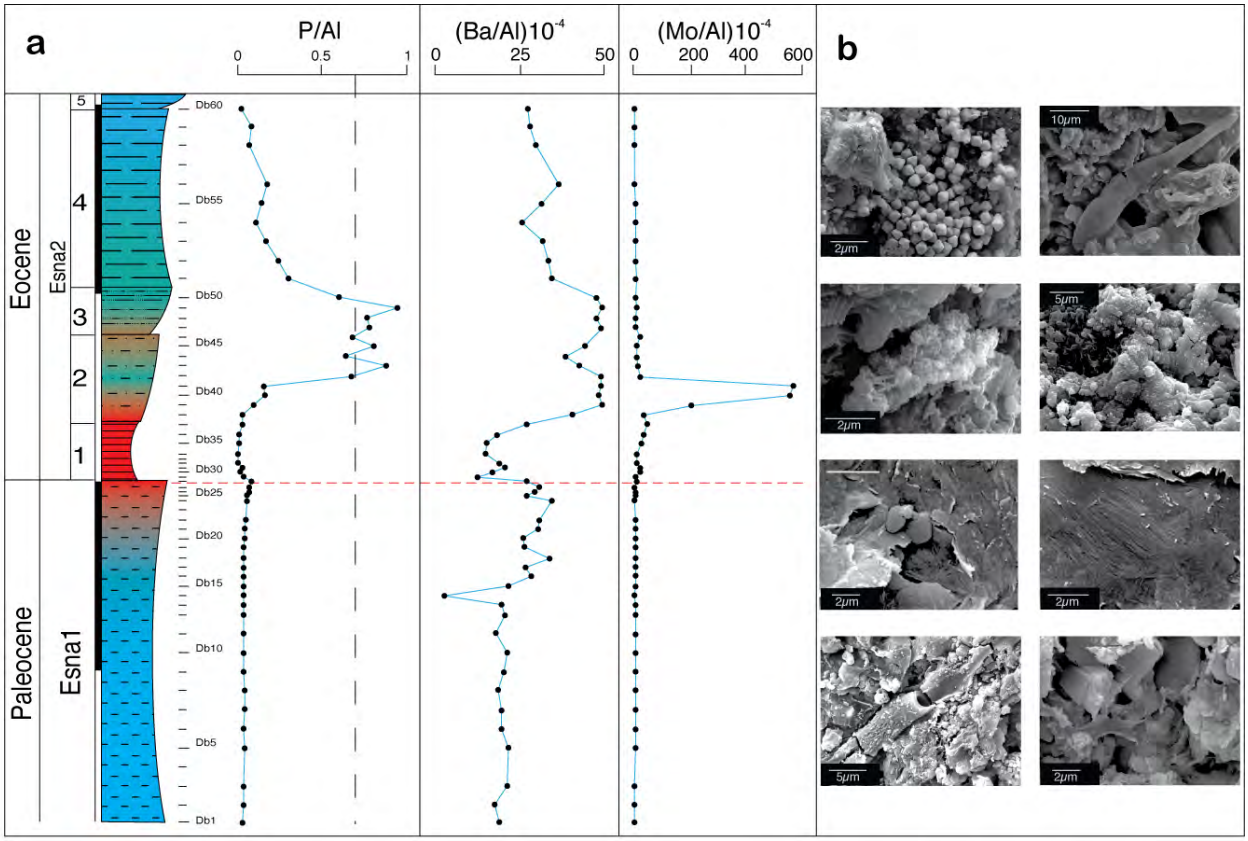

Figure 13: (a) *Plot of paleoproductivity parameters at the Dababiya NWs recovery interval;* ***(b)*** *Different examples of organic matter debris observed at the second anoxic interval at Dababiya NW section.*

Dababiya was part of the southern Tethys margin, which was tectonically stable during the late Paleocene to early Eocene. In these environment Al-normalized contents of chalcophile elements (Algeo & Maynard, 2004; Pujol et al., 2006) and their ratios can also be used to constrain the water column oxygenation during deposition of the PETM sediments.

Schulte et al. (2011; 2013) inferred the presence of one anoxia interval at the Dababiya GSSP, whereas in this study the Ce/Ce* data combined with other redox proxies marks additional interval of anoxia (Fig.12). Most notable are the two Ce/Ce* negative shifts marking intervals of anoxia in the basal part of the PETM at NWs. Each of these anoxic intervals has its own characteristic. The lower anoxic level is characterized by the negative Ce/Ce* shift in with a positive excursions in V/Cr, and V/V+Ni values, a decrease in Mn*, no change in the Al-normalized trace elements V/Al, U/Al, Zn/Al, Cu/Al, and Ni/Al (Figs. 7,12,13) and the presence of disseminated eudiomorphic pyrite crystals. The upper anoxia level is characterized by the negative Ce/Ce* shift coincident with increased V/Cr and a continuous increase in V/V+Ni and depletion in Mn* (Fig. 14). These changes are linked to an abrupt increase in the V/Al, U/Al, Zn/Al, Cu/Al, Ni/Al, common framboidal pyrite and the presence of N-fixing bacteria as observed by steady negative $\delta^{15}N$ values (Figs. 5,10,14). The characteristics of each negative Ce/Ce* anomaly reflects the variable nature of anoxia. If the release of methane was the main reason for the climatic warming, we can explain the lower anoxia by decomposition and oxidation of methane clathrate following the exothermal equation of Circone et al. (2005):

$$CH_4.\, n_wH_2O(s) \rightarrow CH_4(g) + n_wH_2O(s) \qquad (1)$$

and

$CH_4.n_wH_2O(s) \rightarrow CH_4(g) + n_wH_2O$ *(2)*

From the equation 1 and 2

$CH_4 + 2O_2 \rightarrow CO_2 + 2H_2O$ ($\Delta H = -891$ k J/mol (at standard conditions; Circone, et al., 2005). This decomposition and oxidation of methane clathrates from the continental shelf could have led to anoxia and the initial phase of ocean warming. Clathrate melting causes ocean acidification with the warming resulting from exothermal reaction leading to progressive dissolution of carbonate from the deep water and shoaling of the calcite composition depth (CCD) as noted at the SB in Dababiya (NWs) as well as other localities (e.g. Wadi Nukhul, Sinai, Khozyem et al., 2013; Zachos et al., 2005).

Another reason for the rapid sea level rise during the PETM could be the thermal expansion of the seawater (Schulte et al., 2013). In addition, the released CO_2 from the ocean due to clathrate melting acts as atmospheric greenhouse gases. The environmental response is the drawdown excess CO_2 by silicate weathering on land and transport to the ocean by streams particularly during the early stage of the PETM associated with the TST. Mixing of fresh water loaded with suspended nutrients result in water column stratification, and/or development of eutrophic conditions due to the low light penetration as noted by the presence of important bacterial activity, mainly from sulphur reducing and nitrogen-fixing bacteria (Figs. 10, 13, 14).

Figure 14 summarized the link between methane release and anoxic conditions with formation of anhydrite. Whiticar (1999) discussed the relationship between sulphate reduction and methane release and concluded that the release of methane produces free SO^{+4} that easily reduced to HS^- under acidic-anaerobic conditions (HCO_3) at the anaerobic/aerobic interface where the sulphides oxidized in the presence of NO as oxidizing agent (Whiticar, 1999; Campbell 2006; Jenkyns 2010). Based on these processes we suggest that the lower anoxic interval resulted in precipitation of disseminated euhedral pyrite crystals within sediments (Fig. 14b), whereas the upper anoxic level associated with the accumulation of organic matter, precipitation of primary anhydrite and oxidation of framboidal pyrite (<5μm, Fig.14b), formed by bacterial activity under anoxic water column conditions (Wilkin et al., 1996, 1997; Wignal et al., 2005; Riquier et al., 2006) in a medium saturated with dissolved $CaCO_3$ (Fig.14b)

5.6 Toward understanding the PETM event.

The late Paleocene to early Eocene transition experienced a series of progressive changes beginning with the volcanic activity (Courtillot and Renne, 2003) and changes in ocean circulation (Dickens et al. 1995, 1997). New geochemical and mineralogical data from the Dababiya GSSP combined with published data from Bown and Zachos (2010) reveal four main phases of the PETM (Fig. 15):

Phase 1: The North Atlantic volcanic provinces, Caribbean volcanic activity, and mid oceanic volcanism (Storey et al., 2007) all occurred during late Paleocene (Courtillot and Renne, 2003). This led to a gradual increase in ocean temperature and changes in ocean circulation (Dickens et al. 1995, 1997), which negatively affected the methane hydrates stored on continental shelf.

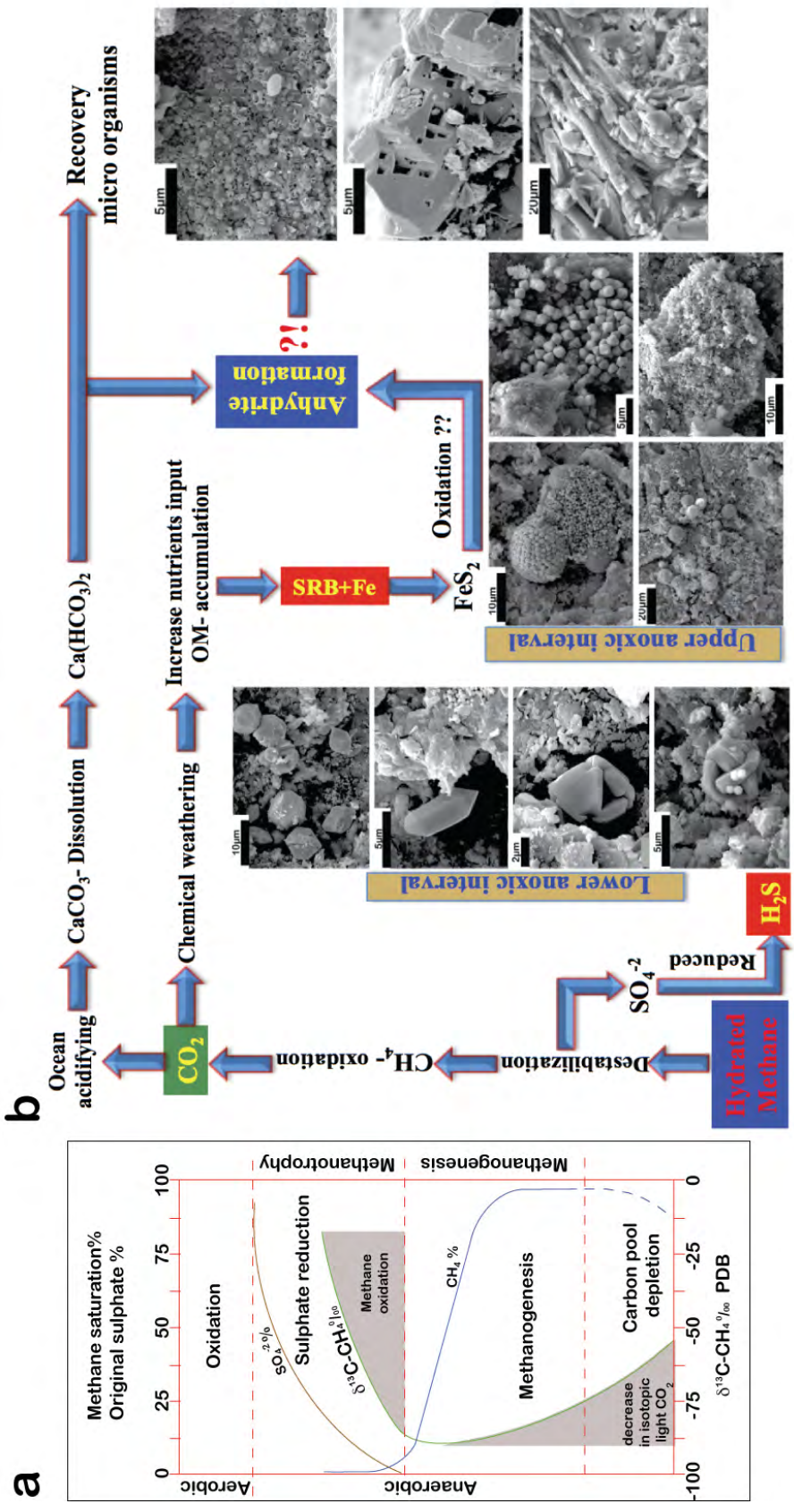

Figure 14: ***(a)*** *Illustration of different processes during methane hydrate release from the continental shelf (after Whiticar, 1999);* ***(b)*** *Schematic diagram showing the differences between the anoxic levels at the NW section linked to with hydrated methane release and deposition of anhydrite.*

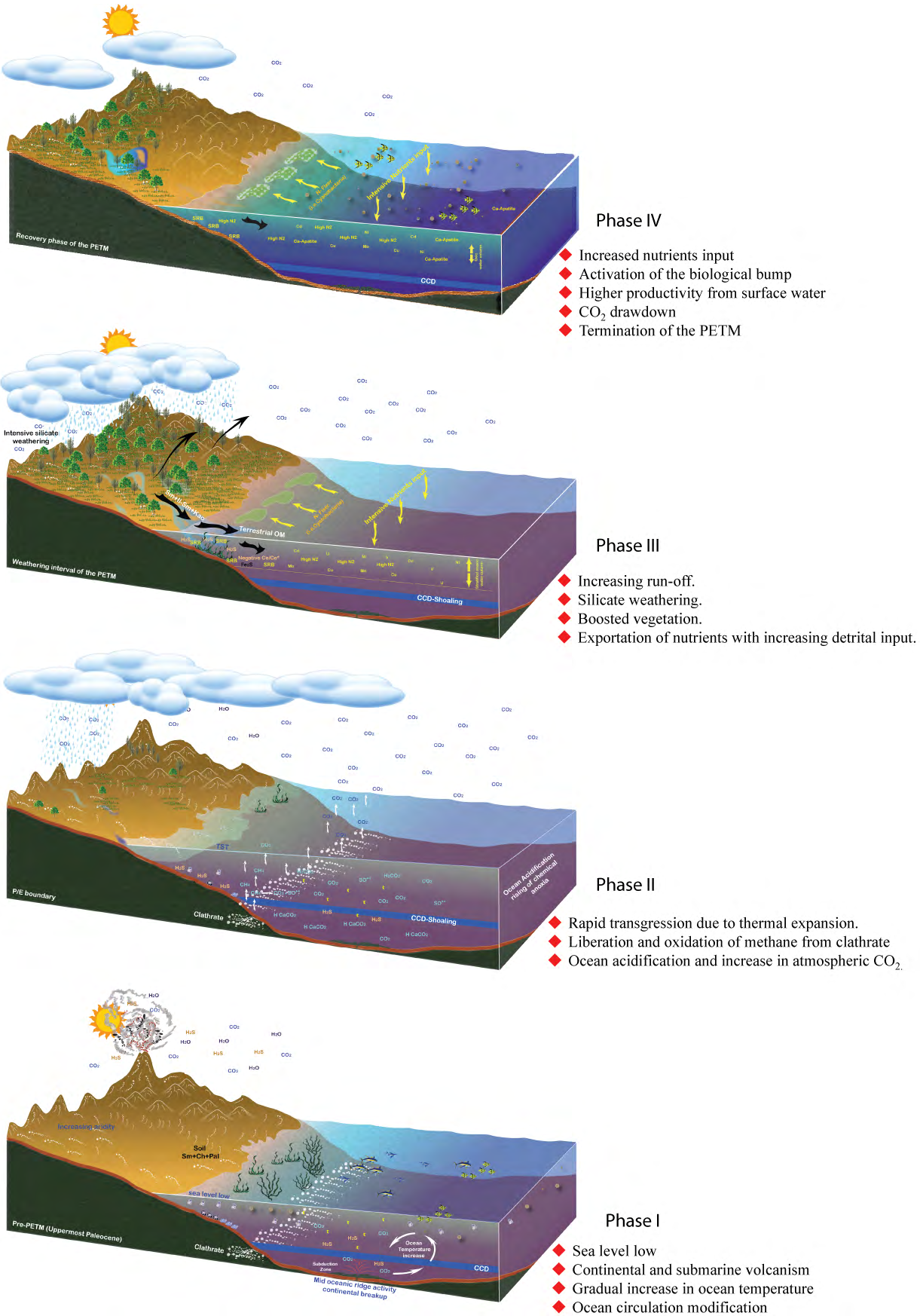

Figure 16: *Hypothetical block diagrams representing four phases of the PETM event using the scenario of Bowen and Zachos, (2010) in combination with results obtained from this study.*

The gradual decrease in $\delta^{13}C_{org}$ and $\delta^{13}C_{carb}$ preceding sequence boundary at Dabbabiya GSSP also observed at Almendilla, Spain reflects this changing environment (Fig. 15).

Phase 2, the global seawater warming of about 5^{o}C due to the submarine volcanism resulted in thermal expansion and a sea level rise of about 5m (Speijer and Wagner, 2002; Sluijs et al., 2008) destabilized methane hydrate. As a result of hot saline water bodies formed on epi-continental seas, and were exported to the deep ocean. Consequently, the change in physic-chemical condition of the ocean (e.g., Releasing and oxidation of ocean methane gas consumed the oxygen in the sea water and led to the first anoxia observed at the base of the weathered PETM, accompanied by acidification observed by shoaling of the CCD (Zachos et al., 2008). This phase is represented at Dababiya NW section by the dissolution (Fig. 15), and lower anoxic interval characterized by negative Ce-anomaly with no change in other redox proxies.

Phase 3: At the water/atmosphere interface, the methane gas oxidized to CO_2. The CO_2 is contributing to greenhouse gases and causing the global hot humid climate with a high precipitation as observed increased kaolinite input (Bolle et al 200; 2001). On land the drawdown excess CO_2 from the atmosphere results in silicate weathering, the uptake of CO_2 by plants during photosynthetic, and the return of CO_2 to the ocean as carbonic acid and leading to increased ocean acidification. The terrestrial weathered materials are transported to the ocean by streams and fluvial discharges (Schulte et al., 2011) accompanying the terrestrial organic matter. The introduced organic matter led to development of anoxic conditions fostering bacterial activity (SRB and Cyanobacteria), and gradually increasing oxygen by fixation of the nutrients. This biospheric feed back during the PETM is a direct response to extremely high tropical temperatures (Huber 2008), seasonal aridity within the continental interiors (Wing et al., 2003), and the release of substantial quantities of C to the ocean/atmosphere system.

Phase 4: the last phase of the PETM is the recovery (Fig. 15). The nutrients transported from the land to the ocean was driven by intensive continental weathering which associated with ocean surface productivity activated the biological bump, thus decreasing ocean acidity. This recovery phase is recognized by gradual increase in carbon isotopes and the abundance of phosphorous with fixation of Ba as a result of the oxic condition.

6. CONCLUSIONS

The expanded sedimentary record of the Dababiya GSSP improves our understanding of the processes leading up to and during the PETM event.

(1) The Dababiya GSSP are deposited in a deepest part of an asymmetric submarine channel as indicated by the paleotopography, and absence of uppermost Paleocene and lowermost Eocene sediments from the E section 25m from the main GSSP outcrop. At 50 m to the NW the sediment beds thin out and disappear at about 150 m from the main GSSP outcrop. Thus, the Dababiya GSSP represent a localized expanded PETM sequence with a maximum extend of about 200m.

(2) At the GSSP, the P/E boundary coincides with a sequence boundary and erosional surface, that can be traced hundreds of km and even to neighboring countries. Consequently, the P/E boundary interval is incomplete with a hiatus spanning the latest Paleocene and the earliest Eocene, as also observed in other sections (e.g. Wadi Nukhul, Khozyem et al., 2013).

(3) $\delta^{13}C_{Carb}$ and $\delta^{13}C_{org}$ profiles show gradual decrease during the latest Paleocene reaching the CIE-minimum at the SB. This interval represents the initiation of the PETM, and may be explained by the onset of the North Atlantic volcanism.

(4) The CIE- minimum in $\delta^{13}C_{Carb}$ is at the SB, and $\delta^{13}C_{org}$ is in the top third of bed 2, marking the onset of the recovery. The depleted recovery in $\delta^{13}C_{org}$ may be due to variable rate of carbon cycle (e.g. continental silicate weathering, increased rate of organic carbon burial, and increased ocean productivity)

(5) Above the middle of bed 3, $\delta^{13}C_{Carb}$ and $\delta^{13}C_{org}$ and the bulk rock composition are return to background values observed below the PETM.

(6) The Ce-anomaly shows two distinctive peaks in the weathering interval. The peak is associated with strong dissolution and may linked to chemical anoxia due to the methane released and oxygen exhalation from the seawater. The second peak is corresponds to an abrupt change change in all redox parameters (V, U, Mo, Cd, etc.) associated with the maximum accumulation of organic matter.

(7) The recovery phase begins at the top of the second anoxia and marked by increase in P, Ba, indicating the return of oxic conditions and ocean re-nitrification.

ACKNOWLEDGEMENTS I thank T. Monnier and J. C. Lavanchy for help in the phosphorus and XRF analyses and P. Vonlanthen for help during SEM analyses. I am grateful to the Egyptian ministry of state for environmental affairs and the president of the international committee of stratigraphy for the providing the necessary official access and permissions to complete these studies. This study was performed at the University of Lausanne and supported by the Egyptian ministry of higher education (mission No.001/013/104) (HK), and the University of Lausanne.

REFERENCES

Adatte, T., Stinnesback, W., and Keller, G., 1996, Lithostratigraphic and mineralogic correlations near K/T boundary clastic sediments in northern Mexico: Implication for origin and nature of deposition: Geological Society of America, special paper, v. 307, pp.211-226.

Agnini, C., Fornaciari, E., Rio, D., Tateo, F., Backman, J., and Giusberti, L., 2007, Responses of calcareous nannofossil assemblages, mineralogy and geochemistry to the environmental perturbations across the Paleocene/Eocene boundary in the Venetian Pre-Alps: Marine Micropaleontology, v. 63, pp.19–38.

Alegret, L., Ortiz, S., and Molina E., 2009, Extinction and recovery of benthic foraminifera across the Paleocene–Eocene Thermal Maximum at the Alamedilla section (Southern Spain): Palaeogeography, Palaeoclimatology, Palaeoecology, v. 279, pp.186–200.

Algeo, T.J., and Maynard, J.B., 2004, Trace-element behavior and redox facies in core shales of Upper Pennsylvanian Kansas-type cyclothems: Chemical Geology, v. 206, pp. 289–318.

Anbar, A.D., 2004, Molybdenum stable isotopes: observations interpretations and directions: Review in Mineralogy and Geochemistry, v. 55, pp. 429–454.

Aubry, M.-P., Berggren, W.A., Van Couvering, J.A. , Ali, J., Brinkhuis, H., Cramer, B., Kent, D.V., Swisher, III, C.C., Gingerich, P.R., Heilmann- Clausen, C., Knox, R.W.O'B., Laga, P., Steurbaut, E., Stott, L.D., and Thiry, M., 2003, Chronostratigraphic Terminology at the Paleocene/Eocene Boundary: In Wing, S.L., Gingerich, P.D., Schmitz, B., and Thomas, E., eds., Causes and Consequences of Globally Warm Climates in the Early Paleogene: Boulder, Colorado, GSA Special Paper 369, Chapter 35, pp. 551–566.

Aubry, M.-P., and Ouda, K., 2003, Introduction, pp. ii-iv. In Ouda, K. and Aubry, M.-P. (eds), The Upper Palaeocene- Early of the Upper Nile Valley, Part 1, Stratigraphy. Micropaleontology Press, New York.

Bains, S., Norris, R.D., Corfield, R.M., and Faul, K.L., 2000, Termination of global warmth at the Palaeocene/Eocene boundary through productivity feedback: Nature, v.407, pp.171–74

Bains, S., Norris, R. D., Corfield, R. M., and Faul, K. L., 2000, Termination of global warmth at the Palaeocene/Eocene boundary through productivity feedback: Nature, v. 407, pp. 171-174

Behar, F., Beaumont, V., and Penteado, H.L.D., 2001, Rock-Eval 6 technology: performances and developments: Oil Gas Science Technology, v. 56, pp.111–134.

Ben-Jacob, E., Cohen, I., and Levine, H., 2000, Cooperative self-organization of microorganisms: Advances in Physics, v. 49, pp. 395–554.

Bertrand, P., Shimmield, G., Martinez, P., Grousset, F., Jorissen, F., Paterne, M., Pujol, C., Bouloubassi, I., Buat Menard, P., Peypouquet, J.-P., Beaufort, L., Sicre, M.-A., Lallier- Verges, E., Foster, J.M., Ternois, Y. and other participants of the Sedorqua Program, 1996. The glacial ocean productivity hypothesis: the importance of regional temporal and spatial studies: Marine Geology, v.130, pp.1–9.

Bodin, S., Godet, A., Matera, V., Steinmann, P., Vermeulen, J., Gardin, S., Adatte, T., Coccioni, R. and Föllmi, K. B., 2006, Enrichment of redox-sensitive trace metals (U, V, Mo, As) associated with the late Hauterivian Faraoni oceanic anoxic event: International Journal of Earth Sciences, v. 96, pp. 327-341.

Bolle, M.-P., Tantawy, A.A., Pardo, A., Adatte, T., Burns, S.J. Kassab, A., 2000, Climatic and environmental changes documented in the upper Paleocene to lower Eocene of Egypt: Eclogae Geologicae Helvetiae, v. 93, pp. 33–51.

Bolle, M.P., and Adatte, T., 2001, Paleocene–Early Eocene climatic evolution in the Tethyan realm: clay mineral evidence: Clay Mineralogy, v. 36, pp. 249–261.

Bowen, G.J., and Zachos, J.C., 2010, Rapid carbon sequestration at the termination of the Palaeocene-Eocene Thermal Maximum: Nature Geoscience, v. 3, pp. 866–69

Bruland, K.W., 1983, Trace Elements in Sea Water. In: J.P. Riiey and R. Chester (Editors): Chemical Oceanography, v. 8. Academic Press, London, pp. 157--220.

Brumsack, H.-J., 2006, The trace metal content of recent organic carbon-rich sediments: implications for Cretaceous black shale formation: Palaeogeography, Palaeoclimatology, Palaeoecology, v. 232, pp. 344–361.

Bybell, L.M., and Self-Trail, J.M., 1997, Late Paleocene and early Eocene calcareous nannofossils from three boreholes in an onshore–offshore transect from New Jersey to the Atlantic continental rise. In: Miller, K.G., Snyder, S.W. (Eds.), Proc. Ocean Drill. Prog., Sci. Results, vol. 150X. Ocean Drilling Program, College Station, TX, pp.91

Calvert, S. E. and Pedersen, T. F., (1993). Geochemistry of recent oxic and anoxic marine sediments: Implications for the geological record: Marine Geology, v. 113, pp. 67-88.

Calvert, S.E., and Pedersen, T.F., 1996, Sedimentary geochemistry of manganese: implications for the environment of formation of manganiferous black shales: Economic Geology, v. 91, pp.36–47.

Campbell, I. H., Czamanske, G. K., Fedorenko, V. A., Hill, R.I., and Stepanov, V., 1992, Synchronismof the Siberian traps and the Permian–Triassic boundary: Science, v. 258, pp.1760–1763.

Cao, Ch., Love, G.D., Hays, L.E., Wang, W., Shen, Sh., and Summons, R.E., 2009, Biogeochemical evidence for euxinic oceans and ecological disturbance presaging the end-Permian mass extinction event: Earth and Planetary Science Letters, v. 281, pp.188–201.

Chamley, H., 1989, Clay sedimentology, 623 pp. (Springer-Verlag, Berlin).

Chamley, H. 1998, Clay mineral sedimentation in the Ocean in Paquet, H., and Clauer, N., eds., Soils and sediments (mineralogy and geochemistry).:Berlin, Springer-Verlag, pp. 269–302.

Circone, S., Kirby, S. H., and Stern, L. A., 2005, Direct Measurement of Methane Hydrate Composition along the Hydrate Equilibrium Boundary: Journal of Physical Chemistry, v.109, pp. 9468-9475

Courtillot, V., and Renne, P., 2003, On the ages of flood basalt events. Comp. Rendus Geoscience, v. 335, pp.113–140.

Crouch, E.M., Dickens, G.R., Brinkhuis,H., Aubry, M.-P.,Hollis, C.J., Rogers, K.M., and Visscher, H., 2003, The Apectodinium acme and terrestrial discharge during the Paleocene–Eocene thermal maximum: new palynological, geochemical and calcareous nannoplankton observations at Tawanui, NewZealand: Palaeogeography, Palaeoclimatology, Palaeoecology, v.194, pp. 387–403.

Cruse, A.M., and Lyons, T.W., 2004, Trace metal records of regional paleoenvironmental variability in Pennsylvanian (Upper Carbonaferous) black shales: Chemical Geology, v. 206, pp.319–345.

Cullers, R. L., 2002, Implications of elemental concentrations for provenance, redox conditions, and metamorphic studies of shales and limestones near Pueblo, CO, USA: Chemical Geology, v. 191, pp. 305-327.

DeConto, R.M., Galeotti, S., Pagani, M., Tracy, D., Schaefer, K., Zhang, T., Pol- lard, D., and Beerling, D.J., 2012, Past extreme warming events linked to massive carbon release from thawing permafrost: Nature, v. 484, p. 87–91, doi:10.1038/nature10929.

Dickens, G., 2011. Down the Rabbit Hole: toward appropriate discussion of methane release from gas hydrate systems during the Paleocene-Eocene thermal maximum and other past hyperthermal events: Climate of the Past, v.7, pp. 831–846.

Dickens, G. R., O'Neil, J. R., Rea, D. K., and Owen, R. M., 1995, Dissociation of oceanic methane hydrate as a cause of the carbon isotope excursion at the end of the Paleocene: Paleoceanography, v. 10, pp. 965-971.

Dickens, G. R., Castillo, M. M., and Walker, J. C. G., 1997, A blast of gas in the latest Paleocene; simulating first-order effects of massive dissociation of oceanic methane hydrate: Geology, v.25, pp. 259-262.

Dickens, G., 2001, Carbon addition and removal during the Late Palaeocene Thermal Maximum: basic theory with a preliminary treatment of the isotope record at ODP Site 1051, Blake Nose, in: D. Kroon, R.D. Norris, A. Klaus (Eds.), Western North Atlantic Palaeogene and Cretaceous Palaeoceanography: Geological Society of London. Special Pub, v.183. pp. 293–305.

Dickens, G.R., Castillo, M.M., and Walker, J.C.G., 1997, A blast of gas in the latest Paleocene: simulating first-order effects of massive dissociation of oceanic methane hydrate: Geology v. 25, pp.259–62

Dumitrescu, M., and Brassell, S.C., 2006, Compositional and isotopic characteristics of organic matter for the Early Aptian Oceanic Anoxic Event at Shatsky Rise ODP Leg 198: Palaeogeography, Palaeoclimatology, Palaeoecology, v. 235, pp.168–191.

Dupuis, C., Aubry, M.-P., Steurbaut, E., Berggren, W.A., Ouda, K., Magioncalda, R., Cramer, B.S., Kent, D.V., Speijer, R.P., and Heilmann-Clausen, C., 2003, The Dababiya Quarry section: lithostratigraphy, clay mineralogy, geochemistry and paleontology. In: Ouda, K., Aubry, M.-P. (Eds.), The Upper Paleocene–Lower Eocene of the Upper Nile Valley: Part 1.Stratigraphy: Micropaleontology, v. 49, pp. 41–59.

Dymond, J., Suess, E., and Lyle, M., 1992. Barium in deep-sea sediments: a geochemical proxy for paleoproductivity: Paleoceanography, v. 7, pp.163–181.

Eaton, A.D., Clesceri, L. S., and Greenberg, A. E., 1995, Standard methods for the examination of water and waste water, v. IXI, pp. 4.113-4.114.

Espitalié, J., Deroo, G. and Marquis, F., 1985, La pyrolyse Rock-Eval et ses applications.Revue de l`Institute francais de Pérole, v. 40, pp. 563-579.

Farrimond, P., Talbot, H.M., Watson, D.F., Schulz, L.K., and Wilhelms, A., 2004, Methylhopanoids: Molecular indicators of ancient bacteria and a petroleum correlation tool. In: Geochimica et Cosmochimica Acta, v. 68, pp. 3873-3882.

Fio, K., Spangenberg J. E., Vlahović, I., Jasenka Sremac, J., Velić, I., and Ervin Mrinjek, E., 2010, Stable isotope and trace element stratigraphy across the Permian–Triassic transition: A redefinition of the

boundary in the Velebit Mountain, Croatia: Chemical Geology, doi:10.1016/j.chemgeo.2010.09.001

Gavrilov, Y.O., Shcherbinina, E.A., and Oberhänsli, H., 2003, Paleocene-Eocene boundary events in the northeastern Peri-Tethys: Geological Society of America, Special Papper, v. 369pp. 147–68

Gradstein, F.M., Ogg, J.G., Smith, A.G., Agterberg, F.P., Bleeker, W., Cooper, R.A., Davydov, V., Gibbard, P., Hinnov, L.A., House, M.R. (2), Lourens, L., Luterbacher, H-P., McArthur, J., Melchin, M.J., Robb, L.J., Shergold, J., Villeneuve, M., Wardlaw, B.R.,Ali,J.,Brinkhuis,H.,Hilgen,F.J.,Hooker,J.,Howarth,R.J., Knoll, A.H., Laskar, J., Monechi, S., Powell, J., Plumb, K.A., Raf®, I., RoÈhl, U., San®lippo, A., Schmitz, B., Shackleton, N.J., Shields, G.A., Strauss, H., Van Dam, J., Veizer, J., van Kolfschoten, Th.&Wilson,D.2004: A Geologic Time Scale 2004.-500pp. Cambridge University Press, Cambridge.

Grosjean, E., Adam, P., Connan, P., and Albrecht, P., 2004, Effects of weathering on nickel and vanadyl porphyrins of a Lower Toarcian shale of the Paris basin. Geochimeca et Cosmochimeca Acta, v. 68, pp. 789–804.

Handley, L., Pearson, P., McMillan, I.K., and Pancost, R.D., 2008, Large terrestrial and marine carbon and hydrogen isotope excursions in a new Paleocene/Eocene boundary section from Tanzania: Earth and Planetary Science, v. 275, pp. 17–25.

Higgins, J. A., Schrag, D.P., 2006, Beyond methane: towards a theory for the Paleocene-Eocene Thermal Maximum: Earth Planetary Science Letter, v. 245, pp. 523–537

Hoffman, P.F., Kaufman, A.J., Halverson, G.P., and Shrag, D.P., 1998, A Neoproterozoic snowball earth: Science, v. 281, pp.1342–1346.

Holser, W.T., 1997, Geochemical events documented in inorganic carbon isotopes: Palaeogeography, Palaeoclimatology, Palaeoecology, v. 132, pp.173–182

Holser, W.T., 1984, Gradual and abrupt shifts in ocean chemistry during Phanerozoic time. In: Holland, H.D., Trendall, A.F. (Eds.), Patterns of Change in Earth Evolution. Springer-Verlag, Berlin, pp. 123–143.

Huber, M. 2008. A hotter greenhouse?: Science, v.321, pp. 353-354

Ingall, E., and Jahnke, R., 1994, Evidence for enhanced phosphorus regeneration from marine sediments overlain by oxygen depleted waters: Geochimica et Cosmochimica Acta, v. 58, no.11, pp. 2571-2575.

Ingall, E., Bustin, R.M., and Van Cappellen, P., 1993., Influence of water column anoxia on the burial and preservation of carbon and phosphorus in marine shale: Geochimeca Cosmochimeca Acta, v. 57, pp. 303–316.

Ingall, E., and Jahnke, R., 1997, Influence of water-column anoxia on the elemental fractionation of C and P during sediment diagenesis: Marine Geology, v. 139, pp. 219–229.

Jarvis, I., Burnett, W.C., Nathan, Y., Almbaydin, F.S.M., Attia, A.K. M., Castro, L.N., Flicoteaux, R., Hilmy, M.E., Husain, V., Qutawnnah, A.A., Serjani, A., and Zanin, Y.N., 1994, Phosphorite geochemistry: state of the art and environmental concerns. Eclogae Geologica Helvetica, v. 87, pp. 643–700.

Jenkyns, H. C., 2010, Geochemistry of oceanic anoxic events, Geochemistry, Geophysics and Geosystem, v.11, Q03004, doi:10.1029/2009GC002788

Joachimski, M.M., Ostertag-Henning, C., Pancost, R.D., Strauss, H., Freeman, K.H., Littke, R., Sinninghe Damsté, J.S., and Racki, G., 2001, Water column anoxia, enhanced productivity and concomitant changes in δ13C and δ34S across the Frasnian–Famennian boundary (Kowala Holy Cross Mountains/Poland): Chemical Geology, v. 175, pp. 109–131.

Joachimski, M.M., Pancost, R.D., Freeman, K.H., Ostertag-Henning, C., and Buggisch, W., 2002, Carbon isotope geochemistry of the Frasnian–Famennian transition: Palaeogeography, Palaeoclimatology, Palaeoecology, v. 181, pp. 91–109.

John, C.M., Bohaty, S.M., Zachos, J.C., Sluijs, A., Gibbs, S., Brinkhuis, H., and Bralower, T., 2008, North American continental margin records of the Palaeocene–Eocene Thermal Maximum:

implications for global carbon and hydrological cycling: Paleoceanography, v. 23. doi:10.1029/2007PA001465.

Katz, M. E., D. R. Katz, J. D. ,Wright, K. G. Miller, D. K., Pak, N. J., Shackleton, & E. Thomas (2003), Early Cenozoic benthic foraminiferal isotopes: Species reliability and interspecies correction factors, Paleoceanography, 18(2), 1024.

Katz, M., Cramer, B., Mountain, G., Katz S., and Miller, K., 2001, Uncorking The Bottle: What Triggered The Paleocene/Eocene Thermal Maximum Methane Release?: Paleoceanography, v. 16, no. 6, pp. 549–562

Katz, M.E., Pak, D.K., Dickens, G.R. and Miller, K.G., 1999, The source and fate of massive carbon input during the Latest Paleocene Thermal Maximum: Science, v. 286, pp.1531–33

Kelly, D.C., Bralower, T.J., Zachos, J.C., Premoli-Silva, I., and Thomas, E., 1996, Rapid diversification of planktonic foraminifera in the tropical Pacific (ODP Site 865) during the late Paleocene Thermal Maximum. Geology, v. 24, p. 423–426.

Kelly, D.C., Zachos, J.C., Bralower, T.J. and Schellenberg, S.A., 2005, Enhanced terrestrial weathering/runoff and surface ocean carbonate production during the recovery stages of the Paleocene Eocene Thermal Maximum:Paleoceanography, v. 20, p.4023

Kennett, J. P., Cannariato, K. G., Hendy, I. L., and Behl R. J., 2002, Methane Hydrates in Qua- ternary Climate Change: The Clathrate Gun Hypothesis, Special Publication,. 54, 224 pp., AGU, Washington, D. C.

Kennett, J.P., and Stott, L., 1991, Abrupt deep-sea warming, palaeoceanographic changes and benthic extinctions at the end of the Palaeocene: Nature, v. 353, pp. 225–229.

Khozyem, H., Adatte, T., Spangenberg, J.E., Tantawy, A.A., and Keller, G., 2013 Paleoenvironmental and climatic changes during the Paleocene-Eocene Thermal Maximum (PETM) at the Wadi Nukhul Section, Sinai, Egypt: Journal of the Geological Society, London, v. 170, pp. 341 –352. doi: 10.1144/jgs2012-046.

Knies, J., Mann, U., Popp, B.N., Stein, R., and Brumsack, H.J., 2008, Surface water productivity and paleoceanographic implications in the Cenozoic Arctic Ocean: Paleoceanography, v. 23, doi:10.1029/2007PA001455.

Kraal, P., Slomp,C.P., and de Lange,G.J., 2010, Sedimentary organic carbon to phosphorus ratios as a redox proxy in Quaternary records from the Mediterranean: Chemical Geology, v. 277, pp. 167-177.

Kübler, B., 1987, Cristallinité de l'illite: méthode normalisées de préparation de mesure, méthode automatique normalisées de mesure: Cahiers de l'Institut de Géologie, Series AX n°3.1 and 3.2.

Kuypers, M.M., Breugel, Y., Schouten, S., Erba, E., and Damsté, J.S., 2004, N_2-fixing cyanobacteria supplied nutrient N for Cretaceous oceanic anoxic events: Geology, v. 32, pp. 853-856, doi:10.1130/G20458.1

Landing, W.M., and Bruland, K.W., 1980, Manganese in the North Pacific: Earth and Planetary Science Letters, v. 49, pp. 45-46

Landing, W.M., and Bruland, K.W., 1987, The contrasting biogeochemistry of iron and manganese in the Pacific Ocean: Geochimica et Cosmochimica Acta, v. 51, pp.29-43

Lu, G., Adatte, T., Keller, G., and Ortiz N.1998. Abrupt climatic, oceanographic and ecologic changes near the Paleocene-Eocene transition in the deep Tethys basin: The Alamedilla section, southern Spain: Ecologica Geologica Helvatica, v. 91, pp.293 306.

Luciani, V., Giusberti, L., Agnini, C., Backman, J., Fornaciari, E., and Rio, D., 2007, Paleocene–Eocene Thermal Maximum as recorded by Tethyan planktonic foraminifera in the Forada section (northern Italy). Marine Micropaleontology, v.64, p.189-214.

Lyons, T.W., Werne, J.P., Hollander, D.J., and Murray, R.W., 2003, Contrasting sulfur geochemistry and Fe/Al and Mo/Al ratios across the last oxic-to-anoxic transition in the Cariaco Basin, Venezuela: Chemical Geology, v.195, pp. 131–157.

Magioncalda, R., Dupuis, C., Smith, T., Steurbaut, E., and Gingerich, P.D., 2004, Paleocene– Eocene

carbon isotope excursion in organic carbon and pedogenic carbonate: direct comparison in a continental stratigraphic section: Geology, v.32, pp. 553–556.

McLennan, S. M., 1989, Rare earth elements in sedimentary rocks: influence of provenance and sedimentary processes. In Lipin, B. R. &McKay, G. A. (eds.) Geochemistry and mineralogy of Rare Earth Elements. Mineralogical Society of America: Review in Mineralogy, v. 21, pp. 169-200.

McManus, J., Berelson, W.M., Klinkhammer, G.P., Johnson, K.S., Coale, K.H., Anderson, R.F., Kumar, N., Burdige, D.J., Hammond, D.E., Brumsack, H.J., McCorckle, D.C., Rushdi, A., 1998a Geochemistry of barium in marine sediments: implications for its use as a paleoproxy: Geochimeca Cosmochimeca Acta, v. 62, pp. 3453–3473.

Meyers, P.A., Bernasconi, S.M., and Forster, A., 2006, Origins and accumulation of organic matter in expanded Albian to Santonian black shale sequences on the Demerara Rise, South American margin: Organic Geochemistry, v. 37, pp.1816–1830

Millot, G., 1970, Geology of Clays: Springer, Berlin Heidelberg New York, 429 p.

Mort, H.P., Adatte, T., Föllmi, K.B., Keller, G., Steinmann, P., Matera, V., Berner, Z. ,and Stüben, D., 2007, Phosphorus and the roles of productivity and nutrient recycling during oceanic anoxic event 2: Geology, v. 35, pp.483-486.

Murphy, A.E., Sageman, B.B., Hollander, D.J., Lyons, T.W., and Brett, C. E., 2000, Black shale deposition and faunal overturn in Devonian Appalachian basin: clastic starvation, seasonal water-column mixing, and efficient biolimiting nutrient recycling: Paleoceanography, v.15, pp. 280–291.

Mutterlose, J., Linnert, Ch., and Norris, R., 2007, Calcareous nannofossils from the Paleocene– Eocene Thermal Maximum of the equatorial Atlantic (ODP Site 1260B): evidence for tropical warming: Marine Micropaleontology, v.65, no.1–2, pp. 13–31.

Nesbitt, H.W., and Young, G.M., 1989, Formation and diagenesis of weathering profiles. Journal of Geology, v. 97, pp.129-147.

Nesbitt, H.W., and Young, G.M., 1984, Prediction of some weathering trends of plutonic and volcanic rocks based on thermodynamic and kinetic considerations: Geochemica et Cosmochemica Acta, v. 48, pp. 1523-1534.

Ohkouchi, N., Kawamura, K., and Taira A.,1997, Molecular paleoclimatology: reconstruction of climate variabilities in the late Quaternary: Organic Geochemistry, v. 27, pp.173– 83.

Ohkouchi, N., Kashiyama, Y., Kuroda, J., Ogawa, N.O., and Kitazato, H., 2006, The importance of diazotrophic cyanobacteria as primary producers during Cretaceous Oceanic Anoxic Event 2: Biogeosciences, v. 3, pp. 467–478.

Piper, D.Z. and Perkins, R.B., 2004, A modern vs. Permian black shale— the hydrography, primary productivity, and water-column chemistry of deposition: Chemical Geology, v. 206, pp. 177–197.

Potter, P.E., Maynard, J.B., and Pryor, W.A., 1980, Sedimentology of Shale: Springer, Berlin Heidelberg New York, 306 p.

Price, J.R., and Velbel, M.A., 2003, Chemical weathering indices applied to weathering profiles developed on heterogeneous felsic metamorphic parent rocks: Chemical Geology, v. 202, pp. 397–416.

Pujol, F., Berner, Z. and Stüben, D., 2006, Chemostratigraphy of some European Frasnian Famennian boundary key sections: Palaeogeography, Palaeoclimatology, Palaeoecology, v.240, pp.120–145.

Revesz, K.M., Landwehr, J.M., and Keybl, J., 2001, Measurement of $\delta^{13}C$ and $\delta^{18}O$ isotope ratios of $CaCO_3$ using a Thermoquest Finnigan GasBench II Delta Plus XL Continuous Flow Isotope Ratio Mass Spectrometer with application to Devils Hole Core DH-11 Calcite. U.S. Geological Survey Open-File-Report 01-257, 17 pp.

Riboulleau, A., Baudin, F., Deconinck, J.-F., Derenne, S., Largeau, C., and Tribovillard, N., 2003, Depositional conditions and organic matter preservation pathways in an epicontinental environment: the Upper Jurassic Kashpir Oil Shales (Volga Basin, Russia): Palaeogeography Palaeoclimatology Palaeoecology, v. 197, pp.171–197.

Rimmer, S.M., 2004, Geochemical paleoredox indicators in the Devonian–Mississippian black shales, central Appalachian Basin (USA): Chemical Geology, v. 206, no. 3–4, pp. 373–391.

Riquier, L., Tribovillard, N., Averbuch, O., Devleeschouwer, X., and Riboulleau, A., 2006, The Late Frasnian Kellwasser horizons of the Harz Mountains (Germany): two oxygen-deficient periods resulting from contrasting mechanisms: Chemical Geology, v. 233, pp.137-155.

Roszak, D.B., and Colwell, R.R., 1987, Survival strategies of bacteria in the natural environment: Microbiology Review, v. 51, no.3, pp. 365-379.

Sageman, B.B., and Lyons, T.W., 2003, Geochemistry of fine-grained sediments and sedimentary rocks, in Holland, H.D., and Turekian, K.K., eds., Treatise on Geochemistry: Amsterdam, Elsevier, Chapter 7.06.

Schmitz, B., Asaro, F., Molina, E., Monechi, S., von Salis, K., and Speijer, R. P., 1997, High-resolution iridium, $\delta^{13}C$, $\delta^{18}O$, foraminifera and nannofossil profiles across the latest Paleocene benthic extinction event at Zumaya, Spain: Palaeogeography, Palaeoclimatology, Palaeoecology, v. 133, pp. 49-68.

Schulte, P., Scheibner, C., and Speijer, R., 2011, "Fluvial discharge and sea-level changes controlling black shale deposition during the Paleocene–Eocene Thermal Maximum in the Dababiya Quarry section, Egypt: Chemical Geology, v.285, pp. 167-183.

Schulte, P., Schwark, L., Stassen, P., Bornemann, A., and Speijer, R.P., 2013, Black shale formation during the Latest Danian Event and the Paleocene-Eocene Thermal Maximum in central Egypt: Two of a kind?: Palaeogeography, Palaeoclimatology, Palaeoecology

Shields, G.A., and Stille, P., 2001, Diagenetic constraints on the use of cerium anomalies as palaeoseawater redox proxies: an isotopic and REE study of Cambrian phosphorites: Chemical Geology, v. 175, pp. 29–48.

Sluijs, A., Brinkhuis, H., Crouch, E.M., John, C.M., Handley, L., Munsterman, D., Bohaty, S.M., Zachos, J.C., Reichart, G.-J., Schouten, S., Pancost, R.D., and Sinninghe Damste, J.S., 2008, Eustatic variations in the Paleocene- Eocene greenhouse world: Paleoceanography, v. 23, PA4216, doi:10.1029/2008PA001615.

Sluijs, A., Brinkhuis, H., Schouten, S., Bohaty, S.M., John, C.M., Zachos, J.C., Reichart, G., Sinninghe Damste, J.S., Crouch, E.M., and Dickens, G.R., 2007, Environmental precursors to rapid light carbon injection at the Palaeocene/Eocene boundary: Nature, v. 450, pp.1218–1221.

Sluijs, A., Schouten, S., Pagani, M., Woltering, M., Brinkhuis, H., Sinninghe Damsté, J.S., Dickens, G.R., Huber, M., Reichart, G.J., and Stein, R., 2006, Subtropical Arctic Ocean temperatures during the Palaeocene/Eocene thermal maximum: Nature, v. 441, pp.610–613.

Slujis, A., Bowen, G.J., Brinkhuis, H., Lourens, L.J., and Thomas. E., 2007, The Palaeocene-Eocene Thermal Maximum super greenhouse: biotic and geochemical signatures, age models and mechanisms of global change. In: Williams, M. Haywood, A.M. Gregory, F.J. and Schmidt, D.N. (Eds.) Deep-time perspectives on climate change: Marrying the signal from computer models and biological proxies. The Micropalaeontological Society, Special Publications. Geological Society of London. pp. 323-350.

Soliman, M.F., Ahmed, E., and Kurzweil, H., 2006, Geochemistry and mineralogy of the Paleocene/Eocene boundary at Gabal Dababiya (GSSP) and Gabal Owaina sections, Nile Valley, Egypt: Stratigraphy, v.3, pp. 31–52.

Spangenberg J.E., Bagnoud-Velásquez, M., Boggiani, P.C., and Gaucher, C., 2013, Redox variations and bioproductivity in the Ediacaran: Evidence from inorganic and organic geochemistry of the Corumbá Group, Brazil: Gondwana Research. Doi:10.1016/j.gr.2013.08.014

Spangenberg, J.E., Fonboté, L., and Macko, S.A., 1999, An evaluation of the inorganic and organic geochemistry of the San Vicente Mississippi Valley-type zinc–lead district, Central Peru: implications for ore fluid composition, mixing processes and sulfate reduction: Economic Geology, v. 94, pp.1067–1092.

Spangenberg, J.E., and Herlec, U., 2006, Hydrocarbon biomarkers in the Topla–Mežica zinc–lead deposits, Northern Karavanke/Drau Range, Slovenia: paleoenvironment at the site of ore formation: Economic Geology, v. 101, pp. 997–1021.

Spangenberg, J.E., and Macko, S.A., 1998, Organic geochemistry of the San Vicente zinc–lead district, eastern Pucará Basin, Peru: Chemical Geology, v. 146, pp. 1–23.

Speijer, R., and Wagner, T., 2002, Sea-level changes and black shales associated with the late Paleocene thermal maximum: Organic-geochemical and micropaleontologic evidence from the southern Tethyan margin (Egypt-Israel): Geological Society of America Special Paper, v. 356, p. 533–549.

Speijer, R.P., Schmitz, B., and Luger, P., 2000, Stratigraphy of late Palaeocene events in the Middle East: Implications for low to middle-latitude successions and correlations: Journal of the Geological Society, London, v. 157, pp. 37-47.

Speijer, R.P., Schmitz, B., and Van der Zwaan, G.J., 1997, Benthic foraminiferal extinction and repopulation in response to latest Paleocene Tethyan anoxia: Geology, v. 25, pp. 683–686.

Srodo. J., 1999, Use of clay minerals in reconstructing geological processes: recent advances and some perspectives: Clay Minerals, v. 34, pp. 27–37

Storey, M., Duncan, R.A., and Swisher C.C., 2007, Paleocene-Eocene Thermal Maximum and the Opening of the Northeast Atlantic: Science, v. 316. p 587

Svensen, H., Planke, S., and Corfu, F., 2010, Zircon dating ties NE Atlantic sill emplacement to initial Eocene global warming: Journal of Geological Society. London, v. 167, pp.433–36

Svensen, H., Planke, S., Malthe-Sorenssen, A., Jamtveit, B., Myklebust, R., et al., 2004, Release of methane from a volcanic basin as a mechanism for initial Eocene global warming: Nature v. 429, pp. 542–45

Torfstein, A., Winckler, G., and Tripati, A., 2010, Productivity feedback did not terminate the Paleocene-Eocene Thermal Maximum (PETM) Climate of the Past, v. 6, pp. 265–272

Tribovillard, N., Algeo, J., Lyons, T., and Riboulleau, A., 2006, Trace metals as palaeoredox and palaeoproductivity proxies: An update: Chemical Geology, v. 232, pp.12–32

Tribovillard, N., Ramdani, A., and Trentesaux, A., 2005, Controls on organic accumulation in Late Jurassic shales of northwestern Europe as inferred from trace-metal geochemistry. In: Harris, N. (Ed.), The Deposition of Organic-Carbon-Rich Sediments: Models, Mechanisms, and Consequences. SEPM Spec. Public., v. 82, pp. 145–164.

Tyrell, T., 1999, The relative influences of nitrogen and phosphorus on oceanic primary production: Nature, v. 400, pp. 525–531.

Weaver, C.E., 1989, Clays, muds, and shales: Developments in sedimentology, v. 44, 819 p.

Weijers, J.W.H., Schouten, S., Sluijs, A., Brinkhuis, H., and Sinninghe Damsté, J.S., 2007, Warm arctic continents during the Palaeocene–Eocene thermal maximum. Earth Planet Science Letter, v. 261, pp. 230–238.

Westerhold, T., Rohl, U., McCarren, H.K., and Zachos, J.C., 2009, Latest on the absolute age of the Paleocene-Eocene Thermal Maximum (PETM): new insights from exact stratigraphic position of key ash layers +19 and −17: Earth Planetary Science Letter, v. 287, pp. 412–19

Whiticar, M. J., 1999, Carbon and hydrogen isotope systematics of bacterial formation and oxidation of methane: Chemical Geology, v.161, pp. 291–314

Wignall, P.B., Newton, R., and Brookfield, M.E., 2005, Pyrite framboid evidence for oxygen-poor deposition during the Permian-Triassic crisis in Kashmir: Palaeogeography Palaeoclimatology Palaeoecology, v. 216, pp. 183-188.

Wilkin, R.T., Arthur, M.A., Dean, W.E., 1997. History of water column anoxia in the Black Sea indicated by pyrite framboid size distributions: Earth Planetary Science Letter, v. 148, pp. 517–525.

Wilkin, R.T., Barnes, H.L., and Brantley, S.L., 1996, The size distribution of framboidal pyrite in modern sediments: an indicator of redox conditions: Geochimeca Cosmochimeca Acta, v. 60, pp. 3897–3912.

Wing, S. L., Harrington, G. J., Bowen, G. J. and Koch, P. L., 2003, Causes and Consequences of Globally Warm Climates in the Early Paleogene Vol. 369 (eds Wing, S. L., Gingerich, P. D., S., Birger & Thomas, E.) 425-440 (Geological Society of America Special Paper, 2003).

Zachos, J. C., Dickens, G. R., and Zeebe, R. E., 2008, An early Cenozoic perspective on greenhouse warming and carbon cycle dynamics. Nature, v. 451, p. 279–283.

Zachos, J., Pagani, M., Sloan, L., Thomas, E., and Billups, K., 2001, Trends, rhythms, and aberrations in global climate 65 Ma to present: Science, v. 292, pp. 686–693.

Zachos, J.C., Röhl, U., Schellenberg, S.A., Sluijs, A., Hodell, D.A., Kelly, D.C., Thomas, E., Nicolo, M., Raffi, I., Lourens, L.J., McCarren, H., and Kroon, D., 2005, Rapid acidification of the ocean during the Paleocene–Eocene Thermal Maximum: Science, v. 308, pp.1611–1615.

Zachos, J.C., Schouten, S., Bohaty, S., Quattlebaum, T., Sluijs, A., Brinkhuis, H., Gibbs, S., and Bralower, T., 2006, Extreme warming of the mid-latitude coastal ocean during the Paleocene–Eocene Thermal Maximum: inferences from TEX86 and isotope data: Geology, v. 34, pp. 737–740.

Zachos, J.C., Wara, M.W., and Bohaty, S., 2003, A transient rise in tropical sea surface temperature during the Palaeocene–Eocene Thermal Maximum: Science, v. 302, pp.1551–1554.

Zeebe, R. E., Zachos, J. C. & Dickens, G. R. 2009. Carbon dioxide forcing alone insufficient to explain Palaeocene-Eocene Thermal Maximum warming: Nature Geoscience, v. 2, pp.576-580.

CHAPTER IV

PALEOCLIMATE AND PALEOENVIRONMENT OF THE NAREDI FORMATION (EARLY EOCENE), KUTCH, GUJARAT, INDIA

HASSAN KHOZYEM[1], THIERRY ADATTE[1], GERTA KELLER[2], JORGE E. SPANGENBERG[1], NACHIAPPAN SARAVANAN[3], SUNIL BAJPAI[3].

[1]Institut des Science de la Terre (ISTE), Université de Lausanne, CH-1015, Switzerland

[2]Department of Geosciences, Princeton University, Guyot Hall, Princeton, NJ 08544, USA

[3]Department of Earth Sciences, Indian Institute of Technology Roorkee, Roorkee, Uttarakhand 247667, India

Journal of Geological Society of India, 2013 inpress

PALEOCLIMATE AND PALEOENVIRONMENT OF THE NAREDI FORMATION (EARLY EOCENE), KUTCH, GUJARAT, INDIA[1]

Abstract. The Naredi Formation in Kutch, Gujarat, India, is early Eocene in age and marks the first marine transgression above the last Deccan traps. Sediment deposition occurred in a shallow inner shelf environment that varied from brackish lagoonal to brackish, normal inner shelf to marginal marine environments. The studied section can be divided into 2 main transgressive cycles interrupted by a regression phase that is marked by a well-defined sequence boundary marked by a roots bearing paleosoil. Three intervals yielded abundant benthic foraminiferal assemblages. Planktic foraminifera are few to rare and restricted to the top of the section, except for *Chiloguembelina trinitatensis.* An early Eocene age can be attributed to the Naredi section based primarily on larger benthic foraminifera (SBZ8 to SBZ11, equivalent to planktic foraminiferal biozones E4 to E6), the stable isotope curve and its correlation with marine sections and sequence stratigraphy. Sediments of the transgression/regression cycles were derived from physical and chemical-weathering processes of basaltic rocks as indicated by the different geochemical proxies. Carbon isotope analyses of bivalve shells and organic matter reveal a negative excursion that is correlative with the global Early Eocene excursion and the presence of fish bones, fish teeth and organic matter can be related to the Early Eocene climatic optimum. Clay mineral data from the Naredi Formation indicate variably hot humid to arid climate conditions.

1. INTRODUCTION

The Kutch region of western India (Gujarat) is a pericratonic rift basin that preserves a predominantly marine sedimentary sequences ranging in age from Jurassic to Recent with repeated transgressive/regressive cycles and stratigraphic breaks. Tertiary strata are exposed in a crescentic belt in the southwestern part of the Kutch District (Fig. 1) and have long attracted attention of geologists and paleontologists because of their high fossil wealth.

The Naredi Formation of Kutch (Biswas, 1992), also called “Gypseous Shales” (Wynne, 1872) and Laki Beds overlies the last Deccan Traps of early Paleocene age. Deposition occurred in a lagoonal to inner shelf environment, which was well developed in the western part of Kutch. The type section consists of 10-20 m high cliffs exposed along the Kakdi River near the Nareda village (Lat: N23°34.602; Long: E68°38.628, Figs. 1, 2).

At the type locality, the Naredi Fm. is subdivided into three main members from base to top (Biswas, 1992): (1) the Gypsiferous Shale Member consists of grey, brown and olive green glauconitic claystones and splintery shales with gypsum, limonite and bands of carbonate concretions. (2) The *Assilina* Limestone Member consists of bedded limestone and yellowish grey marls rich in *Assilina* shells. (3) The Ferruginous Claystone Member marks the uppermost part of the Naredi Fm. and consists of grey, brown iron-rich claystone. Only the lower two members of the Naredi Fm. have been examined in this study with a focus on the Paleocene-Eocene Thermal Maximum (PETM) and Early Eocene climatic Optimum (ETM2) events.

---

[1] ***Hassan Khozyem, Thierry Adatte, Gerta Keller, Jorge E. Spangenberg, N. Saravanan, Sunil Bajpai, 2013, Paleoclimate and paleoenvironment of the Naredi Formation (Eocene), Kutch, Gujarat, India. In Malarkodi, N., Keller, G., Reddy, A.N., and Jaiprakash, B.C. (eds.) Ecology, Biodiversity and Global Bioevents, Geological Society of India, Special Publication, Springer Verlag, vol.1, p. 269-296***

Many authors (e.g. Chattopadhyay, 2004; Chattoraj, et al., 2009; Bajpai have intensively studied the biostratigraphy and lithostratigraphy of Naredi Formation. S., 2009), but no high resolution sequence stratigraphy, geochemistry and chemostratigraphy studies have been achieved so far to reconstruct the paleoenvironemntal variations that prevailed during the first marine deposition above the last phase of Deccan volcanism and more particularly to decipher the climatic changes during the early Eocene climatic optimum (EECO).

Investigations are based on a multi-proxy approach and include: 1) biostratigraphy to provide high-resolution age control of the Naredi deposits, 2) carbon isotope stratigraphy as correlative tool, 3) sedimentology and bulk rock mineralogy to identify environmental and sea-level fluctuations; 4) clay mineralogy to infer paleoclimatic conditions; and 5) trace and major elements geochemistry to determine the original source of Naredi Fm sediments and evaluate the intensity of weathering.

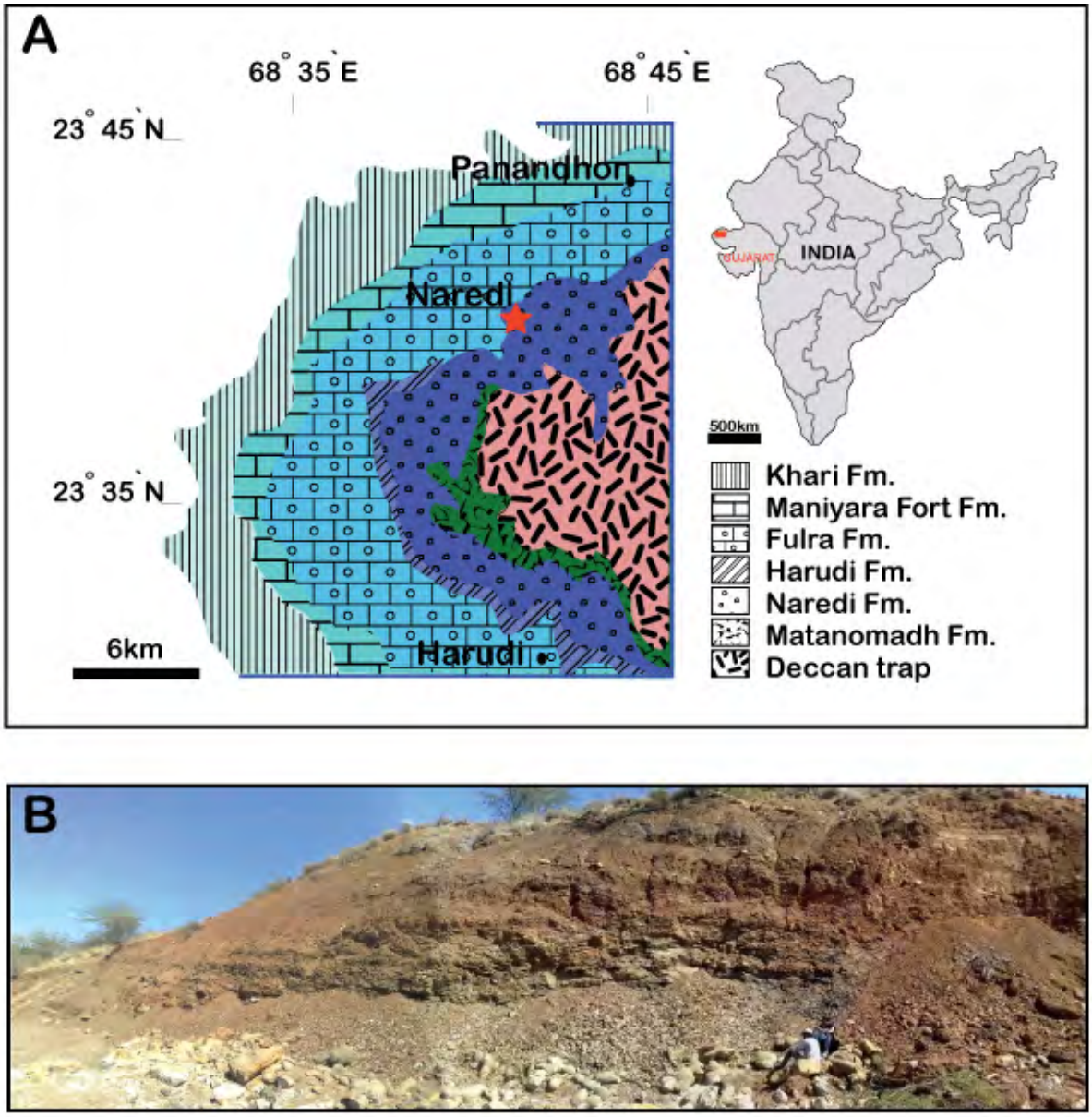

Figure 1. *Geological map of Naredi area with Location of the studied Naredi section (after Biswas, 1992) and picture of the studied outcrop showing the different lithologic units*

2. METHODS

Sampling was carried out at 10 cm intervals spanning 11 m. Samples were processed for microfossils by standard methods (Keller et al., 1995) and washed through a 63 μm screen. Benthic foraminifera were observed primarily in the <100 μm size fraction and assemblages tend to be dominated by one or two species. Preservation is very good and shells are not recrystallized.

Samples for organic-carbon isotope analyses were treated with 10% HCl acid until the carbonate had entirely reacted. The carbon-isotope composition was determined by flash combustion on a Carlo Erba 1108 elemental analyzer (EA) connected to a Thermo Fisher Scientific Delta (IRMS) and operated in the continuous helium flow mode via a Conflo III split interface (EA–IRMS). The $\delta^{13}C_{org}$ values are reported relative to VPDB. The reproducibility was better than 0.1‰ (1σ) for carbon.

Carbon isotope analyses of aliquots of separated bivalves bone and teeth fragments were performed using a Thermo Fisher Scientific (Bremen, Germany) GasBench II preparation device interfaced to a Thermo Fisher Scientific Delta Plus XL continuous flow isotope ratio mass spectrometer (IRMS) (Revesz et al., 2001). The CO_2 extraction was done at 90 °C. The stable carbon and oxygen isotope ratios are reported in the delta (δ) notation as the per mil (‰) deviation relative to the Vienna–Pee Dee belemnite standard (VPDB). Analytical uncertainty (2σ), monitored by replicate analyses of the international calcite standard NBS-19 and the laboratory standards Carrara Marble and Binn Dolomite, are no greater than ± 0.05‰ for $\delta^{13}C_{carb}$. Carbon isotope analyses were done at Isotope lab. (Lausanne University- ISTE).

Whole rock XRD analysis was carried out for all the samples at the Geological Institute of Lausanne University, Switzerland. Samples were prepared following the procedure of Kübler (1987) for whole-rock analysis and Adatte et al. (1996) for the clay-mineral analysis. Whole rock composition was based on methods described Klug and Alexander (1974) and Rolli (1990). The semi-quantification of whole-rock mineralogy is based on XRD patterns of random powder samples by using external standards with an error margin between 5 and 10% for the phyllosilicates and 5% for grain minerals. Clay mineral analysis follows the methods developed by Kübler (1987) and Adatte et al. (1996). The intensities of the identified minerals are measured for a semi-quantitative estimate of the proportion of clay minerals, which is therefore given in relative percent without correction factors because of the small error margin (<5%).

Elemental analysis was carried out at the Institute of Mineralogy and Geochemistry of the Lausanne University, Switzerland, with a FRX Philips PW2400 X-ray fluorescence spectrometer using lithium tetraborate fused pellets for major elements (ME). For the (TEs), the XRF analyses were conducted on powder tablets obtained by pressing 10 g of the sample on a support of polyvinyl alcohol (2%) at over 5000 kg/cm2 (Mori et al., 1999) The detection limits are 0.01% for MEs and 1 to 4 ppm for TEs. The accuracies of the analyses were assessed by analyses of standard reference materials.

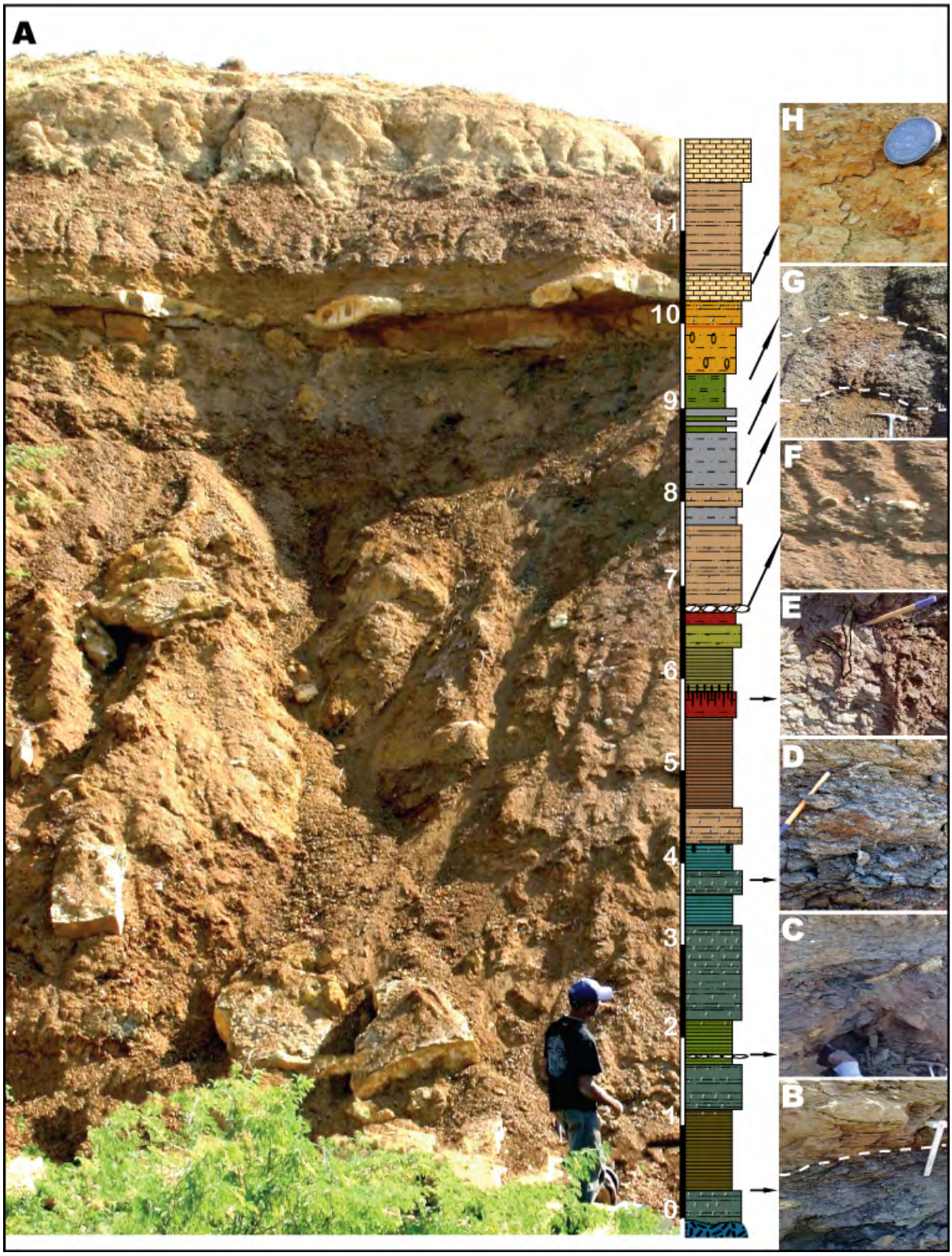

Figure 2. *Field pictures of the studied section showing special field observations. (A) general photograph of the studied section, (B) sharp contact between bivalves bearing claystone and non fossiliferous brown silty claystone, (C) olive silty claystone with calcareous concretions, (D) bivalve bearing silty claystone, (E) paleosoil with root traces, (F) silt stone with large calcareous concretions, (G) non-fossiliferous vary colour silty claystone and (H) Assilina limestone with larger foraminifera.*

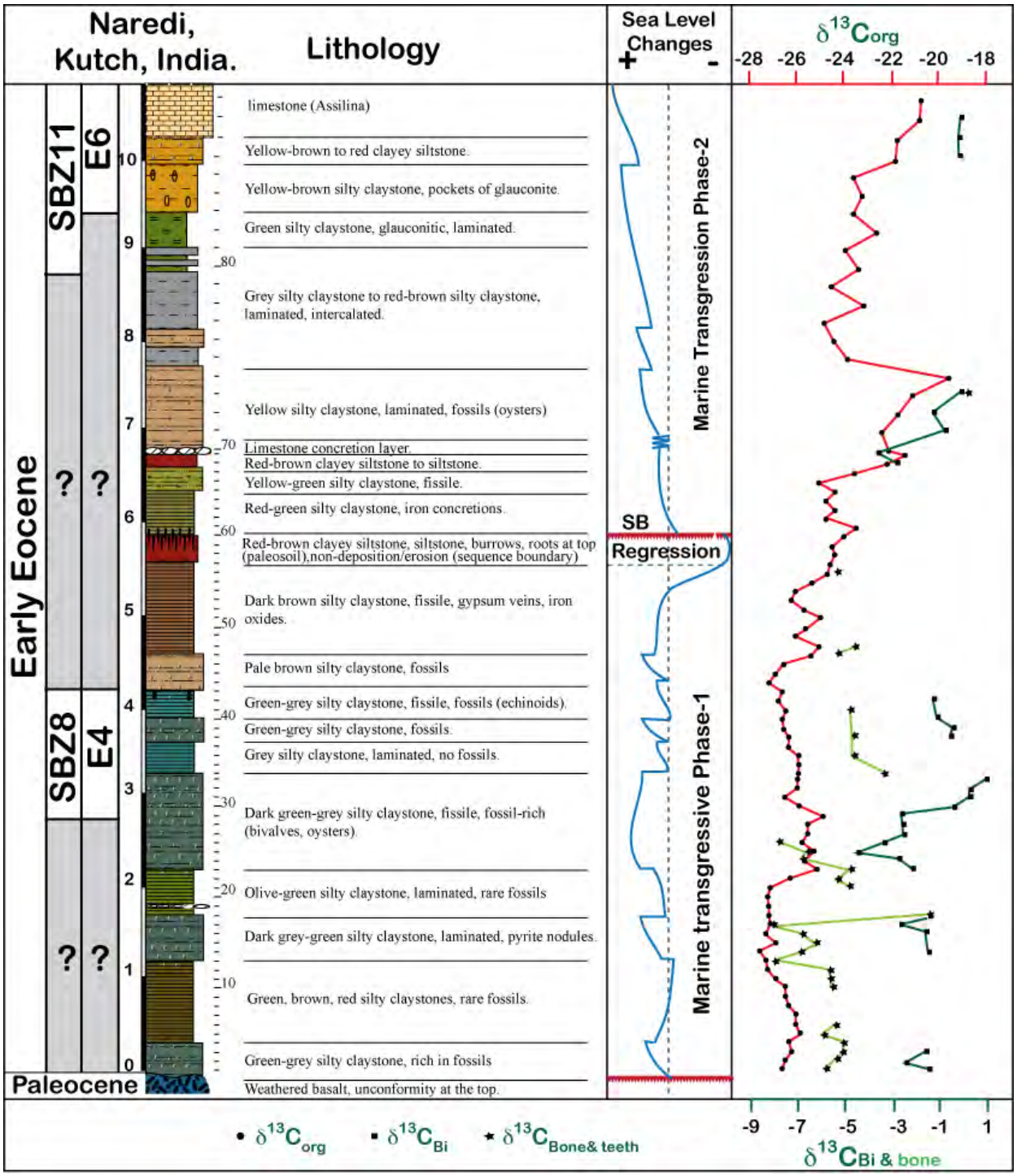

Figure 3. *Lithostratigraphic description of the studied Naredi section, with sea level change curve based on the lithofacies and microfacies and plots of the different carbon isotopic curves ($\delta^{13}C_{org}$, $\delta^{13}C_{Bivalve}$ and $\delta^{13}C_{teth\ +bone}$).*

3. LITHOLOGY

The Naredi section consists predominantly of glauconitic and phosphatic claystone, siltstones and shales with bivalves and larger foraminifera. Sediments were deposited above a laterite paleosoil that developed over basaltic rocks erupted during the last phase of Deccan volcanism in the early Paleocene. The lower 4.5 m contain intervals of fossiliferous marine sediments (e.g., bivalves, benthic, planktonic foraminifera and fish bone and teeth fragments). Glauconitic and phosphatic claystones and shales intercalated with nearly azoic olive green-reddish silty claystones dominate between 4.5-5.5 m (Figs. 2, 3). Above this interval is a 30 cm thick red-brown clayey siltstone with burrows at the base and roots at the top marking a paleosoil. The overlying 50 cm thick red-green silty claystone contains iron concretions but no fossils. This interval is overlain by yellow-green and red-brown silty claystone to clayey siltstones, which are also devoid of fossils. Above a limestone concretions bed at 6.8 m is a laminated yellow silty claystone that contains oysters and larger and small benthic foraminifera marking a return to marginal marine conditions. From 7.8 m to 9.0 m sediments consist of intercalated grey to red-brown silty claystones devoid of microfossils, followed by glauconitic claystone. Between 9.5 to 10.2 m, silty claystones contain common macro- and microfossils marking a return to marginal marine conditions. At the top of the sampled interval is the (*Assilina*) limestone level rich in larger foraminifera (mostly *Nummulites*) (Figs. 2, 3).

4. BIOSTRATIGRAPHY

In the absence of well documented records of planktic foraminifera or any other age diagnostic fossils, the age of the Naredi Formation, and consequently of the earliest marine transgression in Kutch, is a long-standing controversy. An early Eocene (Ypresian) age has been assigned to this formation based on early Eocene snakes (Rage et al., 2003), or early Eocene (Ilerdian) shallow-benthic zones SBZ6 to SBZ11 based mainly on larger foraminifera, such as *Assilina granulosa, Assilina spinosa, Assilina davies, Nummulites atacicus, Nummulites burdigalensis* (Raju et al., 1970; Raju, 1974; Singh and Singh, 1981; Shukla, 2008; Chattoraj et al., 2009; Saraswati et al., 2012). This report and a related study on Foraminifera (see Keller et al., this vol.) also base age control mainly on the larger benthic foraminifera because planktic foraminifera are very rare, of low diversity and only present near the base and top of the section.

Except larger benthic foraminifera and planktic foraminifera recently Garg et al. (2011) reported the age of the formation as Early Eocene on the basis of Dinoflagellate cysts and Anwar Larger foraminifera are common in three intervals of the Naredi section together with small benthic and rare planktic foraminifera and two additional intervals where no small foraminifera are present (Fig. 4). Larger foraminifera from the lower interval (1.5-4.2m) contain *Nummulites globulus nanus* Schaub 1981, indicative of Shallow Benthic Zone (SBZ8), which is correlative with planktic foraminiferal zone E4 (Dr. Lukas Hottinger, written communicaton, 2007; Serra-Kiel et al., 1998). This age determination is in good agreement with studies by Saraswati et al. (2000, 2012) and Shukla, (2008). Saraswati et al. (2012) report larger foraminifera, particularly *Nummulites globulus nanus* from the basal 4 m of the Naredi section overlying the basalts and assigned this interval to SBZ8. The presence of *Acarninia esnaensis* in this assemblage also suggests a zone E4 to possibly E5 age in good agreement with SBZ8.

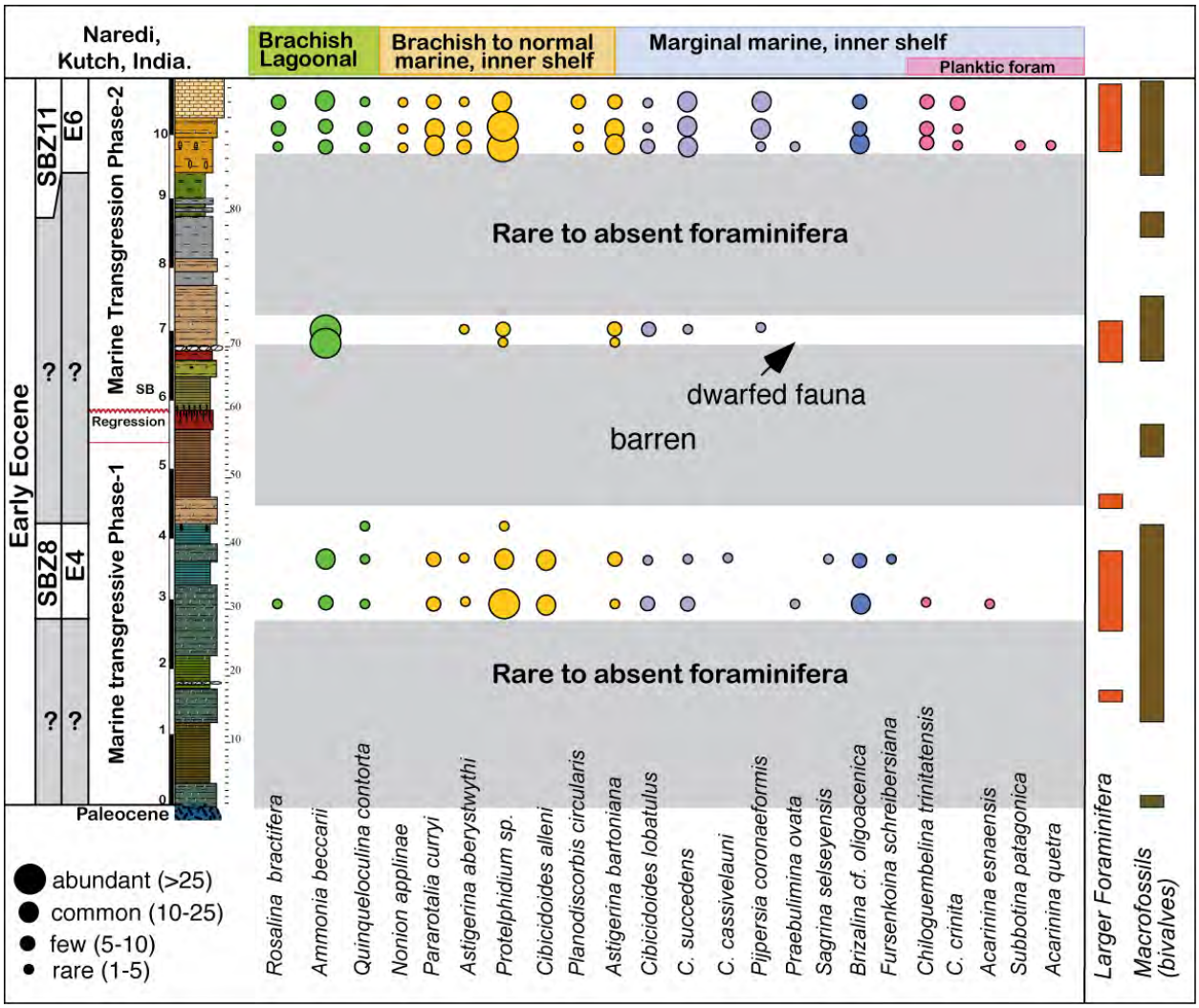

Figure 4. *Combined chart representing benthic, planktic and larger foraminifera distributions along the Naredi regarding to the different carbon isotopic signals.*

et al. (2011) advocated the age of the formation ranges between 50- 55Ma based on strontium isotopic ratios.

Above this interval Saraswati et al. (2012) report a generally barren zone questionably interpreted as SBZ9-10 containing a short interval with only small foraminifera. At this level we observed dwarfed foraminifera and exceptionally small *Nummulites*. The age of this assemblage is unknown. In the limestone at the top of the Naredi section both Hottinger (written communication, 2008) and Saraswati et al. (2012) observed a diverse assemblage of *Nummulites burdigalensis cantabricus, Assilina laxispira, A. spinosa* and *Lockhartia* and assigned it to zone SBZ11 (equivalent to E6 to E7, Fig. 4). Rare planktic foraminifera in this assemblage include *Acarinina quetra* (range E3-E6), which indicates an age no younger than E6 in agreement with the age based on larger foraminifera.

5. RESULTS

5.1. Mineralogy

At Naredi, the bulk rock composition is dominated by phyllosilicates, goethite, feldspars, quartz, calcite and pyrite with some intervals enriched in Ca-apatite (Fig. 5). The presence of

gypsum and hematite reflects late diagenetic processes. In general, Naredi sediments reveal high mineralogic maturity in term of bulk rock mineralogy with a Maturity Index {(MI=Phyllosilicate/Phyllosilicate+quartz+ feldspars; Bathia, 1985}, ranging between (0.85 and 1). From the base of the section up to the sequence boundary (SB, 5.9m) bulk rock composition is dominated by phyllosilicates with values between 60 and 80%. Feldspars and quartz gradually increase reaching their maximum values 1m below the SB (5.4% and 6.2% respectively). Pyrite is primarily restricted to this interval with values ranging between 1.5% and 6.6%, whereas goethite (2.5-13.7%) and hematite (7.58%) are low but variable. Calcite is nearly absent, except for a nodule layer at 1.8 m (Fig. 5). Ca-apatite shows some significant peaks between 1.5 and 2 m. The maturity index (MI) remains high in the 2 m at the base of the section, and then gradually decreases to reach minimum values (0.85) at 1m below the paleosoil, comparable minimum value was also recorded within the second calcareous nodule layer (6.8m), in which the MI reaches maximum values reflecting high phyllosilicates and low quartz and feldspars contents.

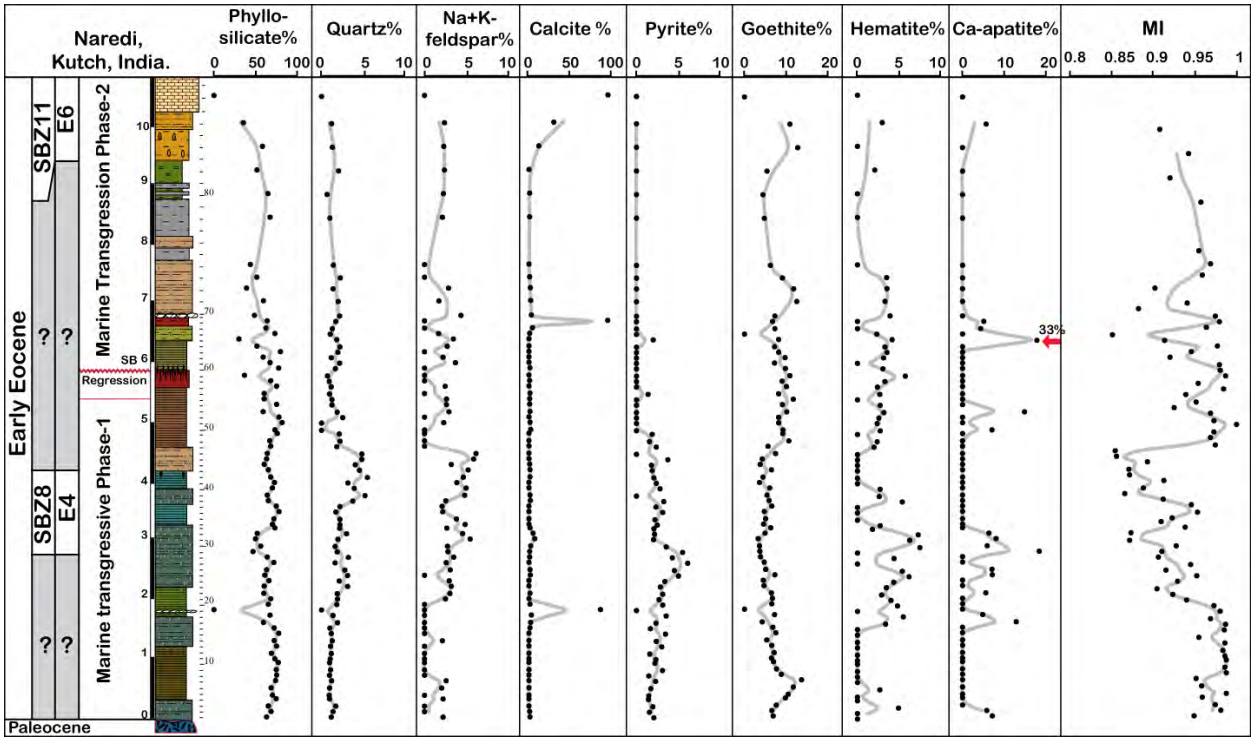

Figure 5. *Bulk rock minerals across the Naredi section. MI is the maturity index determined as MI=Phyllosilicate /phyllosilicate + Quartz + total feldspar. Grey lines represent 3 points average mean values*

Above the SB, the MI is more variable, ranging between 0.88 and 0.98. Quartz and feldspars are less abundant. Pyrite is nearly absent, goethite increases up to 12.8% (sample 88) and calcite increases in the top 1.8 m of the section correlative with marly limestone deposition. At Naredi, clay mineral assemblages are composed of smectite, kaolinite, illite and chlorite (Fig. 6). Glauconite, which is included in illite, is occasionally abundant. The lower part of the section (base to 4.5 m) is dominated by smectite (between 10.1 and 42.6%) and kaolinite (24.4 and 57.8%). Chlorite and illite are less abundant ranging between 5.2 and 23.3% for chlorite and 2 and 22.2% for illite. A notable decrease in smectite and chlorite coincides with an increase of kaolinite and illite in the interval between 3 and 4.5 m. **The** upper part of the section is

characterized by a gradual rise in smectite, culminating up to 65% in the topmost limestones, to the detriment of the kaolinite, chlorite and at lesser extent illite (Fig. 6), between 3 and 4.5 m. All clay mineral contents remain close to the mean value with slight increase in chlorite near the base of the section and from 4.5m up to the paleosoil level (5.8m). Between the paleosoil level and 8.1m, smectite is gradually increasing to the detriment of kaolinite and chlorite and illite is fairly stable. The upper part of the section is characterized by a gradual rise in smectite, culminating up to 65% in the topmost limestones, to the detriment of the kaolinite, chlorite and at lesser extent illite (Fig. 6).

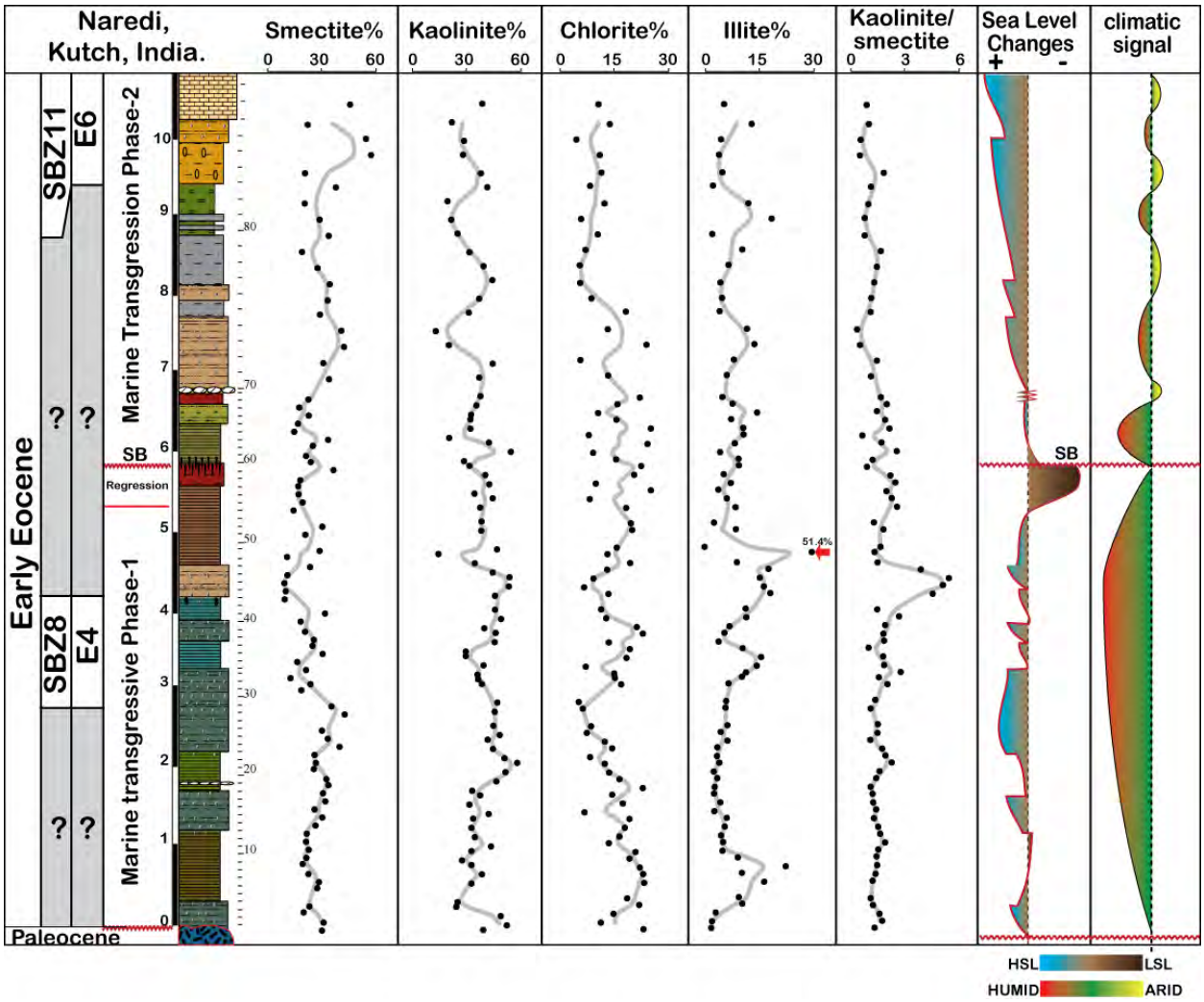

Figure 6. *Clay mineral composition, kaolinite/smectite and kaolinite/(illite+chlorite) ratios against the sea level curve and climatic changes which prevailed during the deposition of Naredi section sediments. Note clay minerals are given in relative percentage. Grey lines represent 3 points average mean values.*

5.2. **Stable Isotopes**

Sediments of the Naredi Fm. vary between carbonate-rich and carbonate-poor intervals. For this reason, analyses are based on organic contents ($\delta^{13}C_{org}$), and the carbonate content of bones, teeth ($\delta^{13}C_{teeth+bones}$) and bivalves ($\delta^{13}Cb_{biv+bones}$) (Fig. 3). Only intervals with high fossil contents yielded good measurements and therefore this data is intermittent through the section.

In the lower part of the section, bivalves show a negative $\delta^{13}C_{Bi}$ shift from -2.5‰ to nearly -5‰, then return to more positive values in the bivalve-rich intervals (3m above the base of the section). At the same level, isotopic values of bones and teeth (Ca-phosphate) show a correlative negative shift from -6‰ to -8‰ (Fig. 3).

The $\delta^{13}C_{org}$ curve at Naredi can be subdivided into three parts, which are independent of lithology (Fig. 4). 1) The lower part of the section (0-4.5 m, samples 1 to 43) is marked by the most negative values ranging between -24.9 and -27.6‰. In this interval, the $\delta^{13}C_{org}$ curve shows minimum values between 1 to 1.8 m and 3 to 4.2 m, respectively, separated by 1.2m characterized by more positive $\delta^{13}C_{org}$ (-25.7‰) values. 2) The middle part consists of a gradual increase $\delta^{13}C_{org}$ values, starting with -26.3‰ at 5.8 m and culminating with -19.6‰ at the fossiliferous claystones at 7.8 m, and 3) the upper part (7.8 m to 8.9 m) $\delta^{13}C_{org}$ values gradually increase (-26.3 to -24‰) followed by a rapid increase to -20.7‰ at the top of the section (Fig. 3).

5.3. **Elemental Geochemistry**

5.3.1. Major elements

Major element concentrations are given in elemental percentage (Fig. 7). The most abundant elements are Si (2.95-21.1%) and Fe (3.7-37.1%), followed by Al (2.1-13.9%) whereas Ca (0.04-33.15%) is only abundant within the bivalves bearing intervals and calcareous concretion layers. Less abundant elements include K, Mg, Ti, P and Na, which fluctuate around 4% in total. Si content is relatively stable and systematically lower than Deccan basalt average composition (DBAC) (Crocket and Paul, 2004) and Post-Archean Australian Shale (PAAS). Three significant drops are observed in Si content: 1) within a nodule layer at 1.8 m, 2) in the paleosoil at 5.8 m, and 3) in the limestone located at the top of the section (Fig. 7).

Al and Ti show similar patterns, although with a larger decrease in Al of the upper part of the section (6-11 m). Fe shows steady values in the lower part of the section with average values of 38% in the paleosoil. Above, Fe remains high but variable up to the top of the section. Note that Fe is enriched relative to PAAS, but comparable to DBAC in the lower part of the section and enriched above the paleosoil. Mn values show a similar trend, except in the uppermost part of the section (8-11 m), where it is depleted relative to Fe and within the calcareous concretion layers in which Mn is linked to Ca. The highest Mn value (0.85%) is observed in the nodule layer (1.8 m). Mn values are comparable to PAAS, but lower than DCAB in the basal 4.6 m. Above this interval, Mn remains generally lower than these two standards, except in the paleosoil and in two samples located at 7.3-7.5 m (yellow silty claystone). Mg values are relatively high (~2.9%) in the basal 4.5 m, exceeding largely PAAS but below DCAB standard values. Mg is significantly depleted between 4.5 to 6.2 m, well below the PAAS value. Above this interval, this element is again abundant (1.2-2.8%, Fig. 7).

Ca contents are close to 0%, except in four intervals respectively located at 1.6 m (first nodule level), between 2.6-3 m (bivalve and oyester bearing claystones), at 6.7 m (second nodule level) and in the uppermost limestone. K contents are minor in the basal 2 m of the section, with values close to the DCAB, but largely lower than the PAAS standards. K values increase significantly from 2 to 4.5 m, and then decrease to DCAB values between 4.5 and 7.3 m and reach minimum content in the paleosoil. Above the paleosoil, a second K enrichment starts in silty claystones (8.5 m) and culminates in the glauconite-rich interval (9-9.5m).

The topmost limestone is significantly depleted in K. Na contents show a different trend with a gradual increase in the lower part of the section and maximum values (3.4%) just below the paleosoil, which is depleted in Na. Above this interval Na is more variable, with a similar trend to that of K, except in the uppermost limestone, which shows a significant increase. Phosphorus shows low contents in comparison with PAAS and DCAB standard values. However, P is enriched at 3 m in the fossiliferous claystone and in the paleosoil at 5.8 m.

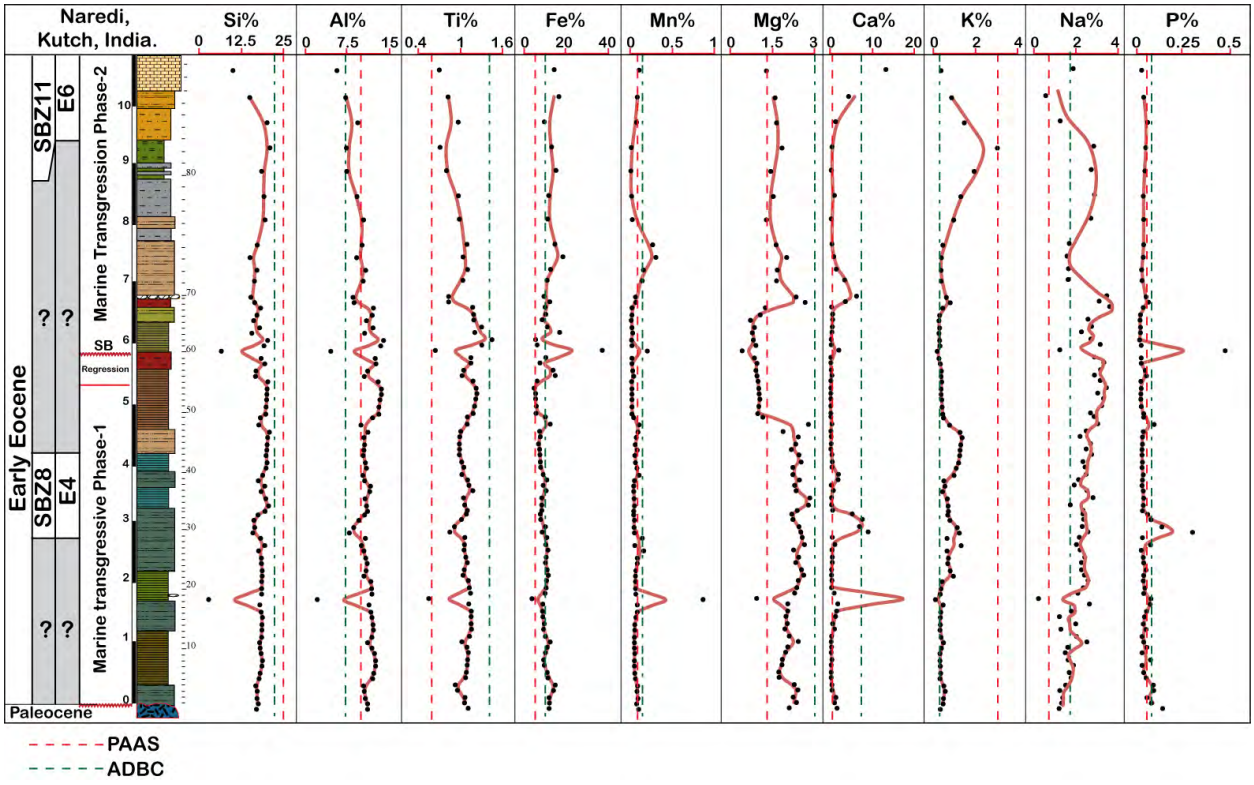

Figure 7. *Distribution of Al-normalized major elements along the studied section in comparison with both Post-Archean Australian Shale (PAAS Taylor and McLennan, 1985) and Deccan basalt Average composition (DBAC. Crocket and Paul, 2004). Red lines represent 3 points average mean values*

5.3.2.Trace elements

Al-normalization is a quick and easy way to represent the authigenic TEs (Tribovillard et al., 2006). The Al- normalized TEs shows enrichments in U, Cu, and Zr at 1.8 m likely linked to the calcareous nodule layer. The overall significant enrichments in Al-normalized TEs near the top of the section are likely an artefact of decreased detrital input. Only Cu/Al values are systematically lower than PAAS and DBAC standards. Al-normalized Zr, Co, Zn and U show some minor variations through the section. Zr/Al ratios show lower values in two short intervals around 5.6 m (below the clayey siltstone topped by paleosoil) and 6.60 m (below and within the nodule layer). An rather high Zn/Al ratio is observed at 6 m just above the discontinuity marked by the paleosoil. Both V/Al and Cr/Al ratios are more variable with maximum concentrations starting 50 cm below the paleosoil horizon and ending at the calcareous concretions level (70 cm above the paleosoil), coinciding with depleted Ni and Co contents. Cu/Al ratios vary significantly particularly in the middle part of the section where minimum values are reached. Significant enrichements in Ni, Co and Zn are observed at 6m in the sediments overlying SB.

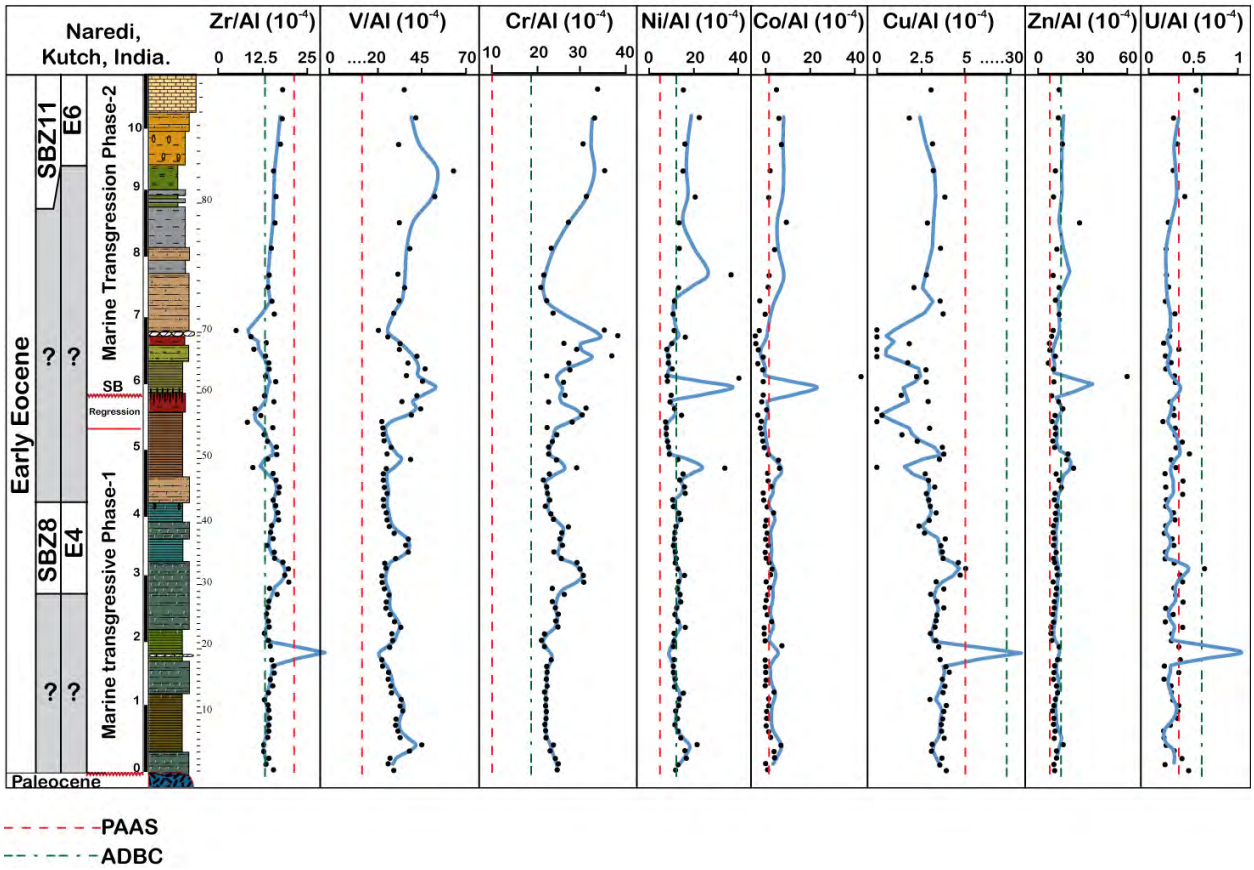

Figure 8. *Distribution of Al-normalized trace elements along the studied section in comparison with both Post-Archean Australian Shale (PAAS) and Deccan basalt Average composition (DBAC. Crocket and Paul, 2004). Blue lines represent 3 points average mean values*

6. DISCUSSION

6.1. Early Eocene Climate Optimum and Carbon isotope signal

The hyperthermal events of the Early Eocene began at the Paleocene-Eocene Thermal Maximum (PETM) at 55.8 Ma, also known as the Eocene Thermal Maximum-1 (ETM1). This hothouse event was followed by another hothouse event termed the Eocene Thermal Maximum-2 (ETM2) at 53.7 Ma, also known as Early Eocene Climatic Optimum (EECO) (Fig.10). A third event followed at ~53.5 Ma termed the Eocene Thermal Maximum-3 (ETM3) Together the first two hothouse events mark the warmest period in Earth's history and are thus an important model for inferring future warming trends in the present climate system. During ~1.5 million years the extreme climate shifts of the Eocene hothouse were accompanied by several biotic changes recorded in the fossil and stable isotope records (Zachos et al., 1994 and 2001; Sloan and Huber, 2001; Woodburne et al., 2009). These climatic and environmental changes resulted in major shifts in the composition of terrestrial and marine communities that led to changes in diversification and extinction rates, and modified the patterns of immigration and emigration over lands (Slujis et al., 2007; Wing et al., 1995).

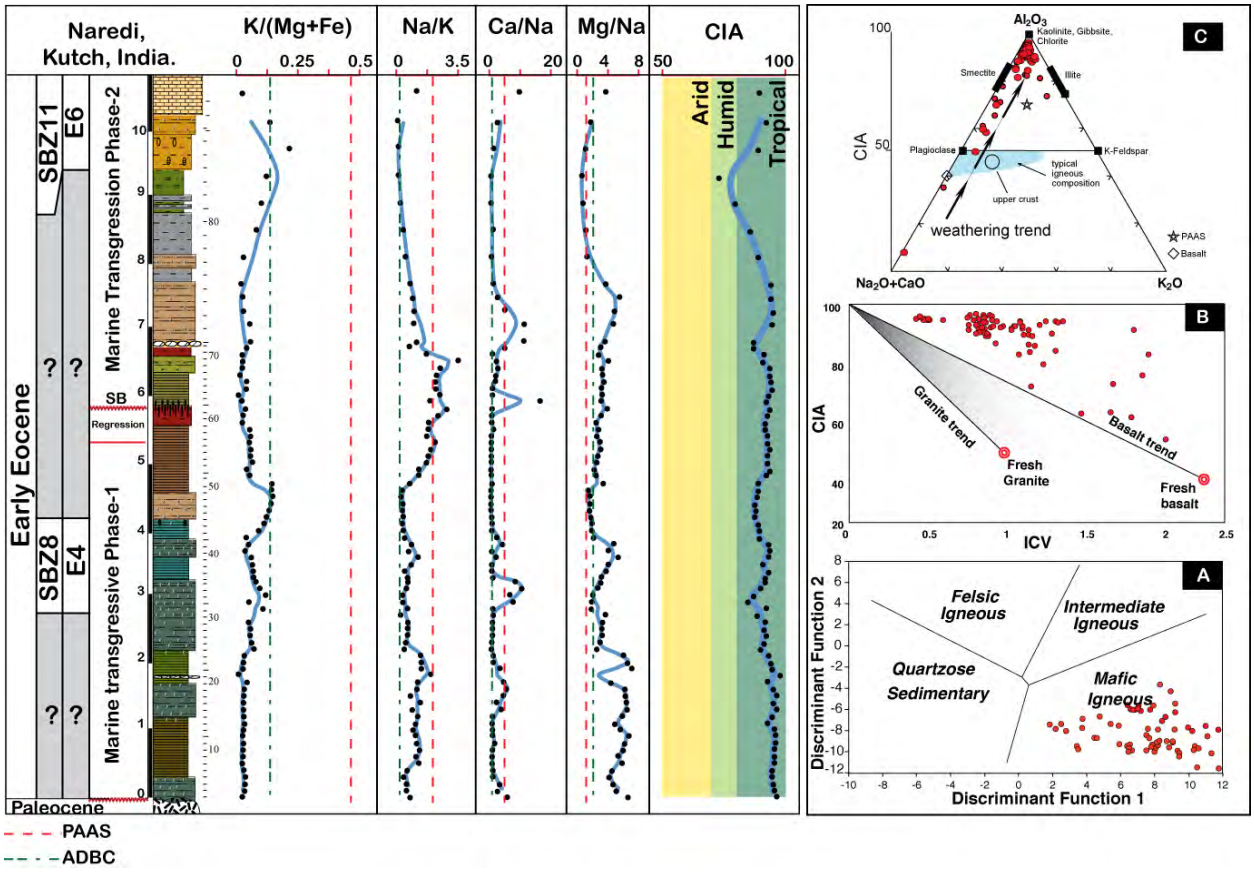

Figure 9. *Summary of environmental proxies used in this study (weathering, basalt weathering, volcanism vs detritism) based on major geochemistry. (A) Discriminant function diagram (Roser and Korsch, 1988) distinguishing the source rock provenances depending on the discriminant function-1 and 2 (B) Cross plot diagram of the two indicators of weathering, Chemical Index of Alteration and Index of Chemical Variation (C) ternary diagram (molar proportion) against the major change in the weathering index and CIA from arid to humid to humid tropical conditions. Blue lines represent 3 points average mean values.*

The Early Eocene Climatic Optimum (EECO) is characterized by a negative carbon isotopic shift in both carbonate and organic carbon. Hothouse events PETM and EECO are globally characterized by pronounced $\delta^{13}C_{carb}$ and $\delta^{13}C_{org}$ negative peaks (Fig.10, Zachos et al., 2001). The isotopic measurements on bivalves, bone and teeth fragments and organic matter highlight the presence of a negative carbon isotope excursion through the basal 4.5 m of the section. This negative shift may be linked to the early Eocene climatic optimum (EECO). Relatively diverse benthic foraminiferal assemblages, rare planktic foraminifera (e.g., *Chiloguembelina, Acarinina esnaensis)* and larger foraminifera (e.g., *Nummulites*) indicative of Early Eocene biozones SBZ8 and E4 mark this interval (Fig. 4, see also Punekar et al., 2010; Saraswati et al., 2012).

The positive $\delta^{13}C_{org}$ excursion correlative with this foraminiferal assemblage could be linked to mixed sources of organic matter or a change toward increased marine organic input (Calvert et al., 1987). This is also suggested by similar positive excursions in $\delta^{13}C_{org}$ coincident with the other two fossil-rich intervals (Fig. 3). Despite their scarcity and intermittent presence, $\delta^{13}C_{biv}$ of bivalves and $\delta^{13}C_{bone}$ show similar positive excursions marking increased marine input.

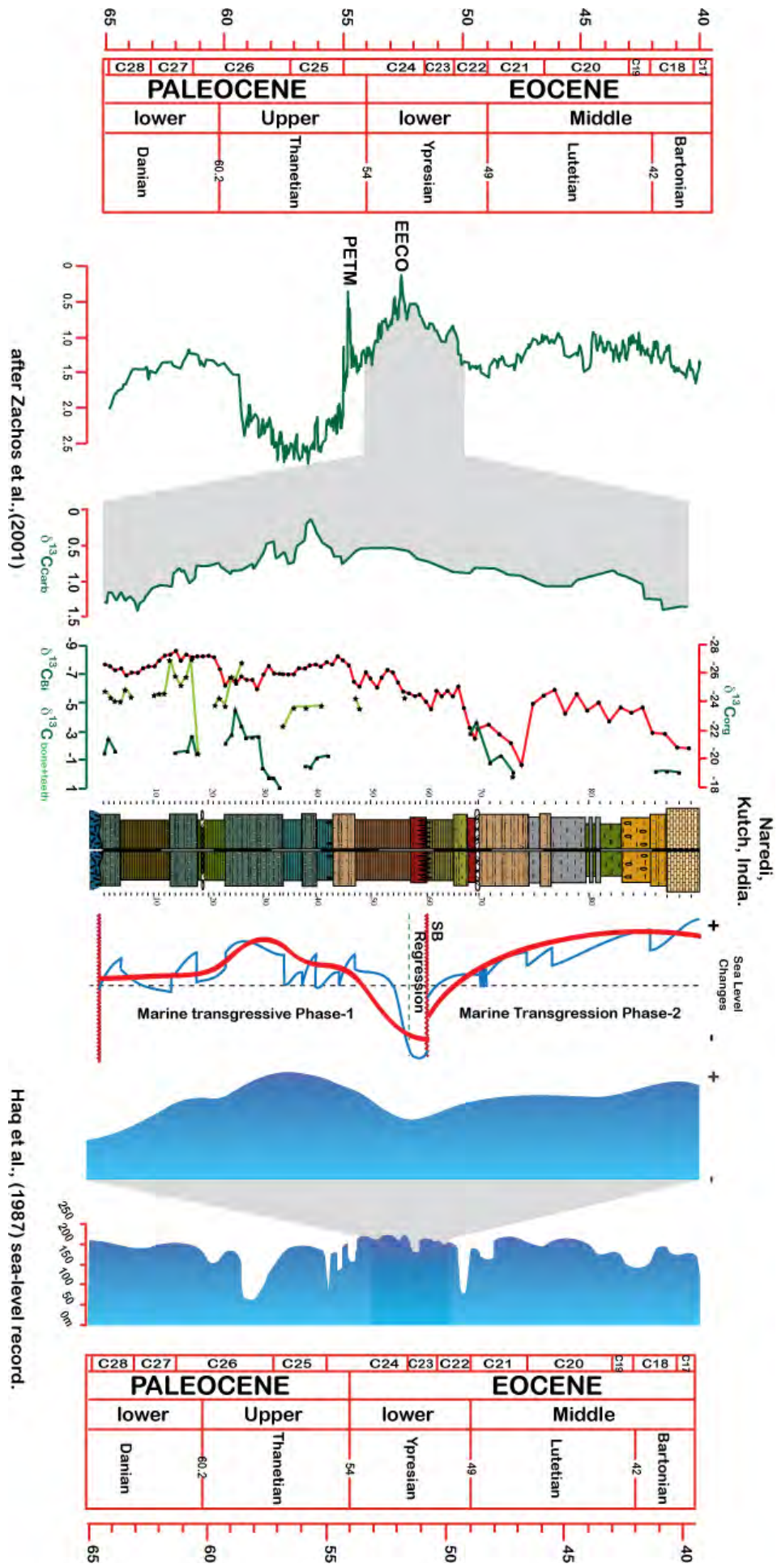

Figure. 10 *correlation chart of both sea lavel curve and carbon isotopic record of Naredi section with global sea level curve of Haq et al., (1987) and global carbon isotooic curve of Zachos et al., (2001)*

The foraminiferal assemblage of the limestone at the top of the section typifies biozones SBZ11 and E6. Based on biostratigraphy and stable isotopes, an early Eocene age (biozones SBZ8-SBZ11, E4-E6) can be attributed to the Naredi section. The stable isotope record can be correlated with the Vastan section of Gujarat, where similar $\delta^{13}C$ excursions and benthic foraminiferal assemblages indicate an early Eocene age (Khozyem et al., in prep.).

6.2. **Sea level**

Sediments of the Naredi section were deposited in a shallow inner shelf environment that varied from brackish lagoonal to normal inner shelf and to marginal marine inner shelf conditions. Sediment deposition alternated from predominantly green glauconitic to brown phosphatic layers. Foraminifera are generally restricted to more phosphatic intervals. The fossiliferous sediments (glauconitic and phosphatic silt-claystones) were deposited in a subtidal environment, whereas the barren intervals probably represent supratidal settings (Chattoraj et al., 2008, 2009). The lower part of the succession (0-5.5 m) is therefore globally trangressive above the basalt and punctuated by short-lived sea-level falls, which corresponds to the barren intervals (Fig. 3, marine transgression phase-1). This overall transgressive trend is interrupted by a sharp discontinuity marked by the deposition of a reddish brown clayey siltstone with root traces that suggest a paleosoil and emergent conditions. The upper part of the section indicates the return to a trangressive phase. Full marine conditions are reached in the uppermost *Assilina* limestone.

Based on our biostratigraphic data, the Naredi section can be tentatively correlated with the sea level curve of Haq et al. (1987) (Fig. 10) and the sequence stratigraphy chart of Hardenbol et al. (1998). The lower transgressive phase-1 (Fig. 3) contains foraminifera indicative of biozones SBZ8 (shallow benthic) and E4 (planktic) that suggest correlation with the sea-level rise preceding the sequence boundary Yp4 of Hardenbol et al., 1998). Therefore, we tentatively correlate the paleosoil in the middle of the Naredi section with the Yp4 sequence boundary (SB, red line, Fig. 3). The upper trangressive phase-2 corresponds to the SBZ11 and E6 biozones, which may correlate with the sea level rise above the major Yp10 sequence boundary of Hardenbol et al. (1998). If this correlation is correct, this would imply that the paleosoil bearing discontinuity at Naredi spans several sequence boundaries from Yp4 (53.6 Ma) to Yp10 (49.5 Ma; Hardenbol et al., 1998), suggesting that this area was emergent during nearly 1 my.

6.3. **Mineralogical proxies**

6.3.1. Bulk rock

Phyllosilicates at Naredi are the most abundant minerals, especially in the lower part of the section corresponding to the first transgression phase. Quartz and feldspars are at a maximum at the end of the first transgression, reflecting increased detrital input (Fig. 5). The dominance of phyllosilicates suggests that chemical weathering prevailed in the lower part of the section, as indicated by the high MI (0.8-1). Decreased MI values observed at the top of the first transgression phase suggest increased erosion and reworking during the maximum regression. The P-enriched mineral (Ca-apatite) is particularly abundant in the glauconitic intervals, which reflect periods of condensed sedimentation and/or increased productivity. Peaks in Ca-apatite often correlate with discrete layers enriched in bivalves and foraminifera. Pyrite is significant in the lower part of the section and may mark dysoxic conditions linked to a rising sea level (fig. 5). Fully anoxic conditions are unlikely given the abundant benthic fauna, the absence of small-sized pyrite framboids and the low amount of redox elements (e.g. U, V, fig.8)

Goethite and hematite are of diagenetic origin and reflect intensive recent weathering typical of the prevailing semi-arid climate in southwestern India at the time. Maximum MI values coincide mainly with the sea level regression (Fig. 5), which is marked by fluctuating but often-high phyllosilicates content with important goethite and hematite linked to the presence of paleosoil. The upper transgressive interval is initially marked by a slight decrease in MI values, followed at the top limestones by an abrupt drop due to very low phyllosilicates and relatively high quartz contents, which implies increased physical weathering under less humid climate conditions or dilution due to high calcite contents.

6.3.2. Clay minerals as paleo-environmental proxies

The clay fraction of the Naredi sediments is composed of smectite, kaolinite, illite and chlorite (Fig. 6). Such clay mineral assemblages reflect continental morphology and tectonic activity, as well as climate evolution and associated sea-level fuctuations (Chamley, 1989, 1997; Weaver, 1989; Li et al., 2000; Adatte et al., 2002, 2005). Illite and chlorite are considered as common byproducts of weathering reactions with low hydrolysis typical of cool to temperate and/or dry climates. Mg-rich chlorite can derive from alteration of mafic igneous rocks (Bettison and Schiffman, 1988; Schiffman and Fridleifsson, 1991). Kaolinite is generally a byproduct of highly hydrolytic weathering reactions in perennially warm humid climates and its formation requires a minimum of 15C° (Gaucher, 1981). The presence of abundant smectite is generally linked to transgressive seas and warm climate with alternating humid and arid seasons but can also reflects volcanic activity (Chamley, 1989, 1997; Deconinck, 1992). The kaolinite/smectite (K/SM) ratio is therefore a usefull climate proxy to infer humid/warm to more dry and seasonal climate variations (Fig. 6) (e.g., Robert and Chamley, 1991; Robert and Kennett, 1992).

Glauconite is quite abundant at Naredi. The neoformation of glauconite requires marine water near normal salinity, reducing conditions, and appropriate source materials. Glauconite production is favored by high organic content in bottom sediments and by slow or negative sedimentation. Glauconite forms in open-sea continental margins at low and moderate latitudes and at a range of depth from 60 m to 1000 m, most often between 60 and 550 m (Odin, 1988). Mineralogically, glauconite is formed through a process analogous to illitization: gradual alteration of neoformed Fe-rich smectite into Fe-K illite through intermediate mixed-layer phases (Odin, 1988). Consequently, glauconite shows an XRD pattern, which is relatively similar to that of the illite. Abundant glauconite makes it difficult to use illite as paleoclimatic indicator. At Naredi, glauconite grains are quite abundant and typify the lower and upper transgressive phases during which, enriched levels in glauconite and phosphate were deposited and remobilized.

Kaolinite is the most abundant clay with lower smectite, chlorite and illite contents at Naredi (Fig. 6). This indicates a fluctuating climate between arid-seasonal to humid and warm conditions. The last Deccan basalt flow underlying the Naredi succession was subject to intensive chemical weathering leading to the formation of soil enriched in smectite or kaolinite depending on the precipitations intensity. Although increased kaolinite may reflect humid conditions, as well as increased erosion during low sea levels, the latter is not the case because there is no strong coeval input of other detrital clay minerals (e.g., mica, chlorite). The lower transgressive phase of the section is characterized by a relatively steady K/SM ratio, with kaolinite slightly more dominant than smectite, except for the upper part of this interval, which

shows a large increase of kaolinite reflecting more humid conditions. A change towards more arid-seasonal conditions is indicated by a decrease in the KSM ratio and coeval increased illite and chlorite. Similarly, the paleosoil interval is marked by higher smectite and chlorite (to a lesser extent illite) and lower kaolinite. Smectite is gradually increasing in the upper part of the section to the detriment of chlorite and kaolinite (decreased K/SM ratio), which reflects drier seasonal conditions that culminated in the limestone at the top. This change from humid to more arid conditions coincides with the reduction and eventual disappearance of lignite deposits that were very common in late Paleocene and early Eocene in western India (Bajpai et al., 2005, 2008, Khozhiem et al, in prep). Note that this climatic shift towards more arid conditions during the early Eocene has been observed at larger scale (e.g. S-Spain, Tunisia, Egypt, Arabian Peninsula, Bolle and Adatte, 2001)

6.4. **Geochemical proxies**

The MEs and TEs and their relative enrichments can be compared to the Deccan Basalt Average Composition (DBAC, Crocket and Paul, 2004) and Post-Archean Australian Shale (PAAS, Taylor, S.R. and Mclennan, S. 1985). Several ratios and cross plots have been used to assess the source and effects of weathering and volcanism during the time of deposition (Figs. 7-9). MEs are a useful tool for identifying different sedimentary provinces based on discrimination diagrams. Roser and Karsch (1988) proposed one to distinguish between the original source rock for sandstone and mudrocks depending on major elements based on the calculation of two discrimination functions:

$F1=-1.773TiO_2 +0.607Al_2O_3+0.76Fe_2O_3-1.5MgO+0.616CaO+0.509Na_2O-1.224K_2O-9.09,$

$F2=0.445TiO_2+0.07Al_2O_3- 0.25Fe_2O_3-1.142MgO+0.438CaO+1.475Na_2O+1.426K_2O-6.86.$

At Naredi, sediments derived predominantly from mafic igneous provinces (Fig. 9A). Therefore, a better discrimination of parent rock types can be achieved by including Fe and Mg. Cox et al. (1995) proposed a measure called the index of compositional variability (ICV): $(CaO+K_2O+Na_2O+Fe_2O_3\ (t)+MgO+MnO+TiO_2)/Al_2O_3$, where Fe_2O_3 (t) = total iron and CaO includes all sources of Ca. In this index, the weight percent of the oxides are used rather than moles, and the values decrease with increasing degrees of weathering. Thus, the ICV allows the differentiation of sediments with basaltic and granitic origins (Fig. 9B).

The feldspar conversion to clay minerals, such as kaolinite can be expressed by the Chemical Index of Alteration (CIA; $CIA=(100)[Al_2O_3/(Al_2O_3+CaO^*+Na_2O+K_2O)]$) (Nesbit and Young, 1984, 1989; Fedo et al., 1995; Maynard et al., 1995; Price et al., 2003). CIA values of 45–55 indicate essentially no weathering. At the other extreme kaolinite, gibbsite, and boehmite all have CIA average values of about 100, whereas smectite and illite range between 70 and 80. This implies that the proportions of clay minerals and primary minerals in a bulk sample will introduce substantial variation in the resulting CIA values (McLennan, 1993).

At the Naredi section CIA values are highest in the lower part of the section, particularly in the basal 1.5 m, then gradually decrease up to 9 m and increase again in the limestone at the top (Fig. 9). As already pointed out by the K/SM ratio, the CIA values in the lower part of the section reflect intense chemical weathering, which gradually decreases upwards. The top limestone is again marked by elevated CIA values, which is not recorded in clay minerals. This increased CIA ratio is explained by a technical artifact due to lower Al, Na and K contents linked

to dilution by carbonate sedimentation.

A plot of CIA against ICV values indicates that most of the Naredi Fm. samples are located along the basaltic field (Fig. 9B) and consequently inherited from basaltic rocks, which underwent intensive chemical alteration as reflected by the high CIA values. Figure 9C shows the distribution of the carbonate-free sediments in the A–CN–K diagram. For comparison, the compositions of the Upper Continental Crust (UCC), PAAS and Deccan basalt are also plotted in the diagram along with the predicted weathering trend for the average upper continental crust (Taylor and McLennan, 1985). This trend encompasses the majority of the Naredi samples.

In the A–CN–K diagram (Fig. 9C), the Naredi sediments indicate a weathering evolution from basaltic parental rocks. However, this trend should be interpreted with caution, especially when there are many factors (e.g., tectonic setting and/or sediment origin) that could modify the weathering trend and hence the inferred climatic conditions. The data in Figure 9C can be interpreted using a mixing model involving two components: (1) a strongly weathered component plotting close to the A-CN axis towards the kaolinite end-member, which is the most abundant clay in the Naredi sediments (Fig. 6); and (2) a relatively mature component, which predominates in the sediments plotting closer to the basalt field. The sediments of the Naredi Formation is therefore derived from a basaltic igneous source that was subjected to intense chemical weathering after the last phase of the Deccan eruption (Fig. 9).

The influence of volcanism was investigated using several volcanic proxies, including Na/K, K/(Fe+Mg), Ca/Na and Mg/Na ratios (Sageman and Lyons, 2003; Pujol et al., 2006, Dessert et al, 2003). Na/K and K/(Fe+Mg) ratios represent the balance between detrital and volcanogenic input and are interpreted to reflect the increase or decrease of riverine siliciclastic flux relative to background volcanic input (Sageman and Lyons, 2003; Keller et al., 2012).

The lower 1.5 m coinciding with the onset of the first transgression phase shows high Na/K and Mg/Na ratios (average of 1.07 and 5.56) with low K/(Fe+Mg) and Ca/Na (average 0.03 and 1.99 respectively). These values are closer to DBAC than PAAS values (Na/K= 4.49, K/(Fe+Mg)= 0.12, Ca/Na= 4.16 and Mg/Na= 2.14; Crocket and Paul, 2004).

A sharp decrease in both K/(Fe+Mg) (0.03) and Ca/Na (2.2) coincides with increased Na/K, and Mg/Na (mean values 2.14 and 2.98 respectively), which reach PAAS values from 1m below the paleosoil to one meter above (Fig. 8). Above this interval, Na/K, Mg/Na and Ca/Na ratios show decreased values coeval with increased K/(Fe+Mg) reaching DBAC values up to the base of the limestone at the top of the section.

Na/K and K/(Fe+Mg) in sediments from the lower transgressive phase reflect a dominant basaltic source, that is linked to intense chemical weathering, which progressively increases reflecting increasing humidity, as suggested by the CIA index and increased weathering of Fe-Mg enriched minerals. Interestingly, the change Na/K, K/(Fe+Mg), Ca/Na and Mg/Na is linked to the intervals with bivalves associated with the first marine transgression, which may represent changes in sediment source and/or weathering intensity. The significant decrease in K/(Fe+Mg) concomitant with increased Ca/Na, Mg/Na and CIA (close to PAAS value) 1m below the paleosoil and up to the carbonate concretions layer (Figs. 3, 9) reflects mixed sources. This could be explained by the long-term emersion represented by the paleosoil and likely involves erosion from different source rocks. Increasing aridity above the carbonate concretions level could also

explain the decrease in Na/K, Ca/Na, Mg/Na and CIA and the increase in K/(Fe+Mg) (Fig. 9). These variations may be due to different climatic conditions and/or the chemical weathering of Ca and Mg rich volcanic rocks, especially in the upper part of the second sea level transgression suggesting decreased weathering. This can be linked to the increased aridity as evidenced by the CIA proxy, which suggests reducing weathering of basalts.

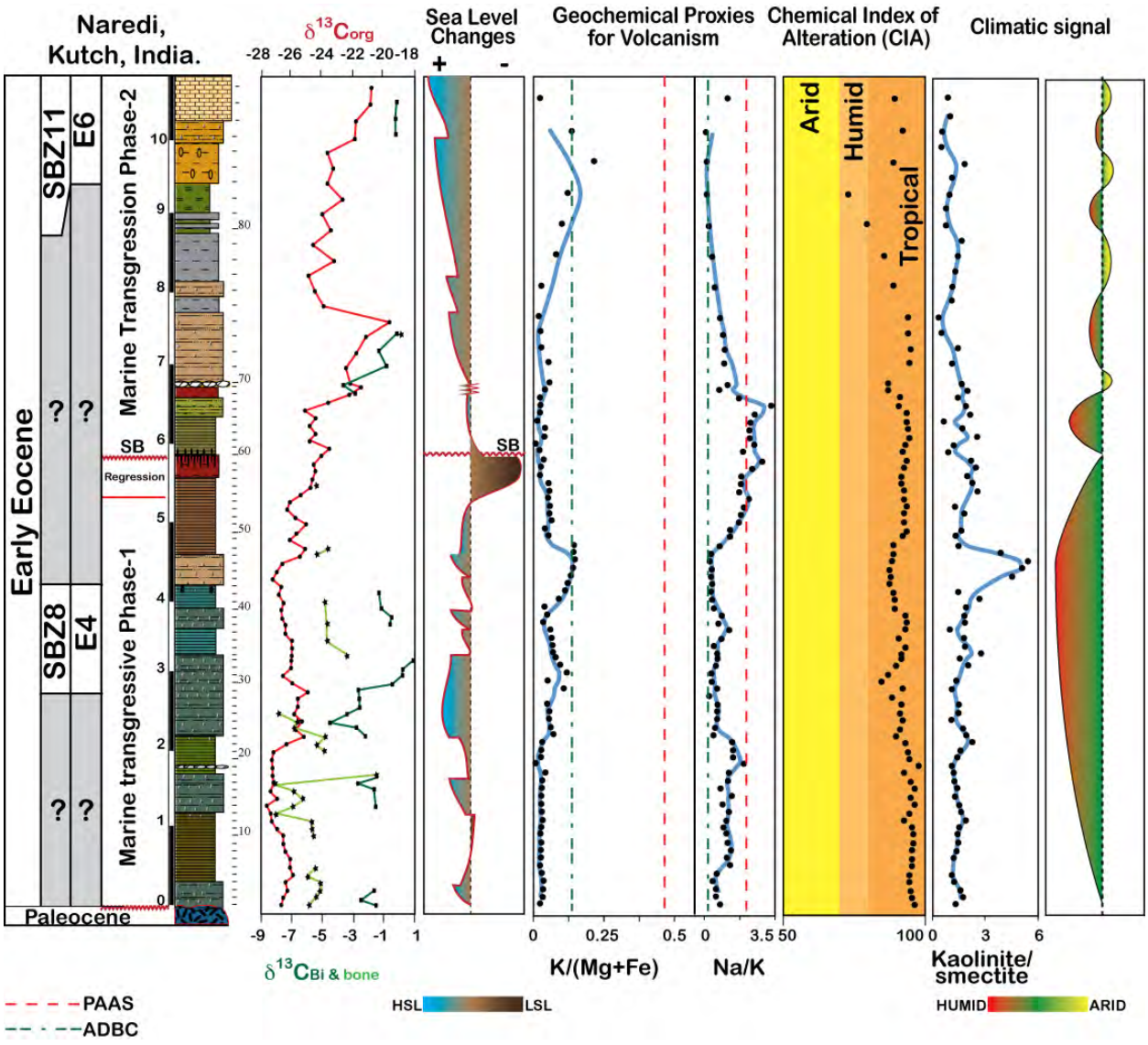

Figure. 11 *Summary of environmental proxies used in this study (different isotopic compositions, sea level, volcanism, weathering and climatic signal of clay minerals) based on major element geochemistry and clay mineralogy.*

7. CONCLUSIONS

The Naredi Formation in southwestern Kutch, India, was deposited during the first marine transgression in the Early Eocene following the last Deccan Trap eruption. Deposition occurred in a shallow inner shelf environment that varied from brackish lagoonal, brackish to normal inner shelf and to marginal marine inner shelf conditions. Two main transgressive phases interrupted by a regression and well-defined sequence boundary typified by a paleosoil can be identified (Fig.11).

Within this sequence three intervals yield common microfaunal assemblages consisting predominantly of small and larger benthic foraminifera. Planktic foraminifera are few to rare and restricted to the bottom and top of the section. An early Eocene age can be attributed to the Naredi sequence, based on larger benthic foraminifera SBZ8 in the lower part and SBZ11 at the top correlative with planktic foraminifera E4 and E6 biozones, respectively. Correlation with stable isotope curves and the sequence stratigraphy supports this age determination.

Sediments characterizing the transgression/regression phases were derived from basaltic rocks due to physical and chemical-weathering (Fig.10 and 11) processes as indicated by different geochemical proxies. A negative carbon isotopic excursion detected in bivalves, fish bones and teeth and organic matter could be related to the Early Eocene Climatic Optimum 2. The clay mineral sequence produced during deposition of the Naredi Formation reflects climatic conditions (see fig. 11) which fluctuated between hot humid to arid climate conditions.

ACKNOWLEDGEMENTS. We dedicate this paper to Prof. Dr. Lukas Hottinger (1933-2011) who passed away before this study was completed. We also thank Monnier, T and Lavanchy, J.C. for technical support and carrying out different types of analyses (phosphorus and XRF analyses). We thank Vonlanthen P. for his help during SEM analyses and Jahnavi Punekar for her precious help during fieldwork. We also thank B. Gertsch for its thorough and usefull review. This study was funded by the Egyptian Ministry of Higher Education (Mission No.001/013/104); and based on work supported by the US National Science Foundation through the Continental Dynamics Program, Sedimentary Geology and Paleobiology Program and Office of International Science & Engineering's India Program under NSF Grants EAR-0207407, EAR-0447171, and EAR-1026271.

REFERENCES

Adatte, T., Keller G. And Stinnesbeck, W. (2002) Late Cretaceousto Early Paleocene climate and sea-level fluctuations. *In:* Remane, J., et al. (eds.), Cretaceous-Paleogene transition in Tunisia. *Palaeogeography, Palaeoclimatology, Palaeoecology*, Special issue, v. 178, pp. 165–196.

Adatte, T., Keller G., Stüben, D., Harting, M., Utz Kramar, U., Stinnesbeck, W., Abramovich, S., And Chaim Benjamini, C. (2005) Late Maastrichtian and K/T paleoenvironment of the eastern Tethys (Israel): mineralogy, trace and platinum group elements, biostratigraphy and faunal turnovers. Bull. Soc. Géol. France, v. 176(1), pp. 37-55.

Adatte, T., Stinnesbeck, W. And Keller, G. (1996) Lithostratigraphic and mineralogic correlations near K/T boundary clastc sediments in northern Mexico: Implication for origin and nature of deposition. Geological Society of America, Special Paper, v. 307, pp. 211-226.

Anwar D., Chaudhary A.K., and Saraswati P.K. (2011). Integrated Biostratigraphy – Strontium Isotope Stratigraphy of Naredi Formation, Kutch. XXIII Indian Colloquium on Micropaleontology and Stratigraphy (ICMS), pp. 26

Bajpai. S. (2009) Biotic perspective of the Deccan volcanism and India–Asia collision: Recent advances, Current trend in science, Platinum Jubilee Special, pp. 505-516

Bajpai, S., Kapur, V.V., Thewissen, J.G.M., Tiwari, B.N., And Das, D.P. (2005a) First fossil marsupials from India: Early Eocene Indodelphis n.gen. and Jaegeria n. gen. from Vastan Lignite Mine, District Surat, Gujarat. Journal of the Palaeontological Society of India, v. 50(1), pp.147-151.

Bajpai, S., Kay, R. F., Williams, B. A., Dash, D. P., Kapur, V. V. And Tiwari, B. N. (2008) The oldest Asian record of Anthropoidea. Proceedings of the National Academy of Sciences, USA, v. 105, pp. 11093- 11098

Bettison, L.A. And Schiffman, R. (1988) Compositional and structural variations of phyllosilicates from the Point Sal ophiolite, California. Am. Mineralogy, v. 73, pp. 62-76

Bhatia, M.R. (1985) Rare earth element geochemistry of Australian Palaeozoic graywackes and mudrocks: provenance and tectonic control. Sedimentary Geology, v. 45, pp. 97–113.

Bolle, MP and Adatte T. (2001)Palaeocene-early Eocene climatic evolution in the Tethyan realm: clay mineral evidence Clay Minerals, v. 36, p. 249-261

Biswas, S.K. (1992) Tertiary stratigraphy of Kutch. Jour. Pal. Soc. India, v.37, pp.1-29.

Calvert, S.E., Fontugne, M.R. (1987) Stable carbon isotopic evidence for the marine origin of the organic matter in the Holocene Black Sea sapropel. Isotope Geosciences, v. 66, pp. 315–322.

Chamley, H. (1997) Clay mineral sedimentation in the Ocean. *In:* PAQUET, H. & CLAUER, N. (Eds.), Soils and sediments. Springer, Heidelberg, pp. 269-302.

Chamley, H. (1989) Clay sedimentology. Springer-Verlag, Berlin 623 pp.

Chattopadhyay, D. (2004) New record of a coral- mollusca reefal community from the early tertiary of Kutch, Gujarat, India, Indian Minerals, v.58, No. 3 & 4

Chattoraj, S., Banerjee, S. And Saraswati, P.K. (2009) Glauconites from the Late Palaeocene - Early Eocene Naredi Formation, Western Kutch and their Genetic Implications JOURNAL GEOLOGICAL SOCIETY OF INDIA v.73, pp.567-574

Chattoraj, S.L., Banerjee, S. And Saraswati, P.K. (2009) Glauconites from the Late Paleocene – Early Eocene Naredi Formation, Western Kutch and their genetic implications. J. Geological Society of India, v. 73, pp. 567-574.

Chattoraj, S.L., Banrejee, S. And Saraswati, P.K. (2008) Sedimentation, palageography and sequence startigraphic framework of the Late Palaeocene to Early Eocene Naredi Formation, Western Kutch, Gujarat. Int. Assoc. Gondwana Res. Conf. Series 5, p.116.

Cox, R., Lowe, D.R. And Cullers, R.L. (1995) The influence of sediment recycling and basement composition of evolution of mudrock chemistry in the southwestern United States. Geochimica et Cosmochimica Acta, v. 59, pp. 2919–2940.

Crocket, J.H., Paul, D.K. (2004) Platinum-group elements in Deccan mafic rocks: a comparison of suites differentiated by Ir contents. Chemical Geology, v. 208, pp. 273–291.

Deconinck, J.-F. (1992) Sédimentologie des argiles dans le Jurassique- Crétacé d'Europe occidentale et du Maroc. – Mém. HDR, Lille I, 266 p.

Dessert, C., Dupre, B., Gaillardet, J., Francois, L. M., And Allegre, C. J. (2003) Basalt weathering laws and the impact of basalt weathering on the global carbon cycle. Chemical Geology. v. 20, pp.1–17.

Fedo, C.M., Nesbitt, H.W. And Young, G.M. (1995) Unraveling the effects of potassium metasomatism in sedimentary rocks and paleosols, with implications for paleoweathering conditions and provenance. Geology, v. 23, pp. 921–924.

Garg, R., Prasad, V., Thakur, B., Singh, I.B. And Ateequzzaman, K. (2011) Dinoflagellate cysts from the Naredi Formation, South western Kutch, India: implication on age and palaeoenvironment. Jour. Paleo. Soc. India, v.56(2), pp. 201-218.

Gaucher, G. (1981) Les facteurs de la pe´dogenese. G. Lelotte, Dison, Belgium, 730 pp.

Haq, B.U., Hardenbol, J. And Vail, P.R. (1987) Chronology of fluctuating sea levels since the Triassic (250 million years ago to present). Science, v. 235, pp. 1156–1167

Hardenbol, J., Thierry, J., Farley, M.B., Jacquin, T., De Graciansky, P.C. And Vail, P. (1998) Mesozoic and Cenozoic sequence chronostratigraphic framework of European basins. *In:* P.C.

Graciansky, et al. (Eds.) Mesozoic and Cenozoic Sequence Stratigraphy of European Basins. SEPM Special Publication v. 60, pp. 3-13.

Keller G., Li, L. And Macleod, N. (l995) The Cretaceous/Tertiary boundary stratotype section at El Kef, Tunisia: How catastrophic was the mass extinction? Palaeogeography, Palaeoclimatology, Palaeoecology, v. 119, pp. 221-254.

Keller, G., Adatte, A., Bhowmick, P.K., Upadhyay, H., Dave, A., Reddy, A.N. And Jaiprakash. B.C. (2012) Nature and timing of extinctions in Cretaceous-Tertiary planktic foraminifera preserved in Deccan intertrappean sediments of the Krishna-Godavari Basin, India. Earth and Planetary Science letters, v. 342-344, pp. 211-221.

Klug, H.P. And Alexander, L.E. (1974) X-ray Difiaction Procedures for Polycrystalline and Amorphous Materials. 2nd Edition, Wiley-VCH, pp. 992

Kübler, B. (1987) Cristallinité de l'illite: méthode normalisées de préparation de mesure, méthode automatique normalisées de mesure. Cahiers de l'Institut de Géologie, Series AX n°3.1 and 3.2.

Li, C., Lightfoot, P.C., Amelin, Y. And Naldrett, A.J. (2000) Contrasting petrological and geochemical relationships in the Voisey's bay and Mushua Intrusions, Labrador, Canada: Implications for Ore Genesis. Economic Geology, v. 95, pp. 771-799.

Maynard, J.B., Morton, J., Valdes-Nodarse, E.L. And Diaz-Carmona, A. (1995) Sr isotopes of bedded barites: Guide to distinguishing basins with Pb-Zn mineralization. Economic Geology and the Bulletin of the Society of Economic Geologists, v. 90, pp. 2058–2064.

Mclennan, S.M., Hemming, S., Mcdaniel, D.K. And Hanson G.N. (1993) Geochemical approaches to sedimentation, provenance, and tectonics. *In:* Johnsson, M.J., Basu, A. (Eds.) Processes controlling the composition of clastic sediments. Geological Society of America Special Paper, v. 284, pp. 21– 40.

Mori, P.E., Reeves, S., Correia, C.T., And Haukka, M. (1999) Development of afused glass disc XRF facility and comparison with the pressed powder pellet technique at instituto de geociencias, Sao Paulo University. Revista Brasileira de Geociencias v. 29(3), pp. 441-446.

Nesbitt, H. W. And Young, G. M. (1984) Prediction of some weathering trends of plutonic and volcanic rocks based on thermodynamic and kinetic considerations. Geochimica et Cosmochimica Acta, v. 48, pp. 1523–1534.

Nesbitt, H.W. And Young, G.M. (1989) Formation and diagenesis of weathering profiles. Journal of Geology, v. 97, pp. 129-147.

Odin, G.S. (1988) Green marine clays. Developments in Sedimentolog, Elsevier, Amsterdam, v. 45, 445 pp

Price, J.R. And Velbel, M.A. (2003) Chemical weathering indices applied to weathering profiles developed on heterogeneous felsic metamorphic parent rocks. Chemical Geology, v. 202, pp. 397–416.

Pujol, F., Berner, Z. And Stueben, D. (2006) Palaeoenvironmental changes at the Frasnian–Famennian boundary in key European sections: chemostratigraphic constraints. Palaeogeography, Palaeoclimatology, Palaeoecology, v. 240, pp. 120–145.

Punekar, J. And Saraswati, P.K. (2010) Age of the Vastan Lignite in Context of Some Oldest Cenozoic Fossil Mammals from India Journal Geological Society Of India v. 76, pp. 63-68

Rage, J-C., Bajpai, S., Thewissen, J.G.M. And Tiwari, B.N. (2003) Early Eocene snakes from Kutch, western India, with a review of the *Palaeophiidae.* Geodiversitas v. 25(4), pp. 695-716.

Raju, D.S.N. (1974) Observations on the Eocene, Oligocene and Miocene foraminiferal biostratigraphy of Kutch, western India. Publication of the Centre of Advanced Study in Geology, Panjab University, Chandigarh, v. 10, pp. 136–155.

Raju, D.S.N., Guha, D.K., Bedi, T.S., Kumar, P. And Bhatttacharya, D.K. (1970) Microfauna,

biostratigraphy and paleoecology of the Middle Eocene to Oligocene sediments in western India. Publication of the Centre of Advanced Study in Geology, v. 7, pp. 155–178.

Revesz, K.M., Landwehr, J.M. And Keybl, J. (2001) Measurement of $\delta^{13}C$ and $\delta^{18}O$ isotope ratios of $CaCO_3$ using a Thermoquest Finnigan GasBench II Delta Plus XL Continuous Flow Isotope Ratio Mass Spectrometer with application to Devils Hole Core DH-11 Calcite. U.S. Geological Survey Open-File-Report 01-257, 17 pp.

Robert, C. And Chamley, H. (1991) Development of Early Eocene warm climates, as inferred from clay mineral variations in oceanic sediments. Palaeogeography, Palaeoclimatology, Palaeoecology, v. 89, pp. 315–331.

Robert, C. And Kennett, J.P. (1992) Paleocene and Eocene kaolinite distribution in the South Atlantic and Southern Ocean: Antarctic climate and paleoceanographic implications. Marine Geology, v. 103, pp. 99-110.

Rolli, M. (1990) Dosage semi-quantitatif RX sur Scintag. Cah. Inst. Geol. Neuchatel, Series ADX 10, 41 pp.

Roser, B.P. And Korsch, R.J. (1988) Provenance signatures of sandstone and mudstone suites determined using discriminant function analysis of major-element data. Chemical Geology, v. 67, pp. 119–139.

Sageman, B.B. And Lyons, T.W. (2003) Geochemistry of fine-grained sediments and sedimentary rocks. *In:* Holland, H.D. and Turekian, K.K. (Eds.), Treatise on Geochemistry, pp. 116-148.

Saraswati, P.K., Patra, P.K. And Banerjee, R.K. (2000) Biometric study of some Eocene *Nummulites* from Kutch and Jaisalmer, India. Journal of the Palaeontological Society of India, v. 45, pp. 91-122.

Saraswati, P.K., Sarkar, U. And Banerjee, S. (2012) *Nummulites solitarius – Nummulites burdigalensis* Lineage in Kutch with Remarks on the Age of Naredi Formation, Journal of the Palaeontological Society of India, v. 7, pp. 476-482.

Schaub, H. (1981) Nummulites et Assilines de la Tethys Paleogene. Taxonomie, Phylogenese et Biostratigraphie. Mem. Suisses Paleontology, v. 236, pp. 104-106

Schiffman, P. And Fridleifsson, G.O. (1991) The smectite-chlorite transition in drillhole NJ-15, Nesjavellir geothermal field, Iceland: XRD, BSE, and electron microprobe investigations. Journal Metamorphic Geology, v. 9, pp. 679-696.

Serra-Kiel, J., Hottinger, L., Caus, E., Drobne, K., Ferrandez, C., Jauhri, A.K., Less, G., Pavlovec, R., Pignatti, J., Samso, J.M., Schaub, H., Sirel, E., Strougo, A., Tambareau, Y., Tosquella, J. And Zakrevskaya, E. (1998) Larger foraminiferal biostratigraphy of the Tethyan Paleocene and Eocene. Bull. Soc. Geol. France, v. 169, pp. 281-299.

Shukla, S. (2008) Atlas of taxonomic and bio-chronostratigraphic studies on Palaeogene Larger Benthic Foraminifera from Indian sedimentary basins. Paleontographica Indica, ONGC, Dehradun, v. 9, 183 pp.

Singh, P. And Singh, M.P. (1991) Nannofloral biostratigraphy of the late middle Eocene strata of Kachchh Region, Gujarat State, India. Geoscience Journal, v. 12, pp. 17–51.

Slujis, A., Bowen, G.J., Brinkhuis, H., Lourens, L.J. And Thomas. E. (2007) The Palaeocene-Eocene Thermal Maximum super greenhouse: biotic and geochemical signatures, age models and mechanisms of global change. *In:* Williams, M. Haywood, A.M. Gregory, F.J. and Schmidt, D.N. (Eds.) Deep-time perspectives on climate change: Marrying the signal from computer models and biological proxies. The Micropalaeontological Society, Special Publications. Geological Society of London. pp. 323-350.

Taylor, S.R. And Mclennan, S. (1985) The Continental Crust: Its Composition and Evolution: Blackwell, Oxford, 312 pp

Weaver, C.E. (1989) Clays, muds and shales. Developments in Sedimentolgy, Elsevier, v. 44, 819 pp.

Woodburne, M.O., Gunnell, G.F. and Stucky, R.K. (2009) Climate directly influences Eocene mammal faunal dynamics in North America. Proceedings of the National Academy of Sciences of the U.S.A. v. 106(32), pp. 13399-13403.

Wynne, A. B. (1872) Memoir on the Geology of Kutch, Memoirs of the Geological Survey of India, v. 9, pp. 1-294,

Zachos, J., Pagani, M., Sloan, L., Thomas, E. And Billups, K. (2001). Trends, rhythms, and aberrations in global climate 65 Ma to present. Science, v. 292, pp. 686–693.

Zachos, J.C., Stott, L.D., and Lohmann, K.C. (1994) Evolution of Early Cenozoic marine temperatures. Paleoceanography, v. 9(2), pp. 353-387.

CHAPTER V

A. PALEOCENE EOCENE THERMAL MAXIMUM (PETM) EVENT: NEW INSIGHTS FROM INDIA

HASSAN KHOZYEM1, THIERRY ADATTE1, GERTA KELLER2, JORGE E. SPANGENBERG1, BANDANA SAMANT 3, AND SURESH MATHUR4.

[1]*Institute of Earth Science (ISTE), University of Lausanne, Géopolis, CH 1015 Lausanne, Switzerland.*

[2]*Department of Geosciences, Princeton University, Guyot Hall, Princeton, NJ 08544, USA*

[3]*Postgraduate Department of Geology, RTM Nagpur University, Nagpur, 440001, India*

[4]*Departement of Geology, J.N.V. University, Jodhpur 342006, India*

B. EARLY EOCENE CARBON ISOTOPE DATA FROM INDIA PROVIDE NEW INSIGHT INTO THE TIMING OF MAMMAL DISPERSAL

HASSAN KHOZYEM[1], THIERRY ADATTE[1], GERTA KELLER[2], JORGE E. SPANGENBERG[1], BANDANA SAMANT [3], AND SURESH MATHUR[4].

[1]*Institute of Earth Science (ISTE), University of Lausanne, Switzerland.*

[2]*Department of Geosciences, Princeton University, Guyot Hall, Princeton, NJ 08544, USA*

[3]*Postgraduate Department of Geology, RTM Nagpur University, Nagpur, 440001, India*

[4]*Departement of Geology, J.N.V. University, Jodhpur 342006, India.*

A. PALEOCENE-EOCENE THERMAL MAXIMUM (PETM): NEW INSIGHTS FROM INDIA[1]

Abstract. Lignite deposits from Gujarat and Rajasthan in northwestern India formed during the early Eocene in a tectonic rift basin that resulted from the rotation and early stage of the India-Asia collision. In coal mines throughout this region, two thick lignite intervals are separated by the early Eocene marine transgression. The source of the organic matter in lignites and intercalated marine sediments is mainly terrestrial and two organic carbon isotope ($\delta^{13}C_{org}$) excursions are recorded. The palynological age linked the lower $\delta^{13}C_{org}$ excursion records the Paleocene Eocene Thermal Maximum (PETM), whereas the upper $\delta^{13}C_{org}$ excursion correlates with the Early Eocene climatic optimum (ETM3) based on benthic foraminifera, palynology, and stable isotope correlation with marine and terrestrial environments.

1. INTRODUCTION

The late Paleocene to early Eocene transition (56 Ma) is marked by the warmest climate interval of the Cenozoic, known as the Paleocene-Eocene Thermal Maximum (PETM). Understanding this rapid warm event is critically important as it bears a striking resemblance to the human-induced climate change unfolding today (Zachos et al., 2001, 2005; Norris et al., 2013). The PETM was caused by massive injections of heat-trapping greenhouse gases into the atmosphere and oceans, comparable in volume to the persistent burning of fossil fuels since the industrial revolution and continuing into the future. Knowing the environmental conditions leading up to the PETM could help predict the looming catastrophe of the future, although oceanic and continental responses to the PETM differed and are not comparable to current conditions.

This PETM marks a global spike in temperature that lasted about 10,000 years and was superimposed over longer term warming. Based on temperature calculations from globally widespread sequences, oceanic deep waters warmed by up to 4-5^{o}C in tropical surface waters and the deep ocean, and by 6-8 ^{o}C in high latitudes, (Kennet & Stott, 1991; LI and Keller, 1998; Zachos et al., 2001, 2003 2005). Associated with this temperature spike are negative isotope excursions of 2-3 permil in carbonate ($\delta^{13}C_{carb}$) and organic matter ($\delta^{13}C_{org}$) linked to a strong perturbation in the carbon cycle over about 150,000 to 220,000 years (Westerhold et al., 2009; McInerney at al., 2011). The main reason for this perturbation is the injection of massive CO_2 into the marine and atmospheric systems. Excess CO_2 in the ocean results in ocean acidification, and a carbonate crisis (Zachos et al., 2005).

Carbonate secreting organisms were most affected by the PETM crisis, which led to: 1) the extinction of deep sea benthic foraminifera (Speijer and Wagner 2002; Alegret et al., 2009); 2) a major turnover in surface dwelling planktic foraminifera, particularly *Acarinina* and *Morozovella,* leading to decreased abundance of extant species and the evolution of several

[1] **Hassan Khozyem, Thierry Adatte, Gerta Keller, Jorge E. Spangenberg, Bandana Samant, and Suresh Mathur, 2013, Paleocene-Eocene Thermal Maximum (PETM): new insights from INDIA. *In preparation***

transient, small, disaster opportunist acarinid species (e.g. *Acarinina africana, A. sibaiyaensis, Morozovella allisonensis*; Kelly et al., 1996, 2002; Lu et al., 1998; Luciani et al., 2007); 3) a faunal turnover in calcareous nannofossils, particularly the transient occurrence of *Rhomboaster–Discoaster* assemblage (Aubrey et al., 2007).

Terrestrial environments responded differently to the PETM. The climate warming and increased atmospheric CO_2 resulted in high precipitation, increased weathering and enhanced runoff, which led to the formation of thick paleosol accumulations (Schmitz and Pujalte, 2007; Lopéz-Martínez and Peláez-Campomanes, 1999. Schmitz and Pujalte, 2003). In shallow areas the humid conditions resulted in wetlands and thick lignite accumulations. During the PETM, modern mammals migrated northward following the climatic belts. However, the timing and tempo of this mammal migration event and whether it originated in Asia or more specifically out of India remains controversial (Smith et al., 2006; Smith, 2012; Rose et al., 2008; Krause and Maas, 1990; Bajbai et al., 2005; Kappeler, 2000; Godinot, 1982; Sloan, 1970; Beard 1998).

The fate of excess carbon at the end of the PETM event is poorly constrained. Drawdown of atmospheric carbon dioxide has been attributed to increased weathering of silicates or to increased rates of organic carbon burial (Zeebe et al., 2009; Bains et al., 2000; Dickens, et al., 1997). The establishment of wetlands could explain the increased rates of organic carbon burial, which also plays an important role in the positive feedback to sustain atmospheric CO_2 via oxidation of coal bed methane (Chakraborty et al., 2011).

Many factors can control the environmental response to the PETM including paleogeography, paleotopography and paleodepth. Most previous studies have concentrated on the marine record, which have provided excellent global carbon and oxygen isotope records that now permit marine-terrestrial correlations of the PETM event. This study examines the terrestrial environment and its response to the PETM and subsequent Early Eocene warm events, known as the Early Eocene Climatic Optimum (EECO) in five lignite mines from Gujarat and Rajasthan, NW India, based on stratigraphy, microfossils, organic matter and organic carbon geochemistry. The main objectives of this study are: 1) develop high-resolution stable isotope records across the PETM and ETM3 in shallow wetland environments; 3) provide improved age control via stable isotope correlation with the marine record; 4) evaluate environmental conditions of the area during the warm events; 5) obtain insights into the age and nature of mammal migration.

2. GEOLOGY and TECTONIC SETTING

During the Jurassic to Cretaceous, the Indian continent separated from Gondwana in its northward migration and by early Eocene began its collision with Asia. In Rajasthan rift basins formed largely controlled by NW–SE and NE–SW trending fault systems (Fig. 1) (Sharma, 1999). In this area lignite formed in the Barmer–Sanchore basin during the early to middle Eocene, and the Bikaner–Nagaur basin and the Barmer–Sanchor basin during the lower Palaeocene to middle Eocene (Bhandari, 1999; Raju and Mathur, 2013).

Further to the south is Gujarat, part of the Saurashtra peninsula, which is surrounded by sea, except for the alluvial plain to the NE. Saurashtra is crossed by faults, including the Cambay Basin fault, Narmada fracture zone, Gulf of Kutch fault and the West Coast fault system in the Arabian Sea (Fig. 1). Biswas and Deshpande (1983) consider the Saurashtra region as a horst surrounded by rift grabens with distinct volcano-tectonic characteristics in the north, south and central areas. On the eastern side of Saurashtra is a sharp contact between alluvium with basalt

extending from Nal Sarovar to Bhavnagar (Fig. 1).

The Saurashtra peninsula is about 65% covered by lava flows (Deccan Traps), overlying Mesozoic sediments in the north and underlying Tertiary to Quaternary sediments along the coast. The Deccan Traps provide the basement for deposition of Tertiary sediments that are exposed in some places. Lignite in the region occurs in the Khadsaliya Clay Formation (? Eocene), which is never exposed. This green to greenish-grey clay contains lignite deposits and carbonaceous clay, which overlie the Supratrappean (Lower Eocene) and Deccan Traps (Cretaceous to Eocene). Lignite seams unconformably overlie the weathered basalt traps, deepen towards the east to northeast and diminish towards sea. Thus, all NW Indian lignite deposits, appear to be linked to tectonic basins that formed during the northward migration and rotation of the India landmass.

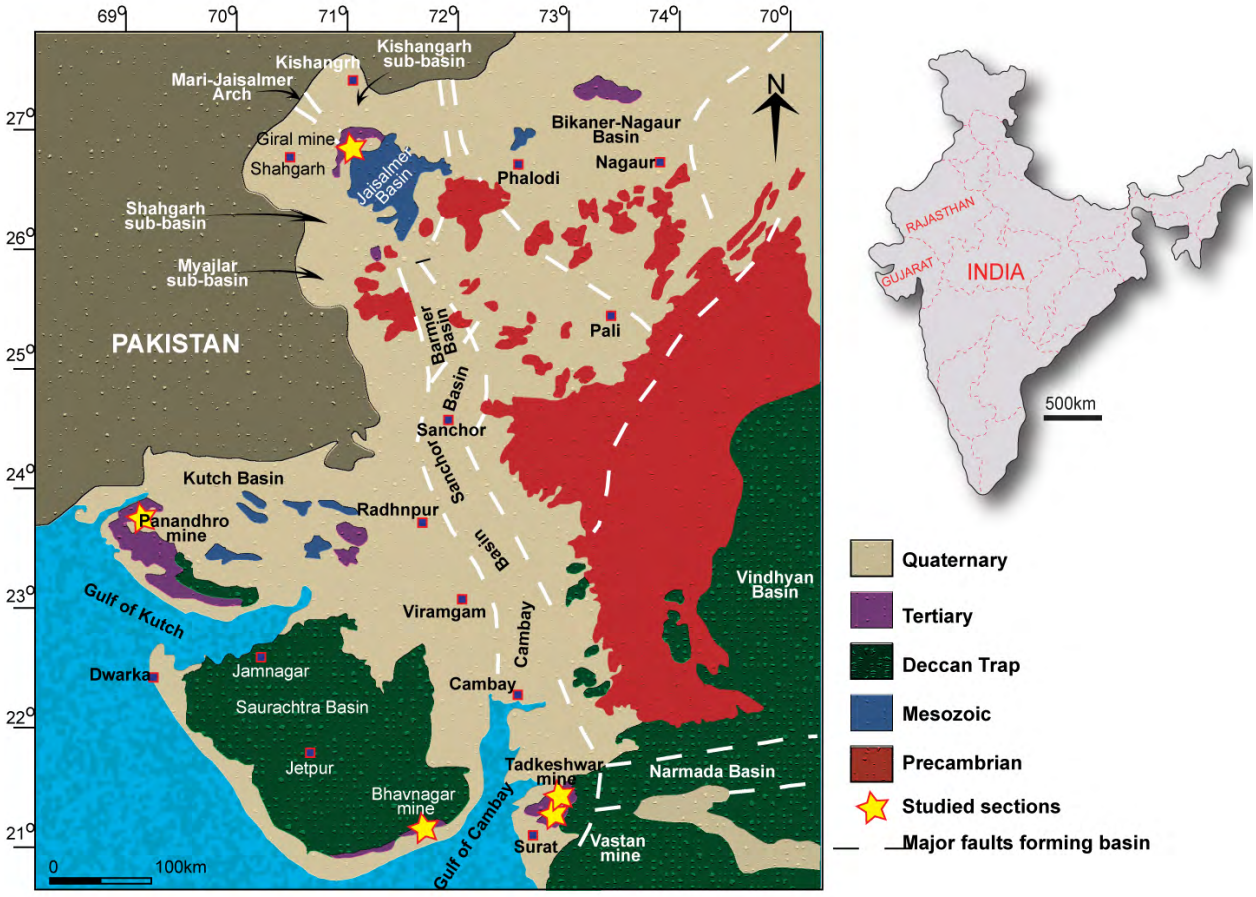

***Figure 1**: Lithostratigraphic and main structural trends of west India showing the exposed lithologic units, distribution of basins and location of the studied section.*

2.1. Geology of lignite mines

Giral Lignite mine, Rajasthan: The Giral mine is located in the Jaisalmere Basin 40km to the north of the town of Barmer, Rajasthan (lat. 26º05'57" Long. 71º25'26", Fig. 1). The 52 m thick strata of the Akli Formation exposed in this mine consist of bentonite, variegated clay, carbonaceous clay, dark grey-green clay, and several grey-green clay bands alternating with up to 1.5 m thick lignite seams and chert nodules. Three carbonaceous horizons can be identified, each comprising a number of lignite bands and carbonaceous clays, and greenish-grey clay partings. Many intervals yield vertebrate fossils, including sharks, rays, lepisosteids,

osteoglossids, pycnodontids, enchodontids and reptiles, such as Squatina, Ginglymostoma, Jaekelotodus and Gymnura including crocodilians and boid snakes (Rana, et al., 2005). This fauna supports a late Paleocene–lower Eocene age (Rana et al., 2005; Raju and Mathur, 2013).

Deposition occurred in coastal floodplains with mangrove-dominated vegetation and frequent marine incursions (Tripathi, et al., 2009). The abundance of biodegraded terrestrial and amorphous organic matter throughout the succession may be attributed to high microbial activity and overall anoxic burial conditions characteristic in the Alki Formation. The lignite beds contain abundant biodegraded amorphous and pyritized amorphous organic matter, which indicate the prevalence of anoxic conditions after burial (Tripathi, et al., 2009).

Panandhro Lignite mine, Gujarat: This lignite mine is located in the Kutch Basin near the village of Panandhro about 130 km to the northwest of Bhuj (lat. 22º42’13”, Long, 64º45’00”, Fig. 1). Tertiary sediments and the lignites are deposited in a basin where Deccan traps are exposed as discontinues patches to the south of the Panandhro mine. The Lower Eocene lignite deposit is associated with the lower member (Carbonaceous Shale Member) of the Panandhro Formation (Biswas & Raju, 1971; Saraswati & Banerji, 1984). The lignite exposed in the Panandhro mine consists of two workable seams separated by grey shale, carbonaceous shale and clay beds. The number of seams varies between 2 to 5 (Nadhamuni, 1976). Generally the Panandhro mine, comprising black pyriteous shale, predominance of argillite and lignite beds are suggestive of low energy lagoonal to marine shelf environments (Biswas & Raju, 1973; Hardas & Biswas, 1973). On the other hand, Saraswati and Banerjee (1984) relate the formation of lignite and carbonaceous shale beds from flood drifted vegetal matter under lacustrine condition.

Bhavnagar Lignite mine, Gujarat: This lignite mine is located in the Cambay Basin near the village of Surkha, 25 km from the town of Bhavnagar (Lat. 21º26’43”, Long. 72º07’30”, Fig. 1). At the base of the mine, lower Eocene bentonites, laterite and reworked bentonite clays unconformably overlie Deccan traps. The lignite seams dip 5-10° to the east-northeast and thin out towards the sea. Another unconformity separates the overlying Eocene Khadsaliya Calys consisting of gray to greenish-gray clays, sandstone and lignite with or without siderite nodules. In the Khadsaliya-Lakhanka Block, lignite is found between depths of 11.99 m to 195.81 m with the thickness of the two seams varying between 0.20 to 11.05 m (source Gujarat Heavy Chemicals Limited report). The lignites are brownish black, fine grained, amorphous and tend to develop cracks when exposed to air. The lignite seams contain specks of resin, pyrite and iron nodules are abundant and can be hand picked (Thakur et al., 2010). Above are lower Miocene shales, sandstones and conglomerates. The Bhavnagar lignite deposits has formed from forest dominated vegetation in a fast subsiding basin, experiencing almost uniform environmental conditions, with slight intermittent fluctuations (Thakur et al., 2010)

Vastan and Tadkeshwar Lignite mines, Gujarat: These two lignite mines are located in the Cambay Basin, about 18 km and 15 km from the railroad station at Kim, respectively (Lat. 21°26’10”N, Long. 73°6’46”E, Lat. 21°22’25”N, Long. 73°04’00”E, Fig. 1). Lignites in these two mines are intercalated in a continuous succession of shales of the Cambay Fm a continuous succession of the Cambay Shale. The main sedimentary facies are lignites and mudstones with or without shells. Minor siltstones and carbonates and rare sandstones are generally in thin layers (<10cm) with parallel laminations. Lignite occurs in multiple beds of varying thicknesses. Two beds referred to as Lignite 1 (younger) and Lignite 2 (older) are particularly thick and persistent

with sharp boundaries. Some beds have pyrite or pyritized organic structures.

The lack of fossils but presence of some rooting structures suggests an environment of coastal grass-flats (McCann, 2010). Singh et al. (2010) inferred that the lignites formed under moderate to high water in limnic environments with influx of fresh water. A marginal marine or coastal environment with influx of fresh water is likely for the deposition of non-shelly mudstones as also suggested by the occurrence of wood logs intensely bored with marine molluscs. Shelly mudstone beds are full of disarticulated molluscan shells. The presence of marine gastropods, pelecypods, ornamented ostracods, foraminifers, shark and ray fishes indicate deposition in a shallow marine setting with varying energy levels.

3. MATERIAL AND METHODS

Samples were collected at 5, 10, 20, 30 and 50 cm intervals from five working lignite mine (Fig.1, Table.1). The samples were analyzed for organic matter content and organic carbon isotopes. Age control is mainly based on palynology and benthic foraminifera.

Table 1. *Location coordinate of the studied section, depositional basins, thickness of collected section and number of samples analyzed.*

Section name	Longitude	Latitude	Basin	Thickness	Samples
Giral mine	71 15' 9.36"E	26 3' 20.52"N	Jaisalmere	31m	188
Panandhro mine	68 46' 15.23"E	23 40' 57" N	Kutch	12m	64
Bhavnagar mine	72°16'30"E	21°43'00"N	Cambay	21.5m	170
Vastan mine	73°07' E	21°25' N	Cambay	9.5m	92
Tadkeshwar mine	73°04'32" E	21°19'26" N	Cambay	17m.	170

3. 1. Rock Eval Pyrolysis.

The content and type of the organic matter were determined by Rock Eval pyrolysis (Rock-EvalTM6, Behar et al., 2001). Total organic carbon contents (TOC, weight %) were obtained using the standard temperature cycle. Samples were calibrated with both IFP160000 and an internal standard with an instrumental precision of <0.2% (Espitalié et al., 1985). Pyrolysis experiments were conducted using a “Turbo” Rock-Eval-6 pyrolyser manufactured by Vinci Technologies®. The full description of the method is given by Lafargue et al. (1998). Briefly, samples were first pyrolysed under an inert N_2 atmosphere and the residual carbon was subsequently burnt in an oxidation oven. The amount of hydrocarbon (HC) released during pyrolysis was detected with a flame ionisation detector (FID), while online infrared detectors continuously measured the released CO and CO_2. The samples were first pyrolysed from 100°C to 650°C at a rate of 25°C/min. The oxidation phase starts with an isothermal stage at 400°C, followed by an increase to 850°C at a rate of 25°C /min to incinerate all the residual carbon. In order to determine the type and degree of maturity of the organic matter contents, the OI vs HI and T-max vs HI were plotted.

3. 2. Organic Carbon isotopes

The kerogen was separated from the samples by HCl treatment, dried (40°C, 16h), and submitted to carbon and nitrogen isotope analyses by flash combustion on a Carlo Erba 1108 elemental analyzer (EA) connected to a Thermo Fisher Scientific Delta S isotope ratio mass spectrometer (IRMS) that was operated in the continuous helium flow mode via a Conflo III split interface (EA–IRMS). The $\delta^{13}C$ values were reported relative to VPDB. The calibration and assessment of the reproducibility and accuracy of the isotopic analyses were based on replicate analyses of laboratory standard and international reference materials. The reproducibility was better than 0.1‰ (1σ).

3.3. Biostratigraphy

For foraminiferal analysis, about 100gr. sediment was processed per sample by standard methods and washed through 63 μm and 38 μm screens to preserve small species (Keller et al., 1995). Biostratigraphic analysis was performed on these two size fractions. Quantitative counts of ~300 specimens were picked from the >63 μm size fraction, mounted on cardboard slides for a permanent record and identified to obtain relative species abundance data. The remaining sample residue for each sample was searched for rare species (analytical work done by G. Keller).

For palynomorph extraction, samples were treated with HCl, HF and HNO_3 followed by 5% solution of KOH. The sample residue was washed with water through a 15μm screen. The slides were prepared in polyvinyl alcohol and mounted in Canada balsam. A Leitz Laborlux-S and Olympus BX51 microscope were used for their study and photomicrography (RTM Nagpur University, Nagpur, India, (analytical work done by B. Samant).

4. RESULTS

4.1. Lithology, Total Organic Content (TOC) and Organic Carbon Isotopes ($\delta^{13}C_{org}$)

All five lignite mines analyzed show similar lithologies with lignite intervals enriched in TOC and separated by shallow marine or lacustrine to fluvial sediments. Strong similarities are observed in the $\delta^{13}C_{org}$ profiles, including two negative carbon isotopic excursions.

4.1.1 Giral Lignite mine

The lithology of the Giral mine section can be divided into three intervals containing well-defined lignite levels with high organic matter contents (Fig. 2). At the base of the exposed section are two lignite layers with total organic matter (TOC) ranging between 12.95% and 63.83% and a mean value of 42.5%. Above is an 8 m thick calcareous claystone and several layers of carbonate concretions with low TOC (0.28-7.75%, mean 1.44%). The middle lignite interval consists of 4 lignite layers between 0.2 m and 1.5 m thick with TOC between 2.24% and 60.24% (mean 22%). This interval is separated from the middle lignite layer by 9 m of calcareous claystone with TOC between 0.6% to 1.7%. The upper lignite interval consists of two beds, each about 2.5 m thick with TOC between 5.3% to 17% (Fig. 2). Between these two lignite layers is a 1.5 m thick calcareous claystone with low TOC (mean 0.4%) similar to the interval below. The OI vs. HI and Tmax vs. HI of the Giral mine reflect immature organic matter of terrestrial origin for both lignite and intercalated calcareous claystones (Fig. 2). The $\delta^{13}C_{org}$ profile shows two distinct $\delta^{13}C_{org}$ excursions in the lower and upper parts of the section.

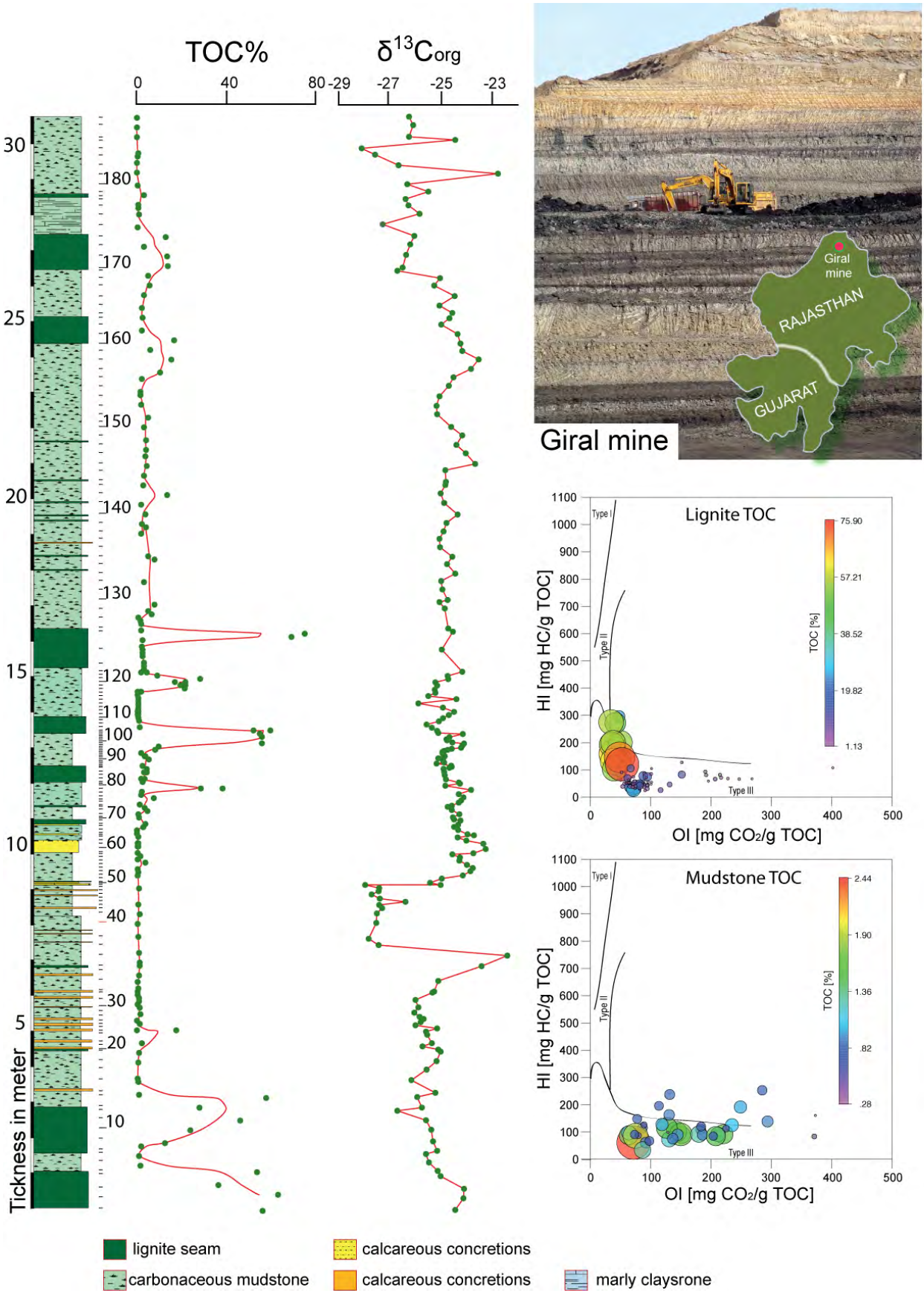

Figure 2: *Giral lignite mine with photo, lithostratigraphy, total organic carbon (TOC), $\delta^{13}C_{org}$, and cross plots of oxygen index (OI) vs. hydrogen index (HI) indicating the terrestrial origin of organic matter.*

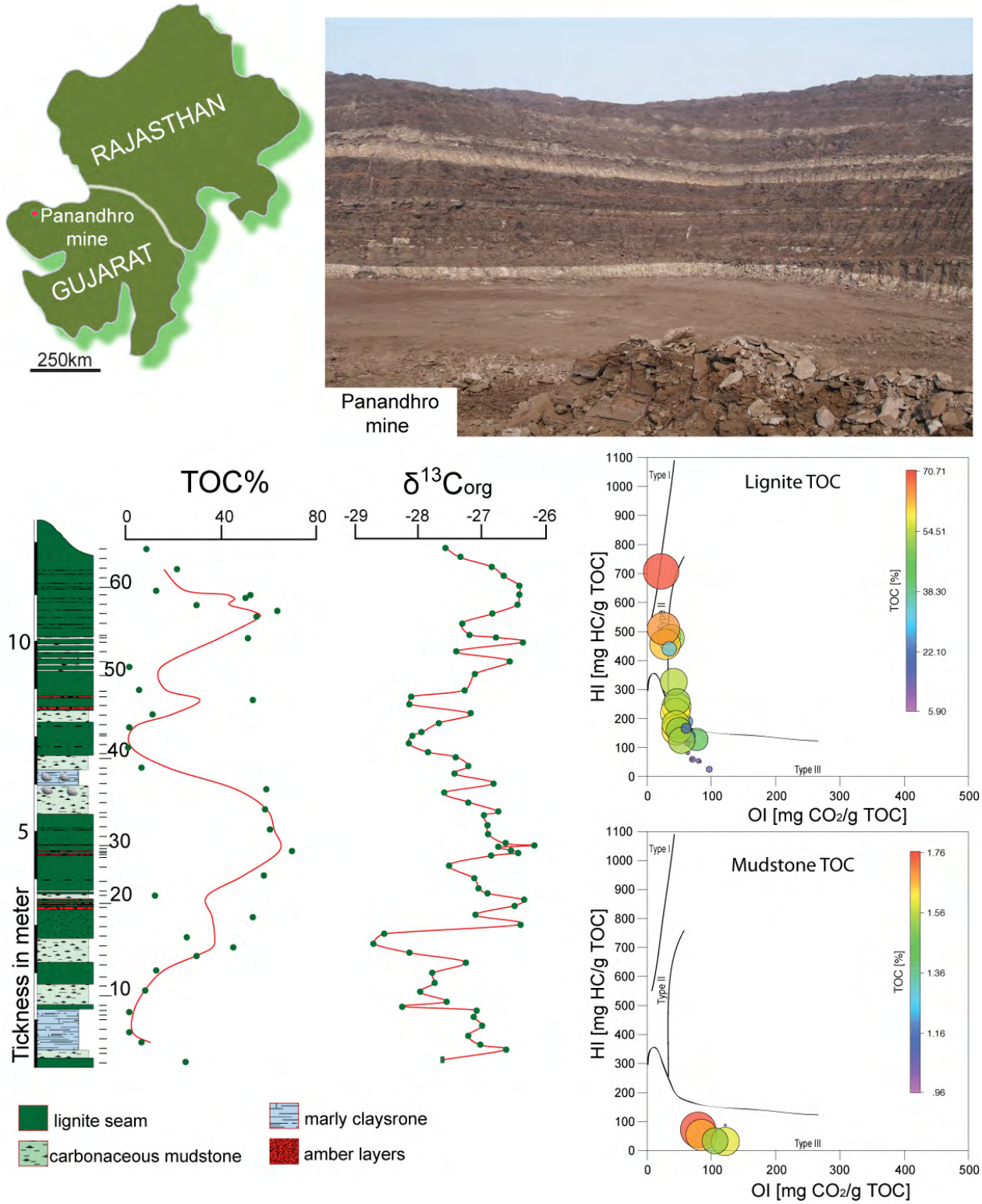

Figure 3: *Panandhro lignite mine with photo, lithostratigraphy, total organic matter (TOC), $\delta^{13}C_{org}$, and cross plots of oxygen index (OI) vs. hydrogen index (HI) indicating the terrestrial origin of organic matter.*

The lower $\delta^{13}C_{org}$ excursion begins 7 m above the base of the section with an abrupt negative shift of about 2‰ (-25.4‰ to -27.4‰), spans 2 m and ends abruptly (Fig. 2). The entire excursion is in calcareous claystone. About 17 m above begins the second more gradual $\delta^{13}C_{org}$ excursion of 2.4‰ (-25‰ to -27.4‰) and values fluctuating around -24.6‰ over the 3.5 m to the top of the exposed sequence. This excursion spans the upper lignite layer and calcareous claystone.

4.1.2 ***Panandhro Lignite mine***

At this mine, two lignite intervals are separated by 1.6 m of calcareous marine mudstone (Fig. 3). The lower lignite interval spans 4 m with intercalations of carbonaceous mudstone. TOC gradually increases over 4.5 m from 8.5% to 70.75% (mean 38.8%). Organic matter content consists of immature organic matter of terrestrial to lacustrine origin. The overlying calcareous marine claystone is enriched in mollusk shells, and has low TOC (0.96%) of immature terrestrial origin. In the upper 4+ m thick lignite layer, TOC gradually increases to a maximum of 64.7% containing immature organic matter of terrestrial to lacustrine origin (Fig. 3). Two $\delta^{13}C_{org}$ excursions are also recorded at the Panandhro mine. The lower $\delta^{13}C_{org}$ excursion shows a gradual decrease (-26.7‰ to -28.7‰) over the 2.8 m at the base of the section reaching minimum values in a calcareous claystone. In the overlying lignite $\delta^{13}C_{org}$ values abruptly increase to -26.3‰, remain heavy but fluctuating over the 2.4 m thick lignite interval. In the overlying 1.5 m calcareous claystones and basal 1 m lignite, the second $\delta^{13}C_{org}$ excursion decreases to minimum values (-28.3‰). In the 2 m overlying lignite $\delta^{13}C_{org}$ fluctuate, but increase to pre-excursion values, decreasing again in the lignite at the top of the section.

4.1.3 Bhavnagar Lignite mine

This mine contains an 8.5 m thick lower lignite interval separated from the two thin upper lignite layers by 6.5 m of marine sediments enriched in molluscs and benthic foraminifera (Fig. 4). The thick lower lignite interval overlies 1.2 m of claystone above the Deccan traps. TOC of the claystone is very low (0.23% to 0.93%). The overlying lignite is enriched with immature organic matter of terrestrial and lacustrine origins ranging between 5.25% to 76.75%. At the base of the marine deposits, TOC abruptly decreases (0.7-1.6%, mean 3.3%) and consists of immature organic matter of terrestrial to lacustrine origin. The two thin upper lignite beds are 0.2 m thick with relatively low TOC (4.25% to 12.75%) and immature lacustrine organic matter (Fig. 4). About 1 m from the base of the section, $\delta^{13}C_{org}$ values show a -2.3‰ negative excursion (-25.4‰ to -27.7‰), followed by gradually increasing values to -26‰ through the thick lignite interval and calcareous claystone above (Fig.4). From the top of calcareous claystones to the top of the section the $\delta^{13}C_{org}$ values fluctuate but decrease to -20.4 ‰.

4.1.4. Vastan Lignite mine

In the Vastan Mine, the Cambay Shale is 20-145 m thick but in the fossiliferous section sampled by us only about 30 m thickness has been exposed so far (Fig. 5). It comprises alternating sequence of lignite beds, dark grey to black and greenish grey shales and clay-marls. There are two main lignite seams, one at the top referred to as Lignite 1 and one at the mine floor referred to as Lignite 2. The thickness of Lignite 1 ranges between 3 and 8 m and that of Lignite 2 between 4 and 6 m. Besides these main lignite seams, there are 4 to 5 thinner seams that are up to one meter or less thick. The top seam or Lignite 1 has a few amber-rich layers, amber is also present but less frequent in Lignite 2.

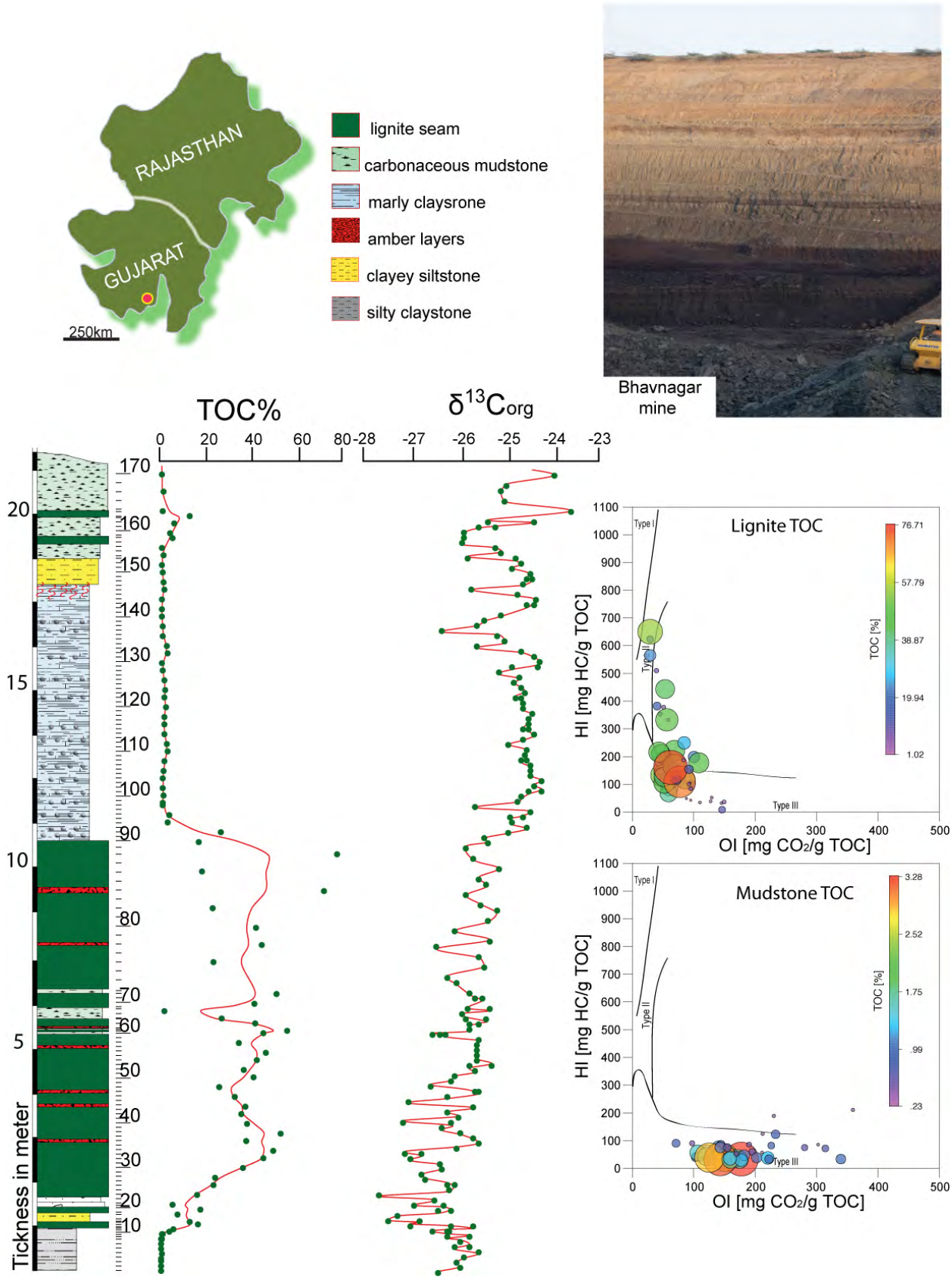

Figure 4: *Bhavnagar lignite mine with photo, lithology,total organic matter (TOC), $\delta^{13}C_{org}$, and cross plots of oxygen index (OI) vs. hydrogen index (HI) indicating the terrestrial origin of organic matter.*

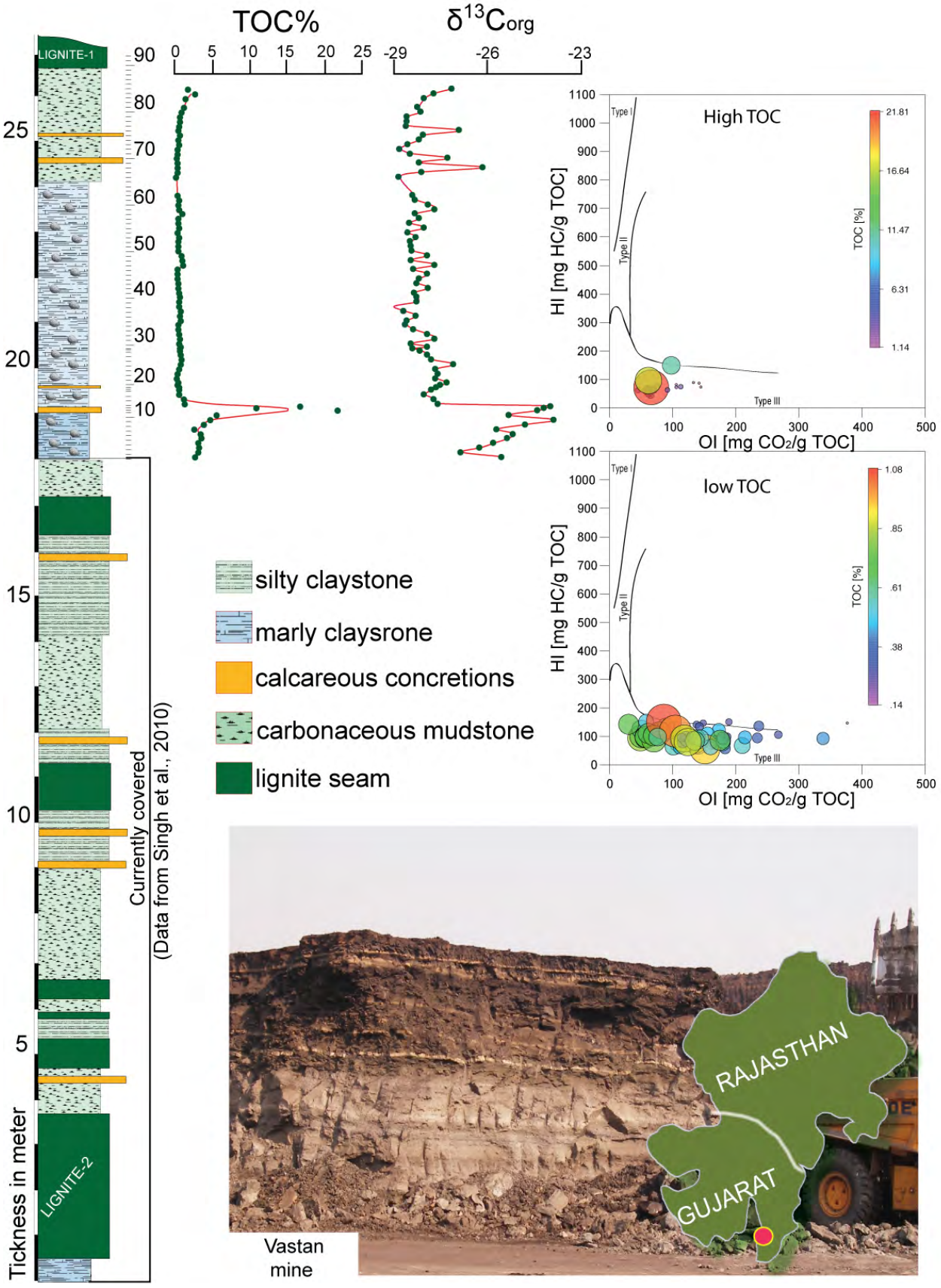

Figure 5: *Vastan lignite mine with photo, lithology, total organic matter (TOC), $\delta^{13}C_{org}$, and cross plots of oxygen index (OI) vs. hydrogen index (HI) indicating the terrestrial origin of organic matter. The lower covered (backfilled) interval is taken from Singh et al., 2010).*

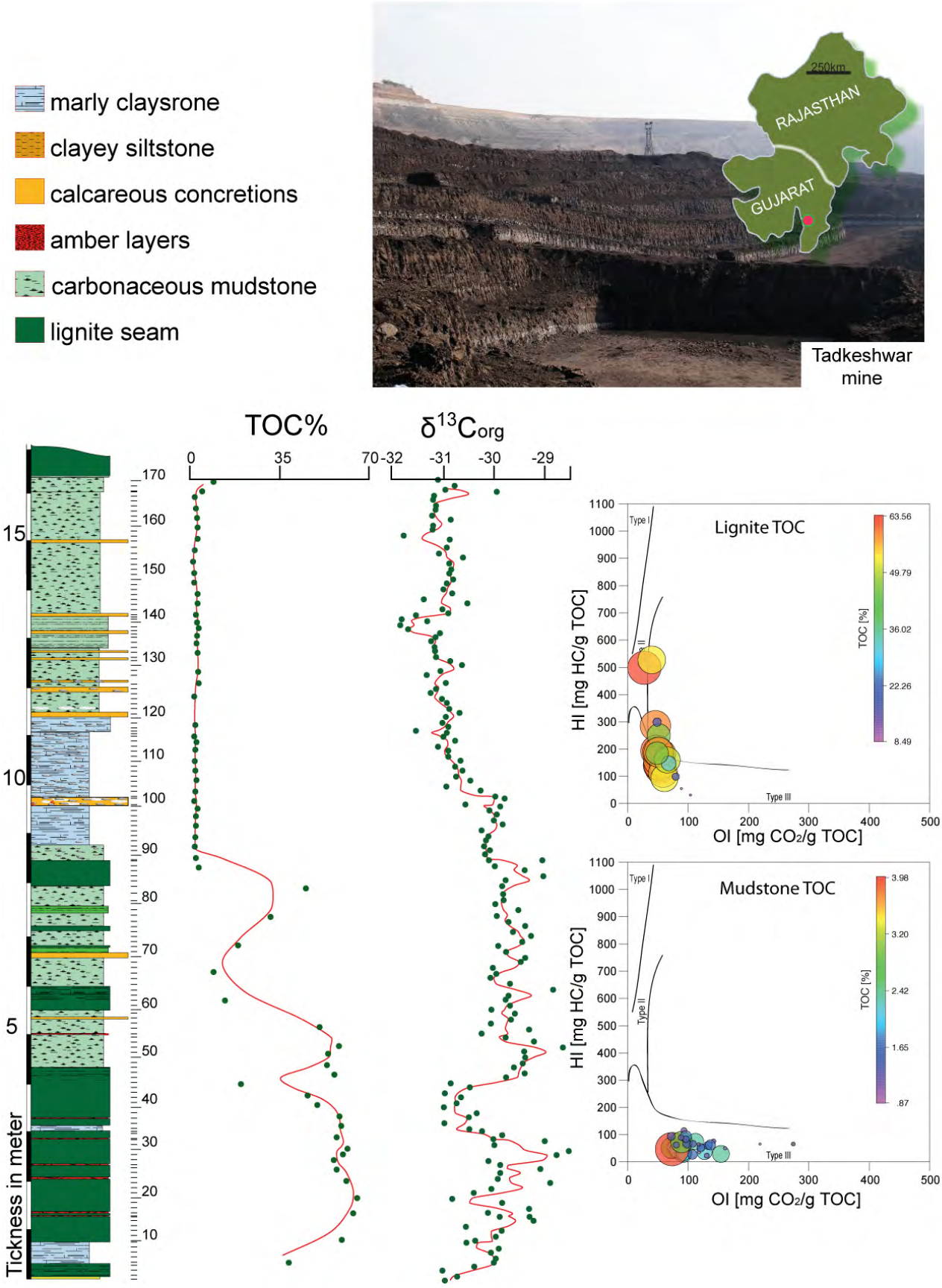

Figure 6: *Tadkeshwar lignite mine with photo, lithostratigraphy, organic matter (TOC), $\delta^{13}C_{org}$, and cross plots of oxygen index (OI) vs. hydrogen index (HI) indicating the terrestrial origin of organic matter.*

The amber from Lignite 1 has yielded some of the finest preserved insect body fossils known (Alimohammadian et al., 2005, 2006). The Vastan section is overall highly fossiliferous. The major groups are plants, molluscs (bivalves, scaphopods as well as gastropods), microvertebrates (fish, amphibians, reptiles as well as mammals) foraminifers and ostracodes. The molluscs are highly concentrated in the lower part of the sequence forming conspicuous shell beds from which a rich assemblage of vertebrate fossils is also recorded (Rana et al., 2004, 2005b; Sahni et al., 2004; Bajpai et al., 2005 a, b, c, 2006; Rose et al., 2006; Nolf et al., 2006). But most of this lithologic succession is now covered due to the mine backfilling processes.

The exposed analyzed sequence was deposited in marine environment with deposition of 6.8 m of calcareous mudstone and 3 m of calcareous claystone (Fig. 5). The lower meter of the calcareous mudstone is characterized by relatively low value TOC (1.14% to 21.8%, and mean value 5.85%). Above the TOC peak an abrupt drop to 0.54% persists to the top of the section with terrestrial organic matter.

In the first meter of the exposed upper section, $\delta^{13}C_{org}$ values gradually increase then abruptly drop ~3‰ (-25.19‰ to -28.12‰) in a marly claystone with calcareous concretions (Fig. 5). In the overlying 5 m of marly claystone, $\delta^{13}C_{org}$ values remain high. In the top 3 m of calcareous claystone with concretion layers, $\delta^{13}C_{org}$ values strongly fluctuate towards more positive values.

4.1.5. Tadkeshwar Lignite mine

The lower 8.5 m of the Tadkeshwar mine section consist of thick lignite layers with calcareous claystone and calcareous concretions (Fig. 6). The basal 2 m of this interval consist of terrestrial to lacustrine organic matter gradually changing to immature terrestrial organic matter. TOC ranges between 8.6% and 65.25% (mean 46.4%). Between 5 m and 6.5 m, TOC abruptly decreases from 70% to 1.6%. Between 8.5 and 11.5 TOC decreased to <2% persisting through the carbonaceous claystone intervals. The second lignite interval at the top of the section has a sharp basal contact.

The $\delta^{13}C_{org}$ profile of the Tadkeshwar mine can be divided into four intervals. At the base (0 to 2.8 m), the $\delta^{13}C_{org}$ values increased gradually from -31‰ to -28.5‰ (mean -29.9‰). The first $\delta^{13}C_{org}$ excursion is gradual (-28.5‰ to -30.9‰, mean -30.4‰) and reaches minimum values between 3.0-4.0 m followed by a rapid increase to pre-excursion values at the lithological change from lignite to calcareous claystone. In the overlying ~5 m of alternating lignite, calcareous claystone and calcareous concretions, values fluctuate between -30.2‰ to -28.6‰ (mean -29.7 ‰). From 9.7 m to 14.5 m, $\delta^{13}C_{org}$ values gradually decrease from -29.7‰ to -31.8‰ (mean -31‰), followed by a gradual increase toward the top of the section (-31.8‰ to -29.9‰, mean -30.9‰).

4.2. Biostratigraphy and Age control.

All five mines show significant sedimentologic, lithologic and $\delta^{13}C_{org}$ carbon isotope similarities but very few contain microfossils that are suitable for age control. This is largely a function of the prevailing shallow water marine to fluvial environment that prevents survival of most marine microfaunas and floras and favors survival of just a few high-stress tolerant species. For the biostratigraphic analysis, we chose the three most promising sections – Tadkeswar, Giral and Vastan mines.

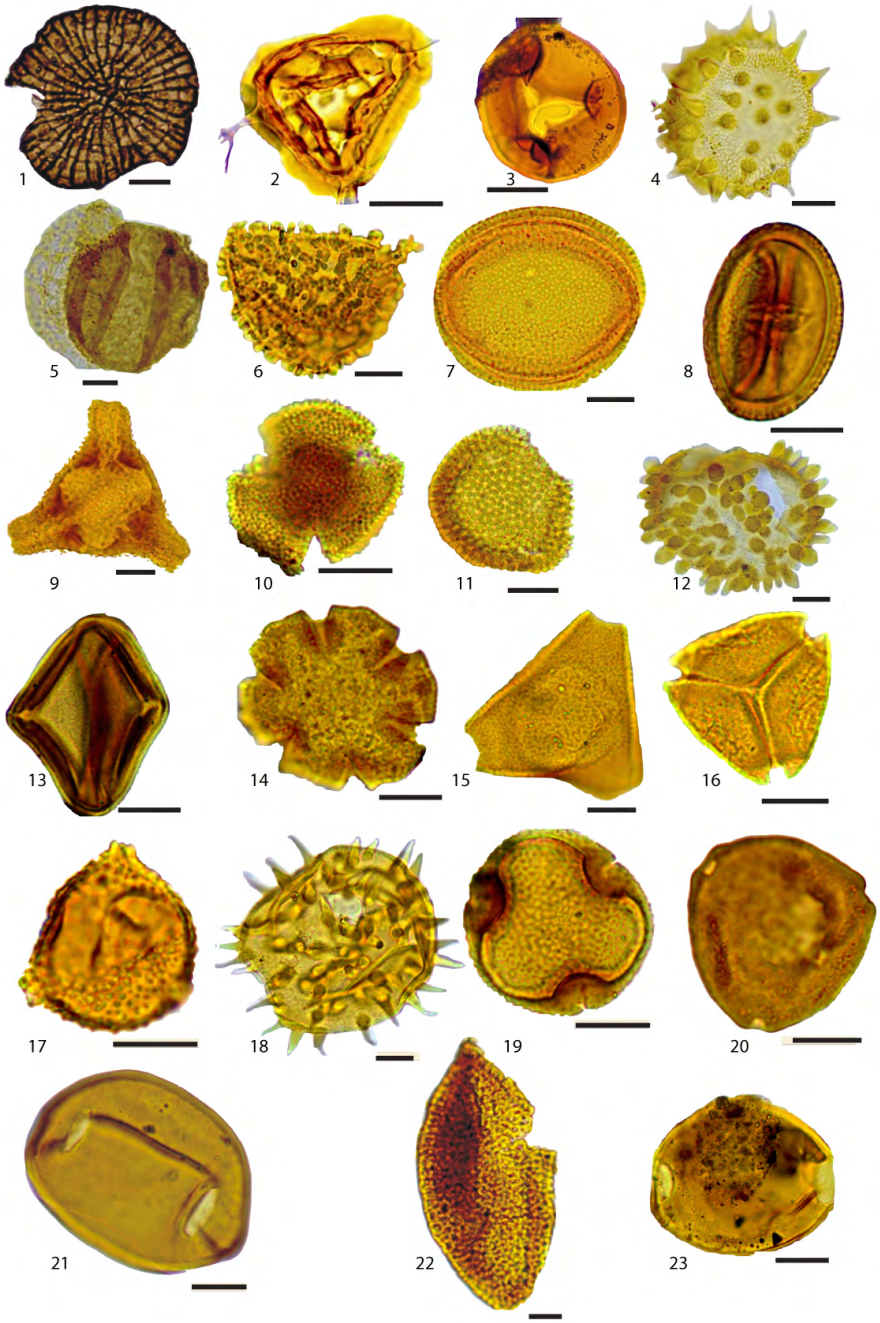

Plate 1: *Pollen species from the Paleocene-Eocene Thermal Maximum (PETM) interval at the Giral mine section. 1. Callimothalus pertusus (Dilcher 1965); 2. Pteridacidites sp. A; 3. Dandotiaspora plicata (Sah et al,. 1971); 4. Spinizonocolpites echinatus (Muller 1968); 5. Podocarpidites sp.; 6. Longapertites sahnii Frederiksen 1994); 7. Proxapertites microreticulatus (Jain, Kar and Singh 1973); 8. Florschuetzia rajpadiensis (Samant and Phadtae, 1997); 9. Grevilloideaepites eocenicus (Biswas) Singh and Mishra, 1991); 10. Warkallipollenites exilis (Frederiksen 1994); 11. Incrotonipollis neyvelli (Jansonius and Hills 1981); 12. Spinizonocolpites adamanteus (Frederiksen 1994); 13. Rhombipollis geniculatus (Frederiksen 1994); 14. Ctenolophonidites sp.; 15. Proteacidites protrudes (Sah and Kar, 1970); 16. Cupanidites flaccidiformis (Venkatachala and Rawat 1972).* 17. *Echitriporites* sp. *A*; 18. *Acanthotricolpites bulbispinosus* (Singh and Misra 1991); 19. *Lacrimapollis* sp. A; 20. *Momipites* sp. A; 21. *Psilodiporites* sp. A; 22. *Matanomadhisulcites maximus* (Kar 1985); 23. *Psilodiporites hammenii* (Venkatachala and Rawat 1962). *Scale bar = 10μm.*

Giral lignite mine: This sequence has a good concentration of pollen, spores, fungi and dinoflagellates across the lower $\delta^{13}C_{org}$ shift. The assemblage is dominated by *Spinizonocolpites* spp. and *Acanthotricolpites* spp. followed by *Kapurdipollenite, Longapertites, Neocouperipollis,* Among spores *Dandotiapora, Foveotriletes, Lygodiumsporeites* and *Triplanosporites* are common. Gymnosperm pollen grains of *Podocarpus* are present along with the epiphyllous fungi microthyriaceae. Fungal spores are present in significant concentration in almost all samples (Plate 1).

The palynoassemblage of pollen from *Echitriporites trianguliformis* (Van Hoeken-Klinkenberg, 1994), *Longapertites sahnii* (Frederiksen, 1994), *Rhombipollis geniculatus* (Frederiksen, 1994), *Warkallipollenites exilis* Frederiksen, 1994 and *Yeguapollis prolatus* (Frederiksen, 1994) which are known only from the Middle-Late Paleocene deposits of the Bara, Lakhara, Hangu and Patals Formations of Pakistan (Frederiksen, 1994). This provides a lower age limit of late Paleocene for the Giral mine section.

Palynomophs restricted to the Paleocene-early Eocene of India include *Dandotiaspora spp, Cupanidites flaccidiformis* (Venkatachala and Rawat, 1972), *Spinizonocolpites adamanteus* (Frederiksen, 1994), *Grevilloideaepites pachyexinus* (Kar and Kumar) Singh and Misra, 1991, *Incrotonipollis neyvelli* (Jansonius and Hills, 1981), K*apurdipollenites baculatus* (Tripathi, 1993), *Longapertites vaneendenburgii, Matanomadhisulcites maximus* (Saxena) (Kar 1985), *Proteacidites protrudus* (Sah and Kar, 1970), *Proxapertites microreticulatus* (Jain Kar and Singh, 1973), *Retistepanocolpites willamsii (*Germeraad, Hopping and Muller, 1968), and *Retiverrumonosulcites barmerensis* (Tripathi, 1993). This assemblage indicates an upper age limit of early Eocene. This is also indicated by the absence of palynotaxa restricted to early-middle Eocene sediments (e.g.,*Meliapollis patchydermis* Navale and Misra, 1979, *M. simplex* Navale and Misra, 1979, *Pseudonothofagidites spp.* (Venkatachala and Kar, 1969), *Retipollenites confuses Gonzalez Guzman, Tricolporocolumellites pilatus (*Kar, 1985), *Tricolporopilites, robustus,* (Kar 1985), *Tripilaorites triangulatus,* (Kar, 1985)). Additional evidence for a late Paleocene-early Eocene (Thanetian-Yprisian) age is the similarity of the Giral lignite palynoassemblage with those recorded from lignite deposits at Akli and Kapurdi in the Barmer District of Rajasthan (Tripathi et al, 2009, Tripathi, 1997). We conclude that the lower $\delta^{13}C_{org}$ excursion represents the Paleocene to Early Eocene (Ypresian) transition the PETM.

Tadkeshwar Lignite mine: No dinoflagellate cysts are present in the interval of the lower $\delta^{13}C_{org}$ excursion. However, typical mangrove pollen (Plate 1) of *Nypa (Spinizonocolpites)* or *Barrigtonia (Barringtoniapollenites)* and other Arecaceae (palms) are present. This suggests deposition in a terrestrial to lagoonal environment. Below the lower $\delta^{13}C_{org}$ excursion, palynomorphs restricted to the Paleocene are present (*Dandotiaspora plicata, Lygodiumsporites lakiensis, Matanomadhiasulcites maximus, Proxapertites cursus, Tricolpites reticulatus, Racemonocolpites maximus). A diverse assemblage of palynomorphs that span the* Paleocene-Eocene are present through the excursion interval (*Ctenolophonidites costatus, Intratricolpites brevis, Iugopollis tetraporites, Lakiapollis ovatus, Longapertites vaneendenburgii, Polycolpites* spp., *Polygalacidites clarus, Pseudonothifagidites kutchensis,. Acanthotricolpites bulbispinosus, Angulocolporites microreticulatus, Cryptopolyporites cryptus Incrotonipollis nyvelli, Neocouperipollis rarispinosus, Retitribrevicolporites matanomadhensis, Retistepanocolpites williamsii Proxapertites cursus, Palmaepollenites kutchensis, P. nadhamunii, P. ovatus).*

This palynoassemblage indicates an Early Eocene age for the lower excursion of the Tadkeshwar section (Plate 1). However, due to presence of some distinct Paleocene taxa (*Matanomadhiasulcites maximus, Retitribrevicolporites matanomadhensis, Neocouperipollis* spp., and *Tricolpites reticulatus* (Dogra and Singh, 1988)) and the palynomorphs *Racemonocolpites maximus* and *Incrotonipollis neyvelii* (species recently recorded from the Paleocene part of intertrappean sediments) the age likely spans the Late Paleocene to Early Eocene interval. However, the observed palynoassemblage is distinctly different from the Barmer basin of Rajasthan (Tripathi et al, 2009; Tripathi and Srivastava, 2010) and the Middle to Late Paleocene deposits of Pakistan (Federikson, 1994). The Tadkeshwar assemblage is also different from that of the nearby Vastan lignite section, which is dated Latest Paleocene-Early Eocene (Garg et al., 2008; Tripathi and Srivastava, 2012). This difference could be due to local variations in the depositional environment. This is suggested by the diverse pteridophytic spores and dominance of the pollen *Acanthotricolpites spp., Matanomadhiasulcites spp, Spinizonocolpites* spp. and *Lakiapollis ovatus* (Tripathi and Srivastava 2012) at Vastan, but near absence of these taxa at Tadkeshwar, except for *Lakiapollis.* Sahni et al. (2006) suggested an estuarine to lagoonal environment for the lower part of the Vastan mine section based on the presence of shell beds, pyritized wood fragments and microvertebrate remains.

Benthic Foraminifera at Vastan and Tadkeshwar: The age diagnostic benthic foraminifer *Nummulites burdigalensis burdigalens* present in the upper half of the Vastan mine section indicates an Early Cuisian (ca. 53 Ma) age of the lignite-bearing sequence (Punekar and Saraswati, 2010). Garg et al. (2008) proposed a Thanetian (Late Palaeocene) to Middle Ypresian (Early Eocene) age for the Vastan lignite deposits based on palynomorphs.

The upper $\delta^{13}C_{org}$ shift is observed in Tadkeshware and Vastan mines linked to marine deposits that yield a distinctive dwarfed foraminiferal assemblage. In the absence of planktic foraminiferal index species, it is difficult to evaluate the age of this dwarfed benthic fauna. Similarly, benthic foraminifera at Tadkeshwar consist of an almost monospecific dwarfed assemblage of *Gyroidinoides angustiumbilicata* associated with the upper $\delta^{13}C_{org}$ shift and climate warming. This species is known from early Eocene brackish to normal marine environments with muddy substrates (Murray et al., 1989, p. 520). In contrast, the nearby Vastan section contains more diverse benthic assemblages, which are similar to marine and marginal marine sediments from the Paleogene of southern England reported by Murray (1989). However, the Vastan fauna is of much lower diversity, consists of very small dwarfed specimens and lacks agglutinated species. Nevertheless, all but one of the 16 species from the Vastan lignite are also present in southern England. Six of these species are reported as restricted to the early Eocene or Eocene of southern England (*Discorbis propinqua, Gyroidinoides angustiumbilicatus, Pararotalia curryi, P. spinigera, Rosalina araucana and Sagrina selseyensis).* The remaining 10 species range from the Paleocene to the Eocene. This suggests an early Eocene age for the Vastan lignite benthic assemblages of the upper $\delta^{13}C_{org}$ excursion.

Benthic foraminifera from the early Eocene interval in the Vastan Lignite mine (Fig. 7) are common to abundant, of low diversity (<18 species) and dwarfed reflecting high stress environmental conditions. All species are hyaline and no agglutinated forms are observed. There are two dominant assemblages. Assemblage one is dominated by brackish to normal marine inner shelf species (*Nonion applinae, Pararotalia curryi, Valvulineria scorbiculata, Astigerina aberystwythi, Goiyroidinoides angustiumbilicata*) and brackish lagoonal species (*Ammonia*

beccarii, Rosalina araucana, Fig. 7, Plate 2). In this assemblage, *A. beccarii* is common and briefly abundant in the lower part of the section, *G. angustiumbilicata* is relatively common throughout the section and *Nonion applinae* appears in great abundance only in two intervals of strong carbonate dissolution. Their high abundance appears to be largely due to dissolution resistance as evident by their strong thick-shelled tests and near absence of species with thinner shells more prone to dissolution.

The second assemblage is dominated by the low oxygen tolerant marginal marine species *Bulimina thanetensis* and *Praebulimina cushmani* (Fig. 7, Plate 2, #8,14). Specimen size of P. *cushmani* is extremely small and generally less than 80 µm, whereas *Bulimina thanetensis* varies from very small to medium size. These two species generally dominate (50-90%) assemblages and indicate low oxygen bottom conditions. A minor marginal marine component consists of *Cibicidoides lobatulus, C. succedens* and *Hanzawaia producta* (Plate 2).

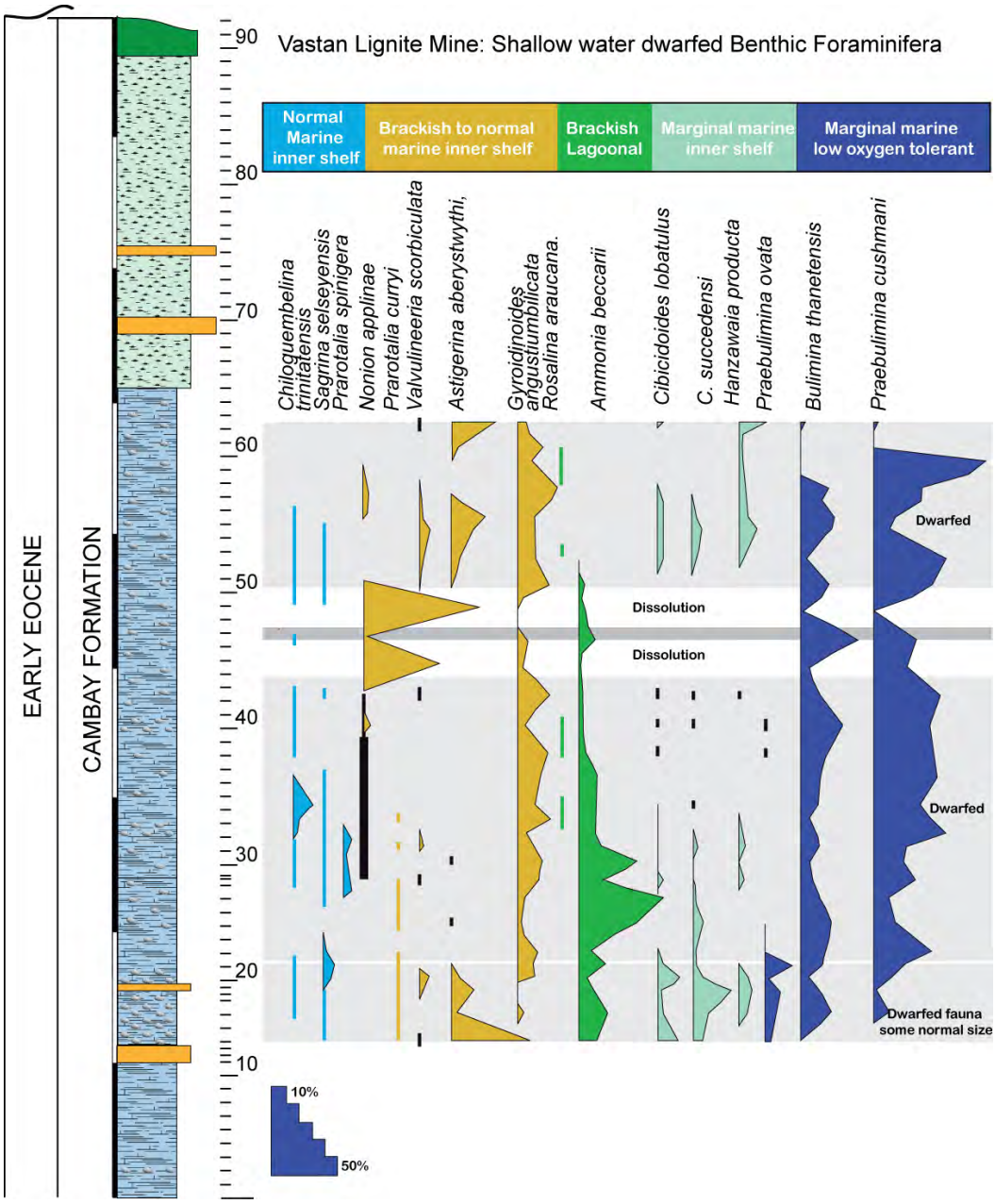

Figure 7: *Relative species abundances of benthic foraminifera (>63µm) in the bivalve bearing interval of the Vastan lignite mine.*

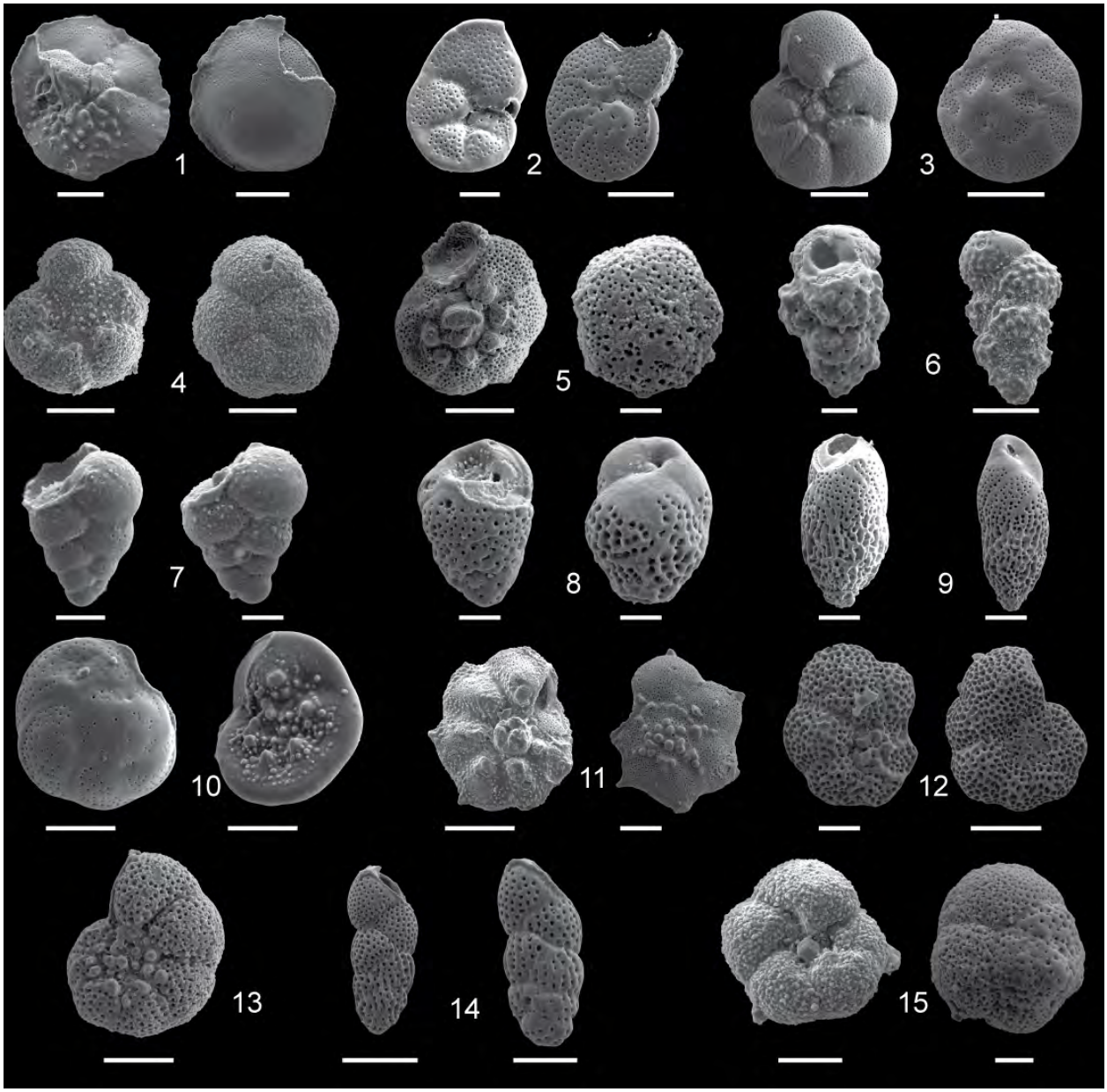

Plate 2: Early Eocene benthic foraminifera from Vastan mine bivalve bearing interval, scale bar 50µm. *1. Astigerina aberystwythi, 2. Cibicidoides lobatulus, 3. Prarotalia curryi, 4. Ammonia beccarii, 5. Gyroidinoides angustiumbilicata, 6. Sagrina selseyensis, 7. Chiloguembelina trinitatensis, 8. Praebulimina cushmani, 9. Praebulimina ovata, 10. Hanzawaia producta, 11. Prarotalia spinigera, 12. Valvulineria scorbiculata, 13. Nonion applinae, 14. Bulimina thanetensis, 15. Rosalina araucana.*

These assemblages are restricted to the base and top of the interval analyzed where low oxygen tolerant species are less abundant. Two species, which are considered to thrive in normal inner shelf marine environments, are rare to few (*Pararotalia spinigera, Sagrina selseyensis,* Plate 2, #6, 11). Their low abundance and sporadic occurrence suggests that normal inner shelf conditions did not exist or persist in this marginal to lagoonal marine environment. Just one biserial planktonic foraminifer is present (*Chiloguembelina trinitatensis* Plate 2, #7). This species is low oxygen tolerant and its extremely small size (45-65 μm) and sporadic occurrence reflects stress conditions. In general, just a few specimens are present, but in one sample (34) *C. trinitatensis* reached 18%. This may reflect a temporary influx of more normal marine waters (e.g., sea level rise or storm).

Murray (2006, p. 318) noted, "in the lagoons and estuaries of Brazil, the highest incidence of deformity occurs in waters that are either hypersaline or undergo natural seasonal acidification followed by regeneration." We can observe the same in the Vastan and Tadkeshwar sections of Gujarat. The assemblages the at Vastan indicate a brackish to lagoonal environment with variable salinity ranging from fresh water to hypersaline, low oxygen, nutrient-rich and acidic leading to test dissolution. In contrast, at Tadkeshwar higher stress conditions are indicated by the nearly monospecific assemblage of *G. angustiumbilicata* suggesting hypersaline and possibly acidic waters (e.g., dissolution effects) and muddy substrate. This may explain the low diversity of palynomorph assemblage at Tadkeshwar.

6. DISCUSSION

During the Paleocene-Eocene (65-36 Ma), lignite deposits in NW India (Rajasthan and Gujarat) formed on alluvial delta plains and swamps with luxuriant vegetation under humid tropical climate conditions (Chakraborty et al., 2011; Raju and Mathur, 2013). Today, these lignite deposits are distributed in a series of basins from Jaisalmer (Rajasthan) to the Cambay basin in the south and Kutch basin (Gujarat) to the southeast (Fig. 1). This distribution reflects the paleotopography of the rift basins that formed during the rotation and subduction of the Indian plate during the early stage of collision with Asia (Gombos et al., 1995; Biswas, 2005). The lignite deposits mined throughout this area consist of two and occasionally three thick intervals generally separated by shallow marine sediments with mollusk shells and benthic foraminifera.

The objective of studying five lignite sequences in Rajasthan and Gujarat was to evaluate the climatic and environmental conditions of the region particularly with respect to the early Eocene climate warm events and more specifically, identify the Paleocene-Eocene thermal maximum (PETM) and early Eocene optimum climate (EECO). Results from previous studies provided clues to the EECO, but not PETM (Clementz et al 2011) This study improves on these results, identifying the PETM as well as EECO (ETM2) based on high-resolution TOC and organic carbon isotope analyses coupled with palynologic and benthic foraminiferal studies.

6.1. Age and Stratigraphy of Lignite sequences

The most difficult aspect of working with terrestrial to shallow marine environments is gaining reliable age control. In open marine environments, relative age control is based on biostratigraphy (calcareous nannofossils, planktic foraminifera, palynomorphs) and the stable isotope record; the latter identifies climate extremes whereas biostratigraphy provides relative age dates for the climatic events. These methods have been applied to deep-sea sequences

worldwide providing reliable age control for the series of climate warming events of the late Paleocene to early Eocene (e.g., Zachos et al., 2001; Cramer et al., 2009), Unfortunately, obtaining high-resolution age control for terrestrial and shallow water environments is difficult because age diagnostic microfossils tend to be rare or absent due to the high-stress conditions in shallow water environments. In such environments, the best age control can be obtained from correlation and integration of bio- and isotope stratigraphies with the marine record.

6.1.1. Biostratigraphy

Palynoflora: Palynoflora assemblages were analyzed for the lower $\delta^{13}C_{org}$ excursion at Tadkeshwar and Giral sections. At the Giral section, a late Paleocene to early Eocene age was determined for the $\delta^{13}C_{org}$ excursion based on palynoflora taxa with known upper age limits of early Eocene. Similar assemblages were recorded from lignite deposits of the nearby Akli and Kapurdi sections of Rajasthan (Tripathi et al, 2009, Tripathi, 1997). At the Tadkeshwar mine section a diverse assemblage of palynomorphs spans the Paleocene-Eocene transition. Similarly, at the nearby Vastan mine section a latest Paleocene-early Eocene assemblage was identified (Garg et al., 2008; Tripathi and Srivastava, 2012). These data indicate that the lower $\delta^{13}C_{org}$ excursion at the Giral, Tadkeshwar and Vastan mine sections span the PETM event.

Benthic foraminifera: In the upper part of the Vastan section, the presence of the larger benthic foraminifer *Nummulites burdigalensis burdigalens* indicates an Early Eocene age (Cuisian, ~53 Ma; shallow benthic zone SZ10; Punekar and Saraswati, 2010). A similar assemblage was recorded in the shallow marine Naredi section in Kutch correlative with the early Eocene climate warming ETM2 (Keller et al., 2013). Thus, larger benthic foraminifera indicate an early Eocene climatic optimum (EECO) age for the upper $\delta^{13}C_{org}$ excursion, and probably the ETM2 event.

Small benthic foraminifera were analyzed for the upper $\delta^{13}C_{org}$ excursion at Tadkeshwar and Vastan sections. At Tadkeshwar this interval is dominated by an almost monospecific, dwarfed benthic assemblage of *Gyroidinoides angustiumbilicata,* a species known from early Eocene brackish to normal marine environments with muddy substrates (Murray et al., 1989, p. 520). In contrast, the nearby Vastan section has relatively diverse, although dwarfed, benthic assemblages indicative of early Eocene age in agreement with the age indicated by larger foraminifera.

Paleoenvironment: Giral, Vastan and Tadkeshwar sections indicate deposition in a terrestrial to lagoonal environment during the lower $\delta^{13}C_{org}$ (PETM) excursion as indicated by typical mangrove pollen of *Nypa* and other Arecaceae (palms). An estuarine to lagoonal environment is also indicated for this interval at Vastan based on shell beds, pyritized wood fragments and microvertebrate remains Sahni et al. (2006). Dwarfed benthic foraminiferal assemblages at Vastan indicate high-stress conditions in a brackish to lagoonal environment with variable salinity ranging from fresh water to hypersaline, nutrient-rich, low oxygen and acidic (evident in test dissolution). Environmental conditions varied locally as indicated by low diversity palynoflora and the nearly monospecific assemblage of *G. angustiumbilicata* at Tadkeshwar, which suggests hypersaline and possibly acidic waters (dissolution effects) and muddy substrate (Murray, 1989).

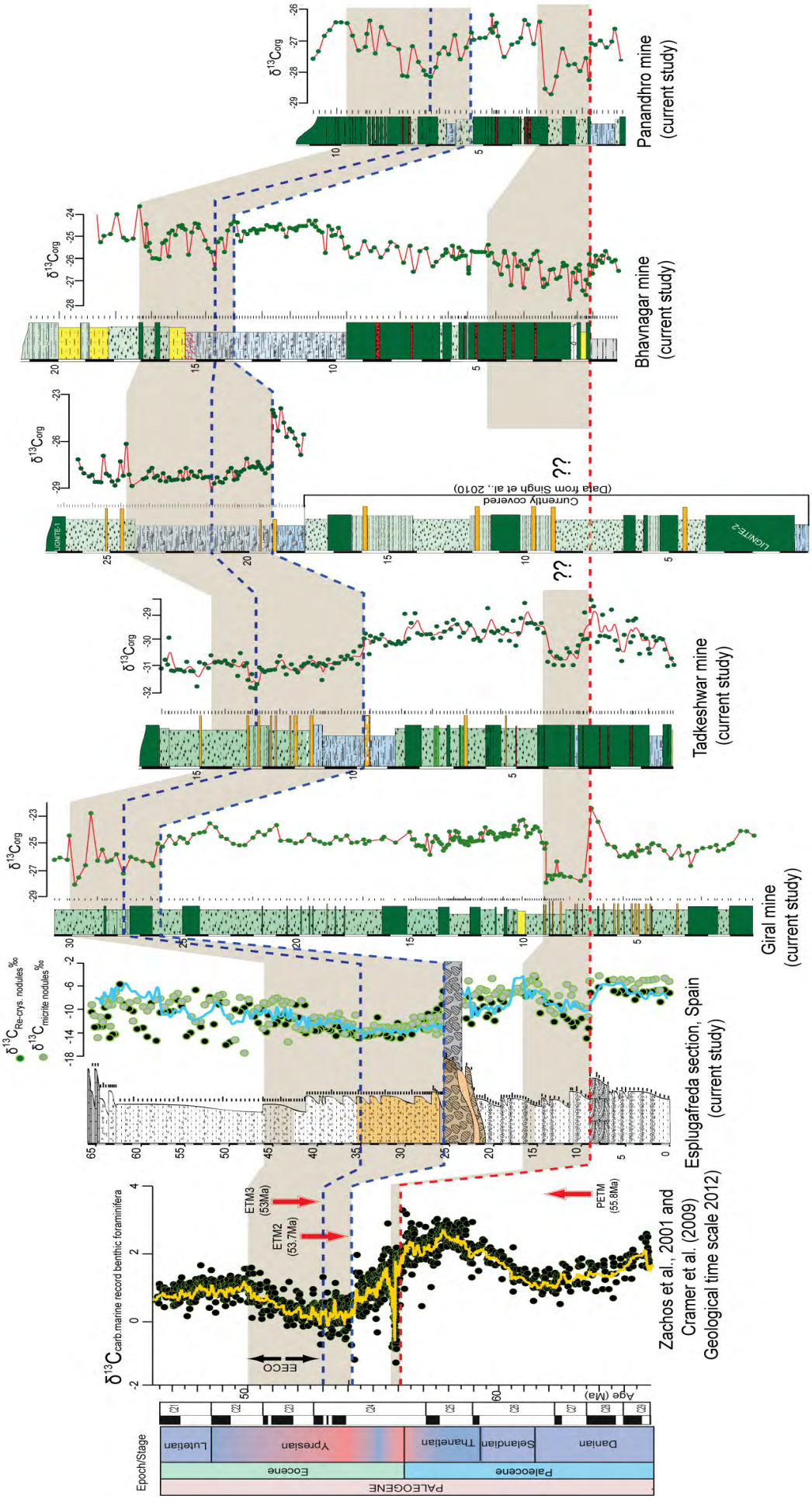

Figure 8: *Chemostratigraphic correlation of the fife studied mines with the existing marine and continental carbon isotopic record (Zachos et al 2001; Cramer at al., 2009;Khozyem et al., in prep)*

6.1.2. Isotope Stratigraphy

The $\delta^{13}C_{org}$ profiles of the studied lignit mines are similar. Two $\delta^{13}C_{org}$ excursions are detected, the lower $\delta^{13}C_{org}$ excursion is linked to PETM events as determined by pollens at Giral mine, this age can be generalize for all the lower $\delta^{13}C_{org}$ in the studied mines. The upper $\delta^{13}C_{org}$ excursion is determined to the ETM2 based on the benthic foraminifera and are recorded in all the studied sections.

The chemo-stratigraphic correlation and biostratigraphic age control of the studied section based on the organic carbon isotopes and integrate the existing marine isotopic record in this correlation (Zachos et al., 2001, and Cramer et al., 2009), and also other terrestrial records such as calcareous nodules of Esplugafreda (Khozyem et al., Ref herein, chapter 6), is confirming the age obtained by pollen and benthic foraminifera. The correlation indicates that the response of both marine and terrestrial isotopic record are identical.

7. SUMMARY AND CONCLUSION

In conclusion, the Lignite deposits in western India are deposited under hot humid condition prevailed due to the Early Eocene Hyperthermal Events. The lower lignite is linked to the PETM warming event in which the lignite accumulation is represent the response of the terrestrial environment to the increase of atmospheric greenhouse conditions, increase of precipitation and less evaporation all these conditions are favourable of wetland establishments as a natural response of the PETM warming. The ETM2 is linked to the first early Eocene transgression depositing the shallow marine sediments, the upper lignite interval observed in all the studied lignite sections are representing the response of the increase of greenhouse gases due to the ETM2 event. Moreoever, the burial of these lignite may have contributed to the CO2 drawdown, which my explain the PETM termination

Therefore, we can summarize that:

- Using of organic carbon isotope profile obtained from single source organic matter (Terrestrial), supported by age control (palynofossils and benthic foraminifera) helps to identify the age of the events responsible of the lignite depositions.
- The observed two $\delta^{13}C_{org}$ excursions are linked to PETM and ETM2 Warming events.
- The high resolution $\delta^{13}C_{org}$ record in combination with biostratigraphic age constrain can provide information helps to solve the old scientific problem of mammals origination and migrations (see chapter 5B)

REFERENCES

Abramovich, S., Keller, G., 2003, Planktonic foraminiferal response to the latest Maastrichtian abrupt warm event: a case study from South Atlantic DSDP Site 525A. Marine Micropaleontology, v. 48, pp. 225-249.

Alegret, L., Ortiz, S., and Molina, E., 2009, Extinction and recovery of benthic foraminifera across the Paleocene–Eocene Thermal Maximum at the Alamedilla section (Southern Spain). Palaeogeography, Palaeoclimatology, Palaeoecology, v.279, pp.186–200.

Alimohammadian, H.; Sahni, N. and Sharma, M.L. 2006. Multi-image analysis of a 52 million year old insect body fossil. Proceedings of National Conference Electron Microscopy and Allied Fields, CSIR-RRL, Thiruvanthapuram, NC-06: 160-161.

Aubry, M-P., Ouda, K., Dupuis, C., Berggren, W.A., Van Couvering, J.A., 2007. The Global Standared Stratotype-section and Point (GSSP) for the base of the Eocene Series in the Dababiya section

(Egypt), Episodes, v.30(4), 271-286.

Bains, S., Norris, R. D., Corfield, R. M., and Faul, K. L., 2000, Termination of global warmth at the Palaeocene/Eocene boundary through productivity feedback. Nature 407, 171_174 (2000).

Bajpai, S. Kapur, V. V. Thewissen, J.G.M.; Das, D.P. and Tiwari, B.N, 2006. New Early Eocene cambay there (Perissodactyla, Mammalia) from the Vastan Lignite Mine (Gujarat, India) and an evaluation of cambay there relationships. - Journal of the Palaeontological Society India, 51 (1): 101-110.

Bajpai, S.; Kapur, V. V.; Thewissen, J. G. M.; Tiwari, B. N. and Das, D. P., 2005b. First fossil marsupials from India: Early Eocene Indodelphis n. gen. and Jaegeria n. gen. from Vastan lignite mine, District Surat, Gujarat. -Journal of the Palaeontological Society of India, 50 (1): 147-151.

Bajpai, S.; Kapur, V.V.; Thewissen, J.G.M.; Das, D.P.; Tiwari, B.N.; Sharma, R. and Saravanan, N., 2005c. Early Eocene Primates from Vastan Lignite Mine, Gujarat, India. -Journal of the Palaeontological Society India, 50 (2): 43-54.

Bajpai, So; Kapur, V. V.; Das, Do P.; Tiwari, B. N.; Saravanan, N. and Sharma, R., 2005a. Early Eocene land mammals from Vastan Lignite Mine, District Surat (Gujarat) , western India. –Journal of the Palaeontological Society of India, 50 (1): 101-113.

Beard, K. C. 1998. East of Eden: Asia as an important center of taxonomic origination in mammalian evolution. Pp. 5-39 in Dawn of the Age of Mammals in Asia (K. C. Beard and M. R. Dawson, eds.). Bulletin of Carnegie Museum of Natural History, No. 34.

Bhandari, A., 1999, Phanerozoic stratigraphy of western Rajasthan India: a review. In Geology of Rajasthan: Status and Perspective (ed. Kataria, P.), MLS University, Udaipur, pp. 126–174.

Biswas, S_ K. & Raju, D. N. S. 1973, The rock-stratigraphic classification of the Tertiary sediments of Kutch. Bull. Oil Natural Cas Commission 10 : 37-45.

Biswas, S. K., 2005, A review of structure and tectonics of Kutch basin, western India, with special reference to earthquakes Current Science, v. 88, no. 10, pp. 1592-1600.

Biswas, S.K. (1980) Structure of Kutch-Kathiawar region, western India. Proc. 3rd Indian Geological Congress, Pune, pp.255- 272.

Biswas, S.K. (1987) Regional tectonic framework, structure and evolution of the western marginal basins of India. Tectonophysics, v.135, pp. 302-327.

Biswas, S.K. And Deshpande, S.V. (1983) Geology and hydrocarbon prospect of Kutch, Saurashtra and Narmada basins. Petroleum Asia Jour., v.6, pp.111-126.

Chakraborty. A., , Tiwari, P.K., and Singh, A.K., 2011, Coalbed Methane Exploration in A Tertiary Lignite Basin, North Gujarat, India, The 2nd South Asain Geoscience Conference and Exhibition,GEOIndia2011, 12-14th Jan,2011,Gearter Noida,New Delhi,India

Cramer, B.S., Toggweiler, J.R., Wright, J.D., Katz, M.E., Miller, K.G., 2009. Ocean overturning since the Late Cretaceous: Inferences from a new benthic foraminiferal isotope compilation. Paleoceanography 24, PA4216. doi:10.1029/2008PA001683.

Dickens, G. R., Castillo, M. M., and Walker, J. C. G., 1997, A blast of gas in the latest Paleocene; simulating first-order effects of massive dissociation of oceanic methane hydrate. Geology 25, 259-262

Dilcher, D. L., 1965. Epiphyllous fungi from Eocene deposits in Western Tennessee, USA. Paleontographica Abt B116, 1-156.

Espitalié, J., Deroo, G., and Marquis, F., 1985, La pyrolyse Rock-Eval et ses applications.Revue de l`Institute francais de Pérole, v. 40, pp. 563-579.

Frederiksen, N. O., 1985. A review of Early Tertiary palynomorph ecology. American Association of Stratigraphic Palynology, 15, 1-91.

Frederiksen, N.O., 1994. Middle and Late Paleocene Angiosperm pollen from Pakistan. Palynology, 18, 91-137.

Garg, R., Ateequzzaman, K., Prasad, V., Tripathi, S.K.M., Singh, I.B., Jauhri, A.K., and Bajpai, S., 2008. Age-diagnostic dinoflagellate cysts from the lignite- bearing sediments of the Vastan Lignite Mine,

Surat District, Gujarat, western India: Journal of Palaeontological Society of India, 53, 99–105.

Godinot, M., 1982. Aspects nouveaux des échanges entre les faunes mammaliennes d'Europe et d'Amérique du Nord à la base de l'Eocène. Geobios, *Mémoire Spécial*, 6,403-412.

Gombos, A.M., Powell, W. G. , Norton, I. O., 1995, The tectonic evolution of western India and its impact on hydrocarbon occurrences: an overview. Sedimentary Geology, v. 96, pp. 119-129

Kappeler, P.M., 2000. Lemur origins: Rafting by groups of hibernators? *Folia Primatologica*, 71, 422-425.

Keller G., Li, L. And Macleod, N., l995, The Cretaceous/Tertiary boundary stratotype section at El Kef, Tunisia: How catastrophic was the mass extinction? Paleogeography, Paleoclimatology, Paleoecology, v. 119, pp. 221-254.

Keller, G., Khozyem, H., and Adatte, A., 2013, Biostratigraphy and Foramiferal Paleoecology of the Eocene Naredi Formation, Kutch, Gujarat, India. In Malarkodi, N., Keller, G., Reddy, A.N., and Jaiprakash, B.C. (eds.) Ecology, Biodiversity and Global Bioevents, Geological Society of India, Special Publication, Springer Verlag, Vol.1, p. 58-92

Keller, G., Stinnesbeck, W., Adatte, T., Holland, B., Stueben, D., Harting, M., De Leon, C., De La Cruz, J., 2003. Spherule deposits in Cretaceous-Tertiary boundary sediments in Belize and Guatemala, Journal of Geological Society of London, v. 160, pp. 1-13.

Kelly, C.D., 2002, Response of Antarctic (ODP Site 690) planktonic foraminifera to the Paleocene-Eocene thermal maximum: Faunal evidence for ocean/climate change. Paleoceanography, v. 17(4), No. 1071, doi:10.1029/2002PA000761, 2002.

Kelly, D.C., Bralower, T.J., Zachos, J.C., Premoli-Silva, I., and Thomas, E., 1996, Rapid diversification of planktonic foraminifera in the tropical Pacific (ODP Site 865) during the late Paleocene Thermal Maximum. Geology, v. 24, p. 423–426.

Kennett, J.P., and Stott, L.D., 1991, Abrupt deep-sea warming, palaeoceanographic changes and benthic extinctions at the end of the Palaeocene. Nature, v. 353, pp. 225–229.

Krause, D. W., and Maas, M. C., 1990. The biogeographic origins of late Paleocene-early Eocene mammalian immigrants to the Western Interior of North America. *Geological Society of America* Special Paper 243, 71–105.

Lopéz-Martínez, N., and Peláez-Campomanes, P., 1999, New mammals from south-central Pyrenees (Tremp Formation, Spain) and their bearing on late Paleocene marine-continental correlations: Bulletin de la Société Géologique de France, v. 170, p. 681–696.

Lu, G., Adatte, T., Keller, G., and Ortiz, N., 1998, Abrupt climatic, oceanographic and ecologic changes near the Paleocene-Eocene transition in the deep Tethys basin: The Alamedilla section, southern Spain. Ecologica Geologica Helvatica, v. 91, pp. 293-306.

Luciani, V., Giusberti, L., Agnini, C., Backman, J., Fornaciari, E., and Rio, D., 2007, Paleocene–Eocene Thermal Maximum as recorded by Tethyan planktonic foraminifera in the Forada section (northern Italy). Marine Micropaleontology, v.64, pp.189-214.

McCann, T., 2010, Chenier plain sedimentation in the Palaeogene of western India. Zeitschrift der Deutschen Gesellschaft für Geowissenschaften, v.161, no.3, pp.335-351.

McInerney, F. A., and Wing, S. L., 2011, The Paleocene–Eocene Thermal Maximum: A perturbation of carbon cycle, climate, and biosphere with implications for the future. Annual Review in Earth Planetary Science, v.39, p.489–516.

Merh, S.S., 1995, Geology of Gujarat. Geological Society India, Bangalore, 222p.

Muller, J., 1964, A palynological contribution to the history iof mangrove vegetation in Borneo. I Cranwell L.M. (eds) Ancient pacific flora, the pollen story, Honolulu. Univ. of Hawaii press, v. 14, pp. 1-37.

Murray, J.W., Curry, J.R. and Haynes, C., 1989, Palaeogene. *In:* Jenkins, D.G. and Murray, J.W. (Eds.) Stratigraphical Atlas of fossil Foraminifera, British Micropalaeontological Society, John Wiley & Sons, pp. 490-536.

Nadhamuni, B. S. 1976. Panandhro lignite deposit Assessment, Development and Utilization. National sem. Open Cast mining, Neyveli, India.

Nolf, D.; Aana, A.S. and Singh, H., 2006. Fish otoliths from the Ypresian (early Eocene) of Vastan, Gujarat, India. -Bulletin de I'lnstitut Royal des Sciences Naturelles de Belgique, Sciences de la Terre, Belgium, 76: 105-118.

Punekar, J., Saraswati, P.K., 2010, Age of the Vastan Lignite in context of some oldest Cenozoic fossil mammals from India. Journal of the Geological Society of India, v. 76, no. 1, pp. 63-68.

Raju, S.V., and Mathur, N. 2013. Rajasthan lignite as a source of unconventional oil. Current Science, v. 104, no. 6, pp. 752-757.

Rana, A.S. and Singh, H., 2005. First record of an exceptionally diverse and well preserved amber-embedded biota from Lower Eocene (-52 Ma) lignites, Vastan, Gujarat.- Current Science, 89 (8): 1328-1330.

Rana, R. S., Kumar, K., Singh, H., and Rose, K. D. 2005. Lower vertebrates from the Late Palaeocene–Earliest Eocene Akli Formation, Giral Lignite Mine, Barmer District, western India. Current Science, Vol. 89, No. 9, 10 November 2005

Rana, R. S.; Kumar, K.; Singh, H. and Rose, K. D., 2005a. Lower vertebrates from the late Palaeocene-earliest Eocene Akli Formation, Giral Lignite Mine, Barmer District, western India. - Current Science, 89: 1606-1613.

Rana, R.S.; Singh, H.; Sahni, A.; Rose, K. D. and Saraswati, P .K., 2005b. Early Eocene chiropterans from a new mammalian assemblage (Vastan Lignite Mine, Gujarat, western peninsular margin): oldest known bats from Asia. -Journal of the Palaeontological Society of India, 50 (1): 93-100.

Rose, K .D., DeLeon, V. B., Missiaen, P., Rana, R. S., Sahni, A., Singh. L., and Smith, T., 2008. Early Eocene lagomorph (Mammalia) from western India and the early diversifi- cation of Lagomorpha; *Proceeding of Royal Society of London*, B 275, 1203–1208.

Rose, K.D.; Smith, T.; Rana, R. S.; Sahni, A.;Singh, H.; Missiaen, P.; and Folie, A., 2006. Early Eocene (Ypresian) continental vertebrate assemblage from India, with description of a new anthracobunid (Mammalia, Tethytheria). –Journal of Vel1ebrate Paleontology, 26 (1): 219-225.

Saraswati, P_ K. & Banerjee, R_ K_ 1984- Lithostratigraphic classification of the Tertiary sequence of northwestern Kutch_ In : Badve, R. M_, Borkar, V. D_, Ghare, M. A_ & Rajshekhar, C 5_ (eds)- Proc_ X Indian Colloq. Micropalaeonl Stratigr_, 1982, Pune : 369- 376. Maharashtra Association for the Cultivation of Science, Pune.

Schmitz, B., and Pujalte, V. 2007 Abrupt increase in seasonal extreme precipitation at the Paleocene-Eocene boundary. Geology 35; no. 3; p. 215–218; doi: 10.1130/G23261A.1; 3

Schmitz, B., and Pujalte, V., 2003, Sea-level, humidity, and land-erosion records across the initial Eocene thermal maximum from a continental-marine transect in northern Spain: Geology, v. 31, p. 689–692, doi: 10.1130/ G19527.1.

Selkirk, D. R., 1975. Tertiary fossil fungi from Kiandra. New South Wales. Proceedings Linnaeus. Society NW 100(1), 70-94.

Sharma, K. K., 1999, K–T magmatism and basin tectonism in western Rajasthan, India. Results from extensional tectonics and not from reunion plume activity.

Singh, P. and Singh, M. P. (1991) Nannofloral biostratigraphy of the late middle Eocene strata of Kachchh Region, Gujarat State, India. Geoscience Journal, v. 12, pp. 17–51.

Singh, P. K., Singh, M. P., and Singh, A. K. 2010. Petro-chemical characterization and evolution of Vastan Lignite, Gujarat, India. International Journal of Coal Geology, 82: 1–16.

Sloan, R.E., 1970. Cretaceous and Paleocene terrestrial communities of western North America, in Yochelson, E.L., ed., Proceedings of the North Ameri- can Paleontological Convention, Two Volumes: Lawrence, Kansas, Allen Press, 427–453.

Smith, T., 2012. Contributions of Asia to the evolution and paleobiogeography of the earliest modern mammals. *Bulletin of Séanc Academic Research of Science*, 57/58.

Smith, T., Rose, K.D., and Gingerich, P.D., 2006. Rapid Asia-Europe-North America geographic dispersal of earliest Eocene primate Teilhardina during the Paleocene-Eocene Thermal Maximum. *Proceeding of the American Academy of Science*, 103, 11223–11227

Thakur, O. P., Singh, A., and Singh, B. D., 2010, Petrographic Characterization of Khadsaliya Lignites, Bhavnagar District, Gujarat. Journal Geological Society Of India, v.76, pp.40-46

Tripathi, S.K. M. (1997) Palynological changes across subsurface Paleocene-Eocene sediments at Barmer, Rajasthan, India. Paleobotanist 46 (1-2), 168-171.

Tripathi, S.K. M., Kumar, M., and Srivastava, D., 2009, Palynology of Lower Paleogene (Thanetian-Ypresian) coastal deposits from the Barmer Basin (Akli Formation, Western Rajasthan, India): Paleoenvironment and paleoclimatic implications. Geologica Acta, 147 -160.

Westerhold, T., Röhl, U., McCarren, H., and Zachos, J., 2009, Latest on the absolute age of the Paleocene–Eocene Thermal Maximum (PETM): New insights from exact stratigraphic position of key ash layers + 19 and – 17. Earth and Planetary Science Letters, v. 287, no. 3–4, pp. 412–419

Zachos, J., Pagani, M., Sloan, L., Thomas, E., and Billups, K., 2001, Trends, rhythms, and aberrations in global climate 65 Ma to present. Science, v. 292, pp. 686–693.

Zachos, J., Wara, M.W., Bohaty, S., Delaney, M.L., Petrizzo, M.R., Brill, A., Bralower, T.J., Premoli Silva, I., 2003. A transient rise in tropical sea surface temperature during the Paleocene-Eocene thermal Maximum. Science 302, 1551-1554.

Zachos, J.C., Röhl, U., Schellenberg, S.A., Sluijs, A., Hodell, D.A., Kelly, D.C., Thomas, E., Nicolo, M., Raffi, I., Lourens, L.J., McCarren, H., and Kroon, D., 2005, Rapid acidification of the ocean during the Paleocene–Eocene Thermal Maximum. Science, v. 308, pp.1161–1611.

Zeebe, R. E., Zachos, J. C., and Dickens, G. R., 2009, Carbon dioxide forcing alone insufficient to explain Palaeocene_Eocene Thermal Maximum warming. Nature Geosci. 2, 576- 580.

B. EARLY EOCENE CARBON ISOTOPE DATA FROM INDIA PROVIDE NEW INSIGHT INTO THE TIMING OF MAMMAL DISPERSAL[1]

Abstract. Carbon isotope analyses and biostratigraphy of three lignite mines located in NW India reveal the presence of both PETM and ETM2 negative organic carbon isotope excursions. In the same sections mammals appear well after the PETM event. In contrast, the dispersal of mammals in Asia, Europe and North America has been recorded earlier during the PETM excursion. This suggests that the early Eocene mammal migration did not originate in India, but entered India, possibly from Asia, well after the PETM event. This delayed appearance in India suggests a barrier to migration that is likely linked to the timing of the India-Asia collision.

1. INTRODUCTION

The late Paleocene to early Eocene transition is marked by severe global warm events with the best known and most extreme warming at 56 Ma known as the Paleocene-Eocene Thermal Maximum (PETM or ETM1), which was followed by the Early Eocene climatic optimum known as ETM2 (53.7 Ma). Several smaller hyperthermal events followed, including H2 (53.6 Ma), I1 (53.3 Ma), I2 (53.2 Ma) and ETM-3 (52.8 Ma) (Zachos et al., 2008). Major negative $\delta^{13}C_{org}$ excursions mark each of these hyperthermal events. The most prominent among these is the PETM, which is accompanied by a rapid global temperature rise of 5–9°C over about 10,000 years, followed by a gradual decrease to pre-excursion $\delta^{13}C_{org}$ values over about 150,000 to 220,000 years (Westerhold et al., 2009; McInerney and Wing 2011). In the marine realm this warm event led to major species extinctions in deep benthic foraminifera (Speijer and Wagner 2002; Alegret et al., 2009) and the diversification in planktic foraminifera (Kelly et al., 1996; Lu et al., 1998; Luciani et al., 2007). In the terrestrial realm it led to the diversification of early Eocene mammals and their migration across the northern continents (Bowen et al., 2002; 2004; Wing et al., 2005). The abrupt appearance of mammals in India at the beginning of the Eocene (Krause and Maas, 1990) sparked strong interest in India as cradle of this migration (Rodriguez, 1999; Bajpai, et al., 2005; 2008; Prasad, et al., 2013).

Mammals dispersed rapidly through Asia, Europe and North America during the PETM event (Smith et al., 2006; Smith, 2012; Rose et al., 2008). However, where the dispersal originated remains controversial. Five possible hypotheses have been proposed: (**i**) Origination in Africa and dispersal through Europe and Greenland to reach North America (Godinot, 1982); (**ii**) origination in North America and dispersal across the Bering route to Greenland, Asia and Europe (Sloan, 1970); (**iii)** origination in India prior to the India/Asia collision near the Paleocene-Eocene (P/E) boundary, followed by dispersal into Asia after the collision (Krause and Maas, 1990; Bajbai et al., 2005; Kappeler, 2000); **(iv)** origination in Asia and dispersed to Europe near the onset of the PETM followed by subsequent migration to North America during the early Eocene (Smith et al., 2006); and **(v)** the East of Aden hypothesis, which suggests

[1] ***Hassan Khozyem, Thierry Adatte, Gerta Keller, Jorge E. Spangenberg, Bandana Samant, and Suresh Mathur, 2013, Early Eocene carbon isotope data from India provide new insight into the timing of mammal dispersal. In preparation***

origination in Asia and migration to north America then to Europe and lastly to India (Beard 1998)

These hypotheses can be tested with reliable chemo- and bio-stratigraphic records of mammal diversification relative to the PETM and EMT2 events. Many early Eocene mammal species first appeared on northern continents shortly after the PETM onset (~56 Ma), which roughly coincides with the onset of the India-Asia collision (Bowen et al., 2004). This led to the hypothesis that early Eocene mammals originated from the Indian subcontinent. However, the best age estimate for the India-Asia collision is between 55 to 53 Ma (Searl et al., 1997; Beck et al., 1996; Clyde et al., 2003), which suggests that this mammal event predates the India-Asia collision.

We tested the "out of India" hypothesis using high-resolution $\delta^{13}C$ records that permit to bracket the early Eocene mammal diversification and dispersal relative to the PETM and ETM2 climate events. Four localities were selected in NW India, one in Rajasthan (Giral lignite mine), two in Gujarat (Vastan and Tadkeshwar lignite mines), and one in Kutch (Naredi, Fig. 1). For these localities we present the first high-resolution $\delta^{13}C$ records that provide a global correlation tool for evaluating the timing and tempo of the mammal diversification and dispersal.

3. RESULTS

In Kutch, the Naredi section consists of a fossil-rich (small and larger Foraminifera, bivalves, ostracods) glauconitic claystones and siltstones deposited in a very shallow marine environment during the Early Eocene climatic optimum (ETM2), which overlies the Deccan Traps (Fig. 1). In Gujarat, the Vastan and Tadkeshwar mines consist of lignite deposits that form upper (lignite-1) and lower (lignite-2) horizons separated by the early Eocene marine transgression that deposited clay and silty clays enriched in bivalves, benthic foraminifera, and ostracods. In Rajasthan, the Giral mine consists of eleven lignite beds that are intercalated with grey to black clays, silty claystone and some calcareous rich layers.

3.1. Stable carbon isotopes

The Paleocene-Eocene thermal maximum (PETM) is present in the Vastan, Tadkeshwar and Giral mines, but currently covered at Vastan (Fig. 1). At the Giral mine the PETM $\delta^{13}C_{org}$ excursion shows an abrupt negative shift of 3.1‰ from values of -25.3‰ to -28.4‰. In the Tadkeshwar mine a similar $\delta^{13}C_{org}$ change from -29 to -31‰ is present in the uppermost part of the lignite-2. In the nearby Vastan mine, the same lignite-2 interval has previously been identified (Tripathi et al., 2009; Singh et al., 2010).

The Early Eocene climatic optimum ETM2 is present in all four sections and supported by $\delta^{13}C_{org}$ and biostratigraphy (Fig. 1). At the Vastan mine the exposed lower Eocene is marked by a sharp $\delta^{13}C_{org}$ excursion from -25.2‰ mean value to -28‰, with lower values persisting for 6 m. The equivalent interval is recorded at Tadkeshwar with a negative excursion from -30 to -32‰ through a thickness of 3 m. At the Giral mine the equivalent interval spans 2.5 m and marked by values from -24.6 to -26.1‰. In the marginal marine Naredi section, values range from -27.6 to -21‰ over an interval of 7.5 m. In all four sections, the top of the ETM2 interval is marked by increased $\delta^{13}C_{org}$ values followed by one or more negative excursions that may be linked to other hyperthermal events.

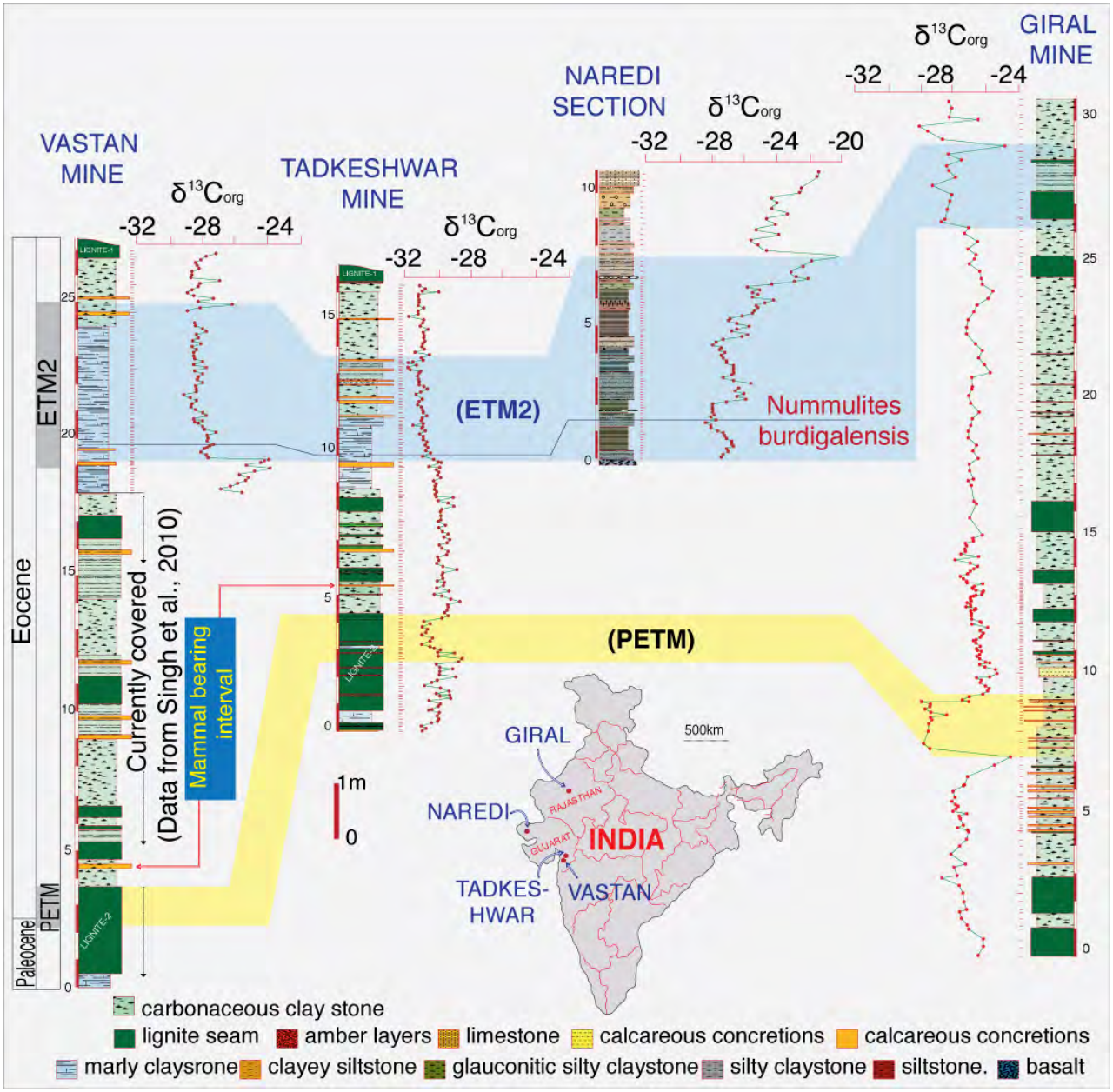

Figure 1: *Vastan and Tadkeshwar mines (Gujarat), Naredi, (Kutch) and Giral mine (Rajasthan). Lithostratigraphy, biostratigraphy and organic carbon isotopes of the PETM and ETM2. The mammal- bearing horizons are above the PETM event. The lithology of the lower part of the Vastan mine is from Singh et al. (2010).*

3.2. Biostratigraphy

Biostratigraphy of these sections is based largely on foraminifera and palynomorphs. At the Vastan mine, the currently covered lower part of the section (PETM) was reported as early Eocene age based on the common presence of larger foraminifera (Sahni et al., 2006; Singh et al., 2010). Uppermost Paleocene dinoflagellates are reported at Vastan from a few meters below the inferred position of the $\delta^{13}C_{org}$ excursion (Gharg et al., 2008) (Fig. 1).

At the Giral mine, the palynomorph assemblage and PETM $\delta^{13}C_{org}$ excursion is mainly restricted to the latest Paleocene to earliest Eocene (Singhet al., 2010) (e.g., *Cupanieidites*

flaccidiformis, Echitriporites trianguliformis, Grevilloideaepites pachyexinus, Kapurdipollenites baculatus, Matanomadhisulcites maximus, Retiverrumonosulcites barmerensis, Spinizonocolpites adamanteus), which indicates deposition no later than early Eocene. Whereas the palynoassemblage *Dandotiaspora plicata, Acanthotricolpites bulbospinosus, Angulocolporites microreticulatus, Cryptopolyporites cryptus, Incrotonipollis neyvellii, Matanomadhiasulcites maximus, Neocouperipollis rarispinosus, Proxapertites cursus, Racemonocolpites maximus, Tricolporopollis matanomadhensis* and *Retistepanocolpites williamsii* recorded from Tadkeshwar are restricted to the late Paleocene early Eocene. Similar palynomorph assemblages are recorded from lignite deposits of the Akli and Kapurdi sections of the Barmer District of Rajasthan (Tripathi, 1997; Tripathi et al., 2009).

At Vastan, Tadkeshwar and Naredi the ETM2 $\delta^{13}C_{org}$ excursion begins below the first appearance of *Nummulites burdigalensis* and abundant small benthic foraminifera (Fig. 1). A comparison with marine and marginal marine sediments from the Paleogene of southern England (Murray et al., 1989) reveals strong similarities with these benthic assemblages, although at Vastan and Tadkeshwar species richness is much lower and most species are dwarfed due to high stress conditions. All but one of the 16 species recorded are also present in southern England. Six of these species are restricted to the early Eocene or Eocene, including *Discorbis propinqua, Gyroidinoides angustiumbilicatus, Pararotalia curryi, P. spinigera, Rosalina araucana and Sagrina selseyensis*. The remaining 10 species range from the Paleocene to the Eocene. This suggests an early Eocene age for the benthic assemblage correlative with a marine transgression.

At Naredi, rare planktic foraminifera and common larger benthic foraminifera indicate the shallow benthic zone SBZ8 equivalent to planktic foraminiferal zone E4. A second fossil-rich interval at the top of the section (*Assilina* limestone) marks SBZ11, equivalent to E6 (Fig. 1) (Saraswati et al., 2012).

3.3. Mammal-bearing horizon

The vertebrate fauna reported from the Vastan mine is from the clayey layer above lignite-2 (Bajbai et al., 2005; Sahni et al., 2006; Clementz et al., 2011; Singh et al., 2010) and includes *Asiadapis cambayensis* (Rose et al., 2007), Ailuravine rodents, *Meldimys musak, M. louisi* and *E. thaleri (Rana et al 2008)*, as well as perissodactyls, artiodactyls, insectivores, proteutherians, apatotherians, marsupials and rodents (Bajpai et al., 2005 a,b), bats and premolarsdescribed as 'Primates?' (Rana et al., 2005). Vertebrate remains, though no mammals, were also recorded in several layers of the Giral mine (Rose et al., 2007).

The age of this fauna was originally attributed to the early Eocene based mainly on its location 'significantly' below the ETM2 carbon isotope excursion (Clementz et al., 2011). Today this mammal-bearing horizon is buried by backfilling and only the upper interval that contains the lignite-1 bed could be sampled (Fig. 1). However, we collected and analyzed the coeval lignite-1 through lignite-2 interval at the Tadkeshwar mine about 5 km to the northeast of the Vastan mine. This new data permits relatively precise correlation of the two sections. At the Vastan mine the ETM2 excursion is 14 m above the mammal-bearing horizon (Fig. 1). The PETM excursion occurs in the upper part of lignite-2 at the Tadkeshwar mine, which is correlative with the lignite-2 layer at Vastan. From earlier vertebrate studies we know that the mammal-bearing horizon is in the clayey interval above lignite-2, which therefore must younger

than the PETM event. This is confirmed by Gharg et al. (2008), who reported latest Paleocene dinoflagellates from a few meters below the mammal-bearing horizon at Vastan, (Fig. 1). Late Paleocene palynomorphs and benthic foraminifera were also reported from the Tadkeshwar and Giral mines (this study).

4. DISCUSSION AND CONCLUSIONS

High-resolution organic carbon isotope and biostratigraphic data from four localities in NW India reveal the $\delta^{13}C_{org}$ excursion of the PETM in the Giral and Tadkeshwar mines and this interval is also present in the lithologically and stratigraphically similar Vastan mine, although the lower part containing the PETM interval is now buried by backfill and inaccessible (Fig. 1). In all four localities analysed, the upper part of the sections is represented by the ETM2 $\delta^{13}C_{org}$ excursion with common *Nummulites burdigalensis* near the base dated as shallow benthic zone SBZ8 correlative with planktic foraminiferal zone E4 (Saraswati et al., 2012). Above the ETM2 another foraminiferal horizon, known as the *Assilina* limestone at Naredi, dates this interval as SBZ11 correlative with E6.

Relatively precise correlation was established between the Vastan and Tadkeshwar mines based on biostratigraphy, lithology (lignite beds) and carbon isotope excursions. From earlier work we know that the mammal-bearing horizon at Vastan is in the clayey interval above the lignite-2 bed, which is correlative with the lignite-2 at Tadkeshwar and the vertebrate-bearing beds above. The present work identified the PETM in the upper part of lignite-2 at Tadkeshwar, which correlates with lignite-2 at Vastan. This indicates that the mammal-bearing horizon is younger than the Paleocene-Eocene boundary, as also confirmed at Vastan by late Paleocene dinoflagellates (Gharg et al., 2008) and at Tadkeshwar by late Paleocene palynomorphs and foraminifera (this study).

Diverse early Eocene mammals first appear across the northern hemisphere during the PETM event, including primates, bats, artiodactyls, perissodactyls, and proboscideans (Bowen et al., 2001; Gingerich, 2003; 2006). Their diversification and dispersal appear to be related to this climate warming marked by the $\delta^{13}C$ excursion (CIE) that defines the Paleocene-Eocene boundary at ~56 Ma (McInerney and Wing, 2011; Gradstein et al., 2012). Asia has long been considered the likely origin of this mammal event (Beard 1998; Beard and Dawson, 1999; Beard et al., 2010), which occurred near the base of the PETM prior to the CIE-minimum. However, the $\delta^{13}C$ excursion is still poorly documented from a single locality in the Nanxiong Basin, China (Fig. 2) (Tong and Wang, 2006; Clyde et al., 2010). In Europe, the first appearance of early Eocene mammals coincides with the CIE-minimum (Smith et al., 1996) whereas in North America this event post-dates the CIE-minimum of the PETM (Koch et al., 1992; 1995) (Fig. 2). In India, we can now place the mammal-bearing horizon of the Vastan mine in a short interval (~1 m) above the PETM $\delta^{13}C_{org}$ excursion (Figs. 1, 2).

Ages for the mammal diversification on each continent can be estimated based on: (a) astronomical cyclostratigraphy (Aziz et al., 2008; Röhl et al., 2007), (b) the age estimate of 56.0 Ma for the CIE onset (P/E boundary), (c) minimum and maximum durations of 150 and 220 ka, respectively, for the PETM, (Westerhold et al., 2009) and (d) the assumption of constant sedimentation rates for the short intervals between the CIE onset and mammal event for each continent.

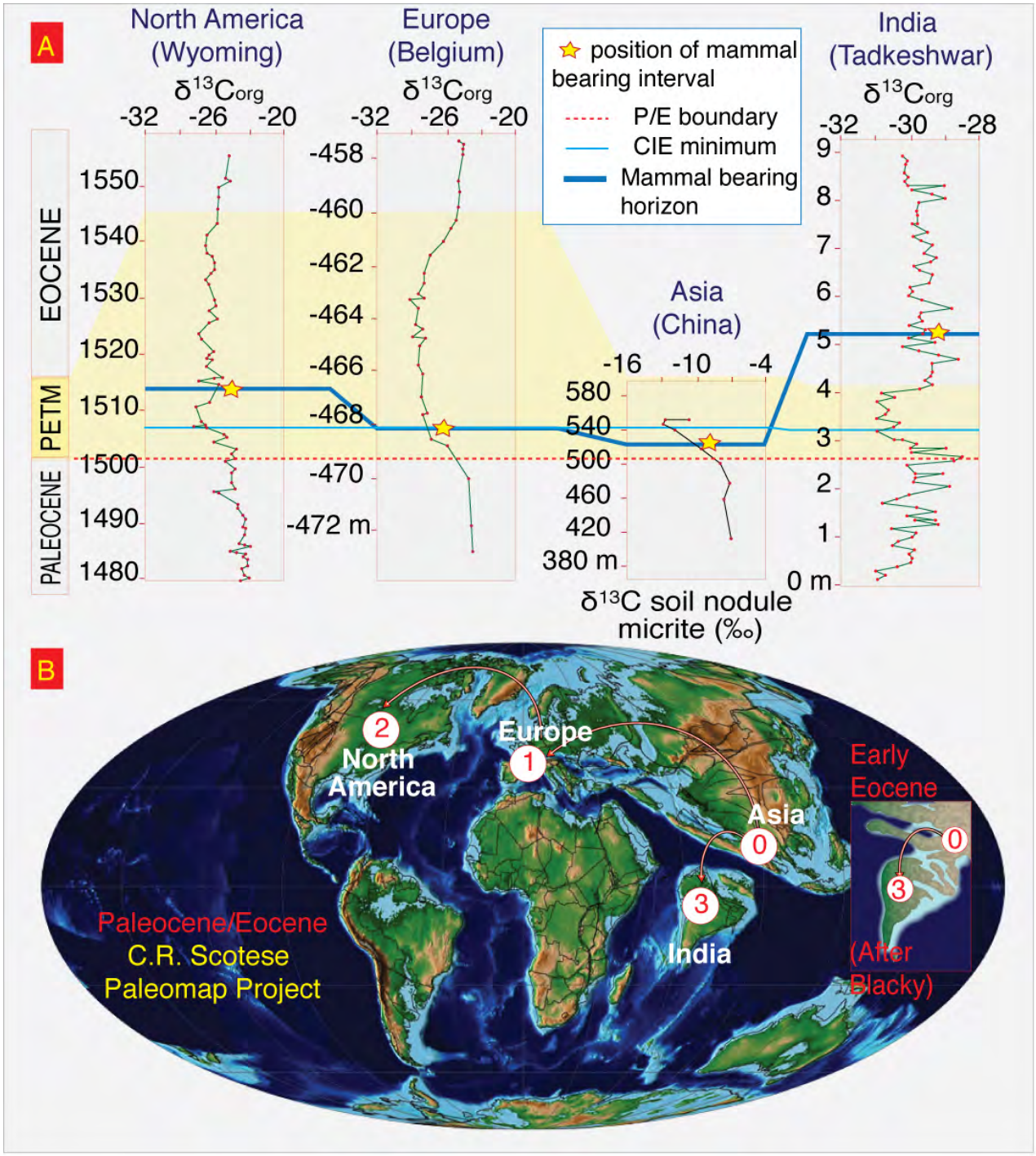

Figure 2: *Global correlation of the modern mammal bearing horizon. (A) Correlation of the mammal-bearing horizon relative to the PETM and CIE-minimum. Note the successively younger ages from the base of the PETM: Asia 12.5-14.3 ka, Europe 25-36.7 ka, North America 42-61.5 ka and India 266.3-390.5 ka indicate migration from Asia to Europe then North America and at least 200-300 ka later from Asia into India. (B) The Paleocene/Eocene paleomap reconstruction illustrates the mammal migration in the northern hemisphere during the early PETM. The delayed migration from Asia into India is linked to the timing and tempo of the India-Asia collision initiated during the early Eocene.*

Based on these factors we calculated sedimentation rates, which are highly variable as they include terrestrial deposition ranging from sandstones to lignite, and derived ages for both minimum and maximum estimated PETM durations. The results are instructive, although they need to be used with caution because of inherent uncertainties in the continuity of sedimentation.

The minimum and maximum age estimates for the early Eocene mammal diversification after the P/E boundary in Asia are 13 ka and 14 ka, respectively, in Europe 25 Ka and 37 ka, in North America 42 ka and 62 ka, and in India 267 ka and 391 ka.

The sequentially younger ages from Asia to Europe to North America during the PETM and subsequently to India well after the PETM suggests a migration path originating from Asia into Europe and North America, followed by a later migration from Asia into India (Fig. 2).

The delayed appearance of early Eocene mammals in India suggests a barrier to dispersal that is likely linked to the timing of the India-Asia collision. Although the onset of this collision is still debated, there is general consensus that it initiated no later than 55–52 Ma based on the ages of post collisional stratigraphic assemblages in north-western Himalaya (Searle et al., 1997; Beck et al., 1996; Ding et al., 2005). The early collision likely resulted in shallow seas dotted with islands between India and Asia (NW Pakistan) (Fig. 2) providing an entry into India via island hopping. This migration scenario waits further testing based on discovery of some Paleocene terrestrial mammal faunas on the Indian subcontinents.

Acknowledgments: We thank the reviewers for their critique and thoughtful suggestions. We are grateful for field assistance and discussion from Prof. S. Bajpai. This study was supported by the Egyptian government (No.001/013/104) (HK), the Lausanne University, the US NSF and Office of International Science & Engineering's India Program (EAR-0207407, EAR-0447171, and EAR-1026271) (GK). BS is thankful to Council of Scientific and Industrial Research, New Delhi (No. 24/297/08-EMR-II) and University Grant Commission Programme- SAP-DRS-I.

METHODS

Samples were collected at 5, 10, 20 and 30 cm intervals depending on lithological changes through the 9 m section of the Vastan mine (90 samples), 17 m thick section at the Tadkeshwar mine (170 samples), 31 m thick section of the Giral mine (188 samples) and 11 m section of Naredi (90 samples).

Total organic carbon separated from the powdered rock samples by acidification was analyzed for the isotopic composition through the use of elemental analysis–isotope ratio mass spectrometry (EA-IRMS). The $\delta^{13}C_{org}$ values are reported relative to VPDB with reproducibility better than 0.1‰ (1σ).

Samples were processed for microfossils by washing through a 63mm screen. Benthic foraminifera are generally small and restricted to the <100mm size fraction. For palynomorph extraction, samples were treated with HCl, HF and HNO_3 followed by 5% solution of KOH. The sample residue was washed with water through a 15µm screen. The slides were prepared in polyvinyl alcohol and mounted in Canada balsam. A Leitz Laborlux-S and Olympus BX51 microscope were used for their study and photomicrography.

REFERENCES

Alegret, L., Ortiz, S., and Molina, E., 2009. Extinction and recovery of benthic foraminifera across the Paleocene–Eocene Thermal Maximum at the Alamedilla section (Southern Spain). *Palaeogeography. Palaeoclimatology. Palaeoecology*, 279, 186–200.

Aziz, H.A., Hilgen, F.J., Luijk, G.M., Sluijs, A., and Kraus, M.J., 2008. Astronomical climate control on paleosol stacking patterns in the upper Paleocene-lower Eocene Willwood Formation, Bighorn Basin, Wyoming. *Geology*, 36, 531–34.

Bajpai, S., Kapur, V.V., Das, D.P., Tiwari, B.N., Saravanan, N., and Sharma, R., 2005a. Early Eocene land mammals from Vastan Lignite Mine, District Surat (Gujarat), western India: *Jour. Palae. Soci. of India*. 50 (1), 101–113.

Bajpai, S., Kapur, V. V., Thewissen, J. G. M., Tiwari, B. N., and Das, D. P. 2005b. First fossil marsupials from India: Early Eocene Indodelphis n. gen. and Jaegeria n. gen from Vastan lignite mine, District Surat, Gujarat. *Jour. Pal. Soc. India*. 50(1), 147-151

Bajpai, S., Kay, R.F., Williams, B.A., Das, D.P., Kapur, V.V., and Tiwari, B.N., 2008. The oldest Asian record of Anthropoidea: *National Academy of Sciences Proceedings*, 105, 11,093–11,098, doi: 10.1073/ PNAS.0804159105.

Beard, K. C. 1998. East of Eden: Asia as an important center of taxonomic origination in mammalian evolution. Pp. 5-39 in Dawn of the Age of Mammals in Asia (K. C. Beard and M. R. Dawson, eds.). Bulletin of Carnegie Museum of Natural History, No. 34.

Beard, K. C., and Dawson, M. R., 1999. Intercontinental dispersal of Holarctic land mammals near the Paleocene/Eocene boundry: paleogeographic, paleoclimatic and biostratigraphic implications. *Bullen of Geological Society of France*, 170, 697-706.

Beard, C.K., Wang, Y.Q., Meng, J., Ni Xi, J., Daniel, L. Gebo. D. L., And Li C. K., 2010. Paleocene Hapalodectes (Mammalia: Mesonychia) From Subeng, Nei Mongol: Further Evidence Of "East Of Eden冶 Dispersal At The Paleocene-Eocene Boundary

Beck, R. A., Burbank, D. W., Sercombe, W. J., Khan, A. M., and Lawrence, R. D., 1996. Late Cretaceous ophiolite obduction and Paleocene India-Asia collision in the westernmost Himalaya, *Geodinamica Acta*, 9, 114 – 144.

Bowen, G. J., Beerling, D. J., Koch, P. L., Zachos, J. C., and Quattlebaum, T., 2004. A humid climate state during the Paleocene–Eocene Thermal Maximum. *Nature*, 432, 495–499.

Bowen, G.J., Clyde, W.C., Koch, P.L., Ting, S., Alroy, J., Tsubamoto, T., Wang, Y., and Wang, Y., 2002. Mammalian dispersal at the Paleocene/Eocene boundary: *Science*, 295, 2062–2065, doi: 10.1126/science.1068700

Bowen, G.J., Koch, P.L., Gingerich, P.D., Norris, R.D., Bains, S., and Corfield, R., 2001. Refined isotope stratigraphy across the continental Paleocene-Eocene boundary on Polecat Bench in the northern Bighorn Basin. *University of Michigan Publications in Paleontology*. 33, 73–88.

Clementz, M., Bajpai, S., Ravikant,V., Thewissen, J.G.M., Saravanan, N., Singh, I.B., and Prasad, V., 2011, Early Eocene warming events and the timing of terrestrial faunal exchange India and Asia. *Geology*, 39, 15-18.

Clyde, W. C., Ting, S., Snell, K.E., Bowen, J.G., Tong, Y., Koch, P.L., Li, O., and Wang, Y., 2010. New Paleomagnetic and Stable-Isotope Results from the Nanxiong Basin, China: Implications for the K/T Boundary and the Timing of Paleocene Mammalian Turnover. *Journal of Geology*, 118, 131-143

Clyde, W.C., Khan I. H., and Gingerich, P.D., 2003. Stratigraphic response and mammalian dispersal during initial India-Asia collision: Evidence from the Ghazij Formation, Balochistan, Pakistan. *Geology*, 31, 1097–1100.

Ding, L., Kapp, P., and Wan, X., 2005. Paleocene–Eocene record of ophiolite obduction and initial India-Asia collision, south central Tibet. *Tectonics*, 24, TC3001.

Garg, R., Ateequzzaman, K., Prasad, V., Tripathi, S.K.M., Singh, I.B., Jauhri, A.K., and Bajpai, S., 2008. Age-diagnostic dinoflagellate cysts from the lignite- bearing sediments of the Vastan Lignite Mine, Surat District, Gujarat, western India: *Journal of Palaeontological Society of India*, 53, 99–105.

Gingerich, P., 2006. Environment and evolution through the Paleocene-Eocene thermal maximum: *Trends in Ecology & Evolution*, 21, 246–253, doi: 10.1016/j.tree.2006.03.006.

Gingerich, P.D., 2003. Mammalian responses to climate change at the Paleocene-Eocene boundary: Polecat Bench record in the northern Bighorn Basin, Wyoming. *Geological Society of America*, 369, 463–78.

Godinot, M., 1982. Aspects nouveaux des échanges entre les faunes mammaliennes d'Europe et d'Amérique du Nord à la base de l'Eocène. Geobios, *Mémoire Spécial*, 6,403-412.

Gradstein, M.F., Ogg, J.G., Schmitz M.D., and Ogg., G.M., 2012. The Geologic Time Scale 2012. *Elsevier*, 1st Ed.

Kappeler, P.M., 2000. Lemur origins: Rafting by groups of hibernators? *Folia Primatologica*, 71, 422-425.

Kelly, D.C., Bralower, T.J., Zachos, J.C., Premoli-Silva, I., and Thomas, E., 1996. Rapid diversification of planktonic foraminifera in the tropical Pacific (ODP Site 865) during the late Paleocene Thermal Maximum. *Geology*, 24, 423–426.

Koch, P. L., Zachos, J. C., and Dettman, D. L., 1995. Stable isotope stratigraphy and paleoclimatology of the Paleogene Bighom Basin (Wyoming, USA). *Palaeogeography. Palaeoclimatology. Palaeoecology*, 115, 61-89.

Koch, P. L., Zachos, J. C., and Gingerich, P., D., 1992. Correlation between isotope records in marine and continental carbon reservoirs near the Paleocene- Eocene boundary. *Nature* 358, 319-322.

Krause, D. W., and Maas, M. C., 1990. The biogeographic origins of late Paleocene-early Eocene mammalian immigrants to the Western Interior of North America. *Geological Society of America* Special Paper 243, 71–105.

Lu, G., Adatte, T., keller, G., and Ortiz, N., 1998. Abrupt climatic, oceanographic and ecologic changes near the Paleocene–Eocene transition in the deep Tethys basin: The Alamedilla section, southern Spain. *Eclogae Geologicae Helvetiae*, 91, 293–306.

Luciani, V., Giusberti, L., Agnini, C., Backman, J., Fornaciari, E., and Rio, D., 2007. Paleocene–Eocene Thermal Maximum as recorded by Tethyan planktonic foraminifera in the Forada section (northern Italy). *Marine Micropaleontology*, 64, 189-214.

McInerney, F. A., and Wing, S. L., 2011. The Paleocene–Eocene Thermal Maximum: A perturbation of carbon cycle, climate, and biosphere with implications for the future. *Annual Review in Earth Planetary Science*, 39, 489–516.

Murray, J.W., Curry, J.R., and Haynes, C., 1989. Palaeogene, in Jenkins, D.G., and Murray, J.W., eds., Stratigraphical atlas of fossil Foraminifera, British Micropalaeontological . Society. John Wiley & Sons. 490-536.

Prasad, V., Singh, I.B., Bajpai, S., Garg, R., Thakur, B., Singh, A., Saravanan. N., and Kapur, V.V., 2013. Palynofacies and sedimentology-based high-resolution sequence stratigraphy of the lignite-bearing muddy coastal deposits (early Eocene) in the Vastan Lignite Mine, Gulf of Cambay, India. *Facies*, DOI 10.1007/s10347-012-0355-8.

Rana, R., Kumar, K., Escarguel, G., Sahni, A., Rose, K., Smith, T., Singh, H, And Singh, L. (2008) An Ailuravine Rodent from the lower Eocene Cambay formation at Vastan, western India, And Its palaeobiogeographic implications. *Acta Palaeontol.* Pol. 53 (1): 1–14, 2008

Rodríguez, J., 1999. Use of cenograms in mammalian palaeoecology. A critical review. *Lethaia*, 32, 331–347.

Röhl, U., Westerhold, T., Bralower, T.J. and Zachos, J.C., 2007. On the duration of the Paleocene-Eocene Thermal Maximum (PETM). *Geochemistry Geophysics and Geosystems*, 8, Q12002. doi:10.1029/2007GC001784

Rose, K .D., DeLeon, V. B., Missiaen, P., Rana, R. S., Sahni, A., Singh. L., and Smith, T., 2008. Early Eocene lagomorph (Mammalia) from western India and the early diversifi- cation of Lagomorpha; *Proceeding of Royal Society of London,* B 275, 1203–1208.

Rose, K.D., Rana, R.S., Sahni, A., and Smith, T., 2007. A new adapoid primate from the early Eocene of India. Contribution of the Museum of Paleontology. *University of Michigan*, 31, 379–385.

Sahni, A., Saraswati, P.K., Rana, R.S., Kumar, K., Singh, H., Alimohammadian, H., Sahni, N., Rose, K.D., Singh, L., and Smith, T., 2006. Temporal Constraints and Depositional Palaeoenvironments of the Vastan Lignite Sequence, Gujarat: Analogy for the Cambay Shale hydrocarbon source rock. *Indian Journal of Petroleum Geology*, 15, 1–20.

Saraswati, P.K., Sarkar, U., and Banerjee, S., 2012. *Nummulites solitarius–Nummulites burdigalensis* Lineage in Kutch with Remarks on the Age of Naredi Formation, *Journal of Geological Society of India*, 7, 476-482.

Searle, M., Stephenson, C. B., and McCarron, J., 1997. Structure of the North Indian continental margin in the Ladakh-Zanskar Himalayas: Implications for the timing of obduction of the Spontang ophiolite, India-Asia collision and deformation events in the Himalaya, *Geological Magazine*, 134, 297–316.

Singh. H., Prasad, M., Kumar, K., Rana, R.S., and Singh, S. K., 2010. Fossil fruits from Early Eocene Vastan Lignite, Gujarat, India: taphonomic and phytogeographic implications. *Current Science*, 98, 1625-1632.

Sloan, R.E., 1970. Cretaceous and Paleocene terrestrial communities of western North America, in Yochelson, E.L., ed., Proceedings of the North Ameri- can Paleontological Convention, Two Volumes: Lawrence, Kansas, Allen Press, 427–453.

Smith, R., Smith, T., and Sudre, J., 1996. Diacodexis gigasein. sp., le plus ancient Artiodactyle (Mammalia) belge, proche de la limite Paléocène-Eocène. *Bulletin de l'Institut royal des Sciences Naturelles de Belgique*, 66, 177-186.

Smith, T., 2012. Contributions of Asia to the evolution and paleobiogeography of the earliest modern mammals. *Bulletin of Séanc Academic Research of Science*, 57/58.

Smith, T., Rana, R.S., Missiaen, P., Rose, K.D., Sahni, A., Singh, H., and Singh, L., 2007. Highest diversity of earliest bats in the Early Eocene of India. *Naturwissenscehaften*, 94, 1003–1009.

Smith, T., Rose, K.D., and Gingerich, P.D., 2006. Rapid Asia-Europe-North America geographic dispersal of earliest Eocene primate Teilhardina during the Paleocene-Eocene Thermal Maximum. *Proceeding of the American Academy of Science*, 103, 11223–11227

Speijer, R.P., and Wagner, T., 2002. Sea-level changes and black shales associated with the late Paleocene thermal maximum: Organic-geochemical and micropaleontological evidence from the southern Tethyan margin (Egypt-Israel): *Geological Society of America*, 356, 533-549.

Tong, Y. S., and Wang, J. W., 2006. Fossil Mammals from the Early Eocene Wutu Formation of Shandong Province. *Palaeontologia Sinica*, 28, 1-195.

Tripathi, S.K.M., 1997. Palynological changes across subsurface Palaeocene-Eocene sediments near Barmer, Rajasthan. *Indian Journal of Palaeobotany*, 46,168-171.

Tripathi, S.K.M., Kumar, M., and Srivastava, D., 2009. Palynology of Lower Paleogene (Thanetian-Ypresian) coastal deposits from the Barmer Basin (Akli Formation, Western Rajasthan, India): Paleoenvironment and paleoclimatic implications. *Geologica. Acta*, 7, 147 -160.

Westerhold, T., Rohl, U., McCarren, H.K., and Zachos, J.C., 2009. Latest on the absolute age of the Paleocene-Eocene Thermal Maximum (PETM): new insights from exact stratigraphic position of key ash layers +19 and −17. *EPSL*, 287, 412–419.

Wing, S.L., Harrington, G.J., Smith, F.A., Bloch, J.I., Boyer, D.M., and Freeman, K.H., 2005. Transient floral change and rapid global warming at the Paleocene–Eocene boundary. *Science*, 310, 993–996.

Zachos, J. C., Dickens, G. R., and Zeebe, R. E., 2008. An early Cenozoic perspective on greenhouse warming and carbon cycle dynamics. *Nature*, 451, 279–283

CHAPTER VI

THE PALEOCENE-EOCENE THERMAL MAXIMUM AT ESPLUGAFREDA, NE SPAIN: NEW EVIDENCE FROM GEOCHEMICAL AND MINERALOGICAL DATA

HASSAN KHOZYEM[1], THIERRY ADATTE[1], JORGE E. SPANGENBERG[1], and GERTA KELLER[2].

[1]Institute of Earth Science (ISTE), University of Lausanne, CH 1015 Lausanne, Switzerland.

[2]Department of Geosciences, Princeton University, Guyot Hall, Princeton, NJ 08544, USA.

THE PALEOCENE-EOCENE THERMAL MAXIMUM AT ESPLUGAFREDA, NE SPAIN: NEW EVIDENCE FROM GEOCHEMICAL AND MINERALOGICAl DATA[1]

Abstract. The Esplugafreda section of northeastern Spain has an excellent terrestrial record of the early Eocene warm events. High-resolution $\delta^{13}C$ and $\delta^{18}O$ analyses of two types of calcareous paleosol nodules reveal two distinct negative excursions. A rapid $8^{o}C$ increase in the lower part of the section corresponds to the Paleocene-Eocene Thermal Maximum (PETM) in accordance with existing regional records of marine and terrestrial environments. A gradual increase from 6 to $8^{o}C$ in the upper part of the section appears to be linked to the Early Eocene Climatic Optimum (ETM2). The well-known Claret conglomerate, previously thought to represent an extreme climatic event in the Pyrenees, occurred therefore between these two climate events and about 10m above the top of the PETM excursion and is therefore not related to the PETM. The $\delta^{13}C_{org}$ is not the best proxy for the PETM when values are overprinted due to oxidized organic matter of older age. A prominent increase in kaolinite content in the PETM implies increased runoff and/or weathering of adjacent soils.

1. INTRODUCTION

The middle Paleocene to Early Eocene (~59-52 Ma) experienced global warming with mean annual temperatures of 17-21ºC (Wilf, 2000; Zachos et al., 2001). An extraordinary warm event, known as the Paleocene-Eocene Thermal Maximum (PETM) marks the Paleocene-Eocene transition 56 Ma ago (Westerhold et al. 2009). Additional warm events are recognized in the Early Eocene, particularly the Early Eocene Climatic Optimum (EECO, ~50-52 Ma; Zachos et al., 2001), which marks the warmest climate of the Paleogene (Lourens et al., 2005; D'Haenens, 2012). Both warm events are accompanied by transient shifts to increased precipitation at higher latitudes (Robert and Kennett, 1994), which enhanced continental weathering (Higgins and Schrag, 2006) and favored kaolinite formation (Gibson et al., 2000; Bolle and Adatte, 2001). These climatic changes strongly affected land plants and were accompanied by major evolutionary changes in mammals (Harrington and Kemp, 2001).

The climatic and environmental changes associated with the PETM affected environments globally including: (1) perturbation in the carbon cycle noted by a -2 to -6 ‰ $\delta^{13}C$ excursion, (2) temperature increase of at least 8 ^{O}C in the polar region and 5 ^{O}C in the tropics, which persisted for several tens of thousands of years (Sluijs et al., 2006; Zachos et al., 2006; Weijers et al., 2007; Handley et al., 2008), (3) extinctions in deep water benthic foraminifers (35–50%) (Alegret et al., 2009), (4) widespread kaolinite formation in marine sediments throughout the Tethys region indicating warm and humid (high rainfall) conditions (Bolle et al., 2000; Bolle and Adatte, 2001), (5) decreased carbonate content linked to dissolution and/or dilution due to high detrital input (Khozyem et al., 2013), (6) formation of wetlands with thick lignite accumulations,

[1] ***Hassan Khozyem, Thierry Adatte, Jorge E. Spangenberg & Gerta Keller, 2013, THE Paleocene-Eocene Thermal Maximum at Esplugafreda, NE SPAIN: new evidence from geochemical and mineralogical data. In preparation***

(7) enhanced fluvial streams and deposition of thick paleosols, and (7) furthered migration and diversification of modern mammals. The origin of this dramatic climate warming is not well understood. Numerous studies document the nature and tempo of the PETM revealing different responses in oceanic and continental environments (Dickens et al., 1995, 2001, 2011; Katz et al., 2001, 2003; Kennett et al., 2002; Zachos et al., 2001, 2005; Speijer et al., 1997; Bowen and Zachos, 2010). Many factors may have controlled these environmental responses, including paleogeography, paleotopography, and paleodeposition.

Over the last ten years, many studies focused on the tempo and timing of the PETM in terrestrial deposits of the Tremp area, most notably the Esplugafreda section in the south central Pyrenees of Spain (Fig. 1) (Manners et al., 2013; Pujalte, et al., 2009a,b; Domingo, et al., 2007; Schmitz and Pujalte, 2007; Lopéz-Martínez and Peláez-Campomanes, 1999; Schmitz and Pujalte, 2003). The Esplugafreda section is an excellent example of the terrestrial response to the PETM event. Sediments consist of a succession of paleosols and a prominent (Claret) conglomerate that developed during the late Paleocene to early Eocene. Previous studies indentified the PETM event within or just above (Schmitz and Pujalte, 2003) or below (Domingo, et al., 2007) this Claret conglomerate and subsequently the PETM climate change was modeled on this basis.

This study revisits this well-known section to re-evaluate the age; depositional nature and climatic events based on high-resolution carbon and oxygen stable isotope analyses of micrite and micro-crystalline nodules, organic carbon analysis of whole rock kerogen, and whole rock and clay mineralogical analyses. The results provide new insights into the timing, tempo and effects of the PETM in terrestrial environments, identify the PETM, and ETM2 events in the Esplugafreda section, correlate these to other sequences of the region, and reveal the Claret conglomerate as independent of the climatic events.

2. LOCATION AND GEOLOGICAL SETTING

The Esplugafreda section is located east of Aren (42º14`50``North; 0º45`13``East, Fig.1) a historical locality at the tributary of the Esplugafreda ravine at the northern margin of the Tremp-Graus Basin (Schmitz and Pujalte 2003, 2007; Pujalte and Schmitz 2005). The section is part of the Tremp syncline and spans the upper part of the Tremp Formation, which was deposited during the late Campanian to early Eocene as determined by biostratigraphy, paleomagnetism and stable isotope studies (Galbrun et al., 1993; López-Martínez et al., 1998; Schmitz and Pujalte, 2003; Dominguo et al., 2009).

3. LITHOLOGY

The Esplugafreda section consists of three Formations as described by Schmitz and Pujalte (2003, 2007) and Pujalte and Schmitz (2005) (Fig. 1). (1) The lower part of the section consists of the Talarn Formation (Danian), an 80 m thick unit of red silty mudstones intercalated with calcarenites and calcareous conglomerates. At the top of this formation is a palustrine limestone overlain by mature paleosol that marks the Mid-Paleocene Unconformity (MPU) (Eichenseer 1988). (2) The Esplugafreda Fm. is 165 m thick with a 10 m thick interval, which consists of grey-purple silty claystones with gypsum seams at the base (Fig. 1D). The claystones contain numerous paleosole horizons with abundant carbonate nodules up to few cm in diameter (Pujalte et al., 2005, 2009). This unit is overlain by red silty mudstones intercalated with calcarenites and calcareous conglomerates.

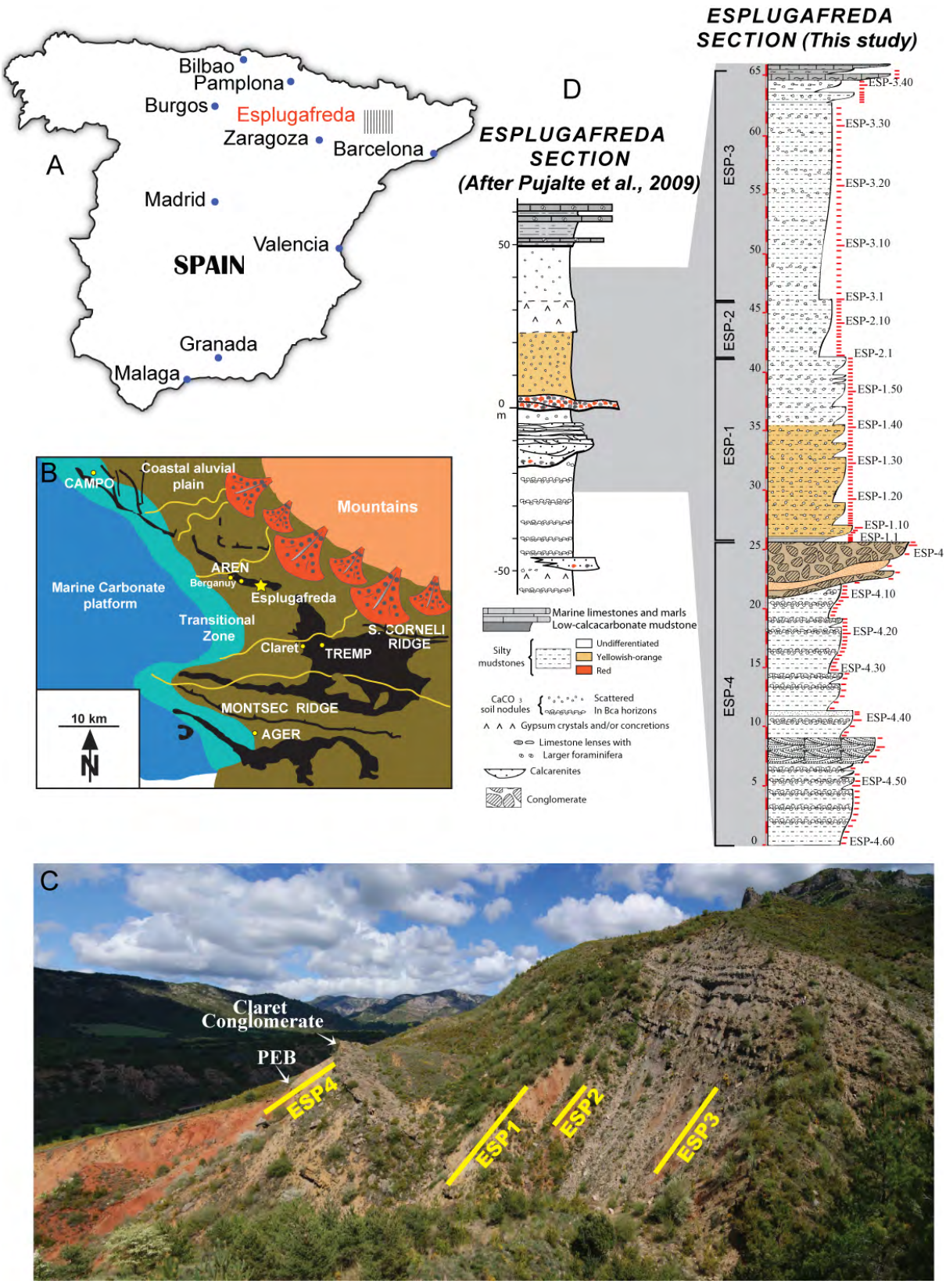

Figure 1. *(A) Location map of Esplugafreda; (B) paleogeographic map with location of the Esplugafreda section; (C) field photograph of the outcrops studied; (D) lithostratigraphic column of the Esplugafreda section.*

Palynological and paleontological data indicate a late Paleocene to early Eocene age for Esplugafreda Formation.

(3) The Claret Formation is 60 to 70 m thick in the studied area and consists of a succession of paleosols intercalated with channelized sandstones and conglomerates.

The most notable feature of the Claret Fm. is the presence of two laterally extended conglomerate beds known as Claret conglomerate (CC). This conglomerate is interpreted as a mega-fan that formed at the onset of the PETM (Schmitz and Pujalte, 2007) or slightly thereafter (Dominguo et al., 2009; Manners et al., 2013). The CC is overlain by a 20 m thick succession of yellow paleosoils (Schmitz and Pujalte, 2003) consisting of silty claystones with minor intercalations of channelized sandstones, which change to silty dark red colored claystone with variable amounts of gypsum veins and root-like concretions. The topmost part of the Claret Fm. consists of light red, silty mudstones with small and scattered carbonate nodules of immature soil conformably overlain by alternating grey marls with marine fossils (Fig. 1). At the Esplugafreda section, the Paleocene-Eocene transition is within the terrestrial part of the Claret Fm. characterized by calcareous nodules and enriched paleosols intercalated with sandstones and conglomerate.

4. METHODS

A Total of 175 samples covering the upper Paleocene to lower Eocene interval (66 m) were collected from a 75 cm deep trench at Esplugafreda (Fig.1). In the laboratory, samples were divided into three parts: 1) powdered samples for bulk rock mineralogy, 2) acidified bulk samples for kerogene extraction and clay mineralogy, and 3) washed residues for obtaining calcareous nodules. All analyses were conducted at the Institute of Earth Science (ISTE), Lausanne University, Switzerland.

For each sample, about 100 gr was washed through a 63μm screen using H_2O_2 and ultrapure water. Different types of calcareous nodules were separated into micrite and micro-crystalline nodules (Fig. 2) and subjected to further cleaning using a cold dilute-buffered solution of hydrogen peroxide to remove organic matter and adhering particles. All nodules were then cleaned three times using di-ionized water and three times using ultrapure water to remove secondary carbonates and organic matter. Cleaned nodules were dried overnight in an oven at 50–70 ^{o}C.

For stable isotope analysis, the nodules were subjected to $\delta^{13}C$ and $\delta^{18}O$ analyses using procedures described by (Revesz et al., 2001). Analyses were conducted using a Thermo Fisher Scientific GasBench II (formerly ThermoQuest/ Finnigan, Bremen, Germany) preparation device interfaced to a Thermo Fisher Scientific Delta Plus XL continuous flow isotope ratio mass spectrometer (IRMS) (Revesz et al., 2001). The $\delta^{13}C$ and $\delta^{18}O$ ratios are reported in the delta (δ) notation as the per mil (‰) deviation relative to the Vienna–Pee Dee belemnite standard (VPDB). Analytical uncertainty (2σ), monitored by replicate analyses of the international calcite standard NBS-19 and the laboratory standards Carrara Marble and Binn Dolomite are no greater than ±0.05‰ for $\delta^{13}C$ and ±0.1‰ for $\delta^{18}O$.

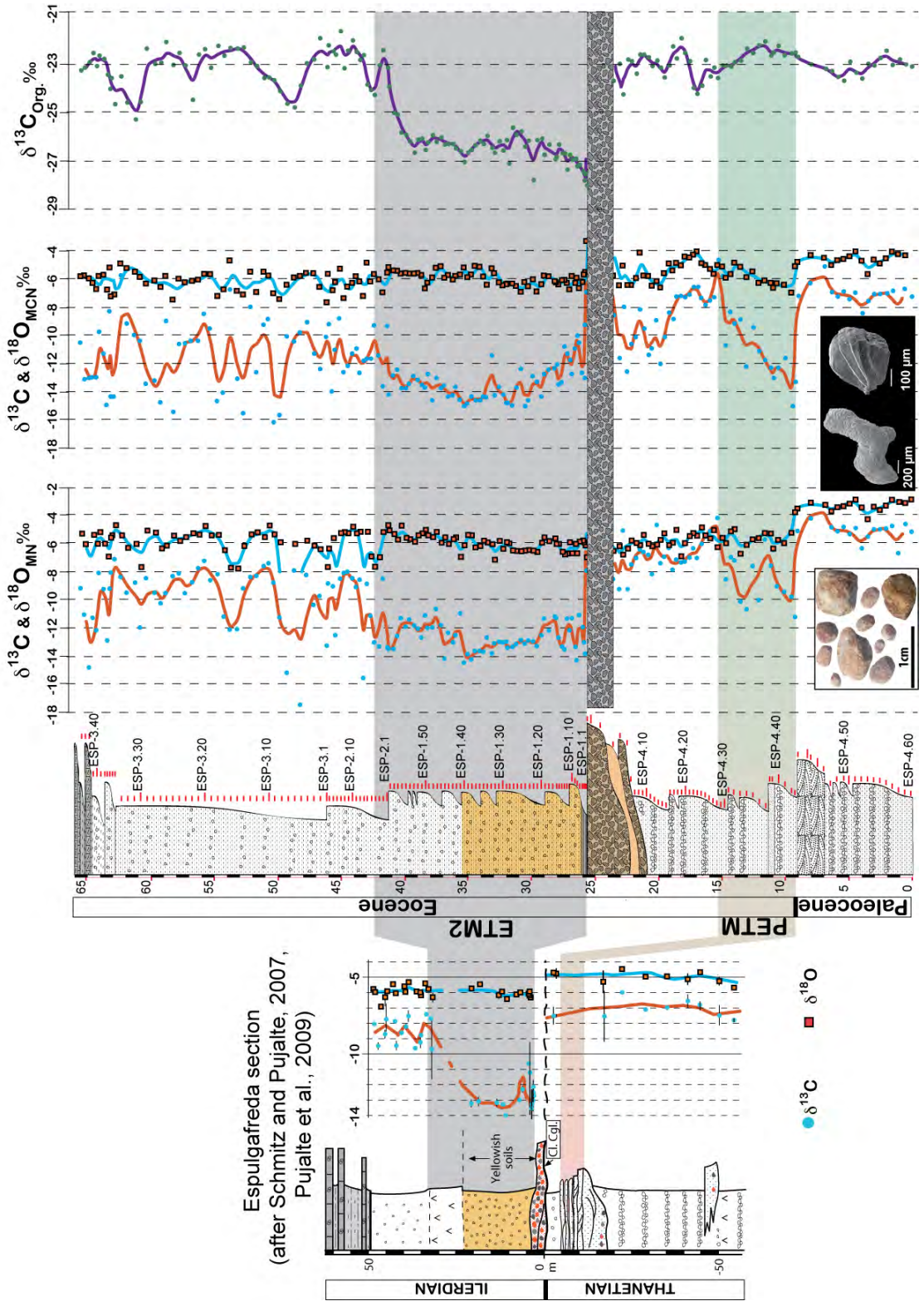

Figure 2. *Correlation of the carbon isotopic record of Esplugafreda section (Pujalte et al., 2009) and Carbon and oxygen isotope profiles of the collected two calcareous soil nodule (micritic, MN and micro-crystalline nodules, MCN) together with organic carbon isotope record of the bulk organic matter.*

For organic carbon isotope analysis, the kerogen was isolated from bulk rock samples by HCl treatment. The carbon isotope composition of kerogen was determined by flash combustion on a Carlo Erba 1108 elemental analyzer (EA) connected to a Thermo Fisher Scientific Delta S isotope ratio mass spectrometer (IRMS) that was operated in the continuous helium flow mode via a Conflo III split interface (EA– IRMS). The $\delta^{13}C$ value is reported relative to VPDB. The reproducibility was better than 0.1‰ (1σ).

For mineralogical analyses, XRD was conducted on bulk rock for all the samples at the Geological Institute of the University of Lausanne, Switzerland. The samples were prepared following the procedure of Kübler (1987). Random powder of the bulk sample is used for characterization of the whole rock mineralogy. About 20 gr. of each rock sample was ground with a "jaw" crusher to obtain small chips (1 to 5 mm). Approximately 5 gr were dried at 60 °C and then ground to a homogenous powder with particle sizes <40μm. 800 mg of this powder was pressed (20 bars) in a powder holder covered with a blotting paper and analyzed by XRD. Whole rock composition was determined by XRD (Xtra Diffractometer, Thermo, Ecublens, Switzerland) based on methods previously described (Ferrero, 1965, 1966; Klug and Alexander, 1974; Kübler, 1983; Rolli, 1990). This method used external standards for semi-quantitative analysis of the bulk rock mineralogy (obtained by XRD patterns of random powder samples).

Clay mineral analyses were based on methods by Kübler (1987). Ground chips were mixed with de-ionized water (pH 7-8) and agitated. The carbonate fraction was removed with the addition of HCl 10% (1.25 N) at room temperature for 20 minutes, or more until all the carbonate was dissolved. Ultrasonic disaggregation was accomplished during 3 minute intervals. The insoluble residue was washed and centrifuged (5-6 times) until a neutral suspension was obtained (pH 7-8). Separation of different grain size fractions (< 2μm and 2-16 μm) was obtained by the timed settling method based on Stokes law. The selected fraction was then pipetted onto a glass plate and air-dried at room temperature. XRD analyses of oriented clay samples were made after air-drying at room temperature and ethylen-glycol solvated conditions. The intensities of selected XRD peaks characterizing each clay mineral (e.g. chlorite, mica, kaolinite, palygorskite, sepiolite, smectite and illite-smectite mixed-layers) were measured to obtain a semi-quantitative estimate of the proportion of clay minerals in the size-fractions <2μm and 2-16μm. Therefore, clay minerals are given in relative percent abundance without correction factors. Content in swelling (% smectite) is estimated by using the method of Moore and Reynolds (1989).

5. RESULTS

5.1. Isotope geochemistry.

5.1a. Micrite nodules (MN)

Stable isotope analyses of the micritic calcareous nodules (MN, $\delta^{13}C_{MN}$ and $\delta^{18}O_{MN}$), ranging in size from several millimeters to few centimeters in diameter, show two distinct negative excursions. Below the lower $\delta^{13}C$ excursion, the $\delta^{13}C_{MN}$ and $\delta^{18}O_{MN\ shows}$ mean values of -5.1‰ and -2.56‰ respectively. The lower $\delta^{13}C$ excursion (marked PETM in Fig. 2) begins with an abrupt shift coincident with a lithologic change from silty mudstone to calcarenite and is characterized by -11.3‰ in $\delta^{13}C_{MN}$ and -3.1‰ in $\delta^{18}O_{MN}$ values at the onset, and spans 5.5m with mean value of -8.67‰ and -5.18‰ for $\delta^{13}C_{MN}$ and $\delta^{18}O_{MN}$ respectively

Between the first $\delta^{13}C$ excursion and the base of the Claret conglomerate, the $\delta^{13}C_{MN}$ are less negative with mean value of -6.8 ‰, whereas the $\delta^{18}O_{MN}$ values remain relatively stable with a mean of -5.5‰ *(*Fig. 2).

Above the Claret conglomerate, the second abrupt shift in $\delta^{13}C_{MN}$ (-7‰, marked ETM2 in Fig. 2) begins 10 cm above the Claret conglomerate and remains low, between -11 to -14‰ for the next 16 m gradually reaches minimum values around 35 m. This long-term decrease in $\delta^{13}C_{MN}$ does not correspond to significant change $\delta^{18}O_{MN}$ values, which remain similar to values below the conglomerate (mean value of -5.7‰). The upper part of the section (45-66m) is marked by fluctuations in both $\delta^{13}C$ (between -8‰ and -12‰), and $\delta^{18}O_{MN}$ (between -4.5‰ and -8‰).

5.1b. Microcrystalline nodules (MCN)

Microcrystalline nodules (<3 mm in diameter) record similar $\delta^{13}C$ trends as micrite nodules (Fig. 2). Relatively stable pre- PETM excursion $\delta^{13}C_{MCN}$ (between -6‰ to -8‰, mean -7.1‰) and between -4.04‰ to -5.68‰, with mean -4.56‰ for $\delta^{18}O_{MCN.}$ The $\delta^{13}C_{MCN}$ and $\delta^{18}O_{MCN}$ values are abruptly shifted from -7.2‰ to-13.3‰, and from -4.8‰ to-5.1‰, followed by gradual recovery over the next 5.5 m to the top of the shaded (PETM) interval with mean values of -11.37‰ and -5.94‰ for $\delta^{13}C_{MCN}$ and $\delta^{18}O_{MCN}$ respectively, contrasting with the double excursion recorded in $\delta^{13}C_{MN}$.

The PETM $\delta^{13}C_{MCN}$ excursion is followed by 3.8m interval that both $\delta^{13}C_{MCN}$ and $\delta^{18}O_{MCN}$ show s less negative values ranging between -5.81‰ and -8.82‰ for $\delta^{13}C_{MCN}$, and -4.06‰ and -5.64‰ for $\delta^{18}O_{MCN}$. The second isotopic $\delta^{13}C_{MCN}$ excursion is started 5m below the Claret conglomerate, gradually reaches its minimum value (-15‰) at 9.5m above the Claret conglomerate, followed 7m interval show gradual increase in $\delta^{13}C_{MCN}$ values to reach - 9.3‰.

Along the ETM2 $\delta^{13}C_{MCN}$ excursion the $\delta^{18}O_{MCN}$ values also show similar trend as observed in the $\delta^{18}O_{MCN}$ with no significant changes. Above the second isotopic excursion, both $\delta^{13}C_{MCN}$ and $\delta^{18}O_{MCN}$ shows rapid and sharp fluctuations between -10 and -16‰ and -4 and -8‰ respectively.

5.1c. Organic carbon isotope

The $\delta^{13}C_{org}$ trend (Fig. 2) differs from of $\delta^{13}C_{MN}$ and $\delta^{13}C_{MCN}$ trends. Below the Claret Conglomerate, the $\delta^{13}C_{org}$ is characterized by heavy values ranging between -24.32‰ and -22.03‰ with a mean value of -23‰. No excursion is recorded correlative with the first $\delta^{13}C$ shift (PETM), which suggests decoupling from the $\delta^{13}C_{carb}$ excursion. Above the Claret conglomerate, $\delta^{13}C_{org}$ records a sharp negative shift, coincident with the second $\delta^{13}C$ excursion, over an interval of 16 m reaching minimum values of around 27‰ (mean value: -25.7‰) and dropping to pre-excursion values at the top. Above this excursion $\delta^{13}C_{org}$ values remain heavier (mean value: -23.4‰) similarly to $\delta^{13}C_{carb}$ records. The uppermost 15 m of the section characterized by three distinct minor negative peaks in $\delta^{13}C_{org}$ averaging -23.9‰, -23.8‰ and -24.4‰ from the bottom to the top.

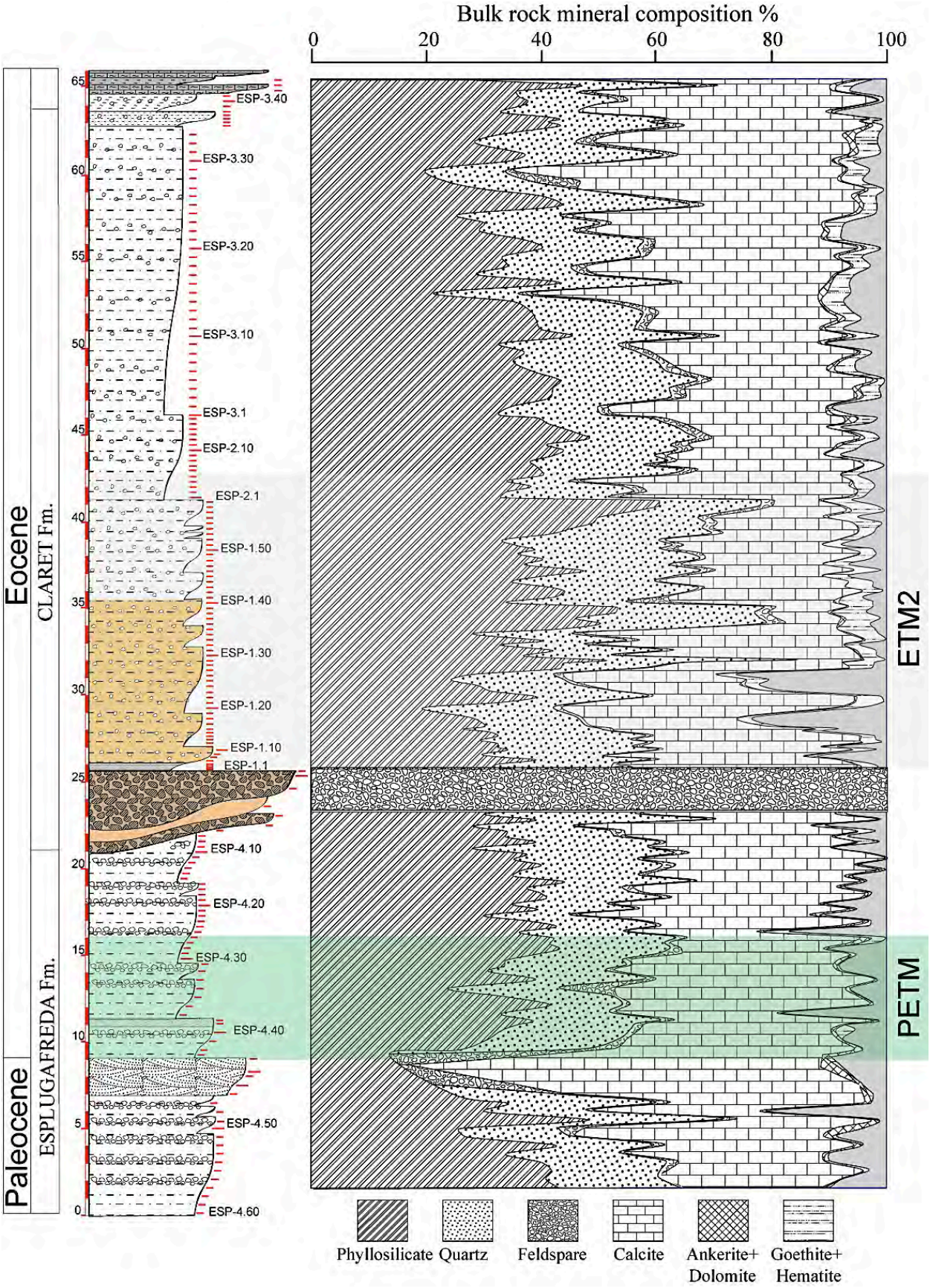

Figure 3. *Bulk rock composition of the studied section in weight percent.*

5.2. **Mineralogy**

5.2a. Bulk Rock mineralogy

Based on bulk mineralogy, the Esplugafreda Fm can be divided into three distinct units: 1) at the base are 7 m of red colored silty mudstones with abundant calcareous nodules, phyllosilicate average 36.1%, calcite 34.2%, quartz 19.2%, feldspar 1.8%, and minor amounts of dolomite, ankerite, hematite and goethite are present (Fig.3). 2) Above the red silty mudstone are 3 m of light brown cross-bedded calcarenite composed of 53.0% calcite, 21.4% phyllosilicate, 16.1% quartz, 2.75% feldspars and minor amounts of dolomite and ankerite, but no iron rich minerals (e.g. hematite, goethite).

3) The upper part (12 m) consists of red-yellow silty mudstone with an average composition of 36.2% phyllosilicate, 34.6% calcite, 19.8% quartz, 1.9% feldspar and minor amounts of dolomite, hematite, goethite and ankerite.

The Claret Fm. unconformably overlies the Esplugafreda Fm. with a 4.5 m thick polymict conglomerate (Figs.1, 3) at the base. Above the conglomerate are undifferentiated vary colored silty mudstone with an average bulk composition of 37.6 % phyllosilicate, 32.2% calcite, 26.7% quartz, and 2.1% feldspar. The Claret Fm. contains abundant calcareous nodules and several intervals with increased phyllosilicate contents, particularly at 10 m and 15 m above the CC.

5.2b. Clay mineralogy

The clay fraction of the Esplugafreda Fm. shows two distinct features. An abrupt increase in kaolinite content (average 20.2%) and decrease in smectite (30%) coincides with the first $\delta^{13}C$ excursion (PETM, Fig. 4). During this interval the maximum kaolinite/smectite ratio (range 0.6 to 4.11) coincides with the negative $\delta^{13}C$ excursion. Increased kaolinite is associated with increased illite (35.0%), illite-smectite (8.0%), and chlorite (6.7%). From the top of the lower $\delta^{13}C$ excursion to the Claret conglomerate, smectite increases gradually along with decreasing kaolinite, illite, IS, chlorite contents and the kaolinite/smectite ratio. Kaolinite content reaches minimum values just below the Claret conglomerate with 7.7%. About 9 m above the Claret conglomerate, kaolinite and illite decrease to minimum values of 10.5% and 15.5% respectively, coincident with maximum smectite content (64%). Above this interval, smectite decreases to minimum values (16.4%) coincident with a sharp increase in kaolinite, illite, smectite, illite-smectite and chlorite. This second peak of kaolinite and illite-smectite (average of 27.32 and 7.8%) spans only 2 m. From 42 m to the top of the section, smectite and kaolinite remain relatively low (mean 36.05%) and illite, illite-smectite and chlorite relatively high (mean 35.5%, 10.26%, and 10.55%, respectively).

6. DISCUSSION

The early Eocene marks the warmest period of the Cenozoic, which is characterized by several early Eocene hyperthermal events. During the early Paleocene, the Tethys region was warm and humid, which turned to seasonally warm climate conditions during the Paleocene-Eocene (P-E) transition (Bolle et al., 2001, Khozyem et al., 2013). Climate warming was accompanied by increased evaporation across the P-E transition in the Tethys region and may have caused a pole-ward increase in atmospheric moisture transport, leaving the Pyrenees seasonally arid (Schmitz et al., 2001, 2003). The resulting climatic and hydrological changes are expected to be recorded in sediments from the Pyrenean region.

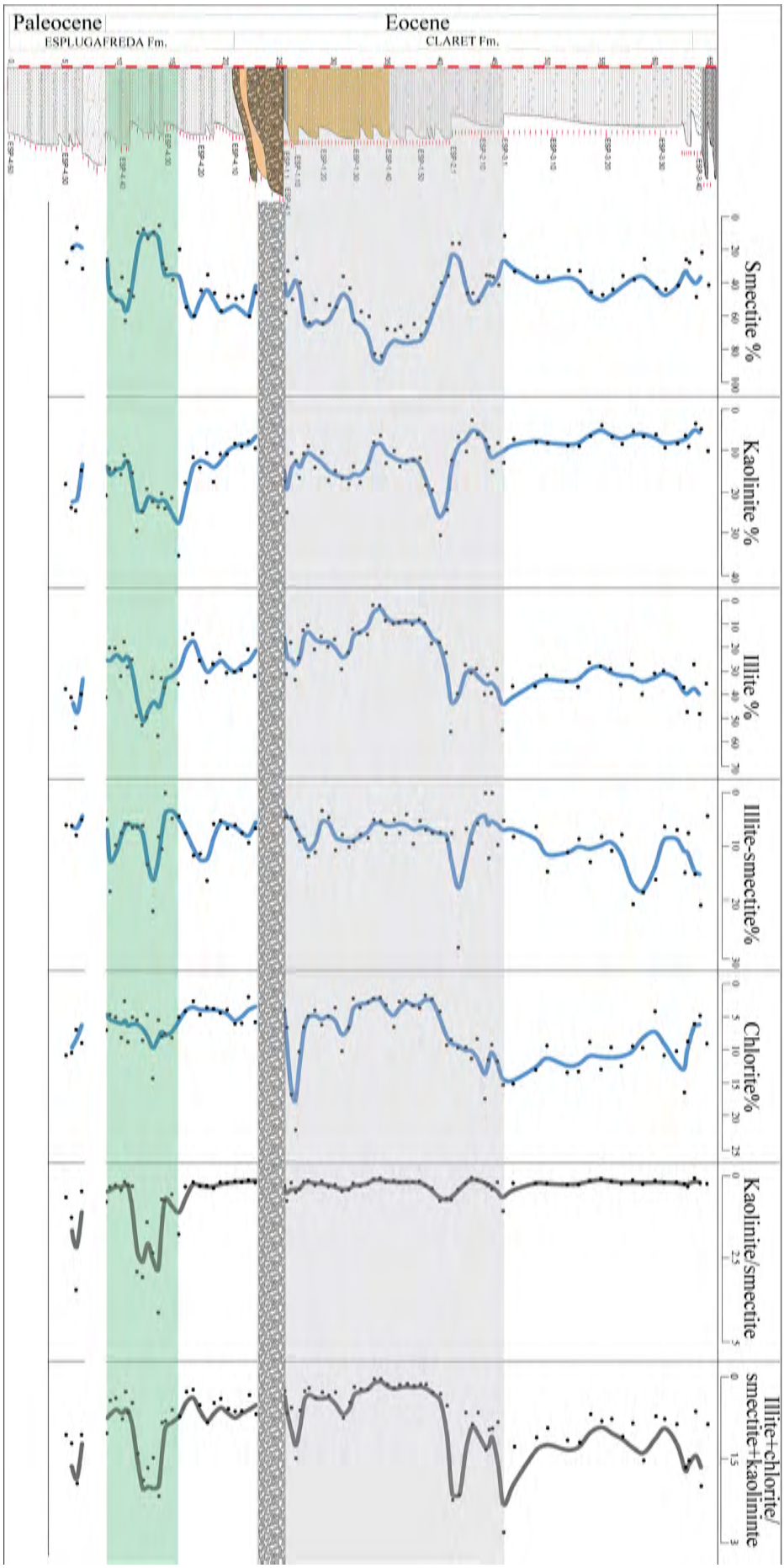

Figure 4. *Clay mineral composition in relative percent together with humidity index (kaolinite/smectite) and PhW/ChW (Illite+chlorite/smectite+kaolinite).*

Numerous publications have investigated the PETM in marine and terrestrial environments of the Pyrenees, thereby redefining the Ilerdian Stage as the beginning of the early Eocene (Pujalte, et al., 2009a,b; Domingo, et al., 2007; Schmitz and Pujalte, 2007; Lopéz-Martínez and Peláez-Campomanes, 1999. Schmitz and Pujalte, 2003; Domingo et al., 2009; Manners et al., 2013). At Esplugafreda, the P-E boundary was placed at the top of the Claret conglomerate based on the correlation of marine and terrestrial sections in the Tremp basin and the abrupt negative $\delta^{13}C$ shift observed in calcareous nodules collected from different paleosoil horizons (Schmitz and Pujalte, 2003, 2007). Pujalte, et al. (2009a) identified the PETM $\delta^{13}C$ excursion over a 20 m interval with amplitude of about -14‰.

6.1. $\boldsymbol{\delta^{13}C}$ of organic matter

The organic carbon isotope reflects the organic matter content and type. In Esplugafreda section the decoupling of the $\boldsymbol{\delta}^{13}C_{org}$ and $\boldsymbol{\delta}^{13}C_{MNand\ MCN}$ at the PETM interval (Fig. 2) can be explain by mixing of oxidized older organic matter derived sediments during the development of the soil profiles (Poppi et al., 1989) with presence of foraminifera species of upper Maastrichtian age. Therefore we cannot depend on the measured $\boldsymbol{\delta}^{13}C_{org}$ to determine the PETM because of overprint of the older organic matter signal.

Recently, Manners et al., (2013) evaluated the organic carbon isotope records from six sections in a continent-marine transect spanning the PETM in northern Spain (e.g., Claret, Tendrui, Esplugafreda, Campo, Ermua, and Zumaia, Fig. 1). Based on the $\boldsymbol{\delta}^{13}C_{org}$ correlation, they concluded that the PETM began prior to deposition of the Claret conglomerate in continental sections, including Esplugafreda, thus contradicting studies by Schmitz and Pujalte (2003, 2007). Our study agrees with Manners et al., (2013) in there overall conclusion of an older PETM age based on $\boldsymbol{\delta}^{13}C$ results, but fails to corroborate their $\boldsymbol{\delta}^{13}C_{org}$ record of Esplugafreda. They neglected to take into consideration the various factors controlling the organic carbon isotope record, such as the type of plants, source and age of organic matter, oxidation and degradation of organic matter and their effect on the isotopic record and the sources of CO_2. In particular, the source and type of organic matter can strongly influence $\boldsymbol{\delta}^{13}C_{org}$, as for example the heavy values observed below the Claret conglomerate that probably reflect reworking and oxidation of older organic matter, thus explaining the decoupling observed between $\boldsymbol{\delta}^{13}C_{org}$ and $\boldsymbol{\delta}^{13}C_{carb\ (MN,\ MCN)}$

6.2. **Emplacement of the PETM and ETM2**

New $\boldsymbol{\delta}^{13}C$ data from two different types of calcareous nodules (micritic and recrystallized) that formed in soils of the Esplugafreda area reveal two well-defined isotopic excursions (Fig. 2). The lower $\delta^{13}C$ excursion spans about 5.5 m and begins with an abrupt negative shift coincident with an unconformity between red soil and calcarenitic fluvial to lacustrine sediments. Previous studies of this section failed to record this $\boldsymbol{\delta}^{13}C$ excursion possibly because of low-resolution sampling (Schmitz and Pujalte, 2003) The upper $\delta^{13}C$ excursion is characterized by a long-term decrease, beginning about 3-4 m below the Claret conglomerate and continuing about 34 m above. Previous workers interpreted this $\boldsymbol{\delta}^{13}C$ excursion interval as PETM.

Correlation with existing marine and terrestrial records outside the Pyreneean region. For the marine record, we chose the combined datasets (Miller et al., 1987; Zachos et al., 1993, 1999, 2001) recalibrated by Cramer et al. (2009) using astronomical tuning, and for the terrestrial record we correlate Esplugafreda with the Tadkeshwar lignite mine in India (Fig. 5).

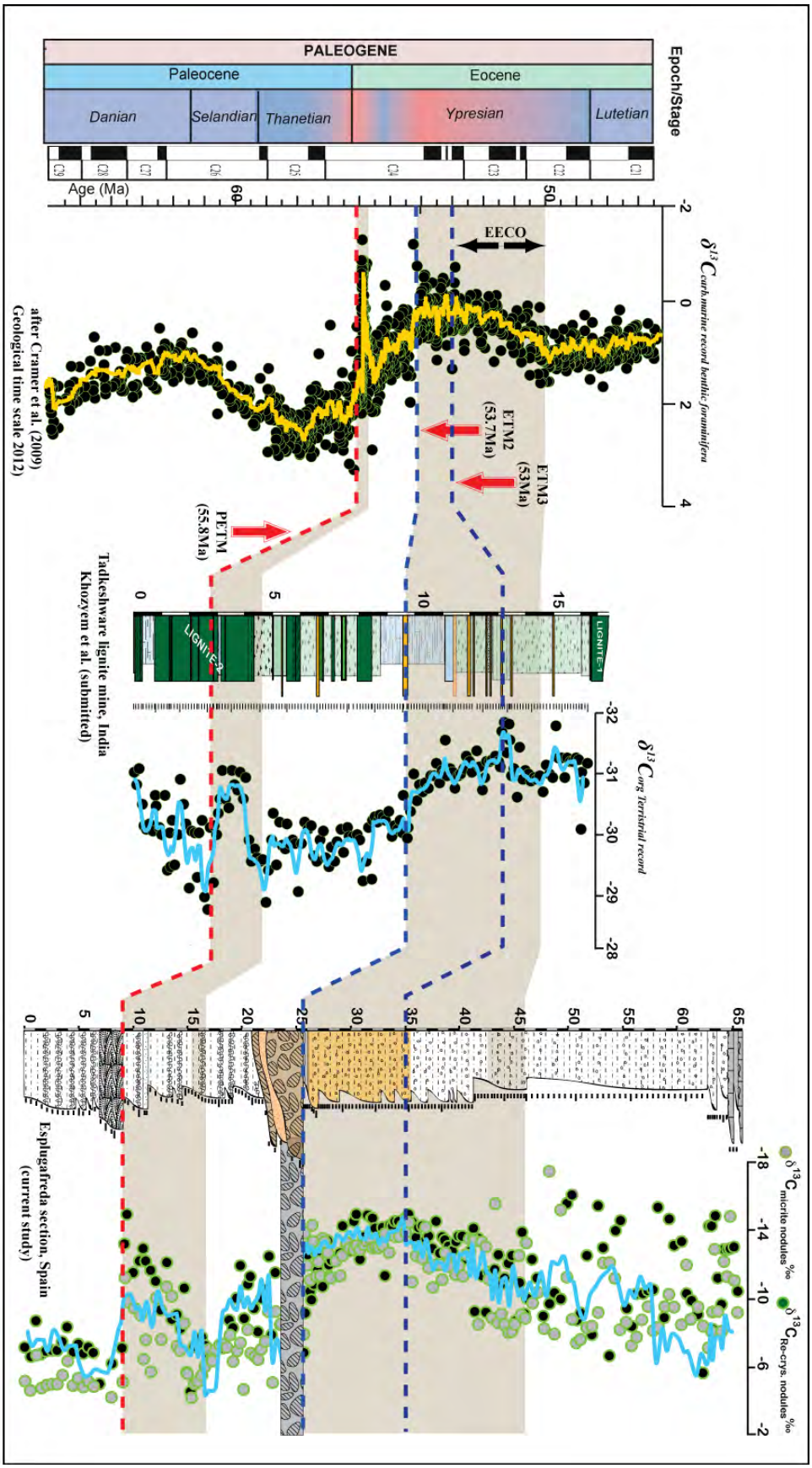

Figure 5. *Correlation of the terrestrial Esplugafreda* $\delta^{13}C_{carb\ (MN\ and\ RN)}$ *with terrestrial organic carbon isotope from Takeswar, India (Khozyem et al., in prep) and the marine isotopic record (Zachos et al., 2001 and Cramer et al. 2009). Note that ages are recalibrated using the GTS 2012.*

Age control for the PETM of the Tadkeshware lignite mine is based on palynology and benthic foraminifera for the ETM2 and correlation with other lignite mines of the area as well as to the marine record (Khozyem in prep.).

We can estimate the age of the two $\boldsymbol{\delta}^{13}C$ excursions at Esplugafreda based on stable isotope

Based on this correlation, the amplitude and stratigraphic position of the lower $\boldsymbol{\delta}^{13}C$ excursion at Esplugafreda correlates well with the PETM in marine sections and the terrestrial $\boldsymbol{\delta}^{13}C_{org}$ record in India (Fig. 5). The Esplugafreda $\boldsymbol{\delta}^{13}C$ record also correlates well with several terrestrial PETM sections across the Bighorn Basin (Koch et al., 2003) and in Asia (Min et al., 2010). The latter studies interpret the PETM excursion in continental environments as result of changing atmospheric CO_2. The upper long-term $\boldsymbol{\delta}^{13}C$ excursion observed above the Claret conglomerate at Esplugafreda correlates well with the undifferentiated Early Eocene Climatic Optimum (EECO) of the marine record, which includes ETM2 event. Within this interval the ETM2 event of Takeshwar, India, and the second excursion at Esplugafreda can be correlated with the lower part of the EECO in the marine record.

Based on these stable isotope correlations, we place the P-E boundary at Esplugafreda at the onset of the lower $\delta^{13}C$ excursion (PETM), which is 10 m below the base of the Claret conglomerate previously identified as PETM age. The climate record (stable isotopes, clay mineralogy) provides additional strong supporting evidence identifying the two climate extremes as PETM and ETM2 events in the Esplugafreda section.

6.3. **Environmental significance of isotope variations**

Cerling (1984, 1991) discussed the relationship between soil formation and carbon isotope composition and defined a two end-member mixing model that relates the isotopic composition of soil calcite to the concentration of atmospheric CO_2 for soils characterized by an open-system, one-dimensional Fickian diffusive, gaseous transport. One of the primary conditions of this model is that soils must be well drained, because carbonate in such profiles is more likely to have formed under open system conditions.

The cross plots of $\delta^{13}C_{org}$ vs the $\boldsymbol{\delta}^{13}C_{carb\ (MN\ and\ MCN)}$ discriminates between the two negative carbon isotopic excursions observed in the Esplugafreda section (Fig. 6). Following Cerling (1991), the $\delta^{13}C_{org}$ versus both $\boldsymbol{\delta}^{13}C_{MN}$ and $\boldsymbol{\delta}^{13}C_{MN}$ cross plots show that the PETM carbon isotopic excursion falls in the field of open soil system (Fig. 6, grey area) that formed in the coastal area where two CO_2 sources influenced the carbon isotopic composition: CO_2 from oxidation of soil organic matter and atmospheric CO_2. The observed heavy $\delta^{13}C_{org}$ values may be linked to oxidation of older organic matter, reworked during the depositional process and/or the presence of C_3 photosynthesizers with typical − 22‰ carbon isotopic values.

If the calcite nodule values originated solely from oxidation of biological material in the soil profile, then the $\delta^{13}C_{nodules\ carb.}$ would at least 14.8‰ heavier than the $\delta^{13}C_{org}$ resulting from oxidizing soil organic matter under open-system conditions. The lower carbon isotopic excursion at Esplugafreda reflects the latter conditions. The minimum isotopic difference between coexisting carbonate and organic matter reflects a 4.4‰ enrichment associated with diffusive transport of biologically derived CO_2 (Cerling, 1991) and an additional 10.4‰ carbon isotope enrichment from gaseous CO_2 to calcite due to carbon isotope fractionation between carbonate species (in slightly alkaline pH; Bottinga, 1968). Consequently, the $\delta^{13}C_{org}$ values characterizing

the PETM at Esplugafreda effectively define a lower limit of acceptable calcite $\delta^{13}C$ values for an open system diffusive exchange between paleosoil CO_2 and global atmospheric CO_2. Such an exchange reflects the prevailing increased runoff and humidity during soil formation at PETM time.

The more negative $\delta^{13}C$ values that characterize the ETM2 suggest that nodule formation occurred (1) under soil conditions that yielded more negative calcite $\delta^{13}C$ values and/or (2) a failed open-system diffusion between soil derived and tropospheric CO_2. This open-system diffusion failure is likely due to the prevailing arid conditions during the ETM2 in the Pyrenean area, as observed by presence of scattered gypsum veinlet at this level.

Alternatively, during the upper climate warming at Esplugafreda, carbonate nodule $\delta^{13}C$ values may record diagenetic alteration. In addition, the positive correlation between $\delta^{13}C_{org}$ and $\boldsymbol{\delta}^{13}C_{carb\ (MN\ and\ RN)}$ indicate a single CO_2 source for the light isotopic compositions in both organic matter and atmosphere. Moreover, the strikingly negative calcite $\delta^{18}O$ values (Fig. 7) are suggestive of diagenetic alteration. However, diagenetic waters are typically carbon-poor, with very little chemical potential to facilitate carbon isotope change (Tucker and Wright, 1990), which argues against diagenetic alteration of $\delta^{13}C$ carbonate values. This suggests that the very negative calcite $\delta^{13}C$ values likely reflect the primary depositional environment (Smith, 1995; Retallack et al., 2003). The lack of a well developed pedogenic structure in the paleosols supports this interpretation, as does the lack of horizontal zonation and soil reddening, which is typical of older, stable, and very well drained soil.

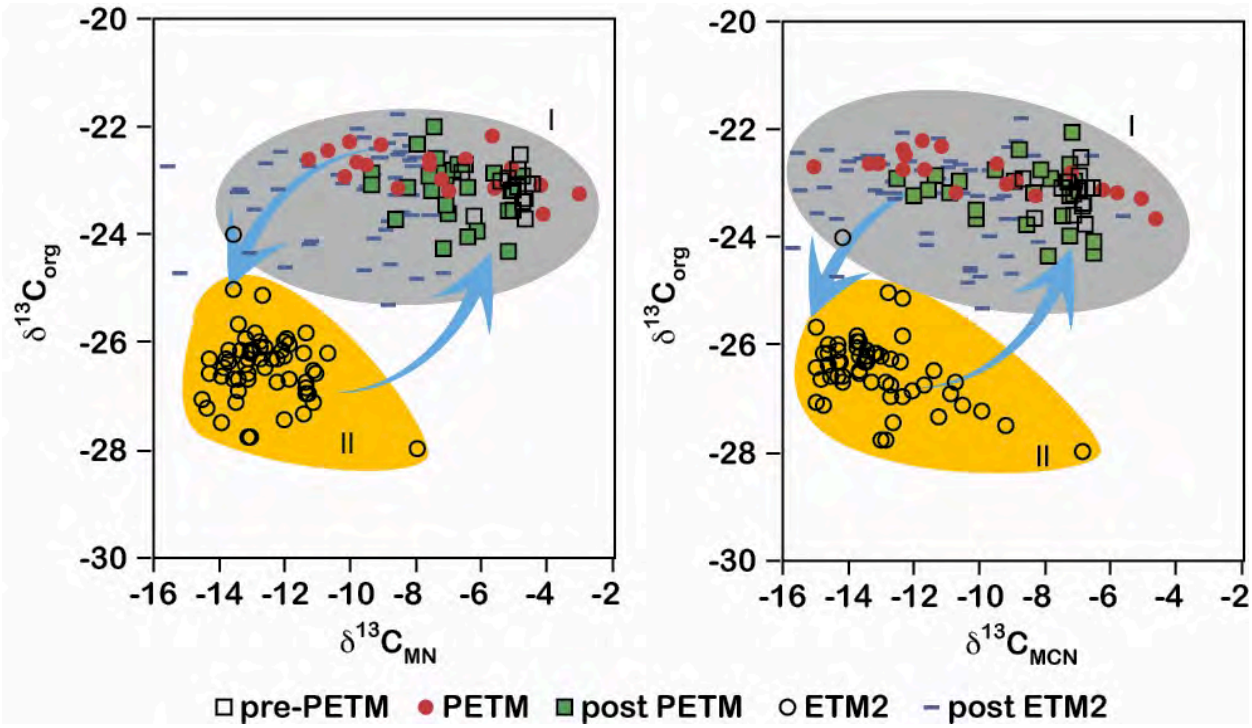

Figure 6. *$\boldsymbol{\delta}^{13}C_{org}$ vs $\boldsymbol{\delta}^{13}C_{carb\ (MN\ and\ RCN)}$; Field- I represents the carbon isotopic compositions of the PETM below the Claret conglomerate; Field-II represents the upper carbon isotopic excursion of the ETM2 interval at Esplugafreda.*

The $\delta^{18}O$ versus $\delta^{13}C$ cross plots for micrite and recrystallized nodules show a similar evolution in isotopic compositions (Fig. 7). Heavy isotope values are linked to the type of fluid percolating through the soil during sediment deposition. Variations in fluids can be detected by

diagenetic overprints in $\delta^{18}O$ versus $\delta^{13}C$ plots. Micritic and recrystallized nodules of the lower climate warm event (PETM) show lower $\delta^{13}C$ values indicating fluid enriched by heavy isotopic compositions.

In the upper warm event (ETM2) both $\delta^{18}O$ and $\delta^{13}C$ values of nodules are less negative and may be linked to fluids with heavier isotopic compositions. This interval indicates a complete change to fluids with lighter isotopic composition and probably carbon-poor meteoric water. Toward the top of the section the isotopic composition gradually returns to more heavier values, which is likely linked to mixing of meteoric and marine waters associated with the sea level rise that resulted in deposition of marine sediments above the paleosols at Esplugafreda (Fig. 2 and 6). We conclude that the variations in the lower and upper carbon isotope excursions at Esplugafreda can mainly be explained by the environmental effects of the climate warming events and more particularly the sources of CO_2 and isotopic compositions of water percolating through soil during deposition and nodule formation.

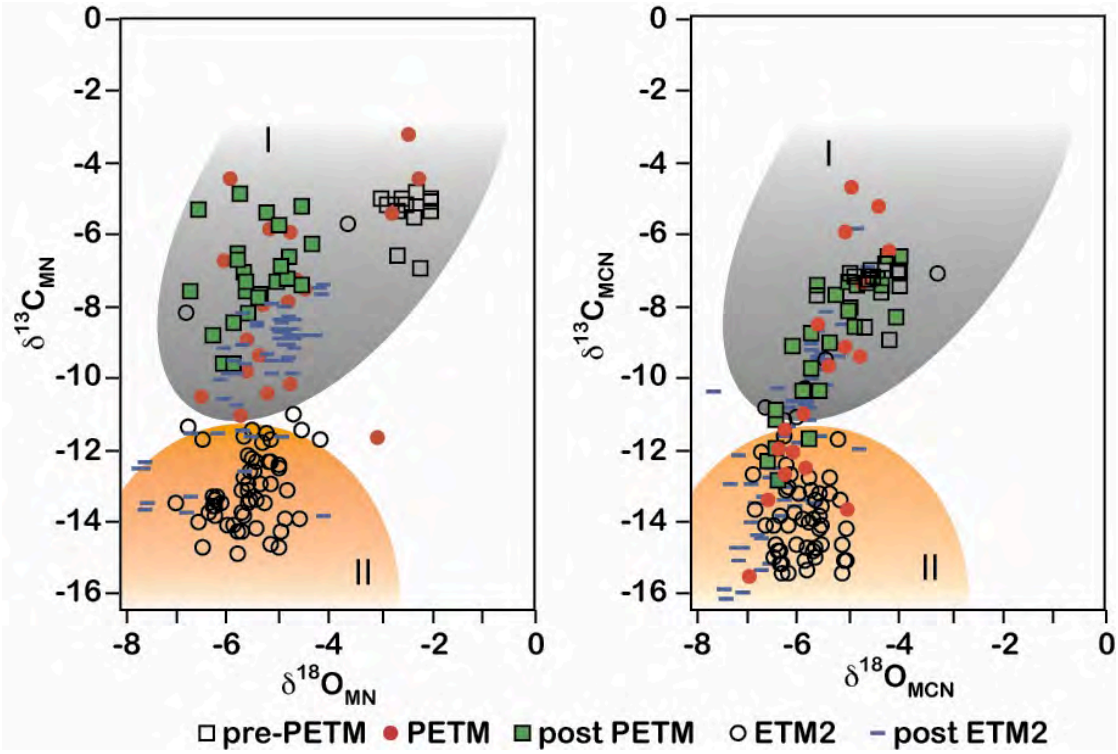

Figure 7. *$\delta^{13}C_{carb\ (MN\ and\ RCN)}$ vs. $\delta^{18}O_{carb\ (MN\ and\ CRN)}$ (fields after Cerling,1991). Field-I coastal plane, field of continental carbonate assuming admixture of atmospheric CO_2 with soil CO_2; Field-II Continental carbonate formation due to single source of CO_2.*

6.4. Paleotemperature fluctuations, evidence of rapid warming

Pedogenic carbonate nodules commonly form in strongly seasonal arid to sub-humid environments due to dissolution–precipitation reactions in the soil (Birkeland, 1999). The Ca^{2+} ions required for carbonate accumulation are provided by rainwater and dissolution of Ca-bearing minerals in the soil parent material (Monger and Wilding, 2006).

The $\delta^{18}O$ of carbonate depends upon the following factors: the $\delta^{18}O$ of seawater from which the carbonate is precipitated, the isotopic fractionation linked to thermodynamic processes, and diagenetic alteration (Faure, 1986). Diagenetic alteration of carbonates is dictated by meteoric water and recrystallization induced by the temperature increase with burial depth. Fresh

(meteoric) waters migrating through pore spaces in sedimentary rocks interact with rock constituents, which results in overprinting by the isotopically lighter meteoric water leaving a more depleted signal compared with primary deposition. When recrystallization occurs at higher temperatures, it can also slightly modify the original carbonate isotope composition.

Temperature-dependent fractionation is one of the most valuable aspects of oxygen isotopes due to its potential for enabling temperature approximations of ancient seawater (Veizer et al., 1999). At higher temperatures, the ^{18}O bond with carbon and hydrogen is more easily broken than at lower temperatures, thus there is less isotopic fractionation with increased temperature. For this reason, carbonates more readily incorporate ^{18}O into their structure at lower temperatures, resulting in heavier $\delta^{18}O$ carbonate values. Due to the potential alteration of $\delta^{18}O$, calculation of absolute temperatures maybe not be realistic. For this reason, this study avoids absolute temperatures in favor of temperature deviation from pre-PETM background mean temperature values.

At Esplugafreda, paleotemperature calculations based on the micritic nodules $\boldsymbol{\delta}^{18}O_{MN}$ and $\boldsymbol{\delta}^{18}O_{MCN}$ (Fig. 8) reveal an abrupt increase of 8 ^{o}C (compared to pre-PETM background mean values) coinciding with the PETM (lower $\boldsymbol{\delta}^{13}C_{carb}$ excursion) and a maximum increase of 7.6 ^{o}C coincident with the ETM2 (upper $\boldsymbol{\delta}^{13}C_{carb}$ excursion) just above the Claret conglomerate. The uppermost part of the section is marked by the same temperature fluctuations as observed from the micritic nodules. Thus, $\boldsymbol{\delta}^{18}O$ of micritic and recrystallized nodules reveal the abrupt PETM warming, though this is largely due to an unconformity, and the long-term $\boldsymbol{\delta}^{13}C_{carb}$ excursion is marked by a rapid and significant warming (+8°C).

6.5. **Clay mineralogy as paleoenvironmental proxies**

Clay minerals and their ratios (kaolinite/smectite and illite+chlorite/smectite+kaolinite) are good proxies to trace the climatic and weathering processes linked with environmental changes. (Chamley, 1989; Weaver, 1989). Deep burial diagenesis may affect clay minerals (e.g. smectite recrystallizes to illite-smectite mixed layers, kaolinite disappears) at depths **of** 2000 m in sediments other than permeable sandstones (Weaver, 1989; Chamley, 1998). At Esplugafreda where overlying Tertiary sediments do not exceed 1000 m, there is no significant deep burial diagenesis, as shown by the presence of smectite and the co-existence of smectite with high kaolinite throughout the section.

Weathering processes are the main trigger for clay mineral formation in soils (Millot, 1970). The origin of clay minerals in modern environments has been widely studied (Robert and Kennett, 1994; Thiry, 2000; Raigemborn et al., 2009). In general, illite and chlorite are indicators of mechanical erosion that affected parent rocks due to cool and dry climate conditions or as a consequence of pronounced topographic relief. Illite, chlorite and mixed layer illite/smectite are the dominant clay minerals of immature soils that have undergone little chemical weathering. On the other hand, smectite and kaolinite are typical of enhanced chemical weathering and soil formation under warm and wet conditions. In particular, kaolinite typically develops in tropical areas with high precipitation and high rates of chemical erosion. Smectite forms in weakly drained soils under warm seasonal climates with alternating wet and dry conditions. The kaolinite /smectite is therefore a useful proxy for humid versus arid conditions (Fig. 4). Kaolinite accumulation during the PETM interval may reflect the increasingly hot humid conditions and/or increasing detrital input linked to high precipitation (Fig. 4).

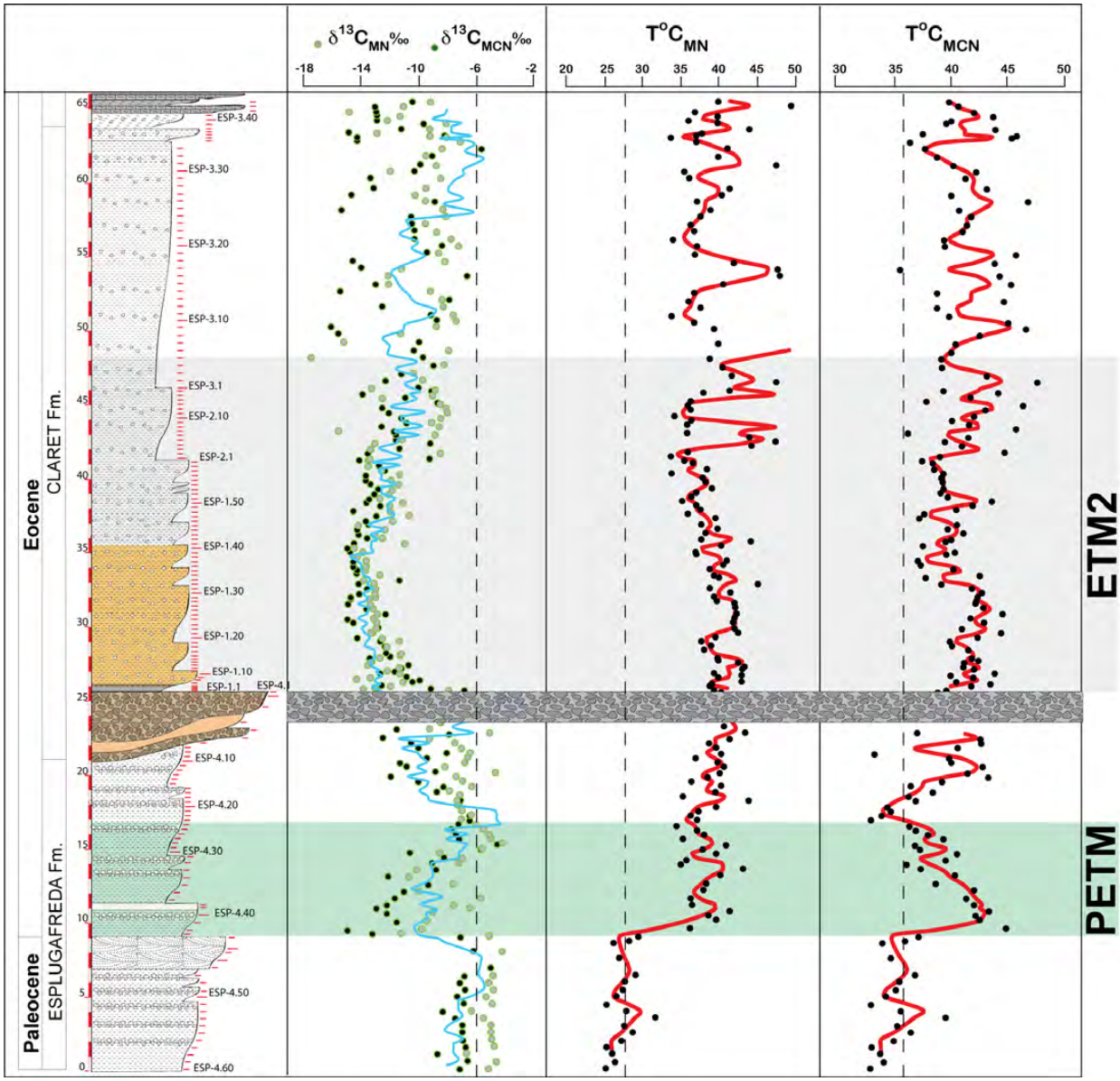

Figure 8. *Temperature anomaly profile calculated from $\delta^{18}O$ measured in micritic and recrystallized calcareous soil nodules of the Esplugafreda section. Dashed line marks pre-PETM temperature.*

However, this interval is characterized by fine sandstone characteristic of fluvial environments that developed under more humid conditions, whereas conglomerate intercalated with paleosols are present below and above.

The calcite nodules from Esplugafreda suggest a semi-arid environment with enhanced climate gradient (Cronholm and Schmitz, 2009). High kaolinite and low smectite contents observed in the PETM interval are associated with increased illite, illite-smectite and chlorite, which suggest increased physical weathering and runoff in the adjacent sedimentary sources enriched in kaolinite (Arostegi et al., 2011). This kaolinite discharge reflects reworking of older soils subject to intense erosion.

In the ETM2 interval, the decrease in the physical weathering index is linked to increased smectite and reflects enhanced aridity. Increasing aridity in the upper part of the section may

correspond to the removal of vegetation linked with a gradual increase in tectonic activity (initiation of the Pyrenean uplift, Vergés et al., 2002, Sinclair et al., 2005). In the uppermost part of the section the illite+chlorite/smectite+kaolinite ratio is constantly higher and suggests dominant physical weathering processes and/or increased tectonic activity (Fig. 4).

6. SUMMARY AND CONCLUSIONS

The Esplugafreda section represents one of the best terrestrial records for the Paleocene Eocene Thermal Maximum (PETM) and early Eocene Climatic Optimum, particularly ETM2.

The developed soil profile reflects denudation and erosion of older sediments from high land area developed during the early stage of Pyrenean orogeny and under arid conditions. The weathered is accumulated at Esplugafreda area that was relatively closer to the shoreline. Changed depositional regime during the early stage of the PETM events led to sharp change in sediment type from mudstone to calcarenite of lacustrine origin enriched with kaolinite indicates a climatic change from arid to more humid with a high runoff rate during the PETM. Above the PETM a short-life climate change took place from humid to slightly arid as observed by abundant soil nodules and smectite, the deposition of the Claret conglomerate reflecting extreme arid conditions. The ETM2 started above the Claret conglomerate with prevailed semi-arid conditions associated with low precipitation and high evaporation rate as indicated by scattered gypsum veinlet. Above the ETM2 $\boldsymbol{\delta}^{13}C$ shift the climate is fluctuated between semi-arid and humid conditions announcing the termination of the extreme early Eocene warming events.

Sum-up of the new findings at Esplugfreda section:

- Two carbon isotopic excursions are recognized based on micritic and recrystallized carbonate soil nodules. 1) The lower $\boldsymbol{\delta}^{13}C$ negative excursion represents the PETM with an abrupt onset due to an unconformity. 2) The upper gradual $\boldsymbol{\delta}^{13}C$ excursion represents the early Eocene climatic optimum (ETM2).
- The $\boldsymbol{\delta}^{13}C_{org}$ data recorded slightly heavy values at the PETM possibly due to oxidation of organic matter and/or deposition in an open soil system formed under more humid conditions where $\boldsymbol{\delta}^{13}C$ values reflect mixed CO_2 sources (atmospheric and oxidation of ancient organic matter). The $\boldsymbol{\delta}^{13}C_{org}$ linked to the ETM2 records more negative values, which could be linked to a closed soil system under more arid conditions.
- The $^{18}O/^{16}O$ paleothermometer shows a rapid increase of $8^{o}C$ at the P/E boundary marked by an unconformity. The ETM2 event shows a gradual increase in temperature from 6 to $8\ ^{o}C$ by the middle of the $\boldsymbol{\delta}^{13}C$ excursion.
- Soil and sediments at Esplugafreda area linked to two different weathering processes. During the PETM sediments are enriched with kaolinite from a detrital source due to denudation from the adjacent areas. The paleosols and sediments associated with the ETM2 event formed under semiarid conditions with weak chemical weathering producing high smectite. In contrast, the increased kaolinite content during the PETM reflects increasing precipitation and enhanced erosion of older kaolinite-rich soils and sediments.

ACKNOWLEDGEMENT

We thank T. Monnier and J. C. Lavanchy for technical support and carrying out different types of analyses, P. Vonlanthen for help during SEM analyses and Alfonso Pardo for assistance with

fieldwork. We gratefully acknowledge Prof. T. Vennemann for stimulating discussion during the preparation of this manuscript. Work was funded by the Egyptian Ministry of Higher Education (Mission No.001/013/104).

REFERENCES

Adatte, T., Stinnesback, W. & Keller, G. 1996. Lithostratigraphic and mineralogic correlations near K/T boundary clastc sediments in northern Mexico: Implication for origin and nature of deposition. *Geological Society of America*, special paper, 307, 211-226.

Alegret, L., Ortiz, S. & Molina E., 2009. Extinction and recovery of benthic foraminifera across the Paleocene–Eocene Thermal Maximum at the Alamedilla section (Southern Spain). *Palaeogeography, Palaeoclimatology, Palaeoecology*, 279, 186–200.

Arostegi, J., Baceta, J . I., Pujalte, V., And Carracedo, M. 2011. Late Cretaceous- Paleocene mid-latitude climates: inferences from clay mineralogy of contenetal- coastal sequences (Tremp-Graus area, southern Pyrenees, N Spain. Clay Minerals, v 46, pp.105–126

Birkeland PW (1999) 'Soils and geomorphology'. 3rd ed. (Oxford University Press: New York).

Bolle M.P. & Adatte T. (2001) Palaeocene_Early Eocene climatic evolution in the Tethyan realm: clay mineral evidence. Clay Minerals, 36, 249_261.

Bolle, M.-P., Tantawy, A.A., Pardo, A., Adatte, T., Burns, S.J. & Kassab, A., 2000. Climatic and environmental changes documented in the upper Paleocene to lower Eocene of Egypt. *Eclogae Geologicae Helvetiae*, 93, 33–51.

Bottinga, 1968

Bowen, G. J., Beerling, D. J., Koch, P. L., Zachos, J. C., and Quattlebaum, T., 2004, A humid climate state during the Paleocene–Eocene Thermal Maximum. Nature, v.432, p.495–499.

Bowen, G.J. and Zachos, J.C. 2010. Rapid carbon sequestration at the termination of the Palaeocene-Eocene Thermal Maximum. Nat. Geosci. 3:866–69

Cerling, T.E., 1984. The stable isotopic composition of modern soil carbonate and its relationship to climate. Earth and Planetary Science Letters 71, 229–240.

Cerling, T.E., 1991. Carbon dioxide in the atmosphere: evidence from Cenozoic and Mesozoic paleosols. American Journal of Science 291, 377–400.

Cerling, T.E., 1992. Use of carbon isotopes in paleosols as an indicator of the PCO2 of the paleoatmosphere. Global Biogeochemical Cycles 6, 307–314.

Chamley, H. 1989. Clay sedimentology, 623 pp. (*Springer-Verlag, Berlin*).

Chamley, H. 1998, Clay mineral sedimentation in the Ocean in Paquet, H., and Clauer, N., eds., *Soils and sediments (mineralogy and geochemistry)*. Berlin, Springer-Verlag, 269–302.

Cramer, B.S., Toggweiler, J.R., Wright, J.D., Katz, M.E., Miller, K.G., 2009. Ocean overturning since the Late Cretaceous: Inferences from a new benthic foraminiferal isotope compilation. Paleoceanography 24, PA4216. doi:10.1029/2008PA001683.

Cronholm, A and Schmitz, B. 2009. A test of kaolinite as proxy of global humidity changes during the initial Eocene Thermal Maximum, 55Ma. Lund Center for studies of Carbon Cycle and Climatic Interaction. LUCCI- Annual Report 2009/2010. Eds. Lindroth, A, Johansson, M., and Hellström, M

Dickens, G., 2001. Carbon addition and removal during the Late Palaeocene Thermal Maximum: basic theory with a preliminary treatment of the isotope record at ODP Site 1051, Blake Nose, in: D. Kroon, R.D. Norris, A. Klaus (Eds.), Western North Atlantic Palaeogene and Cretaceous Palaeoceanography, *Geological Society of London.* Special Pub. 183. 293–305.

Dickens., G.R. 2011 Down the Rabbit Hole: toward appropriate discussion of methane release from gas hydrate systems during the Paleocene-Eocene thermal maximum and other past hyperthermal events. lim. Past, 7, 831-846, 2011 doi:10.5194/cp-7-831-2011

Dickens, G. R., O'Neil, J. R., Rea, D. K. & Owen, R. M., 1995. Dissociation of oceanic methane hydrate as a cause of the carbon isotope excursion at the end of the Paleocene, *Paleoceanography*, 10, 965-971.

Domingo L., Lo´pez-Martı´nez N., Soler-Gijon R., & Grimes S. (2007) A multi-proxy geochemical investigation of the early Paleocene (Danian) continental palaeoclimate at the Fontllonga-3 site (South Central Pyrenees, Spain). Palaeogeography, Palaeoclimatology, Palaeoecology, 256, 71_85.

Ehleringer, J.R., Buchmann, N., Flannagan, L.B., 2000. Carbon isotope ratios in belowground carbon cycle processes. Ecological Applications 10, 412–422.

Ekart, D.D., Cerling, T.E., Montanez, I.P., Tabor, N.J., 1999. A 400 million year carbon isotope record of pedogenic carbonate: implications for paleoatmospheric carbon dioxide. American Journal of Science 299, 805–827.

Faure, G. 1986. Principles of Isotope Geology. New York: Wiley & Sons.

Gibson, T. G., Bybell, L. M., and Mason, D. B., 2000, Stratigraphic and climatic implications of clay mineral changes around the Paleocene/Eocene boundary of the northeastern US margin: Sedimentary Geology, v. 134, p. 65-92.

Handley, L., Pearson, P., McMillan, I.K. & Pancost, R.D. 2008. Large terrestrial and marine carbon and hydrogen isotope excursions in a new Paleocene/Eocene boundary section from Tanzania. *Earth and Planetary Science,* 275, 17–25.

Harrington, G.J., and Kemp, S. J. 2001. US Gulf Coast vegetation dynamics in the latest Palaeocene. Palaeogeography, Palaeoclimatology, Palaeoecology, 167, 1–21.

Higgins JA, and Schrag DP. 2006. Beyond methane: towards a theory for the Paleocene-Eocene Thermal Maximum. Earth Planet. Sci. Lett. 245:523–37

Katz, M. E., D. R. Katz, J. D. Wright, K. G. Miller, D. K. Pak, N. J. Shackleton, & E. Thomas (2003), Early Cenozoic benthic foraminiferal isotopes: Species reliability and interspecies correction factors, *Paleoceanography*, 18(2), 1024.

Katz, M., Cramer, B., Mountain, G., Katz S. & Miller, K. 2001. Uncorking The Bottle: What Triggered The Paleocene/Eocene Thermal Maximum Methane Release? *Paleoceanography*, 16, 6, 549–562

Kennett, J. P., Cannariato, K. G., Hendy, I. L. & Behl R. J. 2002. Methane Hydrates in Qua- ternary Climate Change: *The Clathrate Gun Hypothesis*, Special Publication,. 54, 224 pp., AGU, Washington, D. C.

Khozyem, H., Adatte, T., Spangenberg, E.J., Tantawy, A, Gerta Keller, K. (2013). Paleoenvironmental and climatic changes during the Paleocene-Eocene Thermal Maximum (PETM) at the Wadi Nukhul Section, Sinai, Egypt. Journal of the Geological Society, London, Vol. 170, pp. 341 –352. doi: 10.1144/jgs2012-046.

Klug, H.P. And Alexander, L.E. (1974) X-ray Difiaction Procedures for Polycrystalline and Amorphous Materials. 2nd Edition, Wiley-VCH, pp. 992

Koch, P.L., Clyde, W.C., Hepple, R.P., Fogel, M.L., Wing, S.L., Zachos, J.C., 2003. Carbon and oxygen isotope records from paleosols spanning the Paleocene–Eocene boundary, Bighorn Basin, Wyoming. In: Wing, S.L., Gingerich, P.D., Schmitz, B., Thomas, E. (eds.). Causes and Consequences of Globally Warm Climates in the Early Paleogene. The Geological Society of America, Special Paper, 369, 49-64.

Kübler, B., 1983. Dosage quantitatif des minéraux majeurs des roches sédimentaires par diffraction X. Cahier de l'Institut de Géologie de Neuchâtel,Série AX N°1.1 &1.2

Lopéz-Martínez, N., and Peláez-Campomanes, P., 1999, New mammals from south-central Pyrenees (Tremp Formation, Spain) and their bearing on late Paleocene marine-continental correlations: Bulletin de la Société Géologique de France, v. 170, p. 681–696.

Manners, H.R., Grimes, S.T., Sutton, P.A., Domingo, L., Leng, M.J., Twitchett, R.J., Hart, M.B., Dunkley Jones, T., Pancost, R.D., Duller, R., Lopez-Martinez, N. Magnitude and profile of organic carbon isotope records from the Paleocene-Eocene Thermal Maximum: Evidence from northern

Spain. EPSL. V. 376, pp.202-230

Miller k.G., Fairbanks R.G. and Mountain G.S. (1987) Tertiary oxygen isotope synthesis, sea level history, and continental margin erosion, Paleoceanography, 2, 1-19.

Millot, G. (1970) Geology of Clays. Springer, Berlin Heidelberg New York, 429 p.

Monger, H.C., Wilding, L.P., 2006. Inorganic carbon: composition and formation. In: Lal, R. (Ed.), Encyclopedia of Soil Science. Taylor & Francis, New York pp. 886–889.

Nadelhoffer, K.J., Fry, B., 1988. Controls on natural Nitrogen-15 and Carbon-13 abundance in forest soil organic matter. Soil Science Society of America Journal 52, 1633–1640.

Popp, B.N., Takigiku, R., Hayes, J.M., Louda, J.W., Baker, E.W., 1989, The post-Paleozoic chronology and mechanism of 13C depletion in primary marine organic matter. American Journal of Science v. 289, pp. 436–454.

Pujalte, V., and Schmitz, B., 2005, Revisión de la estratigrafía del Grupo Tremp "Garumniense", Cuenca de Tremp-Graus, Pirineos meridionales): Geogaceta, v. 38, p. 79–82.

Pujalte, V., Schmitz, B., Baceta, J.I., Orue-Etxebarria, X., Bernaola, G., Dinare`s-Turell, J., Payros, A., Apellaniz, E., Caballero, F., 2009a. Correlation of the Thanetian-Ilerdian turnover of larger foraminifera and the Paleocene-Eocene thermal maximum confirming evidence from the Campo area (Pyrenees, Spain). Geologica Acta 7, 161e175.

Pujalte, V., Baceta, J.I., Schmitz, B., Orue-Etxebarria, X., Payros, A., Bernaola, G., Apellaniz, E., Caballero, F., Robador, A., Serra-Kiel, J., Tosquella , J., 2009b. Redefiniton of the Ilerdian Stage (early Eocene). Geologica Acta, 7(1-2), 177-194.

Raigemborn, M., Brea, M., Zucol, A., and Matheos, S. 2009. Early Paleogene Climate at Mid Latitude In South America: Mineralogical and Paleobotanical Proxies From Continental Sequences in Golfo San Jorge Basin (Patagonia, Argentina) Geologica Acta, vol.7, nos 1-2, march-june 2009, 125-145. doi: 10.1344/105.000000269

Retallack G.J., Smith R.M.H., Ward P.D., 2003, Vertebrate extinction across the Permian-Triassic boundary in Karoo Basin, South Africa: Geological Society of America Bulletin, v. 115, p. 1133–1152, doi:10.1130/B25215.1

Revesz, K.M., Landwehr, J.M. And Keybl, J. (2001) Measurement of δ13C and δ18O isotope ratios of CaCO3 using a Thermoquest Finnigan GasBench II Delta Plus XL Continuous Flow Isotope Ratio Mass Spectrometer with application to Devils Hole Core DH-11 Calcite. U.S. Geological Survey Open-File-Report 01-257, 17 pp.

Robert, C., Kennett, J., 1994. Antartic subtropical humid episode at the Paleocene Eocene boundary: clay-mineral evidence. Geology, 22, 211-214.

Schmitz, B., and Pujalte, V., 2003, Sea-level, humidity, and land-erosion records across the initial Eocene thermal maximum from a continental-marine transect in northern Spain: Geology, v. 31, p. 689–692, doi: 10.1130/ G19527.1.

Schmitz, B., and Pujalte, V. 2007 Abrupt increase in seasonal extreme precipitation at the Paleocene-Eocene boundary. Geology 35; no. 3; p. 215–218; doi: 10.1130/G23261A.1; 3

Schmitz, B., Pujalte, V., Nun˜ez-Betelu, K., 2001. Climate and sea-level perturbations during the initial Eocene thermal maximum: Evidence from siliciclastic units in the Basque Basin (Ermua, Zumaia and Trabakua Pass). Palaeogeography, Palaeoclimatology, Palaeoecology 165, 299e320.

Schmitz, B., and Pujalte, V., 2003, Sea-level, humidity, and land-erosion records across the initial Eocene thermal maximum from a continental-marine transect in northern Spain: Geology, v. 31, p. 689–692, doi: 10.1130/ G19527.1. Schweizer et al., 1999

Sinclair, H. D., Gibson, M., Naylor, M., And Morris, R. G. 2005. Asymmetric Growth Of The Pyrenees Revealed Through Measurement And Modeling Of Orogenic Fluxes American Journal of Science, Vol. 305, May, 2005, P. 369 – 406]

Sluijs, A., Schouten, S., Pagani, M., Woltering, M., Brinkhuis, H., Sinninghe Damsté, J.S., Dickens, G.R., Huber, M., Reichart, G.J. & Stein, R. 2006. Subtropical Arctic Ocean temperatures during the Palaeocene/Eocene thermal maximum. *Nature,* 441, 610–613.

Smith, R.M.H., 1995. Changing fluvial environments across the Permian–Triassic boundary in the Karoo Basin, South Africa and possible causes of tetrapod extinctions. Palaeogeography, Palaeoclimatology, Palaeoecology 117, 81–104.

Speijer, R.P., Schmitz, B. & Van der Zwaan, G.J., 1997: Benthic foraminiferal extinction and repopulation in response to latest Paleocene Tethyan anoxia. *Geology* 25, 683–686.

Tabor, N.J., Yapp, C.J., Montanez, I.P., 2004. Goethite, calcite and organic matter from Permian and Triassic soils: carbon isotopes and CO2 concentrations. Geochimica et Cosmochimica Acta 68, 1503–1517.

Thiry, M., 2000. Paleoclimatic interpretation of clay minerals in marine deposits: an outlook from the continental origin. Earth Science Reviews, 49, 201-221. Tucker and Wright, 1990).

Veizer, J., Ala, D., Azmy, K., Bruckschen, P., Buhl, D., Bruhn, F., Carden, G.A.F., Diener, A., Ebneth, S., Godderis, Y., Jasper, T., Korte, C., Pawellek, F., Podlaha, O. and Strauss, H. (1999). "87Sr/86Sr, δ13C and δ18O evolution of Phanerozoic seawater". Chemical Geology 161: 59-88. DOI:10.1016/S0009-2541(99)00081-9.

Tucker, M.E., Wright, V.P., 1990. Carbonate Sedimentology. Blackwell. 482 pp.

Vergés, J., Fernàndez, M. & Martínez, A. 2002. The Pyrenean orogen: pre-, syn-, and post-collisional evolution. In: Rosenbaum, G. and Lister, G. S. 2002. Reconstruction of the evolution of the Alpine-Himalayan Orogen. Journal of the Virtual Explorer, 8, 55 - 74.

Weaver C.E. (1989) Clays, Muds, and Shales. Developments in Sedimentology, 44. Elsevier, Amsterdam.

Weijers, J.W.H., Schouten, S., Sluijs, A., Brinkhuis, H. & Sinninghe Damsté, J.S. 2007. Warm arctic continents during the Palaeocene–Eocene thermal maximum. *Earth Planet Science Letter*, 261, 230–238.

Westerhold T., Röhl U., McCarren H. & Zachos J. 2009. Latest on the absolute age of the Paleocene–Eocene Thermal Maximum (PETM): New insights from exact stratigraphic position of key ash layers + 19 and – 17. *Earth and Planetary Science Letters*. 287, Iss. 3–4, 412–419

Wilf, P., 2000. Late Paleocene–early Eocene climate changes in southwestern Wyoming: paleobotanical analysis. Geological Society of America Bulletin, 112(2), 292-307.

Zachos, J.C., Lohmann, K. C., Walker, J. C. G., and Wise, S. W., 1993, Abrupt Climate Change and Transient Climates in the Paleogene: A Marine Perspective. Journal of Geology, v. 100, p. 191-213.

Zachos, J. C., B. N. Opdyke, T. M. Quinn, C. E. Jones, and A. N. Halliday, 1999, Eocene-Oligocene Climate And Seawater 87Sr/86Sr : Is There A Link? Chemical Geology, special vol., The Chemical Evolution of the Oceans (ed. J. Veizer), v.161, p.165-180

Zachos, J.C., Röhl, U., Schellenberg, S.A., Sluijs, A., Hodell, D.A., Kelly, D.C., Thomas, E., Nicolo, M., Raffi, I., Lourens, L.J., McCarren, H. & Kroon, D., 2005. Rapid acidification of the ocean during the Paleocene–Eocene Thermal Maximum. *Science,* 308, 161–1611.

Zachos, J., Pagani, M., Sloan, L., Thomas, E. And Billups, K. (2001). Trends, rhythms, and aberrations in global climate 65 Ma to present. Science, v. 292, pp. 686–693.

Zachos, J.C., Schouten, S., Bohaty, S., Quattlebaum, T., Sluijs, A., Brinkhuis, H., Gibbs, S.J.& Bralower, T.J. 2006. Extreme warming of mid-latitude coastal ocean during the Paleocene–Eocene Thermal Maximum: inferences from TEX86 and isotope data. *Geology*, 34, 737–740.

CHAPTER VII

CONCLUSIONS

GENERAL CONCLUSIONS

The gradual increase in earth`s surface temperatures marking the transition from the late Paleocene to early Eocene (55.8±0.2Ma) represents an extraordinary warming event known as Paleocene Eocene Thermal Maximum (PETM). During this period, both marine and continental sedimentary records reveal evidences of massive injection of isotopically light carbon. The carbon dioxide injection from multiple potential sources may have triggered the global warming. The importance of the PETM studies is due to the fact that the PETM bears some striking resemblances with the human-caused climate change unfolding today. Most notably, the culprit behind it was a massive injection of heat trapping greenhouse gases into the atmosphere and oceans, comparable in volume to what our persistent burning of fossil fuels could deliver in coming centuries. The exact knowledge of what went on during the PETM could help us to foresee the future climate change. The response of the oceanic and continental environments to the PETM is different. The present work demonstrates that the PETM signal is preserved in marine and continental sedimentary records and underlines an injection of huge amount of CO_2 in both marine and atmospheric systems, but the response of the oceanic and continental environments is different. Our results based on a multiproxy approach show that many factors might have controlled these differences such as paleogeography, paleotopography, paleoenvironment, and paleodepth. The PETM coincides globally with extreme climatic fluctuations that terrestrial environments are therefore very likely to have recorded.

Our new findings obtained from the studied sections and their contribution to a better understanding of the tempo and timing of the Paleocene-Eocene thermal maximum are summarized below.

In the marine realm, our study of the Dababiya GSSP (Luxor, Egypt) provides important clues to understand the warming mechanism before, during and after the PETM events. Before the PETM event (topmost Paleocene), a gradual decreases in $\delta^{13}C_{Carb}$ and $\delta^{13}C_{org}$ are linked to a gradual warming, which may have resulted from the late Paleocene volcanism (North Atlantic magmatic province). This warming reaches to its maximum (at the P/E boundary) leading to the abrupt melting of the methane hydrates stored on continental shelf. Released methane hydrate is associated with some specific criteria such as: (1) Ocean acidification as observed by dissolution of carbonate minerals in Dababiya and elsewhere, (2) anoxic condition that could be linked to oxygen exhalation due to partial oxidation of methane, this anoxia is marked in Dababiya by a negative Ce- anomaly and the precipitation of individual euhedral pyrite crystals within the sediments, and (3) methane oxidation to CO_2 at the water/atmosphere interface. The excess of CO_2 in the atmosphere is acting as greenhouse gases and increases the weathering of silicate rocks. This period of increased weathering is observed at the Dababiya GSSP 60 cm above the P/E boundary and is characterized by high phyllosilicate contents including kaolinite, high CIA and CIW, high Ti, Cr and K input, $\delta^{13}C_{Carb}$ minimum value. The top of that interval is characterized by anoxic conditions marked by: (1) a negative Ce-anomaly, (2) enrichment of redox sensitive trace elements and their ratios (V, U, V/Cr, Ni/Co, V/V+Ni), (3) abundant pyrite framboids (>2μm in diameter), which indicate anoxic conditions within the water column, (4) increased productivity sensitive trace elements (Pb, Zn, Cu, Co and Mo) that could only be

enriched under anoxic conditions associated with high organic matter accumulation leading to the development of anoxic conditions fostering bacterial activity (Sulfur reducing bacteria and Cyanobacteria), and (6) $\delta^{13}C_{org}$ minimum recorded value.

The PETM recovery phase starts at the top of the interval marked by intense weathering (top of the upper anoxic level). The high nutrients input delivered into the ocean reactivates the biological pump leading to the re-establishment of more oxic and suitable conditions as indicated by the increase of productivity indicators such as Ba, P and both $\delta^{13}C_{Carb}$ and $\delta^{13}C_{org}$, which gradually return to the background values observed below the PETM interval.

The PETM at Dababiya GSSP can be therefore divided into four main phases: 1) pre-PETM gradual warming during the latest Paleocene), 2) PETM main phase with methane hydrate release, 3) environmental response (weathering and anoxia), and 4) finally, recovery phase.

At the Wadi Nukhul section, which is characterized by deeper environments, the PETM interval is characterized by: (1) an abrupt negative shift in $\delta^{13}C_{carb}$ followed by $\delta^{13}C_{org}$ shift which suggests a hiatus including the earliest Eocene, this short hiatus is observed in the basal part of the PETM at Wadi Nukhul and also in most of the PETM sections in Egypt except in the Dababiya GSSP (2) a strong and persistent decrease in $\delta^{15}N_{org}$ reflecting significant bacterial activity such as sulfur reducing and cyanobacteria activities as indicated by low N isotope and the presence of EPS-like structures within the PETM interval; (3) a significant increase in P_{tot} content just above the negative isotopes excursion, indicates increased primary productivity induced by increasing nutrients input linked with intense weathering period and prevailing of oligotrophic conditions, (4) a decrease in carbonate content which may be linked to the dissolution and/or the dilution of carbonate due to high detrital input, (5) the presence of small framboidal pyrite (less than 5µm) coincident with high V content and negative Mn*; all are strong evidences of rising dysoxic to suboxic conditions (6) The topmost Paleocene experienced a period of aridity as indicated by the presence of both sepiolite and palygorskite followed by significant increase in kaolinite contents triggered by humid climatic conditions; then returning to semi-arid conditions in the topmost CIE of the PETM interval.

Comparison between the deep and shallow marine records of the PETM events provides some important clues, which can be summarized as follows:

1- In both studied marine sections, the P/E boundary is placed at unconformity surface separates the uppermost Paleocene from the lowermost Eocene.

2- The abrupt negative $\delta^{13}C$ shift present in both Wadi Nukhul in Dababiya East sections reflects the absence of the lowermost Eocene in these two sections whereas the gradual $\delta^{13}C$ shift indicate a rather more complete PETM record at the northwest Dababiya section.

3- At Dababiya, two anoxic intervals are recorded, whereas only the upper one has be identified at Wadi Nukhul.

For better understanding of the response of terrestrial environments to the PETM events, two different terrestrial environments have been studied, (1) the lignite deposits linked to the early Eocene warming events in India, and (2) a paleosoils succession developed during the PETM event in Esplugafreda area, Spain.

The lignite sediments are deposited in west and northwest India (Rajasthan and Gujarat), in two different basins extending northwest southeast. These basins are developed on inherited topography of the rift basins formed during the early stage of India-Asia conversion. Five lignite mine sections have been sampled; similar sedimentary successions are observed in all the studied lignite mines, with two lignite intervals intercalated by marine sediments enriched in bivalves and benthic foraminifera.

The terrestrial origins of organic matter contents strengthen the accuracy of the $\delta^{13}C_{org}$ as a correlation proxy. $\delta^{13}C_{org}$ analyses indicate that two negative carbon isotopic excursions are recorded in all the studied sections. The lower $\delta^{13}C_{org}$ shift is an abrupt excursion, whereas the upper one is more gradual. Palynological results attribute the lower $\delta^{13}C_{org}$ excursion to the PETM event. Benthic foraminifera biostratigraphical data show that the upper $\delta^{13}C_{org}$ excursion which covers the middle part of the marine sediment interval up to the upper lignite interval is linked to the ETM2.

The establishment of wetland and related thick lignite deposits reflect the response of the continental environments to the PETM. This continental climatic shift towards more humid conditions probably led to the migration modern mammals northward following the move of the climatic belts. What remained uncertain is the timing and tempo of modern mammal origination and migration event, and whether it originated in Asia (China) or more specifically out of India.

The dispersal of mammals in Asia, Europe and North America predates or coincides with the PETM excursion. But our $\delta^{13}C_{org}$ based correlation demonstrate that it postdates the PETM in India, suggesting that modern mammals did not originate in India, but moved to India, possibly from Asia, well after the PETM event. The delayed appearance of early Eocene mammals in India suggests a barrier to dispersal that is likely linked to the timing of the India-Asia collision. This migration scenario waits further testing based on discovery of some Paleocene terrestrial mammal faunas on the Indian subcontinents.

In contrast, at Esplugafereda, Spain, the terrestrial environment reacted differently to the PETM warm climate by increased weathering, enhanced runoff and formation of thick paleosoil accumulations enriched in carbonate nodules (*Microcodium* like). Two carbon isotopic excursions are recognized detected in both micritic and recrystallized carbonate soil nodules. Similar to India, the lower $\boldsymbol{\delta}^{13}C$ negative excursion is attributed to the PETM, characterized by an abrupt onset amplified by a sharp unconformity, and, the upper gradual $\boldsymbol{\delta}^{13}C$ excursion represents the early Eocene climatic optimum (ETM2).

The $\boldsymbol{\delta}^{13}C_{org}$ data recorded slightly heavy values at the PETM possibly due to oxidation of organic matter and/or deposition in an open soil system formed under more humid conditions where $\boldsymbol{\delta}^{13}C$ values reflect mixed CO_2 sources (atmospheric and oxidation of ancient organic matter). The $\boldsymbol{\delta}^{13}C_{org}$ linked to the ETM2 shows more negative values, which could be linked to a closed soil system under more arid conditions. The $^{18}O/^{16}O$ paleothermometer shows a rapid increase of $8^{o}C$ at the P/E boundary whereas the ETM2 event shows a gradual increase in temperature from 6 to $8\ ^{o}C$ reaching its maximum in the middle part of the $\boldsymbol{\delta}^{13}C$ excursion.

At Esplugafreda, paleosoils include older sediments from significant relief developed during the early stage of Pyrenean orogeny under arid conditions. The early stage of the PETM coincides with a sharp change in sediment type from mudstone to calcarenite of lacustrine and

fluviatil origin with high kaolinite contents reflecting a climatic change from arid to more humid conditions. Above the PETM, climate evolves rapidly from humid to slightly arid as indicated by the presence of abundant soil nodules and high smectite contents, then to extreme aridity, during the deposition of the Claret conglomerate. The ETM2 starts above the Claret conglomerate under prevailing semi-arid conditions marked by low precipitation and high evaporation rate underlined by scattered gypsum veinlets, and moving of the depositional center far from the shoreline results in a single fluid source (continental) acting in the soil nodule formation as deduced from both $\boldsymbol{\delta}^{18}O$ and $\boldsymbol{\delta}^{13}C$ extreme negative values. Above the ETM2, the climate is fluctuating between semi-arid and humid conditions anticipating the termination of the extreme early Eocene warming events.

In conclusion, this study shows that the response of the oceanic and continental environments to the PETM is different and may be controlled by many factors such as paleogeography, paleoenvironment, and paleodepth. The carbon isotope profiles in both marine and terrestrial environments are identical for both PETM and ETM2, and reveal similarity in the perturbation of carbon cycle.

The PETM represents therefore one of the best analogue of the current warming in term of amplitude and effect, even if the current warming is ten times faster than the PETM.

Future challenges

The PETM events still need more investigations with a special focus on the amplitude of the warming and the causes of the termination of the PETM. Such investigations would include:

a) the use of carbonate clumped isotope technology on the pedogenic carbonate nodules and marine carbonate (foraminifera and nannofossils) deposited during the PETM events. This may bring important clues for a better constraint on the absolute temperatures and intensity of warming during the PETM, and new indications on the difference in terms of warming between the terrestrial and marine realm. By using clumped isotopes and comparing with existing $^{16}O/^{18}O$ records, we can precise and ascertain the source and amplitude of the PETM warming and correlate the paleoclimatic and paleoenvironmental changes linked with these events. The comparison of the response of both marine and terrestrial environments to that abrupt warming event based on clumped isotopes measured on soil calcareous nodules and marine biogenic $CaCO_3$ (foraminifera and nannofossils) may bring crucial clues to understand this exceptional perturbation of the carbon cycle.

b) Study the nature of anoxic intervals linked to the PETM event and the mechanisms leading to the ocean recovery, which played a crucial role in the termination of the PETM event. Unconventional isotope proxies such $^{187}Os/^{188}Os$, $\boldsymbol{\delta}^{6}Li$ and $\boldsymbol{\delta}^{98/95}Mo$ Mo would provide important informations on the nature and intensity of these anoxic episodes and their links with weathering processes. The general P increase observed right above the second anoxia interval, which is correlateable over a long distance (e.g. Sinai, Luxor) is also an important clue to understand the PETM recovery. P speciation would be helpful to know what kind of phosphorus is involved (e.g. authigenic, detrital, linked to organic matter).

APPENDIX - I

AFFILIATED PAPERS

1. **Biostratigraphy and Foramiferal Paleoecology of the Eocene Naredi Formation, Kutch, Gujarat, India.**

2. **Chicxulub Impact Spherules in the NW to SW Atlantic: Age constraints and KTB Hiatus.**

3. **Stratigraphy of the Cenomanian-Turonian Oceanic Anoxic vent OAE2 in shallow shelf sequences of NE Egypt.**

4. **Mineralogy and Geochemistry of the Numidian Formation (Central-Northern Sicily): intra-formation variability and provenance evaluation.**

5. **Late Maastrichtian-Early Danian High-Stress Environments And Delayed Recovery Linked To Deccan Volcanism.**

6. **Atmospheric halogen and acid rains during the main phase of 1 Deccan eruptions: Magnetic and mineral evidence.**

BIOSTRATIGRAPHY AND FORAMIFERAL PALEOECOLOGY OF THE EARLY EOCENE NAREDI FORMATION, SW KUTCH, INDIA[1]

Abstract. The Naredi Formation in southwestern Kutch overlies the last Deccan Trap deposited during the early Paleocene. The lower part of the Naredi Fm (2.8-4.2 m from base) is of early Eocene (Ypresian) age (SBZ8, E4) based on larger foaminifera and rare planktic foraminifera, whereas the upper part (9.3-11 m, including the *Assilina* limestone) is of late early Eocene age (SBZ11, E6). There is no age control for the basal 0-2.8 m and between 4.2-9.3 m because microfossils are rare or absent. Small benthic and rare planktic foraminifera are common in three short intervals and indicate deposition in a brackish to normal marine inner shelf environment (SBZ8, E4), brackish environment (middle of section, no age control) and inner shelf to marginal marine environment (SBZ11, E6). Two phases of marine transgressions can be identified with the maximum transgressions in each phase coincident with the lower and upper foraminiferal assemblages. A paleosoil indicated by root traces and burrows (5.9 m) represents a regression and possibly sequence boundary.

This study is dedicated to Dr. Lukas Hottinger (1933-2011), who passed away before this study was completed. Weremember him for his invaluable contributions to the biostratigraphy, taxonomy and paleoecology of larger Foraminifera and his generous ever cheerful willingness to teach, advise and share his immense knowledge and expertise. We will miss him

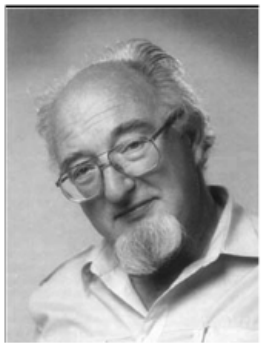

INTRODUCTION

The last Deccan Traps of the early Paleocene are exposed along the base of the Kadi River near the village of Nareda (Lat: N23°34.602'; Long: E68°38.628') in the Kutch District, State of Gujarat in western India (Fig. 1). At this locality about 11 m of predominantly argillaceous sediments disconformably overlie the Deccan Traps and are topped by a limestone rich in *Assilina* species. These sediments have been classified as the Naredi Formation (Biswas and Raju, 1972; Biswas, 1992) and the Kadi River area is known as the Naredi type locality. Sediments consist of shallow marine deposits that are intermittently fossiliferous containing larger foraminifera (e.g., Biswas, 1992; Raju et al., 1970; Punekar et al., 2010; Saraswati et al., 2000, 2012), small benthic and rare planktic foraminifera (Tandon et al., 1980; Jauhri and Vimal. 1978), calcareous nannofossils (Singh and Singh, 1991; Jafar and Rai, 1994; Saravanan, 2007). Microvertebrate fossils include teeth, scales and otoliths of shallow marine fishes including

[1] ***Gerta Keller, Hassan Khozyem, Thierry Adatte (2013). Biostratigraphy and Foramiferal Paleoecology of the Eocene Naredi Formation, Kutch, Gujarat, India. In Malarkodi, N., Keller, G., Reddy, A.N., and Jaiprakash, B.C. (eds.) Ecology, Biodiversity and Global Bioevents, Geological Society of India, Special Publication , Springer Verlag, Vol.1, p. 58-92***

sharks, rays and bony fishes, found together with the freshwater gar fish (*Lepisosteus*), and aquatic snakes (collections made by S. Bajpai). Despite all these studies a precise age has remained elusive, although most workers suggest an early Eocene (early Ypresian) age based on the first calcareous fossil assemblages above the basalt. A recent study on dinoflagellates (Garg et al., 2011) confirmed an early Ypresian age for the Naredi section.

This study contributes to the biostratigraphy and paleoecology of the Naredi Fm. based on rare planktic, abundant small and larger benthic foraminifera and stable isotopes. The main objectives of this study include: a) analysis of planktic foraminifera to obtain good age control – this objective was not fully reached because planktic foraminifera are very rare; b) analysis of small benthic foraminifera to determine their potential for age control and paleoecological interpretations; c) examine larger benthic foraminifera as age indicators and correlate these to small benthic and planktic assemblages; and d) correlate and integrate age control of microfossil assemblages with the stable $d^{13}C$ isotope curves of carbonate and organic carbon to obtain better age constraints of the Naredi section. A companion study by Khozyem et al. (this vol.) details the lithology, mineralogy, major and trace elements and stable isotopes of the same outcrop and the same sample set. Latter was also traced to nearby localities. The trenched section was sampled at 10 cm intervals spanning a sequence of 11 m. Samples were processed for microfossils by standard methods (Keller et al., 1995) and washed through a 63 mm screen. Benthic foraminifera were observed primarily in the 63-100 um size fraction and assemblages tend to be dominated by one or two species. Preservation is very good and shells are not recrystallized. All major species are illustrated by Scanning electron microscopy (SEM; Tescan Mira/LMU) based on gold and carbon coated specimens.

Figure 1: *Geological map of the Naredi area with Location of the studied Naredi section (modified after Garg et al., 2011).*

1. METHODS

The Naredi Fm was sampled along the Kadi River at the type locality. In order to expose fresh rock and avoid contamination of sediments, a section was trenched from the base of the limestone layer near the top of the outcrop down to the river base and Deccan Traps.

Carbon isotope ($\delta^{13}C_{carb}$) analyses were conducted on bivalves, bones and teeth with a Thermo Fisher Scientific (Bremen, Germany) GasBench II preparation device interfaced to a Thermo Fisher Scientific Delta Plus XL continuous flow isotope ratio mass spectrometer (IRMS) (Revesz et al., 2001). Analytical uncertainty (2σ), monitored by replicate analyses of the international calcite standard NBS-19 and the laboratory standards Carrara Marble and Binn Dolomite, are no greater than ± 0.05‰ for $\delta^{13}C_{carb}$. Organic carbon isotope analyses was performed on decarbonated and oven-dried bulk sediment samples by flash combustion on a Carlo Erba 1108 elemental analyser connected to a Thermo Fisher Scientific Delta V isotope ratio mass spectrometer that was operated in the continuous helium flow. The $\delta^{13}C_{org}$ values are reported relative to VPDB. The reproducibility was better than 0.1‰ (1σ). Stable isotope results are fully discussed in Khozyem et al. (this vol.).

2. LITHOLOGY

At the Naredi Formation type locality Biswas (1992) subdivided sediments into three main members: (1) Gypsiferous Shale Member at the base with grey, brown and olive green glauconitic claystones and shales, including gypsum, limonite and siderite concretions; (2) *Assilina* Limestone Member of bedded limestone and yellow-grey marls rich in *Assilina* shells; (3) Ferruginous Claystone Member at the top with grey-brown iron-rich claystone. This study examined the lower two members of the Naredi Fm. Figure 2 shows our detailed outcrop observations of the lithology in the lower two members of the Naredi Fm. In general, sediments consist of glauconitic and phosphatic claystone and siltstones with intervals rich in bivalves, oysters and larger foraminifera. Naredi Fm. sediments unconformably overlie a paleosoil that developed at the top of the weathered basalt that represents the last phase of Deccan volcanism in the early Paleocene. At the base is a grey-green silty claystone rich in fossils (~0.3 m) followed by a green-brown to red silty claystone with only rare fossils (up to 1.1 m, Fig. 2). Sediments between 1.1 m to 4.2 m consist of dark grey-green to olive-green claystones and silty claystone with pyrite nodules at the base and intermittently fossil-rich. Overlying this interval is a pale brown silty claystone (4.2-4.5 m) followed by 1 m of dark brown fissile, silty claystone with gypsum veins and iron oxide. A 30 cm thick red-brown clayey siltstone with burrows and roots at the top (5.5-5.8 m) marks a paleosoil and unconformity (Fig. 2). This interval likely represents a non-deposition and/or erosion surface and may correspond to a sequence boundary. Above the root-bearing (paleosoil) horizon is a 50 cm thick red-green silty claystone devoid of fossils but with iron concretions. This interval is overlain by yellow-green and red-brown silty claystone to clayey siltstone layers also devoid of fossils and followed by a limestone concretions level at 6.8 m. The overlying laminated yellow silty claystone contains oysters and dwarfed foraminifera indicating a return to marginal marine conditions. From 7.8 m to 9.0 m sediments consist of intercalated grey to red-brown silty claystones devoid of fossils, followed by glauconitic claystone. Between 9.5 to 10.2 m silty claystones contain common macro- and microfossils marking a return to marginal marine conditions. At the top of the sampled interval is the (*Assilina*) limestone rich in larger foraminifera (mostly nummulites) (Fig. 2).

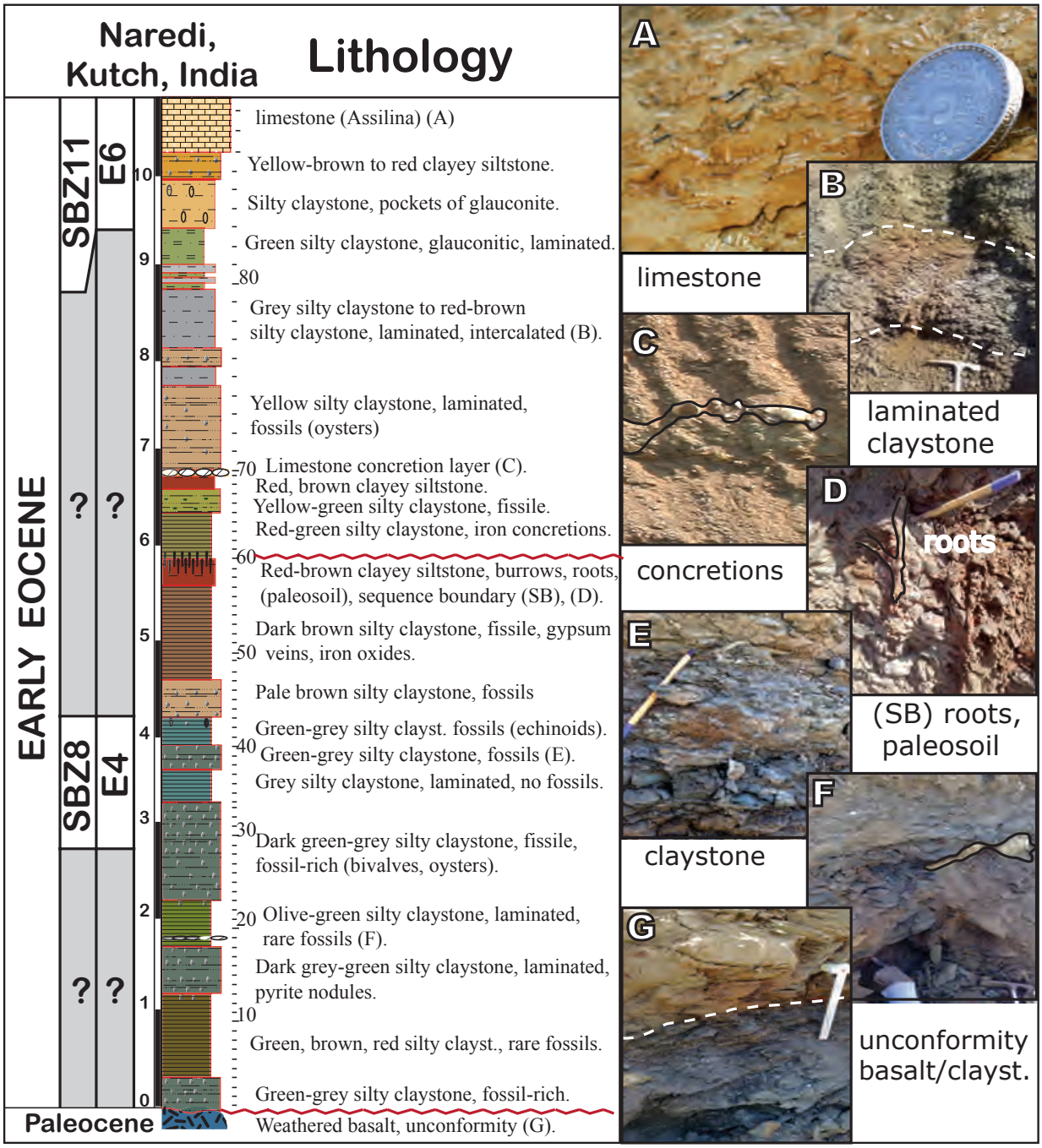

Figure 2: *Lithostratigraphy, description of lithology and photo illustrations of key lithologic horizons of the studied Naredi section.*

3. BIOSTRATIGRAPHY

At the type locality of the Naredi Formation marine microfossil bearing horizons with good assemblages are restricted to three short intervals (2.8-4.1 m, 6.5-7.2 m, 9.8-11 m), with an additional two intervals with larger foraminifera (1.5 m, 4.5 m) (Fig. 3). Macrofossils (primarily bivalves) are distributed more broadly through the section. Foraminiferal assemblages consist mainly of small (63-100 mm) shallow water benthic species. Larger benthic species are common particularly at the top and bottom fosssiliferous intervals. Planktic foraminifera are very rare with just a few mostly long-ranging species, which makes age determination difficult. For this reason we integrate biostratigraphic information from planktic, small and larger benthic foraminifera with the stable isotopes ($\delta^{13}C_{org}$, $\delta^{13}C_{biv+bones}$) in order to obtain a relative age assignment for the Naredi Formation.

3.1. Larger Benthic Foraminifera

Larger benthic foraminifera are common in the three fossiliferous intervals of the Naredi section with rare and mostly dwarfed specimens in two other intervals (Fig. 3). Samples bearing larger foraminifera were sent to the late Dr. Lukas Hottinger for analysis. Because Dr. Hottinger passed away before this study was completed the correspondence is reported here. Hottinger (Jan. 26, 2007) reported: “The nummulites sent by Thierry Adatte contain *Nummulites globulus nanus* Schaub, 1981. This species comes from SBZ8, which corresponds to planktic foraminiferal zone P6 (= E3-E4, Fig. 4). More Details are available in Serra-Kiel et al. (1998). It could have a somewhat broader range because of its extreme habitat, which is not represented at all ages in Europe. The nummulite population is monospecific with only a San-partner of an odd pair [suggesting] much environmental stress: deep and/or dark with lots of turbidity, fine grained mud with some nutrients (some shells are filled with pyrite), which indicates that estuaries are not too far away.” *Nummulites globulus nanus* is illustrated in Figure 5. Hottinger noted: “This species is exceptionally small and therefore escapes notice when associated to a "normal" nummulite assemblage. So far, it was described only from the Tremp area in the Pyrenees where it marks SBZ8 (Ypresian, middle Ilerdian) according to Serra-Kiel et al. (1998). There might be another, larger species but I have only a single specimen that I hesitate to cleave.” When asked whether the small, dwarfed nummulites reflect high stress environmental conditions similar to planktic and benthic foraminifera in this section and elsewhere, Hottinger answered (Jan. 24, 2008): “Yes, I think so. However, there are different kinds of stress. These small sizes seem to be depth-related. I have the same problem with assilinids in the Gulf of Aqaba at the lower end of the photic zone. There I do not know if I have to consider the dwarfed forms as separate species or not. *Nummulites nanus* in the Tremp basin is also in the deepest position where larger forams are still present. The relation with symbiosis (stress by low light levels) remains unclear and in my view improbable. I would rather see a shift in reproduction strategy away from seasonal dependence”. Based on Hottinger’s analysis the larger foraminiferal assemblage of the lower part of the Naredi section indicate an early Eocene SBZ8 age, which is equivalent to planktic foraminiferal zone E4 (=P6b) as shown in the summary of zonations in Figure 4. Hottinger’s age determination and faunal observations are in good agreement with studies by Saraswati et al. (2000, 2012), though Shukla (2008) suggested a late Paleocene age. Saraswati et al. (2012) report larger foraminifera, particularly *Nummulites globulus nanus* from the basal 4 m of the Naredi section overlying the basalts and assigned this interval to SBZ8, which is equivalent to the interval analyzed by Hottinger as SBZ8 (Figs. 3 & 4).

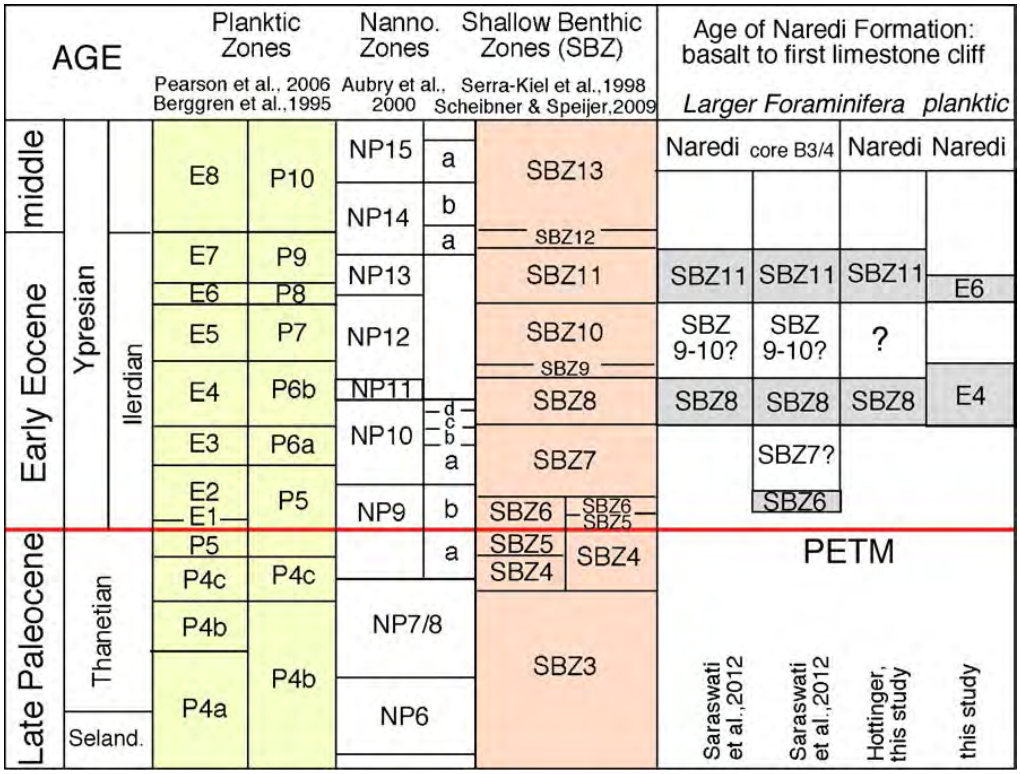

Figure 4. *Correlation of late Paleocene to middle Eocene biozones based on planktic foraminifera (after Pearson et al., 2006; Berggern et al., 1995), nannofossils (Aubry et al., 2000) and larger shallow water benthic foraminifera (Serra-Kiel et al., 1998 and Scheibner et al., 2005), and the age of Naredi Formation based on larger foraminifera (Sarawati et al., 2012) and this study.*

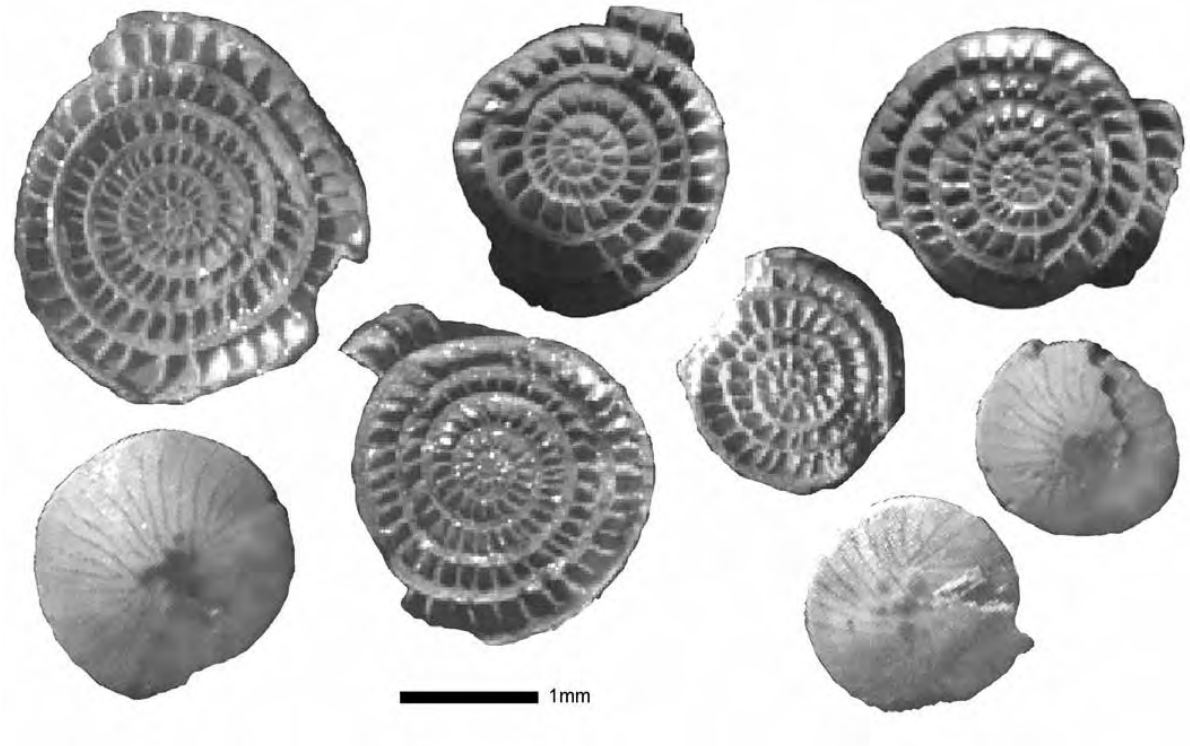

Figure 5: *Micrographs of the external views and equatorial sections of monospecific Nummulites globulusnanus.*

Above this interval Saraswati et al. (2012) report a generally barren zone questionably interpreted as SBZ9-10 containing a short interval with only small foraminifera. At this level we observed dwarfed foraminifera and Hottinger noted "exceptionally small" *Nummulites*. The age of this assemblage is unknown. Near the top of the section, Hottinger, Punekar and Saraswati (2010) and Saraswati et al. (2012) observed a diverse assemblage of *Nummulites burdigalensis cantabricus, Assilina laxispira, A. spinosa and Lockhartia,* which was assigned to zone SBZ11, equivalent to planktic foraminifera zones E6 to E7 (formerly P8-P9) and hence Ypresion (uppermost Ilerdian, Fig. 4). Based on larger foraminifera the 11 m overlying the Deccan basalt at the Naredi type locality is of (early to middle) Ypresian age.

In a borehole about 10 km to the southwest of the Naredi section, Saraswati et al. (2012) recovered a considerably expanded sequence between the basalt and the limestone cliff with similar assemblages and barren intervals as at Naredi. The first 9 m above the basalt are identified as SBZ6 (= lower part of E2, Fig. 4). This is followed by a 14 m interval with rare or no foraminifera, which they questionably identify as SBZ7? At 25 m above the basalt is a second *Nummulites* horizon attributed to SBZ8 (Saraswati et al., 2012). The upper part with the limestone layer has a diverse assemblage of larger foraminifera indicative of SBZ11, similar to Naredi. This suggests that the lower part of the borehole section (SBZ6-SBZ7?) is basal Ypresion in age. This interval appears to be missing at the Naredi outcrop we examined.

3.2. Planktic Foraminifera

Planktic foraminifera are rare, except for chiloguembelinids, and all are present primarily at the base and top of the section. Just five species were identified and all but one are long ranging: *Acarinina quetra* (zones E3-E6), *Acarninia esnaensis* (zones P4-E5), *Chiloguembelina crinita* (early Paleocene to E8), *Chiloguembelina trinitatensis* (zones P5-E3), *Subbotina patagonica* (zones P4-E8) (ranges from Pearson et al., 2006). These rare planktic species can provide only tentative age determinations. The presence of *A. quetra* near the top of the section indicates an age no younger than E6, correlative with the larger benthic zone SBZ11 (Figs. 3 & 4). At the base of the section the presence of *Acarinina esnaensis* suggests an early Eocene age possibly of zone E4 or lower E5, but an older late Paleocene (P4-5) age cannot be excluded. *Chiloguembelina trinitatensis* with a reported upper range limit of zone E3 (Pearson et al., 2006) is relatively common at the top of the section, which suggests that this stress-tolerant species has a longer range than previously reported.

No triserial planktics were observed although they have been reported in Chattoraj et al. (2009) and Saraswati et al. (2000, 2012). Tandon et al. (1980) reported *Globorotalia trinitatensis, G. inconstans, G. rex* and *G. prolata* from the lower part of the Naredi Fm. This assemblage has not been observed to date by other workers, including this team.

4. PALEOENVIRONMENT

4.1. Small Benthic Foraminifera

Small benthic species are generally long ranging and therefore not good age indicators. However, they are excellent environmental proxies as species adapt to changes in sea level, salinity, oxygen, nutrients and substrate. In the Naredi section small benthic foraminifera are relatively common and well preserved in the small size fraction (63-100 mm) in the same three horizons as larger foraminifera and separated by long barren zones (Fig. 3). These barren zones

are partly due to mechanical corrosion, which is most severe in the glauconitic and phosphatic intervals. Dissolution effects in the clayey layers could be related to outcrop weathering. Species assemblages are generally of low diversity with a total of just 18 species. All species have small or dwarfed morphologies characteristic of high stress shallow water environments.

Species identification can be difficult because few well-illustrated records of very small species (<100 mm) in shallow water environments exist. Publications on small benthic species from the Naredi section or other Paleocene-Eocene shallow water environments in India are rare (e.g., Punekar and Saraswati, 2010). A study of shallow water benthic foraminifera by Murray and Wright (1974) based on Eocene sections from the Paris basins, the English Channel and Hampshire, England, was most helpful. Many of the species in the Naredi section are also present in Eocene assemblages of these European sequences, including larger foraminifera suggesting similar environments. We used Murray and Wright (1974) as well as Murray et al. (1989) as guide to the shallow water assemblages from Naredi. All common species from the Naredi section are illustrated in Figures 6-8 and their occurrences and relative abundances recorded and grouped based on known environmental affinities from brackish lagoonal to normal marine inner shelf and marginal marine environments (Fig. 3).

4.2. Paleoecology

Chattoraj et al. (2009, see also Raju, 2008; Khozyem this vol.) interpreted deposition of the Naredi Fm. in a subtidal setting with barren intervals representing supratidal settings. In such shallow water environments faunal assemblages tend to be highly stressed due to fluctuations in salinity, oxygen and nutrients. Species generally adapt to high stress conditions by dwarfing, early sexual maturation and rapid reproduction with many offspring improving chances for survival. Only few species adapt successfully which leads to low diversity assemblages dominated by one or two species. At Naredi the most dominant species are *Ammonia aff. beccarii* and *Protelphidium* sp. 4 (Fig. 3). Common species include *Cibicidoides succedens, Astigerina bartoniana, Pararotalia curryi, Pijpersia coronaeformis and Brizalina.* Different assemblages dominated the fossil-bearing horizons suggesting changing environmental conditions. In this study species associations are grouped into brackish lagoonal, brackish to normal marine inner shelf and marginal marine inner shelf environments (Fig. 3) based on known and inferred affinities from recent analogs and particularly from the extensive Paleogene studies of shallow water environments by Murray and Wright (1974) and Murray et al., (1989).

Ammonia parkinsoniana morphotype assemblage:

Ammonia parkinsoniana (*A. beccarii parkinsonia* of some authors) is a well-known opportunistic species (simiar to *A. beccarii*) that thrives in shallow saline to brackish environments (e.g., Colburn and Baskin 1998; Almogi-Labin et al., 1995) and may live in surface sediments, on hard substrates or attached to macrobenthos in brackish marine or nearby rivers and lakes (Takata et al., 2009).

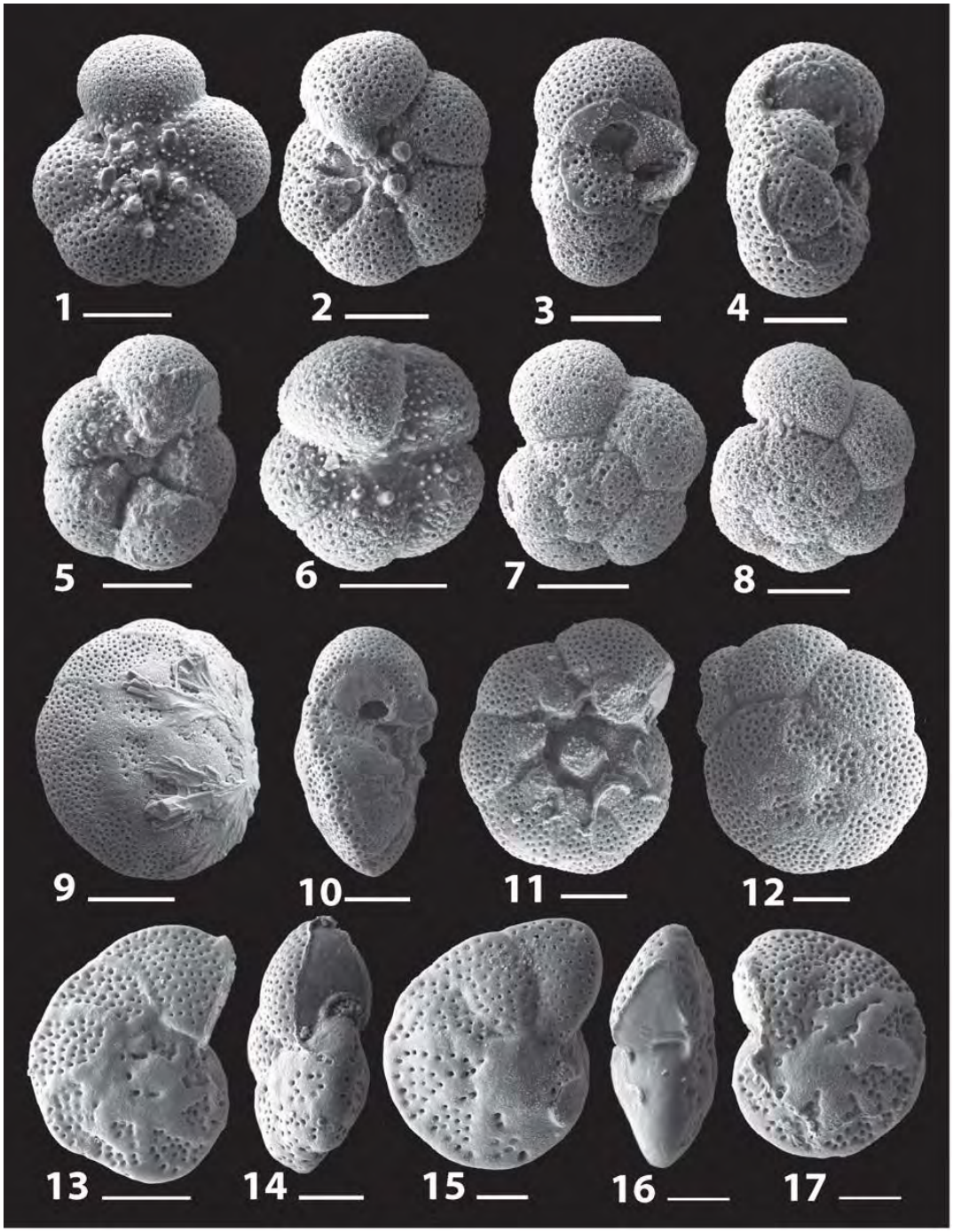

Figure 6. *Benthic foraminifera from the Naredi section of Kutch, India. Scale bar=50 mm. 1-5. Protelphidium sp. 4 of Murray and Wright 1974, Naredi sample NE-32. Description: test planispiral, inflated chambers, rounded, lobate periphery, 5- 6 chambers in Naredi specimens, depressed sutures, umbilicus ornamented with tubercules, aperture interiomarginal row of pores; wall coarsely perforate except on apertural face. Plaeoecology; brackish to normal marine, estuarine and lagoonal .6-8. Protelphidium sp. Naredi sample NE-32. Similar to sp. 4, but 4-5 chambers, less ornamented umbilicus, aperture interiomarginal slit. Paleoecology: brackish to normal marine, shelf, muddy substate. 9-12. Ammonia parkinsonia (d'Orbigny), sample NE-32. 13-14. Cibicides alleni (Pummer), sample NE-32. Paleoecology: marine middle to inner shelf; often associated with current activity.15-17. Cibicides succedens Brotzen, sample NE-32. Paleoecology: marginal marine to middle shelf, may be tolerant of poorly aerated mud bottom.*

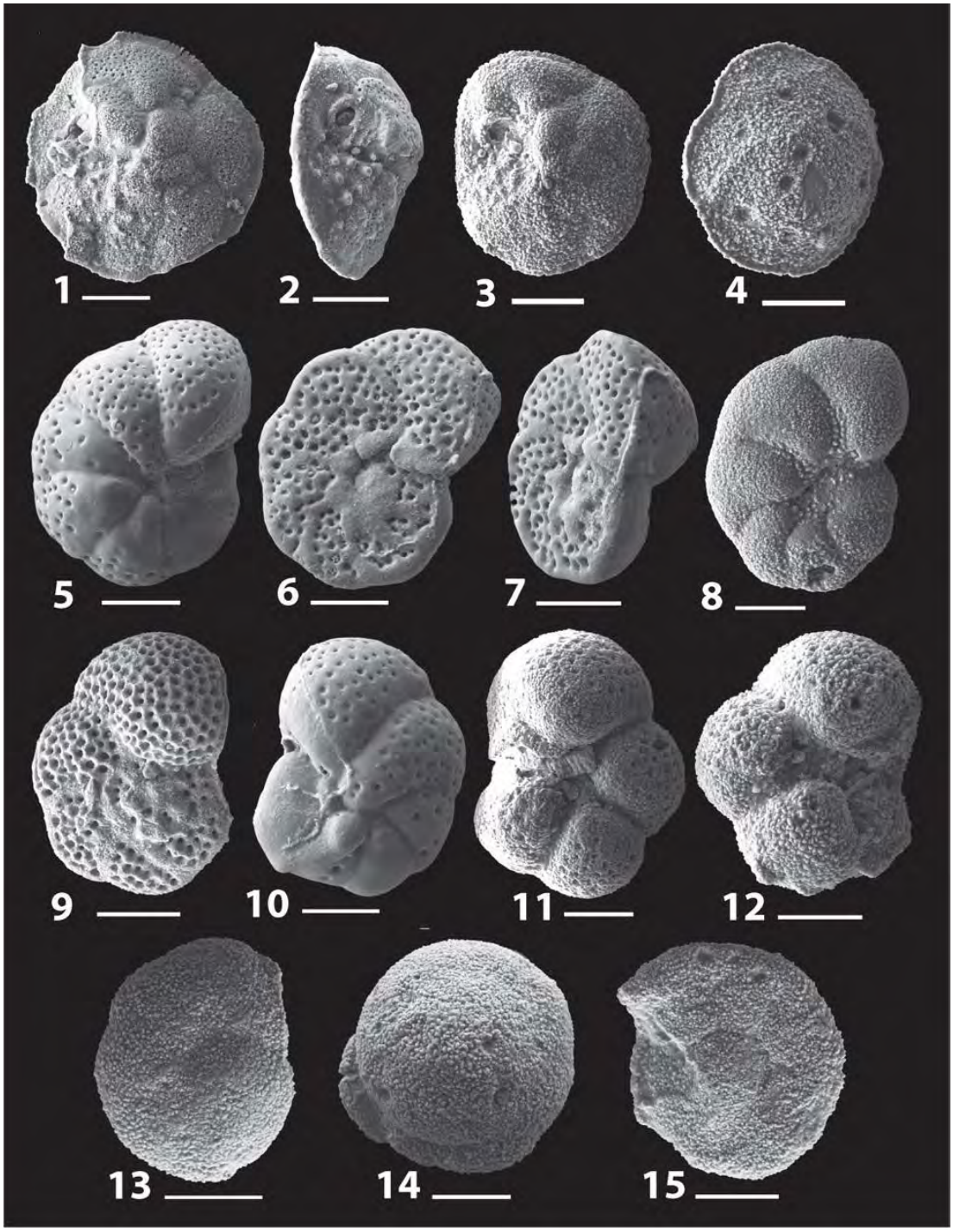

Figure 7*. Benthic foraminifera from the Naredi section of Kutch, India. Scale bar=50 mm. 1-2. Astigerina bartoniana (Ten Dam), sample NE-44. Paleoecology: normal marine, inner shelf. 3-4. Astigerina aberystwythi Haynes, sample NE-87. Paleoecology: noramal marine, ? brackish, inner shelf. 5-7. Cibicidoides lobatulus (Walker and Jacob), sample NE-32. Paleoecology: brackish to normal marine, inner to mid shelf, varied substrates. 8. Nonion applinae Howe and Wallace, sample NE-32. 9-10. Cibicides cassivelauni Haynes, sample NE-39. Paleoecology: normal marine inner to middle shelf. 11-12. Pararotalia cf curryi Loeblich and Tappan, sample NE-86. Specimens less compressed with more rounded periphery than type specimens. Paleoecology: mainly brackish but extending into normal marine inner shelf. 13-15. P. circularis, sample NE-86.*

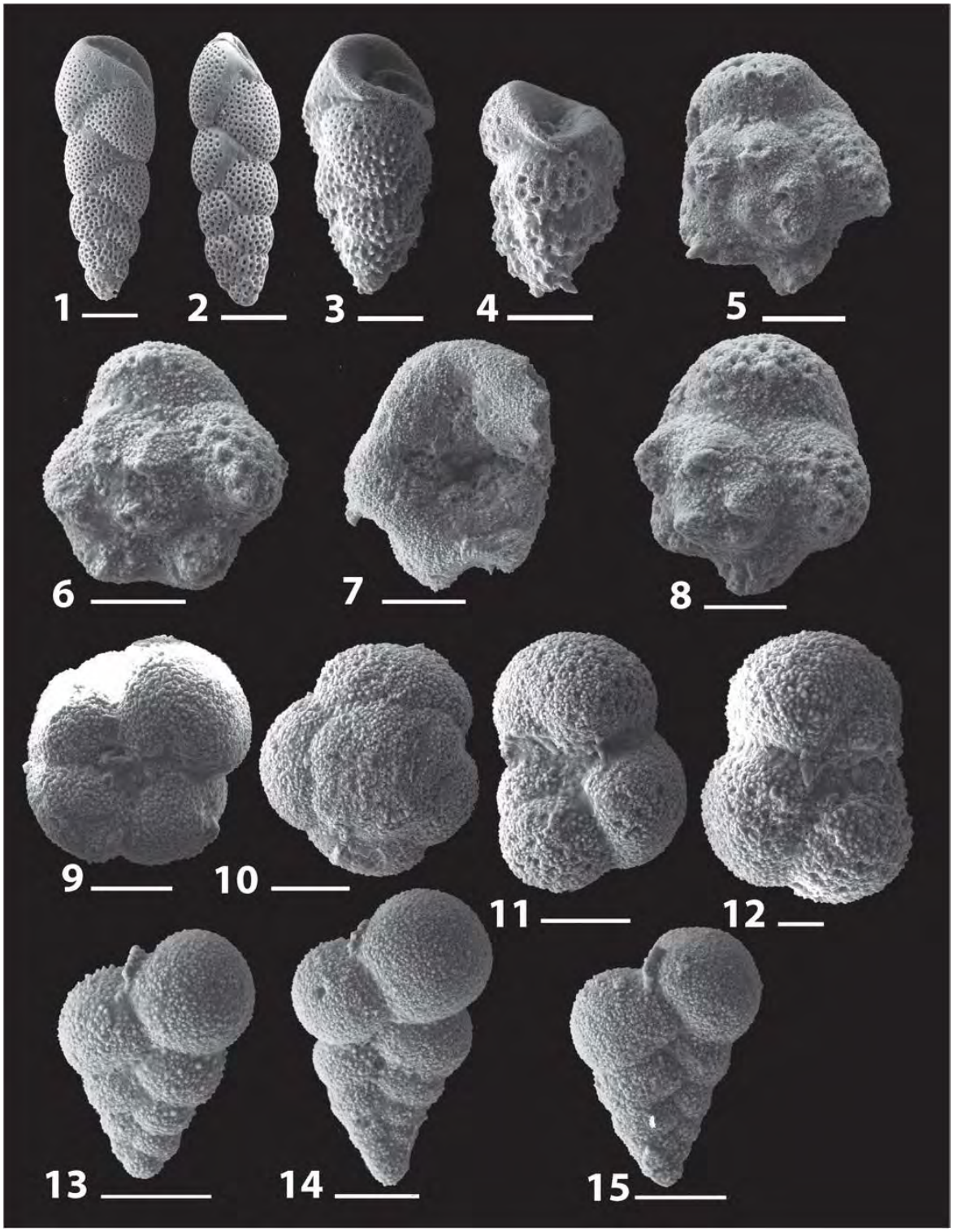

Figure 8. *Benthic and planktic foraminifera from the Naredi section of Kutch, India. Scale bar=50 mm for figs. 1-12 and 20 mm for figs. 13-15. 1-2. Brizalina oligoacenica (Spandel), sample NE-32, Fig. 2. specimen from Vastan lignite mine. Paleoecology: Normal marine shelf, mud substrate. 3-4. Praebulimina spinata (Cushman & Campbell), samples NE-32, NE-39. Sliter 1968, pl. 12 p. 85. 5-8. Pijpersia coronaeformis (Pijpers), sample NE-88. 9-10 ? Protelphidium sp. or Rosalina bractifera? Sample NE-88. 11-12. Subbotina patagonica (Todd and Kniker), sample NE-86. 13-15. Chilogembelina trinitatensis (Cushman and Renz), sample NE-86. Paleoecology: planktic foraminifera, stress tolerant, inner shelf to open marine.*

Colburn and Baskin (1998) observed that *Ammonia parkinsoniana* is one of the most widely distributed and abundant foraminiferans living in nearshore environments of the north-west Gulf of Mexico as well as in Neogene sediments of the Gulf Coast. They have variable test morphologies presumed to be adaptations to environmental changes. Colburn and Baskin (1998) found salinity to be the most important factor affecting morphology. Specimens collected at times of higher salinity (50 ppt) differed from those collected at lower salinity (14 ppt) by having a larger proloculus and fewer chambers in whorls 1 and 2, a smaller umbo diameter and fewer total chambers. Experimental studies on *Ammonia* sp. by Le Cadre et al. (2003) determined that prolonged exposure to low pH results in test dissolution, whereas return to normal pH induces test deformation. Experimental studies by Nigam et al. (2005) and Panchang et al. (2006) exposed species to low oxygen, which revealed a rapid decline in most species, including *A. beccarii* with *Fursenkoina* and *Nonion* species more adatptive.

In the Naredi section a morphotype similar to *A. parkinsonia* (Fig. 6, No. 9-12) dominates a low diversity (8 species) assemblage in a short interval 7 m above the basalt at the base (Fig. 3). Marginal marine species (e.g., *Cibicidoides lobatulus, C. succedens, C. cassivelauni,* Fig. 6, No. 15-17; Fig. 7 No. 5-7, 9-10) and brackish to normal inner shelf species (e.g., *Astigerina bartoniana, A. aberystwythi, Protoelphidium* sp. 4, Fig. 6, No. 1-5) are few to rare varying from <5 to <10 specimens). All species in this assemblage are dwarfed. In addition, a nearly monospecific assemblage of very small specimens of the larger foraminifer *Nummulites globulus nanus* is present and also indicates a high stress environment (Hottinger, written communication, 2008). Based on these assemblage observations we interpret a brackish lagoonal environment. Sediments in washed residues are rich in phosphate suggesting high nutrient influx and possibly dysoxic conditions.

***Protelphidium* sp. 4 assemblage:**

This relatively low diversity assemblage (13 species) is dominated by small 5-6 chambered species with a row of small apertures at the base of the last chamber (Fig. 6, No. 1-5). Two of the three foraminifer horizons at Naredi are dominated by *Protelphidium* sp. 4 (Fig. 3). The species was described by Murray and Wright (l974) as one of several morphotypes abundant in low diversity assemblages of the Paris Basins, English Channel and Hampshire. They interpreted the *Protelphidium* sp. 4 assemblage as indicative of an abnormal environment, possibly hyposaline such as a lagoon or estuary. In the Naredi section a similar environment may have prevailed in the first foraminifer horizon between 2.8-4 m above the basal basalt. At this horizon *Protelphidium* sp. 4 coexists with other brackish to normal marine inner shelf species, including common *Cibicioides alleni* and *Brizalina cf. oligoacenica* (Fig. 6, No. 13-14; Fig. 8. No. 1-2). All other species are few to rare (Fig. 3). Low diversity larger foraminiferal assemblages are also present and dominated by *N. globulus nanus*. However, since sediments are rich in glauconite with minor phosphate this suggests a paloedepth of about 5-10 m with a more open sea connection, rather than a lagoon or estuary.

***Protelphidium* sp. 4 – *Cibicdoides succedens* assemblage:**

The uppermost foraminiferal horizon differs from the two lower ones by higher species diversity (18 species), presence of marginal marine inner shelf benthics with common *C. succedens, C. lobatulus, Brizalina cf. oligoacenica* and *Pijpersia coronaeformis* (Figs. 6-8). Planktic foraminifera are few to rare, including *C. trinitatensis* (Fig. 8, No. 13-15), *C. crinita,*

Subbotina patagonica (No. 11-12) and *Acarinina quetra.* The brackish to normal marine inner shelf benthic assemblage is still common and dominated by *Protelphidium* sp. 4, *Pararotalia curryi, Astigerina aberystwythi* and *A. bartoniana* (Figs. 6, 7). *Ammonia aff. beccarii* is present but significantly reduced in abundance. Most species are larger than in the lower two horizons, suggesting less environmental stress. Larger foraminifera are common and diverse. Sediments are more calcareous with decreased glauconite and phosphate suggesting more oligotrophic conditions. Murray and Wright (1974) interpreted a similar early Eocene assemblage in the European sections as inner shelf with moderate water depth (20-50 m) and slightly hyposaline. The relatively rare and low diversity of planktic foraminifera suggests sluggish connection with the open sea.

5. DISCUSSION

The difficulty in determining the precise age of the Naredi Formation is due to the shallow depositional environment and consequently absence of diverse planktic foraminiferal assemblages that provide excellent age control in marine sequences. Larger shallow benthic foraminifera currently provide good age control indicating an early Eocene Ypresian age (shallow benthic zones SPZ8 to SPZ11), although their intermittent presence leaves age dating at the base of the section and between zones SPZ8 and SPZ11 uncertain (Fig. 4). A recent study by Garg et al. (2011) based on dinoflagellates confirmed an early Eocene age for the Naredi section, but also recovered age diagnostic species in the basal part of the section overlying basalt that indicate a very early Ypresian age (e.g., *Muratodinium fimbriatum, Heterolaucacysta granulata, Operculodinium severinii* and *Ginginodinium palaeocenicum).*

Age resolution can be further refined by integrating all microfossil data and compare and correlate the results with the high-resolution carbon isotope curve of the Naredi section that can be correlated with the global isotope record. This was the main objective of this study and the companion study on geochemistry by Khozyem et al. (this vol.). The carbon isotope curve of the Naredi section is based on $d^{13}C_{org}$ with additional $d^{13}C$ measurements from bivalves, bones and teeth where available through the Naredi section (Fig. 3). The data are discussed in detail in Khozyem et al. (this vol.) and briefly summarized here.

The $d^{13}C_{org}$ curve shows predominantly negative values (-24.9 and -27.6‰) in the basal 4.5 m of the section with minimum values between 1.0-1.8 m and 3-4.2 m (Fig. 3). At the top of this interval (2.8-4.2 m) are the first planktic and benthic foraminiferal assemblages that indicate an early Eocene age (early Ypresian) based on biozones SBZ8 and E4 (Fig. 3) (Saraswati et al., 2012, this study; see also Chattoraj et al., 2009). This foraminiferal and macrofossil-rich assemblage records a strong positive $d^{13}C$ excursion in macrofossil shells, bones and teeth. Microfossils and macrofossils suggest a sea level transgression resulting in a brackish to more normal marine inner neritic environment as indicated by benthic and rare planktic foraminifera and abundant glauconite. In the basal 2.8 m of the section $d^{13}C$ values of bones, teeth and macrofossils show the same negative trend as $d^{13}C_{org}$. No age diagnostic foraminifera species are present. However, dinoflagellates in this interval indicate an early Ypresian age (Garg et al., 2011). The warm early Ypresian climate of the first 4.5 m of the Naredi section may be correlative to the early Eocene climatic optimum (ETM2 at 53.7 Ma) (Zachos et al., 1994; Sloan and Huber, 2001; Slujis et al., 2007; Woodburne et al., 2009). Within this interval and correlative with the first relatively diverse marine assemblages is a major positive $d^{13}C$ excursion

measured in bivalves, bones and teeth and to a lesser extent in $d^{13}C_{org}$. Similar excursions coincide with the other two foraminiferal marine assemblages in the upper part and at the top of the Naredi section (Fig. 3). These positive $d^{13}C$ excursions are likely linked to mixed sources of organic matter or a change toward increased marine organic input (Calvert et al., 1987).

Between 4.5 m and 6.5 m of the Naredi section $d^{13}C_{org}$ values increase fluctuating between -26 to -24‰. This interval is barren of foraminifera and contains rare bones and fish teeth showing a similar positive trend. The major positive excursion in $d^{13}C_{org}$ (6.5-7.6 m) culminates (-19.6‰) in the fossliferous claystones (Fig. 3). Benthic foraminifera in this interval are strongly impoverished with just seven species dominated by a morphotype similar to *Ammonia parkinsonia*, which indicates a brackish to lagoonal environment. In the interval above a rapid negative $\delta^{13}C_{org}$ excursion occurs in an interval devoid of fossils. Between 7.8-9.8m $\delta^{13}C_{org}$ values gradually increase (-26.3 to 24‰) then rapidly reach 20.7‰ at the top of the section (Fig. 3). This rapid $d^{13}C_{org}$ increase occurs in the interval of the most diverse foraminiferal assemblages, which suggest a marginal marine inner shelf environment. Benthic foraminifera are dominated by *Protoelphidium* sp. 4, which indicates brackish to normal marine inner shelf environment. Lithology, foraminifera and stable isotope data thus suggest deposition occurred in a shallow marine environment that varied from brackish to normal marine inner shelf environment. Two transgressive trends are apparent – one in the lower part of the section culminating with the first diverse foraminiferal assemblage and the second in the upper half culminating near the top of the section with the most diverse foraminiferal assemblages (see also Chattoraj et al., 2008). In between these transgressive trends is a root zone horizon representing a paleosoil at 5.9 m that indicates a regression and possibly a sequence boundary (Fig. 3) (see Khozyem et al., this vol. for a detailed discussion and lithology). The intervals with rare and mechanically corroded foraminifera suggest supratidal environments as also indicated by the presence of glauconite.

CONCLUSIONS

The Naredi section is intermittently fossiliferous with bivalves, echinoids, ostracods and larger foraminifera more frequently present than smaller benthic and planktic foraminifera, which are restricted to three intervals. Associated microvertebrates are dominated by teeth, scales and otoliths of shallow marine fishes (sharks, rays, teleosts) and a few aquatic snakes. Based on faunal assemblages and stable isotope data ($\delta^{13}C_{org}$, $\delta^{13}C_{biv+bones+teeth}$) the following age and environmental interpretations can be reached.

1. *Age and Biostratigraphy:* The lower part of the Naredi section is of early Eocene (Ypresian) age (SBZ8, E4) based on larger foaminifera and rare planktic foraminifera in assemblages between 2.8-4.2 m from the base of the section. The top of the section (including the limestone) is of late early Eocene (SBZ11, E6) age (Fig. 3). There is no age control for the lower 2.8 m and between 4.2-9.3 m.
2. *Paleoenvironment*: Small benthic and rare planktic foraminifera are common in three short intervals: the lower assemblage (SBZ8, E4) is indicative of brackish to normal marine inner shelf environments; the middle assemblage represents a brackish environment; the top assemblage (SBZ11, E6) is the most diverse and indicates an inner shelf to marginal marine environment.
3. *Sea level changes*: Two phases of marine transgressions can be identified with the maximum transgressions in each phase marked by the lower and upper foraminiferal assemblages. A

paleosoil indicated by root traces and burrows (5.9 m) represents a regression and possibly a sequence boundary.

ACKNOWLEDGEMENTS: We are grateful to N. Malarkodi and other conveners for organizing the XXIII Colloquium on Micropaleontology and Stratigraphy (ICMS) & International Symposium on Global Bioevents in Earth History, Bangalore Dec. 9-11, 2011. We gratefully acknowledge advise on smaller benthic foraminifera from shallow water environments from Drs. A. Govindan, D.S.N. Raju, P. Kalia and M. Hart. We were fortunate to have the advise on larger foraminifera from Dr. L. Hottinger (1933-2011) who passed away before this study was completed. This study was in part funded by the Egyptian Ministry of Higher Education (Mission No.001/013/104) (HK), the Department of Science and Technology, Government of India (SB), and based upon work supported by the US National Science Foundation through the Continental Dynamics Program, Sedimentary Geology and Paleobiology Program and Office of International Science & Engineering's India Program under NSF Grants EAR-0207407, EAR-0447171, and EAR-1026271 (GK).

REFERENCES

Almogi-Labin, A., Siman-Tov, R., Rosenfeld, A. and Debard, E. (1995) Occurrence and distribution of the foraminifer *Ammonia beccarii tepida* (Cushman) in water bodies, recent and quaternary, of the Dead Sea Rift, Israel, Marine Micropaleontology, v. 6, pp.153–159.

Aubry, M.P., Cramer, B.S., Miller, K.G., Wright, J.D., Kent, D.V. and Olsson, R.K. (2000) Late Paleocene event chronology: unconformities, not diachrony. Bulletin de la Societé Géologique de France, v. 171, pp. 367-378.

Berggren, W.A., Kent, D.V., Swisher, C.C. and Aubry, M.-P. (1995) A revised Cenozoic geochronology and chronostratigraphy. *In:* W.A. Berggren, D.V. Kent, M.-P. Geochronology, Time Scales and Global Stratigraphic Correlation, SEPM, Spec. Publ., no. 54, pp. 129-212.

Biswas, S.K. (1992) Tertiary stratigraphy of Kutch. Jour. Palaeontological Society of India, v.37, p.29.

BISWAS, S.K. and RAJU, D.S.N. (1973) The rock-stratigraphic classification of the Tertiary sediments of Kutch. Bulletin Oil & Natural Gas Commission, v. 10(1- 2), pp. 37-45.

Calvert, S.E., Fontugne, M.R. (1987) Stable carbon isotopic evidence for the marine origin of the organic matter in the Holocene Black Sea sapropel. *Isot. Geosci*ence, v. 66, pp. 315–322.

Chattoraj, S.L., Banerjee, S. and Saraswati, P.K. (2009) Glauconites from the Late Paleocene – early Eocene Naredi Formation, Western Kutch and their genetic implications. J. Geological Society of India, v. 73, pp. 567-574.

Chattoraj, S.L., Banrejee, S. and Saraswati, P.K. (2008) Sedimentation, palageography and sequence startigraphic framework of the Late Palaeocene to Early Eocene Naredi Formation, Western Kutch, Gujarat. Int. Assoc. Gondwana Res. Conf. Series 5, p.116.

Colburn, D.F., Baskin, J.A. (1998) A morphological study of Ammonia parkinsoniana from Laguna Madre and Baffin Bay, Texas. Gulf Coast Association of Geological Societies Transactions, v. 68, pp. 11-20.

Garg, R., Prasad, V., Thakur, B., Singh, I.B., and Khowaja-Ateequzzaman (2011) Dinoflagellate cysts from the Naredi Formation, Southwestern Kutch, India: Implications on age and Paleoenvironment. J. Palaeontological Society of India v. 56(2), pp. 201-218.

Jauhri, A.K. and Vimal, K.P. (1978) Some observations on the foraminifera from the Tertiary rocks of Vinjhan-Miami area, Kutch. Journal of the Geological Society of India, v. 19, pp. 154-159.

Jafar, S.A. and Rai, J. (1994) Late Middle Eocene (Bartonian) calcareous nannofossils. Geophytology, v. 24(1), pp. 23-42.

Keller G., Li, L. and Macleod, N. (l995) The Cretaceous/Tertiary boundary stratotype section at El Kef,

Tunisia: How catastrophic was the mass extinction? Paleogeography, Paleoclimatology, Paleoecology, v. 119, pp. 221-254.

Khozyem, H., Adatte, T., Saravanan, N., Bajpai, S., Keller, G., Spangenberg, J. (this vol.) Paleoclimate and Paleoenvironment of the Naredi Formation, (Early Eocene), Kutch, Gujarat, India. Geological Society of India Special Publication

Le Cadre, V., Deneay, J-P. and Lesourd, M. (2003) Low pH effects on *Ammonia beccarii* test deformation: implications for using test deformation as a pollution indicator. J. Foraminiferal Research, v. 33, pp. 1-9.

Murray, J.W., and Wright, C.A. (1974) Palaeogene Foraminiferida and Palaeoecology, Hampshire and Paris Basins and the English Channel. Special Papers in Palaeontology, No. 14, the Palaeontological Assoc. London, 149 p.

Murray, J.W., Curry, J.R. and Haynes, C. (1989) Palaeogene. *In:* Jenkins, D.G. and Murray, J.W. (Eds.) Stratigraphical Atlas of fossil Foraminifera, British Micropalaeontological Society, John Wiley & Sons, pp. 490-536.

Nigam, R. Saraswat, R., and Panchang, R. (2005) Application on foraminifers in ecotoxicology: retrospect, perstect and prospect. Environ. Int. 32(2), pp. 273-283.

Panchang, R., Nigam R., Linshy, V., Rana, S.S. and Ingole, B. (2006) Effect of oxygen manipulations on benthic foraminifera: a preliminary experiment. Indian J. Mar. Sci. v. 35(3)

Pearson, P.N., Olsson R.K., Huber, B.T., Hemleben, C. and Berggren, W.A. (2006) Atlans of Eocene Planktic foraminifera. Cushman Foundation Special Publication No. 41, 2006, 512 p

Punekar, J., Saraswati, P.K. (2010) Age of the Vastan Lignite in context of some oldest Cenozoic fossil mammals from India. Journal of the Geological Society of India, v. 76(1), pp. 63-68.

Raju, D. S. N. (1974) Observations on the Eocene, Oligocene and Miocene foraminiferal biostratigraphy of Kutch, western India. Publication of the Centre of Advanced Study in Geology, Panjab University, Chandigarh, v.10, pp. 136–155.

Raju, D. S. N. (2008) Stratigraphy of India. Special Issue, ONGC Bulletin v. 43, 44 pp.

Raju, D.S. N., Guha, D. K., Bedi, T. S., Kumar, P. and Bhatttacharya, D. K. (1970) Microfauna, biostratigraphy and paleoecology of the Middle Eocene to Oligocene sediments in western India. Publication of the Centre of Advanced Study in Geology, Panjab University, Chandigarh, v. 7, pp. 155–178.

Revesz, K.M., Landwehr, J.M. and Keybl, J. (2001) Measurement of $\delta^{13}C$ and $\delta^{18}O$ isotope ratios of $CaCO_3$ using a Thermoquest Finnigan GasBench II Delta Plus XL Continuous Flow Isotope Ratio Mass Spectrometer with application to Devils Hole Core DH-11 Calcite. U.S. Geological Survey Open-File-Report 01-257, 17 pp.

Saraswati, P.K., Patra, P.K. and Banerjee, R.K. (2000) Biometric study of some Eocene *Nummulites* from Kutch and Jaisalmer, India. *Jour. Pal. Soc. India,* v. 45, pp. 91-122.

Saraswati, P.K., Sarkar, U. and Banerjee, S. (2012) *Nummulites solitarius – Nummulites burdigalensis* Lineage in Kutch with Remarks on the Age of Naredi Formation, J. Geological Society of India, v. 7, pp. 476-482.

Saravanan, N. (2007) Sequence biostratigraphy of the early Tertiary vertebrate- bearing strata of Gujarat, India. Unpublished Ph.D. thesis, Indian Institute of Technology, Roorkee, India, pp. 242.

Schaub, H. (1981) *Nummulites* et *Assilines* de la Tethys Paleogene. Taxonomie, Phylogenese et Biostratigraphie. Mem. Suisse Paleont., v.104-106, 236 pp.

Scheibner, C. And Speijer, R.P. (2009) Recalibration of the Tethyan shallow-benthic zonation across the Paleocene – Eocene boundary: the Egyptian record. Geologica Acta, v. 7, pp. 195-214.

SERRA-KIEL, J., HOTTINGER, L., CAUS, E., DROBNE, K., FERRANDEZ, C., JAUHRI, A.K., LESS, G., PAVLOVEC, R., PIGNATTI, J., SAMSO, J.M., SCHAUB, H., SIREL, E., STROUGO, A., TAMBAREAU, Y., TOSQUELLA, J. and ZAKREVSKAYA, E. (1998) Larger foraminiferal biostratigraphy of the Tethyan Paleocene and Eocene. Bull. Soc. Geol. France, v. 169, pp. 281-299.

Shukla, S. (2008) Atlas of Taxonomic and Bio-Chronostratigraphic studies on Palaeogene Larger Benthic Foraminifera from Indian sedimentary Basins. Paleontographica Indica, v.9, ONGC, Dehradun, 183 pp.

Singh, P. and Singh, M. P. (1991) Nannofloral biostratigraphy of the late middle Eocene strata of Kachchh Region, Gujarat State, India. Geoscience Journal, v. 12, pp. 17–51.

Sloan, C.L. and Huber, M. (2001) Eocene Oceanic Responses to Orbital Forcing on Precessional Time Scales. Paleoceanography, v. 16(1), pp. 101-111.

Slujis, A., Bowen, G.J., Brinkhuis, H., Lourens, L.J. and Thomas. E. (2007) The Palaeocene-Eocene Thermal Maximum super greenhouse: biotic and geochemical signatures, age models and mechanisms of global change. In: *Deep-time perspectives on climate change: Marrying the signal from computer models and biological proxies. In:* Williams, M., Haywood, A.M., Gregory, F.J. and Schmidt, D.N. (Eds.) Geological Society of London. pp. 323- 350.

Takata, H., Dettman, D.L., Seto K., Kurata, K., Hiratsuka, J. and Khim, B. (2009) *Ammonia "becccarii"* Forma 1 in a macrobenthos community on hard substrates in the Ohashi River, Southwest Japan. J. Foraminiferal Research v. 39(2), pp. 87-96.

Tandon, K.K., Mathur, V.K. and Saxena, R.K. (1980) Paleocene-Early Eocene biostratigraphy in Nareda, southwestern Kutch, Western India. J. Palaeont. Soc. India v. 23,24, pp. 86-91.

Woodburne, M.O., Gunnell, G.F. and Stucky, R.K. (2009) Climate directly influences Eocene mammal faunal dynamics in North America. Proceedings of the National Academy of Sciences of the U.S.A. v.106(32), pp. 13399-13403.

Zachos, J.C., Stott, L.D. and Lohmann, K.C. (1994) Evolution of Early Cenozoic marine temperatures. Paleoceanography, v. 9(2), pp. 353-387.

CHICXULUB IMPACT SPHERULES IN THE NW TO SW ATLANTIC: AGE CONSTRAINTS AND KTB HIATUS[1]

Abstract. The Chicxulub impact is commonly believed to have caused the Cretaceous-Tertiary boundary (KTB) mass extinction and a thin impact spherule layer in the NW to SW Atlantic and Caribbean is frequently cited as proof. We evaluated this claim in the seven best KTB sequences based on high-resolution biostratigraphy, quantitative faunal analyses and stable isotopes (Bass River core, ODP Sites 999B, 1001B, 1049A, 1049C, 1050C, 1259B). Results reveal a major KTB unconformity that spans most of Danian subzone P1a(1) and Maastrichtian zones CF1-CF2 (~400 kyr) in the NW Atlantic, P1a(1) through zones CF1-CF4 (~3 myr) in the Caribbean, and P1a(1), P0 to CF1 (~150-200 kyr) in the SW Atlantic. In all sites examined the impact spherules are reworked into the early Danian subzone P1a(1) about 150-200 kyr after the mass extinction. A similar pattern of erosion and redeposition of impact spherules in Danian sediments has previously been documented from Cuba, Haiti, Belize, Guatemala and southern Mexico and appears to be related to sea level and climate change. The age of the Chicxulub impact cannot be determined from reworked impact spherules.

Keywords: Chicxulub, Impact spherules, KTB unconformity, Atlantic, Caribbean

1. INTRODUCTION

The age of the Chicxulub impact has been a contentious issue ever since the discovery of the impact structure on Yucatan and its initial tentative link to the Cretaceous-Tertiary boundary (KTB also called K-P or K-Pg) mass extinction based mainly on the stratigraphic position of impact spherules relative to the KTB in Haiti and NE Mexico (e.g., Maurasse and Sen, 1991; Smit et al., 1992; Stinnesbeck et al., 1993; Smit, 1999). Over the past 20 years, data from over 80 localities throughout the Caribbean, Central and North America (Fig. 1) have provided variable results.

Multiple spherule layers are present in upper Maastrichtian (zone CF1) sediments from NE Mexico and Texas (Adatte et al., 1996, 2011; Keller et al., 2003a, b, 2007, 2009; Schulte et al., 2003, 2006), and in lower Danian (zone P1a) sediments in the Caribbean, Cuba, Haiti, Belize, Guatemala and southern Mexico (Keller et al., 2003b; Keller, 2008). A single spherule layer between Maastrichtian and Paleocene sediments in the NW Atlantic (Bass River NJ, Blake Nose Site 1049), Caribbean (Site 1001), SW Atlantic (Demerara Rise Site 1259) and southern Mexico (Bochil, Guayal) is interpreted as evidence that the Chicxulub impact is KTB in age (Olsson et al., 1997; Sigurdsson et al., 1997; Kroon et al., 1998; Norris et al., 1999, 2000; Klaus et al., 2000; Martinez-Ruiz et al., 2001; Huber et al., 2002; Norris and Firth, 2002; Arenillas et al., 2006; MacLeod et al., 2007). Schulte et al. (2010) concluded that this single spherule layer proves that the Chicxulub impact caused the KTB mass extinction. In this scenario the

[1] ***Gerta Keller, Hassan Khozyem, Thierry Adatte, Nallamuthu Malarkodi, J.E. Spangenberg, Wolfgang Stinnesbeck (2013). Chicxulub Impact Spherules in the NW to SW Atlantic: Age constraints and KTB Hiatus. Geological magazine, doi:10.1017/S0016756812001069***

stratigraphic variability and presence of multiple spherule layers is attributed to impact generated tsunamis that caused gravity flows, slumps or liquefaction sucking spherules from the KTB into Maastrichtian sediments. An alternative interpretation notes the absence of major slumps, gravity flows or liquefaction and attributes the multiple spherule layers to erosion, reworking and transport during the uppermost Maastrichtian (zone CF1) and lower Danian (zone P1a) as a result of climate and sea level changes (e.g., Keller et al., 2007, 2009; Adatte et al., 2011). In this scenario the stratigraphically oldest spherule layer in zone CF1, up to13 m below the KTB in NE Mexico and ~ 2 m in Texas, represents the Chicxulub impact. The multiple horizons of bioturbation in the sandstone complex (also labeled tsunami deposit, e.g., Smit et al., 1992; Schulte et al., 2003, 2006, 2011) indicate colonization of the ocean floor during deposition and rule out impact-tsunami deposition (Ekdale and Stinnesbeck, 1998; Gale, 2006). Lithified clasts with impact spherules at the base of the sandstone complex and spherule layers in Texas (Brazos) reveal the history of an older spherule layer that was lithified, eroded and redeposited (Keller et al., 2007, 2011; Adatte et al., 2011). The older primary spherule layer is present in undisturbed claystone (Texas) and marl (Mexico, Keller et al., 2009) below the sandstone complex. In this controversy the single thin spherule layer reported from the KTB in the NW-SW Atlantic and Caribbean seems to offer clear evidence that the Chicxulub impact is KTB in age. Indeed, the simplicity of a thin spherule layer separating Maastrichtian and Danian sediments is appealing but difficult to reconcile with regional data. Are these sections complete across the KTB as claimed? If not, is there a pattern of spherule erosion and redeposition? To answer these questions requires high-resolution quantitative planktic foraminiferal biostratigraphy. This permits not only to identify the presence or absence of biozones, but also to assess whether sedimentation is complete in each biozone based on the abrupt onset or termination of species populations. For this reason we examined KTB sequences at Bass River, New Jersey, and ODP Sites 1049A, 1049C, 1050C, 999B, 1001B and 1259B (Fig. 1) based on: 1) high-resolution planktic foraminiferal biostratigraphy, 2) quantitative species abundance data as indicators of biozone truncation and hiatuses, 3) completeness of the KT boundary transition, 4) stable isotopes, and 5) stratigraphic positions of the spherule layer relative to the KTB.

2. METHODS

Cores across the KTB interval at ODP Sites 999B, 1001B, 1049A, 1049C, 1050C and 1259B were sampled at 1 cm, 5 cm and 10 cm intervals. Samples of about 1 cm^3 were taken from central portions of the cores to avoid down-core contamination. For paleontological analyses, samples were processed and washed through 36 mm and 63 mm screens following the procedure described in Keller et al. (1995). Quantitative paleontological analysis was performed on aliquots of 300-400 specimens in the > 63 mm. The 36-63 mm was examined for small species and counts were done for intervals where Danian species are more abundant in this size fraction. All specimens were identified and mounted on microslides for a permanent record. Preservation of foraminifera at Blake Nose ODP Sites 1049-1050 is excellent, though some calcite overgrowth and dissolution effects are apparent in sugary textures in the spherule layer. At Bass River and Site 1259B moderate dissolution resulted in holes of chambers in some Danian species. Strong dissolution and poor preservation at Sites 999B and 1001B prevented quantitative analysis and the species census data was obtained from both washed residues and thin sections. Stable isotope analysis of samples from ODP Sites 1049A, 1049C, 1050C and 1259B were performed on bulk fine fraction (<63 mm).

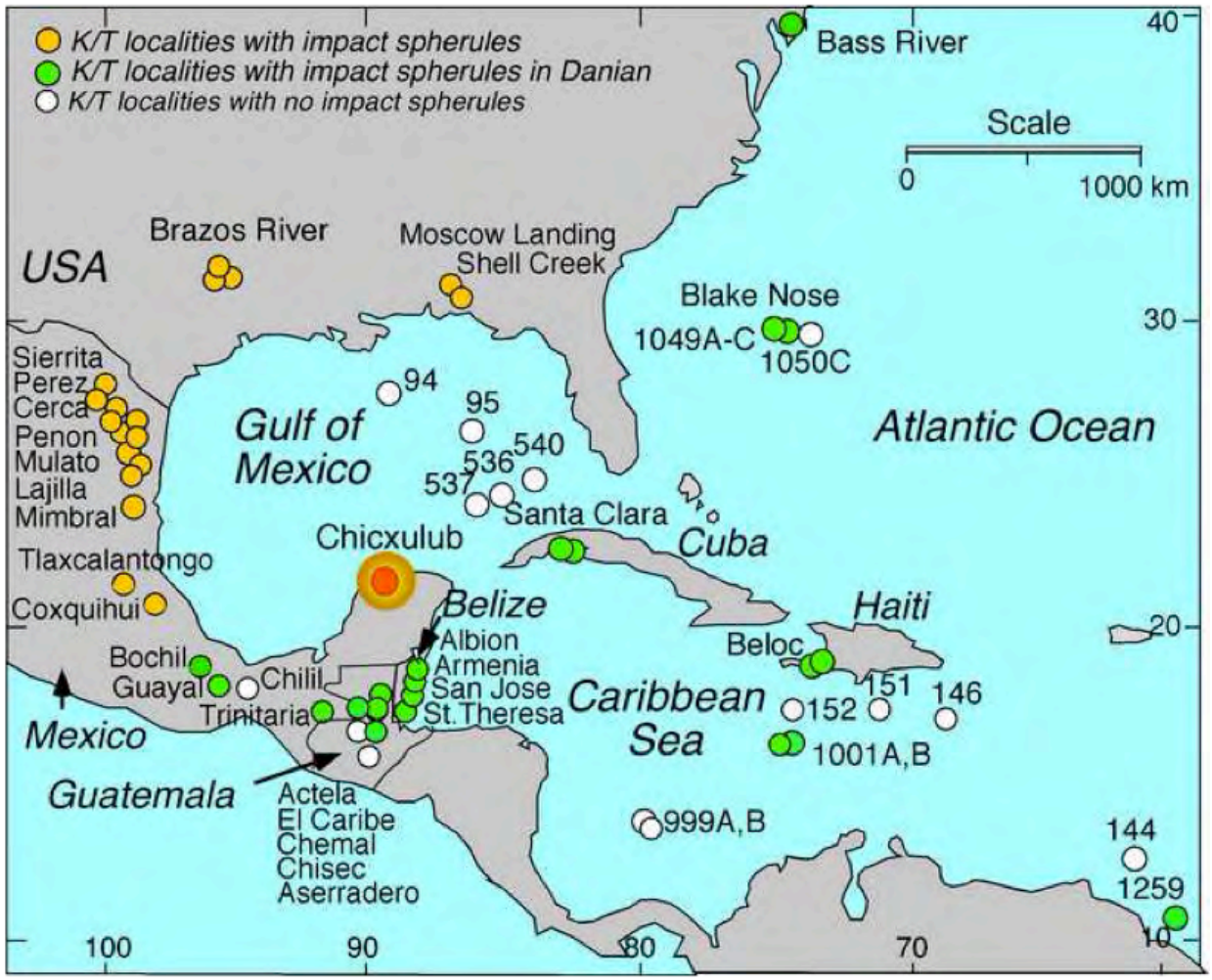

Figure 1*: Cretaceous-Tertiary boundary Localities studied for this report in the NW to SW Atlantic ODP Sites 99B, 1001B, 1049A, 1049C, 1050C, 1259B and Bass River, and other localities with impact spherules surrounding the Chicxulub impact crater on Yucatan with stratigraphic positions of impact spherules.*

The abundance of reworked Cretaceous species in the early Danian of Sites 1049A and 1049C necessitated analysis of the Danian planktic species *Parvularugoglobigerina eugubina* and *Chiloguembelina morsei* to obtain a reliable Danian record.

Analyses were performed at the Institute of Mineralogy and Geochemistry, Lausanne University, using a Thermo Fisher Scientific (Bremen, Germany) GasBench II preparation device interfaced with a Thermo Fisher Scientific Delta Plus XL continuous flow isotope ratio mass spectrometer (IRMS) (Revesz et al., 2001). Stable carbon and oxygen isotope ratios are reported in the delta notation as the per mil (‰) deviation relative to the Vienna Pee Dee belemnite standard (VPDB). Analytical uncertainty (2σ) monitored by replicate analyses of the international calcite standard NBS-19 and the laboratory standards Carrara Marble and Binn Dolomite is no greater than ±0.05‰ for $\delta^{13}C$ and ±0.1‰ for $\delta^{18}O$.

3. KT BOUNDARY DEFINITION AND PLACEMENT

The controversy over the age of the Chicxulub impact is in no small measure the result of redefining the KTB as the impact ejecta layer based on the assumption that this impact caused the end-Cretaceous mass extinction. Unfortunately, this has led to confusion and circular

reasoning. For example, Gradstein et al. (2004) proposed to define the KTB based on just two criteria "the Ir anomaly associated with a major mass extinction." This has proved impractical because small (~ 1 ppb) Ir anomalies may be remobilized and concentrated at redox boundaries thus leading to erroneous KTB placement (e.g., Colodner et al., 2002; Lee et al., 2003; Miller et al., 2010; Gertsch et al., 2011). Partly as a solution, Molina et al. (2006) proposed that any impact ejecta define the KTB (e.g., spherules, breccia, iridium anomaly, shocked quartz, spinels etc). However, defining the Chicxulub impact as KTB age leads to circular reasoning and rules out evaluating the true age of the Chicxulub impact. Moreover, based on the occurrence of impact spherules, the KTB has been placed at the base of clastic deposits in the upper Maastrichtian, at the base of breccia deposits of dubious origins in the Maastrichtian, and at spherule layers reworked into Danian sediments.

These pitfalls can be avoided by returning to the unique defining and supporting KTB criteria of the GSSP, which consistently provide the most reliable KTB identification globally (Keller, 2011). The KTB is globally defined based on five criteria developed at the El Kef stratotype section and point (GSSP) and Elles parastratotype section in Tunisia (Cowie et al., 1989; Keller et al., l995, 2002; Remane et al., 1999). Two of the five are unique defining criteria: the mass extinction of 66% of planktic foraminiferal taxa and a few centimeters above the extinction horizon the first appearance (FA) of five Danian species (*Parvularugoglobigerina extensa, Woodringina hornerstownensis, W. claytonensis, Globoconusa daubjergensis, Eoglobigerina eobulloides*). Three are supporting criteria, which are not unique in the geological record but characterize the KTB: the clay layer, Ir anomaly and negative shift in $d^{13}C$ values. All five criteria have been tested and successfully applied to hundreds of KTB sequences worldwide and their presence is powerful confirmation of environmental changes across this boundary event. These KTB criteria are applied in this study.

4. LITHOLOGY AND BIOSTRATIGRAPHY

Age control is based on high-resolution quantitative planktic foraminiferal biostratigraphy, which provides the best age resolution for palemagnetic chron C29r spanning the KTB (Fig. 2). C29r below the KTB corresponds to planktic foraminiferal zones CF1, CF2 and the top of CF3, which is encompassed by the calcareous nannofossil zone *Micula prinsii*. Above the KTB, C29r corresponds to Danian zones P0, P1a with subzones P1a(1) and P1a(2), which is encompassed by the lower part of nannofossil zone CP1a (or NP1a). Previous studies of the sections analyzed in this report have used standard nannofossil and/or planktic foraminiferal biostratigraphy without quantitative data, which is not well suited for evaluating the completeness of the KTB transition.

4.1. Bass River Core, New Jersey

At Bass River, New Jersey (39°36'422"N, 74°26'122"W) the KTB transition was recovered in a relatively shallow water environment (paleodepth ~100 m; Miller et al., 1998). Upper Maastrichtian sediments consist of calcareous glauconitic silty shale with shells that disconformably underlie a 6 cm thick glauconitic impact spherule layer with clasts (1-6 cm, Fig. 3). A mm thin red-brown limonite layer separates the spherule layer from the overlying glauconitic silty-sandy shale that is interrupted by a dense layer of phosphate clasts and occasional Steinkerns that mark an erosion surface.

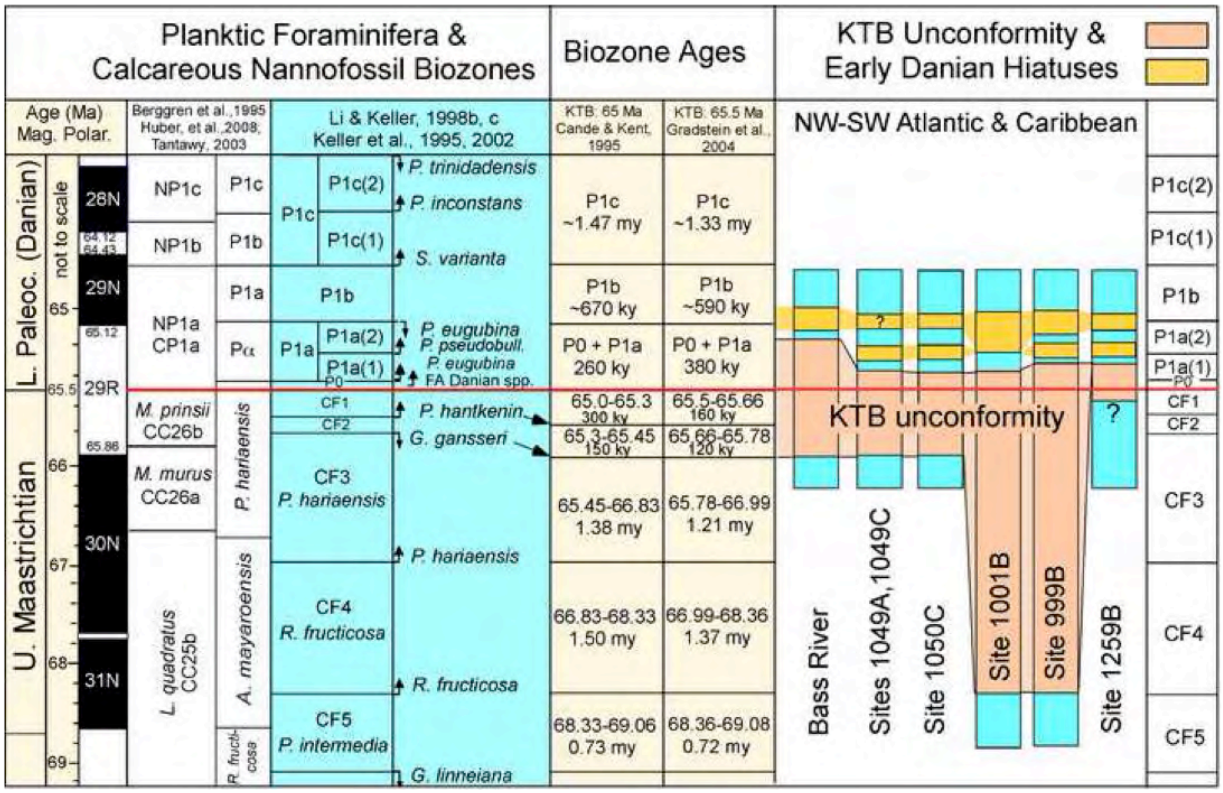

***Figure 2**. High-resolution planktic foraminiferal biostratigraphy in this study is based on Li and Keller (1998b, c) for the Maastrichtian and Keller et al. (1995, 2002) for the early Danian. Biozone ages are calculated based on the time scales of Cande and Kent (1995) and Gradstein et al. (2004). The extent of the KTB unconformity in the NW Atlantic and Caribbean is based on this study.*

About 10 cm above is a burrowed interval truncated by a 16 cm core gap. Above the glauconitic silty shale contains occasional phosphate clasts.

Planktic foraminifera are relatively well preserved, though small, thin walled and fragile. Upper Maastrichtian sediments below the spherule layer contain a typical low diversity middle shelf planktic foraminiferal assemblage indicative of zone CF3 as indicated by the presence of *Gansserina gansseri*, the index species that marks the CF3/CF2 boundary (Fig. 3). This indicates erosion of the CF2-CF1 interval that spans the top 450 kyr or 280 kyr of the Maastrichtian based on Cande and Kent (1995) and Gradstein et al. (2004) respectively (Fig. 2). Olsson et al. (1997) reported *Micula prinsii* in the 8 cm below the spherule layer, which is consistent with the overlap of this species in the upper part of zone CF3 (Fig. 2).

The spherule layer contains a few Cretaceous planktic foraminifera. The 6 cm immediately above the spherule layer contain common small Cretaceous species (KT survivors or reworked) and a diverse (11 species) early Danian assemblage including *Parvularugoglobiergina eugubina, Parasubbotina pseudobulloides* and *Subbotina triloculinoides*, which is characteristic of subzone P1a(2) (upper part of P1a zone, Fig. 3). Thus the total interval missing at the KTB unconformity includes zones CF1, CF2, P0, P1a(1) and most of P1a(2) and spans about 620 kyr, Fig. 2). Just 6 cm above the spherule layer this Danian P1a(2) assemblage and Cretaceous species terminate at the phosphate clast layer, which marks another hiatus between P1a(2) and P1b (Figs. 2, 3).

Above this hiatus the zone P1b assemblage is dominated by *Chiloguembelina morsei, Praemurica taurica* and *Parasubbotina pseudobulloides.*

4.2. NW Atlantic ODP Sites 1049A, 1049C and 1050C

Ocean Drilling Program (ODP) Leg 171 drilled three holes at Site 1049 (A, B, C) on the eastern margin of Blake Nose (30°08'N, 76°06'W) at a water depth of 2671 m (Norris et al., 1998, 1999). In each hole, located just 10 m apart from the next, the KTB transition was recovered along with a 10-15 cm thick impact spherule-rich layer. Site 1050C was drilled at a water depth of 2300 m, 330 m upslope from Site 1049 and at a distance of 10 km (30°05'99'N, 76°14'09'W, Fig. 1). The KTB transition was also recovered but no impact spherules. All three sites analyzed show very similar lithologies, except for the absence of a spherule layer at Site 1050C (Fig. 4).

Upper Maastrichtian sediments at Sites 1049A and 1049C consist of disturbed mottled light and darker gray nannofossil and foraminiferal ooze, which underlie the 10-15 cm thick spherule layer. The spherule layer has a carbonate ooze matrix, irregular bedding, clasts of limestone, chalk and dolomite and is bounded by irregular surfaces (Fig. 4). At Site 1049A a 2 mm thin red-brown limonite layer and 8 cm thick white ooze overlie the spherule layer followed by gray carbonate ooze. At Site 1049C, the limonite layer is also present but discontinuous and white ooze is present in the middle of the spherule layer. Above the limonite layer the 8 cm dark and light gray ooze is strongly mottled and disturbed, followed by light gray ooze. At Site 1050C the KTB transition consists of dark and light gray burrowed ooze with some large horizontal burrows infilled with gray ooze that contains rare Danian species below the KTB. An erosional surface and darker gray layer is correlative with the spherule layer.

Upper Maastrichtian faunal assemblages at all three sites are diverse, abundant and well preserved but lack *Plummerita hantkeninoides,* the zone CF1 index species for the topmost Maastrichtian (Figs. 5-7). However, the presence of *Gansserina gansseri* (and *G. wiedenmayeri* in Site 1050C) and *Pseudoguembelina hariaensis* mark this interval as zone CF3 (Abramovich et al., 2010). *Micula prinsii* was reported from a short interval below the spherule layer (Norris et al., 1999), which is consistent with the upper part of zone CF3 (Fig. 2). This indicates a major hiatus that spans Maastrichtian zones CF1 and CF2 (~ 280 kyr) based on the time scale of Gradstein et al. (2004, Fig. 2).

4.2.1. Impact Spherule layer with early Danian species

The spherule-rich layer above the KTB unconformity at Sites 1049A and 1049C is 15 cm and 10 cm thick, respectively (Fig. 4). Reworked Cretaceous species are common (Figs. 5, 6) along with shallow and deep-water benthic foraminifera that indicate reworking and transport of shallow water sediments into the basin (Alegret and Thomas, 2004). We also observed a dominance of large and thick-shelled species with variable preservation, including discoloration, abrasion and broken shells, and low abundance of small species, all of which indicate reworking and transport. On a quantitative basis 83-95% (>63 mm) of the Maastrichtian species are reworked in the spherule layer and 5-17% are small Danian species.

The relative abundance of Danian species was calculated based on 100-300 specimens per sample (63-100 mm) from the spherule layer (Figs. 5, 6). The presence of diverse assemblages (12 species), including *P. eugubina and P. longiapertura,* but absence of *P. pseudobulloides*

and/or *S. triloculinoides* indicates a subzone P1a(1) assemblage in the spherule layer with the lower part of this subzone and zone P0 missing.

The same Danian assemblage is present in the 8 cm above the spherule layer at Site 1049A and in the 20 cm above the spherule layer at Site 1049C, whereas the abundance of reworked Cretaceous species rapidly decreases to <10% (Figs. 5, 6). The first appearances *P. pseudobulloides, S. triloculinoides* and the sharp increase in *Chiloguembelina morsei* and *Guembelitria* species 8 cm and 20 cm above the spherule layer at Sites 1049A and 1049C marks a hiatus between P1a(1) and P1a(2). At both sites P1a(2) is dominated by *C. morsei* and *G. cretacea*. Reworked Cretaceous species are still present but rare (<2%).

At Site 1050C the comparable P1a(1) and P1a(2) assemblages spans the 60 cm above the KTB unconformity. Reworked species are very rare (Fig. 7). The basal Danian sample is dominated by *P. eugubina* (50%), which indicates that zone P0 and the lower part of P1a(1) is missing along with zones CF1 and CF2 (~400 kyr). Subzone P1a(1) is dominated by *P. eugubina* (55-64%) with common *Eoglobigerina edita* and variable presence of seven other Danian species (Fig. 7).

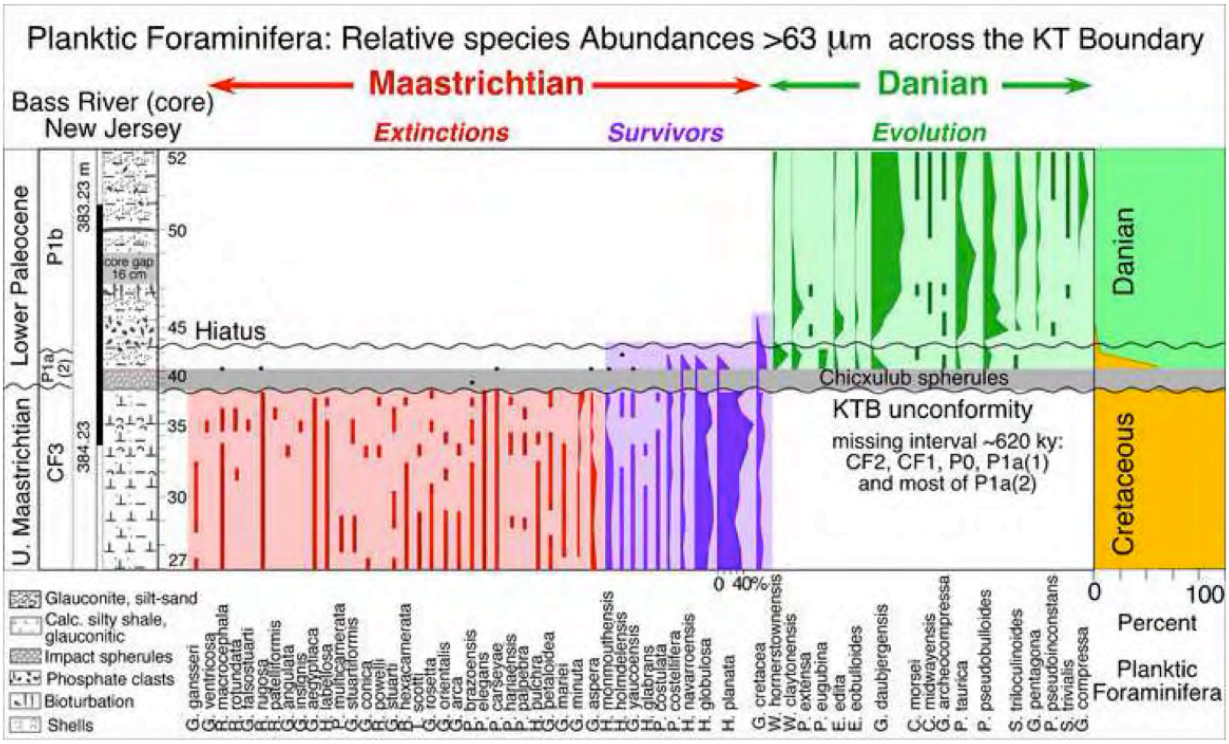

***Figure 3**. Biostratigraphy and relative species abundances of planktic foraminifera (>63 mm) in the Bass River core of New Jersey. An unconformity at the base of the spherule layer spans from the early Danian subzone P1a(2) through P1a(1), P0 and late Maastrichtian zones CF1 and CF2 for a total of about 620 kyr (time scale of Gradstein et al., 2004). Sedimentation resumed in the early Danian, upper part of P1a(2) amplified by reworking, transport and redeposition of impact spherules and Cretaceous species.*

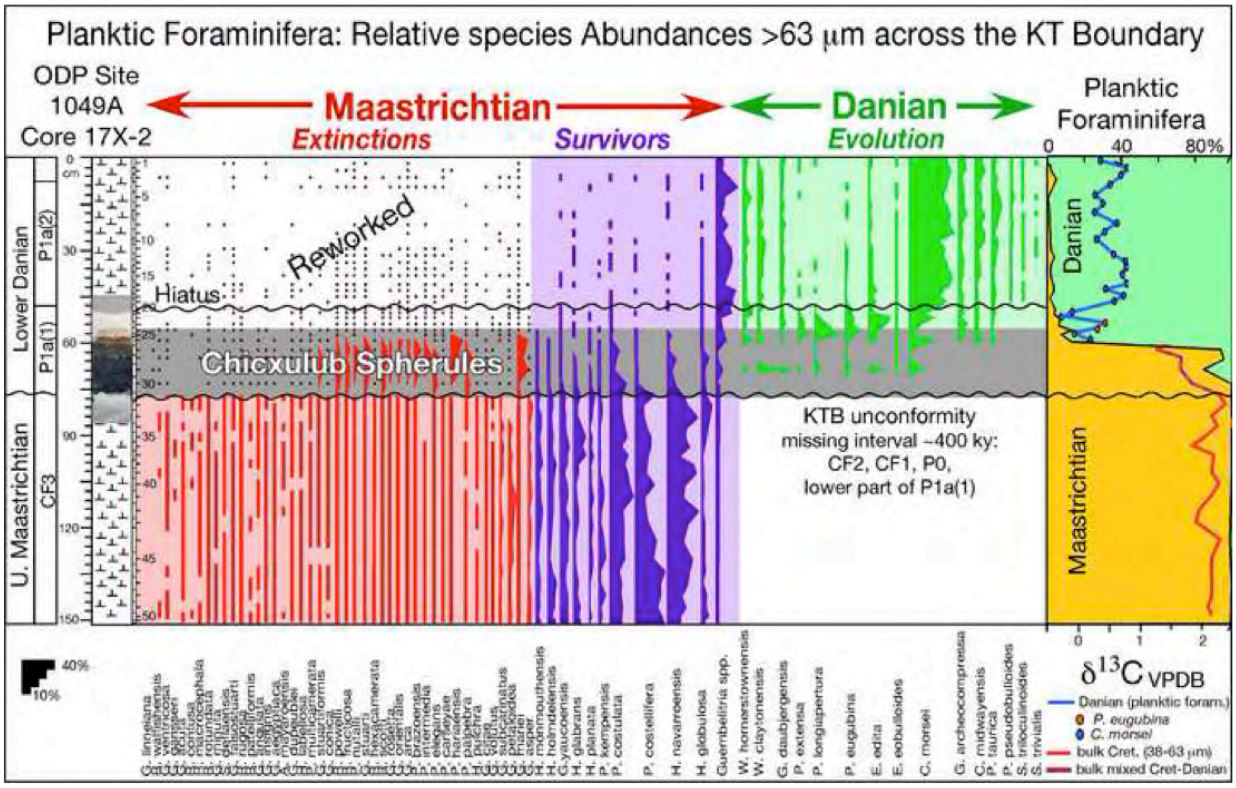

Figure 4*. Lithology of Blake Nose ODP Sites 1049A, 1049C and 1050C in the NW Atlantic. Note the distribution of Chicxulub impact spherules above a major unconformity at Sites 1049A and 1049C, but absence at 1050C. The spherule layer is of light green color due to the impact glass alteration as seen in a photo blow-up from 2006 that also shows the irregular surfaces above and below the spherule layer, the limonite layer at the top, and patches of calcareous ooze in the middle.*

The P1a(1)/P1a(2) boundary is marked by a sharp decrease in *P. eugubina*, concurrent increase in *Guembelitria* spp. and *Chiloguembelina morsei*, first appearances of *P. pseudobulloides* and *P. taurica*. For the next 30 cm *P. eugubina* and *E. edita* dominate along with *C. morsey*. At the top of this interval *E. edita* becomes rare and *P. eugubina* disappears, which marks the P1a/P1b boundary. At this interval the sudden disappearance of *P. eugubina*, decrease in *E. edita*, sudden increase (to 35-40%) in *Guembelitria* spp. and coincident drop in $d^{13}C$ values by nearly 1 permil, suggests another hiatus. During zone P1b *Guembelitria* spp. and *C. morsei* dominate with little change. Comparison between Sites 1049A, 1049C and 1050C reveals both similarities in faunal assemblages and differences in relative abundances of species populations. The latter are primarily due to variable erosion at the KTB and P1a(1)/P1a(2) hiatuses. In zone P1b all sections show the same faunal assemblages dominated by *Guembelitria* sp. and *Chiloguembelina morsei*. Carbon isotope signals also reflect great similarities among these sequences and each hiatus is marked by abrupt shifts in $d^{13}C$ values (see section 5).

4.3. Caribbean ODP Sites 999B and 1001B

ODP Sites 1001A and B were drilled 30 m apart on the Hess Escarpment (lower Nicaragua Rise, 15°45’427’N, 74°54’627’W) at depth of 3259 m (Fig. 1). The KTB transition was recovered at Site 1001B, core 18R-5 (Sigurdsson et al., 1997).

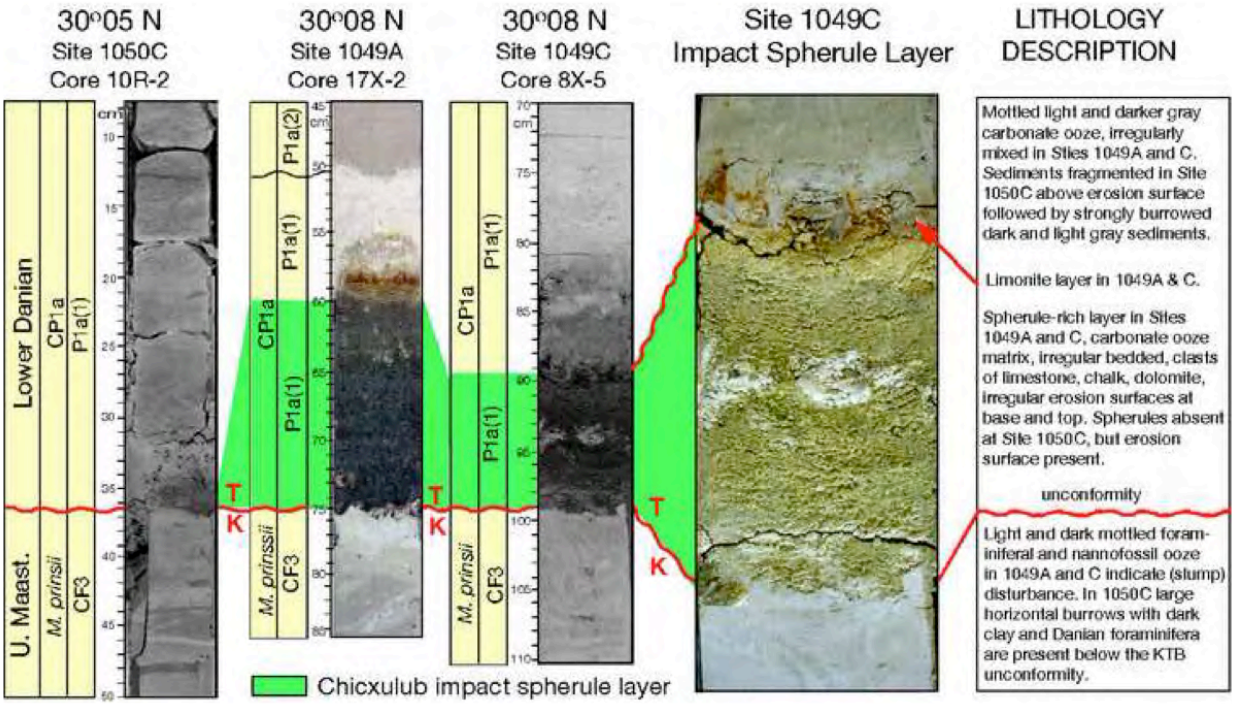

Figure 5*. Biostratigraphy and relative species abundances of planktic foraminifera and d^{13}C values at Site 1049A. An unconformity at the base of the spherule layer spans most of the early Danian subzone P1a(1), P0 and late Maastrichtian zones CF1 and CF2 for a total of about 400 kyr. The spherule layer contains common early Danian subzone P1a(1) species along with abundant reworked Cretaceous species. The d^{13}C curve shows Maastrichtian values below the unconformity and a 2‰ shift in the spherule layer (based on Danian species). Reworked Cretaceous species drop to <10% above the spherule layer. A short hiatus at the P1a(1)/P1a(2) boundary is marked by a 1‰ positive shift marking the initial (temporary) increase in primary productivity after the KTB mass extinction.*

Maastrichtian sediments consist of light gray mottled, burrowed limestone, which in the shipboard photo is speckled with dark flakes from the overlying claystone, but not in the archive core photographed in 2006 (Fig. 8). This limestone contains common *Heterohelix globulosa* and *Rugublobigerina rugosa* but all other species are rare. This low diversity assemblage is partly due to poor preservation and thin-section identification. However, the rarity of globotruncanids, which are more dissolution and break-resistant, and absence of upper Maastrichtian index species indicates a lower upper Maastrichtian zone CF5 age in agreement with the age previously assigned as base *Abathomphalus mayaroensis* (Sigurdsson et al., 1997). This indicates a major KTB hiatus with all or most of the upper Maastrichtian missing (zones CF1-CF4).

Above the unconformity is a 1.5-2.0 cm thick green-grey claystone with impact spherules altered to smectite and containing a lower Danian subzone P1a(1) assemblage (Fig. 8). The overlying 1.5-2.0 cm thick dark green-grey claystone contains abundant clay-altered spherule debris but no foraminifera. No sample was available for this study from the overlying 1.5 cm thick brown-grey claystone.

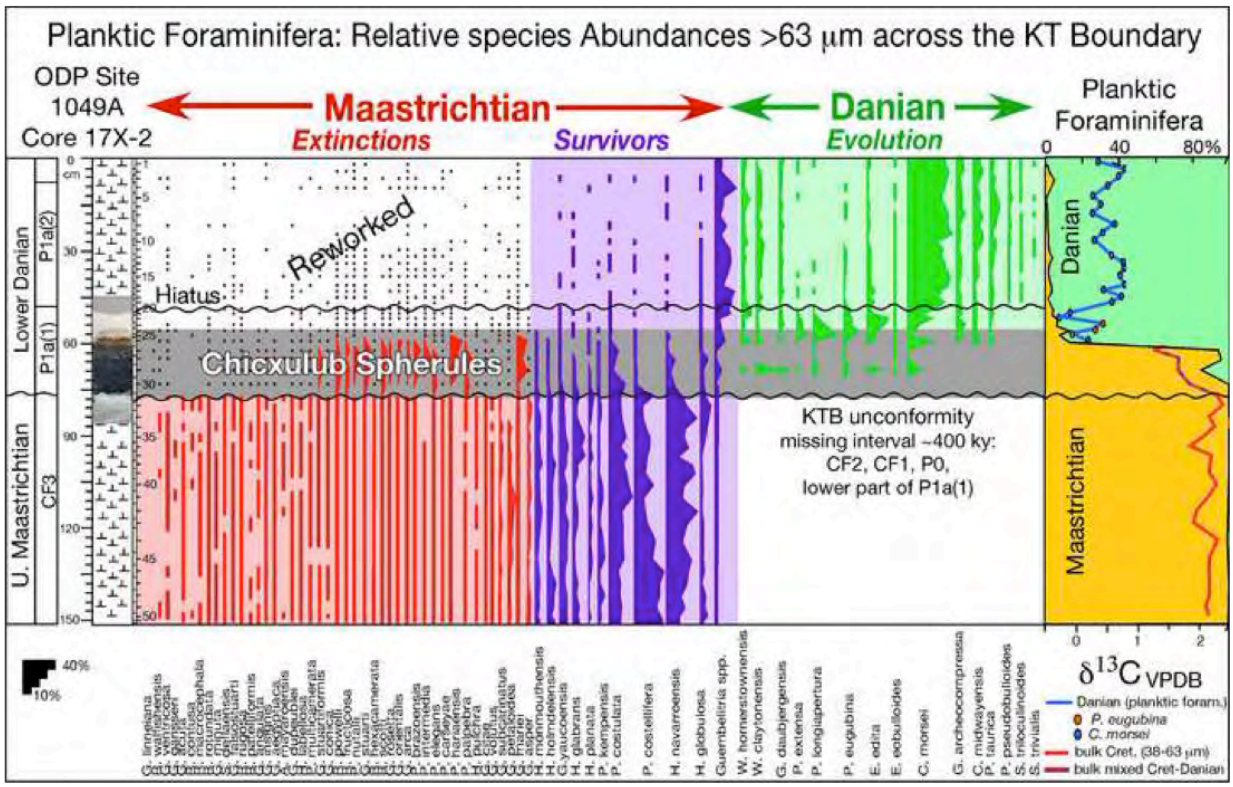

Figure 6. *Biostratigraphy and relative species abundances of planktic foraminifera and d^{13}C values at Site 1049C show a similar pattern to Site 1049A, although with some variability due better preservation notably in the higher abundance of Danian species in the spherule layer. The KTB unconformity spans the same interval as at Site 1049A but reworked Cretaceous species decrease more gradually in the early Danian. d^{13}C values decrease by 2.5‰ across the KTB unconformity followed by the initial early Danian recovery of 1‰ at the P1a(1)/P1a(2) boundary marked by a hiatus.*

Above this claystone is a 2 cm thick white-grey chalk and 3 cm claystone that contain a more diverse subzone P1a(1) assemblage of 9 species (Fig. 8). Sigurdsson et al. (1997) reported the first appearance of lower Danian species in this white-grey chalk. In the overlying claystone the abrupt disappearance of the early Danian species (*P. eugubina, E. edita, W. claytonensis* and *W. hornerstownensis)* and simultaneous first appearance of *S. triloculinoides. P. pseudobulloides* and *S. trivialis* (core 18R-5, 14 cm) marks a hiatus between P1a(1) and P1b with subzone P1a(2) missing. This data suggests a similar KTB and early Danian erosion pattern to Bass River and Blake Nose with impact spherules reworked into early Danian subzone P1a(1). However, erosion of Maastrichtian sediments at the KTB unconformity is more extensive spanning zones CF1-CF4 (~3 myr, Figs. 2, 8).

ODP Site 999B was drilled on Kogi Rise, Colombian Basin (12°44’639’N, 78°44’360’W) at 2828 m depth (Fig. 1). Recovery across the KTB was incomplete. Sigurdsson et al. (1997) assembled a composite section based on three segments (59R-3, 59R-CC and the top of core 60R-1) and placed the KTB at the base of a white limestone (60R-1, 1cm), correlative with their placement at Site 1001B (Fig. 8). No spherules are present and it was suggested they may have been lost in the drilling process.

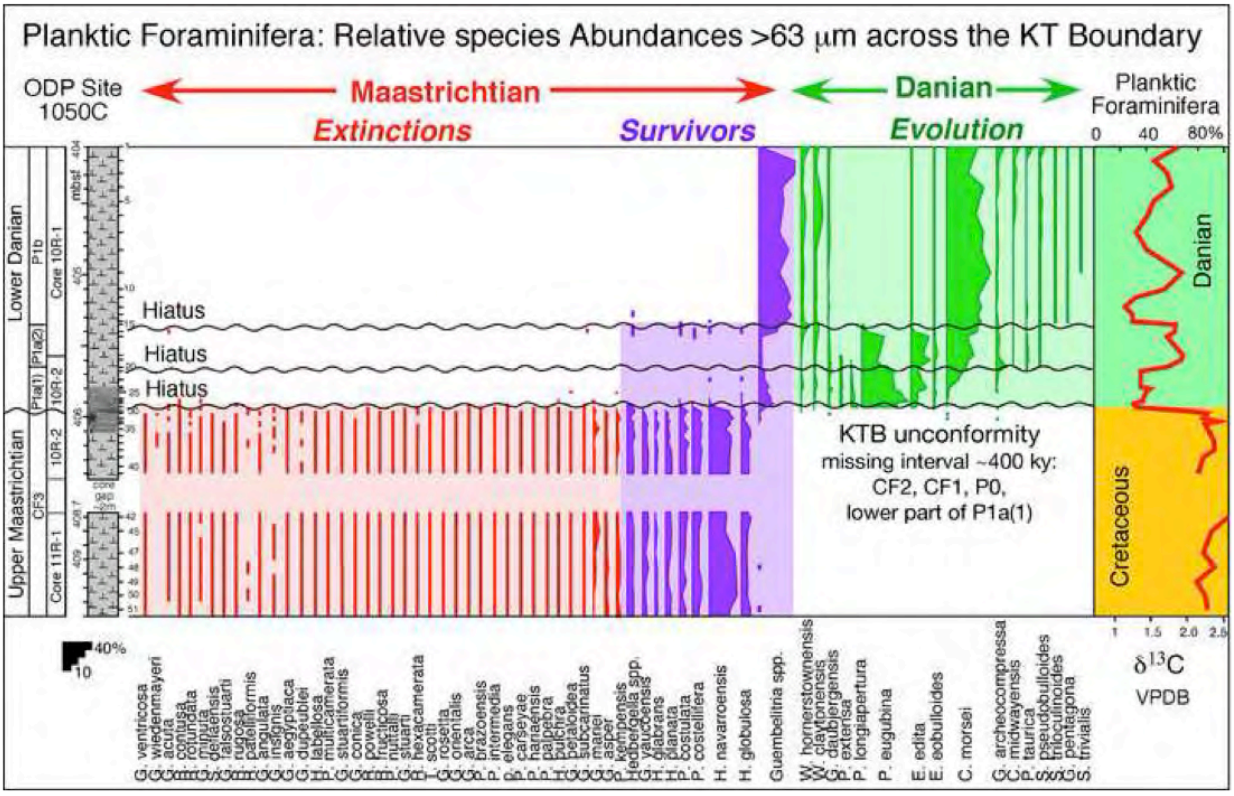

Figure 7. *Biostratigraphy, relative species abundances of planktic foraminifera, $d^{13}C$ values and the KTB unconformity at Site 1050C are very similar to Sites 1049A and 1049C, which are located 300 m downslope and at a distance of 10 km. However, no impact spherule layer is present and reworked Cretaceous species are rare. $d^{13}C$ values (bulk rock) show the negative shift across the KTB unconformity, the temporary recovery marked by a short hiatus at the P1a(1)/P1a(2) boundary and the negative shift at the P1a(2)/P1b hiatus.*

Samples were obtained from the KTB transition. Preservation of foraminifera is poor due to dissolution and the biostratigraphy was determined from species in washed residues and from thin sections. The Maastrichtian limestone at Site 999B (up to 60R-1, 15-18 cm) contains the same impoverished assemblage indicative of zone CF5 as at Site 1001B, which is indicative of the lower upper Maastrichtian (Fig. 2). Sigurdsson et al. (1997) suggested an upper Maastrichtian age of CC26 (*Nephrolithus frequens*) or underlying CC25 zone (*Arkhangelskiella cymbiformis*). They concluded: "*it is not possible to determine whether the K/T boundary at Site 999 is complete from a nannofossil biostratigraphic viewpoint*" (Sigurdsson et al., 1997, p. 154).

Between the grey Maastrichtian limestone and overlying white limestone is a 1-2 cm thick grey claystone with rare Maastrichtian species but abundant *Guembelitria cretacea* and few *W. hornerstownensis, G. daubjergensis* and *P. eugubina*, which indicate deposition in the lower Danian subzone P1a(1). The overlying 10 cm thick white limestone also contains a lower Danian subzone P1a(1) assemblage, similar to the thin white limestone (chalk) at Site 1001B (Fig. 8). Based on this data we place the KTB unconformity between the Maastrichtian limestone and grey claystone with the first Danian assemblage.

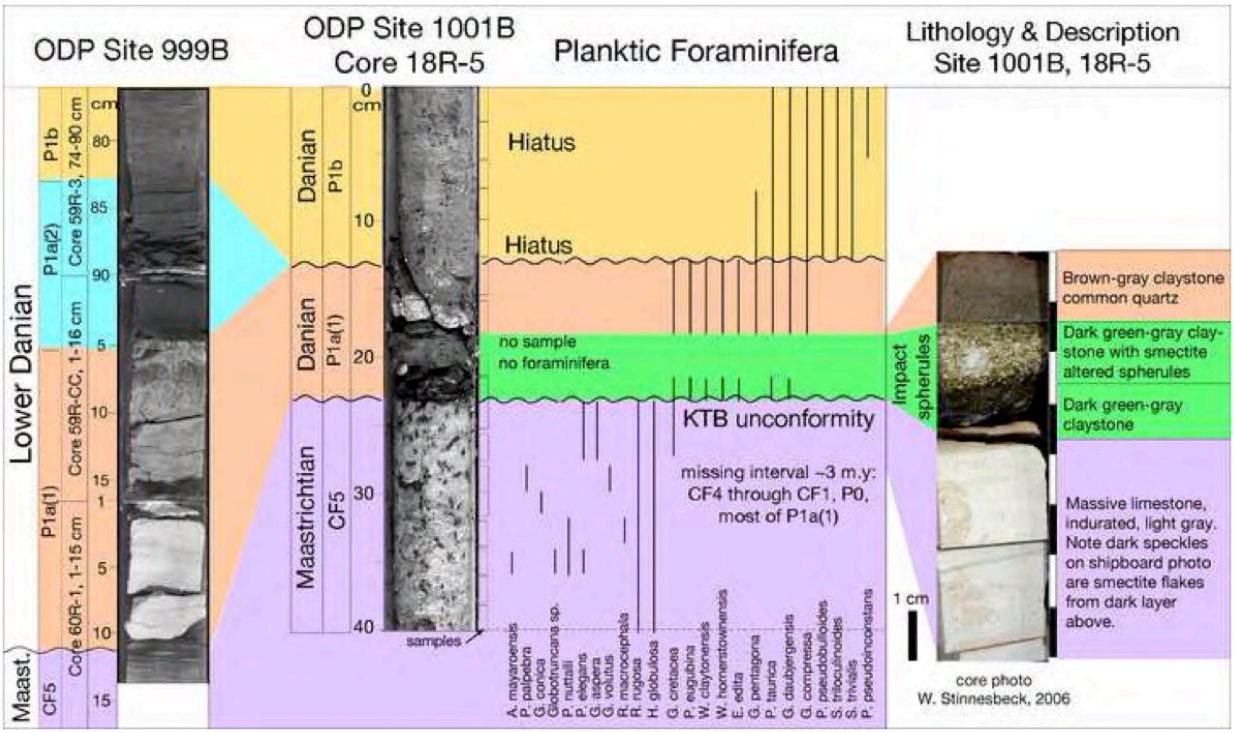

Figure 8*. Biostratigraphy, species ranges and lithology at ODP Site 999B and 1001B. The lithologic description and black & white core photos (with black specks of eroded claystone on Maastrichtian limestone at Site 1001B) are from Sigurdsson et al. (1997). An archive color core photo of Site 1001B from 2006 shows a better image of this interval. Site 999B is a composite of three segments. Planktic foraminiferal data are from washed residues and thin sections. The KTB unconformity spans about 3 myr from the early Danian (most of subzone P1a(1) and zone P0) through the late Maastrichtian (zones CF1-CF4). Another hiatus marks the P1a/P1b boundary with subzone P1a(2) is missing.*

The light grey limestone (59R-CC, 1-15 cm) above the white limestone contains rare and poorly preserved Danian species. Above this layer is a darker grey clay-rich marl that contains a diverse lower Danian subzone P1a(2) assemblage (*G. cretacea, E. edita, P. eugubina, W. hornerstownensis, W. claytonensis, G. daubjergensis, P. taurica, S. triloculinoides, P. pseudobulloides, G. compressa*), which is missing at Site 1001B (Fig. 8). However, the overlying zone P1b assemblage (59R-3, 74-82 cm) is present in both sites. These data indicate a more expanded sediment record across the KTB at Site 999B. However, because this record was pieced together from three different core segments the true sediment record remains uncertain.

4.4. Demerara Rise ODP Site 1259B

ODP Site 1259 was drilled on Demerara Rise (9°18.048'N, 54°11.945') off the SW coast of South America at a water depth of 2354 m (Fig. 1). A 2 cm thick impact spherule layer was recovered at Sites 1259B and 1259C (as well as Sites 1258A, 1260A, Erbacher et al., 2004; MacLeod et al., 2007). Most KTB studies have focused on Sites 1259B and 1259C. We obtained samples from Site 1259B where the spherule layer is in core 13-1, 47-49 cm; 31 samples were analyzed for this report. Sediments below the spherule layer consist of mottled, bioturbated marly chalk with a relatively sharp upper contact. The spherule layer is graded and thin white

chalk layers are present at the base and top, similar to Site 1001B. Danian sediments consist of strongly mottled, bioturbated light and darker gray clayey chalk.

Preservation of planktic foraminifera is good for the Danian and moderate in the Maastrichtian with dissolution effects (thin walls, holes in test chambers). The marly chalk below the spherule layer contains a diverse late Maastrichtian planktic foraminiferal assemblage, including rare *Plummerita hantkeninoides*, the index species for zone CF1 (Fig. 9). Cretaceous assemblages in the >63 mm are dominated by small biserial species (*Pseudoguembelina costulata, Heterohelix planata, H. navarroensis*), whereas *Guembelitria cretacea* is common in the smaller size fraction (36-63 mm). Rare Danian species were obtained from bioturbated grey clay below the KTB unconformity.

One sample was obtained from the spherule layer. Upper Maastrichtian planktic foraminifera are common in the >63 mm and small Danian species are common in the 36-63 mm size fraction where *Guembelitria* species dominate (83-96%) in the spherule layer and 10 cm above it (Fig. 9).

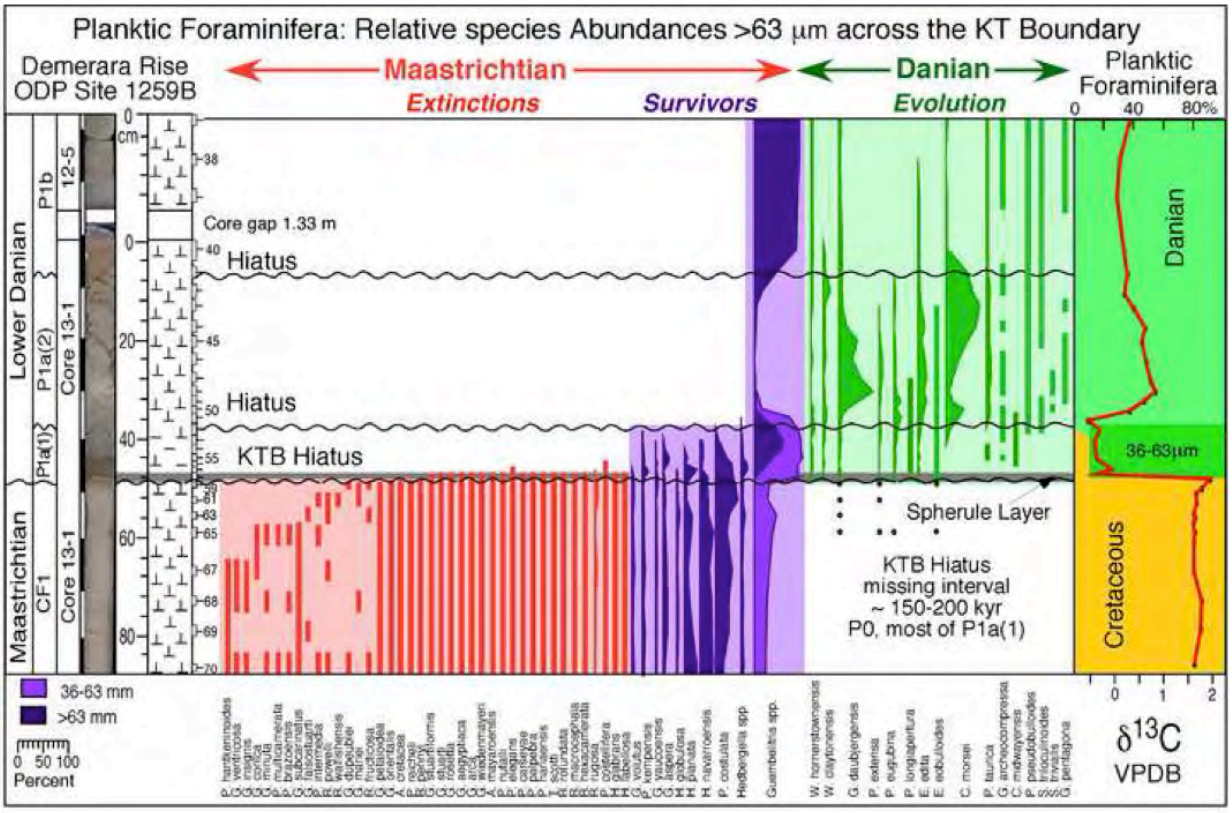

Figure 9. *Biostratigraphy, relative species abundances of planktic foraminifera, $d^{13}C$ values and the KTB unconformity at SW Atlantic Site 1259B. Note the species pattern is similar to NW Atlantic sites although Cretaceous species (mainly KTB survivors) are restricted to the first 10 cm above the unconformity and base of the 2 cm spherule layer. A diverse P1a(1) assemblage of early Danian species is present in the spherule layer and dominates the small size fraction (36-63 mm) with >85% Guembelitria species. Hiatuses are present at the P1a(1)/P1a(2) and P1a(2)/P1b boundaries marked by abrupt species abundance changes.*

The presence of *P. eugubina, G. daubjergensis, W. hornerstownensis, W. claytonensis* and *E. eobulloides* in the spherule layer indicate subzone P1a(1). The same assemblage is present above the spherule layer. The first *P. pseudobulloides* and *Subbotina triloculinoides* appear in sample 13-1, 37-39 cm and mark the P1a(1)/P1a(2) subzone boundary just 8 cm above the spherule layer. *Guembelitria* spp. dominate P1a(1), then rapidly decrease as *Globoconusa daubjergensis* and then *C. morsei* successively dominate in subzone P1a(2). The extinction of *P. eugubina* 37 cm above the spherule layer marks the P1a(2)/P1b boundary. An abrupt assemblage change to dominant *Guembelitria* spp. (85-90%) and abrupt decrease in *C. morsei* suggests another hiatus at the P1a(2)/P1b boundary.

These data reveal a KTB hiatus with most of the Danian subzone P1a(1) and underlying zone P0 missing and an unknown, but likely short interval at the top of the Maastrichtian zone CF1.In addition, short hiatuses are apparent at the P1a(1)/P1a(2) and P1a(2)/P1b boundaries. Similar early Danian erosion and redeposition patterns are apparent at Sites 999B, 1001B, 1049A, 1049C, 1050C and Bass River, although the extent of erosion varies at each location. This is indicated by the variable species abundance patterns between sites although the same biozones P1a(1), P1a(2) and P1b and similar $d^{13}C$ signals are present. For example, at Site 1259B *P. eugubina* is relatively rare, subzone P1a(1) is only 8 cm thick, dominated by *Guembelitria* spp., but with a diverse (14 species) assemblage that indicates an upper P1a(1) interval not observed in the other sections. Subzone P1a(2) is dominated by *C. morsei*, similar to all other sites, but fewer *Guembelitria* spp. Zone P1b differs in its great abundance of *Guembelitria* (~90%) and low abundance of all other species. The difference here is likely due to the core gap of 1.33 m where a critical part of the faunal transition is missing (Fig. 9).

5. Stable Isotope Stratigraphy

One of the characteristic KTB markers is a 2-3 permil negative $d^{13}C$ shift at the base of the Danian, which reflects the productivity crash after the mass extinction. Similarly, the $d^{13}C$ variations in the early Danian mark the delayed marine recovery and setbacks in the aftermath of the mass extinction.

Therefore, carbon isotope stratigraphy, coupled with planktic foraminiferal biostratigraphy, is an excellent and independent method for determining the completeness of the sediment record. No such high-resolution data is published to date for any of the sites analyzed for this study. For Blake Nose (Sites 1049A, 1049B and 1050) and Demerara Site 1259B we analyzed bulk rock fine fraction (36-63mm), which consists primarily of nannoplankton and small planktic foraminifera and is generally a good indicator of primary productivity (Zachos et al., 1989; Schrag et al., 1995). For the Maastrichtian $d^{13}C$ values vary between 1.8-2.2‰, except for Site 1050C which is slightly heavier (2.2-2.4‰, Fig. 10). These values are comparable to those observed in open marine environments, such as South Atlantic Site 525A (Li and Keller, 1998a). No significant changes in $d^{13}C$ are apparent for the intervals of CF3 and CF1 analyzed below the KTB unconformity.

At Sites 1050C and 1259B the KTB unconformity is marked by a sudden 1.2‰ and 2.0‰ drop in $d^{13}C$ values, respectively. At Sites 1049A and 1049C bulk fine fraction yielded a gradual decrease in $d^{13}C$ values well into the early Danian because of the abundance of reworked Cretaceous species (Figs. 5, 6).

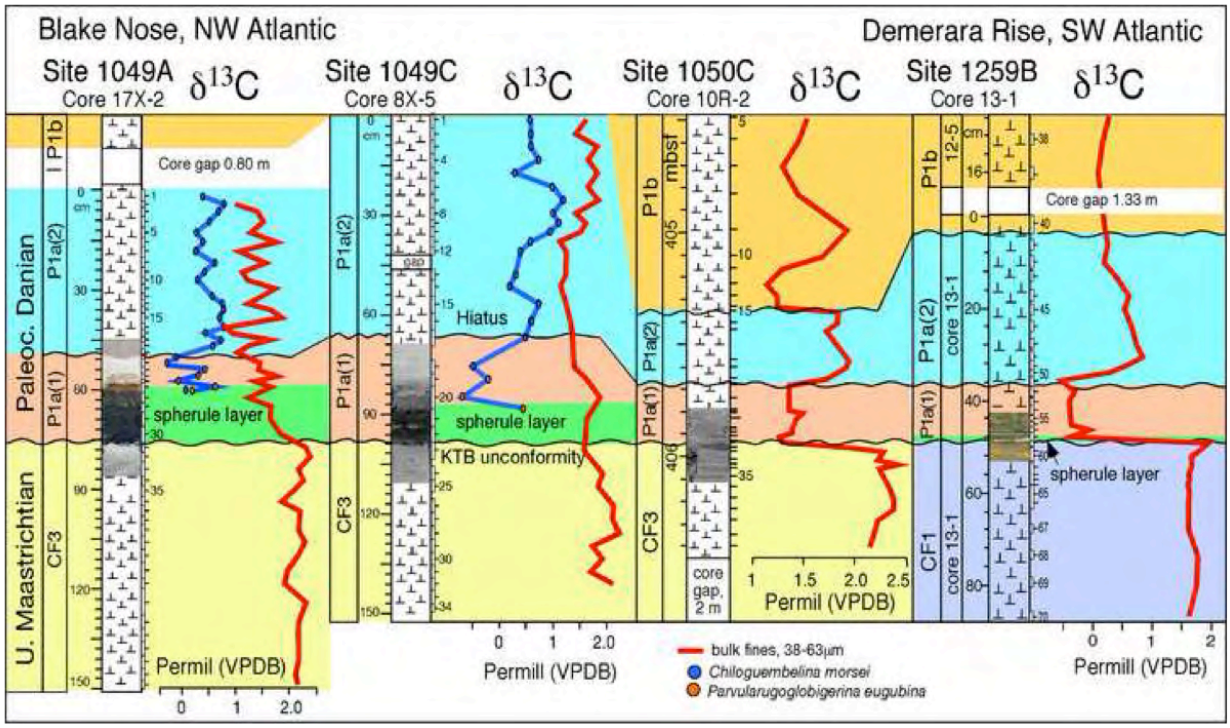

Figure 10. *Bulk rock d^{13}C values from the NW to SW Atlantic ODP sites across the KTB transition and impact spherule layer show a 1.5 to 2.5 permil negative excursion at Sites 1050C and 1259B, but not at Sites 1049A and 1049C due to abundant reworked Cretaceous sediments in the spherule layer and above. However, this signal is recovered in monospecific planktic foraminifera. In all sequences d^{13}C in the early Danian subzone P1a(1) interval record the most negative values. A positive shift of about 1 permil at the P1a(1)/P1a(2) hiatus marks initial recovery after the mass extinction. Another negative d^{13}C excursion marks the P1a(2)/P1b boundary at Site 1050C; core gaps are present at this interval at Sites 1049A and 1259B.*

We obtained an uncompromised lower Danian record from monospecific samples of the Danian species *P. eugubina* and *C. morsei*. In some samples both species were analyzed and the interspecies variation is less than 0.3‰.

Preservation of Danian foraminiferal tests is very good and shell calcite is not recrystallized, but there is minor calcite overgrowth on shell surfaces, which may account for some of the interspecies variation. About 200-300 specimens were picked per sample for analysis. In the lower and middle part of the spherule layer only about 100-150 specimens per species could be obtained (in addition to the quantitative counts that are archived) and this quantity turned out to be insufficient for reliable isotope signals. Nevertheless, in the lower Danian subzone P1a(1), including the top of the spherule layer, the d^{13}C values of Danian species reach lows of -0.5‰ suggesting a drop of about 2‰ across the KTB similar to Site 1259B (Fig. 10). These values are characteristic for the lower Danian above the impact spherule layer in Haiti and the equivalent P1a(1) interval in Tunisia (Keller and Lindinger, 1989; Keller et al., 2001; Stueben et al., 2002).

Major variations in d^{13}C signals through the early Danian that can be correlated despite the frequent hiatuses and variable erosion identified from planktic foraminiferal biostratigraphy and species abundance patterns. The lowest d^{13}C values are known from the early Danian in the aftermath of the mass extinction. In all sites analyzed at least part of this interval is recorded in fine fraction and planktic foraminifera of subzone P1a(1) that includes the spherule layer (Fig.

10). An abrupt positive shift of about 1 permil coincides with the P1a(1)/P1a(2) hiatus. In P1a(2) $d^{13}C$ signals remain relatively high, but do not reach pre-KTB values. The P1a(2) record is fragmented in the sites analyzed due to variable erosion similar to P1a(1). At Site 1050C a negative $d^{13}C$ shift at the P1a(2)/P1b boundary marks the hiatus. This shift was not detected at Sites 1049A and 1259B because of the 0.80 m and 1.33 m core gaps, respectively.

6. DISCUSSION

6. 1. KTB Unconformity

A thin impact spherule layer between Maastrichtian and Paleocene sediments in some KTB sequences from the NW to SW Atlantic and Caribbean is commonly cited as proof that the Chicxulub impact is KTB in age and the sedimentation record complete (e.g., Olsson et al., 1997; Sigurdsson et al., 1997; Norris et al., 1998, 1999; Martinez-Ruiz et al., 2000; MacLeod et al., 2007; Schulte et al., 2010). Results based on high-resolution biostratigraphy, quantitative faunal analyses and stable isotopes show that far from being complete all seven sections analyzed show a major unconformity across the KTB with variable erosion of Maastrichtian sediments.

The maximum extent of erosion can be estimated based on Paleocene and Maastrichtian sediments above and below the unconformity, respectively. At Bass River, New Jersey, the KTB unconformity spans from the early Danian subzone P1a(2) through the upper Maastrichtian zones CF1 and CF2 (~620 kyr, Figs. 2, 3), in NW Atlantic Sites 1049A, 1049C and 1050C from P1a(1) through CF1 and CF2 (~400 kyr, Figs. 5-7), and in the Caribbean Sites 999B and 1001B from P1a(1) through zones CF1, CF2, CF3 and CF4 (~3 myr, Fig. 8). Only at Demerara Rise Site 1259B is erosion or non-deposition more limited spanning most of subzone P1a(1) and all of P0 to the underlying Maastrichtian zone CF1 (~150-200 kyr, Fig. 9). The nearby Site 1258A provides some clues to possible erosion at the top of the Maastrichtian. Just below the KTB Thibault and Gardin (2006) record the abrupt end of the nannofossils *Micula murus* acme that marks the CF1 warm event. In complete sequences, this global warm event ends with the onset of cooling about 50-100 kyr prior to the KTB (Li and Keller, 1998a; Abramovich and Keller, 2003; Abramovich et al., 2011), which suggests erosion of the latest Maastrichtian at Site 1258A and likely at Site 1259B.

We can estimate the missing interval above the KTB based on Danian sediments present within and above the spherule layer. In a complete sequence biozones P0 + P1a(1) + P1a(2) span C29R above the KTB, or 380 kyr based on Gradstein et al. (2004), and half of this is P0 + P1a(1), Fig. 2). In all sections examined zone P0 is absent and P1a(1) is very reduced (missing at Bass River) with abrupt changes in species abundances and $d^{13}C$ shift reflecting a hiatus (Figs. 5-9). Similarly, subzone P1a(2) is reduced with abrupt changes in $d^{13}C$ and species abundances marking a hiatus at the P1a(2)/P1b boundary (Figs. 2-9).

Early Danian P1a hiatuses have been observed in many sections worldwide (e.g., MacLeod and Keller, 1991a,b; Keller et al., 2002, 2003a; Keller, 2008) and may reflect global climate and sea level changes (Adatte et al., 2002). However, NW Atlantic and Caribbean sites differ in the extensive erosion and/or non-deposition in the early Danian (P0-P1a-P1b) and spanning well into the upper Maastrichtian (CF1-CF2) (Fig. 2). We attribute this primarily to tectonic activity in the Caribbean, climate and sea level changes and intensified current circulation (e.g., Gulf Stream, Keller et al., 1993; Watkins and Self-Trail, 2005). The Chicxulub impact may have contributed

mainly via mass wasting of Maastrichtian sediments as suggested by Norris et al. (2000) and Klaus et al. (2001), although these sections do not support this scenario.

6.2. Age and origin of impact spherules

A KTB age for the Chicxulub impact was interpreted based on spherules between Maastrichtian and Danian sediments at the sites investigated (Fig. 11) (e.g., Olsson et al., 1997; Sigurdsson et al., 1997; Norris et al., 1999; MacLeod et al., 2007). There are three key factors that argue against this interpretation: (i) there is a major KTB unconformity in all sequences; (ii) the spherule-rich sediments contain common reworked Maastrichtian species and shallow water benthic foraminifera (Alegret and Thomas, 2004), which argues for erosion and redeposition, and (iii) the spherule layer contains a diverse early Danian P1a(1) species assemblage, which argues for deposition during the early Danian. Earlier studies reported the first Danian species above the spherule layer and thereby justified placing the KTB at its base.

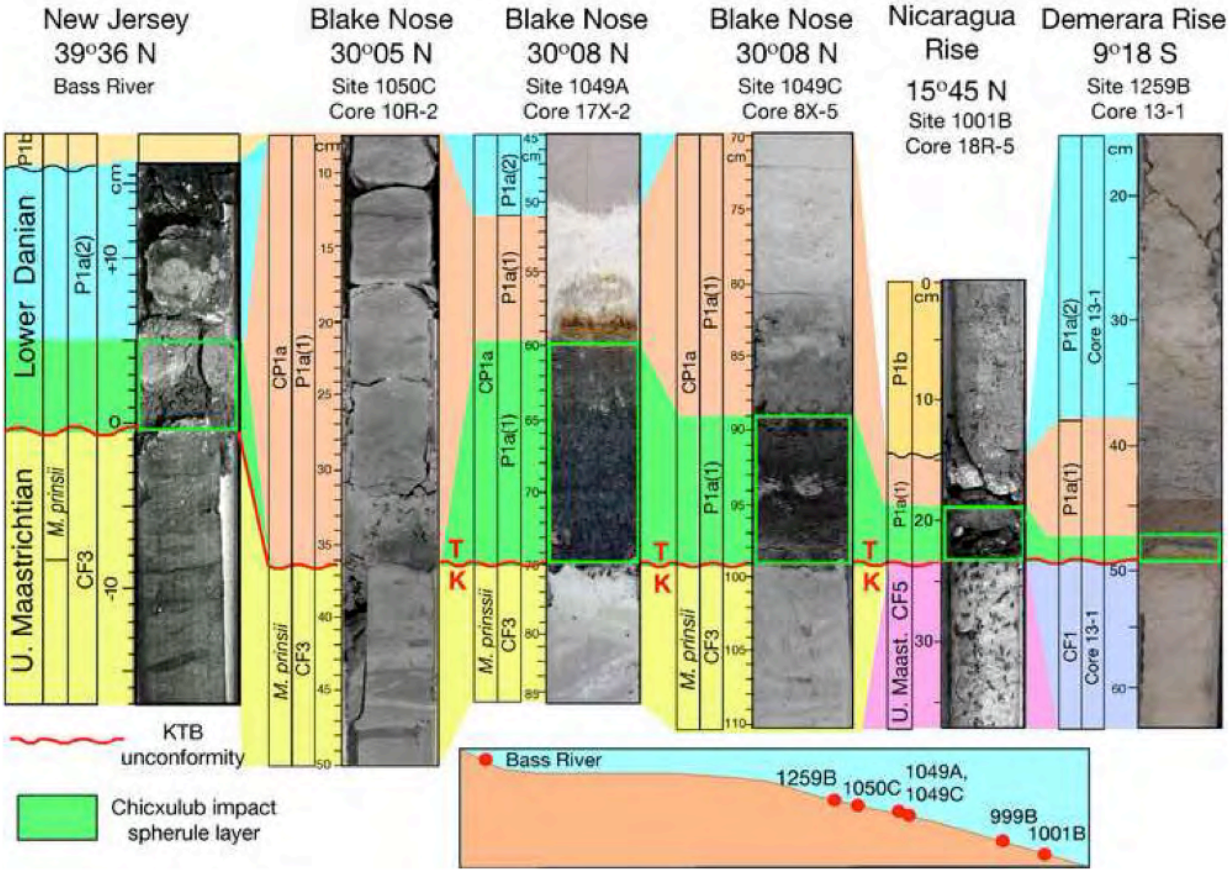

Figure 11. *Biostratigraphic and lithostratigraphic correlation of the KTB transition and Chicxulub impact spherules in cores from the NW to SW Atlantic. A major KTB unconformity is present in all sites with the upper Maastrichtian zones CF1 and CF 2 missing in the NW Atlantic and zones CF1-CF4 missing on Nicaragua Rise. In the early Danian zone P0 and most of subzone P1a(1), or about 150-200 kyr, is missing. When sedimentation resumed impact spherules and Cretaceous species were reworked in subzone P1a(1) at all sites, except at Bass River, New Jersey, where impact spherules are reworked in P1a(2) above the unconformity. A major unconformity is ubiquitous in NW Atlantic and Caribbean sequences (Keller et al., 1993; Bralower et al., 1998) and is likely the result of sea level falls and intensified Gulf Stream circulation.*

It is possible that the early Danian assemblages were not observed because of their small size.

One might argue that the Danian species in the spherule layer are an artifact of bioturbation or leaking of sediments into the more porous spherule layer. Some bioturbation is clearly evident in the lithology of Sites 1049A, 1049C, 1050C (Fig. 4). Similarly at Site 1259B, rare Danian species were observed in burrows below the KTB unconformity (Fig. 9), contrary to Schulte et al. (2009, p. 1185) who noted "*burrows or others signs of bioturbation are totally lacking* ". However, bioturbation may account for some Danian specimens in the spherule layer, but not for an entire assemblage with hundreds of specimens and similar species abundances and diversity as assemblages above.

The presence of these Danian assemblages in the spherule layer above the unconformity indicate that sedimentation resumed in the upper subzone P1a(1) about 150-200 kyr after the KTB mass extinction, except for Bass River NJ where the age is P1a(2). The spherules are thus eroded, transported and redeposited long after the Chicxulub impact. Because the normal early Danian evolutionary pattern is present, except for the missing basal Danian, we can assume that the Danian fauna represents *in situ* deposition interrupted by downslope transport via submarine channel of spherule-rich reworked debris and Maastrichtian foraminifera. The absence of spherules in Site 1050C can be explained by its distant location from the submarine channel. Similar reworking of shallow water sediments and spherules, transport and redeposition into deeper waters is also observed in NE Mexico sections (Alegret et al., 2001). Based on the results from this study the spherules in lower Danian sediments must be reworked from an older primary deposit. Impact spherules have previously been observed in Danian sediments of Haiti, Cuba, Belize, Guatemala and southern Mexico (Keller et al., 2001, 2003b; Alegret et al., 2005; Arenillas et al., 2006; Keller, 2008).

The strongest case for primary spherule deposition precisely at the KTB, and hence precise KTB age for the Chicxulub impact, was made for Demerara Site 1259B by Schulte et al. (2009) based on geochemical and mineralogical analyses. Based on their results (p. 1185) they divided the 1.5-2 cm thick spherule layer into two distinct parts: the upper 0.5-0.7 mm with (i) "*locally enhanced Si, Al, and K contents due to the presence of silicic detritus (i.e., quartz, feldspars, mica), and (ii) local Ca- and Mg-enrichment, indicating the occurrence of calcite and dolomite clasts*". Moreover, they observed a strong negative Nd anomaly, which indicates uptake from contemporaneous ocean water during alteration, which in turn implies a longterm residence time for the spherules in seawater. Schulte et al. (2009, p. 1200) concluded that the Nd isotope systematics "*is best explained by uptake of neodymium from the ocean during the alteration process; this Nd directly reflects fluviatile input from the rather old crustal material in the South American hinterland."* Rather than primary deposition at the time of the Chicxulub impact as argued in their study, these data indicate redeposition of spherules and other detritus that originally accumulated somewhere close to the Guyana craton. This interpretation is consistent with the biostratigraphic results of this study.

6.3. Is there a KTB impact cocktail?

One might argue that the KTB unconformity is unusual and must have an extraordinary cause, such as the Chicxulub impact (e.g., Bralower et al., 1998; Arenillas et al., 2006; Schulte et al., 2010). However, this unconformity is not unique in the NW-SW Atlantic and Caribbean, where major unconformities are the norm (Keller et al., 1993; Bralower et al., 1998; Watkins and

Self-Trail, 2005). Shorter pulses of erosion in the early Danian, as documented in this study, are also widespread (MacLeod and Keller, 1991a,b; Keller et al., 2003a, this study). Moreover, impact spherules are present below the KTB unconformity and in the early Danian P1a sediments in Cuba and southern Mexico, and in Danian sediments in Haiti, Belize, and Guatemala (Alegret et al., 2005; Arenillas et al., 2006; Keller, 2008, 2011). In the shallow water environments of Belize and Guatemala impact spherules are very abundant, frequently in multiple layers and invariably reworked into early Danian P1a(1) to P1a(2) sediments, which overlie Maastrichtian to Campanian limestone (Keller et al., 2003b; Keller, 2008). A similar pattern was observed in Haiti with multiple spherule layers reworked in early Danian P1a(1) to base P1a(2) sediments (Keller et al., 2001).

Most workers ignore spherules in lower Danian sediments, or attribute them to impact-generated tsunami effects, including mass wasting, contamination or leaking of sediments into the more porous spherule layer (e.g., Klaus et al., 2000; Schulte et al., 2009, 2010). However, this cannot be reconciled with the results of this study or of earlier studies in Haiti, Belize, Guatemala and southern Mexico where multiple spherule layers are reworked in lower Danian sediments. To date most effort has gone into explaining the presence of spherule layers in Maastrichtian sediments below the KTB.

For example, Bralower et al. (1998, p. 331) state "*reworked microfossils, impact-derived materials, and lithic fragments occur in sediments at the Cretaceous-Tertiary boundary in the basinal Gulf of Mexico and Caribbean. Recognition of this cocktail is a reliable way to identify the Cretaceous-Tertiary boundary*". Moreover, "*In some sites, cocktail units are separated from underlying Cretaceous and overlying Paleocene strata by unconformities*" (p. 332). This broad all-inclusive "cocktail" permits almost any type of lithologic units to be interpreted as KTB in age. However, out of 12 sites discussed (p. 332), they found only two they considered complete across the KTB. One is Site 1001, which this report demonstrates has a major unconformity (P1a(1) to CF5) and spherules in lower Danian P1a(1) sediments (Fig. 8). The second locality is Beloc, Haiti, where Danian subzone P1a(1) overlies the KTB unconformity and multiple impact spherule layers are reworked in P1a(1) and lower part of P1a(2) (Keller et al., 2001; Keller, 2008) similar to Bass River and Sites 1049A, 1049C, 1001B and 1259B (Figs. 3, 5-9).

Bralower et al. (1998) attribute another four sites (Sites 536-540) to the "boundary cocktail" based on a mix of reworked Cretaceous nannofossils and a few planktic foraminifera below the Paleocene. However, Site 536 is very similar to Sites 999B and 1001B with a truncated zone P1a overlying sediments with a relatively diverse Maastrichtian assemblage (38 species) indicative of the lower to upper Maastrichtian (Keller et al., 1993), equivalent to current zones CF5 or CF6 and nannofossil *L. quadratus* zone (Fig. 2). (Note that the presence of a few reworked older Cretaceous planktonic foraminifera is no indication of tsunami disturbance because rare reworked species can be found in sediments of any age and are the result of normal marine currents.) The similarity in erosion patterns of the Gulf of Mexico, Caribbean and NW Atlantic strongly argues for erosion linked to sea level fluctuations, rather than chaotic mass wasting, gravity slumps, and reworking (e.g., Bralower et al., 1998).

Arenillas et al. (2006, and Schulte et al., 2010) applied the "cocktail" concept to identify impact-tsunami deposits in southern Mexico sections at Bochil and Guyal. Arenillas et al. (2006) concluded the 80 m thick breccia unit and 1-6 m of microbreccia with spherules and an Ir

anomaly in the top 1 cm at Bochil "*is synchronous with the ejecta-rich airfall layer and the Cretaceous-Paleogene (K/Pg) catastrophic mass extinction*" (p.241). However, the breccia consists of alternating conglomerate and reef-derived limestone clasts that are likely collapse breccias common in carbonate slope areas of southern Mexico and Guatemala (Fourcade et al., 1998; Keller et al., 2003b). The spherule-rich microconglomerate is reworked in zone CF1 and truncated at the top by a burrowed erosion surface (Keller, 2011). Above this unconformity is a diverse early Danian P1a(1) assemblage. Beginning at 10 cm above is an 0.8 ppb Ir anomaly with enriched (0.5 ppb) values continuing into the P1a(2), and a thin spherule-rich microconglomerate at 25 cm above the unconformity (see also Fourcade et al., 1998). Limestone breccias and multiple reworked impact spherules are likely related to tectonic activity during the late Maastrichtian when the southern margin of the Yucatan (Maya) block collided with the Greater Antillean Arc, and during the early Paleocene with the Chortis block (e.g., Pindelll and Barrett, 1990; Fourcade et al., 1994; Meschede and Frisch, 1998). Thus, caution must be exercised in interpreting Ir anomalies as KTB markers, spherules as representing the time of the Chicxulub impact, and limestone conglomerates and breccias as related to the Chicxulub impact.

7. CONCLUSIONS

The results of this study reveal a fragmented sedimentary record for the KTB transition in the NW to SW Atlantic and Caribbean with a major unconformity that spans from the lower Danian across the KTB and into the upper Maastrichtian. At these localities Chicxulub impact spherules and Maastrichtian species are reworked and redeposited in lower Danian sediments above the unconformity.

- Bass River core NJ: The KTB unconformity spans from the early Danian subzone P1a(2) through P1a(1), P0, CF1 and CF2 for a total of about 620 kyr (Figs. 3, 12). The 6 cm thick impact spherule layer was eroded and redeposited in the early Danian.
- Blake Nose Sites 1049A, 1049C, 1050C: The KTB unconformity spans from the early Danian subzone P1a(1) through upper Maastrichtian zones CF1 and CF2 for a total of about 400 kyr (Figs. 5, 6, 12). The 10cm and 15 cm thick spherule layer was eroded and redeposited in the early Danian. The same unconformity is also present in Site 1050C where no spherules are present (Fig. 7).
- Caribbean Sites 999B and 1001B: The KTB unconformity at Sites 999B and 1001B spans from Danian subzone P1a(1) through upper Maastrichtian zones CF1, CF2, CF3, CF4 for a total of about 3 myr (Figs. 2, 8). Impact spherules at Site 1001B are eroded and redeposited in the early Danian (no spherules in site 999B).
- Demerara Site 1259B: A KTB hiatus spans most of subzone P1a(1) and zone P0 (total of 150-200 kyr) with erosion likely to the uppermost Maastrichtian warm event in zone CF1. Spherule layer are reworked into early Danian sediments.
- Short hiatuses also occur in the early Danian at the P1a(1)/P1a(2) and Pla(2)/P1b boundaries in all sections examined and are likely linked to climate and sea level fluctuations. Similar hiatuses have been identified in many early Danian sequences worldwide.

- Abrupt negative and positive $d^{13}C$ shifts observed in Sites 1049A, 1049C, 1050C, 1259B support the KTB and early Danian hiatuses and reflect low primary productivity and delayed post-KTB recovery of the ecosystem into zone P1b.
- The widespread erosion and sedimentation pattern through the NW-SW Atlantic and Caribbean and the reworked impact spherules in lower Danian sediments rule out this area as indicator of the age of the Chicxulub impact.

ACKNOWLEDGEMENTS: Samples for this research were obtained from the Integrated Ocean Drilling Program (IODP), Bremen Core Repository (BCR), Germany, during two sampling visits in 2006 and 2011. We are grateful to Walter Hale, Repository Superintendent for his kind assistance during sampling. The material for this study is based upon work supported by the US National Science Foundation through the Continental Dynamics Program and Sedimentary Geology and Paleobiology Program under NSF Grants EAR-0207407 and EAR-0447171.

REFERENCES

Abramovich, S., Keller, G., 2003. Planktonic foraminiferal response to the latest Maastrichtian abrupt warm event: a case study from South Atlantic DSDP Site 525A. Marine Micropaleontology 48, 225-249.

Abramovich, S., Yovel-Corem, S., Almogi-Labin, A., Benjamini, C., 2010. Global climate change and planktic foraminiferal response in the Maastrichtian. Paleoceanography 25, PA2201.

Adatte, T., Stinnesbeck, W., Keller, G., 1996. Lithostratigraphic and mineralogical correlations of near-K/T boundary clastic sediments in northeastern Mexico: Implications for origin and nature of deposition, in*:* Ryder G., et al. (Eds), The Cretaceous-Tertiary event and other catastrophes in Earth History. Geological Society of America, Special Paper 307, 211-226.

Adatte, T., Keller, G., Stinnesbeck, W., 2002. Late Cretaceous to early Paleocene climate and sea-level fluctuations. Paleogeogr., Paleoclimatol., Paleoecol., 178, 165-198.

Adatte, T. Keller, G., Stueben, D., Harting, M., Kramar, U., Stinnesbeck, W., Abramovich, S. and Benjamini, C., 2005. Late Maastrichtian and K/T paleoenvironment of the eastern Tethys (Israel): mineralogy, trace element and platinum group elements, biostratigraphy and faunal turnovers. Bulletin Société Géologique de France. 176, 1, 35-53.

Adatte, T., Keller, G., Baum, G., 2011. Age and origin of the Chicxulub impact and sandstone complex, Brazos River, Texas: Evidence from Lithostratigraphy, Sedimentology and Sequence Stratigraphy, in: Keller, G., Adatte, T., (Eds.), The End-Cretaceous Mass Extinction and the Chicxulub Impact in Texas, SEPM Special Publication No. 100, 43-80.

Alegret, L., Thomas, E., 2004. Benthic foraminifera and environmental turnover At the Cretaceous/Paleogene boundary at Blake Nose (ODP Hole 1049C, Northwestern Atlantic). Paleogeography, Paleoclimatology, Paleoecology 208, 59-83.

Alegret, L., Arenillas, I., Arz, J.A., Diaz, C., Grajales-Nishimura, J.M., Melendez, A., Molina, E., Rojas, R., Soria, A.R., 2005. Cretaceous-Paleogene boundary deposits at Loma Capiro, central Cuba: Evidence for the Chicxulub impact. Geology 33(9), 721-724.

Arenillas, I., Arz, J.A., Grajales-Nishimura, J.M., Murillo-Muneton, G., Alvarez, W., Camargo-Zanguera, A., Molina, E., Rosales- Dominguez, C., 2006. Chicxulub impact event is Cretaceous/Paleogene boundary in age: New micropaleontological evidence. Earth and Planetary Science Letters 249, 241-257.

Berggren, W.A., Kent, D.V., Swisher, C.C., Aubry, M.-P., 1995. A revised Cenozoic geochronology and chronostratigraphy. in: Berggren, W.A., Kent, D.V., Aubry, M.-P., Hardenbol, J. (Eds.),

Geochronology, Time Scales and Global Stratigraphic Correlation, SEPM Special Publication 54, 129-212.

Bralower, T.J., Paull, C.K., Leckie, R.M., 1989. The Cretaceous-Tertiary boundary cocktail: Chicxulub impact triggers margin collapse and extensive sediment gravity flows. Geology 26, 331-334.

Brooks, R.R., Hoek, P.L., Peeves, R.D., Wallace, R.C., Johnston, J.H. Ryan, D.E., Hozbecher, J., Collen, J.D., 1985.Weathered spheroids in a Cretaceous-Tertiary boundary shale at Woodside Creek, New Zealand. Geology 13, 735-740.

Cande, S., KENT, D.V., 1995. Revised calibration of the geomagnetic polarity Timescale for the Late Cretaceous and Cenozoic, Journal of Geophysical Research 100, 6093-6095. Colodner, D.C., Boyle, E.A., Edmond, J.M., Thomson, J., 1992. Post-depositional mobility of platinum, iridium, and rhenium in marine sediments. Nature 358, 402–404.

Cowie, J.W., Ziegler, W., Remane, J., 1989. Stratigraphic Commission accelerates Progress, 1984 to 1989. Episodes 12, 79-83.

Elliot, C.W., Aronson, J.L., Millard, H.T. Gierlowski-Kordesch, E., 1989. The origin of clay minerals at the Cretaceous-Tertiary boundary in Denmark. Geol. Soc. America Bull. 101, 702-710.

Ekdale, A.A., Stinnesbeck, W., l998. Ichnology of Cretaceous-Tertiary (K/T) boundary beds in northeastern Mexico: Palaios 13, 593-602.

Erbacher, J., Mosher, D.C., Malone, M.J., et al., Site 1259. Proceedings of the Ocean Drilling Program, Initial Reports, Volume 207, College Station, Texas, Ocean Drilling Program p. 1-110.

Fourcade, E., Méndez, J., Azéma, J. et al., 1994. Dating of the settling and drowning of the carbonate platform and of the overthrusting of the ophiolites on the Maya Block during the Mesozoic (Guatemala). Newsletter on Stratigraphy 30, 33-43.

Fourcade, E., Rocchia, R., Gardin, S., Bellier, J-P., Debrabant, P., Masure, E., Robin, E. and Pop, W.T. 1998. Age of the Guatemala breccias around the Cretaceous-Tertiary boundary: relationships with the asteroid impact on the Yucatan. Comptes Rendues de l' Academie Scientifique Paris, Sciences de la Terre et des planètes 327, 47-53.

Gale, A., 2006. The Cretaceous-Tertiary boundary on the Brazos River, Falls County, Texas; evidence for impact-induced tsunami sedimentation? Proceedings of theGeologists' Association 117, 1-13.

Gertsch, B., Keller, G., Adatte, T., Berner, Z., 2011. Platinum Group Element (PGE) Geochemistry of Brazos Sections, Texas, in: Keller, G., Adatte, T. (Eds.), The End-Cretaceous Mass Extinction and the Chicxulub Impact in Texas, SEPM Special Publication 100, 228-249.

Gradstein, F., Ogg, J., Smith, A., 2004. A Geologic Time Scale. Cambridge, U.K.Cambridge University Press, 598 pp.

Graup, G., Spettel, B., 1989. Mineralogy and phase-chemistry of an Ir-enriched pre-K/T layer from the Lattengebirge, Bavarian Alps, and significance for the KTB problem. Earth and Planetary Science Letters 95, 271-290.

Huber, B.T., MacLeod, K.G., Norris, R.D., 2002. Abrupt extinction and subsequent reworking of Cretaceous planktonic foraminifera across the K/T boundary: evidence from the subtropical North Atlantic, in: Koeberl, C., MacLeod, K. (Eds.), Catastrophic Events and Mass Extinctions: Impacts and Beyond. Geological Society of America, Special Paper 356, 227–289.

Huber, B.T., MacLeod, K.G., Tur, N.A., 2008. Chronostratigraphic framework for upper Campanian-Maastrichtian sediments on the Blake Nose (Subtropical North Atlantic). Journal of Foraminiferal Research 38 (2), 162-182.

Keller, G., 2008. Impact Stratigraphy: old principle - new reality, in: Evans, K.R., Horton, J.W., King, D.T., (Eds.), The Sedimentary Record of Meteorite Impacts. Geological Society of America, Special Paper 437, 147-178.

Keller, G., 2011. Defining the Cretaceous - Tertiary Boundary: A practical Guide and Return to first Principles, in: Keller, G., Adatte, T., (Eds), The End-Cretaceous Mass Extinction and the Chicxulub Impact in Texas, SEPM Special Publication No. 100, 23-42.

Keller, G., Lindinger, M., 1989. Stable isotopes, TOC and CaCO3 record across the Cretaceous-Tertiary boundary at El Kef, Tunisia. Paleogeogr. Paleoclimatol., Paleoecol., 73(3/4), 243-265.

Keller, G., Lyons, J.B., MacLeod, N., Officer, C.B., 1993. Is there evidence for Cretaceous-Tertiary boundary impact deposits in the Caribbean and Gulf of Mexico? Geology 21, 776-780.

Keller, G., Li, L., MacLeod, N., 1995. The Cretaceous/Tertiary boundary stratotype section at El Kef, Tunisia: How catastrophic was the mass extinction? Paleogeography, Paleoclimatology, Paleoecology 119, 221-254.

Keller, G., Adatte, T., Stinnesbeck, W., Stueben, D., Berner, Z., 2001. Age, chemo- and biostratigraphy of Haiti spherule-rich deposits: a multi-event K-T scenario. Canadian Journal of Earth Sciences 38, 197-227.

Keller, G., Adatte, T., Stinnesbeck, W., Luciani, V., Karoui, N., Zaghbib-Turki, D., 2002. Paleoecology of the Cretaceous-Tertiary mass extinction in planktic foraminifera. Paleogeography, Paleoclimatology, Paleoecology 178, 257-298.

Keller, G., Stinnesbeck, W., Adatte, T., Stueben, D., 2003a. Multiple Impacts across the Cretaceous-Tertiary boundary. Earth Science Reviews 62,327-363.

Keller, G., Stinnesbeck, W., Adatte, T., Holland, B., Stueben, D., Harting, M., De Leon, C., De La Cruz, J., 2003b. Spherule deposits in Cretaceous-Tertiary boundary sediments in Belize and Guatemala. J. Geological Society of London 160, 1-13.

Keller, G. Adatte, T., Berner, Z. Harting, M. Baum, G. Prauss, M. Tantawy A. A., Stueben, D., 2007. Chicxulub Impact Predates K-T Boundary: New Evidence from Texas. Earth and Planetary Science Letters 255, 339-356.

Keller, G., Adatte, T., Berner, Z., Pardo, A., Lopez-Oliva, L., 2009a. New Evidence concerning the Age and Biotic Effects of the Chicxulub impact in Mexico. J. Geological Society of London 166, 393-411.

Klaus, A., Norris, R.D., Kroon, D., Smit, J., 2000. Impact-induced mass wasting at the K-T boundary: Blake Nose, western North Atlantic. Geology 28, 319–322.

Kramar, U., Stueben, D., Berner, Z., Stinnesbeck, W., Philipp, H., Keller, G., 2001. Are Ir anomalies sufficient and unique indicators cosmic events? Planetary Space Science 49, 831-837.

Lee, C-T, A., Wasserburg, G.J., Kyte, F. T., 2003. Platinum-group elements (PGE) and rhenium in marine sediments across the Cretaceous-Tertiary boundary: Constraints on Re-PGE transport in the marine environment. Geochimica et Cosmochimica Acta 67(4), 655-670.

Li, L., Keller, G., l998a. Abrupt deep-sea warming at the end of the Cretaceous. Geology 26(11), 995-998.

Li, L., Keller, G., l998b. Diversification and extinction in Campanian-Maastrichtian planktic foraminifera of northwestern Tunisia. Eclogae Geologica Helvetica 91, 75-102.

Li, L., Keller, G., l998c. Maastrichtian climate, productivity and faunal turnovers in planktic foraminifera in South Atlantic DSDP Sites 525A and 21. Marine Micropaleontology 33, 55-86.

Maurrasse, F. J-M. R., Sen, G., 1991a. Impacts, tsunamis, and the Haitian Cretaceous-Tertiary boundary layer. Science 252, 1690-1693.

MacLeod, N. and Keller, G., 1991a. Hiatus distribution and mass extinctions at the Cretaceous-Tertiary boundary. Geology 19, 497-501.

MacLeod, N. and Keller, G., 1991b. How complete are Cretaceous/Tertiary Boundary sections? A Chronostratigraphic estimate based on graphic correlation. Geol. Soc. Amer. Bull., 103: 1439-1457.

MacLeod , K. G., Whitney, D. L., Huber, B.T., Koeberl, C., 2007. Impact and extinction in remarkably complete Cretaceous-Tertiary boundary sections from Demerara Rise, tropical western North Atlantic. Geological Society of America Bulletin 119, 101-115.

Martinez-Ruiz, F., Ortega-Huertas, M., Palomo-Delgado, I., Smit, J., 2001. K-T boundary spherules from Blake Nose (ODP Leg 171B) as a record of the Chicxulub ejecta deposits, in: Kroon, D., Norris, R.D., Klaus, A. (Eds.), Western North Atlantic Paleogene and Cretaceous Paleoceanography. Geological Society of London Special Publication 183, 149–161.

Meschede, M., Frisch, W., 1998. A plate-tectonic model for the Mesozoic and early Cenozoic history of the Caribbean Plate. Tectonophysics 296, 269-291.

Miller, K.G., Sugarman, P.J., Browning, J.V., et al., 1998. Bass River Site. Proceedings of the Ocean Drilling Program, Initial Reports, College Station, Texas 174AX, 1-39.

Miller, K.G., Sherrell, R.M., Browning, J.V., Field, M.P., Gallagher, W., Olsson, R.K., Sugarman, P.J., Tuorto, S., Wahyudi, H., 2010. Relationship between mass extinction and iridium across the Cretaceous-Paleogene boundary in New Jersey. Geology 28, 867-870.

Molina , E., Alegret , L., Arenillas , I., Arz, J. A., Gallala, N., Hardenbol , J., Von Salis, K., Steurbaut , E.,Vandenberghe , N., Zaghbib-Turki, D., 2006. The Global Boundary Stratotype Section and Point for the base of the Danian Stage (Paleocene, Paleogene, "Tertiary", Cenozoic) at El Kef, Tunisia - Original definition and revision. Episodes 29, 263-273.

Norris, R.D., Kroon, D., Klaus, A., et al., 1998. Site 1049. Proceedings of the Ocean Drilling Program, College Station, Texas, Initial Reports 171B, 47-86.

Norris, R. D., Huber, B. T., Self-Trail, B.T., 1999. Synchroneity of the KT oceanic mass extinction and meteorite impact: Blake Nose, western North Atlantic. Geology, 27, 419–422

Norris, R.D., Firth, J., Blusztajn, J., Ravizza, G., 2000. Mass failure of the North Atlantic marign triggered by the Cretaceous–Paleogene bolide impact. Geology 28, 1119–1122.

Olsson, R. K., Miller, K.G., Browning, J.V., Habib, D., Sugarmann, P.J., 1997. Ejecta layer at the Cretaceous-Tertiary boundary, Bass River, New Jersey (Ocean Drilling Program Leg 174AX). Geology 25, 759–762.

Pindell, J.L., Barrett, S.F., 1990.Geological evolution of the Caribbean region: a plate tectonic synthesis. In: Dengo, G. & Case, J.E. (Eds.) The Caribbean Region: the Geology of North America. Geological Society of America, Boulder, CO, 405-432.

Remane, J., Keller, G., Hardenbol, J., Ben Haj Ali, M., l999. Report on the International Workshop on Cretaceous-Paleogene Transitions. Episodes 22(1), p. 47-48.

Revesz, K.M., Landwehr, J.M., Keybl, J., 2001. Measurement of δ13C and δ18O isotope ratios of CaCO3 using a Thermoquest Finnigan GasBench II Delta Plus XL Continuous Flow Isotope Ratio Mass Spectrometer with application to Devils Hole Core DH-11 Calcite. U.S. Geological Survey Open-File-Report 01-257, 17 pp.

Sigurdsson, H., Leckie, R.M., Acton, G.D., et al., 1997. Caribbean volcanism, Cretaceous/Tertiary impact, and ocean-climate history: Synthesis of leg 165. Proceedings of the Ocean Drilling Program, College Station, Texas, Initial Reports 165, 377-400

Schulte, P., Stinnesbeck, W., Stueben, D., Kramar, U., Berner, Z., Keller, G., Adatte, T., 2003. Fe-rich and K-rich mafic spherules from slumped and channelized Chicxulub ejecta deposits in the northern La Sierrita area, NE Mexico. International J. Earth Sciences 92, 114-142.

Schulte, P., Speijer, R.P., Mai, H., Kontny, A., 2006. The Cretaceous-Paleogene (K-P) boundary at Brazos, Texas: Sequence stratigraphy, depositional events and the Chicxulub impact. Sedimentary Geology 184, 77-109.

Schulte, P., and 40 others, 2010. The Chicxulub asteroid impact and mass extinction at the Cretaceous-Paleogene boundary. Science 327, 1214-1218.

Schrag, D.P., DePaolo, D.J., Richter, F.M., 1995. Reconstructing past sea surface temperatures from oxygen isotope measurements of bulk carbonate. Geochim. Cosmochim. Acata 59, 2265-2278.

Smit, J., 1999. The global stratigraphy of the Cretaceous-Tertiary boundary impact ejecta. Annual Review Earth Planet Science 27, 75–113.

Smit, J., Montanari, A., Swinburne, N. H. M., Alvarez, W., Hildebrand, A. R., Margolis, S. V., Claeys, P., Lorie, W., Asaro, F., 1992. Tektite-bearing, deep-water clastic unit at the Cretaceous-Tertiary boundary in northeastern Mexico. Geology 20, 99-103.

Stinnesbeck, W., Barbarin, J.M., Keller, G., Lopez-Oliva, J.G., Pivnik, D.A., Lyons, J.B., Officer, C.B., Adatte, T., Graup, G., Rocchia, R., Robin, E., 1993. Deposition of near K/T Boundary clastic sediments in NE Mexico: Impact or Turbidite Deposits*?* Geology 21, 797-800.

Stueben, D., Kramer, U., Berner, Z., Eckhardt, J.D., Stinnesbeck, W., Keller, G., Adatte, T. and Heide, K. 2002. Two anomalies of platinum group elements above the Cretaceous-Tertiary boundary at Beloc, Haiti: Geochemical context and consequences for the impact scenario. Geological Society of America, Special Volume 356, 163-188.

Stueben, D., Kramar, U., Harting, M., Stinnesbeck, W., Keller, G., 2005. High-resolution geochemical record of Cretaceous-Tertiary boundary sections in Mexico: New constraints in the K/T and Chicxulub events. Geochim. Et Cosmochim. Acta 69, 2559-2579.

Tantawy A.A. 2003. Calcareous nannofossil biostratigraphy and paleoecology of the Cretaceous-Tertiary transition in the western desert of Egypt. Marine Micropaloentology 47, 323-356.

Thibault, N., Gardin, S., 2006. Maastrichtian calcareous nannofossil biostratigraphy and paleoecology in the Equatorial Atlantic (Demerara Rise, ODP Leg 207 Hole 1258A). Reviue de micropaléontology 49, 199-214.

Watkins, D.K., Self-Trail, J.M., 2005. Calcareous nannofossil evidence for the existence of the Gulf Stream during the late Maastrichtian, Paleoceaonography20, PA3006.

Zachos, J.C., Arthur, M.A., Dean, W.E., 1989. Geochemical evidence for suppression of pelagic marine productivity at the Cretaceous/Tertiary boundary. Nature 337, 61- 64.

STRATIGRAPHY OF THE CENOMANIAN-TURONIAN OCEANIC ANOXIC VENT OAE2 IN SHALLOW SHELF SEQUENCES OF NE EGYPT[1]

Abstract. Two shallow water late Cenomanian to early Turonian sequences of NE Egypt have been investigated to evaluate the response to OAE2. Age control based on calcareous nannoplankton, planktic foraminifera and ammonite biostratigraphies integrated with $\delta^{13}C$ stratigraphy is relatively good despite low diversity and sporadic occurrences. Planktic and benthic foraminiferal faunas are characterized by dysoxic, brackish and mesotrophic conditions, as indicated by low species diversity, low oxygen and low salinity tolerant planktic and benthic species, along with oyster-rich limestone layers. In these subtidal to inner neritic environments the OAE2 $\delta^{13}C$ excursion appears comparable and coeval to that of open marine environments. However, in contrast to open marine environments where anoxic conditions begin after the first δ13C peak and end at or near the Cenomanian-Turonian boundary, in shallow coastal environments anoxic conditions do not appear until the early Turonian. This delay in anoxia appears to be related to the sea level transgression that reached its maximum in the early Turonian, as observed in shallow water sections from Egypt to Morocco.

Keywords: Cenomanian-Turonian; OAE2; Shallow water sequences; Egypt

1. INTRODUCTION

The mid-Cretaceous (120–80 Ma) represents one of the warmest periods in Earth's history (Norris et al., 2002; Gustafsson et al., 2003; Forster et al., 2007) characterized by high atmospheric CO2 levels (Arthur et al., 1985, 1991), high tropical sea-surface temperatures accompanied by relatively low latitudinal temperature gradients (Huber et al., 2002; Norris et al., 2002; Forster et al., 2007; Pucéat et al., 2007), a high sea level (Haq et al., 1987; Hallam, 1992; Voigt et al., 2006, 2007) and faunal and floral turnovers (Jarvis et al., 1988; Hart et al., 1993; Keller et al., 2001, 2008; Leckie et al., 2002; Erba and Tremolada, 2004; Keller and Pardo, 2004; Gebhardt et al., 2010; Gertsch et al., 2010b; Linnert et al., 2010). These greenhouse conditions coincided with a worldwide pulse in the production of new oceanic crust (Sinton et al., 1998; Courtillot and Renne, 2003; Snow et al., 2005; Turgeon and Creaser, 2008; Seton et al., 2009). Within this time interval, repeated widespread deposition of organic-rich shale, associated with major δ13C excursions mark perturbations in the carbon cycle and enhanced burial of 13C-depleted organic carbon during five Oceanic Anoxic Events (OAEs) (e.g., Hart and Leary, 1989; Erbacher et al., 1999; Leckie et al., 2002; Pucéat, 2008).

Among these oceanic anoxic events, OAE2 represents the climax of a cycle of black shale deposition in the latest Cenomanian planktic foraminiferal Rotalipora cushmani Zone (e.g., Hart et al., 1993; Leckie et al., 1998; Keller et al., 2001, 2004, 2008; Keller and Pardo, 2004; Kuhnt et

[1] ***Ahmed El-Sabbagh, Abdel Aziz Tantawy, Gerta Keller, Hassan Khozyem, Jorge Spangenberg, Thierry Adatte and Brian Gertsch (2011). Stratigraphy of the Cenomanian-Turonian Oceanic Anoxic vent OAE2 in shallow shelf sequences of NE Egypt. Cretaceous Research. Vol. 32, Iss. 6, Pages 705–722.***

al., 2005; Voigt et al., 2006, 2007, 2008; Gebhardt et al., 2010). OAE2 is characterized by a ~2-3‰ positive shift in carbon isotopes and up to 6‰ in organic carbon that reflects an increase in productivity and/or carbon burial (Arthur et al., 1990; Keller et al., 2001, 2004; Kolonic et al., 2005; Jarvis et al., 2006; Voigt et al., 2006, 2007, 2008; Mort et al., 2008; Gebhardt et al., 2010; Linnert et al., 2010).

Black organic-rich shale characterizes OAE2 in deeper waters (outer shelf-upper slope), upwelling areas and basin settings of the North Atlantic, Mediterranean and surrounding margins (Kuhnt et al., 1997; Kolonic et al., 2002, 2005; Voigt et al., 2006, 2007, 2008; Keller et al., 2008; Mort et al., 2008). However, in shallow marine platform and coastal areas (e.g., eastern Tethys) organic-rich black shales are generally absent, either because they were not deposited or not preserved (van Buchem et al., 2002; Lüning et al., 2004; Gertsch et al., 2010a). In these shallow marine settings, faunal assemblages are characterized by low diversity, sporadic occurrences and long-ranging stress resistant species that provide relatively poor age control (Keller and Pardo, 2004; Gebhardt et al., 2010; Gertsch et al., 2010a, b). This study examines carbon isotopes, micro- and macrofossil biostratigraphies and faunal turnovers of the latest Cenomanian OAE2 in two shallow water coastal sequences (Wadi Dakhl and Wadi Feiran) of northeastern Egypt (Fig. 1). The results are correlated with published OAE2 records from other shallow water sequences in Egypt (Wadi El Ghaib, eastern Sinai, Gertsch et al., 2010a), Pueblo, Colorado (stratotype section and point, GSSP, Keller et al., 2004; Keller and Pardo, 2004), and NW Morocco (Azazoul section, Gertsch et al., 2010b, Fig. 2A). Specific objectives include: (1) stable carbon isotopes to evaluate the extend of the OAE2 δ13C excursion in marine-coastal areas, (2) biostratigraphy and age control based on macrofossils and microfossils (e.g., ammonites, oysters, planktic foraminifera, calcareous nannoplankton) and (3) evaluate faunal turnovers in shallow marine sequences insofar as the sporadic fossil record permits.

2. GEOLOGICAL SETTING

During the Cenomanian-Turonian, Egypt was part of a broad Tethyan Seaway with open marine circulation to the Indo-Pacific in the east and the Atlantic-Caribbean- Pacific in the west (Fig. 2B) (Said, 1990; Lüning et al., 1998, 2004; Issawi et al., 1999). Sediment deposition in Egypt occurred mainly during the sea-level transgression that progressively advanced to the south. Carbonate deposition marks the northern deeper part of the seaway (northern Sinai and the northern part of the Western Desert), whereas to the south (central and southern Sinai and the Eastern Desert) clastic sedimentation dominates (Kerdany and Cherif, 1990; Issawi et al., 1999; El-Sabbagh, 2000, 2008; Wilmsen and Nagm, 2009; Gertsch et al., 2010a). In shallow basins of the south, episodic sea level fluctuations associated with high terrigenous influx are indicated by rapid facies changes of carbonates alternating with sandstones (Bachmann and Kuss, 1998; Lüning et al., 1998; Bauer et al., 2001, 2003).

Along the margins west and east of the Gulf of Suez rift, the Cenomanian- Turonian strata have an extensive aerial distribution and form distinct rock units lying almost directly on different horizons of the pre-Cenomanian Nubian Sandstone (Kerdany and Cherif, 1990; Issawi et al., 1999). They include beds with common to abundant macrofauna (e.g., ammonites, oysters) and intervals enriched in microfauna (e.g., foraminifera, nannoplankton) as reported in various publications (e.g., Said, 1962, 1990; Malchus, 1990; Kassab and Obaidalla, 2001; El-Sabbagh, 2008; Gertsch et al., 2010a; Nagm et al., 2010a, b).

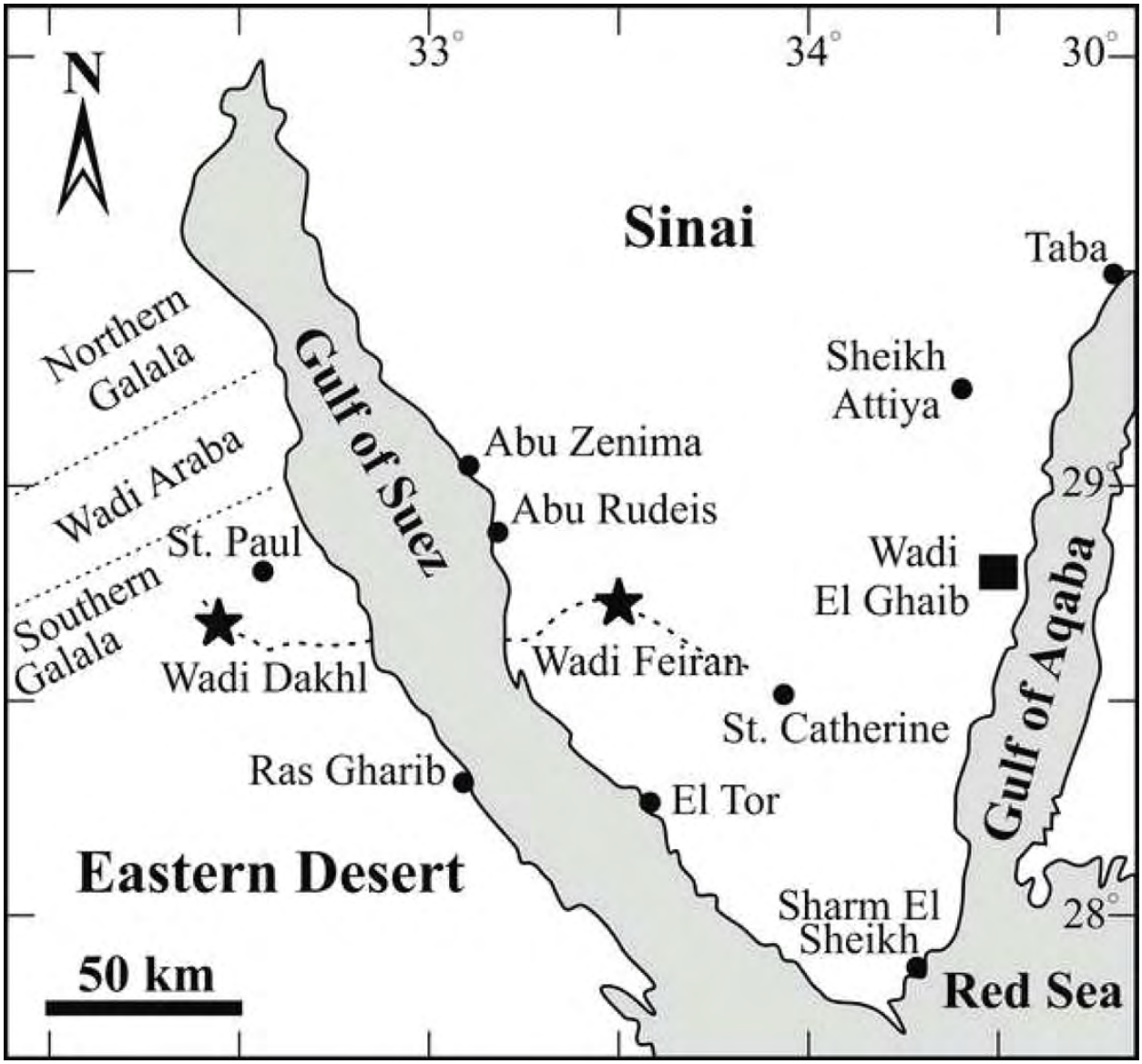

Fig. 1. *Location map showing the sections analyzed across the Gulf of Suez and the Wadi El Ghaib section of Gertsch et al. (2010a) in the eastern Sinai.*

in the southern part of the Southern Galala Plateau west of the Gulf of Suez with the Wadi Dakhl section located north of Bir Dakhl, about 30 km southwest of the Monastery of St. Paul (32°25\ E, 28°41\ N, Fig. 1). Wadi Feiran trends east-west in the southwestern Sinai and the section is located near the village of Mukattab, about 18 km from the Feiran traffic station at the road entrance to the Monastery of St. Catherine (33°31\ E, 28°47\ N).

Outcrops at Wadi Dakhl and Wadi Feiran represent parts of the margins west and east of the Gulf of Suez rift, respectively. The main bedrock outcrops are distributed in two major highly fractured elongated platforms running parallel to the Gulf of Suez (Said, 1962, 1990; Kerdany and Cherif, 1990). Wadi Dakhl is located

3. METHODS

The Wadi Dakhl and Wadi Feiran sections were examined in the field for lithological changes, burrows, macrofossils, hardgrounds and erosion surfaces, which were described, measured and sampled.

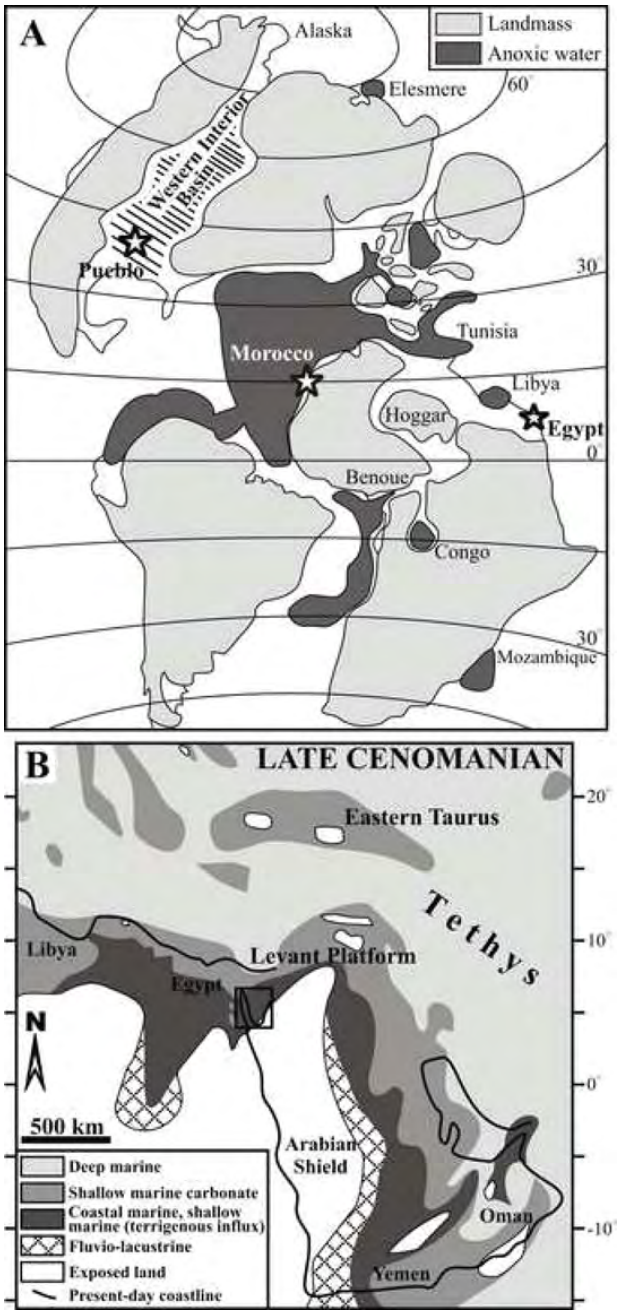

Fig. 2*. A, Geographic distribution of the Cenomanian-Turonian (C-T) organic-rich deposits in the Atlantic and adjacent areas (modified after De Graciansky et al., 1986). Stars mark the locations of studied sections (Egypt) and other C-T sections in Morocco and the U.S. Western Interior Basin. B, Late Cenomanian palaeogeographic map of the Peri-Tethyan domain with main depositional environments (modified after Philip,* 2003*). Square marks the study area of Figure 1.*

A total of 119 rock samples were collected at an average of 30-50 cm intervals for the Wadi Dakhl outcrop and 57 rock samples for the Wadi Feiran outcrop at intervals of about 25 cm. At Wadi Dakhl, macrofossil assemblages were collected throughout the sequence wherever present. At Wadi Feiran only few macrofossils were observed. In the laboratory, sediment samples were processed for foraminiferal analysis using standard methods (Keller et al., 1995). Planktic and benthic foraminifera were analyzed in the >63 µm size fraction, mounted on microslides and identified. Planktic foraminifera are generally rare, though common in some intervals in both

sections. Benthic foraminifera are common to abundant. Quantitative estimates of foraminifera were obtained from at least 100 planktic specimens, and up to 600 benthic specimens. Identification of planktic and benthic species follows that of Cushman (1946), Omara

(1956), Sliter (1968), Robaszynski and Caron (1979, 1985), and Bolli et al. (1994). Preservation of foraminiferal tests is good to moderate. Calcareous nannofossils were processed by standard smear slide preparation from raw sediment samples as described by Perch-Nielsen (1985). Smear slides wereexamined using a light photomicroscope with 1000x magnification. Each slide was observed under cross-polarized light. Preservation and abundance of nannofossils are moderate to poor throughout the Wadi Feiran section. Calcareous nannofossil species abundances were semiquantitatively evaluated as follows: common: >1 specimen per field of view (FOV); few: 1 specimen per 1–10 FOV; rare: 1 specimen per >10 FOV. Carbon isotope composition of bulk rock carbonates was determined using a Thermo Fisher carbonate-preparation device and GasBench II connected to a Thermo Fisher Delta Plus XL continuous He flow isotope ratio mass spectrometer (IRMS). CO2 extraction was done with 100% phosphoric acid at 70°C for calcite and 90°C for dolomite. The stable carbon isotope ratios are reported in the delta (δ) notation as the permil (‰) deviation relative to the Vienna-Pee Dee belemnite standard (VPDB). Analytical uncertainty (2 σ), monitored by replicate analyses of the international calcite standard NBS-19 and the laboratory standards Carrara Marble and Binn Dolomite was better than ±0.05‰ for $\delta^{13}C$.

4. LITHOLOGY

At Wadi Dakhl and Wadi Feiran, the Cenomanian-Turonian sequences are composed of siliciclastic sediments in the lower part, mixed siliciclastic carbonates in the middle part, and mostly carbonates in the upper part (Figs. 3, 4). Different lithostratigraphic schemes have been proposed to describe the Cenomanian-Turonian deposits in the northern Eastern Desert, Gulf of Suez and western Sinai despite lithologic and faunal similarities (e.g., Cherif et al., 1989; Kerdany and Cherif, 1990; Kora et al., 2001; El-Sabbagh, 2008; Wilmsen and Nagm, 2009). As a result, the Cenomanian-Turonian deposits of the Wadi Dakhl and Wadi Feiran sections were included in the Raha (early-late Cenomanian), Abu Qada (late Cenomanian-early Turonian) and Wata (late Turonian) Formations (Figs. 3, 4). The Raha Formation (Ghorab, 1961) is well represented in the Wadi Dakhl section by sandstone, shale, marl, dolomite and limestone (Fig. 3) that reflect the first shallow marine transgression in northeastern Egypt during the Cenomanian (Kerdany and Cherif, 1990; Issawi et al., 1999). Around the Gulf of Suez, the top of a sandstone interval (i.e., the Mellaha Sand Member of Ghorab, 1961) marks the Raha/Abu Qada transition

(Cherif et al., 1989; Kora et al., 2001; El-Sabbagh, 2008). At the Wadi Dakhl section, sandstone deposition ends at 33.7 m, which may represent the Raha/Abu Qada boundary. The lower part of the Raha Formation is poorly fossiliferous with oysters, trigonid bivalves, gastropods and a few bioturbated levels. The middle part contains more common oysters, gastropods, bivalves, ammonite, rudists and echinoids, whereas the sandstones of the upper part are largely devoid of macrofossils. The Abu Qada Formation (Ghorab, 1961) is well developed in the Wadi Dakhl and Wadi Feiran sections (Figs. 3, 4) and consists of shales, marls, nodular marls, limestones and oyster-rich limestone beds.

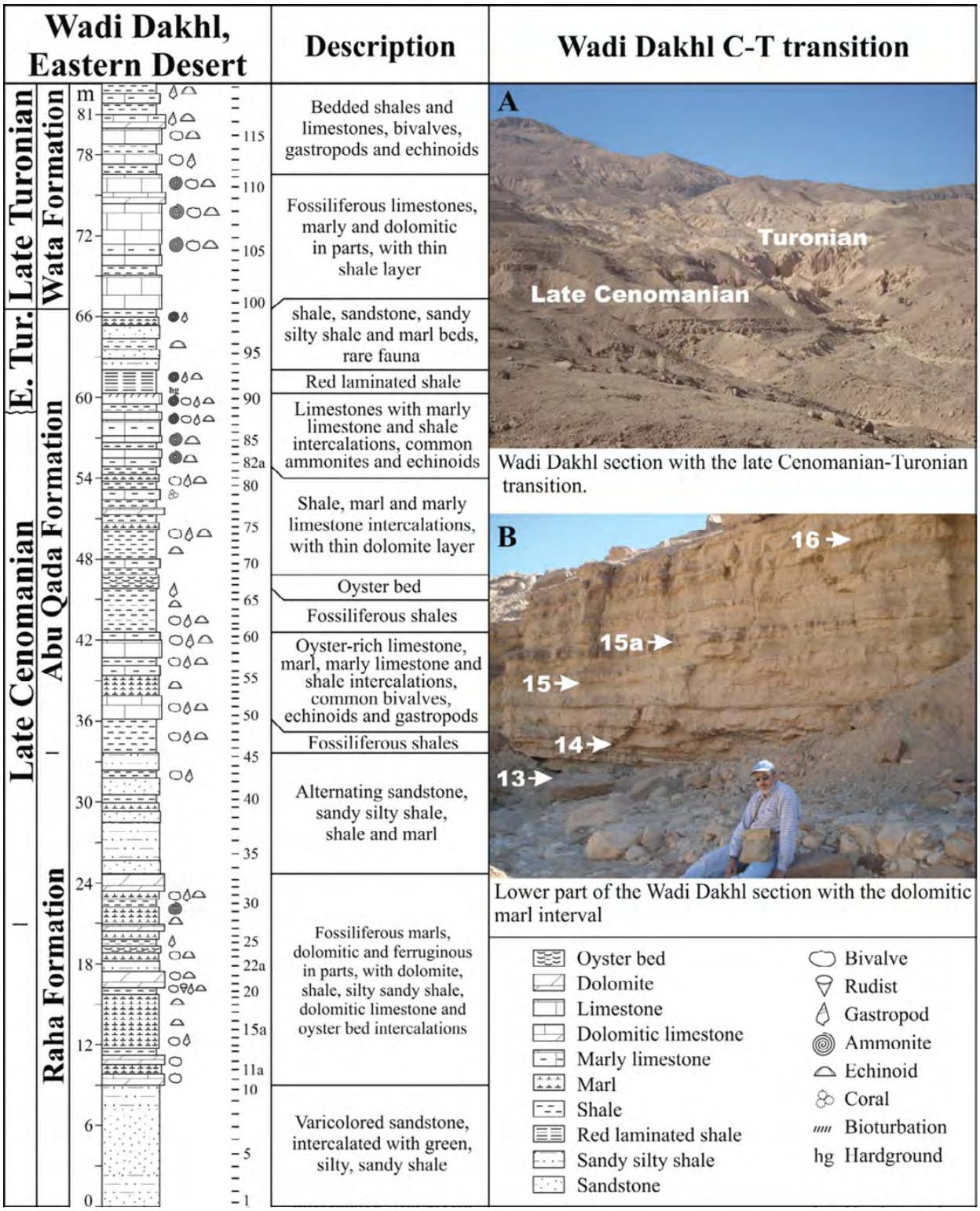

***Fig. 3**. Lithological descriptions of the Wadi Dakhl section and photos of the outcrop showing part of the lower marl interval and the Cenomanian-Turonian transition.*

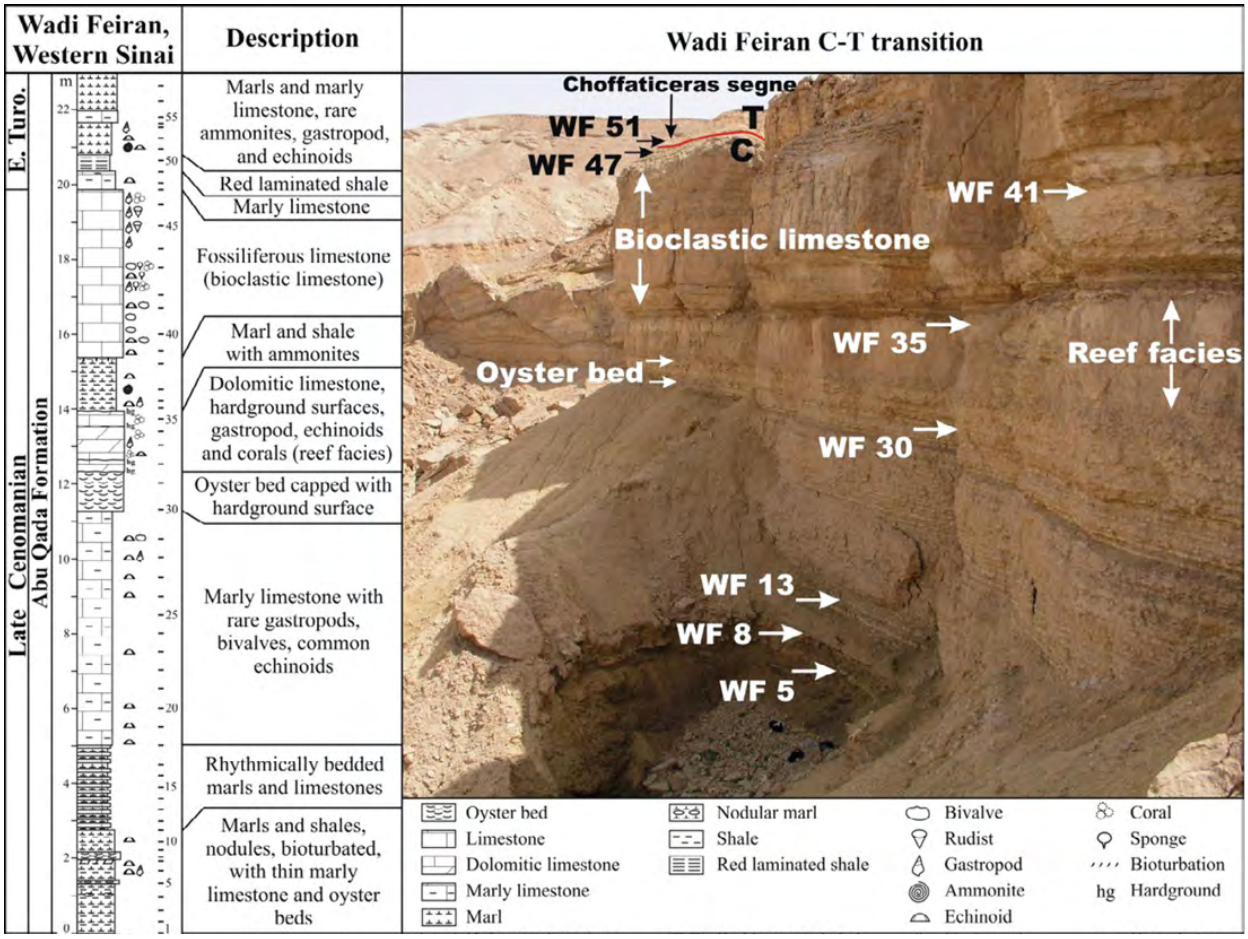

Fig. 4*. Lithological descriptions of the Wadi Feiran section and photo of the outcrop showing different rock facies, sample positions and the Cenomanian-Turonian boundary.*

The Wata Formation (Ghorab, 1961) in Wadi Dakhl is represented by a carbonate facies consisting of limestone, marly limestone and shales with common ammonites, bivalves, gastropods and echinoids (Fig. 3). The Wadi Dakhl section spans from the lower Cenomanian to the upper Turonian. The basal 9.0 m consist of sandstone intercalated with sandy silty shale in the lower and upper parts. Between 9.0-24.7 m, sediments consist of alternating marl (Fig. 3B), dolomite, dolomitic limestone, shale and silty-sandy shale layers. A unique 0.5 mthick oyster bed is present at 18.8 m (Fig. 3). A clastic interval between 24.7-36.1 m consists of alternating sandstone, shale, silty sandy shale, a thin marl bed at 29.3 m and a thick shale layer at the top. Oyster-rich limestone and marly limestone layers (36.1- 42.6 m) overlie this interval and are intercalated with marl and shale layers. Above is a thick shale layer followed by a 1.0 m thick oyster bed and an interval of alternating shale, marl, marly limestone and thin dolomite layers (42.6-55.0 m). Limestone, marly limestone and thin shale layers with common ammonites and echinoids dominate lithologies between 55.0-60.3 m. A disconformity is indicated at the top of this unit by the strongly bioturbated limestone followed by a red laminated shale layer (1.8 m thick) that marks the transition to a poorly fossiliferous interval (62.1-66.6 m) of silty-sandy shale, sandstone, shale and marl layers (Fig. 3). Near the top of the section is a thick fossiliferous marly limestone, partly dolomitic (66.6-76.6 m) with a 0.8 m thick shale bed. Shale, marly and partly dolomitic limestones mark the uppermost part of the section.

The Wadi Feiran section outcrops in a cliff and spans the late Cenomanian to early

Turonian (Fig. 4). The lower part of the section (0-2.7 m) consists of alternating marl and shale layers with thin nodular marly limestone (10 cm thick) and oyster (20 cm thick) beds. Marls contain rare nodules and are poorly fossiliferous. Rhythmically bedded thin marl and limestone layers overlie this interval (2.7-5.0 m). A thick marly limestone bed (5.0-11.3 m) terminates at a 1.1 m thick oyster bed with an erositional surface at the top (Fig. 4). Between 12.4-14.0 m is a fossiliferous dolomitic limestone layer with multiple hardground surfaces indicating nondeposition and/or erosion (reef facies). Alternating marls and shales with ammonites (14.0-15.5 m) underlie a thick bed of highly fossiliferous (bioclastic) limestone (15.5-19.9 m). This unit terminates at a 0.5 m thick marly limestone layer containing rare echinoids. Above is a red laminated shale layer (0.4 m thick). The top of the section (20.8-23.0 m) consists of a thick marl layer with a 0.3 m thick marly limestone layer in the middle part (Fig. 4).

5. ISOTOPE STRATIGRAPHY

In shallow water sequences, carbonates are likely to undergo diagenesis that alters the primary isotopic signals and limits their role in paleoenvironmental interpretations (Jenkyns et al., 1994; Schrag et al., 1995). Diagenesis strongly affects oxygen isotopes by recrystallization and/or interstitial fluids, which leads to significant lowering of δ18O values and obliterates the original seawater temperature signals, though trends tend to be preserved (Jenkyns et al., 1994; Mitchell et al., 1997; Paul et al., 1999). In contrast, δ13C values are little affected by diagenesis due to the low carbon content of pore waters (Schrag et al., 1995), except in sediments influenced by organogenic carbon incorporation (Marshall, 1992). Carbon isotopes therefore closely track environmental changes.

Wadi Feiran: In the basal part of the Abu Qada Formation, δ13C data show low values (-1.4-1.5‰) with a drop to -0.3‰ just below an oyster bed (1.9 m), followed by a sharp increase to 2.9‰ in a 0.2 m thick oyster bed and a further increase to 4.6‰ at 3 m (Fig. 5A). This δ13C shift marks the global OAE2 excursion and the first (peak 1) of two δ13C maxima, as observed worldwide (e.g., Kuhnt et al., 1997, 2005; Keller et al., 2001, 2004, 2008; Leckie et al., 2002; Kolonic et al., 2005; Jarvis et al., 2006; Voigt et al., 2006, 2007, 2008; Gebhardt et al., 2010; Gertsch et al., 2010a, b; Linnert et al., 2010). After the first peak, δ13C values drop to 2.5‰ then gradually increase to 4.5‰ at 6.5 m, which probably marks the second peak of the global δ13C excursion (Fig. 5A). $\delta^{13}C$ values remain relatively high and steady up to 20.6 m where they gradually decrease to 2‰ in the upper part of the Abu Qada Formation. Wadi Dakhl: Samples that contain sufficient carbonate for stable isotope analysis are relatively few at the shallower Wadi Dakhl section (Fig. 5B). In the middle part of the Raha Formation (18.5 m) the δ13C curve shows low values (0.19‰). An increase to 1.4‰ occurs in a 0.5 m thick oyster bed (18.8-19.3 m), followed by a decrease to -0.3‰ in the overlying marl (21.3 m). Between 21.3 m to 36.0 m carbonate values are too low for stable isotope analysis. In the lower part of the Abu Qada Formation (36-50.4 m), δ13C values fluctuate between 0.4 and 1.9‰ with values up to 2.2‰ at 41 m. Between 50.4-55.1 m, no samples are available (dashed line in $\delta^{13}C$ curve, Fig. 5B). Above this level, δ13C values reach 4.3‰ and mark the upper part of the OAE2 excursion below the C/T boundary. Just above the C/T boundary, an abrupt drop in δ13C to -1.2‰ at 60 m marks a major hiatus with early Turonian sediments above it.

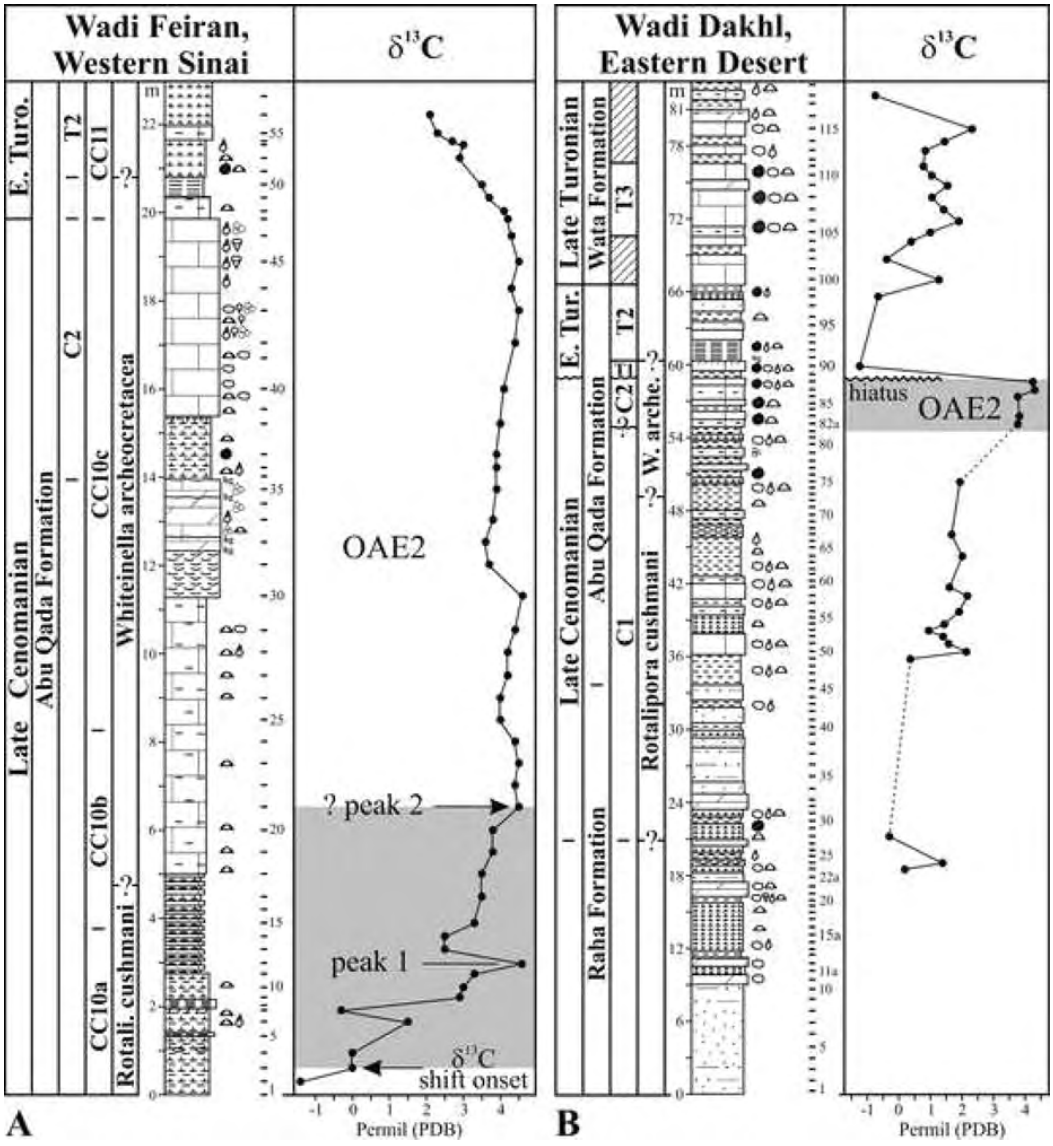

Fig. 5*. δ13C curves of the (A) Wadi Feiran and (B) Wadi Dakhl sections. $\delta^{13}C$ record at the Wadi Feiran section shows the characteristic positive excursion of the late Cenomanian OAE2. At Wadi Dakhl the $\delta^{13}C$ curve shows only a small part of the OAE2 plateau.*

Table 1*. Inter-regional correlation of the late Cenomanian-early Turonian ammonite zones for the Wadi Dakhl section.*

Stage	Western Interior Kennedy et al. (2000)	Europe Hardenbol et al. (1998)	North Africa Caron et al. (2006), Amédro and Robaszynski (2008)	The Middle East Lewy and Raab (1976), Lewy et al. (1984)	Egypt Kassab and Obaidalla (2001), Gertsch et al. (2010a), this study
Early Turonian	*M. nodosoides*	*M. nodosoides*	*M. nodosoides*	*Ch. luciae*	*Ch. segne* (T2)
	V. birchbyi	*W. coloradoense*	*T. rollandi*	*Ch. quaasi* *Ch. securiforme*	
	P. flexuosum		*P. flexuosum*	*V. pioti*	*V. proprium* (T1)
	W. devonense	*W. devonense*	*Watinoceras* sp.		
Late Cenomanian	*N. scotti* *N. juddii*	*N. juddii*	*P. pseudonodosoides*	*V. cauvini*	*V. cauvini* (C2)
	S. gracile	*M. geslinianum*	*M. geslinianum*	*Kanabiceras* sp.	*N. vibrayeanus* (C1)
	M. mosbyense	*C. naviculare/* *E. pentagonum/* *C. guerangeri*	*E. pentagonum*	*Calycoceras* sp.	
	C. canitaurinum			*N. vibrayeanus*	

The absence of the characteristic two $\delta^{13}C$ peaks and prolonged plateau indicates that this hiatus spans most of the OAE2 excursion. In the upper Turonian Wata Formation, δ13C values fluctuate between -0.4-2.4‰. The relatively small-scale cyclical oscillations in this interval may be largely the result of lithological changes (Paul et al., 1999; Keller et al., 2001; Voigt et al., 2006).

6. BIOSTRATIGRAPHY

6.1. Ammonites

In shallow water Cenomanian-Turonian sequences of the southern Tethys, ammonites offer good age control and regional correlations (Robaszynski and Caron, 1995; Hardenbol et al., 1998). Low diversity and endemism has led to a number of regional ammonite biozonations, including Egypt (Table 1). These biozonations have been widely discussed (Kora and Hamama, 1987; Kassab, 1991, 1994, 1999; Kassab and Ismael, 1994; El-Sabbagh, 2000, 2008; Kassab and Obaidalla, 2001; El-Hedeny, 2002; Zakhera and Kassab, 2002; Nagm et al., 2010a, b) and correlated with the Pueblo, Colorado, stratotype section and point (GSSP) based on carbon isotope stratigraphy (e.g., Gertsch et al., 2010a, b).

6.1.1. Neolobites vibrayeanus interval zone (Zone C1)

Zone C1 is defined by the total range of the zonal marker N. vibrayeanus (Fig. 6). In the Wadi Dakhl section occurrences of the index species were observed between 21.0-23.4 m, which tentatively identify the base of zone C1 (Fig. 7). Associated with these occurrences is the oyster Ilymatogyra (Afrogyra) africana, a characteristic early late Cenomanian species of Egypt (Malchus, 1990; El-Sabbagh, 2000, 2008). In the Wadi El Ghaib section, zone C1 spans up to the first appearance of Vascoceras cauvini, which is coincident with the first peak of the d13C shift at 4.5‰ (Gertsch et al., 2010a). At Wadi Dakhl, C1 also spans the interval below the d13C excursion, though the C1/C2 boundary is uncertain because the $d^{13}C$ shift and most of the plateau are missing (Fig. 7). Zone C1 was not sampled in the Wadi Feiran section.

In Egypt, zone C1 is generally confined to the upper part of the Raha Formation (Abdel-Gawad, 1999; Kassab and Obaidalla, 2001; El-Sabbagh, 2008; Gertsch et al., 2010a). However, in the field the boundary placement between the Raha and Abu Qada Formations is uncertain. The Mellaha Sand Member of Ghorab (1961) is considered a marker horizon. However, a sandstone unit is not a unique marker in shallow water sequences that frequently contain sandstones. In the absence of distinct lithologic markers, the boundary between the Raha and Abu Qada Formations remains unknown. For these reasons, we tentatively identify the upper part of the Raha Formation as equivalent to zone C1.

6.1.2. Vascoceras cauvini interval zone (Zone C2)

Zone C2 is defined by the first occurrence (FO) of the zonal marker V. cauvini at the base and/or the last occurrence (LO) of N. vibrayeanus. The top of zone C2 is marked by the LO of V. cauvini and/or the FO of V. proprium, an early Turonian ammonite that marks the Cenomanian-Turonian (C/T) boundary. In Egypt, the base of zone C2 coincides with the trough between the $\delta^{13}C$ excursion peak 1 and peak 2, whereas the top coincides with the end of the δ13C plateau at or near the C/T boundary (Gertsch et al., 2010a).

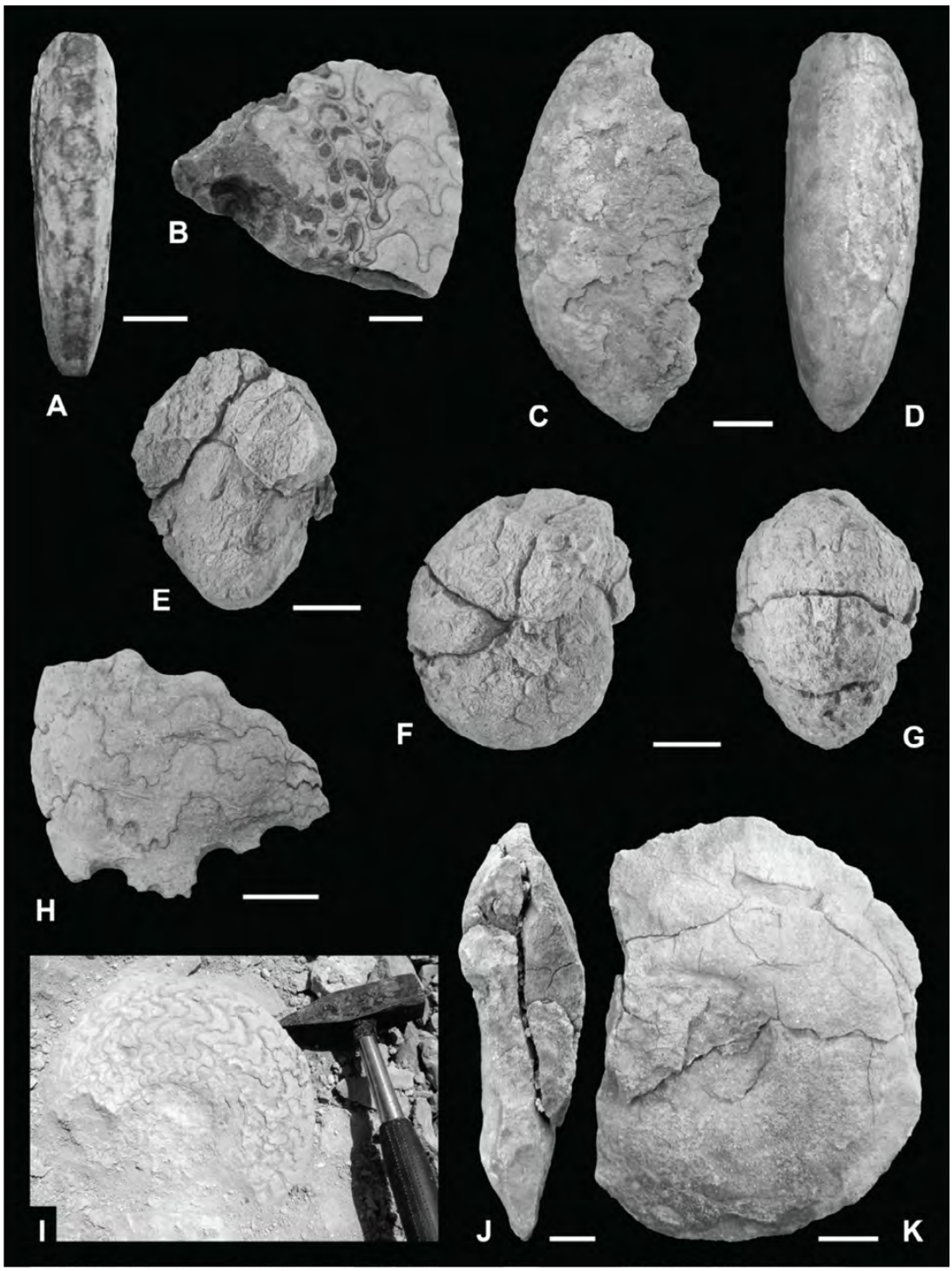

Fig. 6: *Some selected late Cenomanian - late Turonian ammonite index species from the Wadi Dakhl section. A-B, Neolobites vibrayeanus (d'Orbigny, 1841), UpperCenomanian Raha Formation. A: ventral view, B: lateral view; scale bars = 1cm. C-D, Vascoceras cauvini Chudeau, 1909, Upper Cenomanian Abu Qada Formation. C: lateral view, D: ventral view; scale bar = 2 cm. E-G, Vascoceras proprium (Reyment, 1954), Lower Turonian Abu Qada Formation. E: apertural view, F: lateral view, G: ventral view; scale bars = 1.5 cm. H-I, Choffaticeras segne (Solger, 1903), Lower Turonian Abu Qada Formation. H: lateral view, scale bar = 1.5 cm; I: lateral view. J-K, Coilopoceras requienianum (d'Orbigny, 1841), Upper Turonian Wata Formation. J: apertural view, K: lateral view; scale bars = 2 cm.*

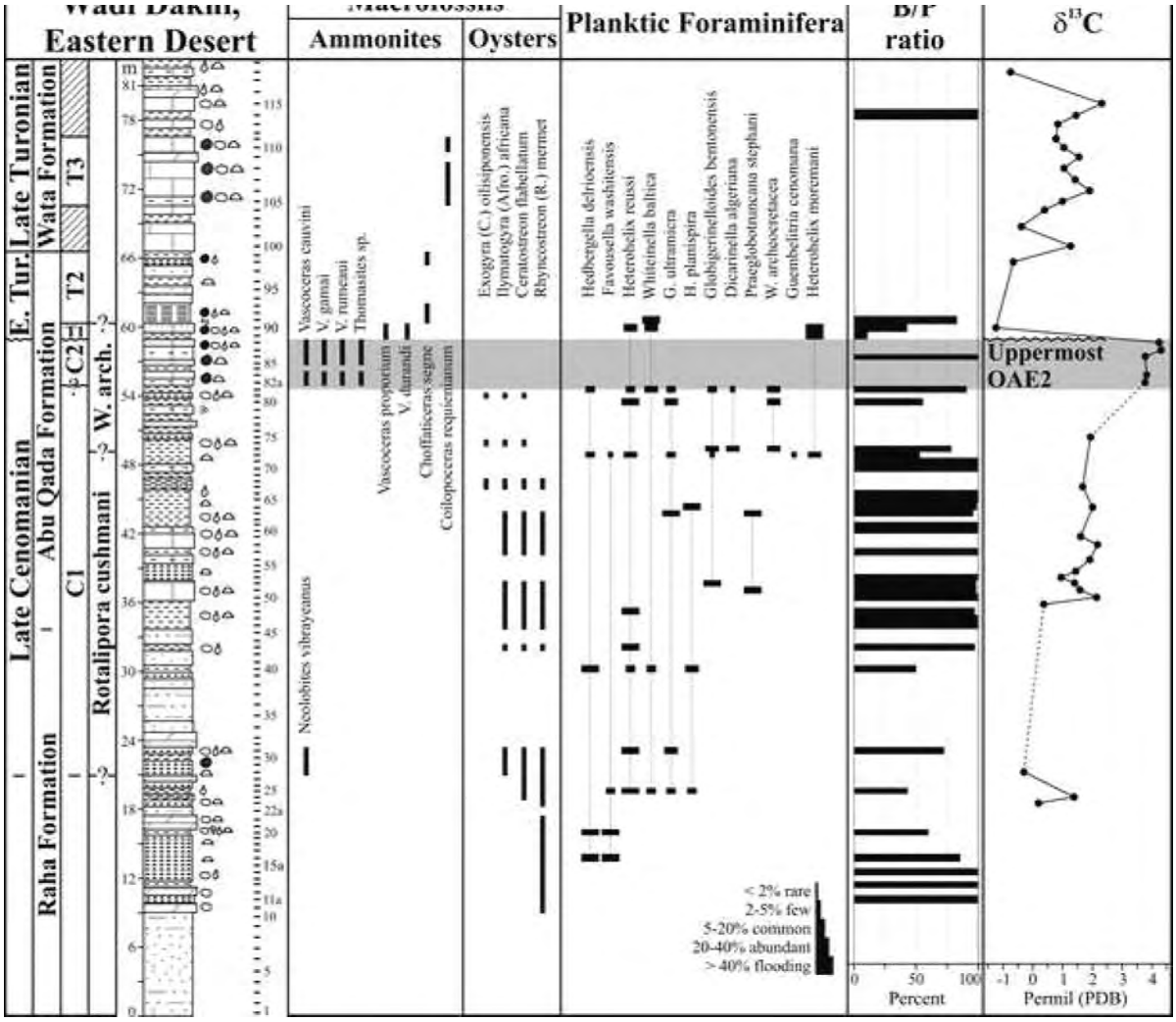

Fig. 7. *Late Cenomanian-late Turonian biostratigraphy of ammonites, oysters and planktic foraminifera with the benthic/planktic ratio and the δ13C record of the Wadi Dakhl section. Biostratigraphic interpretation is based on fauna, the δ13C curve and local and regional correlations*

At the Wadi Dakhl section, the δ13C excursion and plateau are mostly missing due to one or more hiatuses. Only a short interval of high δ13C values (3.8-4.3 ‰) is present and probably represents part of the plateau. In this interval V. cauvini is present and marks zone C2 (Figs. 6, 7). The oyster Exogyra (Costagyra) olisiponensis, which marks the latest Cenomanian in the Tethys seaway (Kennedy et al., 1987; Meister et al., 1992; Chancellor et al., 1994; Kassab and Obaidalla, 2001; Wilmsen and Nagm, 2009), was observed below the FO of V. cauvini. Above this interval, δ13C values abruptly drop to <1‰ and indicate a hiatus at or near the C/T boundary (Fig. 7). Above the hiatus, the early Turonian ammonites V. proprium and V. durandi are present. Below the interval of high δ13C values the onset of the δ13C excursion and maximum values (peak 1 and peak 2) are missing, which indicates another hiatus. At Wadi Feiran, the base of C2 can be tentatively inferred by the rare occurrenceof V. cauvini, which coincides with the upper part of the δ13C plateau (Fig. 8).

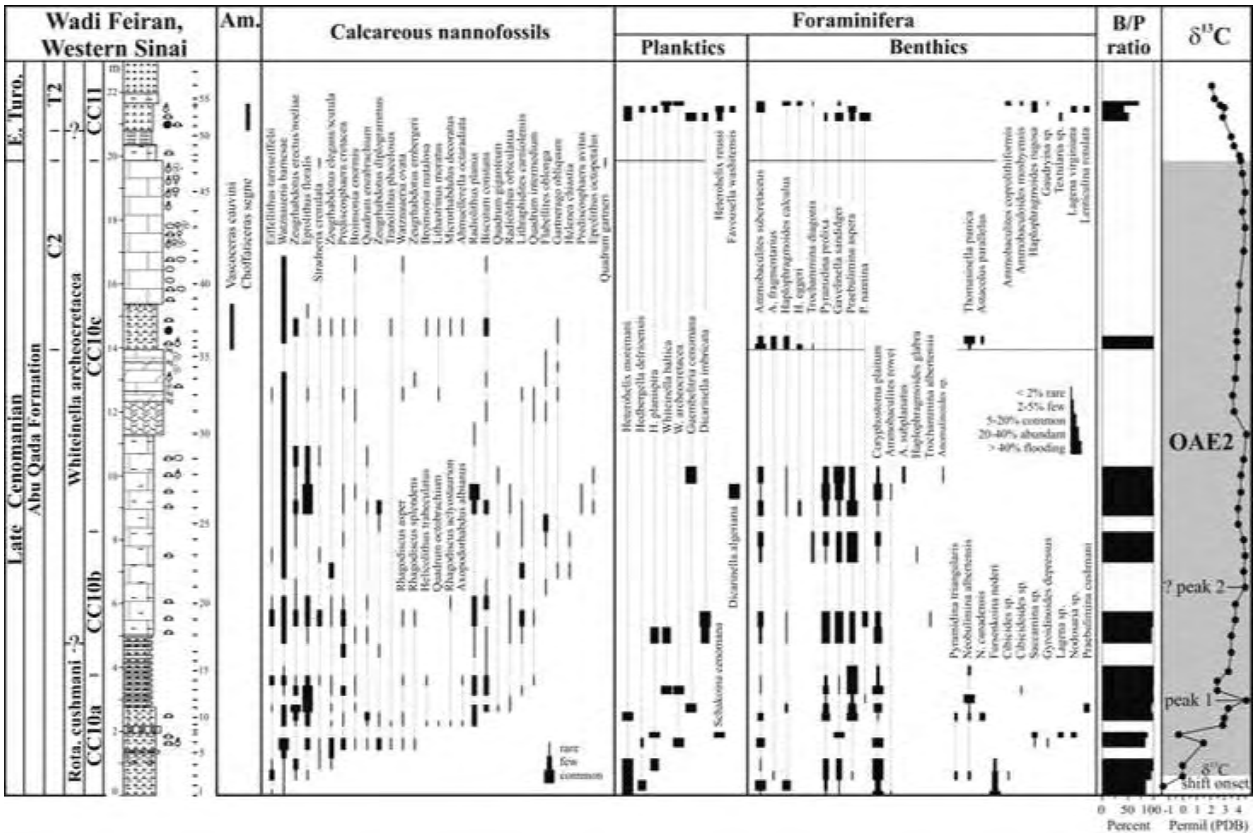

Fig. 8. *Late Cenomanian-early Turonian biostratigraphy of ammonite, nannoplankton and planktic and benthic foraminifera with the benthic/planktic ratio and the δ13C record of the Wadi Feiran section. Biostratigraphic interpretation is based on fauna, flora, the $\delta^{13}C$ curve and local and regional correlations.*

The characteristic ammonites that define the C/T boundary were not observed, although Kassab and Obaidalla (2001) reported them earlier. The C/T boundary was therefore placed at the end of the $\delta^{13}C$ plateau excursion, coincident with the position of this boundary event globally.

6.1.3. Vascoceras proprium total range zone (Zone T1)

Zone T1 is defined by the total range of the zonal index species V. proprium. These globose vascoceratids (Fig. 6) are good biostratigraphic indicators for the early Turonian in the southern Tethys (Hardenbol et al., 1993; Robaszynski and Gale, 1993; Chancellor et al., 1994). At Wadi Dakhl, V. proprium was observed along with V. durandi in a very short interval (59.0-60.4 m) above the hiatus evident in the δ13C curve (Fig. 7). This indicates that most of zone T1 is missing. At Wadi Feiran, the zone T1 index species was not observed. V. proprium is common in the early Turonian Pseudoaspidoceras flexuosum Zone in the Tethyan realm (Meister and Rhalmi, 2002; Meister and Abdallah, 2005) and US Western Interior (Kennedy et al., 1987; Kennedy and Cobban, 1991). Zone T1 is thus considered equivalent to the P. flexuosum Zone and probably the Watinoceras devonense Zone (Table 1).

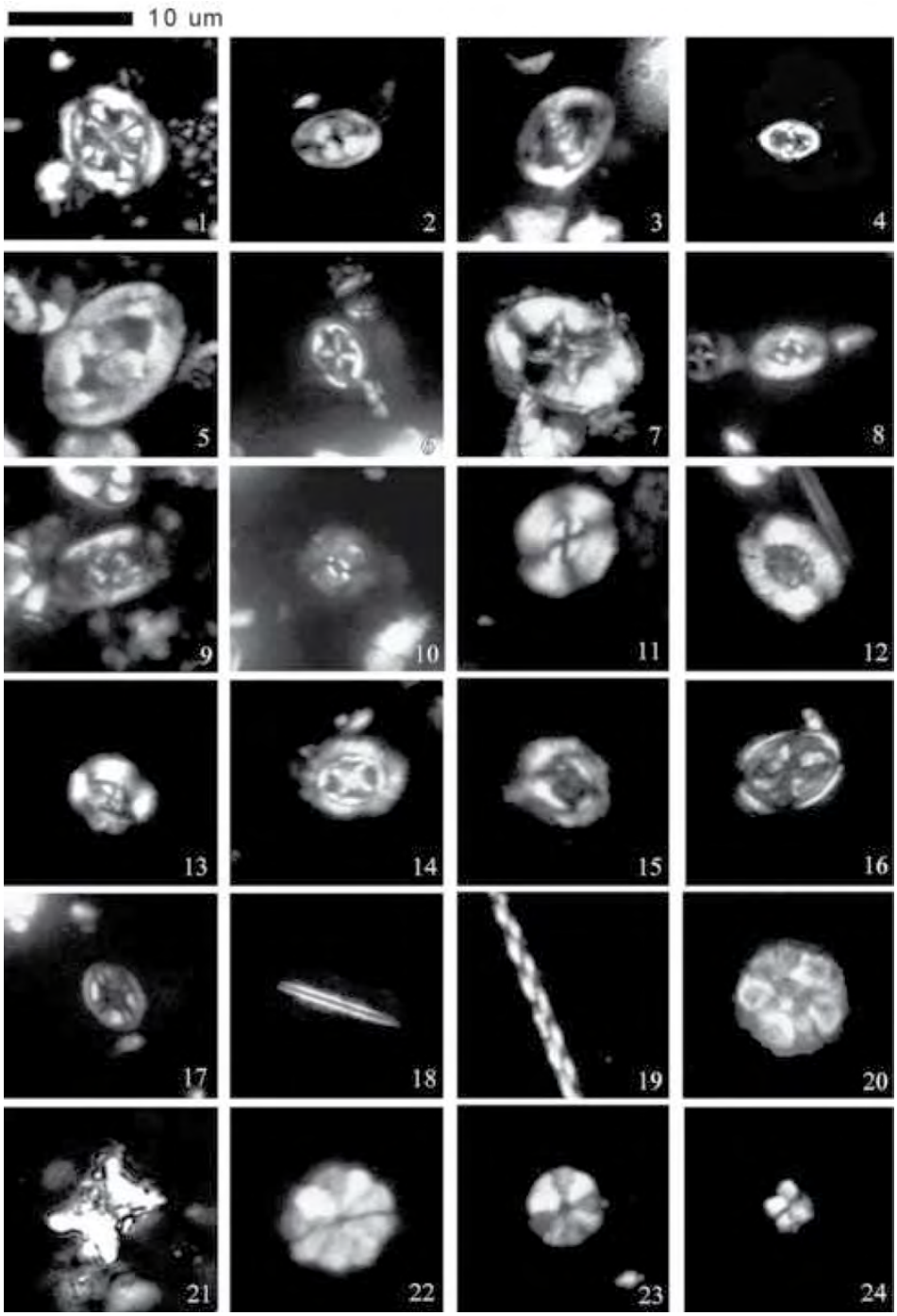

Fig. 9*. Light microscope photographs of some selected calcareous nannofossil species from the Wadi Feiran section. All figures were taken under cross-polarized light. 1, Axopodorhabdus albianus, sample 14. 2, Tranolithus phacelosus, sample 5. 3, Zeugrhabdotus scutula, sample 22. 4, Zeugrhabdotus erectus, sample 10. 5, Zeugrhabdotus embergeri, sample 33. 6, Helicolithus trabeculatus, sample 14. 7, Eiffellithus turriseiffelii, sample 19. 8, Rhagodiscus achlyostaurion, sample 20. 9, Rhagodiscus splendens, sample 19. 10, Biscutum constans, sample 38. 11, Watznaueria barnesae, sample 5. 12, Retecapsa crenulata, sample 38. 13, Helenea chiastia, sample 24. 14, Prediscosphaera cretacea, sample 17. 15, Flabellites oblonga, sample 33. 16, Gartnerago obliquum, sample 38. 17, Broinsonia matalosa, sample 38. 18, Lithraphidites carniolensis, sample 22. 19, Microrhabdulus decoratus, sample 38. 20, Eprolithus octopetalus, sample 28. 21-22, Eprolithus floralis, sample 26. 23, Radiolithus planus, sample 27. 24, Quadrum gartneri, sample 47*

6.1.4. Choffaticeras segne total range zone (Zone T2)

Zone T2 is defined by the total range of the nominate species (Fig. 6). At Wadi Dakhl, zone T2 is recognized between 60.4-66.6 m in the upper part of the Abu Qada Formation, and at Wadi Feiran between 20.8-23.0 m. In both sections zone T2 coincides with low δ13C values (Figs. 7, 8).

6.1.5. Coilopoceras requienianum total range zone (Zone T3)

Zone T3 is defined by the total range of the zonal index species. Coilopoceras requienianum was observed in the Wadi Dakhl section (Fig. 6) with the first appearance about 4 m above Ch. segne. Therefore, the T2/T3 boundary is tentatively identified (dashed interval, Fig. 7). The last occurrence was observed at 76.6 m. Zone T3 and thus spans an interval from 70.6-76.6 m at Wadi Dakhl. Coilopoceras requienianum is a well-known late Turonian ammonite index species (e.g., Cobban and Hook, 1980; Wright et al., 1984; Nagm et al., 2010a, b).

6.2. **Planktic foraminifera**

Planktic foraminiferal assemblages are present only in sporadic intervals and rotaliporid index species generally rare or absent in the shallow water sequences of Egypt (Cherif et al., 1989; Shahin and Kora, 1991; Kora et al., 1994; Gertsch et al., 2010a). Relative age interpretations can be made based on these sporadic assemblages and integration with calcareous nannofossils and carbon isotope stratigraphies. Wadi Dakhl: In this section, the Cenomanian-Turonian planktic foraminiferal assemblages range from few to common (Fig. 7). In the marl and shale layers below the high δ13C values, heterohelicids, hedbergellids and globigerinellids are sporadically common and whiteinellids are present (e.g., Praeglobotruncana stephani, Dicarinella algeriana). This interval is tentatively placed in the Rotalipora cushmani Zone. Whiteinella archeocretacea are present between 49.2-54.9 m, an interval that is tentatively placed in the W. archeocretacea Zone (Fig. 7). Above this interval, high $\delta^{13}C$ values indicative of the OAE2 plateau indicates the upper part of the W. archeocretacea Zone, although the interval is barren (Keller and Pardo, 2004; Keller et al., 2008; Caron et al., 2006). Globigerinelloides bentonensis, which generally disappears above the $\delta^{13}C$ excursion peaks (Keller et al., 2001; Keller and Pardo, 2004), is absent. This indicates that the lower part of the OAE2 $\delta^{13}C$ excursion is missing at the Wadi Dakhl section. The uppermost planktic foraminiferal assemblage occurs in the shale and limestone layers between 59.0-61.0 m above the high δ13C values. This assemblage contains abundant heterohelicids and whiteinellids, which is generally indicative of the early Turonian, though no zonal index species are present. Wadi Feiran: In this section, planktic foraminifera range from few to common with the first sporadic assemblages of heterohelicids, hedbergellids, whiteinellids and dicarinellids in marl, shale and marly limestone layers between 0-10.3 m. (Fig. 8). Whiteinella archeocretacea first appears at 1.5 m, near the onset of the δ13C excursion, as also observed in the Wadi El Ghaib section in the eastern Sinai (Gertsch et al., 2010a) and elsewhere (Nederbragt and Fiorentino, l999; Keller et al., 2001, 2008; Leckie et al., 2002; Keller and Pardo, 2004; Caron et al., 2006; Gebhardt et al., 2010; Gertsch et al., 2010b). Rotaliporids are absent in this shallow water environment.

The base of the W. archeocretacea Zone is defined globally by the extinction of all Rotalipora species, including the index species R. cushmani (Caron, 1985; Robaszynski and Caron, 1995). This extinction datum occurs in the trough between $\delta^{13}C$ peaks 1 and 2 (e.g., Keller et al., 2001, 2008; Leckie et al., 2002; Kuhnt et al., 2005; Gebhardt et al., 2010; Gertsch et

al., 2010b), except for the Pueblo stratotype section, where the R. cushmani extinction coincides with the $\delta^{13}C$ peak 1 as a result of condensed sedimentation (Keller and Pardo 2004). At Wadi Feiran, we tentatively place the R. cushmani/W. archeocretacea Zone boundary in the trough (4.75 m) between the two $\delta^{13}C$ peaks and just below the FO of D. imbricata, as also observed in the Pueblo stratotype section (Fig. 8). Above the OAE2 δ13C excursion (21.1-21.8 m), a relatively diverse planktic foraminiferal assemblage of heterohelicids, hedbergellids and whiteinellids is indicative of early Turonian age, though the index species Helvetoglobotruncana helvetica is absent. The C/T boundary is tentatively placed at the end of the δ13C excursion plateau, correlative with the Pueblo stratotype section and elsewhere (Hart et al., 1993; Keller and Pardo, 2004; Voigt et al., 2006, 2007; Gebhardt et al., 2010; Gertsch et al., 2010b).

6.3. Calcareous Nannofossils

Calcareous nannofossils at Wadi Feiran are generally rare, poorly preserved and limited to distinct lithostratigraphic units (Fig. 8). Sixty-three species attributable to 21 genera were identified, including the index taxa, which allow reasonably good biostratigraphic resolution (Fig. 9). This study mainly follows the standard cosmopolitan zonations of Sissingh (1977) and Perch-Nielsen (1979, 1985) and incorporates additional bioevents from Bralower (1988) and Burnett (1998). Two nannofossil zones (CC10 and CC11) and three subzones (CC10a-c) have been identified and correlated regionally (e.g., Sinai, Jordan, Tunisia, Morocco, Table 2). Zone CC10 spans the late Cenomanian (Perch-Nielsen, 1985) and is defined by the interval from the first occurrence (FO) of Lithraphidites acutus and/or FO of Microrhabdulus decoratus to the FO of Quadrum gartneri. Manivit et al. (1977) and Perch-Nielsen (1985) subdivided Zone CC10 into a lower CC10a, or Microstaurus chiastius subzone, based on the last Burnett (1998) divided the same interval into four zones: Zone UC3 - Zone UC6 (Table 2). Recently, Tantawy (2008) subdivided Zone CC10 into three subzones (a, b and c) based on the successive last occurrences of Axopodorhadbus albianus and Helenea (Microstaurus) chiastia (Fig. 8, Table 2). These events order consistently relative to other marker species and provide reliable indices (Bralower, 1988). At the Wadi Feiran section, subzone CC10a spans the basal 3.8 m of the Abu Qada Formation (Fig. 8). Preservation in the lower part of this subzone is generally poor with low abundances and species richness. Subzone CC10b is recognized between 3.8-8.3 m of the Abu Qada Formation. The base of this subzone occurs just above the $\delta^{13}C$ excursion peak 1, whereas the top lies above peak 2. The same correlation was observed in the Tarfaya basin, southern Morocco (Tantawy, 2008). Subzone CC10c is 11.6 m thick at Wadi Feiran and occupies the upper part of the Abu Qada Formation. Near the top of the section nannofossil preservation is poor and most samples are barren. The top of CC10c coincides with the end of the δ13C plateau at or near the C/T boundary (Fig. 8). Subzones CC10b and CC10c correspond to Zones UC5 and UC6, respectively, of Burnett (1998). Zone CC11 spans the Early and Middle Turonian (Perch-Nielsen, 1985) and is defined by the interval from the FO of Quadrum gartneri at the base to the FO Eiffellithus eximius (e.g., Cepek and Hay, 1969; Perch-Nielsen, 1985) and/or FO of Lucianorhabdus maleformis (e.g., Sissingh, 1977) at the top. Zone CC11 corresponds to Zone UC7 of Burnett (1998) and spans the uppermost part of Abu Qada Formation (Fig. 8). Preservation is poor and only 2 species are present. The base of CC11 (FO Q. gartneri) approximates the C/T boundary (Birkelund et al., 1984; Perch-Nielsen, 1985; Robaszynski et al., 1990; Nederbragt and Fiorentino, 1999). In the Tarfaya basin, southern Morocco, this level is observed near the top of the δ13C plateau, about 45 cm below the FO of Helvetoglobotruncana

helvetica, which approximates the C/T boundary based on planktic foraminifera (Keller et al., 2008; Tantawy, 2008; Gertsch et al., 2010b). In contrast, Bralower (1988) and Bralower et al. (1995) noticed Quadrum gartneri below the C/T boundary (their IC48 Zone), whereas others placed the FO of this species in the early Turonian (e.g., Burnett, 1998; Luciani and Cobianchi, 1999; Lees, 2002) (Table 2).

7. PALEOENVIRONMENT

7.1. Microfossils as environmental proxies

7.1.1. Planktic foraminifera

In shallow environments, planktic foraminifera reflect high stress conditions by generally low diversity, dwarfing and sporadic presence. In Wadi Dakhl only a narrow interval of the OAE2 δ13C excursion is preserved due to erosion. No planktic foraminifera are present in this interval (Fig. 7). Immediately below is a low diversity assemblage of whiteinellids, heterohelicids, globigerinellids and hedbergellids that indicates a shallow environment. During the late Cenomanian (13-45 m) only 2 to 5 planktic foraminiferal species are sporadically present and reflect high stress conditions. In the interval above the δ13C excursion, high stress conditions are indicated by the presence of only Heterohelix species and W. baltica. Heterohelix generally dominates nearshore assemblages in areas with salinity or oxygen fluctuations (e.g., Nederbragt, 1991, 1998; Premoli Silva and Sliter, 1999; Keller and Pardo, 2004; Pardo and Keller, 2008; Gebhardt et al., 2010), and in upwelling areas, such as Tarfaya, Morocco (Keller et al., 2008; Gertsch et al., 2010b). Planktic foraminifera reappear above the hiatus that spans most of the $\delta^{13}C$ excursion, but are absent in red shale that marks anoxic conditions during the early Turonian. It is well known that in shallow water facies organic matter is not preserved (e.g., oxidized), and, consequently, black shale is replaced by red shale (e.g., Voigt et al., 2006, 2007; Keller et al., 2008; Gertsch et al., 2010a, b). At Wadi Feiran, the OAE2 δ13C excursion interval is relatively complete (Fig. 8). Planktic foraminiferal assemblages below the δ13C peak 1 consist of low oxygen and low salinity tolerant species (e.g., heterohelicids, hedbergellids, whiteinellids and guembelitrids) that reflect nutrient-rich, dysoxic conditions in a coastal environment. The low salinity tolerant hedbergellids (e.g., Hedbergella delrioensis, H. planispira), low oxygen tolerant heterohelicids (e.g., Heterohelix reussi, H. moremani) and disaster opportunist Guembelitria cenomana are among the last survivors in shallow inner neritic environments (Hart, 1980, 1999; Leckie, 1987; Leckie et al., 1998, 2002; Keller and Pardo, 2004; Pardo and Keller, 2008; Keller and Abramovich, 2009). Above the $\delta^{13}C$ peaks 1 and 2, planktic foraminifera are absent, except for one isolated occurrence of G. cenomana and D. algeriana. This absence coincides with very a shallow water environment and consequently extreme stress conditions, as indicated by oyster beds and bioclastic limestones (Fig. 4). Planktic foraminifera reappear only above the $\delta^{13}C$ excursion in the early Turonian, similar to Wadi Dakhl (Figs. 7, 8), and are absent in the red layer that represents anoxic conditions.

7.1.2. Benthic foraminifera

Late Cenomanian to early Turonian benthic foraminiferal assemblages in the Wadi Feiran and Wadi Dakhl sections are more diverse and abundant than planktic species, which reflects the shallow water environment (Figs. 8, 10). Benthic foraminiferal assemblages are dominated by low oxygen tolerant agglutinated (e.g., Ammobaculites, Haplophragmoides, Spiroplectammina, Cribrostomoides, Thomasinella) and hyaline species (e.g., Coryphostoma plaitum, Praebulimina

aspera, Pyramidina prolixa, P. nannina, Neobulimina albertensis, Fursenkoina nederi, Gavelinella sandidgei) (Murray, 1973). Within these assemblages, infaunal species (deposit feeders that profit from high food availability) are more abundant than epifaunal species, which indicates dysoxic seafloor conditions (Jarvis et al., 1988; Hart et al., 1993; Koutsoukos et al., 1990; Perty and Lamolda, 1996; Gebhardt et al., 2010). Benthic foraminifera are nearly absent during the δ13C plateau (oyster and bioclastic limestones) and in the early Turonian red shale that reflects delayed anoxic conditions. 7.1.3. Calcareous nannofossils The composition and distribution of nannofossil taxa are generally indicative of paleoecological and paleoenvironmental conditions (e.g., nutrient supply, surface sea water temperature, water depth). However, the effects of diagenetic processes and poor preservation strongly affect the original assemblages (Fig. 9). Effects of dissolution are indicated by high abundance of dissolution-resistant species, such as Watznaueria barnesae and Eprolithus floralis (Roth and Krumbach, 1986; Erba et al., 1992) and rare occurrence of solution-susceptible species (e.g., Eiffellithus species, Tranolithus phacelosus, Prediscosphaera spinosa (Thierstein, 1980; Roth and Krumbach, 1986; Paul et al., 1999; Linnert et al., 2010). Watznaueria barnesae, which is common in the Late Cenomanian CC10a, b subzones, is widely used as a preservation indicator. Roth and Krumbach (1986) and Tantawy (2008) pointed out a good linear correlation between diversity and relative abundance of W. barnesae, although ecological factors may also have affected the distribution (Eshet and Almogi-Labin, 1996; Bauer et al., 2001). Eprolithus floralis shows an increased in abundance at the topmost part of CC10a and lower CC10c (Fig. 8). The species is relatively resistant to dissolution (e.g., Thierstein, 1980; Roth and Krumbach, 1986; Bralower, 1988; Linnert et al., 2010), and high abundance around the C/T boundary is at least partly a preservational artifact. Similar preservational trends and low diversity in Cenomanian–Turonian nannofossil assemblage have been observed regionally (e.g. Sinai: Bauer et al., 2001, 2003; Jordan: Schulze et al., 2004; Morocco, Tantawy, 2008; Gertsch et al., 2010b).

The tropical Watznaueria barnesae is common in most low to mid latitude Cretaceous assemblages but absent from high latitudes in the Cretaceous (Bukry, 1973; Thierstein, 1981; Shafik, 1990; Watkins et al., 1996; Lees, 2002; Tantawy, 2008). Rhagodiscus spices, which are considered a paleotemperature proxy indicative of warm water conditions (Mutterlose, 1989), are rarely present in the lower part of the section (Fig. 8). Common Zeugrhabdotus erectus+spp., Eprolithus floralis, Biscutum constans, and few Rhagodiscus asper/splendens in the lower half of the section (Figs. 8, 9) are interpreted as indicators of high surface-water productivity in upwelling regions (Roth, 1981; Roth and Krumbach, 1986; Erba, 1987; Erba et al., 1992; Mutterlose et al., 1994; Premoli Silva et al., 1999; Howe et al., 2000; Linnert et al., 2010). In the Wadi Feiran section, common Eprolithus floralis and Zeugrhabdotus species in association with oyster-rich limestone may reflect eutrophic conditions (e.g., Roth and Krumbach, 1986; Premoli Silva et al., 1999). High abundance of the nannofossil Broinsonia characterizes neritic chalk seas in SE Europe, Texas and the south of France (Roth and Bowdler, 1981; Roth and Krumbach, 1986). Bralower (1988) observed high abundance of this taxon in upper Cenomanian samples from England, Germany and N. America and interpreted this as indicating shallow water, reduced salinity or high fertility. Linnert et al. (2010) confirmed high abundance in late Cenomanian, but recorded low abundance and hence low fertility during the OAE2 interval. In the Sinai Wadi Feiran section, the shallow water depth is probably the main factor controlling the distribution of Broinsonia species, as well as the low diversity and abundance of other

calcareous nannofossils.

***Table 2**. Comparison between commonly used calcareous nannofossil zonal schemes.*

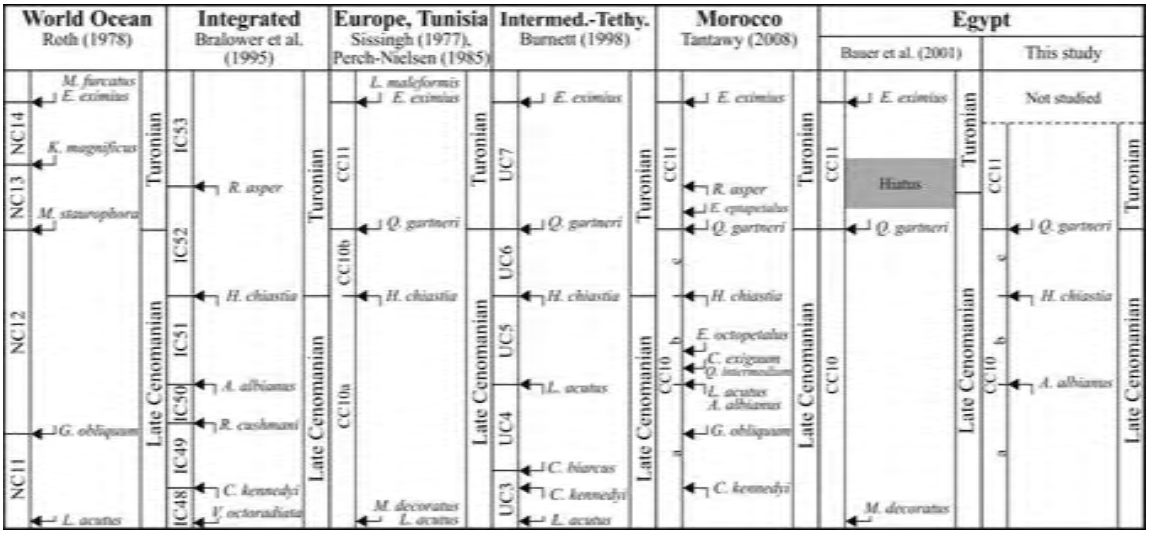

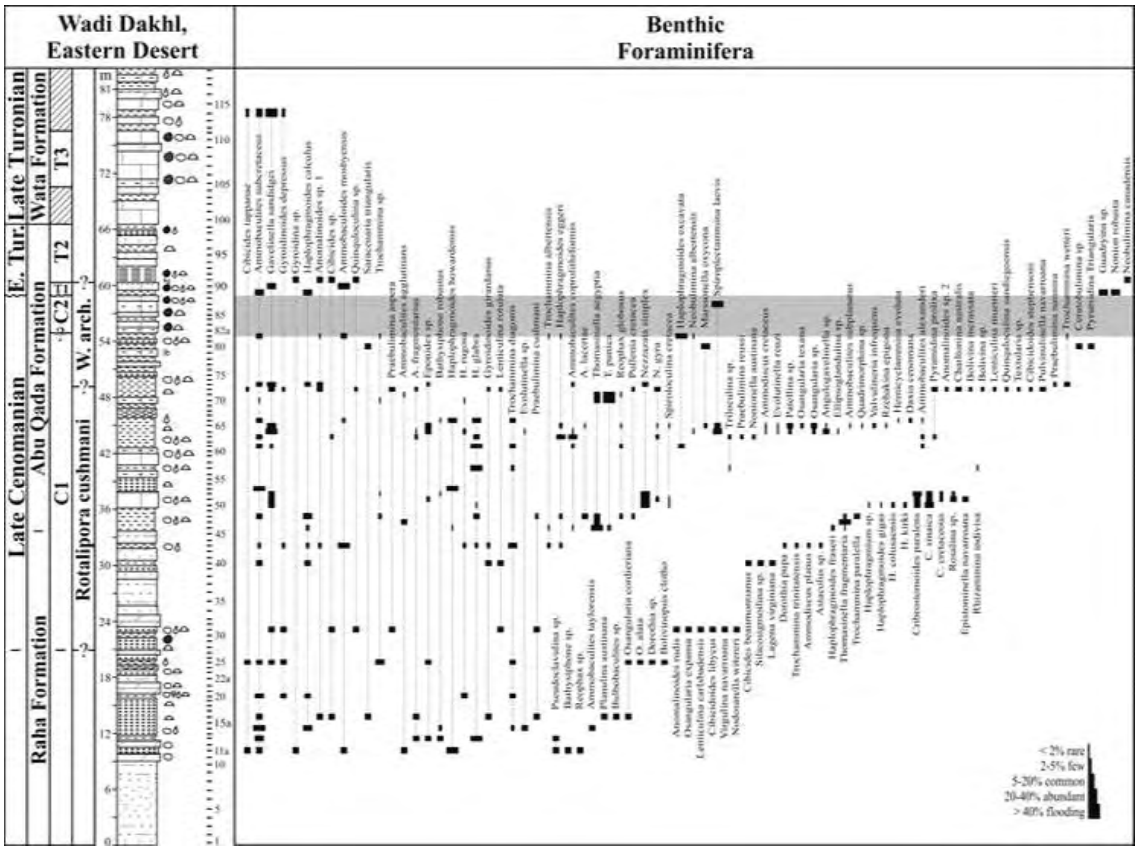

Fig. 10. Cenomanian-late Turonian benthic foraminifera of the Wadi Dakhl section. Note that most benthic foraminiferal assemblages are diversified, sporadic and dominated mainly by agglutinated species.

7.1.3. **Oyster biostromes**

Biotic stressed conditions in the Wadi Dakhl and Wadi Feiran sections are also indicated by the presence of oyster-rich limestone layers that form tabular oyster biostromes as a result of high nutrient flux and rising sea level (Glenn and Arthur, 1990; Abed and Sadaqh, 1998; Dhondt et al., 1999; Pufahl and James, 2006). In the studied sections and through North Africa, oyster biostromes are commonly associated with the onset of the δ13C excursion (Gertsch et al., 2010a, b). Oysters are efficient filter feeders, tolerate a wide range of environmental conditions and can respond quickly to environmental perturbations. They typically occur in high energy, shallow (<20 m) and faunally restricted environments with low salinity, mesotrophic nutrient levels and turbid water column (Pufhal and James, 2006). Such environments are generally unfavorable for planktic and most benthic foraminifera and explain their absence during the δ13C plateau.

8. LATE CENOMANIAN OAE2

The severity of the late Cenomanian oceanic anoxia (i.e., black shale deposition) in the water column depends largely on distance to the coast and water depth, terrestrial influx, marine primary productivity, organic matter preservation, oxidation in the water column, and rates of sedimentation (Pedersen and Calvert, 1990; Canfield, 1994; Arthur and Sageman, 1994). Deeper basins near upwelling areas (i.e., typical anoxic settings; e.g., Tarfaya basin, Morocco) reveal very high sedimentation rates and organic contents (Kuhnt et al., 2005; Kolonic et al., 2005; Keller et al., 2008; Mort et al., 2008). Shallower middle shelf sequences of the U.S. Western Interior at Pueblo, England, Croatia, Portugal, Italy and Spain reveal higher terrigenous influx and lower organic contents (Hart et al., 1993, 2008; Drzewiecky and Simo, 1997; Sageman et al., 1998; Davey and Jenkyns, 1999; Gale et al., 2000; Keller et al., 2004; Keller and Pardo, 2004; Parente et al., 2007; Gebhardt et al., 2010). Among these well-known shelf settings, e.g., in southern England, Jarvis et al. (1988) suggested that organic matter preservation and reductions in microfaunal assemblages (planktic and benthic foraminifera and nannofossils) indicate dysoxic but never anoxic, brackish and mesotrophic conditions during the OAE2. However, Gale et al. (2000) argued, largely on the basis of macrofauna and trace fossil evidences, that there was not even dysaerobic and that diversity reductions were due to oligotrophic nutrient levels.

8.1. OAE2 in shallow near-shore areas

Paleoenvironmental reconstructions for the Cenomanian-early Turonian of Egypt suggest that there was no significant carbonate platform at that time (Lüning et al., 1998, 2004). During the late Cenomanian, shallow subtidal, calcareous deposits covered almost the entire Sinai (Cherif et al., 1989; Kora et al., 1994; Lüning et al., 1998; Bauer et al., 2003) and Eastern Desert (Bandel et al., 1987; Kuss, 1992; Kassab, 1994). In the northern Sinai, shoal carbonates were attached to the shelf edge (Kuss and Bachmann, 1996), whereas in the southern Sinai and Eastern Desert, a thin belt of sandstones interfingered with fluvial deposits (Bandel et al., 1987; Kuss and Bachmann, 1996). At Wadi Dakhl and Wadi Feiran, the Cenomanian-Turonian sequences reflect atypical shallow near-shore environment deepening with the late Cenomanian to early Turonian sea level rise as indicated by dominant carbonate deposition (Figs. 3, 4). Such shallow marine environments are often characterized by high nutrients due to terrigenous runoff and low salinity due to fresh water influx (Keller et al., 2004; Keller and Pardo, 2004; Gertsch et al., 2010a, b). In this shallow inner neritic depositional environment of Egypt, the OAE2 δ13C

excursion shows characteristics similar to the GSSP section at Pueblo (Leckie et al., 2002; Keller and Pardo, 2004; Caron et al., 2006; Gertsch et al., 2010a), as well as deeper marine sequences of Tunisia and Morocco (Accarie et al., 1996; Nederbragt and Fiorentino, 1999; Kolonic et al., 2005; Caron et al., 2006; Voigt et al., 2006, 2007; Keller et al., 2008; Mort et al., 2008; Gertsch et al., 2010b).

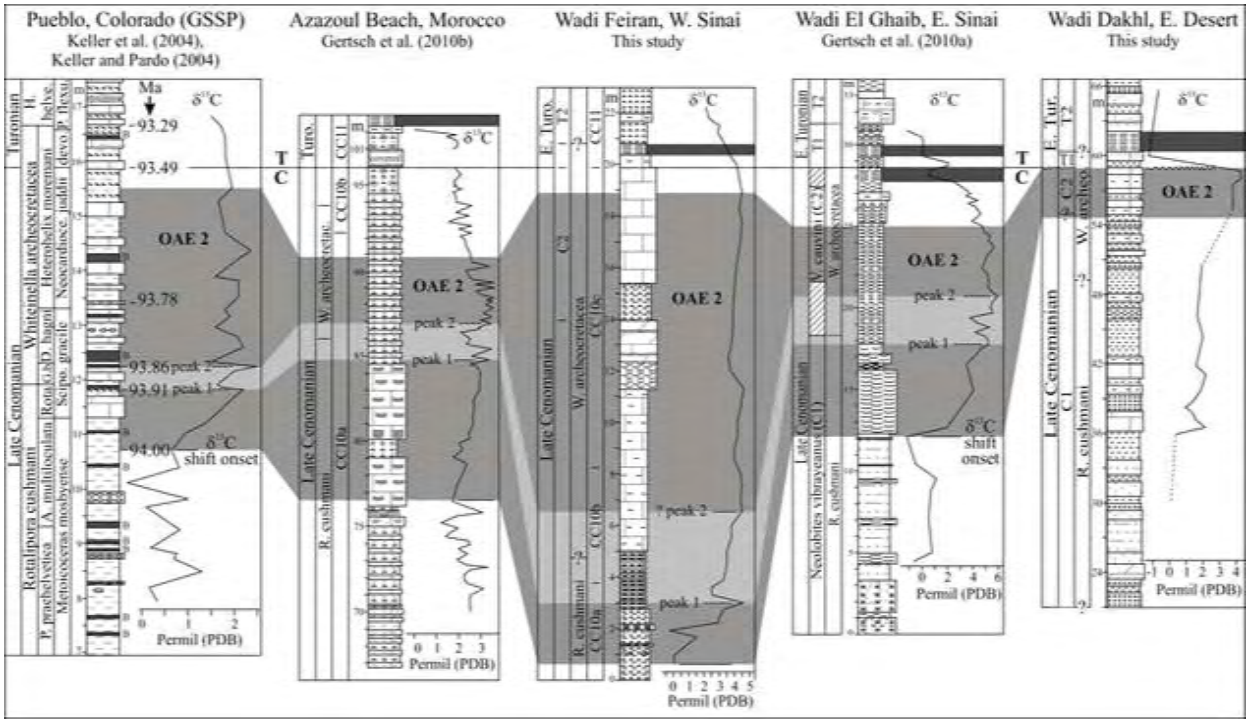

Fig. 11. *$\delta^{13}C$ correlation of the late Cenomanian OAE2 excursion in Egypt, Morocco and Pueblo. Note that the OAE2 δ13C excursion is comparable in all sections. The absence of the characteristic two δ13C peaks at the Wadi Dakhl section indicates a major hiatus. Dark grey areas mark OAE2, whereas light grey marks the interval between peaks 1 and 2. No anoxic conditions are observed during OAE2 in these shallow environments, but delayed anoxic conditions are observed in the early Turonian in Egypt and Morocco (darker grey areas). These delayed anoxic/dysoxic conditions are correlated with the maximum sea level transgression in shallow environments.*

The magnitude of the OAE2 δ13C excursion (~4.5‰) is comparable to the Wadi El Ghaib section in the eastern Sinai (5‰, Gertsch et al., 2010a), Eastbourne, England (~5‰, Jarvis et al., 2006), Tarfaya and Agadir, Morocco (3-4‰, Keller et al., 2008; Mort et al., 2008; Gertsch et al., 2010b), but higher than at Pueblo, Colorado (~2.5‰, Keller et al., 2004) and Azazoul, Morocco (~3‰, Gertsch et al., 2010b) (Fig. 11). This reveals that the OAE2 δ13C excursion, which is mainly known from black shale deposits of deeper marine environments, reached into inner shelf and coastal environments, as earlier observed by Gertsch et al. (2010a, b) and confirmed in this study. However, the characteristic anoxic conditions of the δ13C plateau are not apparent in the lithology of the studied sections (Figs. 3, 4).

8.2. Delayed OAE2 anoxia

Gertsch et al. (2010a, b) observed that in shallow near-shore environments anoxic conditions were not reached until the early Turonian and well after the OAE2 δ13C plateau in

the Wadi El Ghaib section of the Sinai and in northern Morocco (Azazoul section). This study confirms these observations in the Wadi Dakhl and Wadi Feiran sections. Lithologically, the delayed anoxic conditions are indicated by the presence of red laminated shales in the early Turonian of shallow C/T sections in Egypt and Morocco (Fig. 11). These red shales are diagentic products of the originally dark organic-rich shales (Voigt et al., 2006, 2007; Gertsch et al., 2010a, b). Neither planktic nor benthic foraminifera are observed in these red shales, which suggest anoxia comparable to the δ13C plateau. The delay in anoxic conditions is considerable and probably encompasses most of ammonite zone T1. In all sections it occurs after the OAE2 δ13C plateau in the early Turonian, although the timing appears to depend on local environmental conditions. The delayed anoxic conditions in inner shelf areas appears to be related to the sea level transgression, which reached its maximum in the early Turonian transporting low oxygen waters shoreward, which resulted in organicrich shale deposition (see also Gertsch et al., 2010a, b). Despite this delay, the δ13C excursion that characterizes OAE2 in marine environments is comparable and coeval to that in deeper open marine environments, including the stratotype at Pueblo, Colorado (Fig. 11).

9. CONCLUSIONS

Biostratigraphic control in shallow water sequences is difficult due to low diversity and sporadic occurrences, though integrated macro- and microfossil biostratigraphy and stable isotope stratigraphy yields good age control for late Cenomanian to early Turonian sequences. Subtidal to inner neritic environments during the late Cenoamnian OAE2 excursion at Wadi Dakhl and Wadi Feiran are characterized by dysoxic, brackish and mesotrophic conditions, as indicated by low species diversity, low oxygen and low salinity tolerant planktic and benthic species, along with oyster-rich limestone layers. The late Cenomanian OAE2 $\delta^{13}C$ excursion is recorded in shallow inner neritic environments of NE Egypt, and appears coeval with the OAE2 $\delta^{13}C$ excursion in open marine environments. Anoxic conditions characteristic of the late Cenomanian OAE2 are delayed until the early Turonian in shallow shelf sequences. This delay appears to be associated with the maximum sea level transgression in the early Turonian that transported low oxygen waters shoreward.

ACKNOWLEDGEMENTS We thank the reviewers M. Hart, D. Horne and one anonymous, for comments and helpful suggestions. This study was supported through a grant from the Binational Fulbright Commission in Egypt to A. El-Sabbagh while visiting Princeton University, and partly supported by the U.S. National Science Foundation under Grant No. 0217921.

REFERENCES

Abdel-Gawad, G., 1999. Biostratigraphy and facies of the Turonian in West Central Sinai, Egypt. Annals of the Geological Survey of Egypt 22, 99-114.

Abed, A.M., Sadaqah, R., 1998. Role of upper Cretaceous oyster bioherms in the deposition and accumulation of high-grade phosphorites in central Jordan. Journal of Sedimentary Research 68, 1009–1020.

Accarie, A., Emmanuel, L., Robaszynski, R., Baudin, F., Amedro, F., Caron, M., Deconinck, J., 1996. Carbon isotope geochemistry as stratigraphic tool. A case study of the Cenomanian/Turonian boundary in central Tunisia. Comptes Rendus de l'Académie des Sciences Paris (2a) 322, 579–586.

Amédro, F., Robaszynski, F., 2008. Zonation by ammonites and foraminifers of the Vraconian-Turonian interval: A comparison of the Boreal and Tethyan domains (NW Europe/Central Tunisia). Carnets de Géologie Letter 2 (CG2008-LO2), 1- 5.

Arthur, M.A., Allard, D., Hinga, K.R., 1991. Cretaceous and Cenozoic atmospheric carbon dioxide variations and past global climate change. Abstract Program, Geological Society of America 23, 5178.

Arthur, M.A., Dean, W.E., Schlanger, S.O., 1985. Variations in the global carbon cycle during the Cretaceous related to climate, volcanism, and changes in atmospheric CO2. In: Sundquist, E.T., Broecker, W.S. (Eds.), The Carbon Cycle and Atmospheric CO2: Natural Variations Archean to Present, American Geophysical Union Monograph, vol. 32, pp. 504– 529.

Arthur, M.A., Jenkyns, H.C., Brumsack, H.J., Schlanger, S.O., 1990. Stratigraphy, geochemistry and paleoceanography of organic carbon-rich Cretaceous sequences. In: Ginsburg, R.N., Beaudoin, B. (Eds.), Cretaceous Resources, Events and Rhythms: Background and Plans for Research. NATO ASI series, pp. 75–119.

Arthur, M.A., Sageman, B.B., 1994. Marine black shales: depositional mechanisms and environments of ancient deposits. Annual Review of Earth and Planetary Sciences 22, 499–551.

Bachmann, M., Kuss, J., 1998. The middle Cretaceous carbonate ramp of the northern Sinai: sequence stratigraphy and facies distribution. In: Wright, V.P., Burchette, T.P. (Eds.), Carbonate ramps. Journal of the Geological Society, London, Special Publication 149, pp. 253-280.

Bandel, K., Kuss, J., Malchus, N., 1987. The sediments of Wadi Qena area, Eastern Desert, Egypt. Journal of African Earth Sciences 6, 427-455.

Bauer, J., Kuss, J., Steuber T., 2003. Sequence architecture and carbonate platform configuration (Late Cenomanian–Santonian), Sinai, Egypt. Sedimentology 50, 387–414.

Bauer, J., Marzouk, A.M., Steuber, T., Kuss, J., 2001. Lithostratigraphy and biostratigraphy of the Cenomanian-Santonian strata of Sinai, Egypt. Cretaceous Research 22, 497-526.

Birkelund, T., Hancock, J.M., Hart, M.B., Rawson, P.F., Remane, J., Robaszynski, F., Schmid, F., Surlyk, F., 1984. Cretaceous Stage boundaries, proposals. Bulletin of the Geological Society of Denmark 33, 3-20.

Bolli, H.M., Beckmann, J.-P., Sauders, J.B., 1994. Benthic foraminiferal biostratigraphy of the south Caribbean region. Cambridge University press, 408 pp.

Bralower, T.J., 1988. Calcareous nannofossil biostratigraphy and assemblages of the Cenomanian-Turonian boundary interval: implications for the origin and timing of oceanic anoxia. Palaeoceanography 3, 275-316.

Bralower, T.J., Leckie, R.M., Sliter, W.V., Thierstein, H.R., 1995. An integrated Cretaceous microfossil biostratigraphy. Society of Economic Paleontologists and Mineralogists Special Publication 54, 65-79.

Buchem, F.S.P., Van, Razin, P., Homewood, P.W., Heiko Oterdom, W., Philip J., 2002. Stratigraphic organization of carbonate ramps and organic-rich intraself: Natih Formation (middle Cretaceous) of northern Oman. American Association of Petroleum Geologists 86, 21-53.

Bukry, D., 1973. Coccolith and silicoflagellate stratigraphy, Tasman Sea and southwestern Pacific Ocean, Deep Sea Drilling Project Leg 21. Initial Reports of the Deep Sea Drilling Project 21, 885-893.

Burnett, J.A., 1998. Upper Cretaceous. In: Bown, P.R. (Ed.), Calcareous nannofossil biostratigraphy. British Micropalaeontological Society Publication Series, Chapman and Hall Ltd. Kluwer Academic Publisher, London, pp. 132-165.

Canfield, D.E., 1994. Factors influencing organic carbon preservation in marine sediments. Chemical Geology 114, 315–329.

Caron, M., 1985. Cretaceous planktonic foraminifera. In: Bolli, H.M., Saunders, J.B., Perch-Nielsen, K. (Eds.), Plankton Stratigraphy. Cambridge University Press, Cambridge, pp. 17–86.

Caron, M., Dall'Agnolo, S., Accarie, H., Barrera, E., Kauffman, E.G., Amedro, F., Robaszynski, F., 2006. High-resolution stratigraphy of the Cenomanian- Turonian boundary interval at Pueblo (USA) and Wadi Bahloul (Tunisia): stable isotope and bio-events correlation. Geobios 39, 171–200.

Cepek, P., Hay, W.W., 1969. Calcareous nannoplankton and stratigraphic subdivision of the Upper

Cretaceous. Transactions of the Gulf Coast Association of Geological Societies 19, 323-336.

Chancellor, G.R., Kennedy, W.J., Hancock, J.M., 1994. Turonian ammonite faunas from Central Tunisia. Journal of the Geological Society, London, Special Papers in Palaeontology 50, 1-118 p.

Cherif, O.H., Al-Rifaiy, I.A., Al-Afifi, F.I., Orabi, O.H., 1989. Foraminiferal biostratigraphy and paleoecology of some Cenomanian-Turonian exposures in West-Central Sinai (Egypt). Revue de Micropalèontologie 31, 243-262.

Cobban, W.A., Hook, S.C., 1980. The Upper Cretaceous (Turonian) ammonite Family Coilopoceratidae Hyatt in the western Interior of the United States. US Geological Survey Professional Paper 1192, 1-28.

Courtillot, V.E., Renne P.R., 2003. On the ages of flood basalt events. Comptes Rendus Geoscience 335, 113-140.

Cushman, J.A., 1946. Upper Cretaceous foraminifera of the Gulf Coast region of the United States and adjacent areas. US Geological Survey Professional Paper 206, 1-241.

Davey, S.D., Jenkyns, H.C., 1999. Carbon-isotope stratigraphy of shallow-water limestones and implications for the timing of Late Cretaceous sea-level rise and anoxic events (Cenomanian Turonian of the peri-Adriatic carbonate platform, Croatia). Eclogae Geologicae Helvetiae 92, 163-170.

Dhondt, A.V., Malchus, N., Boumaza, L., Jaillard, E., 1999. Cretaceous oysters from North Africa: origin and distribution. Bulletin de la Société géologique de France 170, 67–76.

Drzewiecky, P.A., Simo, J.A., 1997. Carbonate platform frowning and oceanic anoxic events on a mid-Cretaceous carbonate platform, south-central Pyrenees, Spain. Journal of Sedimentary Research 67, 698-714.

El-Hedeny, M.M., 2002. Cenomanian-Coniacian ammonites from west-central Sinai, Egypt, and their significance in biostratigraphy. Neues Jahrbuch für Geologie und Paläontologie Monatshefte 7, 397-425.

El-Sabbagh, A.M., 2000. Stratigraphical and paleontological studies of the Upper Cretaceous succession in Gebel Nezzazat and Bir El-Markha areas, West- Central Sinai, Egypt. Unpublished PhD Thesis, Alexandria University, Faculty of Science, 209 pp.

El-Sabbagh, A.M., 2008. Shallow-water macrofaunal assemblages of the Cenomanian- Turonian sequence of Musabaa Salama area, west central Sinai, Egypt. Egyptian Journal of Paleontology 8, 63-86.

Erba, E., l987. Mid-Cretaceous cyclic pelagic facies from the Umbria-Marchean basin: what do calcareous nannofossils suggest? International Nannofossil Association Newsletter 9, 52-53.

Erba, E., Castradori, D., Guasti, G., Ripepe, M., 1992. Calcareous nannofossils and Milankovitch cycles: the example of the Albian Gault Clay Formation (southern England). Palaeogeography, Palaeoclimatology, Palaeoecology 93, 47–69.

Erba, E., Tremolada, F., 2004. Nannofossil carbonate fluxes during the early Cretaceous: phytoplankton response to nutrification episodes, atmospheric CO2, and anoxia. Paleoceanography 19, 1008. doi:10.1029/2003PA000884.

Erbacher, J., Hemleben, Ch., Huber, B.T., Markey, M., 1999. Correlating environmental changes during early Albian oceanic anoxic event 1B using benthic foraminiferal paleoecology. Marine Micropaleontology 38, 7-28.

Eshet, Y., Almogi Labin A., 1996. Calcareous nannofossils as paleoproductivity indicators in Upper Cretaceous organic-rich sequences in Israel. Marine Micropaleontology 29, 37-61.

Forster, A., Schouten, S., Baas, M., Sinninghe Damsté, J.S., 2007. Mid-Cretaceous (Albian-Santonian) sea surface temperature record of the tropical Atlantic Ocean. Geology 35, 919–922.

Gale, A.S., Smith, A.B., Monks, N.E.A., Young, J.A., Howard, A., Wray, D.S., Huggett, J.M., 2000. Marine biodiversity through the Late Cenomanian-Early Turonian: paleoceanographic controls and sequence stratigraphic biases. Journal of the Geological Society, London 157, 745-757.

Gebhardt, H. Friedrich, O. Schenk, B., Fox, L., Hart, M., Wagreich, M., 2010. Paleoceanographic changes at the northern Tethyan margin during the Cenomanian-Turonian Oceanic Anoxic Event (OAE2). Marine Micropaleontology 77, 25-45.

Gertsch, B., Adatte, T., Keller, G., Tantawy, A.A., Berner, Z., Mort, H.P., Fleitmann, D., 2010b. Middle and late Cenomanian oceanic anoxic events in shallow and deeper shelf environments of NW Morocco. Sedimentology 57, 1430-1462.

Gertsch, B., Keller, G., Adatte, T., Berner, Z., Kassab, A.S., Tantawy, A.A., El- Sabbagh, A.M., Stueben, D., 2010a. Cenomanian-Turonian transition in shallow water sequence of the Sinai, Egypt. International Journal of Earth Sciences (Geologische Rundschau) 99, 165–182.

Ghorab, M.A., 1961. Abnormal stratigraphic features in Ras Gharib oilfield. Third Arab Petroleum Congress, Alexandria, pp. 1-10.

Glenn, C.R., Arthur, M.A., 1990. Anatomy and origin of a Cretaceous phosphoritegreen sand giant, Egypt. Sedimentology 37, 123-148.

Graciansky, P.C., de, Deroo, G., Herbin, J.P., Jacquin, T., Magni, F., Montadert, I., Müller, C., 1986. Ocean-wide stagnation episodes in the Late Cretaceous. Geological Rundschau 75, 17– 41.

Gustafsson, M., Holbourn, A., Kuhnt W., 2003. Changes in Northeast Atlantic temperature and carbon flux during the Cenomanian/Turonian paleoceanographic event: the Goban Spur stable isotope record. Palaeogeography, Palaeoclimatology, Palaeoecology 201, 51-66.

Hallam, A., 1992. Phanerozoic Sea Level Changes. Columbia University Press, New York, 266 pp.

Haq, B.U., Hardenbol, J., Vail, P.R., 1987. Chronology of fluctuating sea levels since the Triassic. Science 235, 1156–1167.

Hardenbol, J., Caron, M., Amedro, F., Dupuis, Ch., Robaszynski, F., 1993. The Cenomanian-Turonian boundary in central Tunisia in the context of a sequencestratigraphic interpretation. Cretaceous Research 14, 449-454.

Hardenbol, J., Thierry, J., Farley, M.B., de Graciansky, P.C., Vail, P.P., 1998. Mesozoic and Cenozoic sequence chronostratigraphic framework of European basins. Chart 4: Cretaceous sequence chronostratigraphy. In: de Graciansky, P.C., Hardenbol, J., Jacquin, T., Vail, P.P. (Eds.), Mesozoic and Cenozoic sequence stratigraphy of European basins, Society for Sedimentary Geology Special Publication 60, pp. 3-13.

Hart, M.B., 1980. A water depth model for the evolution of the planktonic foraminifera. Nature 286, 252–254.

Hart, M.B., 1999. The evolution and biodiversity of Cretaceous planktonic Foraminiferida. Geobios 32, 247–255.

Hart, M.B., Callapez, P.M., Fisher, J.K., Hannant, K., Monteiro, J.F., Price, G.D., Watkinson, M.P., 2008. Micropaleontology and stratigraphy of the Cenomanian/Turonian boundary in the Lusitanian Basin, Portugal. Journal of Iberian Geology 31, 311-326.

Hart, M.B., Dodsworth, P., Duane, A.M., 1993. The late Cenomanian Event in eastern England. Cretaceous Research 14, 495-508.

Hart, M.B., Leary, P.N., 1989. The stratigraphic and paleoceanographic setting of the late Cenomanian ‘‘anoxic’’ event. Journal of the Geological Society, London 146, 305–310.

Howe, R.W., Haig, D.W., Apthorpe, M.C., 2000. Cenomanian-Coniacian transition efrom siliciclastic to carbonate marine deposition, Giralia Anticline, Southern Carnarvon Platform, Western Australia. Cretaceous Research 21, 517–551

Huber, B.T., Norris, R.D., MacLeod, K.G., 2002. Deep-sea paleotemperature record of extreme warmth during the Cretaceous. Geology 30, 123-126.

Issawi, B., El Hinnawi, M., Francis, M., Mazhar, A., 1999. The Phanerozoic geology of Egypt: A geodynamic approach. Geological Survey of Egypt 76, 1-462.

Jarvis, I., Carson, G.A., Cooper, M.K.E., Hart, M.B., Leary, P.N., Tocher, B.A., Horne, D. and Rosenfeld, A., 1988. Microfossil assemblages and the Cenomanian/Turonian (Late Cretaceous)

Oceanic Anoxic Event. Cretaceous Research 9, 3-103.

Jarvis, I., Gale, A.S., Jenkyns, H.C., Pearce, M.A., 2006. Secular variation in Late Cretaceous carbono isotopes: a new δ13C carbonate reference curve for the Cenomanian-Campanian (99.6-70.6 Ma). Geological Magazine 143, 561-608.

Jenkyns, H.C., Gale, A.S., Corfield, R.M., 1994. Carbon- and oxygen-isotope stratigraphy of the English Chalk and Italian Scaglia and its palaeoclimatic significance. Geological Magazine 131, 1–34.

Kassab, A.S., 1991. Cenomanian-Coniacian biostratigraphy of the northern Eastern Desert, Egypt, based on ammonites. Newsletters on Stratigraphy 25, 25–35.

Kassab, A.S., 1994. Upper Cretaceous ammonites from the El-Sheikh Fadl-Ras GharibRoad, Northeastern Desert, Egypt. Neues Jahrbuch für Geologie und Paläontologie Monatshefte 2, 108-128.

Kassab, A.S., 1999. Cenomanian–Turonian boundary in the Gulf of Suez region, Egypt: towards an inter-regional correlation, based on ammonites. Geological Society of Egypt, Special Publication 2, 61–98.

Kassab, A.S., Ismael, M.M., 1994. Upper Cretaceous invertebrate fossils from the area northeast of Abu Zeneima, Sinai, Egypt. Neues Jahrbuch für Geologie und Paläontologie Abhandlungen 191, 221–249

Kassab, A.S., Obaidalla, N.A., 2001. Integrated biostratigraphy and interregional correlation of the Cenomanian–Turonian deposits of Wadi Feiran, Sinai, Egypt. Cretaceous Research 22, 105–114.

Keller, G., Abramovich, S., 2009. Lilliput effect in late Maastrichtian planktic foraminifera: Response to environmental stress. Palaeogeography, Palaeoclimatology, Palaeoecology 284, 47-62.

Keller, G., Adatte, T., Berner, Z., Chellai, E.H., Stueben, D., 2008. Oceanic events and biotic effects of the Cenomanian-Turonian anoxic event, Tarfaya Basin, Morocco. Cretaceous Research 29, 976-994.

Keller, G., Berner, Z., Adatte, T., Stueben, D., 2004. Cenomanian-Turonian $\delta^{13}C$ and $\delta^{18}O$, sea level and salinity variations at Pueblo, Colorado. Palaeogeography, Palaeoclimatology, Palaeoecology 211, 19–43.

Keller, G., Han, Q., Adatte, T., Burns, S., 2001. Paleoenvironment of the Cenomanian- Turonian transition at Eastbourne, England. Cretaceous Research 22, 391–422.

Keller, G., Li, L., MacLeod, N., 1995. The Cretaceous/Tertiary boundary stratotype section at El Kef, Tunisia: how catastrophic was the mass extinction? Palaeogeography, Palaeoclimatology, Palaeoecology 119, 221-254.

Keller, G., Pardo, A., 2004. Age and paleoenvironment of the Cenomanian-Turonian global stratotype section and point at Pueblo, Colorado. Marine Micropaleontology 51, 95–128.

Kennedy, W.J., Cobban, W.A., 1991. Stratigraphy and interregional correlation of the Cenomanian-Turonian transition in the Western Interior of the United States near Pueblo, Colorado, a potential boundary stratotype for the base of the Turonian stage. Newsletters on Stratigraphy 24, 1–33.

Kennedy, W.J., Walaszezyk, I., Cobban, W.A., 2000. Pueblo, Colorado, USA, candidate Global Boundary Stratotype Section and Point for the base of the Turonian Stage of the Cretaceous and for the base of the middle Turonian Substage, with a revision of the Inoceramidae (Bivalvia). Acta Geologica Polonica 50, 295–334.

Kennedy, W.J., Wright, C.W., Hancock, J.M., 1987. Basal Turonian ammonites from West Texas. Palaeontology 30, 27–74.

Kerdany, M.T., Cherif, O.H., 1990. Mesozoic. In: Said, R. (Ed.), The geology of Egypt. Balkema Publishers, pp. 407-438.

Kolonic, S., Sinninghe Damsté, J.S., Bottcher, M.E., Kuypers, M.M.M., Kuhnt, W., Beckmann, B., Scheeder, G., Wagner, T., 2002. Geochemical characterization of Cenomanian/Turonian black shales from the Tarfaya Basin (SW Morocco) – relationships between palaeoenvironmental conditions and early sulphurization of sedimentary organic matter. Journal of Petroleum Geology 25, 325–350.

Kolonic, S., Wagner, T., Forster, A., Sinningh Damsté , J.S., Walsworth-Bell, B., Erba, E., Turgeon, S., Brumsack, H.J., Chellai, E.H., Tsikos, H., Kuhnt, W., Kuypers, M.M.M., 2005. Black shale

deposition on the northwest African shelf during theCenomanian-Turonian oceanic anoxic event: climate coupling and global organic carbon burial. Paleoceanography 20, 1006. doi:10.1029/2003PA000950.

Kora, M., Hamama, H.H., 1987. Biostratigraphy of the Cenomanian-Turonian successions of Gebel Gunna, southeastern Sinai, Egypt. Mansoura Faculty of Science Bulletin 14, 289-301.

Kora, M., Khalil, H., Sobhy, M., 2001. Stratigraphy and microfacies of some Cenomanian-Turonian successions in the Gulf of Suez Region. Egyptian Journal of Geology 45, 413-439.

Kora, M., Shahin, A., Semiet, A., 1994. Biostratigraphy and paleoecology of some Cenomanian successions in the West-Central Sinai, Egypt. Neues Jahrbuch für Geologie und Paläontologie Monatshefte 10, 597-617.

Koutsoukos, E.A.M., Leary, P.N., Hart, M.B., 1990. Latest Cenomanian-earliest Turonian low-oxygen tolerant benthonic foraminifera: a case study from the Sergipe Basin (N.E. Brazil) and the western Anglo-Paris Basin (Southern England). Palaeogeography, Palaeoclimatology, Palaeoecology 77, 145–177.

Kuhnt, W., Luderer, F., Nederbragt, S., Thurow, J., Wagner, T., 2005. Orbital scale record of the late Cenomanian-Turonian Oceanic Anoxic Event (OAE2) in the Tarfaya Basin (Morocco). International Journal of Earth Sciences 94, 147–159.

Kuhnt, W., Nederbragt, A., Leine, L., 1997. Cyclicity of Cenomanian-Turonian organiccarbon- rich sediments in the Tarfaya Atlantic Coastal Basin (Morocco). Cretaceous Research 18, 587-601.

Kuss, J., 1992. Facies and stratigraphy of Cretaceous limestones from northeast Egypt, Sinai, and southern Jordan. Geology of the Arab World, Cairo University, 283- 302.

Kuss, J., Bachmann, M., 1996. Cretaceous paleogeography of the Sinai Peninsula andneighboring areas. Comptes rendus de l'Academie des Sciences, Serie II, Sciences de la Terre et des Planetes 322, 915-933.

Lamolda, M.A., Gorostidi, A., Paul, C.R.C., 1994. Quantitative estimates of calcareous nannofossil changes across the Plenus Marls (latest Cenomanian), Dover, England; implication for the generation of the Cenomanian-Turonian boundary event. Cretaceous Research 15, 143-164.

Leckie, R.M., 1987. Paleoecology of the mid-Cretaceous planktic foraminifera: a comparison of open ocean and epicontinental sea assemblages. Micropaleontology 33, 164–176.

Leckie, R.M., Bralower, T.J., Cashman, R., 2002. Oceanic anoxic events and plankton evolution: biotic response to tectonic forcing during the mid-Cretaceous. Paleoceanography 17, 1041. doi:10.1029/2001PA000623.

Leckie, R.M., Yuretich, R.F., West, L.O.L., Finkelstein, D., Schmidt, M., 1998. Paleoceanography of the southwestern Western Interior Sea during the time of the Cenomanian-Turonian boundary (Late Cretaceous). In: Dean, W.E., Arthur, M.A. (Eds.), Concepts in Sedimentology and Paleontology. Society of Economic Paleontologists and Mineralogists 6, pp. 101–126.

Lees, J., 2002. Calcareous nannofossil biogeography illustrates palaeoclimate change in the Late Cretaceous Indian Ocean. Cretaceous Research 23, 537-634.

Lewy, Z., Kennedy, J. and Chancellor, G., 1984. Co-occurrence of Metoicoceras geslinianum (d'Orbigny) and Vascoceras cauvini Chudeau (Cretaceous Ammonoidea) in the southern Negev (Israel) and its stratigraphic implications. Newsletters on Stratigraphy 13, 67-76.

Lewy, Z., Raab, M., 1976. Mid-Cretaceous stratigraphy of the Middle East. Annals du Muséum d'Histoire Naturelle de Nice 4 (XXXII), 1-17.

Linnert, C., Mutterlose, J., Erbacher, J., 2010. Calcareous nannofossils of the Cenomanian/Turonian boundary interval from the Boreal Realm (Wunstorf, northwest Germany). Marine Micropaleontology 74, 38–58.

Luciani, V., Cobianchi, M., l999. The Bonarelli level and other black shales in the Cenomanian-Turonian of the northeastern Dolomites (Italy): calcareous nannofossil and foraminiferal data. Cretaceous Research 20, 135-167.

Lüning, S., Kolonic, S., Belhadj, E.M., Cota, L., Baric, G., Wagner, T., 2004. Integrated depositional model for the Cenomanian-Turonian organic-rich strata in North Africa. Earth-Science Reviews 64, 51-117.

Lüning, S., Marzouk, A., Morsi, A., Kuss, J., 1998. Sequence stratigraphy of the Upper Cretaceous of central-east Sinai, Egypt. Cretaceous Research 19,153–196.

Malchus, N., 1990. Revision der Kreide-Austern (Bivalvia: Pteriomorphia) Ägyptens (Biostratigraphie, Systematik). Berliner Geowissenschäftliche Abhandlungen A125, 1-231.

Manivit, H., Perch-Nielsen, K., Prins, B., Verbeek, J.W., 1977. Mid Cretaceous calcareous nannofossil biostratigraphy. Proceedings of the Koninklijke Nederlandse Akademie van Wetenschappen, Series B80, 169-181.

Marshall, J.D., 1992. Climatic and oceanographic isotopic signals from the carbonate rock record and their preservation. Geological Magazine 129, 143-160.

Meister, C., Abdallah, H., 2005. Précision sur les successions d'ammonites du Cénomanien-Turonien dans la région de Gafsa, Tunisie du centre-sud. Revue de Paléobiologie 24, 111-199.

Meister, C., Allzuma, K., Mathey, B., 1992. Les ammonites du Niger (Afrique occidentale) et la Transgression Transsaharienne au cours du Cenomanien– Turonien. Geobios 25, 55–100

Meister, C., Rhalmi, M., 2002. Quelques ammonites du CénomanieneTuronien de la région d'Errachidia-Boudnid-Erfoud (partie méridionale du Haut Atlas Central, Maroc). Revue de Paléobiologie 21, 759-779.

Mitchell, S.F., Ball, J.D., Crowley, S.F., Marshall, J.D., Paul, C.R.C., Veltkamp, C.J., Samir, A., 1997. Isotope data from Cretaceous chalks and foraminiferal environmental or diagenetic signals? Geology 25, 691–694.

Mort, H., Adatte, T., Keller, G., Bartels, D., Föllmi, K., Steinmann, P., Berner, Z., Chellai, E.H., 2008. Organic carbon deposition and phosphorus accumulation during Oceanic Anoxic Event 2 in Tarfaya, Morocco. Cretaceous Research 29, 1008-1023.

Murray, J.W., 1973. Deposition and ecology of living benthic foraminiferids. Russak and Co, Carne, pp 1–274.

Mutterlose, J., 1989. Temperature-controlled migration of calcareous nannofossils in the north-west European Aptian. In: Crux, J.A., van Heck, S.E. (Eds.), Nannofossils and their applications. Chichester (Ellis Horwood), pp. 122–142.

Mutterlose, J., Bornemann, A., Herrle, O., 2005. Mesozoic calcareous nannofossils – state of the art. Paläontologische Zeitschrift 79, 113–133.

Mutterlose, J., Kessels, K., 2000. Early Cretaceous calcareous nannofossils from high latitudes: implications for palaeobiogeography and palaeoclimate. Palaeogeography, Palaeoclimatology, Palaeoecology 160, 347–372.

Mutterlose, J., Luppold, F.W., Grenda, F., 1994. Floren- und Faunenverteilung in rhythmisch gebankten Serien des Hauterive (Unterkreide) NW Deutschlands. Berichte der Naturhistorischen Gesellschaft Hannover 136, 27–65.

Nagm, E., Wilmsen, M., Aly, M., Hewaidy, A., 2010a. Upper Cenomanian – Turonian (Upper Cretaceous) ammonoids from the western Wadi Araba, Eastern Desert, Egypt. Cretaceous Research 31, 473-499.

Nagm, E., Wilmsen, M., Aly, M., Hewaidy, A., 2010b. Biostratigraphy of the Upper Cenomanian - Turonian (lower Upper Cretaceous) successions of the western Wadi Araba, Eastern Desert, Egypt. Newsletters on Stratigraphy 44, 17-35.

Nederbragt, A.J., 1991. Late Cretaceous biostratigraphy and development of Heterohelicidae (planktic foraminifera). Micropaleontology 37, 329-372.

Nederbragt, A.J., 1998. Quantitative biogeography of late Maastrichtian planktic foraminifera. Micropaleontology 44, 385-412.

Nederbragt, A., Fiorentino, A., 1999. Stratigraphy and paleoceanography of the Cenomanian-Turonian

boundary event in Oued Mellegue, northwestern Tunisia. Cretaceous Research 20, 47–62.

Norris, R.D., Bice, K.L., Magno, E.A., Wilson, P., 2002. Jiggling the tropical thermostat in the Cretaceous hothouse. Geology 30, 299–302. Omara, S., 1956. New foraminifera from Cenomanian of Sinai, Egypt. Journal of Paleontology 30, 883-890.

Pardo, A., Keller, G., 2008. Biotic effects of environmental catastrophes at the end of the Cretaceous and early Tertiary: Guembelitria and Heterohelix blooms. Cretaceous Research 29, 1058–1073.

Parente, M., Frijia, G., Di Lucia, M., 2007. Carbon-isotope stratigraphy of Cenomanian- Turonian platform carbonates from the southern Apennines (Italy): a chemostratigraphy approach to the problem of correlation between shallow water and deep-water successions. Journal of the Geological Society, London 164, 609-620.

Paul, C.R.C., Lamolda, M.A., Mitchell, S.F., Vaziri, M.R., Gorostidi, A., Marshall, J.D., 1999. The Cenomanian-Turonian boundary at Eastbourne (Sussex, UK): a proposed European reference section. Palaeogeography, Palaeoclimatology, Palaeoecology 150, 83–121.

Pedersen, T.F., Calvert, S.E., 1990. Anoxia vs. Productivity: what controls the formation of organic-carbon-rich sediments and sedimentary rocks? American Association of Petroleum Geologists 74, 454-466.

Perch-Nielsen, K., 1979. Calcareous nannofossils from the Cretaceous between the North Sea and the Mediterranean. Aspekte der Kreide Europas. International Union of Geological Sciences Series A6, 223–272.

Perch-Nielsen, K., 1985. Cennozoic calcareous nannofossils. In: Bolli, H.M., Saunders, J.B., Perch-Nielsen, K. (Eds.), Plankton Stratigraphy. Cambridge University Press, Cambridge, pp. 422-454.

Perty D., Lamolda, M., 1996. Benthonic foraminiferal mass extinction and survival assemblages from the Cenomanian–Turonian boundary event in the Menoyo section, northern Spain. In: Hart, M. (Ed.), Biotic recovery from mass extinction events. Journal of the Geological Society, London, Special Publication 102, pp. 245–258.

Philip, J., 2003. Peri-Tethyan neritic carbonate areas: distribution through time and driving factors. Palaeogeography, Palaeoclimatology, Palaeoecology 196, 19-37.

Premoli Silva, I., Erba, E., Salvini, G., Verga, D., Locatelli, C., 1999. Biotic changes in Cretaceous anoxic events. The Journal of Foraminiferal Research 29, 352-370.

Premoli Silva I., Sliter W.V., 1999. Cretaceous paleoceanography: evidence from planktonic foraminiferal evolution. In: Barrera E., Johnson C.C. (Eds.), Evolution of the Cretaceous ocean-climate system. Geological Society of America, Special Paper 332, pp. 301-328.

Pucéat, E., 2008. A new breath of life for anoxia. Geology 36, 831-832.

Pucéat, E., Lécuyer, C., Donnadieu, Y., Naveau, P., Cappetta, H., Ramstein, G., Huber, B.T., Kriwet, J., 2007. Fish tooth δ18O revising Late Cretaceous meridional upper ocean water temperature gradients. Geology 35, 107–110.

Pufahl, P.K., James, N.P., 2006. Monospecific Pliocene oyster buildups, Murray Basin, South Australia: Brackish water end member of the reef spectrum. Palaeogeography, Palaeoclimatology, Palaeoecology 233, 11-33.

Robaszynski, F., Caron, M., 1979. Atlas de foraminifères planctoniques du Crètacè moyen (Mer Boreale et Tethys), première partie. Cahiers de Micropalèontologie 1, 1-185.

Robaszynski, F., Caron, M., 1995. Foraminifères planctoniques du Crétacé: Commentaire de la zonation Europe-Méditerranée. Bulletin de la Société géologique de France 166 (6), 681-692.

Robaszynski, F., Caron, M., Dupuis, C., Amédro, F., Gonzalez Donoso, J. M., Linares, D., Hardenbol, J., Gartner, S., Calandra, F., Deloffre, R., 1990. A tentative integrated stratigraphy in the Turonian of central Tunisia: formations, zones and sequential stratigraphy in the Kalaat Senan area. Bulletin des Centres de Recherches Exploration-Production Elf Aquitaine 14, 213-384.

Robaszynski, F., Gale, A.S., 1993. The Cenomanian–Turonian boundary: a discussion held at the final session of the colloquium on the Cenomanian–Turonian events, Grenoble, 26th May 1991 (France).

Cretaceous Research 14, 607–611.

Roth, P.H., 1978. Cretaceous nannoplankton biostratigraphy and oceanography of the northwestern Atlantic Ocean. In: Benson, W.E., Sheridan, R.E. (Eds.), InitialReports of the Deep Sea Drilling Project 44. U.S. Government Printing Office, Washington, DC, pp. 731–759.

Roth, P.H., 1981. Mid-Cretaceous calcareous nannoplankton from the Central Pacific: Implication for paleoceanography. Initial Report of the Deep Sea Drilling Project 62, 471-489.

Roth, P.H., Bowdler, J.L., 1981. Middle Cretaceous calcareous nannoplankton biostratigraphy and oceanography of the Atlantic Ocean. Society of Economic Paleontologists and Mineralogists Special Publication 32, 517-546.

Roth, P.H., Krumbach, K.R., 1986. Middle Cretaceous calcareous nannofossil biogeography and preservation in the Atlantic and Indian oceans: implications for palaeoceanography. Marine Micropaleontology 10, 235-266.

Sageman, B.B., Rich, J., Arthur, M.A., Dean, W.E., Savrda, C.E., Bralower, T.J., 1998. Multiple Milankovictch cycles in the Bridge Creek Limestone (Cenomanian- Turonian), Western Interior Basin. In: Dean, W.E., Arthur, M.A. (Eds.), Stratigraphy and Paleoenvironments of the Cretaceous Western Interior Seaway, USA. SEPM Concepts in Sedimentology and Paleontology 6, pp. 153-171.

Said, R., 1962. The Geology of Egypt. Elsevier, Amsterdam, 377 pp.

Said, R., 1990. The Geology of Egypt. Balkema Publishers, 734 pp.

Schrag, D.P., DePaolo, D.J., Richter, F.M., 1995. Reconstructing past sea surface temperatures: correcting for diagenesis of bulk marine carbon. Geochimica et Cosmochimica Acta 59, 2265–2278.

Schulze, F., Marzouk, A.M., Bassiouni, M.A., Kuss, J., 2004. The late Albian-Turonian carbonate platform succession of west-central Jordan: stratigraphy and crises. Cretaceous Research 25, 709-737.

Seton, M., Gaina, C., Müller, R.D., Heine, C., 2009. Mid-Cretaceous seafloor spreading pulse: Fact or fiction? Geology 37, 687-690.

Shafik, S., 1990. Late Cretaceous nannofossil biostratigraphy and biogeography of the Australian western margin. Bureau of Mineral Resources, Geology and Geophysics, Report 295, 1-164.

Shahin, A., Kora, M., 1991. Biostratigraphy of some Upper Cretaceous successions in the eastern Central Sinai, Egypt. Neues Jahrbuch für Geologie und Paläontologie Monatshefte 11, 671-692.

Sinton, C.W., Duncan, R.A., Storey, M., Lewis, J., Estrada, J.J., 1998. An oceanic flood basalt province within the Caribbean Plate. Earth and Planetary Science letters 155, 221– 235.

Sissingh, W., 1977. Biostratigraphy of Cretaceous calcareous nannoplankton. Geologie en Mijnbouw 56, 37-65.

Sliter, W.V., 1968. Upper Cretaceous foraminifera from southern California and northwestern Baja California, Mexico. University of Kansas Paleontological Contributions 49, 1-141.

Snow, L.J., Duncan, R.A., Bralower, T.J., 2005. Trace element abundances in the Rock Canyon Anticline, Pueblo, Colorado, marine sedimentary section and their relationship to Caribbean plateau construction and oxygen anoxic event 2. Paleoceangraphy, 20, PA3005. doi:10.1029/2004PA001093.

Tantawy, A.A., 2008. Calcareous nannofossil biostratigraphy and paleoecology of the Cenomanian-Turonian transition in the Tarfaya Basin, southern Morocco. Cretaceous Research 29, 996-1007.

Thierstein, H.R., 1980. Selective dissolution of late Cretaceous and earliest Tertiary calcareous nannofossils: Experimental evidence. Cretaceous Research 2, 165-176.

Thierstein, H.R., 1981. Late Cretaceous nannoplankton and the change at the Cretaceous-Tertiary boundary. Society of Economic Paleontologists and Mineralogists Special Publication 32, 355-394.

Turgeon, S.C., Creaser, R.A., 2008. Cretaceous oceanic anoxic event 2 triggered by a massive magmatic episode. Nature 454, 323-326.

Voigt, S., Aurag, A., Leis, F., Kaplan, U., 2007. Late Cenomanian to middle Turonian high-resolution carbon isotope stratigraphy: New data from the Münsterland Cretaceous Basin, Germany. Earth and

Planetary Science Letters 253, 196-210.

Voigt, S., Erbacher, J., Mutterlose, J., Weiss, W., Westerhold, T., Wiese, F., Wilmsen, M., Wonik, T., 2008. The Cenomanian – Turonian of the Wunstorf section- (North Germany): global stratigraphic reference section and new orbital time scale for Oceanic Anoxic Event 2. Newsletters on Stratigraphy 43, 65-89.

Voigt, S., Gale, A.S., Voigt, T., 2006. Sea-level change, carbon cycling and palaeoclimate during the Late Cenomanian of northwest Europe; an integrated palaeoenvironmental analysis. Cretaceous Research 27, 836-858.

Watkins, D.K., Wise, S.W., Pospichal, J.J., Crux, J., 1996. Upper Cretaceous calcareous nannofossil biostratigraphy and paleoceanography of the Southern Ocean. In: Moguilevsky, A., Whatley, R. (Eds.), Microfossils and oceanic environments. University of Wales, Aberystwyth Press, Aberystwyth, pp. 355–381.

Wilmsen, M., Nagm, E., 2009, Biofacies, stratigraphy and facies development of the Galala and Maghra El Hadida formations (Cenomanian-Turonian, Wadi Araba, Eastern Desert, Egypt). 8th International Symposium on the Cretaceous System, Abstract Volume, pp. 153-154.

Wright, C.W., Kennedy, W.J., Hancock, J.M., 1984. Introduction. In: Wright, C.W., Kennedy, W.J. (Eds.), The Ammonoidea of the Lower Chalk: Part I. Monograph of the Palaeontographical Society, London 1, pp. 1–37.

Zakhera, M., Kassab, A.S., 2002. Integrated macrobiostratigraphy of the Cenomanian- Turonian transition, Wadi El-Siq, west central Sinai, Egypt. Egyptian Journal of Paleontology 2, 219-233

MINERALOGY AND GEOCHEMISTRY OF THE NUMIDIAN FORMATION (CENTRAL-NORTHERN SICILY): INTRA-FORMATION VARIABILITY AND PROVENANCE EVALUATION*

Abstract. Mud rocks and sandstones of Numidian Formation in Sicily have been analysed for mineralogical, petrographic, major element and selected trace element compositions to constrain the intra-formational variability and the sediment provenance. The mudrocks are characterized by a kaolinite-rich signature while the sandstones have a quartz-arenitic composition. The high Chemical Index of Alteration and Plagioclase Index of Alteration strongly suggest that recycling processes have been responsible for the present compositions. The mudrocks geochemical data suggested a compositional variability function of the paleogeographic depositional environments. In particular, the Numidian Formation of the more external Serra Del Bosco Unit is affected by the terrigenous contribution of epicontinental- type sediments. With regard to provenance, the geochemical data indicate a derivation from post-Archean sedimentary siliciclastic rocks. The contribution of African cratonic sediments was confirmed by the trace elements ratios and by the end-member modeling processed on mudrocks compositional data. In particular the suitability of the Nubian sediments as one of the sources of sediment supply is also attested.

KEY WORDS: Numidian Formation, Mineralogy, Geochemi - stry, Provenance, Sicily.

1. Introduction

The Oligocene-Miocene Numidian Formation is one of the most widespread formations in the Mediterranean region, outcropping throughout the Apenninic-Maghrebian Chain, from southern Spain and northern Africa to the southern Apennines. Owing to its great importance, several studies have been focused on the Numidian Formation with the majority of them focused on the petrographic/ geochronologic data of the sandstones (Cazzola & Critelli, 1987; Critelli, 1991; Patacca Et Alii, 1992; Critelli & Le Pera, 1995; Critelli, 1999; Critelli Et Alii, 2011), whilst mineralogical and chemical data of mudrocks and the chemical analysis of sandstones are still missing.

In addition some unsettled issues still remain about the compositional variation inside the sedimentation basin and the role of this Formation in the Neogene paleo – geoghaphic framework of the Mediterranean area. The main matter of a long-term debate is the provenance of Numidian sediment and the location of the source region: this latter has been previously described as northern, from European terrains (Fildes Et Alii, 2010, and references therein), or southern, from the African craton (Thomas Et Alii, 2010, and references therein) supported by geochronological zircon data which indicate Eburnian and Pan- African age, but none Hercynian

* ***Giovanni Barbera, Germana Barone, Paolo Mazzoleni, Diego Puglisi, Hassan Khozyem and Osama Mashaly (2013). Mineralogy and Geochemistry of the Numidian Formation (Central-Northern Sicily): intra-formation variability and provenance evaluation. Ital. J. Geosci. (Boll. Soc. Geol. It.), Vol. 132, No. 3, doi: 10.3301/IJG.2013.07***

and Alpine age (see FILDES et alii, 2010, and reference therein).

The source area must be a region hundreds of thousands of km wide, peneplaned for a long time period and covered by very thick, ultra-mature, quartz-rich and kaolinitic regoliths (e.g., GUERRERA et alii, 2012, and reference therein). Around the western Mediterranean realm, North Africa is the only regional domain that satisfies these requirements whilst no source in Europe has enough surface area to supply the huge amount of ultra-mature and polycyclic siliciclastic detritus required for the Numidian Formation (Guerrera Et Alii, 2012).

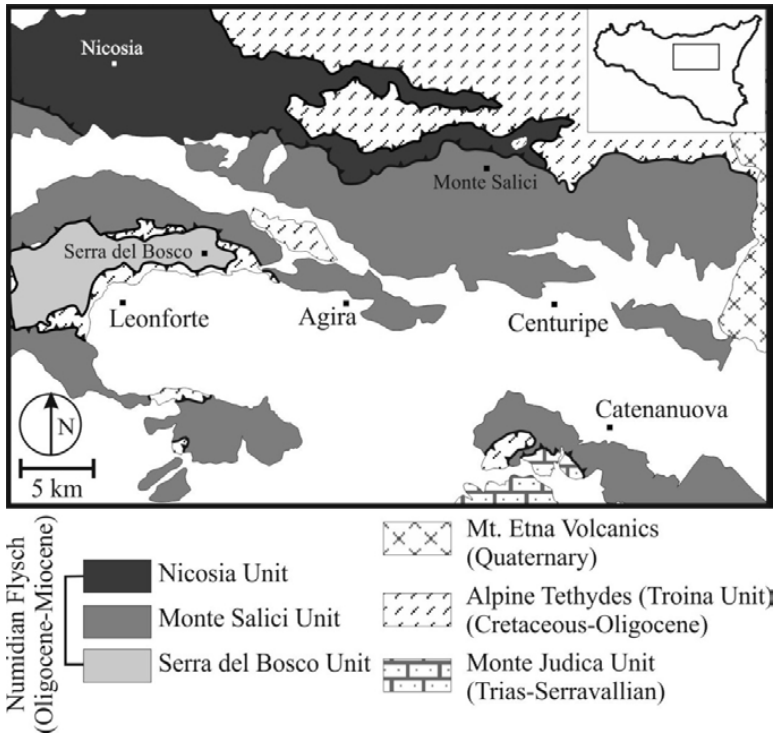

Fig. 1 - Geological sketch map of the studied area (modified after CARBONE et alii, 1990).

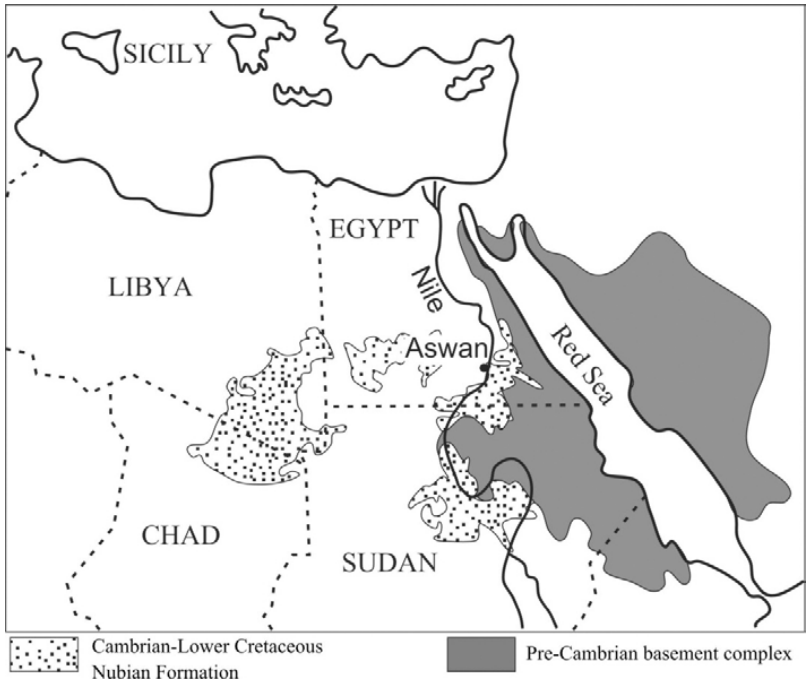

Fig. 2 - Outcropping area of the Nubian Formation in the north eastern Africa.

With regard to the supposed source rocks, supporters of a southern source have variously suggested the Continental Intercalaire of western and central Africa (Moretti Et Alii, 1991), the Nubian sandstone (Wezel, 1970; Johansson Et Alii, 1998) and Permo-Triassic and Ordovician continental sandstones of southern Tunisia (Gaudette Et Alii, 1979).

In this work, new mineralogical and petro-chemical data are discussed in order to: 1) characterize the Numidian sediments also taking into account the effects of sedimentary and post-sedimentary processes (Mongelli, 1993; Nesbitt & Young, 1989; Nesbitt & Young, 1996; Zhang Et Alii, 1998; Mongelli, 2004; Lopez Et Alii, 2005); 2) evaluate the compositional variability inside the formation; 3) evaluate the provenance of sediment by considering the major and trace element compositions and considering the likeliness of the African provenance hypothesis and the Nubian Formation as one of the likely sources for the Numidian Formation.

GEOLOGICAL SETTING

The structural framework in Eastern Sicily displays: northward the Calabride crystalline basement, belonging to the European palaeo-margin, overlains the Alpine Tethys Units (also known as “Sicilide units”) representing different sectors of an original accretionary wedge formed by broken formations and melange terranes. Southward, the Meso-Cenozoic successions of the subducted Ionian Tethys basin are represented by distinct thrust sheets derived from the deformation of sedimentary successions referred to shallow water platforms (Panormide Unit) and deep-water deposits (i.e., Imerese and Mt. Judica Units).

In this framework, the Numidian Formation, represents a new sedimentary supply (GRASSO et alii, 1987) forming the earliest terrigenous Oligocene-Miocene foredeep deposit at the onset of collision between the European and African plates: northward the Internal-Intermediate Numidian sequence (GUERRERA et alii, 1992) covers the Alpine Tethydes domain (LENTINI et alii, 1991) whilst to the south the External Numidian sequence affects the domains of the Ionian Tethys domain (Imerese basin).

In the study area (fig. 1), the Numidian Formation is formed by three tectonic units: Nicosia, Serra del Bosco and Monte Salici. In all these units the stratigraphic successions consist in mudrocks levels prevailing at the bottom and quartz-arenites prevailing upward; a specific feature characterizing the upper part of the Serra del Bosco Unit is the occurrence of typical glauconitic arenaceous horizons very similar to the Upper Oligocene-Serravallian levels of the Monte Judica.

The Numidian sedimentation began during Middle- Upper Eocene (JOHANSSON et alii, 1998) in the platformbasin system settled in the Sicilian area at the end of the Jurassic to middle Cretaceous ocean rifting stage (CATALANO & D’ARGENIO, 1978). From the Early Oligocene the entire region had been transformed into a shallow open shelf northward deepening to a trench slope subducting below the Alpine Tethydes accrectionary prism in front of which the foredeep represented the depositional system of the Numidian Formation (BENOMRAN et alii, 1987).

The deposition took place on the Panormide platform and the Imerese basin (MONTANARI, 1987). Northward, also the Alpine Tethydes domain, already structured as tectonic nappes, experienced the deposition of Numidian sediments. Serra del Bosco mudrocks were deposited in a basin intermediate with respect to the Panormide+Imerese domains and the southeastern African Continental shelf. During Langhian times, a glauconitic sedimentation took place

TABLE 1

Mineralogical compositions of the numidian mudrocks.

Whole rock: Qtz=quartz, F=feldspars, Cc=calcite, Fe Ox=Iron Oxides, Tot NC=total non-clay minerals; K=kaolinite, Sm=smectites, Il=illite, Chl=chlorite, Tot CM=total clay minerals. <2µm: I/SR0=illite/smectite mixed layered with 50% of illite, I/SR1=illite/smectite mixed layered with 70-80% of illite

	Whole rock										<2µm					
Sample	**Qtz**	**F**	**Cc**	**Fe-Ox**	**Tot NC**	**K**	**Sm**	**Il**	**Chl**	**Tot CM**	**DiSm**	**I/SR0**	**I/SR1**	**Kao**	**I**	**DiChl**
UN1	44	14	n.d.	n.d.	58	20	n.d.	18	4	42	n.d.	4	32	51	12	1
UN2	11	6	n.d.	n.d.	17	36	22	14	10	82	1	35	2	52	10	n.d.
UN3	14	7	n.d.	n.d.	21	9	32	17	21	79	n.d.	30	26	26	15	2
UN4	10	7	n.d.	n.d.	17	22	30	14	17	83	n.d.	39	19	34	7	n.d.
UN5	21	5	1	1	28	19	17	25	11	72	n.d.	12	41	36	11	n.d.
UN6	18	4	n.d.	1	22	24	21	26	7	78	n.d.	29	31	28	10	1
UN7	7	6	n.d.	1	14	38	20	13	14	86	1	18	10	59	10	2
UN8	5	7	n.d.	n.d.	12	42	19	13	12	87	1	19	11	60	10	n.d.
UN9	14	6	n.d.	n.d.	20	31	25	10	14	79	1	21	5	63	10	n.d.
UN10	12	9	n.d.	1	21	37	20	8	14	79	1	21	12	59	7	n.d.
UN11	13	7	n.d.	n.d.	19	41	19	13	8	81	1	4	18	68	9	n.d.
USB4	29	6	1	2	38	12	17	20	13	62	1	10	42	34	13	n.d.
USB5	21	8	3	2	34	20	32	5	9	66	1	40	9	36	13	n.d.
USB6	20	7	n.d.	n.d.	27	23	23	22	5	73	n.d.	35	20	34	10	n.d.
USB7	13	6	1	2	22	18	33	19	8	78	2	50	6	30	12	n.d.
USB8	18	6	n.d.	1	25	18	27	25	6	75	1	36	25	26	11	1
USB9	20	5	n.d.	n.d.	25	23	27	18	5	74	1	44	6	38	10	n.d.
USB10	27	6	5	3	40	13	30	7	10	60	n.d.	18	76	4	2	n.d.
USB11	28	7	1	n.d.	36	14	41	4	5	64	n.d.	35	29	34	2	n.d.
USB12	28	6	n.d.	n.d.	34	15	41	6	3	66	n.d.	9	48	38	5	n.d.
USB13	22	7	3	n.d.	32	11	39	8	11	68	n.d.	9	52	26	10	3
UMS1	12	5	n.d.	n.d.	17	26	25	26	6	83	n.d.	39	26	24	8	3
UMS3	7	5	n.d.	n.d.	12	9	46	21	12	88	1	40	17	29	11	2
UMS4	12	5	n.d.	n.d.	18	28	22	28	4	82	n.d.	17	28	42	12	n.d.
UMS5	14	7	n.d.	n.d.	21	28	27	18	6	79	1	19	24	47	9	n.d.
UMS6	19	3	n.d.	n.d.	22	29	28	11	10	77	n.d.	n.d.	11	70	19	n.d.
UMS7	9	6	n.d.	2	17	37	25	9	11	83	n.d.	28	13	52	5	1
UMS8	23	8	n.d.	n.d.	31	27	19	22	2	69	n.d.	23	18	46	13	n.d.
UMS9	18	5	n.d.	n.d.	24	36	14	23	4	76	n.d.	21	20	50	9	n.d.
UMS10	11	3	n.d.	4	18	22	27	23	11	82	n.d.	18	20	55	7	n.d.
UMS11	6	3	n.d.	n.d.	9	48	22	17	2	90	1	19	21	48	11	n.d.
UMS12	10	7	n.d.	n.d.	17	32	25	25	1	83	1	37	8	44	7	2
UMS13	11	6	n.d.	n.d.	17	27	31	19	5	83	2	47	n.d.	41	10	n.d.
UMS14	15	4	1	1	20	29	27	21	3	80	n.d.	5	32	52	10	n.d.
UMS15	28	3	n.d.	n.d.	31	28	24	18	n.d.	69	2	55	n.d.	35	6	2
min	5	3	1	1	9	9	14	4	1	42	1	4	2	4	2	1
mean	17	6	2	2	24	26	26	17	8	76	1	26	23	42	10	2
max	44	14	5	4	58	48	46	28	21	90	2	55	76	70	19	3

southward in the Sicanian-Saccense domain, where the deposition of the epicontinental glauconitic sandstones that form the uppermost part of the Monte Judica Unit occurred; accordingly, the lithological similarities of the Serra del Bosco succession with the Monte Judica Unit, drawn by the occurrence of some glauconitic horizons in the former, could point a likely interference between their source and depositional systems.

MATERIALS AND ANALYTICAL METHODS

Thirty-five Numidian mudrocks and nineteen sandstones were collected for this work. Macroscopically the sandstones mainly consist in massive-hard quartzose rocks whilst the mudrocks are grey to brown (tobacco) and frequently characterized by scaly fabric. For the purposes of this work we also analyzed 8 mudrocks sampled from the Monte Judica Unit, one kaolin sample and 14 sandstones belonging to the Nubian formation (Aswan area, Egypt; fig. 2). Regarding the X ray diffraction and X ray fluorescence, the analytical methodology description are extensively reported in recent authors publications (BARBERA et alii, 2009, 2011). Nine samples were analysed for REE + Cs, Th, U, Hf, Ta, Zn and Sc by iNAA at the SGS mineral service laboratories (Ontario, Canada).

The statistical methodology is mainly based on the log-ratio technique introduced by Aitchison (1986) and employed in order to avoid the constant sum problem; the centered logratio transformation (clr) of data is applied as follows:

$$x \in SD \rightarrow y = \log (xD/gD (x)) \in RD$$

Where x = composition, xD = (x1, x2, ….xD), y = log transformed composition and gD(x) = D√(x1x2.....xD).

This operation transforms the data from their constrained sample space, the simplex Sd, into the real space Rd where parametric statistical methods can be applied to the transformed data. Next the clr-transformed dataset is explored by biplots of two principal components. Both clr-transformation and biplots processing have been obtained by means of CoDaPack (THIO-HENESTROSA & MARTIN-FERNANDEZ, 2005).

RESULTS

MUDROCKS: WHOLE ROCK AND CLAY-SIZED FRACTION

MINERALOGY

The whole rock and <2μm mineralogical compositions are listed in tab. 1. Quartz is the most abundant component of the non-clay fraction (mean 17 wt.%) ranging from 5 wt.% (sample UN8) to 44 wt.% (UN1). Feldspars can be considered as accessory phases as the mean value is 6 wt.% and the range is from 3 wt.% (UMS 6-10-11-15) to 14 wt.% (UN1). Very low contents of Fe Oxides have been detected whilst calcite is almost absent except for detectable amounts in samples USB5 and USB13. Amongst clay minerals kaolinite and smectite are the most abundant mineral phases (mean 26 wt.%) characterized by highest values in the order of 50 wt.% (UMS11 and USB12-13 respectively). Illite and chlorite are subordinate phases.

The mineralogy of the <2μm fraction is on the whole controlled by kaolinite, and, subordinately by illite and illite/smectite mixed-layered minerals; discrete smectite and chlorite reach detectable amounts only in few samples (tab. 1). In the diffraction traces, kaolinite minerals are characterized by very sharp peaks at 12.3 2θ (0.71 nm) and 24.6 2θ (3.58 nm) and this is suggestive of thick crystals (fig. 3). Mixed-layered minerals exhibit a clear asymmetry in the (001) mica reflection and several weak reflections in the 16.29-17.05 2θ region (0.54-0.52 nm) which confirm the presence of several types of mixed-layered illite/smectite with different amounts of expandable phases ranging from 20% to 50% with I/S 50 R0 and I/S 80 R1 prevailing.

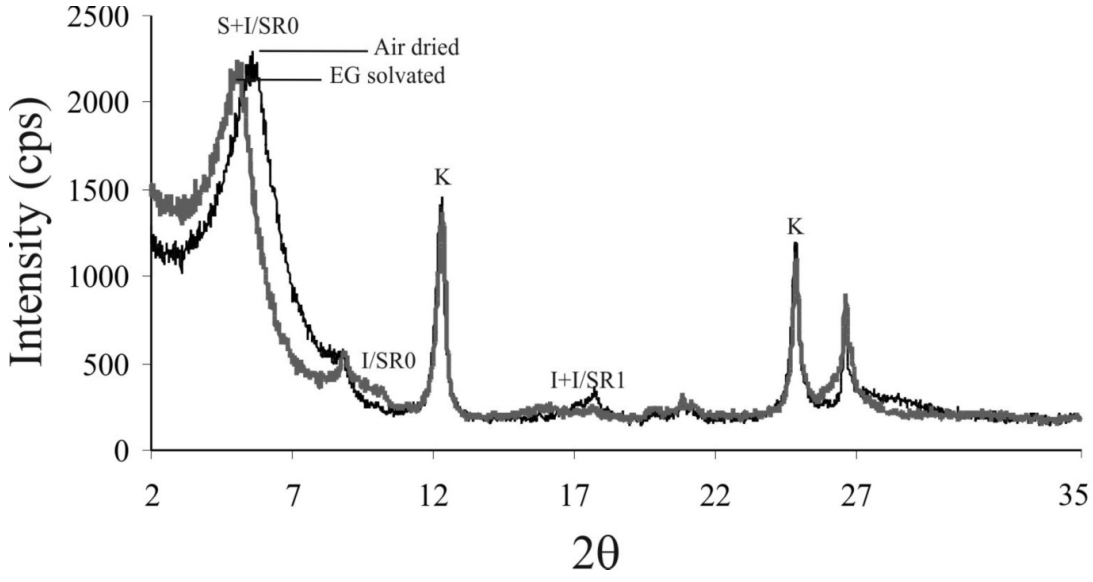

Fig. 3 - Air-dried and Ethylene Glycol-solvated diffraction traces of a representative sample (USB7) showing the mineral phases in the <2μm fraction. I/S = mixed layered illite/smectite, I = illite, K = kaolinite, S = smectite.

TABLE 2

Composition of the Numidian Flysch

	Rif Morocco[1] n= 8	Rif Morocco[2], n= 5	Tell Algeria[3] n= 15	Lucanian Apennine southern Italy[4] n= 15	Lucanian Apennine southern Italy[5] n= 59	Daunian Apennine southern Italy[6] n= 9)
Q	80.7	90.3	83.4	86.8	89.0	70.7 ÷ 81.6 **(n. d.)**
P	0.1	0.2	1.1	1.8	2.7	0.0 ÷ 0.5
K	2.6	0.1	1.7	-	4.2	0.3 ÷ 3.2
Lc	-	-		-		0.0 ÷ 0.9
Lm	-	-	0.7 **(n.d.)**	-	3.2 **(n.d.)**	0.0 ÷ 0.8
Ls	-	-		1.1		-
Ch	-	-	0.3	0.5	-	0.0 ÷ 0.0
M	15.0	-	1.0	0.9	0.1	0.0 ÷0.3
Op	-	0.5	1.1		-	0.1 ÷ 0.8
Om	-	0.3	0.6	0.3	0.8	0.0 ÷ 0.2
Mt	-	1.6	8.6	4.7	-	
Cm[1]	-	0.2	-	-	-	11.7 ÷ 24.1 **(n.d.)**
Cm[2]	1.6	-	0.6	3.8	-	-
Cm[3]	-	6.8	0.9	0.1	-	-
Sum	**100.0**	**100.0**	**100.0**	**100.0**	**100.0**	
Q	96.8	99.7	95.6	96.1	89.8	-
F	3.2	0.3	3.2	2.1	7.0	-
L	-	-	1.2	1.8	3.2	-
Sum	**100.0**	**100.0**	**100.0**	**100.0**	**100.0**	-

sandstones along the Maghrebian-Apennine Chain. Q=total quartzose grains; F=P+K, where: F=total feldspar grains, P and K=plagioclase and k-feldspar single grains, respectively; L=Lc+Ls+Ch, where: L=unstable fine-grained rock fragments (<0.06 mm) including Lc=carbonate, Ls=sedimentary clasts and Ch=chert; M=micas and/or chlorites in single grains; Om=other mineral grains (mainly heavy minerals), Mt=siliciclastic matrix; Cm1=silica cement, Cm2=carbonate cement, Cm3=other cements; n.d.=not determined: 1) CHIOCCHINI et alii, 1980; 2) CRITELLI, 1984-1985; 3) MORETTI et alii, 1991; 4) CARBONE et alii, 1987; 5) LOIACONO et alii, 1983; 6) ARDITO et alii, 1985.

SANDSTONES PETROGRAPHY

The Numidian sandstones composition and texture are well known along all the Betic-Maghrebian Chain and southern Apennines. With the aim to compare the Nubian sandstone data we report in tab. 2 the literature composition of the Numidian Sandstones along the Apenninic-Maghrebian Chain. These sandstones are characterized by a high compositional maturity (more than 95% of modal quartz, usually with high/very high roundness) and are commonly ascribed to the quartzarenite clan (sensu FOLK, 1974; fig. 4).

The Nubian Sandstones are often described in literature without detailed microscopic and/or chemical data. Thus, new modal data of these rocks, collected from southern Egypt (Aswan area; Cretaceous Nubian Group Formations; KHEDR, 1990), are shown in tab. 3 and in fig. 4. Detrital frameworks of the Nubian Sandstones are characterized by a dominant non-carbonate extrabasinal fraction, made up of abundant sub-angular to subrounded quartz grains, very low percentages of feldspars and lithic fragments (fig. 5). Opaque minerals are often present as single detrital grains or locally forming abundant and very fine-grained interstitial matrix and/or Fe-oxide cement. Sili ca cement locally occurs, represented by quartz overgrowths and by other silica-phases, such us chalcedony up to crypto- and or microcrystalline quartz (fig. 5).

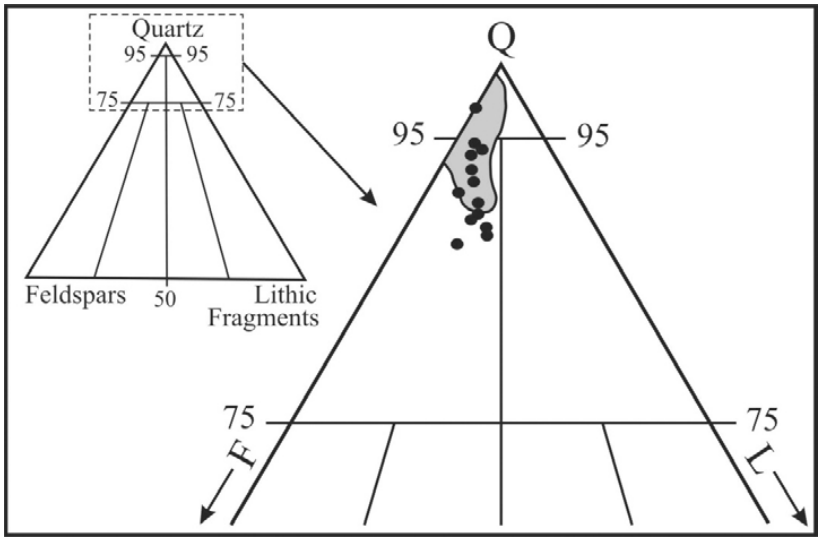

Fig. 4 - Total quartz-feldspar-lithic fragment (Qt-F-L) ternary plot of Numidian sandstones (grey area; see tab. 3 and text for references) and Nubian Sandstones (closed black circles; see tab. 4).

TABLE 3: Modal composition of the Nubian Sandstones.Q=Qm+Qp, where: Q=total quartzose grains including Qm=monocrystalline quartzose grains, subdivided into Qm'=with low undulosity (≤5°) and Qm''=with high undulosity (>5°), Qp=polycrystalline quartzose grains which have been subdivided in Qp'=with few subgrains (≤4 crystalline units per grain) and Qp''=with many subgrains (>4 crystalline units per grain); F=P+K, where: F=total feldspar grains, P and K=plagioclase and k-feldspar single grains, respectively; L=Lc+Ls, where: L=unstable finegrained rock fragments (<0.06 mm), including: Ls=sedimentary clasts, Lc=carbonate clasts and Ch=chert; Lt=L+Qp, where: Lt=total lithic fragments (both unstable and quartzose); M=micas and/or chlorites in single grains; Om=other mineral grains (mainly heavy minerals), Mt=siliciclastic matrix; Cm1=Fe-oxide cement, Cm2=Silica cement.

	NS 1	NS 2	NS 3	NS 4	NS 5	NS 6	NS 7	1	214	215/216	245	QZ 1	QZ 2	x	⍰
Qm'	17.5	22.4	18.4	14.6	12.2	15.4	15.4	11.0	32.5	26.2	29.7	11.1	14.3	18.8	7.07
Qm''	29.2	28.5	26.5	18.7	17.8	19.2	27.5	19.3	18.2	19.7	14.8	20.3	19.5	21.8	4.70
Qp'	12.9	15.1	17.1	18.2	19.7	16.3	12.3	19.3	14.7	20.2	26.5	16.3	19.5	16.5	6.11
Qp''	25.9	19.7	21.0	26.9	28.3	24.7	23.1	26.1	14.4	1 5.9	6.4	28.1	25.0	22,1	6.42
Ch	3.2	1.3	2.2	2.6	3.6	3.2	1.7	3.1	1.2	2.1	1.2	2.5	2.9	2.5	0.83
Ps	-	-	0.8	1.4	-	1.2	0.8	-	0.4	-	-	-	-	0.3	0.46
Ks	2.4	2.1	2.1	2.6	2.3	3.5	1.6	3.1	0.8	1.5	1.5	3.8	2.3	2.4	0.84
Lc	-	0.7	0.8	0.8	1.2	0.8	0.8	1.2	-	-	-	-	-	0.5	0.49
Ls	-	2.2	1.9	2.2	2.4	2.7	1.2	3.1	2.4	1.9	1.5	3.3	2.9	2.1	0.87
Ms	-	-	0.8	0.9	1.8	0.8	-	-	0.8	1.1	0.4	-	-	0.5	0.58
Op	2.2	1.4	1.9	2.3	1.2	1.6	2.4	1.9	1.6	-	0.8	1.2	2.9	1.6	0.76
Om	-	-	-	0.8	-	-	0.4	0.6	-	0.8	-	0.8	-	0.3	0.36
Mt	2.9	2.4	1.9	2.3	3.2	2.2	3.1	1.9	4.4	3.7	4.5	3.1	-	2.8	1.18
Cm^1	3.8	4.2	4.6	5.7	4.2	4.5	9.7	6.3	8.6	6.9	12.7	-	4.2	5.9	3.17
Cm^2	-	-	-	-	2.1	3.9	-	3.1	-	-	-	9.5	6.7	1.9	3.09
Sum	100.0	100.0	100.0	100.0	100.0	100.0	100.0	100.0	100.0	100.0	100.0	100.0	100.0	100.0	
Q	97.4	93.1	92.3	89.2	89.2	86.9	92.8	87.7	94.3	93.7	94.9	88.7	90.6	91.6	3.15
F	2.6	2.3	2.3	4.5	2.6	5.4	2.8	3.6	1.4	1.7	1.8	4.4	2.7	2.9	1.20
L	-	4.6	5.4	6.3	8.2	7.7	4.4	8.7	4.3	4.6	3.3	6.9	6.7	5.5	2.34
Sum	100.0	100.0	100.0	100.0	100.0	100.0	100.0	100.0	100.0	100.0	100.0	100.0	100.0	100.0	
Qm	51.3	55.3	49.4	37.9	34.3	39.8	50.8	35.1	59.9	45.9	54.5	36.8	39.2	46.7	8.66
F	2.6	2.3	2.3	4.5	2.6	5.4	2.8	3.6	1.4	1.7	1.8	4.4	2.7	2.9	1.20
Lt	46.1	42.4	48.3	57.6	63.1	54.8	46.4	61.3	38.7	52.4	43.7	58.8	58.1	50.4	7.2
Sum	100.0	100.0	100.0	100.0	100.0	100.0	100.0	100.0	100.0	100.0	100.0	100.0	100.0	100.0	

GEOCHEMISTRY

The chemical compositions of the Numidian mudrocks and sandstones are listed in tabs. 4 and 5 together with the composition of the Nubian kaolin and sandstones and the Monte Judica mudrocks. The geochemical data have been processed by comparing the elemental abundances to the global subducting sediment (GLOSS; PLANK & LANGMUIR, 1998).

Mudrocks

The normalised patterns to GLOSS are reported in fig. 6 showing a strong depletion in CaO, Na2O and MnO whereas K2O, SiO2, Fe2O3, MgO and P2O5 are similar to the GLOSS composition. By contrast TiO2 and Al2O3 are characterized by a enrichment with respect to the GLOSS.

The trace element patterns normalised to GLOSS are displayed in fig. 6B, where both XRF and INAA (9 samples) data are reported; amongst the large ionic litophile elements, Sr and Ba are on the whole depleted relative to GLOSS whilst Rb and Cs are slightly to strongly enriched. Thorium and Uranium are slightly enriched. The transition element are on the whole GLOSS-like or slightly depleted except Cr, Sc and V that are enriched reflecting the chief role of clay minerals in their distributions. Finally, HFS elements are characterized by enriched patterns with respect to GLOSS.

The behaviour of Monte Judica Miocene mudrocks, also showed in figs. 6A and 6B, is similar to the Numidian mudrocks except for the minor depletions in Na2O and MnO amongst major elements and LILE amongst trace elements. Concerning the Nubian formation, the kaolin sample is characterized by several elements below the detection limits (tab. 4); nevertheless, the enriched factors for the measured elements showed significant enrichments in Al2O3 and TiO2 and depletions in CaO and NaO whilst the SiO2 and P2O5 compositions are similar to the Numidian mudrocks. The trace element pattern is characterized by strong Ba-Sr and moderate V-Co-Zn depletions and Cr, Th, Zr, Y, Nb, La and Ce enrichments whilst Ni is similar to the GLOSS composition.

Sandstones

Sandstones are characterized by an overall depletion in the major elements (fig. 6C). Only silica is enriched in response to the quartz-rich signature of the Numidian sandstones. The whole trace elements are depleted with respect to the GLOSS whilst marked enrichments occur only for Zr (fig. 6D). The average composition of the Nubian Sandstones is also shown in fig. 6 (C, D) the distribution of major and trace elements is fairly similar to the Numidian sandstones.

DISCUSSION

SOURCE AREA WEATHERING AND DIAGENESIS

The chemical index of alteration [CIA = 100Å~Al2O3/ (Al2O3 + Na2O + CaO* + K2O)], defined by NESBITT & YOUNG (1982), and the plagioclase index of alteration [PIA = 100Å~(Al2O3-K2O)/(Al2O3 + CaO* + Na2O-K2O)], defined by FEDO et alii (1996), are both very high for the overall Numidian mudrocks then suggesting a strongly weathered source. These results are reinforced by the data plotted into the ACNK ternary diagram (fig. 8), where all the studied samples plot near the A-K line indicating an intense feldspar alteration (NESBITT et alii, 1996).

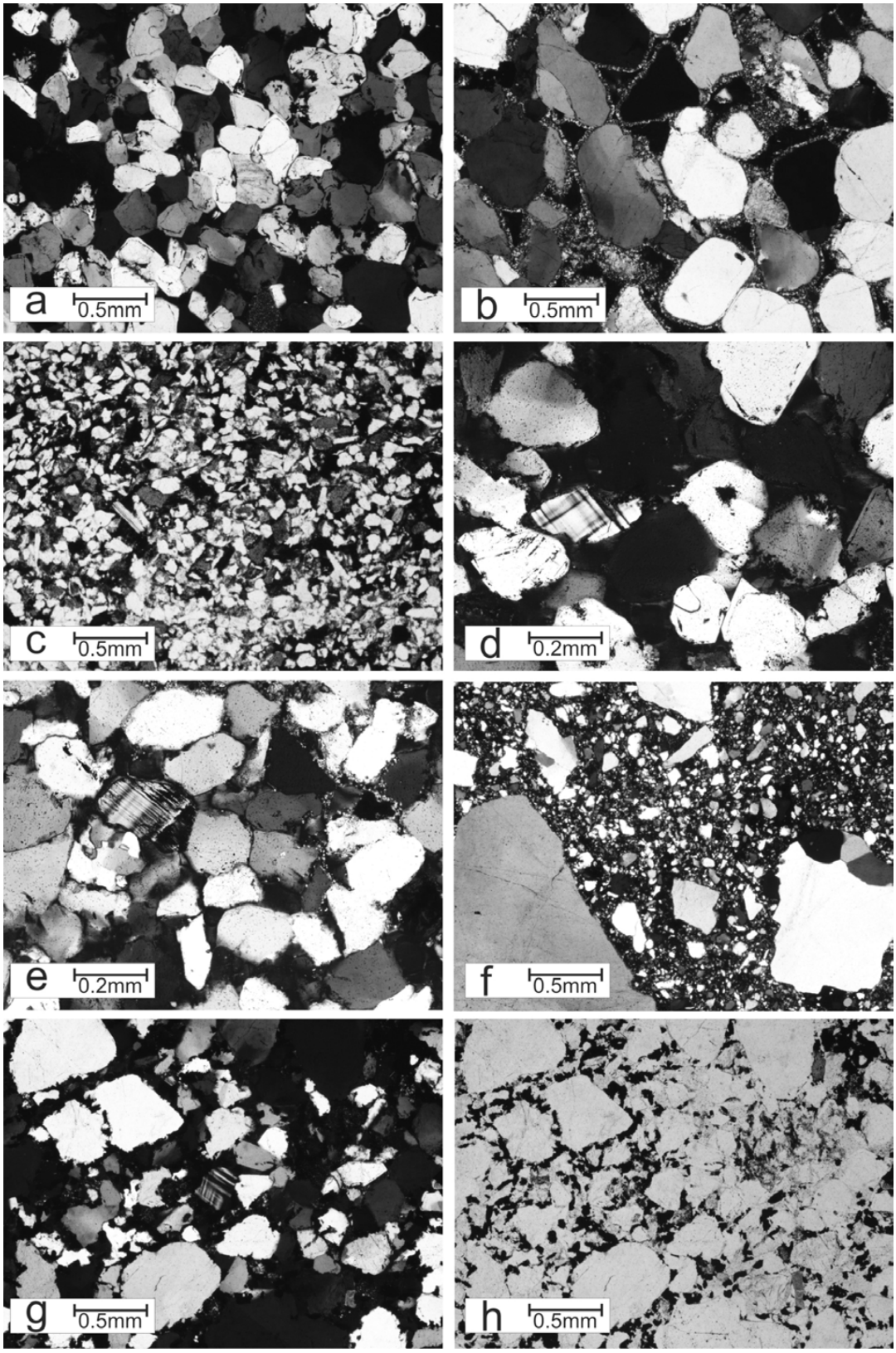

Fig. 5 - Thin section microphotographs of different Nubian Sandstone samples. Silica cement due (a) to synaxial overgrowths of authigenic quartz on detrital quartz grains and (b) to the formation of chalcedony up to crypto- and microcrystalline quartz; (c) Fe-oxide cement; (d) and (e) feldspar grains; (f) very poor sorting; (g) and (h) same microphotograph with crossed and parallel nicols, respectively, showing feldspar grains together with polycrystalline and high undulosity detrital quartz grains and Fe-oxide cement.

TABLE 4

Chemical compositions obtained by XRF analysis; the UN data have been already published in BARBERA *et alii* (2009); M=Mudrock; S=Sandstone; b.d=below detection limits.

Sample			SiO2	TiO2	Al2O3	Fe2O3	MnO	MgO	CaO	Na2O	K2O	P2O5	LOI	V	Cr	Co	Ni	Rb	Sr	Y	Zr	Nb	Ba	La	Ce	Th	CIA	PIA
UN1	NUMIDIAN FORMATION	M	67.4	1.34	18.3	2.30	0.01	1.05	0.16	0.50	2.29	0.08	6.57	119	97	11	18	84	146	42	566	32	449	53	108	17	84	95
UN2		M	52.7	1.52	24.8	3.63	0.02	1.46	0.43	0.23	1.89	0.08	13.3	191	163	14	38	116	175	42	316	47	383	84	166	25	89	96
UN3		M	54.2	1.12	19.8	6.80	0.03	3.26	0.61	0.28	3.22	0.10	10.6	213	171	24	67	147	184	38	290	35	397	67	122	22	80	92
UN5		M	54.0	1.09	20.1	6.78	0.02	2.13	1.34	0.19	2.57	0.08	11.8	186	148	20	40	134	179	31	233	32	220	57	118	19	79	87
UN7		M	49.8	1.40	25.1	6.80	0.04	1.76	0.68	0.18	1.93	0.09	12.3	221	168	19	49	116	172	41	251	48	400	87	155	25	88	95
UN8		M	50.2	1.50	26.2	4.89	0.01	1.60	0.61	0.17	1.97	0.08	12.8	215	168	11	36	116	182	36	265	49	389	95	179	26	89	95
UN9		M	56.4	1.49	23.6	3.39	0.02	1.49	0.16	0.30	1.94	0.10	11.1	184	150	14	38	98	147	42	321	39	358	73	142	20	90	97
UN11		M	53.2	1.65	26.0	3.49	0.01	1.39	0.40	0.20	2.02	0.11	11.5	200	166	10	34	109	226	45	411	49	385	102	178	25	90	97
UNQ1		S	91.6	0.28	3.92	0.55	b.d.	b.d.	0.36	0.68	1.03	0.02	1.63	5	12	b.d.	b.d.	14	130	5	281	b.d.	207	12	18	b.d.	/	/
UNQ2		S	95.8	0.22	1.81	0.90	0.01	b.d.	0.04	0.21	0.43	0.02	0.55	b.d.	8	b.d.	b.d	5	23	6	216	b.d.	90	8	16	b.d.	/	/
UNQ3		S	96.3	0.20	1.62	0.57	b.d.	b.d.	0.05	0.16	0.27	0.02	0.80	b.d.	10	b.d.	b.d	b.d.	20	b.d.	209	b.d.	70	9	12	b.d.	/	/
UMS1		M	57.9	1.22	20.8	4.02	0.01	1.77	0.19	0.16	2.40	0.05	11.5	173	147	11	26	126	133	28	253	35	281	70	114	20	87	97
UMS3		M	53.0	1.13	18.6	8.41	0.04	2.30	1.60	0.17	2.29	0.17	12.3	191	171	20	40	121	196	40	257	48	197	68	123	19	78	85
UMS5		M	56.3	1.35	22.8	4.33	0.01	1.36	0.40	0.27	2.25	0.84	10.1	176	140	15	28	114	191	48	402	37	377	83	148	20	93	98
UMS6		M	50.1	1.50	23.3	7.62	0.05	1.50	0.95	0.39	1.94	0.19	12.5	208	167	23	37	112	173	52	434	42	371	77	155	23	85	92
UMS8		M	58.3	1.39	22.0	3.11	0.01	1.35	0.30	0.46	2.68	0.07	10.4	163	135	7	18	106	153	32	451	40	401	67	110	22	85	94
UMS9		M	53.4	1.52	24.5	3.46	0.01	1.24	0.60	0.21	1.90	0.16	13.1	168	147	11	27	100	194	38	399	45	434	81	144	23	89	95
UMS10		M	55.4	1.21	21.7	5.20	0.01	1.83	0.64	0.15	2.27	0.06	11.5	172	156	16	27	118	188	30	297	33	314	63	127	20	85	94
UMS11		M	51.6	1.60	27.1	3.61	0.02	1.21	0.18	0.18	2.00	0.08	12.3	208	165	16	51	118	192	51	388	53	421	101	195	27	91	98
UMS13		M	55.0	1.18	22.3	4.30	0.02	1.71	0.88	0.16	1.93	0.06	12.4	175	136	12	27	109	196	28	279	35	348	70	139	17	85	92
UMS14		M	54.1	1.00	21.5	5.83	0.02	1.59	2.17	0.18	2.05	0.37	11.2	179	156	14	28	108	178	29	229	26	288	57	119	27	79	85
UMS15		M	57.2	1.44	21.6	4.55	0.01	1.59	0.67	0.32	1.97	0.08	10.6	169	134	12	26	110	186	46	439	41	398	77	149	29	85	93
UMSQ1		S	95.9	0.23	1.97	0.53	b.d.	b.d.	0.08	0.29	0.54	0.02	0.51	b.d.	9	b.d.	b.d.	6	28	b.d.	238	b.d.	227	6	27	b.d.	/	/
UMSQ2		S	91.5	0.31	4.34	1.28	b.d.	0.05	0.09	0.18	0.84	0.04	1.36	10	16	b.d.	b.d.	15	33	5	217	b.d.	164	12	23	5	/	/
UMSQ3		S	91.0	0.28	3.98	2.05	b.d.	0.04	0.09	0.17	0.77	0.04	1.57	9	17	5	b.d.	14	32	11	186	b.d.	155	14	21	b.d.	/	/
UMSQ4		S	96.4	0.13	1.61	0.33	0.01	0.01	0.09	0.23	0.39	0.02	0.85	b.d.	6	b.d.	b.d.	b.d.	24	b.d.	106	b.d.	89	6	13	b.d.	/	/
USB4		M	56.7	1.13	20.3	7.09	0.16	1.78	1.51	0.23	2.10	0.11	8.93	149	121	23	45	99	192	28	266	24	230	46	110	14	80	86
USB5		M	55.0	1.07	19.4	7.62	0.04	1.26	2.47	0.12	1.57	0.12	11.3	140	120	16	32	73	146	26	311	23	253	43	100	12	76	80
USB7		M	54.4	1.23	19.9	6.52	0.05	1.74	1.68	0.47	1.85	0.05	12.2	159	133	13	29	97	174	23	238	25	160	50	131	15	78	83
USB9		M	58.6	1.33	22.2	4.41	0.00	1.06	0.16	0.11	1.59	0.07	10.5	141	126	14	29	89	102	26	257	32	195	58	156	16	92	98
USB10		M	54.0	1.05	17.4	6.75	0.06	1.44	4.16	0.30	1.46	0.10	13.4	133	113	18	37	81	233	27	266	24	309	35	122	10	65	67
USB11		M	58.7	1.18	18.5	7.18	0.06	1.22	1.30	0.32	1.30	0.08	10.2	137	113	20	34	83	157	29	322	27	308	42	138	12	82	86
USB13		M	54.6	1.28	19.7	6.22	0.04	1.26	2.31	0.34	2.42	0.14	11.8	144	114	13	35	103	161	32	325	28	265	46	150	14	74	79
USBQ1		S	93.7	0.23	2.94	1.48	b.d.	0.05	0.03	0.15	0.10	0.03	1.29	5	13	b.d.	b.d.	b.d.	19	9	181	b.d.	20	13	21	b.d.	/	/
USBQ2		S	96.0	0.21	1.61	1.04	b.d.	b.d.	0.05	0.12	0.08	0.02	0.89	5	8	b.d.	b.d.	b.d.	17	5	244	b.d.	42	11	15	b.d.	/	/

continue

Continued Table 4

AG1		M	54.0	1.04	18.1	7.00	0.12	1.71	3.11	0.27	1.50	0.09	13.0	146	120	19	44	92	232	26	242	24	376	55	98	14	71	74
AG3		M	60.3	1.12	18.5	7.20	0.02	1.18	0.47	0.23	1.80	0.12	9.05	142	125	13	34	95	163	26	200	24	228	55	115	13	86	95
AG4		M	58.2	1.16	19.1	7.48	0.10	1.28	0.84	0.21	1.65	0.11	9.90	149	117	20	38	89	170	28	191	24	280	50	107	14	85	92
AG5		M	60.0	1.12	18.4	7.17	0.03	1.14	0.65	0.31	1.76	0.13	9.29	140	119	17	35	93	173	29	200	24	441	45	89	13	85	92
AG6		M	52.5	1.56	25.7	5.91	0.05	1.13	0.63	0.26	1.97	0.12	10.2	176	135	19	36	95	181	33	353	37	569	74	144	17	88	95
AG9		M	58.8	1.12	18.3	5.62	0.03	1.31	3.36	0.34	1.68	0.10	9.42	115	98	11	32	79	195	27	386	23	402	35	98	11	69	72
AG10		M	58.5	1.11	17.8	6.36	0.04	1.38	2.76	0.34	1.75	0.12	9.79	120	106	15	36	84	185	27	294	23	241	38	103	13	71	75
NS1		S	97.6	0.51	0.67	0.58	b.d.	b.d	0.11	0.10	0.22	0.02	0.20	b.d.	40	b.d.	b.d.	b.d.	26	10	119	b.d.	52	9	23	b.d.	/	/
NS2		S	98.0	0.21	0.62	0.42	b.d.	b.d	0.11	0.17	0.26	0.02	0.19	b.d.	7	b.d.	b.d.	b.d.	22	8	75	b.d.	60	9	6	b.d.	/	/
NS3		S	98.0	0.26	0.60	0.49	b.d.	b.d	0.09	0.09	0.20	0.02	0.23	b.d.	13	b.d.	b.d.	b.d.	25	8	76	b.d.	56	10	19	b.d.	/	/
NS4		S	97.2	0.21	0.97	0.81	b.d.	b.d	0.14	0.10	0.17	0.02	0.38	7	16	b.d.	b.d.	b.d.	24	9	104	b.d.	51	7	26	b.d.	/	/
NS5		S	97.1	0.49	0.94	0.71	b.d.	b.d	0.12	0.11	0.23	0.03	0.28	4	22	b.d.	b.d.	b.d.	30	10	102	b.d.	53	12	20	b.d.	/	/
NS6		S	97.8	0.28	0.90	0.26	b.d.	b.d	0.16	0.09	0.18	0.01	0.33	b.d.	11	b.d.	b.d.	b.d.	21	8	65	b.d.	65	8	7	b.d.	/	/
NS7		S	78.0	1.61	7.70	7.05	0.70	b.d	0.63	0.52	0.94	0.05	2.79	6	56	25	5	19	96	29	549	14	409	19	61	9	/	/
1		S	96.8	0.18	0.21	1.72	b.d.	b.d	0.21	0.09	0.01	0.02	0.80	23	11	b.d.	b.d.	b.d.	84	7	87	b.d.	42	8	11	b.d.	/	/
214		S	89.2	0.78	3.57	5.06	b.d.	b.d	0.07	0.03	b.d	0.02	1.26	73	25	30	b.d.	b.d.	17	11	559	13	38	5	11	5	/	/
215/216		S	88.5	1.02	6.89	1.12	b.d.	b.d	0.05	0.06	b.d	0.02	2.32	9	27	10	6	b.d.	20	10	743	24	29	13	28	9	/	/
245		S	75.2	0.98	7.39	10.1	0.06	0.87	0.09	0.22	0.32	0.08	4.69	41	39	47	53	10	115	26	372	6	70	31	62	b.d.	/	/
QZ1		S	98.4	0.09	0.07	0.93	b.d	b.d	0.07	0.08	0.00	0.01	0.31	7	7	b.d.	b.d.	b.d.	17	6	36	b.d.	18	5	b.d.	b.d.	/	/
QZ2		S	96.7	0.15	0.12	2.25	b.d.	b.d	0.10	0.08	0.00	0.09	0.50	25	5	b.d.	b.d.	b.d.	27	8	60	b.d.	24	9	b.d.	b.d.	/	/
227		S	94.4	0.76	1.51	1.80	0.02	b.d	0.08	0.15	0.18	0.02	1.04	6	22	26	7	b.d.	26	9	260	b.d.	42	10	13	b.d.	/	/
Kao		M	47.5	3.38	38.9	0.87	b.d.	b.d	0.08	0.07	b.d.	0.10	9.84	73	213	10	55	b.d.	53	146	1244	179	61	167	364	34	/	/

NUBIAN FORMATION **MONTE JUDICA**

TABLE 5

Chemical composition of selected mudrocks obtained by

INAA analysis.

	UN4	UN6	UN10	USB6	USB8	USB12	UMS4	UMS7	UMS12
SiO_2	52.0	56.6	52.5	57.1	55.8	57.0	50.0	52.3	54.9
TiO_2	1.30	1.09	1.63	1.34	1.30	1.30	1.28	1.68	1.48
Al_2O_3	22.6	21.6	25.8	22.0	20.3	20.2	23.0	26.0	23.3
Fe_2O_3	5.81	4.48	5.03	4.74	7.77	7.93	6.05	5.19	3.60
MnO	0.03	0.01	0.04	0.01	0.01	0.04	0.03	0.01	0.01
MgO	2.68	1.87	1.50	1.27	1.36	1.02	1.71	1.12	1.50
CaO	0.34	0.16	0.17	0.46	0.29	0.52	0.35	0.11	0.10
Na_2O	0.19	0.16	0.25	0.19	0.18	0.33	0.16	0.21	0.21
K_2O	2.45	2.46	2.01	2.24	2.25	1.84	2.39	1.56	2.03
P_2O_5	0.08	0.06	0.07	0.06	0.07	0.10	0.08	0.12	0.13
LOI	12.6	11.5	11.0	10.6	10.7	9.70	15.0	11.7	12.7
Sc	20.0	18.2	20.4	17.9	16.9	16.2	19.5	20.4	20.0
V	205	195	195	159	162	153	207	198	185
Cr	180	150	164	141	144	126	174	162	148
Co	18	16	22	12	13	21	20	20	12
Ni	49	40	45	28	22	41	38	41	35
Zn	80	80	100	88	102	101	80	80	70
Rb	136	128	112	110	110	96	135	99	111
Sr	147	134	166	142	146	147	151	188	185
Y	31.0	27.0	48.0	29.2	25.8	33.3	38.0	57.0	38.0
Zr	306	220	416	292	289	266	255	398	353
Nb	36.0	33.0	50.0	25.2	25.5	26.8	34.0	52.0	45.0
Cs	8.3	7.9	6.4	7.4	7.9	5.8	8.3	5.8	7.0
Ba	357	214	456	225	258	356	276	415	320
La	58.2	55.5	74.5	52.9	48.1	54.8	60.2	79.9	63.7
Ce	107	111	142	98	93	109	121	162	119
Nd	42	46	58	43	39	50	55	69	48
Sm	6.9	6.5	10.8	7.2	6.3	8.6	9.2	12.7	8.2
Eu	1.3	1.1	2.2	1.5	1.2	1.7	1.8	2.7	1.6
Tb	1.0	0.8	1.4	0.8	0.6	1.0	1.0	1.4	1.0
Yb	2.8	2.3	3.9	2.6	2.4	3.1	3.0	4.6	3.4
Lu	0.45	0.39	0.61	0.42	0.4	0.47	0.49	0.71	0.54
Hf	8.6	6.6	11.0	7.7	7.3	7.0	7.2	11.0	10.0
Ta	2.2	1.7	2.8	1.5	1.6	1.7	1.5	2.8	2.5
Th	16	13	19	13	14	14	16	20	16
U	2.0	2.6	2.8	2.3	1.7	3.0	2.6	2.8	3.5
$(La/Yb)_n$	19.04	21.98	16.16	11.86	11.92	11.64	16.85	13.55	16.29
Eu/Eu*	0.59	0.56	0.66	0.72	0.69	0.67	0.68	0.73	0.65
Th/U	8	5	6.79	5.65	8.24	4.67	6.15	7.14	4.57
CIA	87	88	90	87	93	91	86	87	86
PIA	96	98	98	97	99	99	95	96	94

The REE Chondrite-normalized patterns (fig. 7) are commonly observed in the upper continental crust rocks characterized by LREE enrichment (mean Lan/Ybn = 15.26, tab. 5) and significant Eu negative anomaly (average Eu/Eu* = 0.67, tab. 5).

With regard to the sandstones, the major element compositions characterized by very low Al2O3 contents, make the weathering chemical indexes above described meaningless. Nevertheless, the high compositional maturity given by the high abundances of detrital quartz grains and by its high and/or very high roundness can be interpreted as testifying prolonged transports and, more probably, a polycyclic origin of these sandstones. After the deposition, the most significant diagenetic process was the smectite- illite transition via the formation of mixed-layered clay minerals. Mineralogical data and the diffraction patterns of the analysed samples point up the presence of not only one kind of interstratification but, in contrast, different mixed-phases with different proportions of illite and smectite layers were recognized; this suggests that the transition is likely not complete but otherwise it was in progress prior to the involving of those terrains in the tectonic events that characterized the Formation.

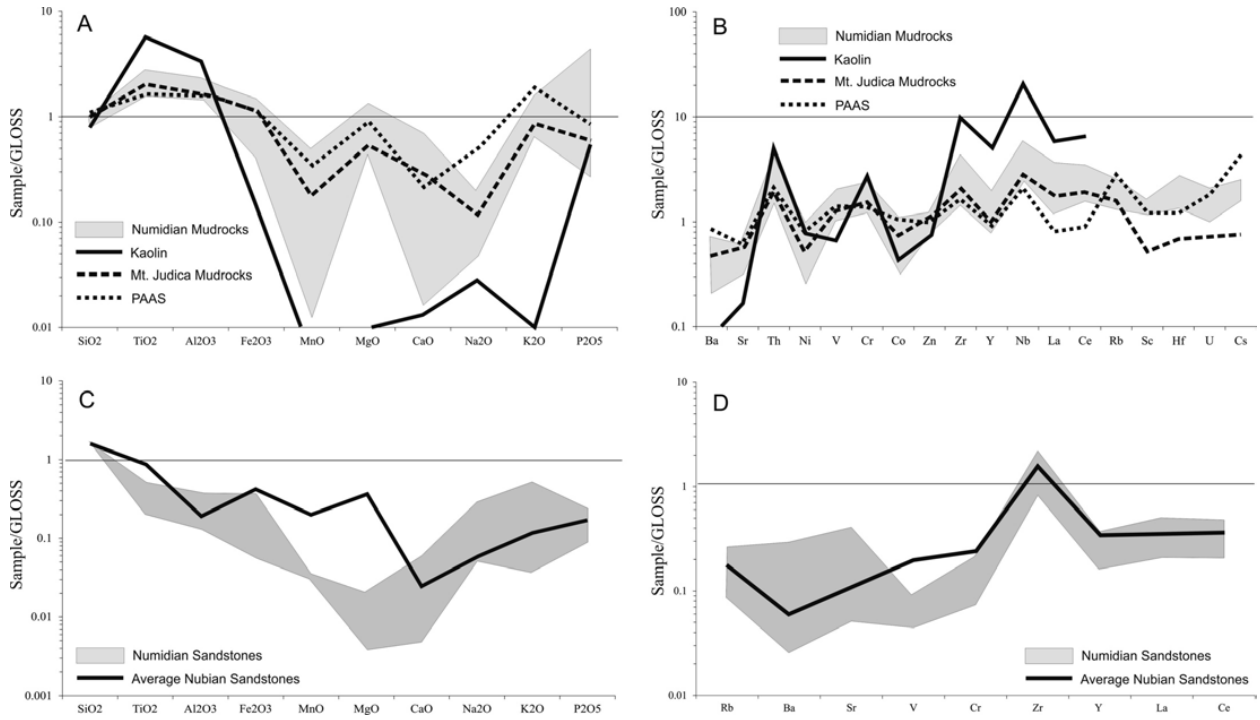

Fig. 6 - Major (A) and trace (B) elements of the analysed mudrocks and sandstones (C, D) normalized to the GLOSS composition (data from PLANK & LANGMUIR, 1998).

IS THE NUMIDIAN FORMATION HOMOGENEOUS WITHIN ITS TECTONIC UNITS?

In order to evaluate the compositional variability between the tectonic units (i.e. Nicosia, Monte Salici, Serra del Bosco) forming the Numidian Formation, the mudrocks compositional data have been processed by means of multivariate statistical analysis. The biplots of the first two principal components computed on a subset of selected major (fig. 9A) and trace elements (fig. 9B) evidenced the relationships between the four groups; Nicosia and Monte Salici Unit mudrocks are separated from the Monte Judica Unit samples, whereas the cases representing

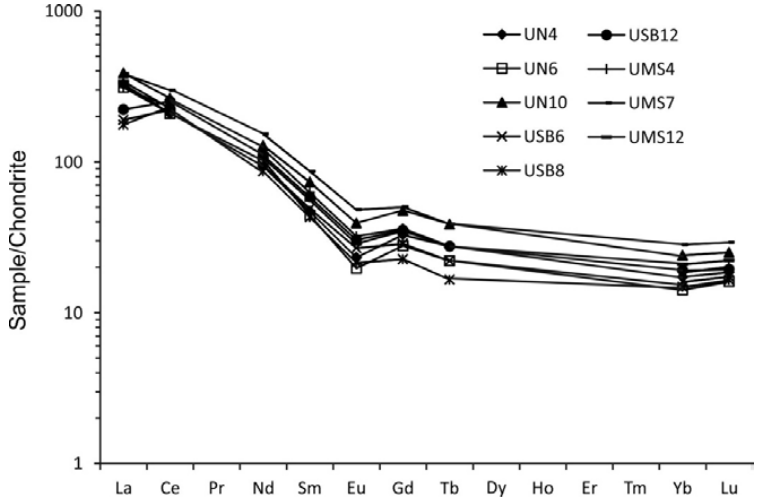

Fig. 7 - REE patterns normalized to chondrite (ANDERS & GREVESSE, 1989). Gd* is calculated using the formula: Gd* = (Sm·Tb2)1/3.

Serra del Bosco Unit show a very high dispersion with a spread distribution.

On the whole, the statistical analysis highlighted that the Miocene succession of Serra del Bosco Unit possesses a geochemical signature that seems to be intermediate between the compositions of the other Numidian units (i.e., Nicosia and Monte Salici) and the compositions of the Monte Judica mudrocks. This result may be due to the mixture of strictly Numidian sediments and Monte Judica-like detrital pulses in accordance with the paleogeographic position of the Serra del Bosco Unit between the Numidian basin and the African continental shelf.

PROVENANCE AND RECYCLING SEDIMENTS ASSESSMENT

The provenance study is mainly based on the mudrocks data since the quartzarenitic composition of sandstones preclude many geochemical considerations. A general evaluation of sediment provenance has been performed by considering the La-Th-Sc relationships (fig. 10A) suggesting a derivation from post-Archean sedimentary siliciclastic rocks also confirmed by the (Gd/Yb)ch vs. Eu/Eu* diagram (fig. 10B).

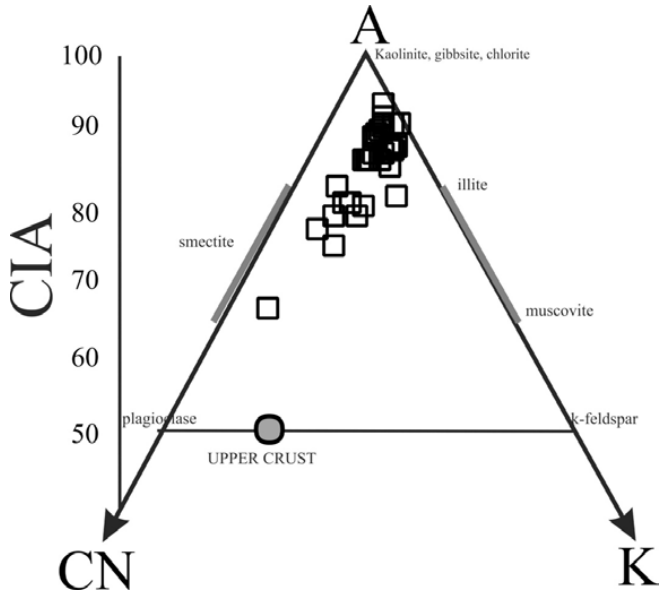

Fig. 8 - Molar proportions of Al2O3–(CaO*+Na2O)–K2O plotted in triangular A-CN-K diagram (CaO* represents CaO of the silicate fraction only).

In the Th/Sc vs Zr/Sc diagram (fig. 11), the Numidian mudrocks plot along the zircon addition trend interpreted as due to sedimentary sorting and recycling (MCLENNAN et alii, 1993; PERRI et alii, 2013). In this context, the Th/U ratios (ranging from 4.5 to 8.2, tab. 5), on average higher than values found for GLOSS (4.11) and post-Archean Australian Shale (PAAS) (4.71), may be due to the oxidation and loss of U during erosion and redeposition cycles (MCLENNAN et alii, 1993). As evidenced by BARBERA et alii (2009) the mineralogical and geochemical features of the Numidian Formation are in contrast with the compositions of the older Alpine Tethydes whose provenance from the European crust has been already constrained (BARBERA et alii, 2009, 2011); thus the alternative provenance hypothesis (i.e., from the African Craton) has been evaluated. For this purpose, several trace element ratios have been considered for the comparison of the Numidian Formation and the Nubian sediments (sandstones and kaolin). In the diagram of fig. 12, the mudrocks are well matched by the Nubian kaolin while the sandstone mimics the Nubian sandstones trends. A further constraining of the Numidian provenance has been attempted by evaluating the Zr/Y vs. Zr/Nb ratios (fig. 13). On the whole, the Zr/Y ratio of the studied mudrocks is higher than the relative average values of the magmatic rocks and cratonic shales reported by CONDIE (1993) and of the Alpine Tethydes reported by

BARBERA et alii (2009, 2011). Even if the Zr/Y and Zr/Nb ratios may be influenced during the sedimentary recycling processes by zircon enrichment (PERRI et alii, 2013), the trend due to the adding of this mineral may not justify the low Y/Nb ratio (0.8-1.2) of the Numidian mudrocks. Conversely, the Zr/Y and Zr/Y ratios of several African alkaline rocks such as the Ethiopian and Sudan granitoid suites and the average compositions of the cratonic sandstones reported by CONDIE (1993) are characterized by similar or higher ratios with respect to the Numidian mudrocks. Worth of note is that the analysed Nubian kaolin lies in the field of the Numidian mudrocks strongly suggesting a likely contribution of African sediments. The African provenance is also accounted by THOMAS et alii (2010) in their extensive review about the source of the Numidian Formation, who reported Precambrian zircon ages thus supporting a provenance from the African Craton.

With the purpose to evaluate the contribution of the African Nubian sediments, an end-member modeling of mudrocks compositional data has been performed following WELTJES's (1997) approach to the mixing problem. Starting from initial composition, the end memberwere iteratively calculated. The analysis was performed by considering the major oxides, excluding MnO and P2O5 as their contents are very close to the detection limits, and excluding K2O in response to its high susceptibility to diagenetic transformations.

The factor variance analysis indicates that four end members (high Silica-A, high MgO-B, high Al2O3-C, and high CaO-D) are adequate for the compositional modelling of the selected mudrocks. The compositions of the initial end members were selected on the basis of the previous geochemical and paleo-geographical considerations; the end members A, C and D are representative of the Nubian sandstones, Nubian kaolin and Monte Judica mudrocks respectively. With regard to the end member B, we decided to consider the composition of sample UN3 in response to its high MgO contents. The relative contributions of each end member for each sample are displayed in the histograms of fig. 14.

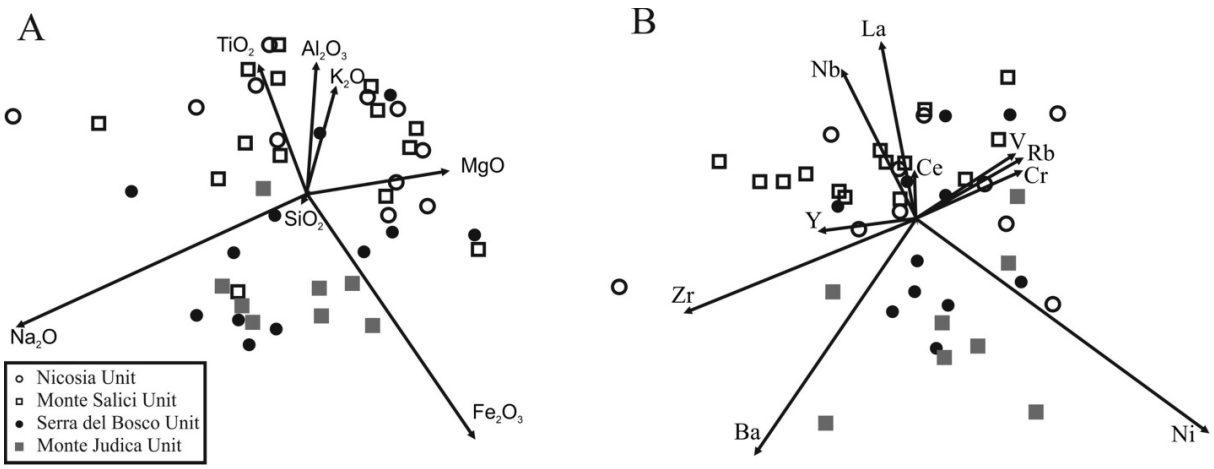

Fig. 9 - Biplots of major (A) and trace (B) elements; the horizontal scale is the first principal components direction (PC1), the vertical scale represent the direction of the second principal component (PC2). PC1 + PC2 explain the 73% and 66% of the total variance in A and B respectively.

The Nicosia and Monte Salici are more influenced by the African end-members (i.e., A and C) and by the high MgO end-member whereas the Serra del Bosco samples reflect a higher contribution of the high CaO end member confirming the suggested mixing with terrigenous epicontinental- type sediments represented by the clays of the Monte Judica Unit. In order to further investigate and to verify the mixing modelling, also the trace elements compositions were considered; in particular the composition of end members was calculated by means of ordinary

Least Squares The diagram of fig. 15 shows that, even if the absolute Zr values for the high silica (A) and high Alumina (C) end members are significantly high, their trace elements patterns are as a whole similar to that of the Nubian sand stones and kaolin respectively, thus supporting the results of the major oxides end member modelling.

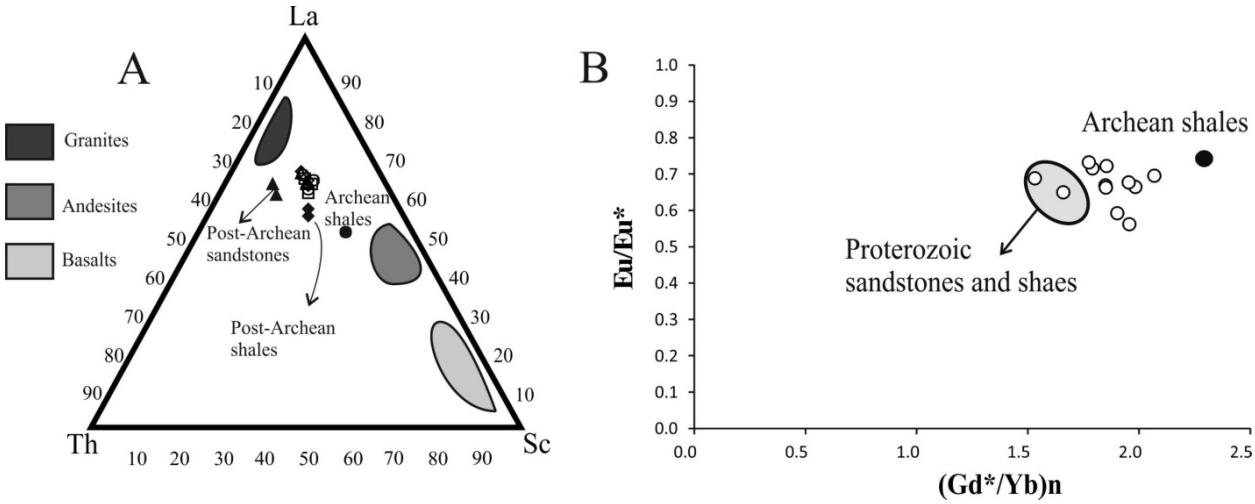

Fig. 10 - A) La-Th-Sc ternary plot; data for reference rocks from CONDIE (1993); B) Eu/Eu* versus (Gd*/Yb)n systematics.

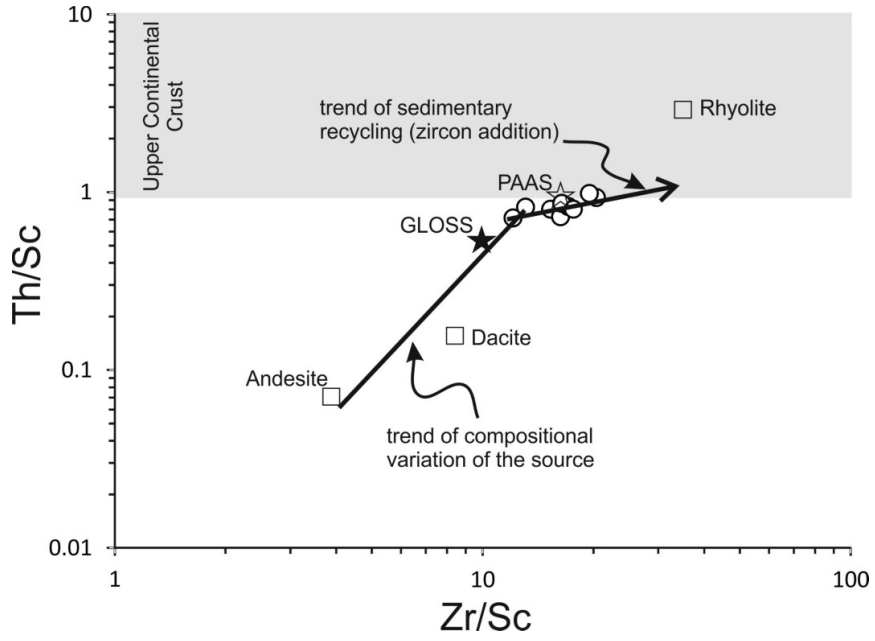

Fig. 11 - Th/Sc vs. Zr/Sc plot (MCLENNAN et alii, 1993; PERRI et alii, 2013).

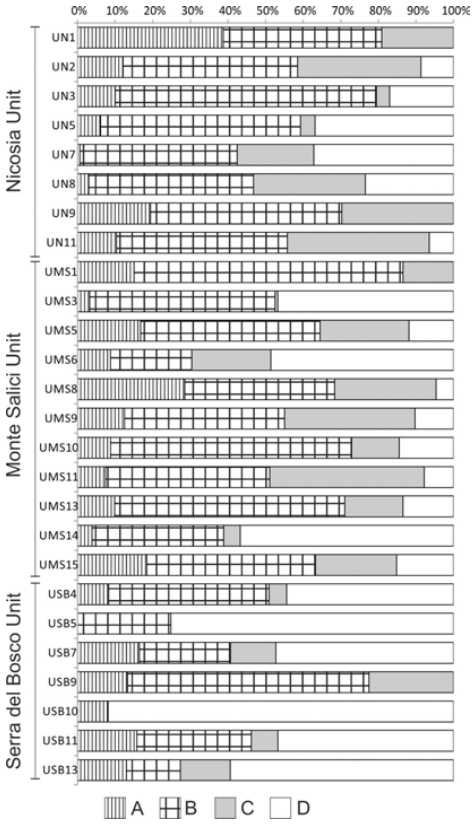

Fig. 12 - Multi-element diagram of selected ratios critical for provenance evaluation. A particularly well matching of the kaolinitic mudrocks and the numidian mudrock can be observed.

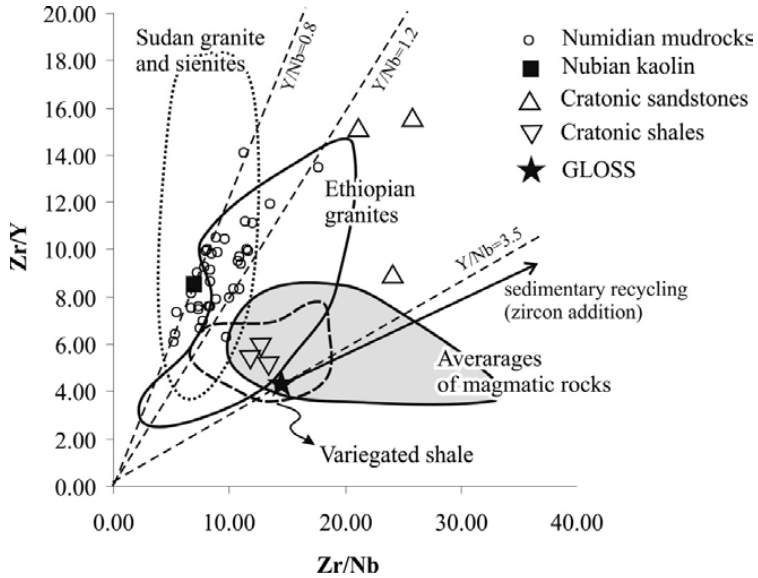

Fig. 13 - Zr/Y vs. Zr/Nb relationships: the following bibliographic data have been considered: Cratonic shales and sandstones + average of several magmatic rocks (basalts + andesites + granitoids; CONDIE 1993); Alpine Tethydes shales (BARBERA et alii, 2009); Ethiopian granites (KEBEDE & KOEBERL, 2003; TEKLAY et alii, 1998); Sudan granites and syenites (O'HALLORAN, 1985).

CONCLUSIONS

A mineralogical and geochemical characterization of the Numidian Formation was realized in order to unravel two important issues: the compositional variability amongst the tectonic units of the Numidian formation and the location of the source area. The statistical analysis of compositional data highlighted significant differences both in major and in trace elements contents between the samples of the Nicosia + Monte Salici Units (Numidian pelites) and Monte Judica Unit (Not-Numidian pelites). By contrast the statistical pattern of Serra del Bosco mudrocks seems to be not very clear because of the scattering of the analyzed samples both within the compositional fields of Numidian and not-Numidian mudrocks.The geochemical signature of Serra del Bosco Unit could be related to its palaeo-geographic position between the Numidian basin and the continental shelf represented by the Monte Judica Miocene succession. In this framework the Miocene succession of Serra del Bosco Unit may be considered as the result of detrital pulses of sediments coming from Numidian source and alternatively from not-Numidian source. The nature of the source rock and the hypothesis of an African derivation were addressed by considering the trace elements compositions; the hypotheses that the source rocks could be located in the African Craton was supported by the comparative analysis of Numidian Formation with the Nubian Sandstones and by the results of end-member mixing modelling that also showed the possible contribution of other sources Hence the results of our work are consistent with the hypothesis of a southern provenance of the Numidian debris and indicate that the reworking of older sedimentary sequences was a likely process for the origin of the Numidian debris and that one of the source rocks could represent by the Nubian sandstones. This conclusion is also supported by the petro graphic characters of the Numidian sandstones of all the Apenninic-Maghrebian Chain that are very similar to those observed within Oligocene-Miocene deposits of the external Rifian domains (Tangier Unit Auct.; CAZZOLA & CRITELLI, 1987; ZAGHLOUL et alii, 2005), whose provenance is exclusively linked to the African Craton.

REFERENCES

ARDITO M.C., COLALUCE G., DAZZARO L., DEL GAUDIO V., LOPS B., MORESI M., PICCARRETA G. & RAPISARDI L. (1985) - Le arenarie dell'Appennino Dauno. Osservazioni geologiche, mineralogiche e petrografiche. Atti 3° Conv. Naz. "Attività estrattiva dei minerali di II categ.". ANIM, ed., PEI, Parma, Bari, 50-53.

BARBERA G., CRITELLI S. & MAZZOLENI P. (2011) - Petrology and Geochemistry of Cretaceous Sedimentary Rocks of the Monte Soro Unit (Sicily, Italy): Constraints on Weathering, Diagenesis, and Provenance. The Journal of Geology, 119, 51-68.

BARBERA G., LO GIUDICE A., MAZZOLENI P. & PAPPALARDO A. (2009) - Combined statistical and petrological analysis of provenance and diagenetic history of mudrocks: Application to Alpine Tethydes shales (Sicily, Italy). Sedimentary Geology, 213, 27-40.

BASU A. (1985) - Reading provenance from detrital quartz. In: Zuffa G.G. (ed.), Provenance of arenites. Reidel, Dordrecht, 231-247.

BENOMRAN O., NAIRIN A.E.M. & SCHAMEL S. (1987) - Source and dispersal of mid-Cenozoic clastic sediments in the central Mediterranean region. Mem. Soc. Geol. It., 38, 47-68.

BIANCHI F., CARBONE S., GRASSO M., INVERNIZI G., LENTINI F., LONGARETTI G., MERLINI S. & MOSTARDINI F. (1987) – Sicilia Orientale: profilo Nebrodi-Iblei. Mem. Soc. Geol. It., 38

CARBONE S., LENTINI F., SONNINO M. & DEROSA R. (1987) - Il Flysch Numidico di Valsinni (Appennino Lucano). Boll. Soc. Geol. It., 106, 331-345.

CATALANO R. & D'ARGENIO B. (1978) - An essay of palinspastic restoration across western Sicily.

Geologica Romana, 6, 145-159.

CAZZOLA C. & CRITELLI S. (1987) - Litostratigrafia e petrologia delle quarzoareniti torbiditiche oligo-mioceniche di Asilah (Catena del Rif, Marocco nord-occidentale). Mineralogica et Petrographica Acta, 30, 203-226.

CHIOCCHINI U., FRANCHI R., GUERRERA F., RYAN W.B.F. & VANNUCCI S. (1980) - Geologia di alcune successioni torbiditiche cretacicoterziarie appartenenti ai "Flysch Maurétanien" e alla "Nappe Numidienne"del Rif settentrionale (Marocco). Studi Geologici Camerti, 4, 37-66.

CONDIE K.C. (1993) - Chemical composition and evolution of the upper continental crust: Contrasting results from surface samples and shales. Chemical Geology, 104, 1-37.

CRITELLI S. (1991) - Evoluzione delle mode detritiche delle successioni arenitiche terziarie dell'Appennino meridionale. Mem. Soc. Geol. It., 47, 55-93.

CRITELLI S., MUTO F., TRIPODI V. & PERRI F. (2011) – Relationships between lithospheric flexure, thrust tectonics and stratigraphic sequences in foreland setting: the Southern Apennines foreland basin system, Italy. In: Tectonics 2 (ed., By Schattner U.), Chapter 6, Intech Open Access Publisher [ISBN 979-953-307- 199-1], 121-170.

CRITELLI S. & LE PERA E. (1995) - Tectonic evolution of the Southern Apennines thrust-belt (Italy) as reflected in modal compositions of Cenozoic sandstone. The Journal of Geology, 103, 95-105.

CRITELLI S. (1999) - The interplay of lithospheric flexure and thrust accommodation in forming stratigraphic sequences in the southern Apennines foreland basin system, Italy. Memorie dell'Accademia Nazionale dei Lincei, 10, 257-326.

FEDO C.M., ERIKSSON K.A. & KROGSTAD E.J. (1996) – Geochemistry of shales from the Archean (–3.0 Ga) Buhwa Greenstone Belt, Zimbabwe: Implication for provenance and source-area weathering. Geochimica et Cosmochimica Acta, 60, 1751-1763.

FILDES C., STOW D., RIAHI S., SOUSSI M., PATEL U., MILTON J.A. & MARSHET S. (2010) - European provenance of the Numidian Flysch in northern Tunisia. Terra Nova, 22, 94-102.

FOLK R.L. (1974) - Petrology of Sedimentary Rocks. Austin, Texas, Hemphill Press, 182 pp.

GAUDETTE H.E., HURLE P.M. & LAJMI T. (1979) - Provenance studies in Tunisia by U-Pb ages of detrital zircons. AAPG Bulletin, 63, 456.

GUERRERA F., LOIACONO F., PUGLISI D. & ELVIO M. (1992) – The Numidian nappe in the Magrebian Chain: state of art. Boll. Soc. Geol. It., 111, 217-253.

GUERRERA F., MARTÍN-ALGARRA A. & MARTÍN-MARTÍN M. (2012) - Tectono-sedimentary evolution of the 'Numidian Formation' and Lateral Facies (southern branch of the western Tethys): constraints for central-western Mediterranean geodynamics. Terra Nova, 24, 34-41.

JOHANSSON M., BRAAKENBURG N.E., STOW D.A.V. & FAUGÈRES J.C. (1998) - Deep-water massive sands: facies, processes and channel geometry in the Numidian Flysch, Sicily. Sedimentary Geology, 115, 233-265.

KEBEDE T. & KOEBERL C. (2003) - Petrogenesis of A-type granitoids from the Wallagga area, western Ethiopia: constraints from mineralogy, bulk-rock chemistry, Nd and Sr isotopic compositions. Precambrian Research, 121, 1-24.

KHEDR E.S. (1990) - Major subdivision of the Red Sea Continental Margin Sequence, Southern Egypt. Academy of Scientific Research and Technology Cairo Bull., 40, 1-15.

LENTINI F., CARBONE S., CATALANO S., GRASSO M. & MONACO C. (1991) - Presentazione della carta geologica della Sicilia centroorientale. Mem. Soc. Geol. It., 47, 145-156.

LOIACONO F., PAGLIONICO A. & PELLEGRINO M.C. (1983) - Le quarzareniti del Flysch Numidico di Campomaggiore (PZ): indagini per l'utilizzazione in campo industriale. Geol. Appl. Idrogeol., 18, 73-80.

LOPEZ J.M.G., BAULUZ B., FERNANDEZ-NIETO C. & OLIETE A.Y. (2005) - Factors controlling the trace element distribution in finegrained rocks: the Albian kaolinite-rich deposits of the Oliete basin (NE Spain). Chemical Geology, 214, 1-19.

MCLENNAN S.M. & TAYLOR S.R. (1991) - Sedimentary rocks and crustal evolution: tectonic setting and secular trends. Journal of Geology, 99, 1-21.

MCLENNAN S.M., HEMMING D.K. & HANSON G.N. (1993) – Geochimical aproaches to sedimentation, provenance and tectonics. Geological Society of America Special Papers., 284, 21-40.

MONGELLI G. (1993) - REE and other trace elements in a granitic weathering profile from "Serre", southern Italy. Chemical Geology, 103, 17-25.

MONGELLI G. (2004) - Rare-earth elements in Oligo-Miocenic politic sediments from Lagonegro Basin, Southern Appennines, Italy: implications for provenance and source area weathering. Int. J. Earth Science (Geol. Rundsch), 93, 612-620.

MONTANARI L. (1987) - Lineamenti stratigrafico-paleogeografici della Sicilia durante il ciclo alpino. Mem. Soc. Geol. It., 38, 361-406.

MORETTI E., COCCIONI R., GUERRERA F., LAHONDERE C., LOIACONO F., PUGLISI D. (1991) The Numidian sequence between Guelma and Constantine (Eastern Tell, Algeria). Terra Nova, 3, 153-165.

NARDI L.V.S., FORMOSO M.L.L., MÜLLER I.F., FONTANA E., JARVIS K. & LAMARÃO C. (2013) - Zircon/rock partition coefficients of REEs, Y, Th, U, Nb, and Ta in granitic rocks: Uses for provenance and mineral exploration purposes. Chemical Geology, 335, 1-7.

NESBITT H.W. & YOUNG G.M. (1989) - Formation and diagenesis if weathering profiles. The Journal of Geology, 97, 129-147.

NESBITT H.W. & YOUNG G.M. (1996) - Petrogenesis of sediments in the absebce of chemical weathering: effects of abrasion and sorting on bulk composition and mineralogy. Sedimentology, 43, 341-358.

O'HALLORAN D.A. (1985) - Rased Dom migrating ring complex: A-type granites and syenites from the Bayuda Desert, Sudan. Journal of African Earth Sciences, 3, 61-65.

PATACCA E., SCANDONE P., BELLATALLA M., PERILLI N. & SANTINI U. (1992) - The Numidian-sand event in the southern Apennines. Mem. Sc. Geol., Univ. Padova, 43, 297-337.

PERRI F., CRITELLI S., MARTÍN-ALGARRA A., MARTÍN-MARTÍN M., PERRONE V., MONGELLI G. & ZATTIN M. (2013) Triassic red beds in the Malaguide Complex (Betic Cordillera-Spain): Petrography, geochemistry and geodynamic implications. Earth-Sci. Rev. 117, 1-28.

TAYLOR S.R. & MCLENNAN S. (1985) - The continental crust: its composition and evolution. Blackwell Scientific Publications, Oxford, 312 pp.

TEKLAY M., KRONER A., MEZGER K. & OBERHANSLI R. (1998) - Geochemistry, Pb-Pb single zircon ages and Nd-Sr isotope composition of Precambrian rocks from southern and eastern Ethiopia: implications for crustal evolution in East Africa. Journal of African Earth Sciences, 26, 207-227.

THIO-HENESTROSA S. & MARTIN-FERNANDEZ J.A. (2005) – Dealing with Compositional Data: The Freeware CoDaPack. Mathematical Geology, 37, 773-793.

THOMAS M.F.H., BODIN S., REDFERN J. & IRVING D.H.B. (2010) – A constrained African craton source for the Cenozoic Numidian Flysch: Implications for the palaeogeography of the western Mediterranean basin. Earth-Science Reviews, 101, 1-23.

WELTJE G. (1997) - End-member modeling of compositional data: Numerical-statistical algorithms for solving the explicit mixing problem. Mathematical Geology, 29 (4), 503-549.

ZAGHLOUL M.N., DI STASO A., GIGLIUTO L.G., MANISCALCO R. & PUGLISI D. (2005) - First evidence of Lower and Middle Miocene strata within the succession of the External Tanger Unit: stratigraphy, provenance, palinspastic and geodynamic implications (Intra-Rif Sub-Domain, External Domain; Rif, Morocco). Geologica Carpathica, 56, 517-530.

ZHANG L., SUN M., WANG S. & YU X. (1998) - The composition of shales from the Ordos basin, China: effects of sorce weathering and diagenesis. Sedimentary Geology, 116, 129-141.

LATE MAASTRICHTIAN-EARLY DANIAN HIGH-STRESS ENVIRONMENTS AND DELAYED RECOVERY LINKED TO DECCAN VOLCANISM*

Abstract. Deccan volcanism occurred in three intense phases of relatively short duration: Phase-1 spanning the paleomagnetic chron C30r/C30n boundary (planktic foraminiferal zone CF4), phase-2 in the latest Maastrichtian C29r (zones CF1-CF2), and phase-3 in the early Danian C29n (zone P1b). The mass extinction and subsequent recovery coincide with phase-2 and phase-3, based on planktic foraminifera in intertrappean sediments from quarries and subsurface cores of the Krishna-Godavari Basin, India. This study explores the nature of paleoenvironmental changes correlative with the three volcanic phases as observed in Central Egypt and the Sinai based on planktic foraminifera, stable carbon and oxygen isotopes. Results show that high-stress assemblages dominated by *Guembelitria* blooms are prominent though not exclusive to all three volcanic phases. *Guembelitria* blooms are well known from the aftermath of the mass extinction in zones P0-P1a, the intertrappean interval between volcanic phase-2 and phase-3. *Guembelitria* blooms in zone CF4 (phase-1) are relatively minor (<45%) although a substantial component of the planktic foraminiferal assemblages. Maximum *Guembelitria* blooms (>80%) are observed in zone CF1, which spans the last 160 ky of the Maastrichtian marked by rapid global climatic warming and cooling correlative with phase-2. Major *Guembelitria* blooms (50-75%) are also observed in zone P1b, which is marked by climate warming (Dan-C2 event) and a major negative carbon isotope excursion correlative with phase-3. This high-stress event precedes full marine biotic recovery after the mass extinction.

Key Words Deccan Volcanism; KTB mass extinction; delayed recovery, *Guembelitria* blooms

1. INTRODUCTION

A large meteorite impact and one of the world's largest volcanic eruptions, the Deccan Traps in India, occurred in the latest Maastrichtian, an interval leading up to the Cretaceous-Tertiary boundary (KTB also known as Cretaceous-Paleogene or K-Pg, KPB). Of these two catastrophes, the meteorite impact is popularly assumed to be the sole cause for the KTB mass extinction (Alvarez et al., 1980; Schulte et al., 2010). However, major climate, environmental and faunal changes during the late Maastrichtian and early Danian rule out a single cause. Deccan volcanism has been proposed as likely long-term cause (McLean, 1985; Courtillot et al., 1986, 1988) but a direct link with the mass extinction remained elusive until recently. Improved paleomagnetic and radiometric dating have identified three major phases of Deccan volcanism (Chenet et al., 2007, 2008). The initial phase-1 (67.5±1 Ma, C30n/C30r) accounts for ~6% of Deccan eruptions, the main phase-2 (C29r below the KTB) accounts for 80% of the total lava pile, and the last phase-3 (onset at C29r/C29n boundary) accounts for 14%. The discovery of marine deposits in intertrappean sediments of the Krishna-Godavari Basin quarries and subsurface cores (Keller et al., 2008, 2011a, 2012), and in outcrops of central India (Madhya Pradesh) (Keller et al., 2009a,b), have recently provided the first direct links between the KTB

* ***Jahnavi Punekar, Gerta Keller, Hassan Khozyem, Carl Hamming, Thierry Adatte and Abdel, A. Tantawy (2013) Late Maastrichtian- Early Danian high-stress environments and delayed recovery may be linked to Deccan Volcanism. Cretaceous Research, in press***

mass extinction and volcanic phase-2, as well as the long-delayed (>0.5 m.y.) post-KTB recovery and Deccan phase-3. These two volcanic phases, which account for 94% of the total volume of Deccan eruptions, are recognized as containing the world's largest and longest lava mega-flows >1000 km across India and out into the Bay of Bengal (Keller et al., 2008; Self et al., 2008).

The sheer volume of CO_2, SO_2 and Cl_2 associated with these volcanic eruptions suggest that Deccan volcanism had the potential of causing serious global environmental destruction (Self et al. 2005, 2008; Chenet et al., 2009). This is evident in intertrappean sediments between the C29r lava mega-flows of the Krishna-Godavari Basin (SE India) where the mass extinction is rapid and ends with the last phase-2 mega-flows at the KTB (Keller et al., 2011a, 2012). In Meghalaya (NE India) located ~800 km from the main Deccan province, blooms of the disaster opportunist *Guembelitria cretacea* dominate (>95%) in phase-2 with only rare Maastrichtian species present and all go extinct at the KTB, which is also marked by a large (12 ppb) Ir anomaly and negative $d^{13}C$ excursion (Gertsch et al., 2011). These observations now permit the evaluation of faunal assemblages and particularly *Guembelitria* blooms correlative with Deccan volcanism on a global basis. For example, *Guembelitria* blooms have previously been observed from the Middle East during the late Maastrichtian (zones CF1-CF2 and CF4 and in the early Danian zone P1b, although the cause(s) for these stress conditions remained unexplained (Keller and Benjamini, 1991; Abramovich et al., 1998; Keller, 2002).

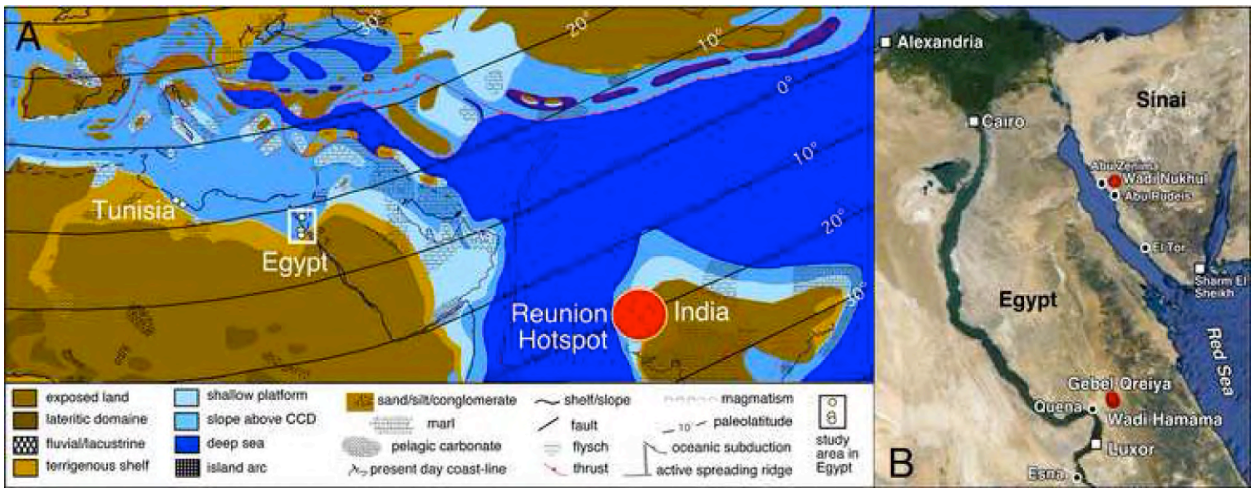

Figure 1*. (A) Paleogeography of Tethys, India and Reunion hotspot during the Cretaceous-Tertiary transition, modified after Dercourt et al. (1993); (B) Google Earth image showing the present day location of the studied sections in Central Egypt and Sinai.*

The objective of this study is to test the hypothesis that high-stress planktic foraminiferal assemblages observed in late Maastrichtian and early Danian sequences are caused by climatic and environmental changes that resulted directly from the main phases of Deccan volcanic eruptions in Indian. We chose central Egypt and the Sinai as test case because of this region's proximity to the paleolatitude of India and the Reunion hotspot that resulted in the Deccan volcanic province (Fig. 1A), and because of the previously observed enigmatic *Guembelitria* blooms in the late Maastrichtian and early Danian in Israel (e.g., Keller and Benjamini, 1991; Abramovich et al., 1998). Three sections were chosen from the Central Eastern Desert (Wadi Hamama, Gebel Qreiya) and the Sinai (Wadi Nukhul, Fig. 1B). The fauna is relatively well

preserved and spans late Maastrichtian through the early Danian. Investigations concentrate on: 1) biostratigraphy, 2) faunal turnovers, 3) *Guembelitria* blooms, 4) carbon and oxygen isotope stratigraphy 5) correlation of *Guembelitria* blooms with Deccan volcanism, and 6) potential causes of biologic stress.

2. LOCATION

Gebel Qreiya and Wadi Hamama are located in the central eastern Desert of Egypt (26°21'N 33°01'E, Fig. 1B) at the southern tip of the Wadi Qena. Gebel Qreiya is 50 km northeast of Qena city and 18 km north of the Km53 marker on the Qena-Safaga road, whereas Wadi Hamama is ~28 km south of Gebel Qreiya and 10 km south of the Km44 marker on the Qena-Safaga road (26°18'N 33°02'E). During the late Maastrichtian and early Paleocene sediment deposition occurred in a middle shelf (~100-200 m) environment marked by sea-level fluctuations and erosion (Said, 1961; Luger, 1988; Keller, 2002; Keller et al., 2002; Tantawy, 2003). Wadi Nukhul is located in the southwestern Sinai about 6 km south of Abu Zenima City, on the eastern side of the Gulf of Suez (29°01' N 33°15' E, Fig. 1). Sedimentation occurred in an outer shelf environment at a paleodepth >200 m.

3. LITHOLOGY

At Gebel Qreiya and Wadi Hamama the Dakhla Formation spans the upper Maastrichtian and lower Danian (Abdel Razik, 1972; Soliman et al., 1986), which was sampled and analyzed in a 24 m interval at Gebel Qreiya (Fig. 2) and 22 m in the Wadi Hamama (Fig. 3). For Gebel Qreiya the biostratigraphy (planktic foraminifera and nannofossils), sedimentology, mineralogy and stable isotopes of the upper 14 m were previously published (Keller, 2002; Keller et al., 2002; Tantawy, 2003) and only a brief summary is given here. This study added a 10 m interval at the bottom of the section for a more complete upper Maastrichtian record. The nannofossil biostratigraphy, faunal and floral turnovers are similar in both sections (Tantawy, 2003).

At Gebel Qrieya, the basal 9 m consist of monotonous grey marly shale devoid of macrofossils (Fig. 2); this interval was not collected at Hamama. The grey shale grades into darker grey marly shale with abundant *Pecten farafrensis* shell fragments at Qreiya, though the equivalent interval at Wadi Hamama is devoid of macrofossils (Fig. 3). The *Pecten*-rich interval grades into monotonous marly shale with rare *P. farafrensis* and ends abruptly at a disconformity ~1.8 m below the KT boundary at Gebel Qreiya, but 3 m below the KTB at Wadi Hamama. (Note the KTB is identified by the mass extinction in planktic foraminifera immediately followed by the evolution of the first Danian species). Marly shale devoid of macrofossils overlies the disconformity in both sections and ends at another disconformity at the KTB in both sections (Fig. 3). At Qreiya, the KTB erosional surface overlies a 10 cm thick bioturbated, fossiliferous marly shale (Fig. 2). Above this hiatus is a 1-cm- thick red clay layer devoid of calcareous microfossils, but enriched with gypsum and a 5.4 ppb Ir anomaly marks this KTB unconformity (Keller et al., 2002; Tantawy, 2003). In contrast, there is no marked erosional surface or red layer observed at the KTB at Wadi Hamama (Fig. 3). At Qreiya and Hamama, a <0.5 m thick fissile dark-grey shale overlies the red layer and contains the earliest Danian (zone P1a) faunal assemblages. Above this interval, grey marly shale marks sedimentation in the early Danian.

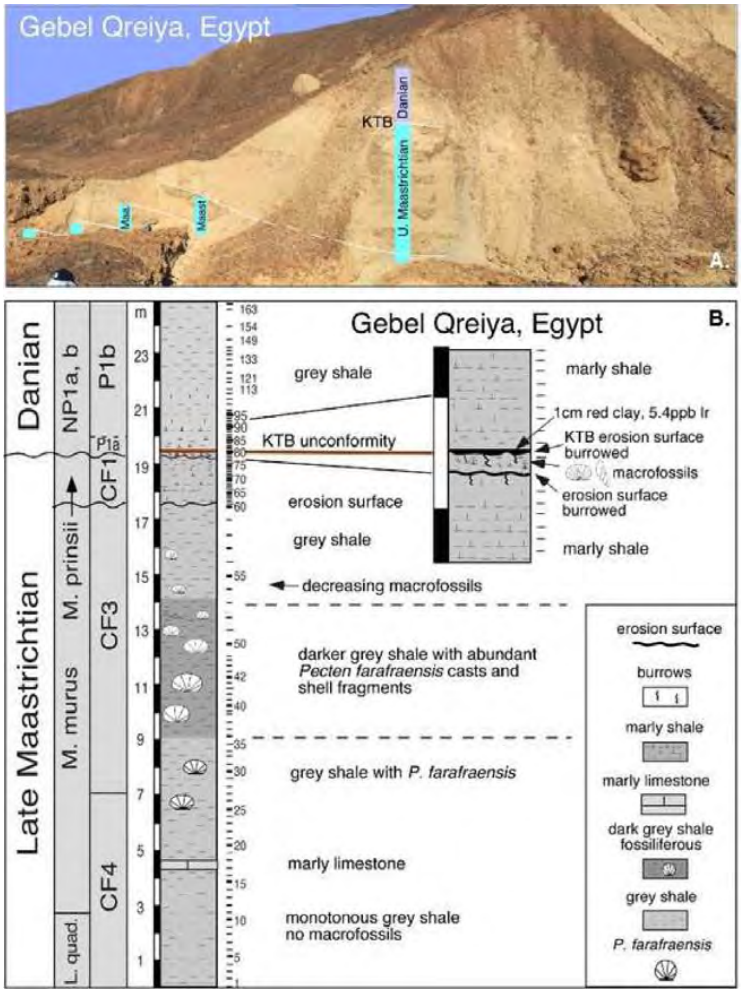

Figure 2. *(A) Gebel Qreiya, Egypt, with Maastrichtian to early Paleocene sequence. (B) Lithology and description of the interval analyzed*

The Wadi Nukhul contains one of the most continuous sedimentary sequences across the Cretaceous-Tertiary and Paleocene-Eocene transitions in Egypt (Fig. 4A). Most of the Maastrichtian consists of the Sudr Formation, which is characterized by white chalk intercalated with thin lamina of yellow calcareous shale. The contact between the Sudr Formation and the overlying Dakhla Formation is marked by a change to grey and yellow marly limestone at the top of a cliff. The lower part of the Dakhla Formation consists of an increasingly bioturbated, marly limestone with burrows infilled with gray shale (Fig. 4B, C). Fissile marly limestone grades into silty marl and shale with a gypsum layer at the top that marks the KTB unconformity. Above the unconformity yellow-grey marls are intercalated with ferruginous brown-red claystone with gypsum seams (samples Nua 112-116, Fig. 4B, A and B). The overlying Danian sediments consist of argillaceous limestone grading into gray calcareous shale (0.8 m thick). Above this interval is a prominent 5 cm thick red-brown ferruginous claystone with gypsum seams. The overlying calcareous shale is 1.4 m thick and multicolored (grey, brown, black, green, yellow) interrupted by two thin silty claystone layers (Fig. 4B).

4. MATERIAL AND METHODS

For all three sections analyzed samples were collected at 10-30 cm intervals and at closer spacing (~5 cm) across the KTB. In the laboratory, samples were crushed into small fragments and left overnight in 3% hydrogen peroxide solution to oxidize organic carbon. After disaggregation of sediment particles, the samples were washed through >63µm and >36µm sieves to obtain clean foraminiferal sample residues (Keller et al., 1995). Complete removal of

clay is important to avoid clump formation upon drying. Washed residues were oven dried at 50°C. Foraminifera from Maastrichtian limestone and marly limestone of the Wadi Nukhul section are difficult to free from adhering sediments even after boiling with $NaHCO_3$ and ultrasonic treatment and no reliable quantitative data could be obtained. Thin section analysis is not suitable for quantitative faunal studies because species identification is limited to a small number of specimens with species-specific characteristic crosscuts.

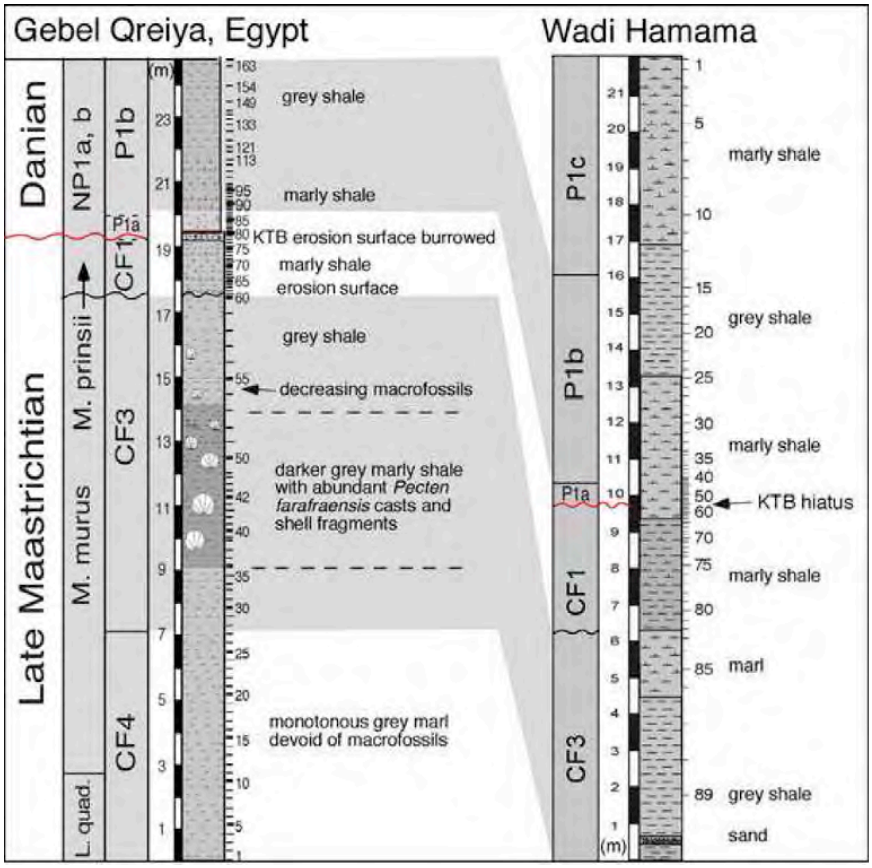

Figure 3*. Lithology and description of the Maastrichtian to early Paleocene sequence at Wadi Hamama compared with Gebel Qreiya, Egypt.*

To obtain a statistically valid representation of the species population, each sample was split with an Otto micro-splitter to obtain approximately 300 specimens from the >63µm size fraction. Planktonic foraminifera were picked from each sample split, sorted and mounted on micro-slides and identified. The entire remaining sample residue was thoroughly searched for rare species. Identification of species is based on standard taxonomic concepts (e.g., Robaszynski et al., 1983-1984; Nederbragt, 1991; Olsson et al., 1999). Some of the typical species are illustrated in Plates 1-IV.

Stable carbon and oxygen isotope analyses were performed on well-preserved shells of monospecific planktic and benthic foraminiferal species for samples from Gebel Qreiya consistent with the dataset of Keller et al. (2002). At Wadi Hamama and Wadi Nukhul bulk rock samples were analyzed due to poor foraminiferal preservation. These analyses were conducted at the Earth Sciences Institute (ISTE) of the University of Lausanne, Switzerland, using a Thermo Fisher GasBench II preparation device interfaced with a Thermo Fisher Delta Plus XL continuous flow isotope ratio mass spectrometer. The stable carbon and oxygen isotope ratios are reported in the delta (δ) notation as the per mil (‰) deviation relative to the Vienna Pee Dee

belemnite standard (VPDB). The reproducibility was better than ±0.05‰ for $\delta^{13}C$ and ±0.1‰ for $\delta^{18}O$.

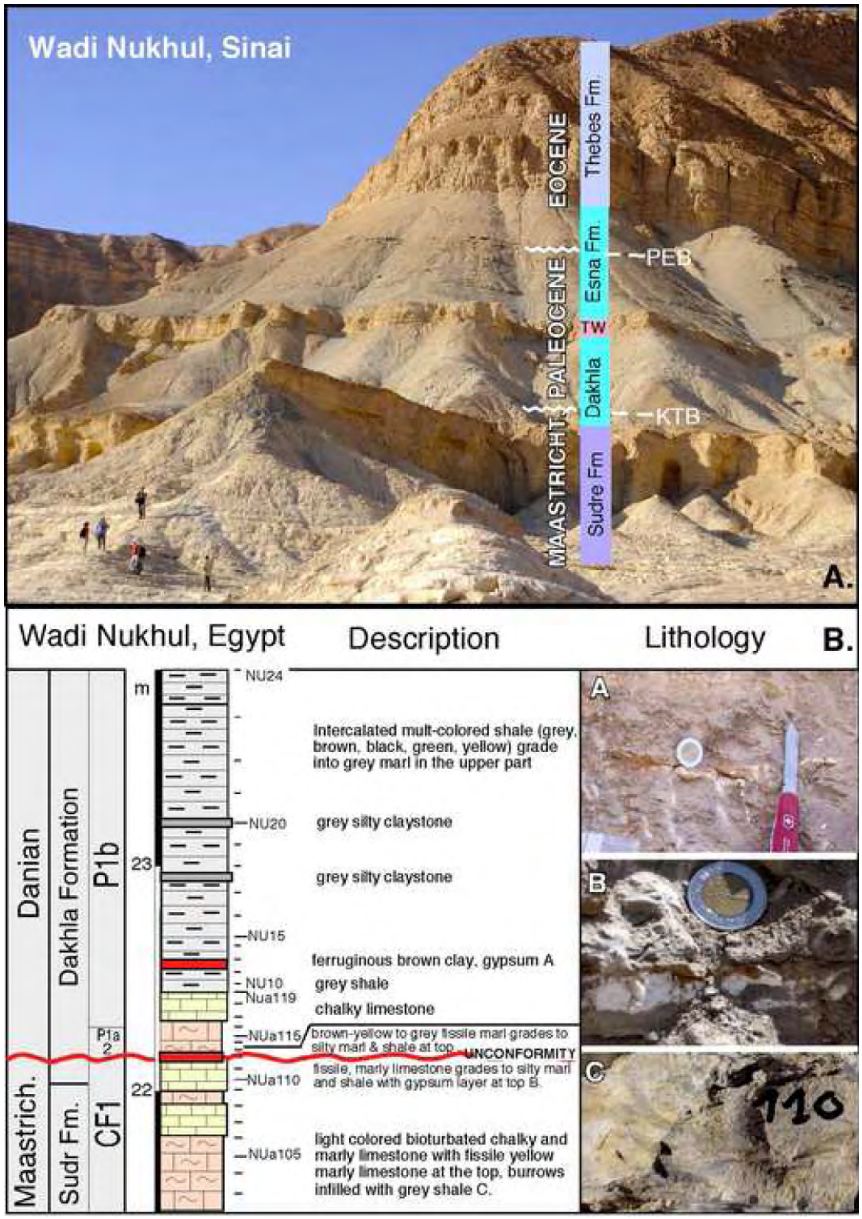

Figure 4*. (A) Maastrichtian through Paleogene sequence at Wadi Nukhul, Egypt. (B) Lithology and description of the interval analyzed.*

5. BIOSTRATIGRAPHY

The Cretaceous Foraminiferal (CF) biozonation of Li and Keller (1998a) and Danian biozonation of Keller et al. (1995, 2002) are applied in this study (Fig. 5). Biozone ages are calculated based on the paleomagnetic time scales of Cande and Kent (1995) and Gradstein et al. (2004). Previous studies recognized most late Maastrichtian to early Danian planktic foraminiferal and nannofossil biozones at Gebel Qreiya, Wadi Hamama and Wadi Nukhul (Keller, 2002; Keller et al., 2002; Tantawy, 2003).

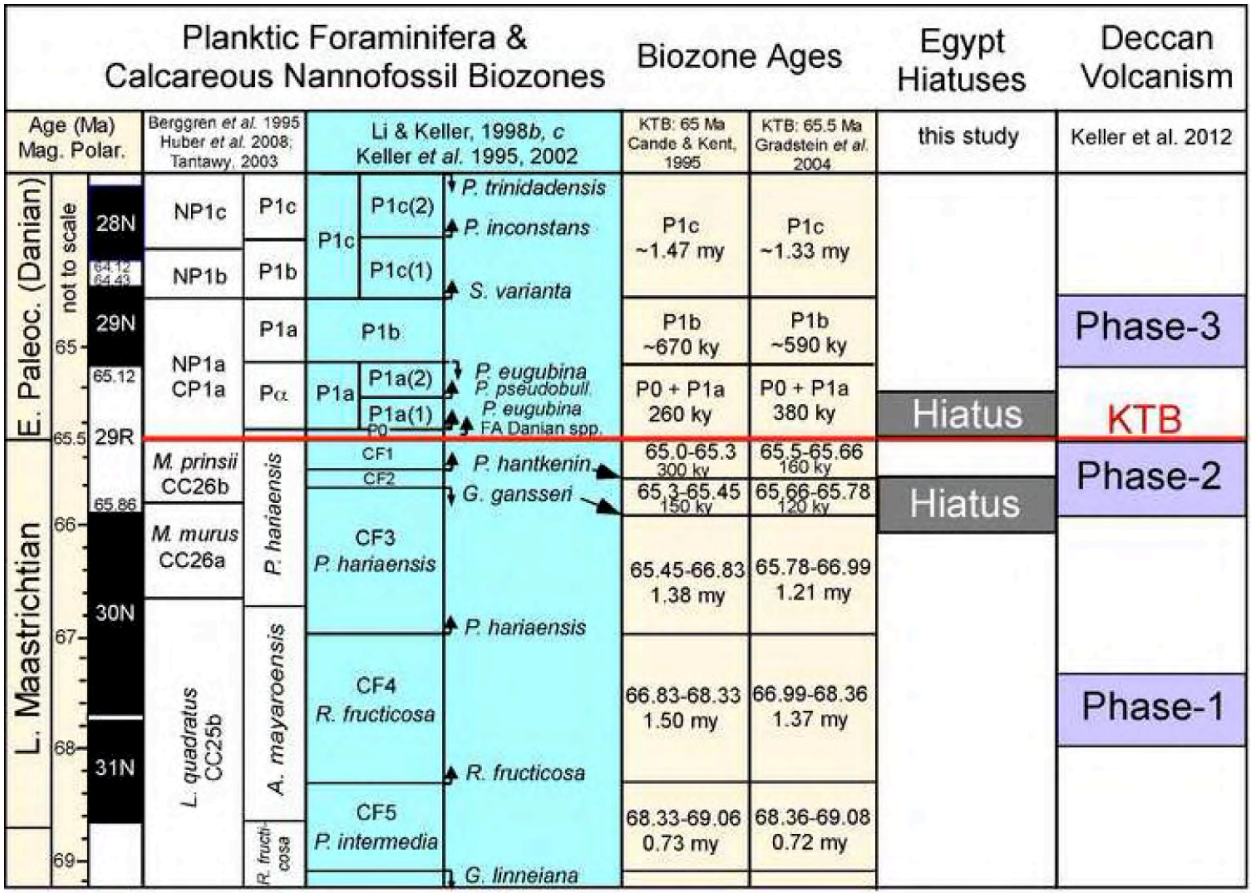

Figure 5*. Biozonation scheme applied in this study compared with alternative biozonations Ages for biozones are given for the time scales with the KTB at 65 Ma and at 65.5 Ma. Hiatuses observed in Egypt and ages of the three phases of Deccan volcanism are indicated.*

Zone CF4 (66.99-68.36 Ma): This zone spans the interval between the first occurrences (FO) of *Racemiguembelina fructicosa* and *Pseudoguembelina hariaensis* (Fig. 5). Zone CF4 is tentatively identified in the basal 7 m of the Gebel Qreiya section based on the presence of rare *R. fructicosa* and absence of *P. hariaensis* (Fig. 6). The faunal assemblage is dominated by *Heterohelix navarroensis*, *H. planata* and *H. globulosa*, *H. costulata* and *H. costellifera* (Plate I, 5-6). *Guembelitria cretacea* (Plate IV, 12) shows two abundance maxima at 1.5 m and 6-7 m from the base. *Globotruncana bulloides* and *Rosita fornicata* disappear after the first *G. cretacea* peak (Fig. 6). *Rosita plummerae* and *R. plicata* disappear before the second *G. cretacea* peak and *Archaeoglobigerina cretacea*, *A. blowi* and *G. wiedenmayeri* disappear coincident with this *Guembelitria* peak. The disappearance of *G. bulloides*, *R. plummerae* and *R. fornicata* was previously reported from zone CF4 in DSDP 525A and Madagascar (Li and Keller, 1998a and Abramovich et al., 2002).

Zone CF3 (65.78-66.99 Ma): This zone spans the interval from the FO of *Pseudoguembelina hariaensis* (Plate I, 4) to the last occurrence (LO) of *Gansserina gansseri* (Fig. 5). At Gebel Qreiya, CF3 spans 10.5 m (7-17.5 m, Fig. 6). *Guembelitria* blooms dominate faunal assemblages by 60% between 9.3-10.8 m and 11.8-13.3 m (peaks 3, 4). Near the top of CF3, *Guembelitria* blooms dominate assemblages by 80-90% (peak 5, Fig. 6). At the same time, species richness drops 19% (from 47 to 38 species). Heterohelicids continue to be the second most dominant group in the assemblage, but decrease in abundance during *G. cretacea* blooms. A hiatus marks the top of zone CF3 with zone CF2 and an unknown interval of CF3 is missing.

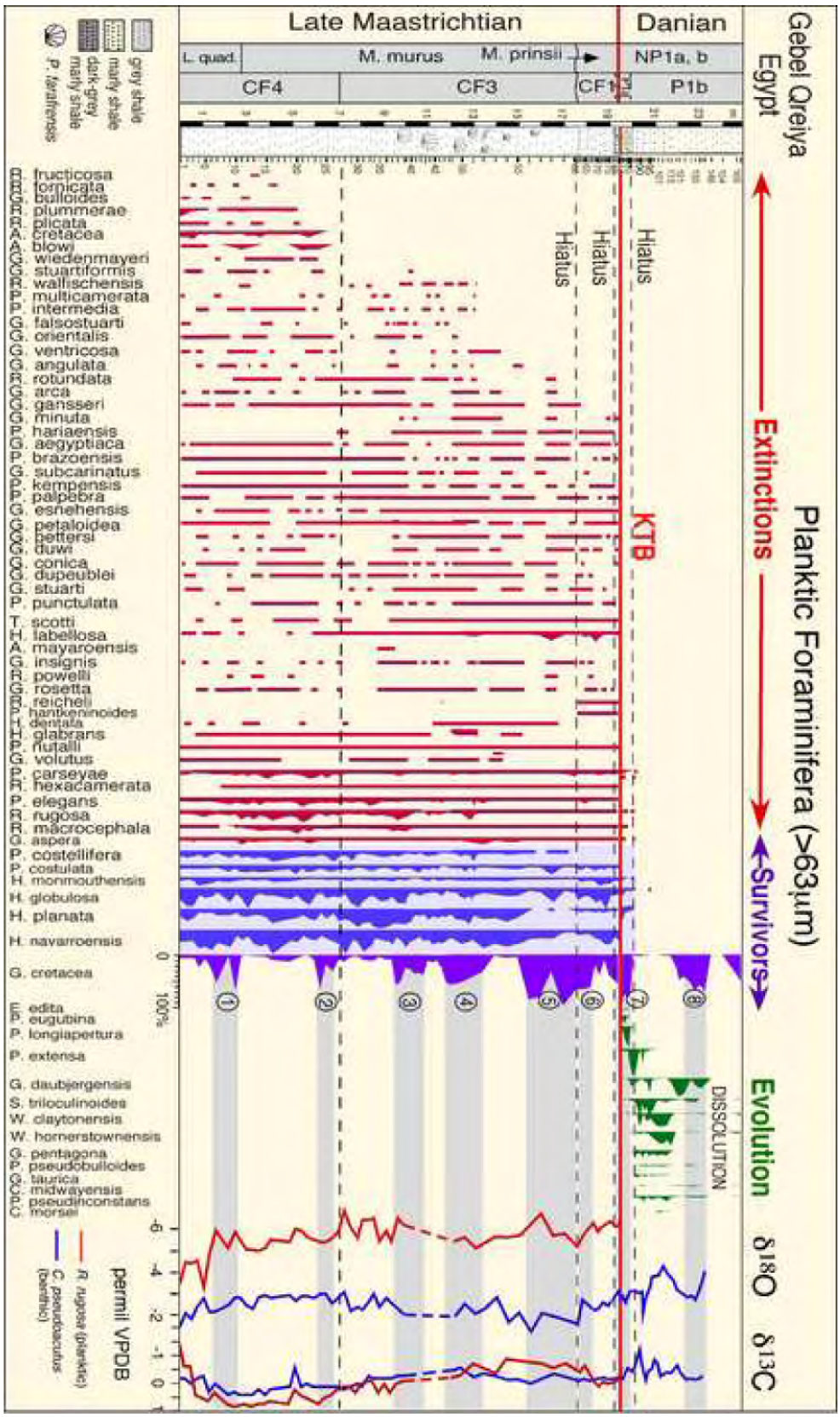

Figure. 6. *Relative species abundances and turnover of planktic foraminifera (>63µm) at Gebel Qreiya, Egypt. Note the gradual disappearances of species during the Late Maastrichtian culminating in the mass-extinction at the KTB, and the abundance peaks of Guembelitria cretacea that mark intervals of environmental stress. Nannofossil zones are based on Tantawy (2003).*

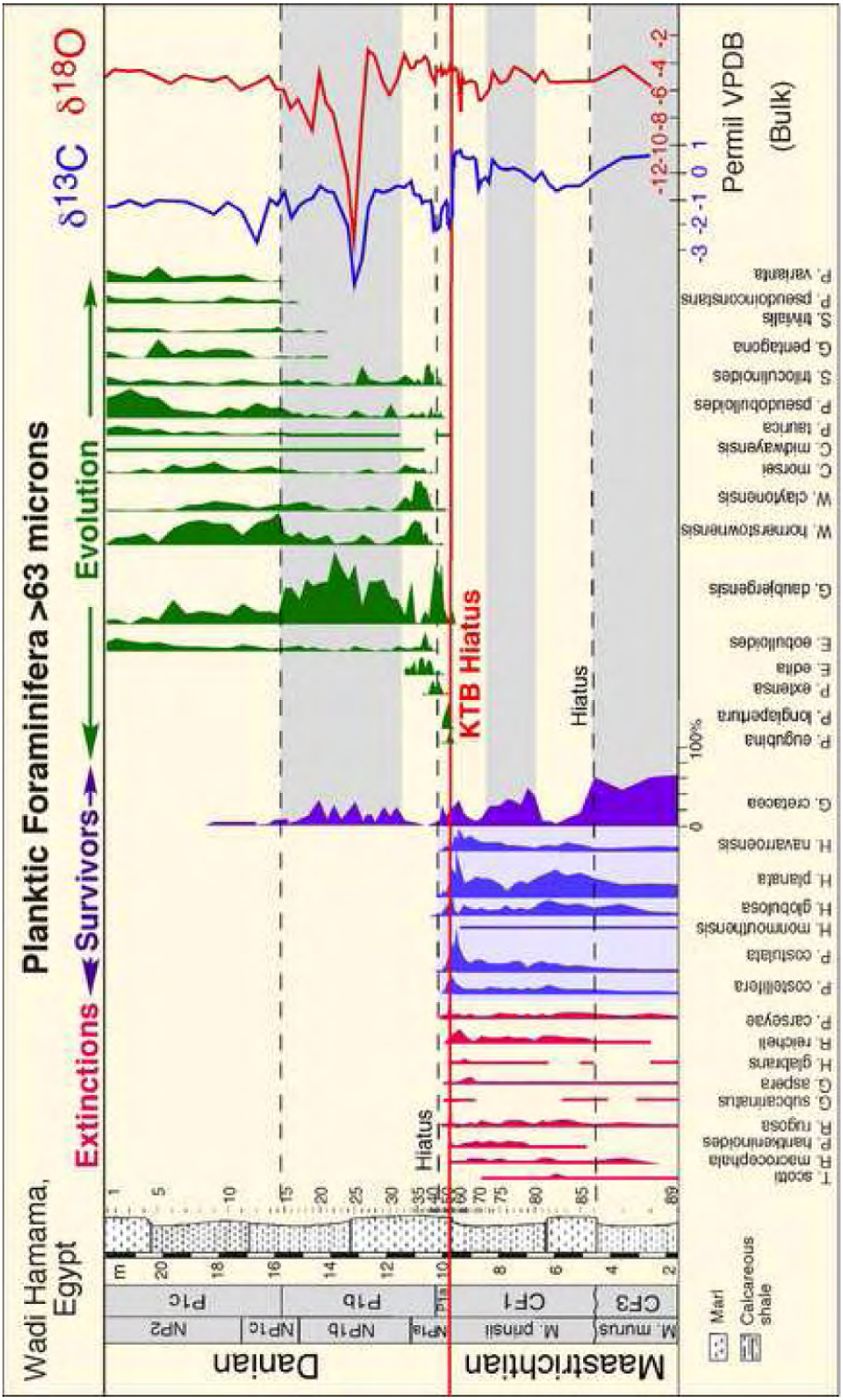

Figure. 7. *Relative species abundances of planktic foraminifera (>63μm) and $\delta^{13}C$ at Wadi Hamama, Egypt. High abundances of Guembelitria cretacea mark intervals high environmental stress. Globoconusa daubjergensis reflects high-stress in subzone P1a(2) and zone P1b. Negative $\delta^{13}C$ excursions at the KTB and in zone P1b coincide with lithological changes and a KTB hiatus.*

At Wadi Hamama, zone CF3 marks the base of the section (1.5-4.5 m), which is dominated by *Guembelitria* blooms (60%, Fig. 7). Heterohelicids are common and globotruncanids very rare (Plate II). *Guembelitria* blooms abruptly end at the lithologic change from grey shale to marl marking a hiatus between CF3 and CF1 similar to Gebel Qreiya.

***Zone CF2 (65.66-65.78 Ma)*:** This zone is defined by the interval between the LO of *Gansserina gansseri* and FO of *Plummerita hantkeninoides* (Fig. 5). At Gebel Qreiya and Wadi Hamama, the co-occurrence of these index species indicates a hiatus (Figs. 6, 7) with at least zone CF2 missing (~150ky based on Cande and Kent (1995) or 120ky based on Gradstein (2004), Fig. 5) and probably part of zone CF3. Zone CF2 is present in the Negev sections of Israel, which were deposited in a deeper outer shelf to upper bathyal (300-500 m) environment (Adatte et al., 2005).

***Zone CF1 (65.50-65.66 Ma)*:** The total range of the index species *P. hantkeninoides* defines zone CF1. At Gebel Qreiya, zone CF1 spans a 2 m interval below the KTB (17.5-19.5 m, Fig. 6) with *P. hantkeninoides* (Plate I, 11-14) consistently present. The CF1 assemblage is considerably lower (~20-30%) in species richness compared with older Maastrichtian biozones. Globotruncanids (Plate II) are very rare. Heterohelicids and *G. cretacea* alternate in dominating the assemblages. Two peaks of *G. cretacea* are observed within CF1 although the distribution is uncertain due to hiatuses at the top and bottom of the zone (Fig. 6).

At Wadi Hamama, zone CF1 spans about 5 m below the KTB, but, just as at Gebel Qreiya this biozone is truncated by hiatuses at the top and bottom leaving the true distribution of *Guembelitria* peaks uncertain. However, similar to Qreiya *Guembelitria* blooms dominate various intervals (Fig. 7). Most globotruncanids (Plate II) and rugoglobigerinids (Plate I, 9-16) disappeared at or below the KTB and species diversity is very low.

At Wadi Nukhul (Sinai), less than 1 m of zone CF1 was analyzed quantitatively because species could not be freed from the limestones below this interval (Fig. 8). In the lower part of the analyzed interval, heterohelicids dominate especially *H. navarroensis, H. planata, H. globulosa, H. costulata* and *H. costellifera* whereas *G. cretacea* remains very low (<15%). In the 20 cm below the KTB heterohelicids decrease and *G. cretacea* dominates (~50%). Species richness (25 species) reflects deposition in a middle to outer shelf environment (Keller and Abramovich, 2009). Globotruncanids and rugoglobigerinids are rare to few, although this is partly an artifact due to sample processing from limestones.

Definition of the KT boundary

The KT boundary is one of the easiest epoch boundaries to identify, whether based on lithological changes in the field, geochemical analysis in the laboratory, or fossil content. A set of five KTB-identifying criteria, originally proposed by the ICS working group during 1980 - 1990s, have proven globally applicable and independently verifiable: (1) mass extinction of Cretaceous planktic foraminifera, (2) evolution of the first Danian species, (3) KTB clay and red layer, (4) Ir anomaly, and (5) $\delta^{13}C$ shift (review in Keller, 2011). In Central Egypt, the Sinai and Israel the KTB transition is generally marked by erosion and condensed sedimentation of the earliest Danian and across the KTB (e.g., Keller and Benjamini, 1991; Keller, 2002; Keller et al., 2002, 2004; Tantawy, 2003). Nevertheless, the KT transition can be easily identified based on the defining criteria, except for the Ir anomaly, which may be concentrated at the hiatus due to redox concentrations.

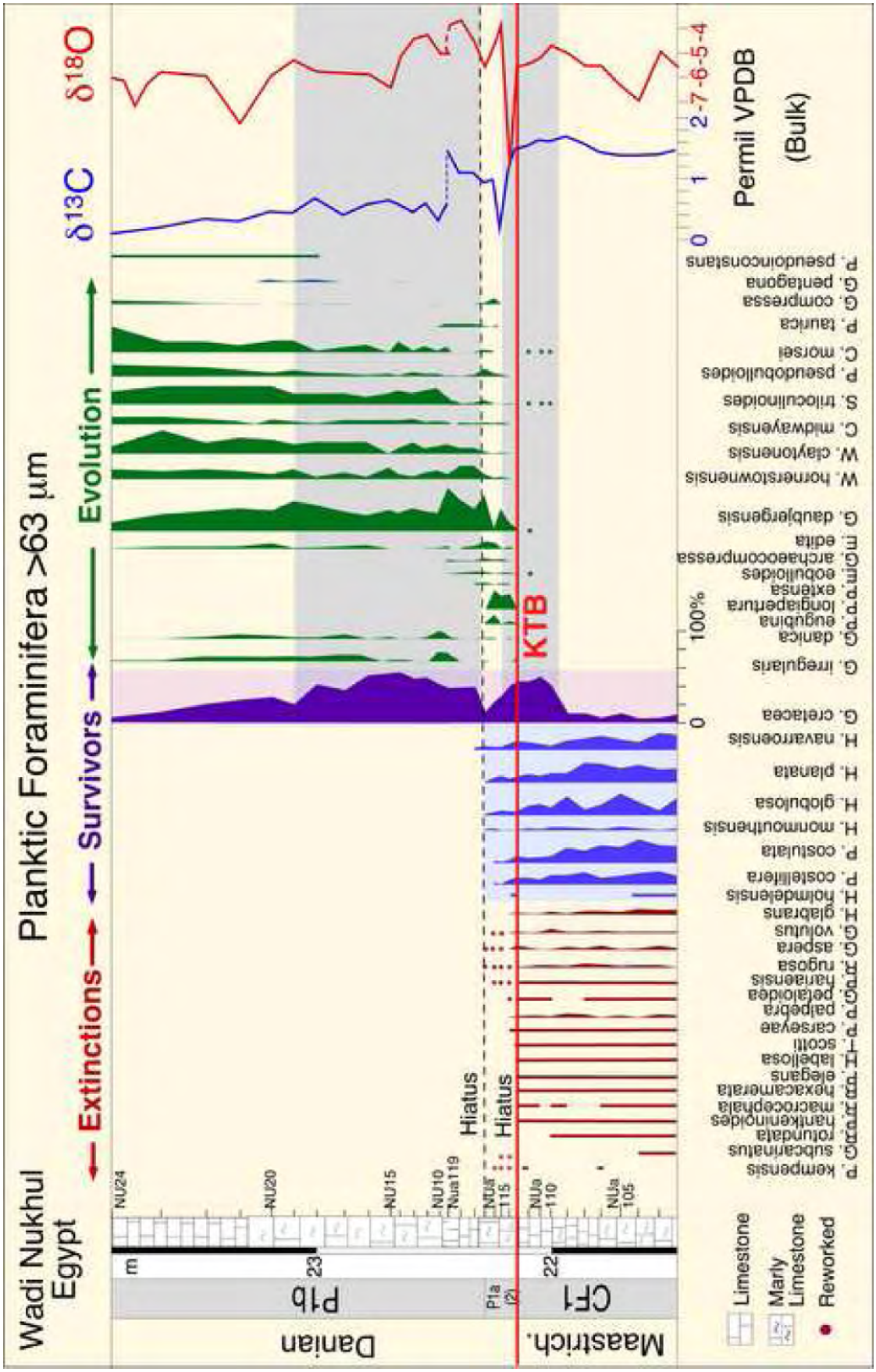

***Figure**. 8. Relative abundances of planktic foraminifera (>63µm), oxygen and carbon isotopes at Wadi Nukhul, Sinai. Note the $\delta^{18}O$ excursion near the KTB hiatus is due to abundant reworked Cretaceous species in bulk sediments analyzed. $\delta^{13}C$ exursions are observed in the upper subzone P1a(2) and lower part of zone P1b.*

Zone P0: This zone marks the base of the Danian in the interval between the mass extinction horizon and the first occurrence of *Parvularugoglobigerina eugubina* (Fig. 5). In complete KT sequences, zone P0 consists of a dark organic-rich KT clay layer with a 2-4 mm thin red oxidized layer enriched in iridium (Molina et al., 2006; Keller, 2011). Zone P0 is likely absent in Egyptian sections because of the KTB hiatus. At Gebel Qreiya, a thin dark clay and 1 cm red clay layer with a 5.4 ppb Ir anomaly overlies an erosional surface that truncates burrows of the underlying marl unit (Figs. 5, 6, Keller, 2002). This rather small anomaly is likely linked to fluctuating redox conditions commonly associated with condensed sedimentation (e.g., Donovan et al., 1988; Bruns et al., 1997; Miller et al., 2010; Gertsch et al., 2011). At Wadi Hamama, no clay layer is present and the KTB hiatus is marked by a lithologic change from marly shale to marl (Fig. 7). At Wadi Nukhul, the KTB clay layer is also missing and the boundary is marked by an undulating erosional surface (Figs. 4, 8). Reworked Cretaceous species are common in the overlying early Danian sediments.

Zone P1a**:** This zone is identified by the total range of *Parvularugoglobigerina eugubina* (Plate III, 13-14) and can be subdivided into P1a(1) and P1a(2) based on the FO of *Parasubbotina pseudobulloides* and/or *Subbotina triloculinoides* (Fig. 5, Plate III, 5-6 and 1-2, respectively). At all three sections examined, subzone P1a(2) directly overlies the KTB. This indicates that the earliest Danian subzone P1a(1) and zone P0 are missing. Erosion of the earliest Danian is commonly observed in KTB sections throughout Egypt, Sinai and the Negev (Keller and Benjamini, 1991; Keller, 2002; Keller et al., 2002; Tantawy, 2003; Adatte et al., 2005), as well as Madagascar (Abramovich et al., 2002), South Atlantic (Li and Keller, 1998a), South America (Brazil, Argentina; Keller et al., 2007; Gertsch et al., 2013), Central America, (Keller et al., 2003, 2009b) and North Atlantic (Keller et al., 1993; 2013).

At Gebel Qreiya and Wadi Hamama, subzone P1a(2) spans 50 cm of dark-grey marly shale, whereas at Wadi Nukhul only 15 cm is present (Figs. 6-8). *Parvularugoglobigerina* spp. dominate and show peak abundance ranging from 50-60% at Qreiya and Hamama and ~30% at Wadi Nukhul. *Guembelitria* is the other dominant group with maximum abundances of 75% at Qreiya, 50% at Wadi Nukhul and 30% at Hamama. The high variability in *Guembelitria* abundance between sections is mainly due to hiatuses and the resultant fragmented stratigraphic record of zone P1a with only part of subzone P1a(2) present. *Chiloguembelina* spp. (Plate IV, 5, 8) and *Woodringina* spp. (Plate IV, 6-7) are present but not abundant.

A hiatus is identified at the top of P1a(2) in all three sections by the abrupt termination of abundant *Parvularogoglobigerina* and *Guembelitria* species followed by the abrupt dominance of *Globoconusa daubjergensis* (Plate IV, 3-4, 9-12). In more complete stratigraphic records termination and onset of these species is significantly more gradual. Apart from *Guembelitria cretacea*, other Cretaceous survivor species (e.g., *Heterohelix globulosa, H. planata, H. navarroensis, P. costulata, Hedbergella monmouthensis, H. holmdelensis)* are identified based on their consistent presence and early Danian stable isotope signals in zone P0 and subzone P1a(1) in expanded and relatively complete KTB sequences (Barrrera and Keller, 1990; Pardo and Keller, 2008). In Egypt and Israel where the early Danian is very incomplete with P0 and P1a(1) missing (Keller and Benjamini, 1991; Keller, 2002), the sporadically present Cretaceous survivor species in P1a(2) may be reworked.

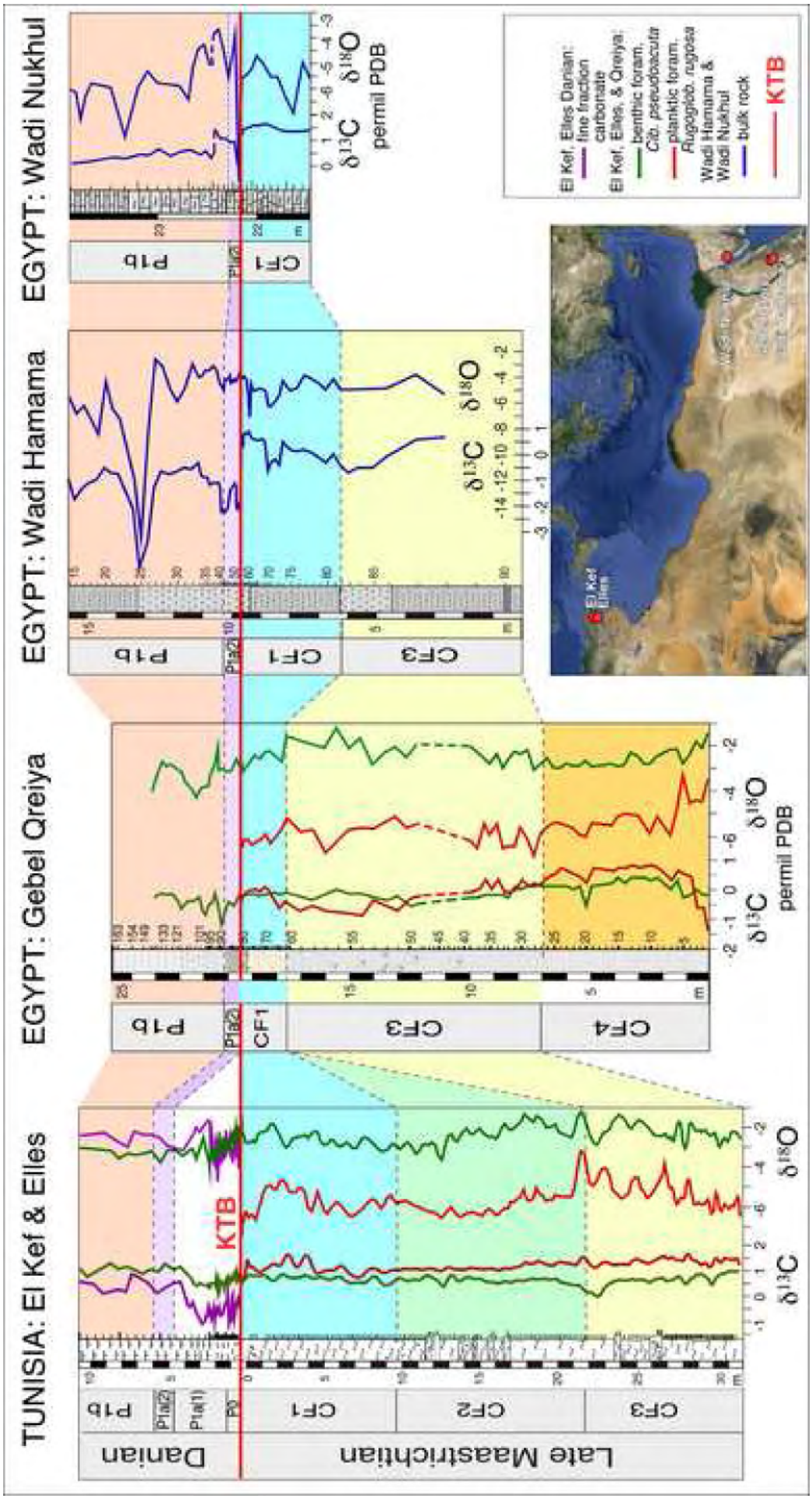

***Figure**. 9. Carbon and oxygen isotopes of three sections from central Egypt and Sinai compared with Elles, (Maatrichtian, Stüben et al., 2003) and El Kef, Tunisia (Danian, Keller and Lindinger, 1989). Inset shows the present day location of these sections.*

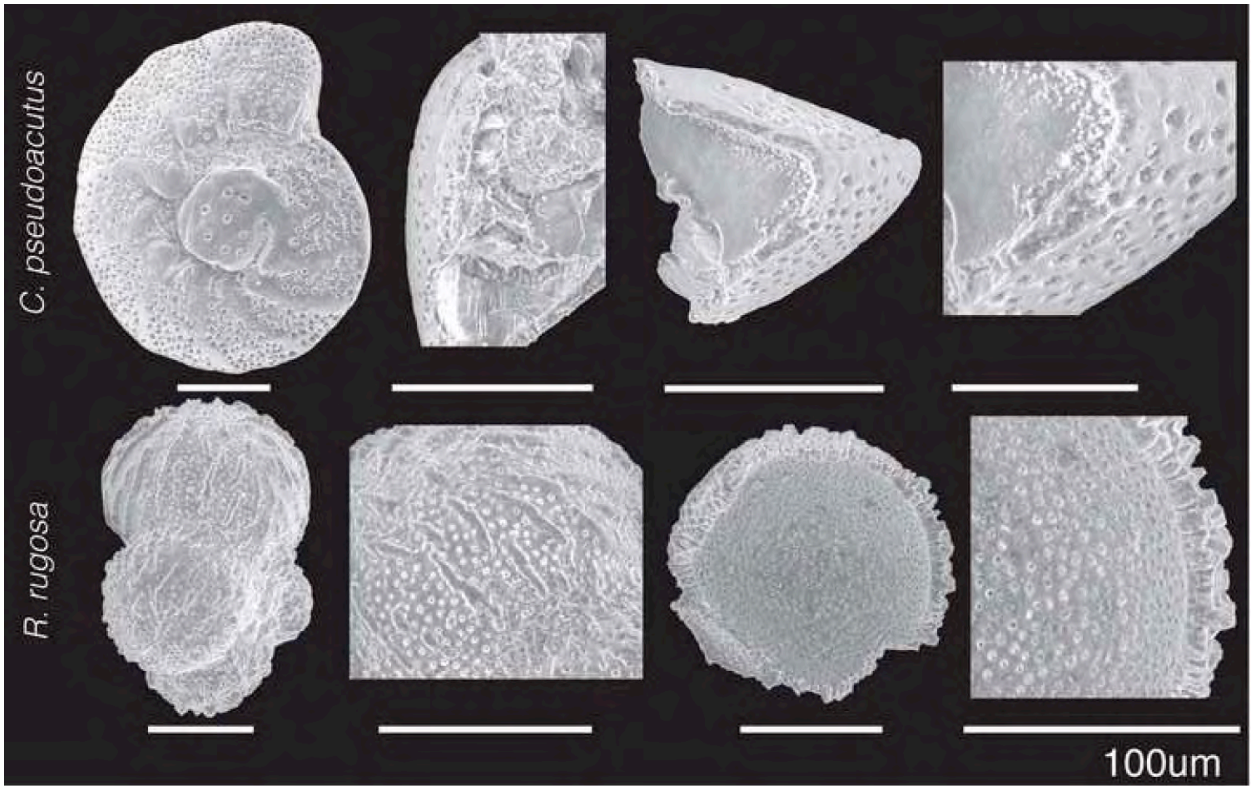

Figure 10*. Scanning electron micrograph (SEM) images of planktic (R. rugosa) and benthic (C. pseudoacutus) foraminifers analyzed for stable isotopes. Note that the relatively well-preserved planktic tests show some recrystallization and calcite overgrowth and benthic foraminiferal tests are infilled with secondary calcite.*

Biozone P1b**:** This zone is the interval between LO of *P. eugubina* and FO of *Subbotina varianta* (Fig. 5). Zone P1b spans ~5 m at Gebel Qreiya, 6 m at Wadi Hamama and the top 1.5 m of Wadi Nukhul (Figs. 6-8). *Parvularugoglobigerina extensa* (Plate III, 15-16) and *E. edita* (Plate IV, 1-2) disappear in the lower part of zone P1b. Most of the P1b species assemblages include survivors from zone P1a. *Praemurica pseudoinconstans* first appears in zone P1b, as also observed in the northwest Atlantic (Keller et al., 2013). Zone P1b is dominated by alternating abundances of *Guembelitria* spp. (*G. cretacea, G. trifolia, G. irregularis;* Plate IV, 9, 10, 12), *Globoconusa daubjergensis* (Plate IV, 3-4) and biserial species (*Woodringina hornerstownensis, W. claytonensis, Chiloguembelina morsei;* Plate IV, 5-8) suggesting a succession of variable high-stress environments (Figs. 6-8). At the top of zone P1b *Guembelitria* spp. and *G. daubjergensis* decrease sharply and biserial species dominate in P1c. This changeover is a secondary marker for the P1b/P1c boundary.

Biozone P1c**:** Biozone P1c spans the interval between FO of *Subbotina varianta* (Plate III, 3-4) and FO of *Praemurica trinidadensis.* Zone P1c was recovered at Wadi Hamama (Figs. 5, 7). Most of the P1c species assemblage includes survivors of zone P1b. Biserial species dominate zone P1c and the overall species richness, species size and morphology increases in P1c.

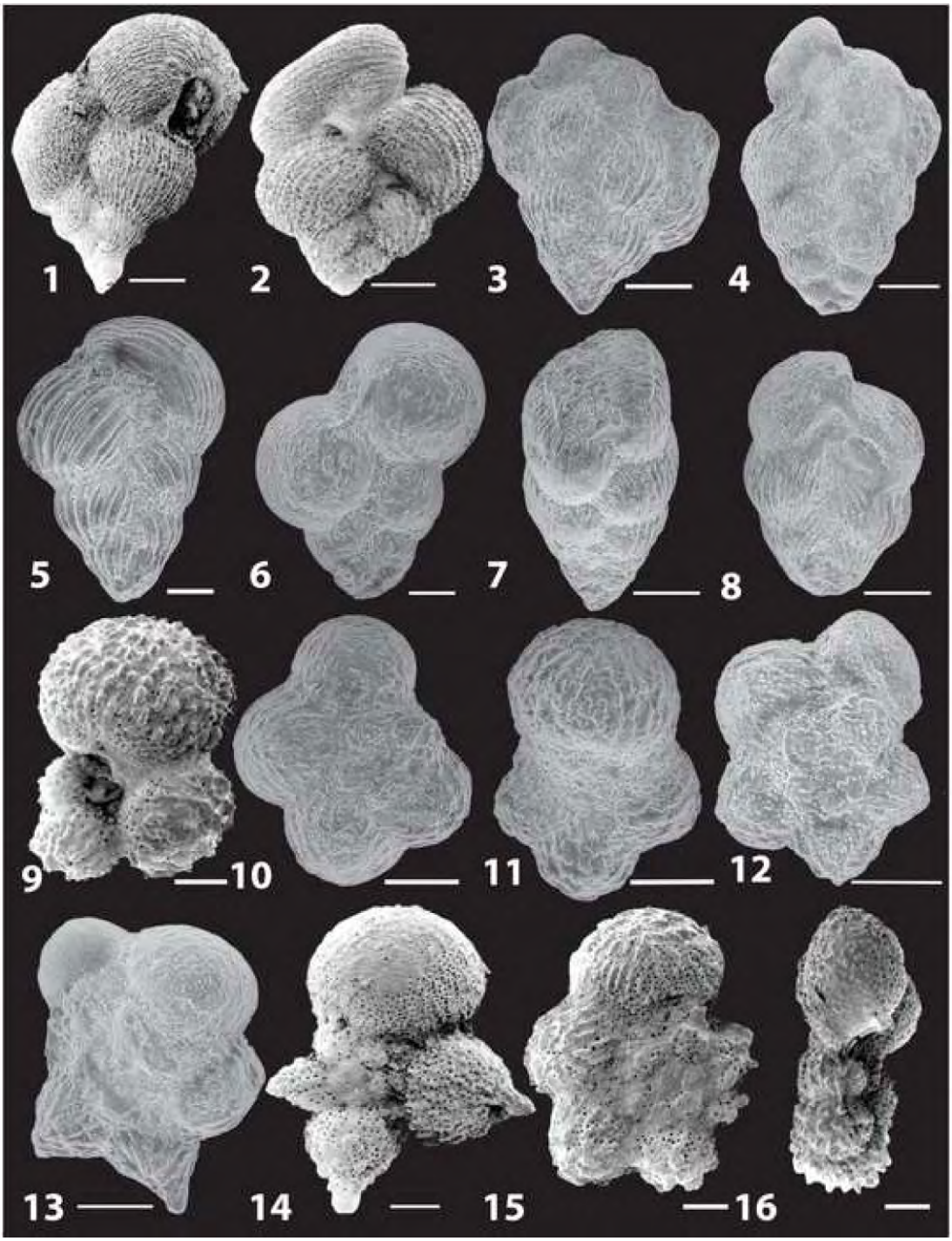

Plate 1. Maastrichtian planktic foraminifera from Gebel Qreiya (SEM images from Keller, 2002) and Wadi Nukhul, Egypt, scale bar = 50 μm.

1. Planoglobulina carseyae (Plummer), Gebel Qreiya., *2. Pseudoguembelina palpebra* (Brönniman and Brown), Gebel Qreiya. *3. Planoglobulina brazoensis* (Martin), Wadi Nukhul. *4. Pseudoguembelina hariaensis* (Nederbragt), Wadi Nukhul. *5. Pseudoguembelina costulata* (Cushman), Wadi Nukhul. *6. Heterohelix globulosa* (Ehrenberg), Wadi Nukhul. *7. Pseudotextularia elegans* (Rzehak), Wadi Nukhul. 8. *Heterohelix labellosa* (Nederbragt), Wadi Nukhul. *9. Rugoglobigerina macrocephala* (Brönniman), Gebel Qreiya. *10. Rugoglobigerina rugosa* (Plummer), Wadi Nukhul. *11-13. Rugoglobigerina rugosa- Plummerita hantkeninoides* intermediate morphologies, Wadi Nukhul. *14. Plummerita hantkeninoides* (Brönniman), Gebel Qreiya. *15-16. Trinitella scotti* (Brönniman),Wadi Nukhul.

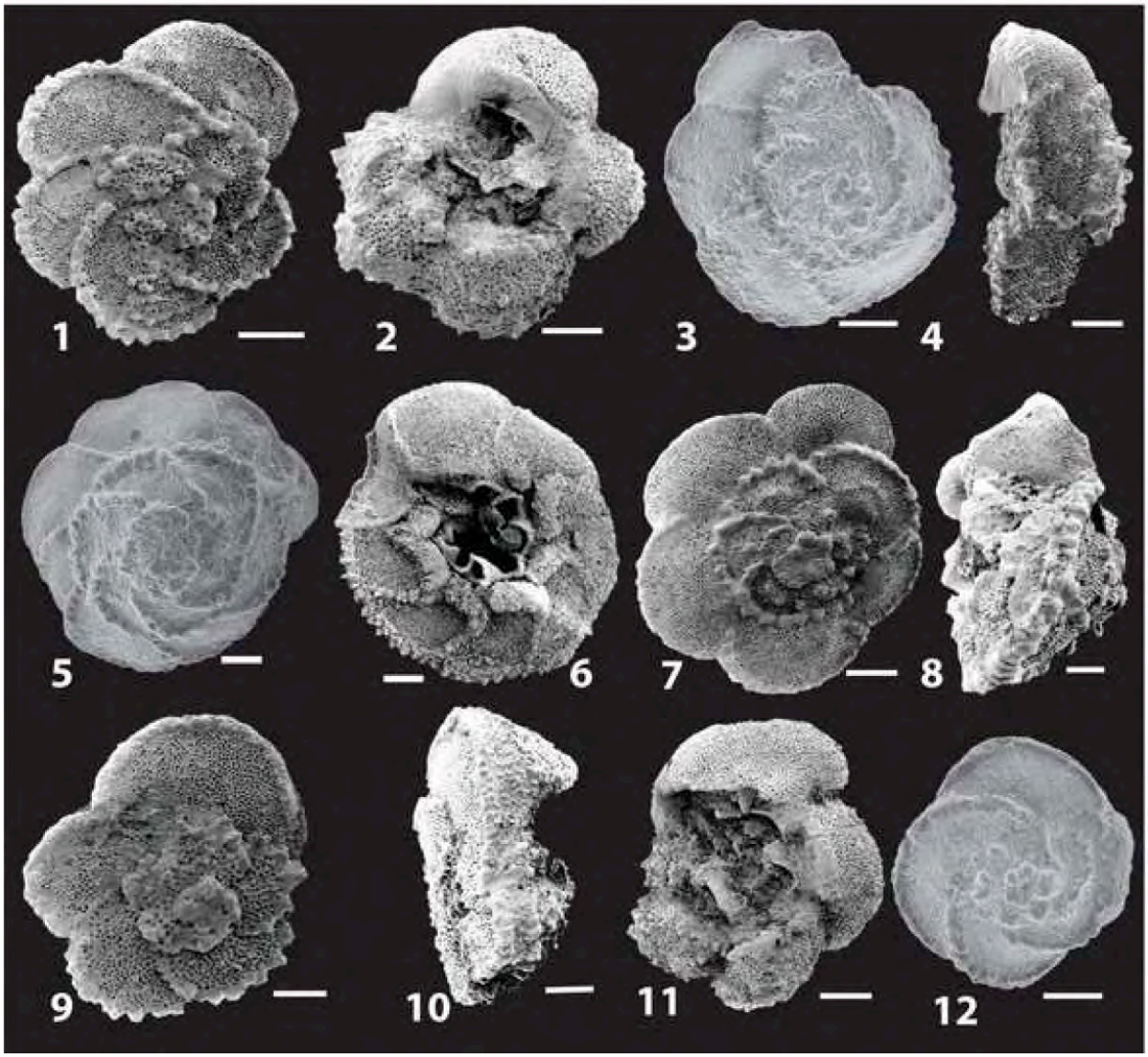

Plate 2. Maastrichtian planktic foraminifera from Gebel Qreiya (SEMS images from Keller, 2002) and Wadi Nukhul, Egypt, scale bar = 50 µm.

1-2. *Globotruncana rosetta* (Carsey), Gebel Qreiya. 3-4. *Globotruncanita conica* (White), spiral view- Wadi Nukhul, side view- Gebel Qreiya. *5-6. Globotruncanita stuarti* (de Lapparent), spiral view- Wadi Nukhul, umbilical view- Gebel Qreiya. *7-8. Globotruncana dupeublei* (Caron), Gebel Qreiya. *9-11. Globotruncana aegyptiaca* (Nakkady), Gebel Qreiya. *12. Globotruncanita pettersi* (Gandolfi),Wadi Nukhul.

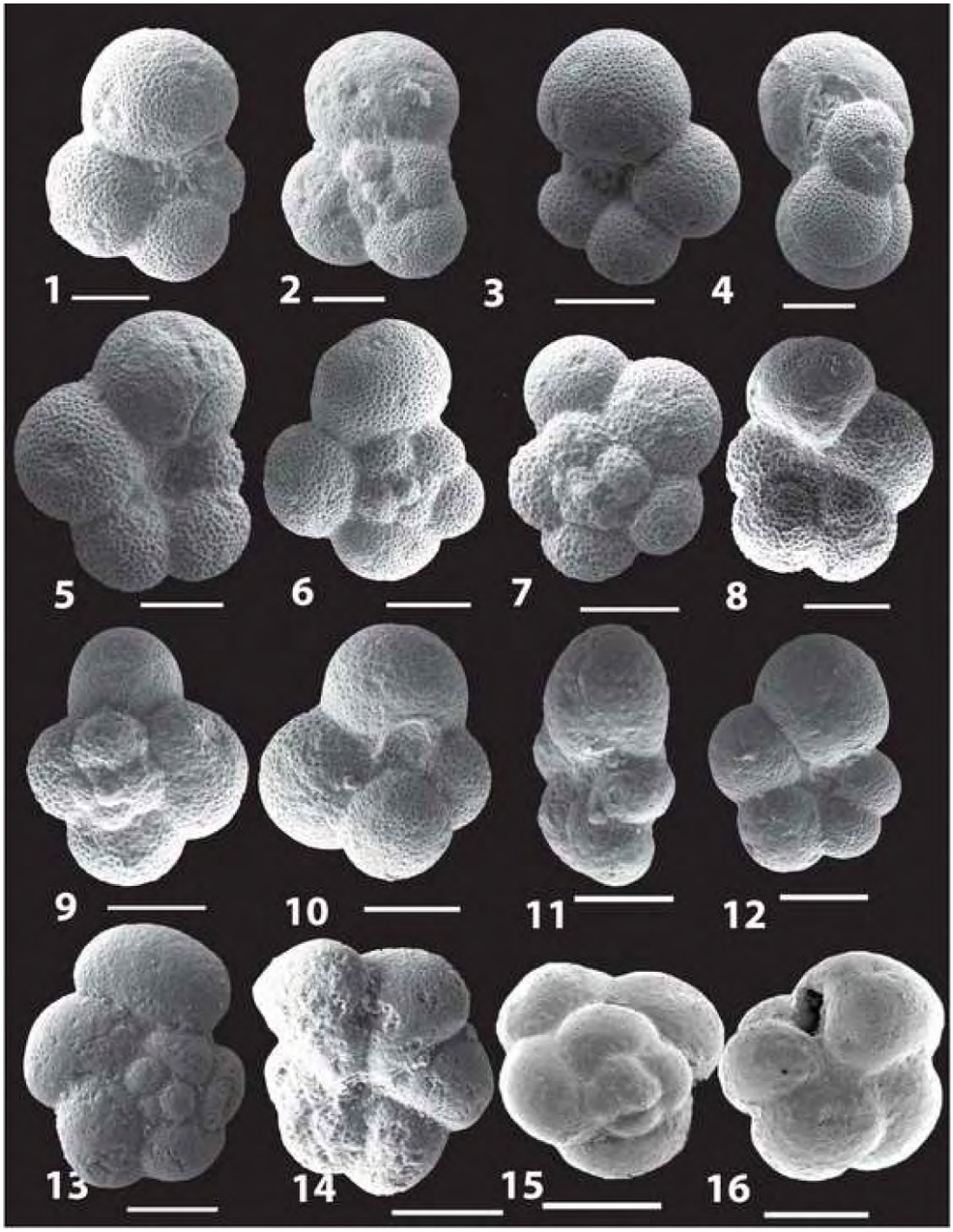

Plate 3. Danian planktic foraminifera from Gebel Qreiya (SEM images from Keller, 2002) and Wadi Nukhul, Egypt, scale bar = 100 µm.

1-2. *Subbotina triloculinoides* (Plummer), Wadi Nukhul. 3-4. *Parasubbotina varianta* (Subbotina), Wadi Nukhul. 5-6. *Parasubbotina pseudobulloides* (Plummer), Wadi Nukhul. 7-8. *Globigerina (Eoglobigerina) pentagona* (Morozova), Wadi Nukhul. 9-10. *Subbotina trivialis* (Subbotina), Wadi Nukhul. 11-12. *Globanomalina compressa* (Plummer), Wadi Nukhul. 13-14. *Parvularugoglobigerina eugubina* (Luterbacher and Premoli Silva), Wadi Nukhul. 15-16. *Parvularugoglobigerina extensa* (Blow), Gebel Qreiya.

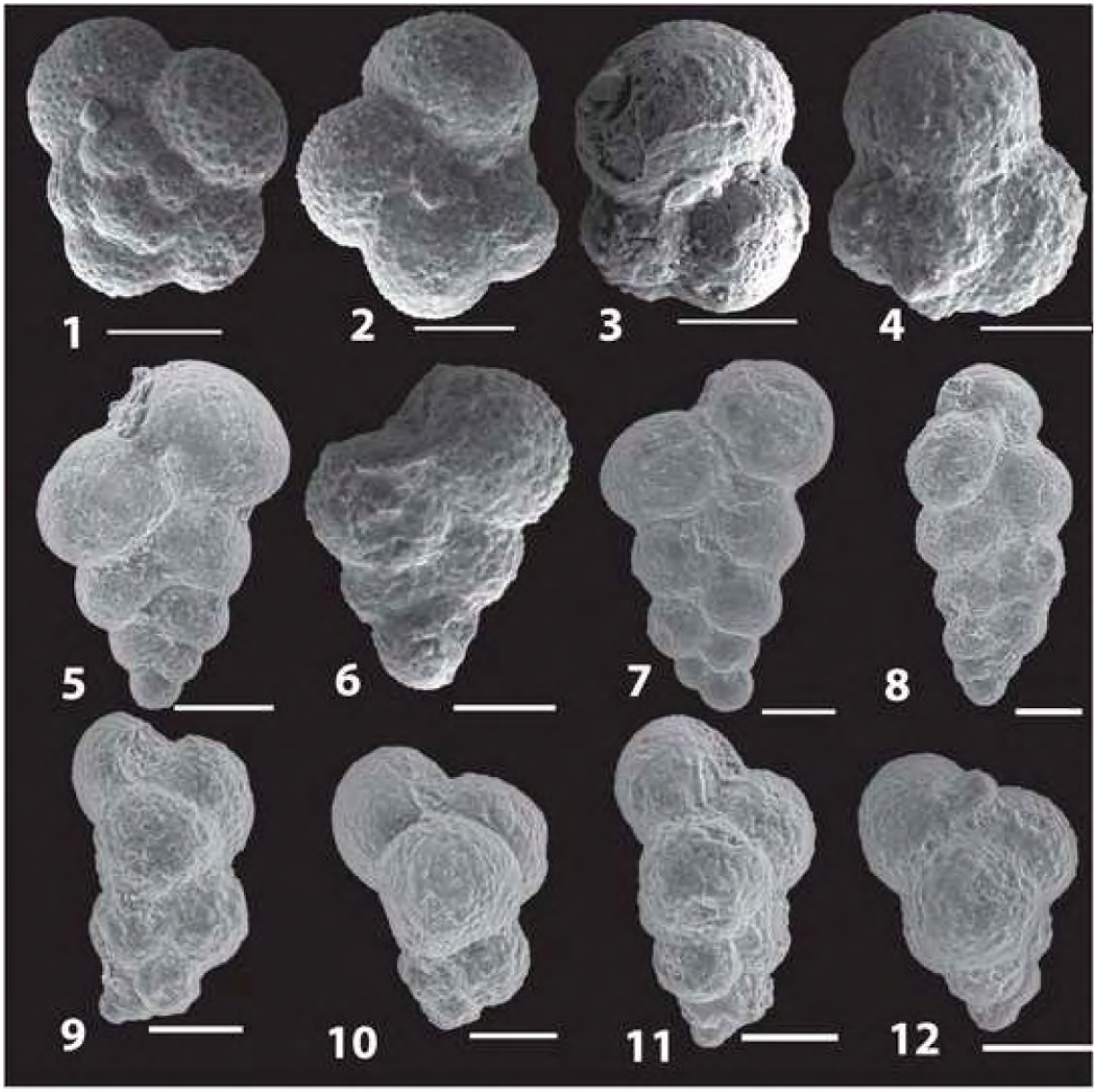

Plate 4. Danian planktic foraminifera from Wadi Nukhul, Egypt, scale bar = 50 µm.
1-2. *Eoglobigerina edita* (Subbotina) 3-4. *Globoconusa daubjergensis* (Brönnimann) 5. *Chiloguembelina midwayensis* (Cushman) 6. *Woodringina claytonensis* (Loeblich & Tappan) 7. *Woodringina hornerstownensis* (Olsson) 8. *Chiloguembelina morsei* (Kline) 9-10. *Guembelitria irregularis* (Morozova) 11. *Guembelitria danica* (Hofker) 12. *Guembelitria cretacea* (Cushman)

6. STABLE ISOTOPES

Stable isotopes ($\delta^{13}C$ and $\delta^{18}O$) measured for all three sections from Egypt (Tables 1-3) are compared with data from Elles and El Kef, Tunisia, for the Maastrichtian-Danian interval (Keller and Lindinger, 1989; Stüben et al., 2003; Fig. 9). Although overall trends are similar for the late Maastrichtian, direct comparison is difficult due to the presence of hiatuses in Egypt.

The $\delta^{13}C$ record for the KTB transition at Gebel Qreiya was discussed in Keller et al. (2002). The key features include the decreasing surface-to-deep $\delta^{13}C$ trend with a reversal in planktic and benthic values in the upper part of zone CF3 (planktic $\delta^{13}C$ 0.2-0.8‰ lighter than benthic

values, Fig. 9). In zone CF1, planktic values increase by 0.7‰ and decrease by 0.5‰ at the KTB hiatus. In contrast, at Elles, El Kef and globally planktic $\delta^{13}C$ values decrease 2-3‰ at the KTB. This difference is due to the hiatus in the Egypt sections with the KTB interval missing. Benthic values gradually decrease in zone P1a(2) reach minimum values at the P1a(2)/P1b hiatus and fluctuate in P1b.

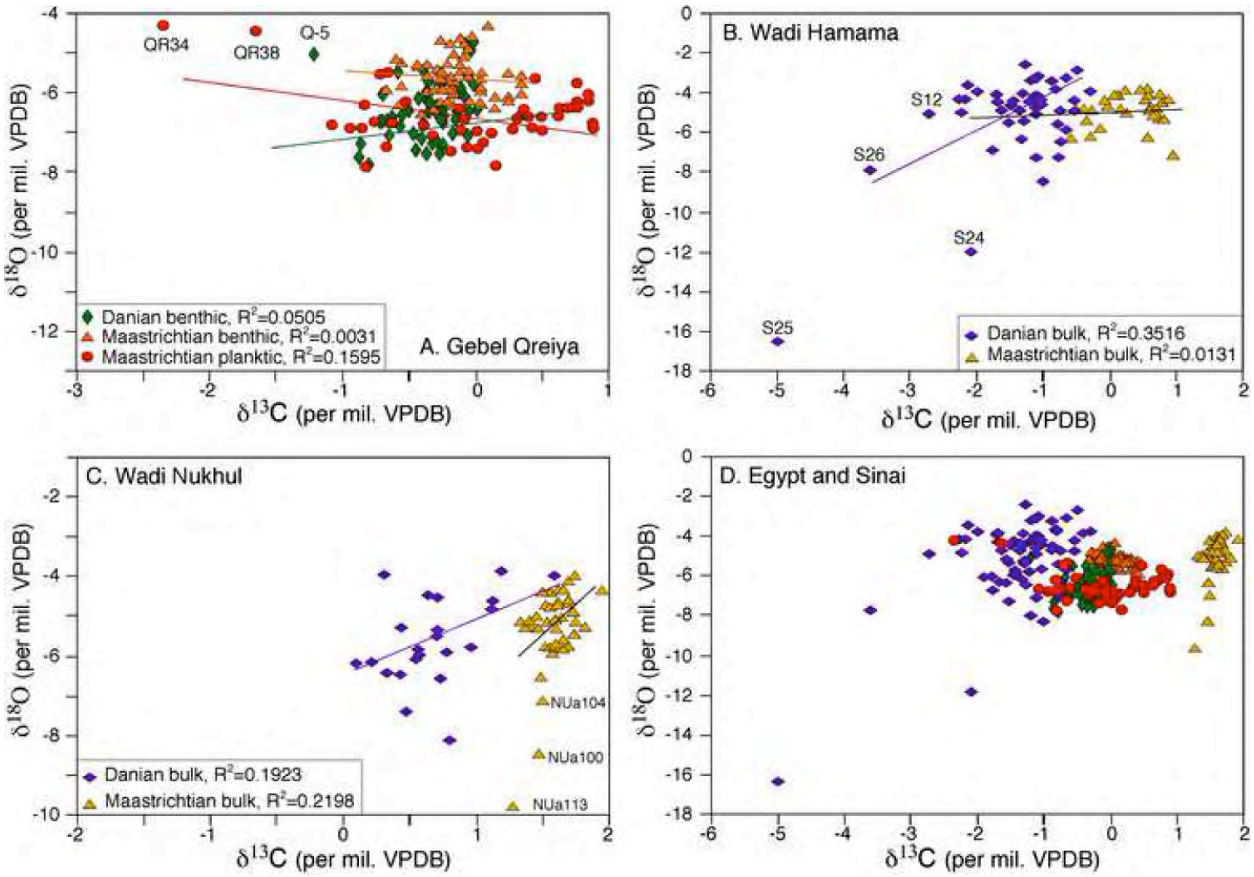

Figure 11. *$\delta^{13}C$ and $\delta^{18}O$ cross-plots for the three sites analyzed in Egypt. The generally low correlation coefficient indicates a limited degree of diagenetic alteration. Gebel Qreiya, planktic foraminiferal tests show a slightly higher R^2 value, indicating the higher susceptibility of thin planktic tests to diagenesis as compared to thick-walled benthics.*

At Wadi Hamama and Wadi Nukhul only bulk rock isotope analyses were performed because of poor preservation and insufficient quantity of early Danian planktic foraminifera for analysis. The late Maastrichtian $\delta^{13}C$ trend at Hamama is similar to the planktic $\delta^{13}C$ record of Gebel Qreiya with low values in zone CF3, increased values in zone CF1 and a negative shift coincident with the KTB hiatus also observed at Wadi Nukhul (Fig. 9). Above the KTB the earliest Danian is reduced to a small part of subzone P1a(2) due to erosion. A 1‰ negative excursion at or near the P1a(2)/P1b hiatus is followed by partial recovery although $\delta^{13}C$ values remain about 2‰ below Maastrichtian values. At Wadi Hamama, a major negative excursion in zone P1b at a lithologic change from marl to dark shale occurs nearly 3 m above the hiatus. This interval was not recovered in the other Egypt or Tunisia localities, but was observed in Israel (Magaritz et al., 1992).

The $\delta^{18}O$ record at Gebel Qreiya shows a 2‰ negative shift in planktic $\delta^{18}O$ and 1.5‰ in benthic $\delta^{18}O$ values in the basal part of zone CF4. In zone CF3, increases in planktic and benthic

$\delta^{18}O$ values (0.5-0.7 ‰) are similar to Elles. The entire zone CF2 and the lower part of CF1 are missing at Gebel Qreiya and Wadi Hamama (Figs. 6, 7). All three localities show minimum $\delta^{18}O$ values at the top of CF3, although the CF3-CF1 hiatus prevents direct comparison with Elles. The top of zone CF1 at Qreiya and Hamama is reduced due to erosion at the KTB. Bulk isotopes at Wadi Hamama and Wadi Nukhul show the same trends as the planktic $\delta^{18}O$ values for Elles and Gebel Qreiya, although there are unique local short-term shifts (e.g., Danian of Wadi Hamama, about 3.5 m above the KTB, Fig.9).

7. DISCUSSION

7.1. Stable isotopes and Diagenesis

At Gebel Qreiya, the planktic and benthic foraminifera (*R. rugosa, Cibicidoides pseudoacutus)* analyzed show diagenetic alteration of test calcite. This is evident in the foraminifer test wall structure with calcite overgrowth and the benthic tests commonly infilled with secondary calcite (Fig. 10). Recrystallization of foraminiferal tests tends to shift $\delta^{18}O$ values towards more positive values and carbon isotopes towards more negative values, thus biasing isotopic values towards cooler temperatures and lower productivity, although trends tend to be preserved (Schrag et al., 1995; Pearson et al., 2001).

Diagenetic effects can be observed in all three Egyptian sections analyzed. Maastrichtian $\delta^{18}O$ values for planktic foraminifera and bulk fine fraction carbonate vary between -4 to -6 ‰ in all sections, including Elles and El Kef, with an isolated larger excursion at Wadi Hamama. Therefore, the $\delta^{18}O$ values cannot be used for calculation of absolute temperature, although trends are preserved. Very limited recrystallization can result in the observed negative values as indicated by the very low correlation coefficients of $\delta^{13}C$-$\delta^{18}O$ cross plots (Fig. 11) and relatively constant diagenetic effects indicated by the surface-to-bottom water $\delta^{18}O$ gradient of 3-4‰. Burial diagenesis typically decreases this gradient (Schrag et al., 1995; Pearson et al., 2001; Stüben et al., 2003).

Climate trends in Tunisia and Egypt indicate warming in zone CF4 (Qreiya) followed by cooling in CF3 (Qreiya and Elles), which culminates in maximum cooling at the CF3/CF2 boundary coincident with a major sea level regression and erosion in shelf areas (Li and Keller, 1998a; Keller et al., 2002). At Elles, the expanded zones CF1-CF2 record shows several intervals of surface warming, including two in CF1 (Fig. 9, Stüben et al., 2003).

At Qreiya, only a single warm interval is recorded in CF1 due to the KTB hiatus and similarly incomplete CF1-CF2 records are present at Wadi Hamama and Wadi Nukhul. The early Danian record in Egypt is also very incomplete with a hiatus between zones P1a/P1b, and another hiatus with the earliest Danian subzone P1a(1) and zone P0 missing (~100 ky) along with the uppermost part of Maastrichtian zone CF1 (Fig. 5).

In zone P1b, major negative $\delta^{18}O$ excursions are observed at lithologic changes that are partly due to diagenesis, but also record climate warming as indicated by blooms of *G. cretacea* and *G. daubjergensis* (Fig. 9). This warm interval may correspond to the early Danian Dan-C2 warm event near the top of C29r correlative with phase-3 Deccan volcanism (Quillévéré et al., 2008; Punekar et al., in press).

***Table 1**. Gebel Qreiya, Egypt, carbon and oxygen stable isotope data (per mil. VPDB) for planktic (Rugoglobigerina rugosa) and benthic (Cibicidoides pseudoacutus) foraminifera.*

Benthic			Planktic		
Sample	δ13C	δ18O	Sample	δ13C	δ18O
37	-1.73	-3.34	37	-3.43	-6.72
36	-2.37	-3.23	36	-3.67	-6.18
35	-0.3	-3.0	35	-0.1	-7.2
34	-0.3	-3.3	34	0.0	-7.5
33	-0.2	-3.6	33	0.3	-6.4
32	-0.2	-3.8	32	0.0	-6.9
31	-0.2	-3.4	31	0.3	-6.4
30	-0.2	-4.0	30	-0.1	-7.5
29	-0.3	-3.7	29	-0.1	-7.4
28	0.1	-3.3	28	0.0	-7.4
27	0.0	-3.4	27	0.3	-6.6
26	0.1	-3.2	26	0.1	-7.1
25	0.2	-4.1	25	0.1	-7.8
24	0.1	-3.8	24	0.2	-6.8
23	0.1	-3.6	23	0.4	-6.6
22	0.1	-4.0	22	0.5	-6.4
21	0.1	-4.0	21	0.7	-6.4
20	0.1	-3.8	20	0.6	-6.5
19	0.0	-3.9	19	0.5	-6.6
18	0.1	-3.9	18	0.4	-6.9
17	-0.6	-3.7	17	0.2	-7.0
16	0.1	-3.9	16	0.7	-6.4
15	0.2	-3.8	15	0.6	-6.5
14	0.3	-3.9	14	0.7	-6.2
13	0.2	-3.8	13	0.7	-6.0
12	0.4	-3.3	12	0.8	-14.2
11	0.4	-3.5	11	0.7	-6.1
10	0.4	-3.8	10	0.8	-6.9
9	0.3	-3.8	9	0.8	-6.8
8	0.4	-3.5	8	0.7	-6.2
7	0.0	-3.2	7	0.3	-6.9
6	0.3	-3.2	6	0.6	-5.8
5	-0.3	-3.7	5	-2.0	-4.3
4	-0.2	-3.4	4	0.4	-5.6
3	0.0	-2.7	3	-0.6	-5.4
2	-0.2	-3.1	2	-0.6	-5.5
1	-0.2	-2.4	1	-1.4	-4.5

Table 1. Continued

	Benthic			Planktic	
Sample	δ13C	δ18O	Sample	δ13C	δ18O
48	-2.9	-4.9	48	-7.68	-9.34
47	-1.8	-3.6	47	-2.61	-7.78
46	-2.8	-4.1	46	-6.66	-7.96
45	-2.4	-3.4	45	-2.11	-7.51
44	-2.9	-4.0	44	-2.27	-7.80
43	-3.7	-3.9	43	-4.71	-7.73
42	-1.8	-3.0	42	-2.60	-7.24
41	-3.0	-3.7	41	-6.71	-7.19
40	-2.2	-3.8	40	-3.81	-7.29
39	-1.8	-3.6	39	-1.95	-7.10
38			38	-2.85	-7.09

Some puzzling features in the oxygen and carbon isotope trends at Gebel Qreiya seem to have variable origins. For example, the reverse $\delta^{13}C$ gradient (more negative planktic than benthic values) can be explained by the relatively constant terrestrial ^{12}C influx and greater recrystallization of planktic tests due to the thinner and more porous wall structure (Keller et al., 2002; Stüben et al., 2003). Intervals of low $\delta^{13}C$ planktic values are correlative with a major reduction in large specialized species (thermocline dwellers), and assemblages dominated (75-90%) by the disaster opportunist *G. cretacea* or *H. globulosa* (Fig. 12). Keller et al. (2002) attributed these changes to the maximum cooling and sea-level regression in CF3-CF2 resulting in restricted circulation in central and southern Egypt. Alternatively, the low $\delta^{13}C$ values of Dissolved Inorganic Carbon (DIC) may be due to increased terrestrial weathering and detrital influx due to drawdown of higher atmospheric pCO_2 and/or low $\delta^{13}C$ of atmospheric CO_2 associated with surface ocean acidification (recorded in partially to completely dissolved foraminifer tests). All these phenomena and the global climate warming of Zones CF2-CF1 are consistent with large-scale Deccan volcanism as observed during the main phase-2.

7.2. Paleoenvironment inferred from planktic foraminifera

Species Richness:

Low species richness (the number of species per sample) is a measure of environmental stress because high-stress environments generally exclude specialized species due to changes in oxygen, nutrient, salinity and watermass stratification (Keller and Abramovich, 2009). However, during the late Maastrichtian the constant variation between 30 and 40 species in central Egypt provides little information on stress conditions. In contrast, cumulative species richness provides an estimate of long-term evolutionary trends. Cumulative species richness is defined as the total number of species that are theoretically present in a sample based on the assumption that a

***Table 2**. Wadi Hamama, Egypt, bulk carbon and oxygen stable isotope data (per mil. VPDB).*

Sample	δ13C	δ18O	Sample	δ13C	δ18O
S1	-1.31	-4.61	S46	-2.25	-4.28
S2	-1.28	-4.01	S47	-2.10	-3.78
S3	-1.06	-4.12	S48	-1.67	-4.41
S4	-1.30	-4.13	S49	-1.42	-4.37
S5	-1.08	-4.49	S50	-1.30	-4.24
S6	-1.09	-4.94	S51	-1.12	-4.35
S7	-1.12	-4.43	S52	-1.28	-4.11
S8	-1.36	-4.69	S53	-1.97	-3.92
S9	-1.60	-4.80	S54	-2.11	-3.57
S10	-1.14	-4.48	S55	-1.69	-4.03
S11	-1.49	-5.54	S56	0.55	-4.14
S12	-2.71	-5.04	S57	0.43	-3.89
S13	-1.02	-4.57	S58	0.73	-4.07
S14	-1.26	-5.42	S59	0.84	-4.28
S15	-0.74	-5.48	S60	0.78	-5.35
S16	-1.74	-6.87	S61	0.91	-7.15
S17	-1.31	-6.27	S62	0.74	-4.49
S18	-1.10	-7.20	S63	0.67	-4.79
S19	-0.98	-8.41	S64	0.67	-5.05
S20	-0.52	-4.34	S66	0.59	-4.73
S21	-0.72	-6.44	S67	0.57	-4.83
S22	-0.76	-7.20	S68	0.63	-5.16
S24	-2.08	-11.94	S69	0.54	-6.29
S25	-4.99	-16.44	S70	-0.59	-6.25
S26	-3.57	-7.89	S71	-0.31	-6.24
S27	-1.27	-2.56	S72	-0.16	-5.80
S28	-0.65	-3.19	S73	-0.36	-5.45
S29	-0.73	-4.80	S74	0.52	-4.33
S30	-0.64	-5.80	S75	0.23	-5.06
S31	-0.49	-2.88	S76	0.15	-4.81
S32	-0.53	-4.87	S77	0.21	-3.87
S33	-0.28	-3.93	S78	0.09	-4.12
S34	-0.82	-3.83	S79	-0.09	-4.40
S35	-0.86	-3.40	S80	-0.29	-4.88
S36	-0.85	-3.40	S81	0.05	-4.17
S37	-1.17	-3.34	S82	-0.41	-4.80
S38	-1.09	-3.16	S83	-0.71	-4.94
S39	-1.13	-3.30	S84	-0.48	-4.80
S40	-1.08	-4.39	S85	-0.47	-4.80
S41	-1.09	-4.66	S86	-0.05	-4.73
S42	-1.31	-4.71	S87	0.54	-3.79
S44	-2.23	-4.97	S88	0.71	-5.31
S45	-2.14	-4.24			

Sample	δ13C	δ18O
Nu-25	0.08	-6.04
Nu-24	0.21	-5.96
Nu-23	0.32	-6.26
Nu-22	0.46	-7.27
Nu-21	0.42	-6.28
Nu-20	0.58	-5.73
Nu-19	0.56	-5.90
Nu-18	0.80	-8.00
Nu-17	0.53	-5.91
Nu-16	0.70	-5.26
Nu-15	0.77	-5.74
Nu-13	0.57	-5.80
Nu-12	0.73	-6.39
Nu-11	0.43	-5.11
Nu-10	0.69	-4.40
Nu-9	0.63	-4.27
Nu-8	0.70	-5.12
Nua-119	1.58	-3.80
Nua-118	1.18	-3.67
Nua-117	1.12	-4.50
Nua-116	0.95	-5.57
Nua-115	1.10	-4.63
Nua-114	0.30	-3.75
Nua-113	1.27	-9.63
Nua-112	1.60	-5.56
Nua-111	1.66	-5.44
Nua-110	1.75	-5.23
Nua-109	1.74	-4.68
Nua-108	1.83	-5.07
Nua-107	1.69	-5.53
Nua-106	1.55	-5.54
Nua-105	1.49	-6.32
Nua-104	1.50	-6.97
Nua-103	1.56	-4.93
Nua-102	1.58	-5.61

Table 3*. Wadi Nukhul, Egypt, bulk carbon and oxygen stable isotope data (per mil. VPDB).*

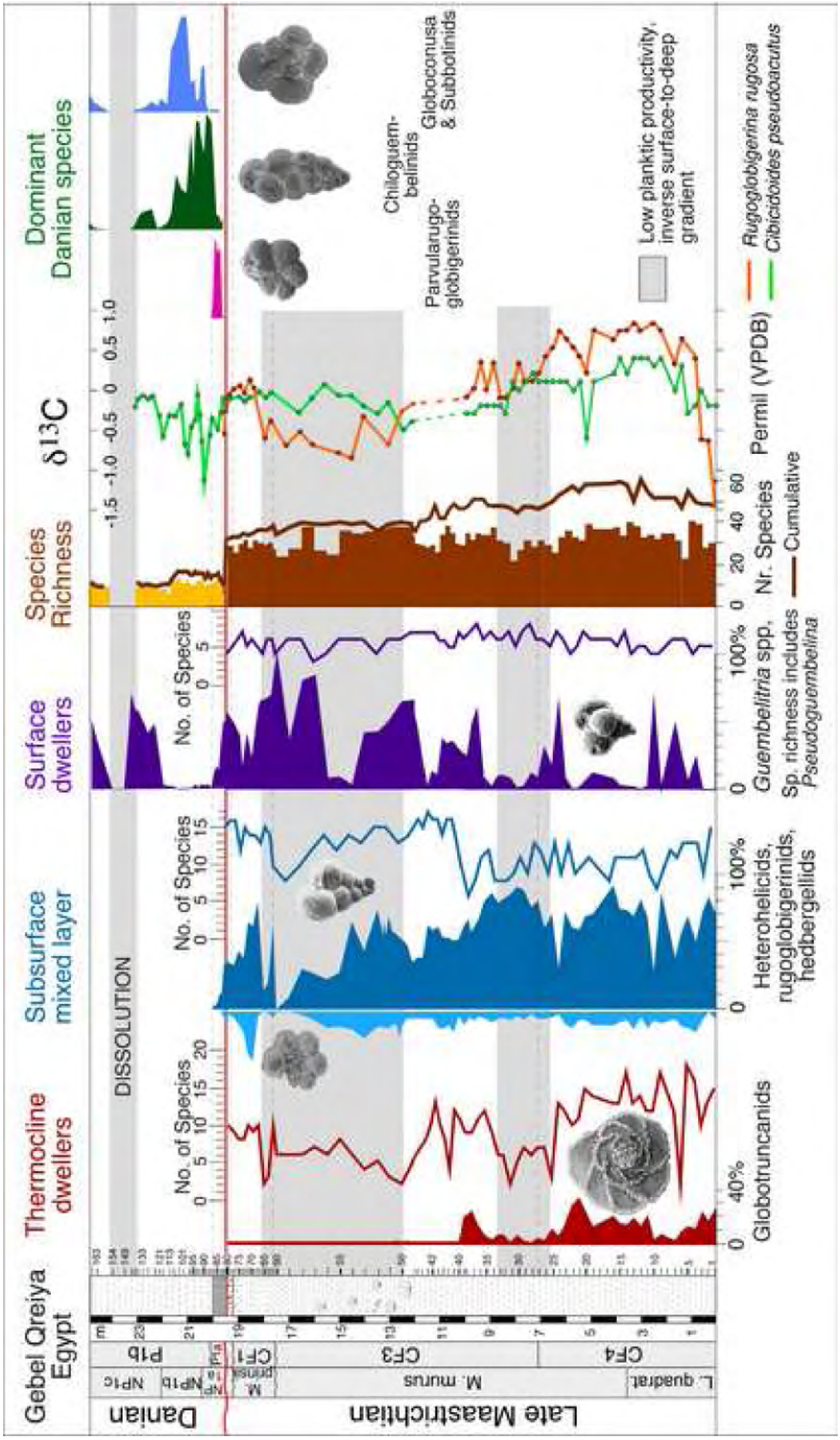

***Figure** 12. Paleoenvironmental interpretation of late Maastrichtian to early Danian planktic foraminifera and stable isotopes at Gebel Qreiya. Note the strong decrease in abundance and species diversity of globotruncanids (thermocline dwellers) in zone CF3 well before the KTB. See text for discussion*

species is present from its evolutionary first appearance to its extinction. At Gebel Qreiya, this index reveals a decreasing trend from a high of 60 species in zone CF4 to a low of 30 species at the KTB hiatus (Fig. 12). This decreasing trend parallels the surface productivity ($\delta^{13}C$), except that during the climate warming of zone CF1 species richness fails to recover probably due to continued high-stress conditions. This relationship between stress conditions and non-recovery leading up to the KTB mass extinctions is still under investigation. Species abundance variations are another index of environmental stress because they are highly sensitive to changes in oxygen, salinity, temperature, nutrients and a host of still unknown other environmental parameters.

Large specialized species: Intermediate or thermocline dwellers

We can group species based on stable isotope depth ranking into surface, subsurface mixed layer, intermediate or thermocline and deep-water dwellers (Abramovich et al., 2003). Large ornate tropical and subtropical species, such as planoglobulinids, recemiguembelinids and globotruncanids (Plate II), tend to be highly specialized (K-selected) species that require specific food sources, occupy narrow ecological niches and produce few offspring (Abramovich et al., 2003). At times of environmental stress, this large group of species (50% at Qreiya) is the first to disappear and their extinction is complete by the KTB (Keller, 2001). Globotruncanids are the largest and most diverse group of large, specialized species. They lived at intermediate or thermocline depths and include photosymbiotic species such as *Racemiguembelina* and *Contusotrunca* (Abramovich et al., 2010).

In central Egypt, globotruncanids in zone CF4 reached a maximum diversity of 25 species (42%) and peak abundance of 30%, although only 18 species are present in any given sample (Figs. 6, 11). This ending phase for globotruncanids likely coincides with a time of maximum surface productivity, increased surface-to-deep gradient and climate warming as indicated by $\delta^{13}C$ and $\delta^{18}O$ respectively (Figs. 9, 11). However, this coincidence requires further validation by other proxies. Near the top of zone CF4 and into CF3, globotruncanid diversity declined to 3-7 species and <10% abundance correlative with decreasing surface productivity to the level of benthic $\delta^{13}C$ values and climate warming. An increase in species richness in the lower part of CF3 to 12 species and ~20% abundance (9.7-10.1 m) correlates with a temporary increase in surface productivity and climate cooling. Thereafter, species richness dropped to 3-7 species totaling no more than 3% in relative abundance correlative with the inverse $\delta^{13}C$ surface-to-deep gradient (Fig. 12). A similar inverse gradient is observed at the base of the section. During the zone CF1 global warming globotruncanids briefly recovered to 10 species but relative abundance remained low up to their extinction at the KT boundary. Earlier studies of the CF1 warm event documented decreased diversity and dwarfed species, including globotruncanids, pseudotextularids (e.g. *P. elegans*, Plate I, 7) and pseudoguembelinids (e.g Plate I, 2, 4, 5) (Li and Keller, 1998a, b; Abramovich and Keller, 2003). These data suggest that globotruncanids and photosymbiotic forms thrived in a well-stratified oligotrophic water column (Abramovich et al., 2010).

Small morphologies: Subsurface mixed layer

Subsurface mixed layer dwellers include a large group of relatively small species with simple morphologies and minor surface ornamentation, including heterohelicids, rugoglobigerinids, hedbergellids and globigerinelloidids (Abramovich et al., 2003, 2010). Their habitat, frequent association with unstable environments suggest that these species are more tolerant of environmental fluctuations (r-selected), feed on diverse food sources, adapt to wide ecological niches, and multiply rapidly with more offspring thus increasing chances of survival (Pardo and

Keller, 2008; Keller and Abramovich, 2009). The small heterohelicids, including *Heterohelix globulosa, H. navarroensis* and *H. planata* (Fig. 6-8) are dominant in this group.

At Qreiya, the surface mixed layer group includes 10-13 species dominated by heterohelicids (70-90%) from zone CF4 to the base of CF3 (0-9 m), except for very short intervals of *Guembelitria* blooms (Fig. 12). In the middle and upper zone CF3, species richness reaches a maximum of 16 and gradually decreases to 8, correlative with decreasing population abundance from 60% to nearly 0 by the CF3/CF1 hiatus. This decrease coincides with the inverse surface-to-deep gradient, common globigerinelloidids and rare globotruncanids. Abramovich et al. (2010) observed a similar species distribution in Israel and suggested mesotrophic conditions, whereas in oligotrophic open-marine conditions globotruncanids are more common and globigerinelloidids rare (e.g., DSDP site 525a, Li and Keller 1998a; Tunisia, Abramovich and Keller, 2002). During the climate warming and high productivity of zone CF1 subsurface dwellers increased to 16 species with high population abundance (~90%) including 30% rugoglobigerinids (Fig. 12). A similar increase in rugoglobigerinids is observed in the Negev sections in zones CF1-CF2 (Abramovich et al., 2010).

Biserial morphologies

In oligotrophic environments, surface dwellers consist of a small group of biserial species that includes *Pseudoguembelina costulata, P. costellifera, P. palpebra* and *P. hariaensis* (Abramovich et al., 2003, 2010). These species are most abundant and characterized by lighter $\delta^{13}C$ values relative to other species (except *G. cretacea*). In Central Egypt and Sinai, *P. palpebra* and *P. hariaensis* are present but rare and the combined abundance of *P. costulata* and *P. costellifera* reaches a maximum of 25% during warm intervals (Figs. 6-8). Their low abundance indicates a less oligotrophic environment, consistent with the mesotrophic environment in the eastern Tethys (Abramovich et al., 2003; 2010).

Guembelitria blooms: high-stress environment

Among late Maastrichtian to early Danian planktic foraminifers, the tiny triserial *Guembelitria cretacea* species have the lightest $\delta^{13}C$ values marking them as living in the uppermost part of the surface ocean (Abramovich et al., 2010; Pardo and Keller, 2008). A more diverse group of *Guembelitria* morphotypes evolved in the early Danian (*G. trifolia, G. danica, G. dammula, G. irregularis;* Plate IV, 9-12) with significantly (p=0.0264) lighter $\delta^{13}C$ values (Pardo and Keller, 2008). Among planktic foraminifera, *Guembelitria* morphotypes, especially *G. cretacea*, are unique as they erupt in great blooms during times of high environmental stress and quickly disappear when conditions return to normal. They are usually associated with mesotrophic environments such as near-shore continental shelf, upwelling areas and regions under volcanic influence (Keller and Abramovich, 2009; Keller and Pardo, 2004; Pardo and Keller, 2008). *Guembelitria cretacea* are therefore interpreted to have a wider range of tolerance enabling them to survive in high-stress conditions detrimental to other species (Abramovich and Keller, 2003; Keller, 2005; Keller and Abramovich, 2009). The “blooms” strongly indicate r-selected behavior, which is a common survival strategy in unpredictable and stressful environments where quick reproduction betters the chances of survival (Pardo and Keller, 2008; Keller and Abramovich, 2009).

Guembelitria blooms were first noted in the aftermath of the KTB mass extinction and have since been observed during the late Maastrichtian and early Danian invariably in high-stress environments where few other species thrived or even survived (reviews in Keller and Pardo, 2004; Pardo and Keller, 2008; Keller and Abramovich, 2009). Abramovich et al. (2010, p. 12)

suggest that the low $\delta^{13}C$ values of *Guembelitria* can be attributed to living in the uppermost part of the surface waters where photosynthesis is inhibited by high UV radiation and therefore uninhabited by other foraminifers such as symbiotic species and nutrition-deprived heterotrophs. This adaptation could explain the opportunistic *Guembelitria* blooms at times when most or all other species decrease or disappear. Once crises conditions abate, *Guembelitria* blooms disappear. The return to normal, more-diverse assemblages thus indicates an abatement of crisis conditions.

At Gebel Qreiya, multiple *Guembelitria* blooms reach 60% relative abundance in zones CF4 and CF3, with maximum abundance of 80-90% at the top of CF3 below the CF3/CF1 hiatus (Fig. 12). Similar blooms are observed in CF1 at Gebel Qreiya, Wadi Hamama and Wadi Nukhul (Figs. 6-8). Each *Guembelitria* bloom correlates with a relative decrease in heterohelicid abundance as well as other mixed layer species. In zone CF1, *Guembelitria* blooms reach a maximum of 50-70%, but strongly decrease during the climate warming when the biserial species dominate the assemblages. The relationship between *Guembelitria* blooms and surface productivity appears more complicated (Fig. 12). Abramovich et al. (2010) observed that *Guembelitria* blooms in zones CF3-CF4 and CF2-CF1 of the Negev coincide with two major warm events. However, in the shallow shelf environment of Texas, *Guembelitria* blooms of zone CF1 show no strong correlation with low productivity, higher temperatures or freshwater influx (Abramovich et al., 2011). Similarly, no strong correlation with climate warming is observed in the Sinai and Central Egypt.

The immediate post-KTB record cannot be assessed based on Central Egypt, Sinai, or Negev sections because the basal Danian is missing including zone P0 and most of zone P1a. In the upper part of zone P1a (upper subzone P1a(2) above the KTB hiatus), *Guembelitria* blooms rapidly decrease from 55% and reappear in zone P1b throughout this area (Keller and Benjamini, 1991; Keller, 2002; Keller et al., 2002, this study). In between these two early Danian *Guembelitria* blooms there is a suc1cessive dominance of small Danian species beginning with *Parvularugoglobigerina (P. eugubina, P. longiapertura* and *P. extensa)* followed by *Woodringina* and *Chiloguembelina (W. hornerstownensis, W. claytonensis, C. morsei, C. midwayensis*) and ending with *Globoconusa daubjergensis* (Fig. 12). These rapid shifts in dominance suggest an unstable high-stress environment during the early post- KTB recovery phase, followed by the *Guembelitria* bloom dominated high- stress environment in zone P1b.

It is interesting to note that blooms of dinoflagellate *Thoracosphaera* spp. at Wadi Hamama (Fig. 9) and nannofossil *Braarudosphaera bigelowii* at Gebel Qreiya (Fig. 8, Tantawy, 2003) exist in NP1b/NP1c (C28n), which is well above planktic foraminiferal zone P1b (Fig. 5). There appears to be no consistent correlation of these blooms with *Guembelitria* or *G. daubjergensis* blooms, suggesting that they do not respond to the same environmental stresses. However, a good correlation was observed in the late Maastrichtian between *Guembelitria cretacea* and calcareous nannofossil blooms (*Micula decussata, Arkhangelskiella cymbiformis, Watznaueria barnesia*) in volcanically induced stress environments in the Indian Ocean (Tantawy et al., 2009).

8. *GUEMBELITRIA* BLOOMS LINKED WITH DECCAN VOLCANISM

Late Maastrichtian Deccan Phase-1 ~ 67.4±0.6 Ma

It is tempting to link global *Guembelitria* blooms to major catastrophic events, such as the three major phases of Deccan volcanism and associated environmental and climatic consequences. The earliest Deccan eruption phase-1 (6% of the total lava pile) in C30r (~67.4±0.6 Ma) is correlative with zone CF4 (Fig. 5). A major *Guembelitria* bloom was observed in Madagascar in zone CF4 (Abramovich et al., 2002), in south Atlantic DSDP Site 525 (Li and Keller, 1998a), in deep wells of the Cauvery Basin of southern India, in outcrops of the Negev and Texas (Abramovich et al., 2010, 2011; Keller et al., 2012) and now at Qreiya in Central Egypt (Figs. 6, 11). Two short-lived *Guembelitria* blooms are present at Gebel Qreiya, of which one near the CF4/CF3 boundary is associated with the disappearance of *G. bulloides, R. plummerae and R. fornicata.* This extinction event is noted not only in Egypt but also in Madagascar (Abramovich et al., 2002) and South Atlantic Site 525 (Li and Keller, 1998a). The age of this interval correlates well with Deccan Volcanic phase-1 (67.4Ma). There are also major *Guembelitria* blooms in zone CF3 at various localities, which may be linked to Deccan volcanism, or possibly Ninetyeast Ridge volcanism in the Indian Ocean, which coincides with zone CF3 and may have resulted in *Guembelitria* blooms and nannofossil species blooms at least regionally (Keller, 2003; Tantawy et al., 2009). These blooms may be related to major volcanism and associated climate change, increased continental weathering and drawdown of excess atmospheric CO_2.

Late Maastrichtian Deccan Phase-2: C29r zone CF1

The most massive Deccan volcanic eruptions occurred during phase-2 with about 80% of the total lava pile. The worlds largest and longest lava flows erupted at this time spanning over 1000 km across India and out into the Bay of Bengal (Keller et al., 2008; Self et al., 2008). A total of four of these longest lava flows were documented in deep wells of the Krishna-Godavari Basin correlative with zone CF1. Intertrappean sediments between these lava flows reveal the rapid and devastating species extinctions after each lava flow with the fourth lava flow ending with the mass extinction at the KT boundary (Keller et al., 2011a, 2012). In Meghalaya, NE India, 800 km from the Deccan Volcanic Province high-stress deformed *Guembelitria* blooms dominate (>95%) faunal assemblages of zone CF1 correlative with phase-2 Deccan volcanism (Gertsch et al., 2011). In Egypt, *Guembelitria* blooms are also observed in CF1, although this interval is incomplete due to hiatuses, and similar blooms are present in CF3 (Fig. 12). Zone CF1 *Guembelitria* blooms have been documented globally from nearshore to open marine environments from India, to Madagascar, eastern Mediterranean, Texas, Brazil, and Argentina (Abramovich et al., 2002, Keller et al., 2007, 2011b; Abramovich et al., 2010, 2011; Gertsch et al., 2013). These *Guembelitria* blooms generally coincide with the zone CF1 global warming, which has been linked to Deccan volcanism (Li and Keller, 1998a, b; Wilf et al. 2003; Thibault and Gardin, 2007; Abramovich et al., 2010; Keller et al., 2012).

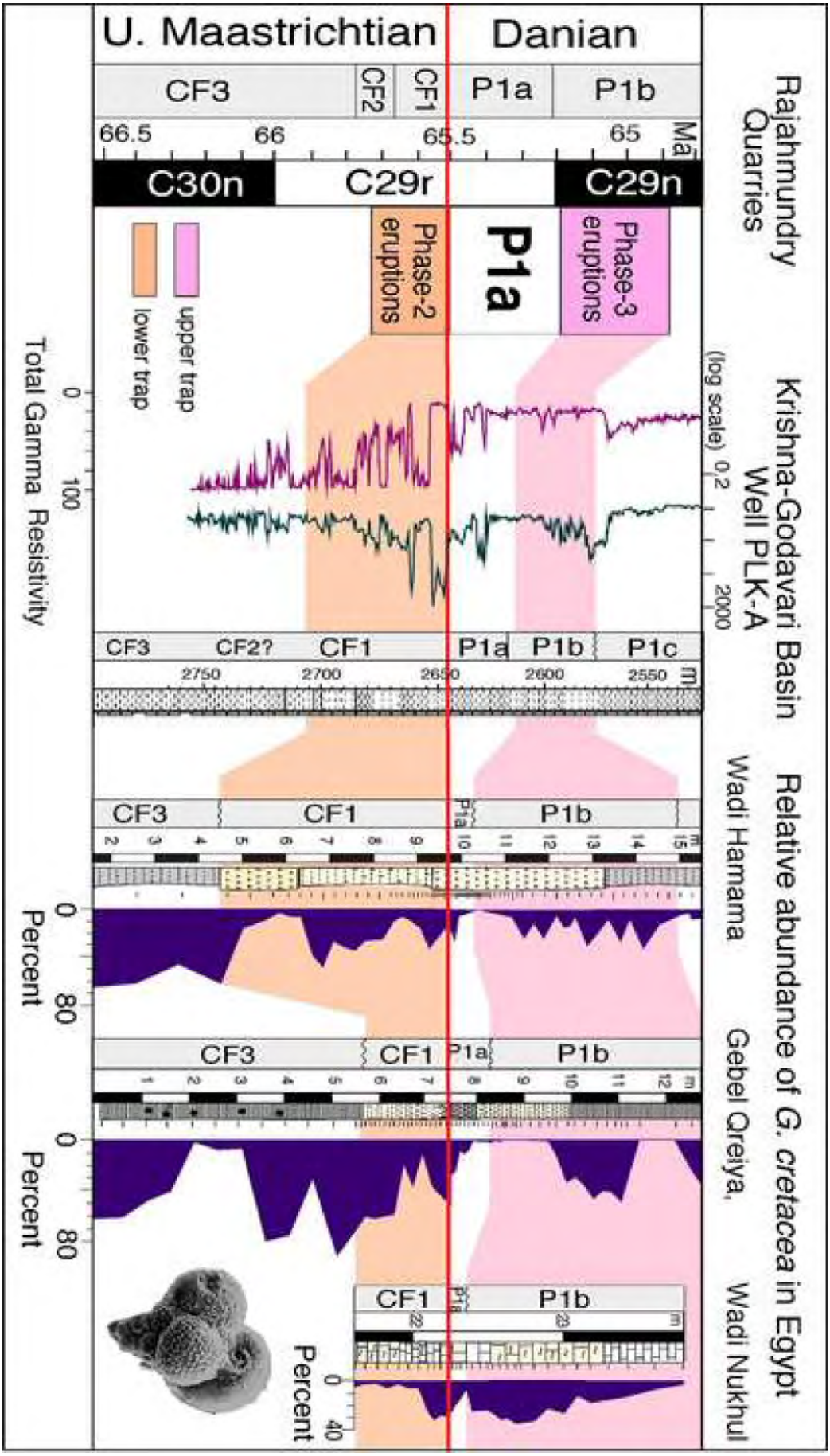

***Figure** 13. Phase-2 and phase-3 Deccan volcanism and intertrappean sediments in outcrops and subsurface cores of the Krishna-Godavari Basin correlated with late Maastrichtian zone CF1 and early Danian zone P1b high-stress environments marked by Guembelitria blooms in Egypt.*

Early Danian Deccan Phase-3: C29n zone P1b

Keller and Benjamini (1991) first observed *Guembelitria* blooms in a clay layer from the early Danian zone P1b in the Negev coincident with a major negative $d^{13}C$ excursion similar to the KT boundary mass extinction (Magaritz et al., 1992). This *Guembelitria* event remained an enigma until recently. The discovery of planktic foraminifera in intertrappean sediments of deep wells from the Krishna-Godavari basin yielded not only age control for the KT boundary relative to phase-2 eruptions, but also for the early Danian phase-3. This last phase of Deccan volcanism began in the early Danian near the base of C29n correlative with zone P1b and *Guembelitria* blooms (Fig. 13). Phase-3 accounts for ~14% of the total Deccan Traps with four megaflows across India similar to Deccan phase-2 (Keller et al., 2012). Intertrappean sediments yield dwarfed, low diversity planktic foraminiferal assemblages. Return to normal sized morphologies and more diverse species assemblages occurred only after the last phase-3 lava flows. The same pattern is observed in Meghalaya, NE India, and Cauvery Basin of southern India (Keller unpublished data). Zone P1b *Guembelitria* blooms have now been documented from Egypt (Figs. 6-10), North Atlantic and Texas (Keller et al., 2011b). This suggests that the long delayed post-KTB recovery was likely due to Deccan volcanism and that normal conditions for marine plankton only returned after the end of Deccan volcanism.

9. CONCLUSIONS

Planktic foraminiferal assemblages from the late Maastrichtian through early Paleocene reveal a series of high-stress intervals marked by *Guembelitria* blooms, low diversity assemblages, species dwarfing and reduced abundance of keeled globotruncanids associated with low surface productivity rapid global climate warming and associated changes in the water-mass stratification. These high-stress assemblages are prominent in late Maastrichtian zones CF4-CF3, CF1 and early Danian zones P0-P1a and P1b in Egypt with predominantly global distributions. The three main Deccan eruptions closely correspond with these high-stress intervals.

1) Phase-1 in C30r (zone CF4) coincides with the disappearance of *G. bulloides, R. plummerae and R. fornicata* also recorded in Madagascar and South Atlantic Site 525, bracketed by two brief *Guembelitria* blooms.
2) Phase-2 in C29r (zone CF1) ends at the KTB mass extinction and may have been the principle contributor to the long-term climatic and environmental stresses of the late Maastrichtian leading to the KTB mass extinction.
3) Phase-3 near the C29r/C29n boundary (zone P1b) in the early Danian appears to be the cause for the long delayed recovery after the mass extinction. The onset of full biotic recovery is observed in assemblages of zone P1c, after the cessation of phase-3 volcanism.

Acknowledgements. We are grateful to Peter Harris and two anonymous reviewers for their insightful comments and suggestions. The material for this study is partially based upon work supported by the US National Science Foundation through grant NSF OISE-0912144, EAR-0207407, EAR-0447171, EAR-1026271 and Princeton University's Scott and Tuttle Funds. The isotope analyses were conducted at the University of Lausanne and supported by the Egyptian ministry of higher education (mission No.001/013/104) (HK).

REFERENCES

Abdel Razik, 1972. Comparative studies on the Upper Cretaceous–Early Paleogene sediments on the Red Sea coast, Nile Valley and Western Desert, Egypt. Sixth Arab Petroleum Congress, Algiers 71, 1-23.

Abramovich, S., & Keller, G., 2002. High stress late Maastrichtian paleoenvironment: inference from planktonic foraminifera in Tunisia. Palaeogeography, Palaeoclimatology, Palaeoecology 178, 145-164.

Abramovich, S., & Keller, G., 2003. Planktonic foraminiferal response to the latest Maastrichtian abrupt warm event: a case study from South Atlantic DSDP Site 525A. Marine Micropaleontology 48(3-4), 225-249.

Abramovich, S., Almogi-Labin, A., & Benjamini, C., 1998. Decline of the Maastrichtian pelagic ecosystem based on planktic foraminifera assemblage change: Implication for the terminal Cretaceous faunal crisis. Geology 26(1), 63-66.

Abramovich, S., Keller, G., Adatte, T., Stinnesbeck, W., & Hottinger, L., 2002. Age and paleoenvironment of the Maastrichtian to Paleocene of the Mahajanga Basin, Madagascar : a multidisciplinary approach. Marine Micropaleontology 47, 17-70.

Abramovich, S., Keller, G., Stüeben, D., & Berner, Z., 2003. Characterization of late Campanian and Maastrichtian planktonic foraminiferal depth habitats and vital activities based on stable isotopes. Palaeogeography, Palaeoclimatology, Palaeoecology 202(1-2), 1-29.

Abramovich, S., Yovel-Corem, S., Almogi-Labin, A., & Benjamini, C., 2010. Global climate change and planktic foraminiferal response in the Maastrichtian. Paleoceanography 25(2), 1-15.

Abramovich, S., Keller, G., Berner, Z., Cymbalista, M. & Rak, C., 2011. Maastrichtian Planktic Foraminiferal Biostratigraphy and Paleoenvironment of Brazos River, Falls County, Texas, in: Keller, G. & Adatte ,T. (Eds.), 100SEPM Special Publication, 123-156.

Adatte, T., Keller, G., Stüeben, D., Harting, M., Kramer, U., Stinnesbeck, W., Abramovich, S., & Benjamini, C., 2005. Late Maastrichtian and K / T paleoenvironment of the eastern Tethys (Israel): mineralogy, trace and platinum group elements, biostratigraphy and faunal turnovers. Bulletin de la Société Géologique de France 176(1), 37-55.

Almogi-Labin, A., Bein, A., & Sass, E., 1993. Late Cretaceous upwelling system along the southern Tethys margin (Israel): interrelationship between productivity, bottom water environments, and organic matter preservation. Paleoceanography 8(5), 671-690.

Alvarez, W., Kauffman, E. G., Surlyk, F., Alvarez, L. W., Asaro, F., & Michel, H. V., 1980. Impact Theory of Mass Extinctions and the Invertebrate Fossil Record. Advancement Of Science 223(4641), 1135-1141.

Barrera, E., and Keller, G., 1990, Foraminiferal stable isotope evidence for gradual decrease of marine productivity and Cretaceous species survivorship in the earliest Danian: Paleoceanography 5, 867-890.

Berggren, W.A., Kent, D.V., Swisher, III, C.C. & Aubry, M.-P., 1995. A revised Cenozoic geochronology and chronostratigraphy, in: Berggren, W.A., Kent, DV., Aubry, M.-P. and Hardenbol, J. (Eds.), Geochronology, Time Scales and Stratigraphic Correlation. Society of Economic Paleontologists and Mineralogists, Special Volume 54, Cambridge, U.K. Cambridge University Press, pp. 129-212.

Bruns, P., Rakoczy, H., Pernicka, E. & Dullo, W.-C., 1997. Slow sedimentation and Ir anomaly at the Cretaceous/Tertiary boundary. Geologische Rundschau 86, 168–177.

Cande, S. C., & Kent, D. V., 1995. Revised calibration of the geomagnetic polarity timescale for the Late. Journal of Geophysical Research 100, 6093-6095.

Chenet, A. -L., Quidelleur, X., Fluteau, F., Courtillot, V., & Bajpai, S., 2007. ^{40}K–^{40}Ar dating of the Main Deccan large igneous province: Further evidence of KTB age and short duration. Earth and Planetary Science Letters 263(1-2), 1-15.

Chenet, A. -L., Fluteau, F., Courtillot, V., Gérard, M., & Subbarao, K. V., 2008. Determination of rapid Deccan eruptions across the Cretaceous-Tertiary boundary using paleomagnetic secular variation:

Results from a 1200-m-thick section in the Mahabaleshwar escarpment. Journal of Geophysical Research 113(B4).

Chenet, A. -L., Courtillot, V., Fluteau, F., Gérard, M., Quidelleur, X., Khadri, S. F. R., Subbarao, K. V., Thordarson, T., 2009. Determination of rapid Deccan eruptions across the Cretaceous-Tertiary boundary using paleomagnetic secular variation: 2. Constraints from analysis of eight new sections and synthesis for a 3500-m-thick composite section. Journal of Geophysical Research 114(B6), 1-38.

Courtillot, V., Besse, J, Vandamme, D., Montigny, R., Jaeger, J. -J. & Cappetta, H., 1986. Deccan flood basalts at the Cretaceous/Tertiary boundary? Earth and Planetary Science Letters 80(3-4), 361-374.

Courtillot, V., Féraud, G., Maluski, H., Vandamme, D., Moreau, M. G. & Besse, J., 1988. Deccan flood basalts and the Cretaceous/Tertiary boundary. Nature 333, 843 – 846.

Dercourt, J., Ricou, L.E., & Vrielynck, B., 1993. Atlas Tethys Paleoenvironmental Maps, Gauthier-Villars, Paris, pp. 307.

Donovan, A.D., Baum, G.R. Blechschmidt, G.L. Loutit, T.S. Pflum, C.E., & Vail, P.R., 1988. Sequence stratigraphic setting of the Cretaceous–Tertiary Boundary in Central Alabama, in: C.K. Wilgus, B.K. Hastings, H. Posamentier, J. Van Wagoner, C.A. Ross, C.G.St.C. Kendall (Eds.), Sea-Level Changes—An integrated Approach, SEPM Special Publication 42, 299–307.

Gertsch, B., Keller, G., Adatte, T., Garg, R., Prasad, V., Berner, Z., & Fleitmann, D., 2011. Environmental effects of Deccan volcanism across the Cretaceous–Tertiary transition in Meghalaya, India. Earth and Planetary Science Letters 310(3-4), 272-285.

Gertsch, B., Keller, G., Adatte, T., & Berner, Z., 2013. The Cretaceous- Tertiary boundary (KTB) transition in NE Brazil. Journal of the Geological Society of London 170, 249-262.

Gradstein, F. M., Ogg, J. G., & Smith, A. G., 2004. *A geologic time scale*. Cambridge, U.K. Cambridge University Press, pp. 598.

Huber, B. T., MacLeod, K. G., & Tur, N. A., 2008. Chronostratigraphic framework for upper Campanian-Maastrichtian sediments on the Blake Nose (subtropical North Atlantic). The Journal of Foraminiferal Research 38(2), 162-182.

Keller, G., 2001. The end-cretaceous mass extinction in the marine realm: year 2000 assessment. Planetary and Space Science, 49(8), 817-830.

Keller, G., 2002. Guembelitria-dominated late Maastrichtian planktic foraminiferal assemblages mimic early Danian in central Egypt. Marine Micropaleontology 47, 71-99.

Keller, G., 2003. Biotic effects of impacts and volcanism: Earth and Planetary Science Letters 215, (1-2), 249-264.

Keller, G., 2011. Defining the Cretaceous–Tertiary Boundary: A PracticaL Guide and Return to First Principles. Society for Sedimentary Geology Special Volume 100, 23-42.

Keller, G. & Abramovich, S., 2009. Lilliput effect in late Maastrichtian planktic foraminifera: Response to environmental stress. Palaeogeography, Palaeoclimatology, Palaeoecology 284(1-2), 47-62.

Keller, G., & Benjamini, C., 1991. Paleoenvironment of the Eastern Tethys in the Early Paleocene. Palaios 6, 439-464.

Keller, G. & Lindinger, M., 1989. Stable isotope, TOC and $CaCO_3$ record across the cretaceous/tertiary boundary at El Kef, Tunisia. Science 73, 243-265.

Keller, G., & Pardo, A., 2004. Disaster opportunists Guembelitrinidae: index for environmental catastrophes. Marine Micropaleontology 53(1-2), 83-116.

Keller, G., Li, L. & MacLeod, N., 1995. The Cretaceous/Tertiary boundary stratotype section at El Kef, Tunisia: How catastrophic was the mass extinction? Palaeogeography Palaeoclimatology Palaeoecology 119(3), 221–254.

Keller, G., Barrera, E., Schmitz, B., & Matsson, E., 1993. Gradual mass extinction, species survivorship, and long term environmental changes across the Cretaceous-Teriary boundariy in high latitudes. Geological Society of America Bulletin 105(8), 979–997.

Keller, G., Adatte, T., Burns, S. J., & Tantawy, A. A., 2002. High-stress paleoenvironment during the late Maastrichtian to early Paleocene in Central Egypt. Palaeogeography, Palaeoclimatology, Palaeoecology 187, 35-60.

Keller, G., Stinnesbeck, W., Adatte, T., & Stüben, D., 2003. Multiple impacts across the Cretaceous–Tertiary boundary. Earth-Science Reviews 62(3), 327-363.

Keller, G., Adatte, T., Tantawy, a. a., Berner, Z., Stinnesbeck, W., Stueben, D., & Leanza, H. A., 2007. High stress late Maastrichtian – early Danian palaeoenvironment in the Neuquén Basin, Argentina. Cretaceous Research 28(6), 939-960.

Keller, G., Adatte, T., Gardin, S., Bartolini, A., & Bajpai, S., 2008. Main Deccan volcanism phase ends near the K–T boundary: Evidence from the Krishna–Godavari Basin, SE India. Earth and Planetary Science Letters 268(3-4), 293-311.

Keller, G., Adatte, T., Bajpai, S., Mohabey, D. M., Widdowson, M., Khosla, A., Sharma, R., Khosla, S. C., Gertsch, B., Fleitmann, D. & Sahni, A., 2009a. K–T transition in Deccan Traps of central India marks major marine Seaway across India. Earth and Planetary Science Letters 282(1), 10-23.

Keller, G., Abramovich, S., Berner, Z., & Adatte, T., 2009b. Biotic effects of the Chicxulub impact, K–T catastrophe and sea level change in Texas. Palaeogeography, Palaeoclimatology, Palaeoecology *271*(1), 52-68.

Keller, G., Bhowmick, P. K., Upadhyay, H., Dave, A., Reddy, A. N., Jaiprakash, B. C. & Adatte, T., 2011a. Deccan Volcanism Linked to the Cretaceous-Tertiary Boundary Mass Extinction : New Evidence from ONGC Wells in the Krishna-Godavari Basin. Journal of the Geological Society of India 78, 399-428.

Keller, G., Abramovich, S., Adatte, T., and Berner, Z., 2011b. Biostratigraphy, Age of the Chicxulub impact, and depositional environment of the Brazos River KTB sequences, in: The End-Cretaceous Mass Extinction and the Chicxulub Impact in Texas, Keller, G., Adatte, T., eds., Society for Sedimentary Geology (SEPM) Special Publication 100, 81-122.

Keller, G., Adatte, T., Bhowmick, P. K., Upadhyay, H., Dave, A., Reddy, A. N., & Jaiprakash, B. C., 2012. Nature and timing of extinctions in Cretaceous-Tertiary planktic foraminifera preserved in Deccan intertrappean sediments of the Krishna–Godavari Basin, India. Earth and Planetary Science Letters 341, 211-221.

Keller, G., Khozyem, H.M., Adatte, T., Malarkodi, N., Spangenberg, J.E., and Stinnesbeck, W., 2013, Chicxulub Impact Spherules in the North Atlantic and Caribbean: age constraints and Cretaceous-Tertiary boundary hiatus: Geological

Magazine, doi:10.1017/S0016756812001069.

Khozyem, H., Adatte, T., Spangenberg, J. E., Tantawy, A. A. & Keller, G., 2013. Palaeoenvironmental and climatic changes during the Palaeocene–Eocene Thermal Maximum (PETM) at the Wadi Nukhul Section, Sinai, Egypt. Journal of the Geological Society London 170(2), 341-352.

Li, L., & Keller, G., 1998a. Maastrichtian climate, productivity and fauna1 turnovers in planktic foraminifera in South Atlantic DSDP sites 525A and 21. Marine Micropaleontology 33, 55-86.

Li, L., & Keller, G., 1998b. Abrupt deep-sea warming at the end of the Cretaceous. Geology 26, 995-998.

Luger, P., 1988. Maastrichtian to Paleoocene facies evolution and the Cretaceous-Tertiary boundary in Middle and Southern Egypt. Revista española de paleontología 1, 83-90.

Magaritz, M., Benjamini, C., Keller, G., & Moshkovitz, S., 1992. Early diageneitc isotopic signal at the Cretaceous/Tertiary boundary, Israel. Palaeogeography, palaeoclimatology, palaeoecology 91(3), 291-304.

McLean, D., 1985. Deccan traps mantle degassing in the terminal Cretaceous marine extinctions. Cretaceous Research 6(3), 235-259.

Miller, K. G., Sherrell, R. M., Browning, J. V., Field, M. P., Gallagher, W., Olsson, R. K. Sugarman, P. J., Tuorto, S., & Wahyudi, H., 2010. Relationship between mass extinction and iridium across the Cretaceous-Paleogene boundary in New Jersey. Geology 38(10), 867-870.

Molina, E., Alegret, L., Arenillas, I., Arz, J., Gallala N., Hardenbol, J., von Salis, K., Steurbaut, E., Vanhenberghe, N., & Zaghbib-Turki, D., 2006. The Global Boundary Stratotype Section and Point for the base of the Danian Stage (Paleocene, Paleogene, "Tertiary", Cenozoic) at El Kef, Tunisia -Original definition and revision. Episodes 29(4), 263-273.

Nederbragt, A. J., 1991. Late Cretaceous biostratigraphy and development of Heterohelicidae (planktic foraminifera). Micropaleontology 37, 329–372.

Olsson, R.K., Hemleben, C., Berggren, W.A., Huber, B.T., 1999. Atlas of Paleocene Planktonic Foraminifera. Smithsonian Contribution to Paleobiology No. 85, Smithsonian Institution Press, Washington D.C., pp. 252.

Pardo, A., & Keller, G., 2008. Biotic effects of environmental catastrophes at the end of the Cretaceous and early Tertiary: Guembelitria and Heterohelix blooms. Cretaceous Research, 29(5-6), 1058-1073.

Pearson, P. N., Ditchfield, P. W., Singano, J., Harcourt-Brown, K. G., Nicholas, C. J., Olsson, R. K., Shackleton, N. J. & Hall, M. A., 2001. Warm tropical sea surface temperatures in the Late Cretaceous and Eocene epochs. Nature 413(6855), 481-487.

Punekar, J., Mateo, P. & Keller, G., 2014. Environmental and biological effects of Deccan volcanism: A global survey. In press.

Quillévéré, F., Norris, R. D., Kroon, D., & Wilson, P. A., 2008. Transient ocean warming and shifts in carbon reservoirs during the early Danian. Earth and Planetary Science Letters, 265(3), 600-615.

Robaszynski, F., Caron, M., Gonzales Donoso, J.M & Wonders, A.A.H., 1984. Atlas of Late Cretaceous Globotruncanids. Revue de Micropaléontologie 26, 145–305.

Said, R., 1961. Tectonic framework of Egypt and its influence on distribution of foraminifera. AAPG Bulletin 45(2), 198-218.

Schrag, D. P., Depaolo, D. J., & Richter, F. M., 1995. Reconstructing past sea surface temperatures : Correcting for diagenesis of bulk marine carbonate. Geochemica et Cosmochimica Acta 59(11), 2265-2278.

Schulte, P., Alegret, L., Arenillas, I., Arz, J. A., Barton, P. J., Bown, P. R., Bralower, T. J., Christeson, G. L., Claeys, P., Cockell, C. S., Collins, G. S., Deutsch, A., Goldin, T. J., Goto, K., Grajales-Nishimura, J. M., Grieve, R. A. F., Gulick, S. P. S., Johnson, K. R., Kiessling W, Koeberl C, Kring DA, MacLeod KG, Matsui T, Melosh J, Montanari A, Morgan, J. V., Neal, C. R., Norris, R. D., Pierazzo, E., Ravizza, G., Rebolledo-Vieyra, M., Reimold, W. U., Robin E, Salge T, Speijer, R. P., Sweet, A. R., Urrutia-Fucugauchi, J., Vajda, V., Whalen, M.T., Willumsen, P. S., 2010. The Chicxulub asteroid impact and mass extinction at the Cretaceous-Paleogene boundary. Science 327(5970), 1214-1218.

Self, S., Thordarson, T., & Widdowson, M., 2005. Gas Fluxes from Flood Basalt Eruptions. Elements 1(5), 283-287.

Self, S., Blake, S., Sharma, K., Widdowson, M., & Sephton, S., 2008. Sulfur and chlorine in late Cretaceous Deccan magmas and eruptive gas release. Science 319(5870), 1654-7.

Soliman, M., Habib, M. and Ahmed, E., 1986. Sedimentologic and tectonic evolution of the Upper Cretaceous-Lower Tertiary succession at Wadi Qena, Egypt. Sedimentary Geology 46, 11-133.

Stüben D., Kramar, U., & Berner, Z.A., 2003. Late Maastrichtian Paleoclimatic and Paleoceanographic Changes Inferred from Sr/Ca Ratio and Stable Isotopes. Palaeogeography, Palaeoclimatology, Palaeoecology 199, 107–127.

Tantawy, A. A., 2003. Calcareous nannofossil biostratigraphy and paleoecology of the Cretaceous/Tertiary transition in the central eastern desert of Egypt. Marine Micropaleontology 47, 323-356.

Tantawy, A.A., Keller, G., Pardo, A., 2009. Late Maastrichtian volcanism in the Indian Ocean: Effects on calcareous nannofossils and planktic foraminifera. Palaeogeography, Palaeoclimatology, Palaeoecology 284, 63-87.

Thibault, N., & Gardin, S., 2007. The late Maastrichtian nannofossil record of climate change in the South Atlantic DSDP Hole 525A. Marine Micropaleontology 65(3), 163-184.

Wilf, P., Johnson, K.R. & Huber, B.T., 2003. Correlated terrestrial and marine evidence for global climate changes before mass extinction at the Cretaceous–Paleogene boundary. Proceedings of the National Academy of Sciences, USA 100 (2), 599–604.

ATMOSPHERIC HALOGEN AND ACID RAINS DURING THE MAIN PHASE OF DECCAN ERUPTIONS: MAGNETIC AND MINERAL EVIDENCE*

Abstract. Environmental changes linked to Deccan volcanism are still poorly known. ENREF_3 A major limitation resides in the paucity of direct Deccan volcanism markers and in the geologically short interval where both impact and volcanism occurred, making it hard to evaluate their contributions to the mass extinction. We investigated the low magnetic susceptibility interval just below the Iridium-rich layer of the Bidart (France) section, which was recently hypothesized to be the result of palaeoenvironmental perturbations linked to paroxysmal Deccan phase-2. Results show a drastic decrease of detrital magnetite and presence of scarce akaganeite, a hypothesized reaction product formed in the aerosols derived from reaction of the volcanic plume with water and oxygen in the high atmosphere. A weathering model of the consequences of acidic rains on a continental regolith reveals nearly complete magnetite dissolution after about 31,000 years, which is consistent with our magnetic data and fall within the duration of the Deccan phase-2. These results highlight the nature and importance of the Deccan-related environmental changes leading up to the end-Cretaceous mass extinction.

Keywords: Deccan volcanism, akaganeite, acid rain, mass extinction, rock magnetism, weathering model

1. INTRODUCTION

The history of the Earth is punctuated by five severe global climatic and environmental catastrophes that led to nearly total mass extinctions of calcareous marine and many continental species. The most famous case is the Cretaceous-Palaeogene boundary (KPB or KTB) mass extinction, which is still the center of acrimonious debates between partisans of the bolide impact theory (Schulte et al., 2010) and those who favour a terrestrial origin linked to Deccan Traps volcanism (Courtillot, 2012; Keller et al., 2012). Others argue that each process, individually, is unlikely to cause a global biological collapse and a scenario of multiple causes is preferred (White and Saunders, 2005; Keller et al., 2009; Renne et al., 2013).

In recent years Deccan volcanism studies resulted in major advances that now facilitate recognition and evaluation of its global effects such as attempted in this study. For example, three discrete Deccan volcanism phases with variable intensity have been dated based on magnetostratigraphy and ^{40}K-^{40}Ar ages (Chenet et al., 2007): Phase-1 in the early late Maastrichtian (base magnetozone C30n, ~67.4 m.y.) accounts for ~6% of the total lava pile, which today forms mountain peaks of 3500 m (Self et al., 2008b). Most of the lava pile (80%)

---

* ***Eric Font, Sébastien Fabre, Anne Nédélec, Thierry Adatte, Gerta Keller, Cristina Veiga Pires, Jorge Ponte, Hassan Khozyem and Jorge Spangenberg. (2013) Magnetic and mineral markers of atmospheric halogen and acid rains during the end-Cretaceous major episode of Deccan volcanism. GSA, inpress.***

erupted during phase-2 in the latest Maastrichtian paleomagnetic chron C29r. The final phase-3 erupted in the early Danian base of C29n and accounts for ~14% of total Deccan eruptions (Chenet et al., 2007; Chenet et al., 2008; Keller et al., 2011; Keller et al., 2012). The original size prior to erosion is estimated to have been 1.5 million km^2 and the volume of lava extruded about 1million km^3 (Self et al., 2006; Chenet et al., 2007). Most critical for the current study is Deccan volcanism phase-2, which has been directly linked to the KPB mass extinction in outcrops and deep wells of the Krishna-Godavari Basin in India (Keller et al., 2011; Keller et al., 2012). These studies revealed Earth's longest lava mega-flows (Self et al., 2008) 1500 km across India near the end of phase-2 with the final mega-flow at the KPB mass extinction (Keller et al., 2008).

Current research thus narrows the main phase-2 of Deccan volcanism to the geologically short interval of the Cretaceous planktic foraminiferal zone CF1, which spans the last ~160,000 years below to the KPB, whereas the Chicxulub impact is commonly placed at the KPB (Schulte et al., 2010) or within zone CF1 preceding the mass extinction (Keller et al., 2012). This short interval limits our ability to separate the main Deccan volcanic phase (i.e. phase-2) from the Chicxulub impact within resolvable radiometric ages and to evaluate their respective biotic effects and their contributions to the KPB mass extinction. Radiometric (K-Ar and Ar-Ar) methods are subject to intrinsic errors (~1-2%), linked to inter-laboratory calibration, imprecise K and Ar isotopic standard (Fish Canyon standard) and uncertainty of decay constants (Kuiper et al., 2008; Channell et al., 2010; Renne et al., 2010; Renne et al., 2013), preventing any precise radiometric age correlation between continental Deccan flood basalts and the mass extinction recorded in marine sections. In addition, because volcanic mineralogical markers (aerosol) are generally restricted to the vicinity of the volcanic source, the discrimination between Deccan phase-2 and the Chicxulub impact in distal section is even harder within such a short temporal interval. Are volcanic signals present but unrecognized outside India? A recent study of KPB sections at Bidart, France, and Gubbio, Italy, suggests so (Font et al., 2011). In these sections, a 50 cm thick yellow-red interval of very low magnetic susceptibility (MS) directly underlies the KPB (Fig. 1), as also observed in Oman (Ellwood et al., 2003) and other marine sections. Preliminary data indicate that this low MS interval contains an enigmatic antiferromagnetic (i.e. high coercivity) Cl-rich iron oxyhydroxide that could have formed by interaction between HCl-rich volcanic gas and aerosols in the high atmosphere (Font et al., 2011)_ENREF_12. Plate-like morphology and well-preserved texture of this newly discovered mineral strongly contrast with the detrital aspect of titanomagnetite and suggest an aeolian origin for its transport. Recent numerical modelling showed that penetrative convection driven by the cooling of the Deccan lavas may have generated buoyant atmospheric plumes (Kaminski et al., 2011). In such a situation, aerosols would have been able to rise to the stratosphere providing an explanation for a rather long halogen residence time in the atmosphere and the eventual transport of their reaction products to Bidart and Gubbio sections.

The main objective of this study is to evaluate the magnetic and mineralogical characteristic of the uppermost Maastrichtian at Bidart, France, in order to determine the potential signature of Deccan volcanism. To achieve this objective the following evaluations were performed: (1) Determine the presence of zone CF1 (latest Maastrichtian correlative with Deccan phase-2) based on high-resolution biostratigraphy and chemostratigraphy (carbon and oxygen isotopes).

(2) Perform high-resolution (cm-scale) magnetic analyses and microscope observations

focused on the last meter of the Maastrichtian including the low MS interval to determine its mineral content and origin. (3) Identify the enigmatic Cl-bearing iron oxyhydroxide and evaluate its possible formation and subsequent transport in relation with the Deccan volcanism. (4) Quantify the effects of acid rains on a continental regolith using a numerical weathering model.

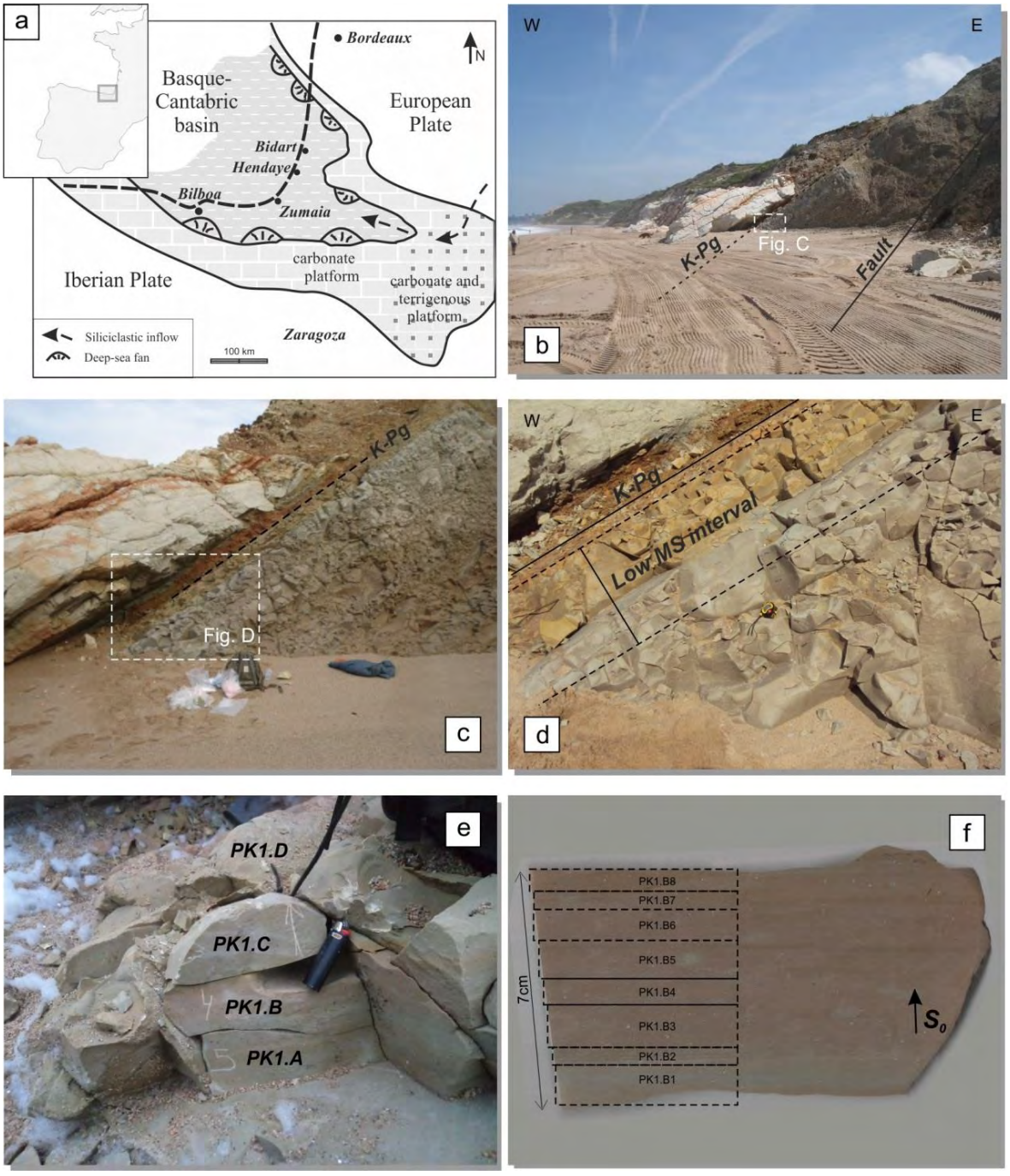

Figure 1. *Geological settings and biostratigraphy of the Bidart section.* ***a,*** *Palaeoenvironmental context of the Biscay Bay.* ***b,*** *The Erretegia Beach showing the white-pink Danian limestones and the Maastrichtian marls cut by a fault.* ***c,*** *The K-Pg boundary showing* ***d,*** *the typical dark clay layer and the yellow-red interval of low MS values in the upper Maastrichtian.* ***e,*** *Example of hand block collected at the outcrop.* ***f,*** *Example of a block cut into small plates, by using a non-magnetic dremel-saw, for subsequent magnetic analyses.*

2. METHODS

For biostratigraphic and faunal analyses samples were processed using standard methods (Keller et al., 1995). Samples were washed through 38mm and 63mm sieves and oven dried at 50ºC. Species preservation is generally good though shells are recrystallized and affected by dissolution. Dissolution effects are apparent below the KPB coincident with the low magnetic susceptibility (MS) interval and a major increase in benthic species. In the 25 cm below the Cretaceous-Paleogene boundary almost all carbonate shells are dissolved due to intense dissolution. Faunal analysis was conducted on three size fractions (38-63mm, 63-150mm, >150mm) with the quantitative analysis based on 38-63mm and 63-150mm).

We measured magnetic susceptibility (MS), saturation isothermal remanent magnetization (SIRM) and coercivity ($IRM_{-0.3T}/IRM_1$=S-ratio, $B_{1/2}$) dependent magnetic properties. Mass specific magnetic susceptibility is mainly controlled by content in ferromagnetic (i.e. iron oxides) and paramagnetic (i.e. clays) material whereas isothermal remanent magnetization (IRM) is mostly sensitive to ferro/ferri- and antiferromagnetic particles even in very low amounts. Magnetic susceptibility was measured with a MFK1 (AGICO) apparatus at the Institute Dom Luís laboratory (Portugal) and reported relative to mass specific m^3/kg by dividing by density. Samples were cleaned by alternating fields (AF) treatment and submitted to Isothermal (IRM) measurements using an impulse magnetizer (IM-10-30). IRM curves were then analysed using a cumulative Log-Gaussian function (Kruiver et al., 2001) in order to discriminate magnetic phases by their respective coercivity spectra. Fresh rock fragments were also observed under a Hitachi S-3700N Scanning Electron Microscope (SEM) coupled to a Bruker XFlash® 5010 Energy Dispersive Spectra (EDS) detector at the Hercules laboratory (Evora, Portugal). EDS provides semi-quantitative compositional analysis.

We also measured the colour by using Diffuse Reflectance Spectrophotometry (DRS) analysis, which are based on the percentage reflectance of a sample relative to white light and provides qualitative information about mineralogical and grain size variations. DRS data were converted into a colour by using the Munsell Colour System and represented in L*a*b* coordinates following the Commission International de l'Éclairage (CIE, 1976), where L* is the lightness/darkness, a* is the redness/greenness and b* is the yellowness/blueness. Data were obtained using a X-Rite® Colortron™ spectrophotometer from 86 rock powders, in order to avoid grain size effects, and after three series of measurements.

Isotopic analyses were performed at the University of Lausanne on a Thermo Fisher Scientific (Bremen, Germany) GasBench II carbonate preparation device connected to a Thermo Fisher Scientific Delta Plus XL continuous flow isotope ratio mass spectrometer (IRMS). CO_2 was extracted at 70°C. Isotopic ratios of carbon and oxygen are reported in the delta (d) notation as the per mil (‰) deviation relative to the ViennaPee Dee belemnite standard (VPDB). The analytical reproducibility estimated from replicate analyses of the international calcite standard NBS-19 and the laboratory standards Carrara Marble was better than ±0.05‰ for $d^{13}C_{carb}$ and ±0.1‰ for $d^{18}O_{carb}$.

In order to discuss the origin of the loss in detrital magnetite just below the Cretaceous-Paleogene boundary, we processed a numerical weathering model. We used the PHREEQC program (Appelo and Parkhurst, 1999)_ENREF_39 developed by the U.S. Geological

Survey for modelling water-rock interactions, coupled with the Laurence Livermore National Laboratory database. The program determines the chemical speciation of aqueous solutes, the fugacities of gases, and attributes each component of the solution to stable aqueous species. It also calculates the activity coefficients of water and the aqueous species, as well as the saturation index of the solution with respect to all the solid phases of the database. The weathered "rock" material is a monolithologic sandy regolith, assumed to have the same mineral composition of the mean continental upper crust (or typical granodiorite) and forming a layer subjected to drainage conditions and reacting with rainwater initially equilibrated with volcanic gases. In our hypothesis the initial magnetic particles accumulate from the parent rock during pedogenesis. _ENREF_43. The regolith alteration is assumed to proceed by a continuous batch process in water-saturated sediment, where the pore water is being periodically replaced by an equivalent volume of fresh rain water at each rain event (Fabre et al., 2011; Fabre and Berger, 2012). The surface percentage of magnetite is taken equal to 1.8% (Table 1). The mineral reactive surface (A) is calculated according a simple parametric law assumed to be a correct approximation of the solid Brunauer Emmet Teller (BET) surface ((i.e. method of adsorbing-desorbing gases at the mineral surface in order to measure the surface area; Brunauer et al., 1938; Sverdrup and Warfvinge, 1995):

$A = (8.0x_{clay} + 2.2x_{silt}+0.3x_{sand}+0x_{coarse}).\rho$ [E1]

Where x_{clay}, x_{silt}, x_{sand} and x_{coarse} represent fractions of clay, silt, sand and coarse materials in the sandy regolith. ρ is the regolith density in g/m^3. Other relevant characteristics of the regolith are reported in Table 2.

The rain frequency is linked to the presumed Maastrichtian climate, namely tropical hot and humid. The runoff is taken as equal to present-day values: 11 $L/s.km^2$ (Gaillardet et al., 1999). Numerous studies of current conditions indicate the potential role of acidic rainwater in the mobilisation of metals (Floor et al., 2011). In this study, we assume a pH between 3.3 and 4.3, which is typical of rainwater resulting from the mixing between volcanic plumes and atmospheric aerosols (Chudaeva et al., 2006; Calabrese et al., 2011; Floor et al., 2011). These values were measured in the neighbourhood of active volcanoes such as Mt Etna. After each rain event, magnetite and rainwater react to reach equilibrium. The overall dissolution rate of the minerals, $R_{k,}$ considered as a first-order law, is equal to:

$$R_k = \left(\frac{dn}{dt}\right) = k_o A S_w \left(1 - \frac{Q}{K_k}\right) \quad \text{[E2]}$$

Where R_k stands for bulk dissolution rate of mineral k, ko is the dissolution rate constant in $mol.m^{-2}.s^{-1}$, A the reactive surface area of the solid (m^2/m^3), S_w the soil moisture (fixed at 30% as a mean value (Sverdrup and Warfvinge, 1995)), and Q/K the saturation ratio. Thermodynamic constants are taken from Fabre et al. (2011) and White et al. (1994)_ENREF_43. No specific precipitation law was imposed for secondary phases, assuming that secondary phase formation is controlled by the dissolution of source minerals. Moreover, we assume that the reaction is not controlled by the diffusion through the oxide layer as observed in closed reactors _ENREF_41(White et al., 1994). The number of dissolved magnetite in moles is calculated during each increment. The final value is the time required to dissolve a significant percentage of

the initial magnetite mass (90% corresponding to the observed magnetic susceptibility decrease.

3. AGE AND CORRELATION WITH DECCAN PHASE-2

The Bidart section is generally considered as one of the most complete KPB sections worldwide because of a thin clay layer and Ir anomaly (Bonté et al., 1984; Ward and Kennedy, 1993; Vonhof and Smit, 1997; Galbrun and Gardin, 2004). However, in previous studies the zone CF1 index species was not observed leaving doubt as to the presence of a complete sediment record below the KPB. In this study the zone CF1 index species (*Plummerita hantkeninoides*) was observed confirming the presence of the correlative interval with Deccan phase-2.

A second independent test for the presence of the uppermost Maastrichtian can be obtained from oxygen and carbon isotopes, and more specifically the global climate warming, which begins in zone CF2 and continues into the lower part of CF1 and the subsequent cooling prior to the KPB (Li and Keller, 1998; Stuben et al., 2003; Wilf et al., 2003; Abramovich et al., 2010) (Fig. 2). We measured carbon and oxygen isotope compositions for the entire section (~6 m) at 20 cm intervals as well as at higher resolution (5 cm intervals) for the low MS interval of the top 1 m with comparable results (Figs. 2-3; Table X1). These data show the climate warming beginning in zone CF2 and proceeding into CF1 followed by cooling correlative with South Atlantic Site 525 (Fig. 2). Note that zones CF2 and CF1 span the last 160 and 120 kyr at the end of the Maastrichtian, respectively. This study thus demonstrates the presence of the latest Maastrichtian at Bidart correlative with Deccan phase-2.

In this study we hypothesize that Deccan volcanism caused acid rain and ocean acidification. If this is the case, then it should be reflected in the calcareous shells of planktic foraminifera and more specifically by the loss of dissolution-prone thin-walled species. We observed increasing dissolution effects in planktic foraminifera at the Bidart section in the 50 cm below the KPB and correlative with the low MS interval with maximum dissolution effects (nearly all species dissolved) in the 20 cm below the KPB (Fig. 2). Increased carbonate dissolution below the KPB has been observed in many sequences (e.g., Smit, 1990; Pardo et al., 1996) but no systematic recording is available to date because the cause remained unknown. Only recently has Deccan volcanism been identified as potential cause.

4. MAGNETIC AND SEM DATA

The Bidart section was sampled at 1 cm intervals to determine the magnetic properties in the last meter of the Maastrichtian marls (Fig. 1e-f). The enigmatic Cl-rich iron oxide present in the low MS interval is extremely rare, with concentration below the detection limit of common analytical methods (X-ray diffraction) and with grain-size (~10 mm) too small to allow accurate microprobe analysis. However, it is extremely sensitive to induced magnetic fields (i.e. Isothermal Remanent Magnetization=IRM), having high values of mean acquisition field (B1/2 on Fig. 3 and 4), making magnetic methods an adequate tool for its detection (Font et al., 2011). Our new high-resolution mass specific magnetic susceptibility analyses confirm the presence of the low MS interval from -5 to -50 cm below the KPB boundary (Fig. 3). The transition to the more characteristic MS values of the Maastrichtian marls at the base of the interval is gradual suggesting a progressive change in palaeoenvironmental conditions rather than the existence of a hiatus or a fault.

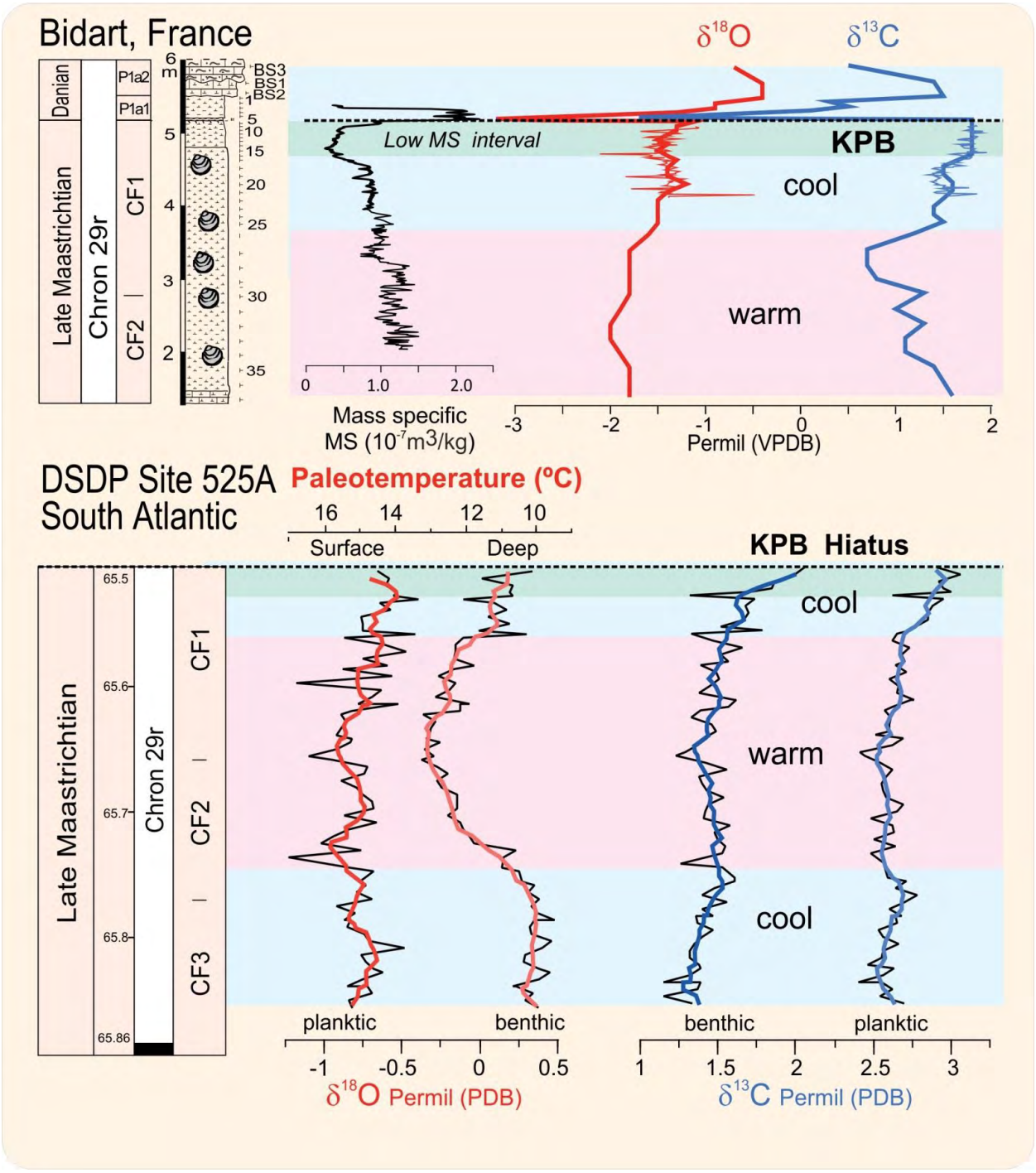

Figure 2. *C and O isotopic compositions of the Bidart section and correlation with the South Atlantic (DSDP Site 525A) (Li and Keller, 1998). The mass specific magnetic susceptibility profile compiled from Font et al. (2011) and the present study is also shown.*

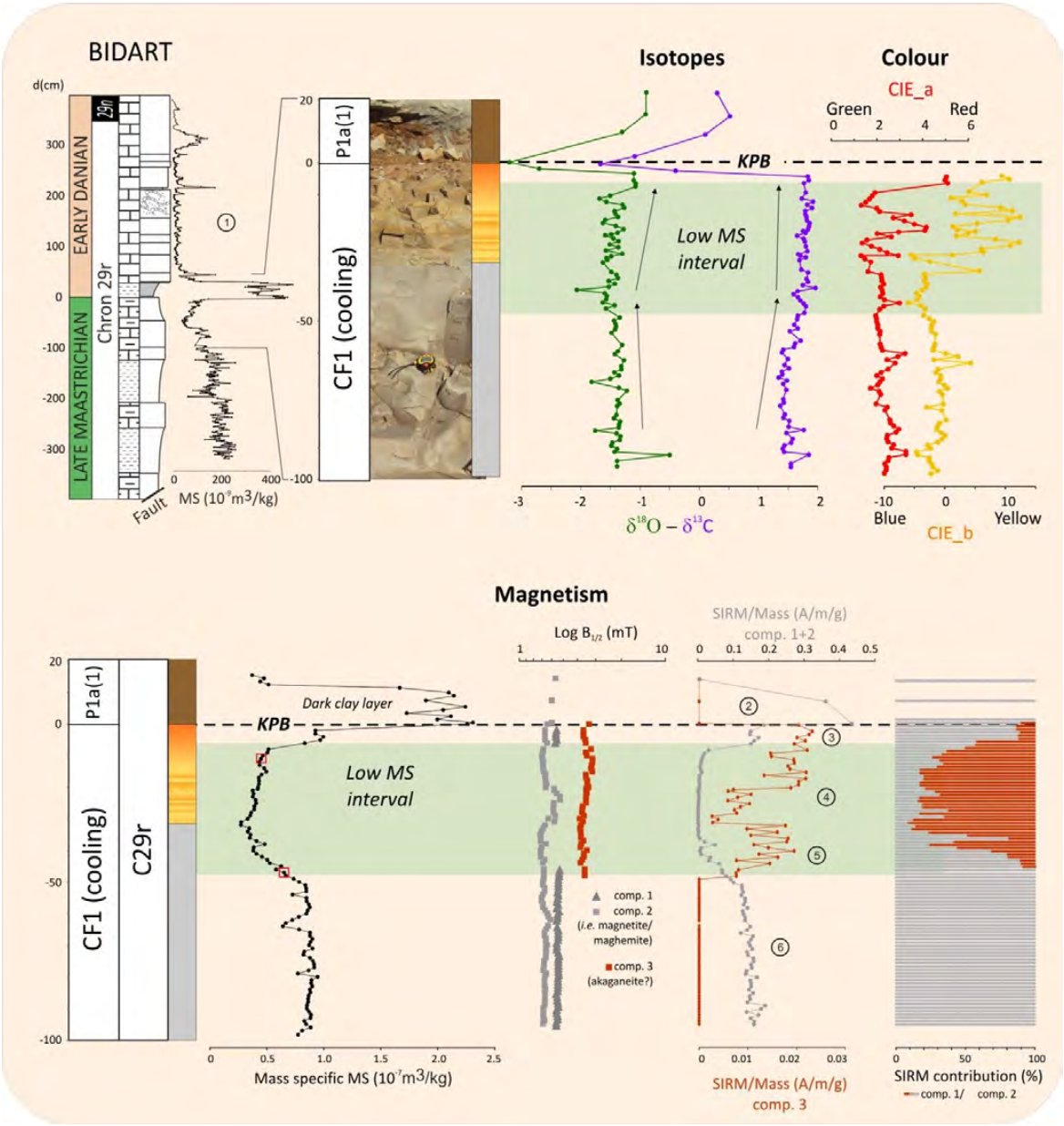

***Figure 3**. **a,** Mineralogical and isotopic (C and O) data of the entire Maastrichtian cropping out at Bidart (above the fault indicated at Fig. 1b). The magnetic susceptibility profile compiled from Font et al. (2011) and this study is also shown. **b,** High-resolution mass specific magnetic susceptibility (MS) and IRM parameters ($B_{1/2}$, SIRM and contribution) of the last meter of Maastrichtian marls and the KPB. The figure shows that detrital titanomagnetite is the principal magnetic carrier in Maastrichtian and Danian sediments, while the peculiar low MS interval is dominated by (antiferromagnetic) akaganeite. Red squares on the MS profile show samples analysed by SEM-EDS and illustrated in Figure 5. Numbered intervals (from 1 to 6) refer to IRM data (cf. Fig. 3). **c,** Diffuse Reflectance Spectrophotometry show an increase in red-yellow coloured iron oxides (i.e. akaganeite) in the interval of low MS values concomitantly with a decrease in clay content and an increase in carbonate (X-ray diffraction); C and O isotopes are coherent with the uppermost CF1 (cooling) interval (cf. Fig. 2).*

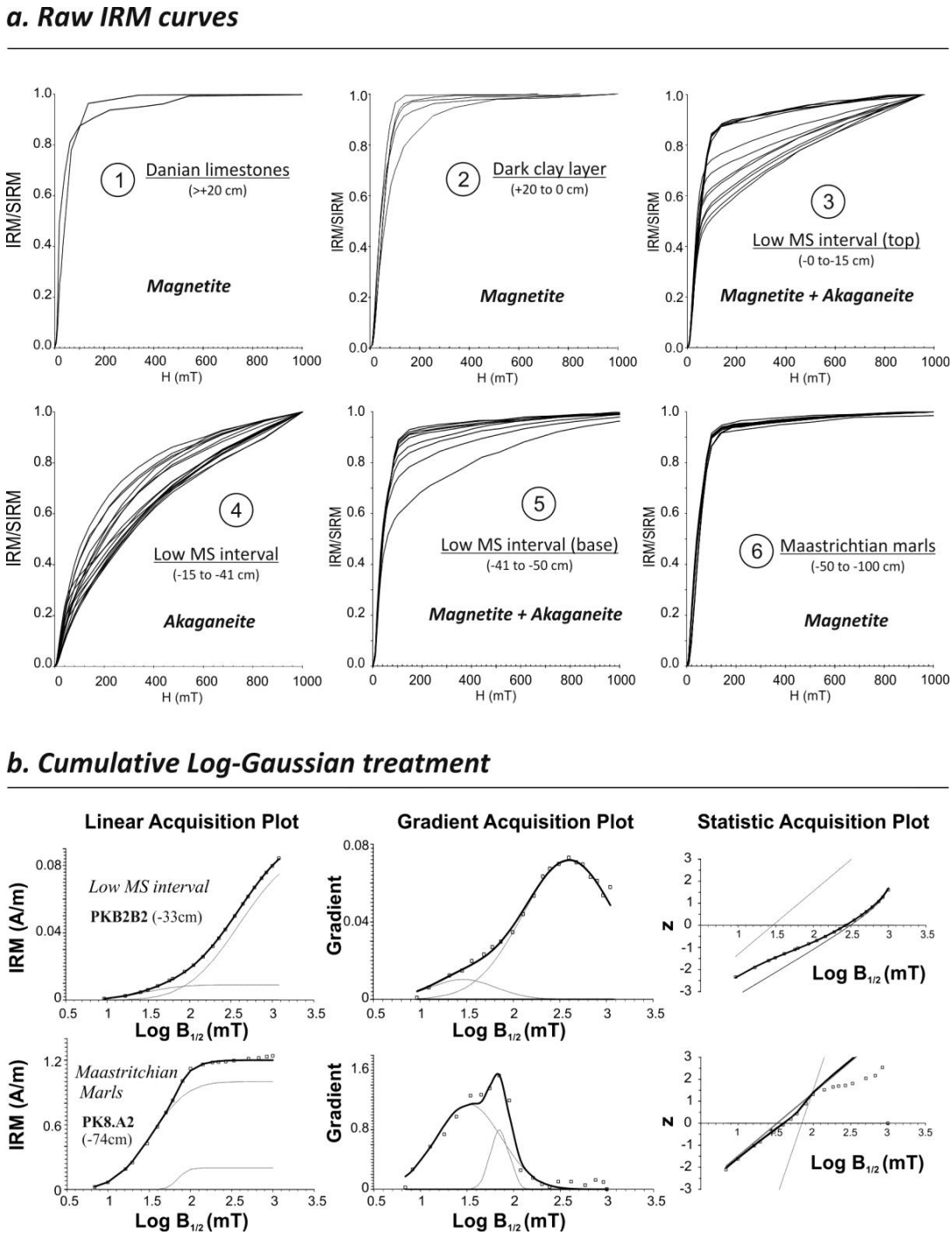

Figure 4. a, *Raw Isothermal Remanent Magnetization curves of the Bidart section show that all sedimentary intervals are dominated by unimodal distribution of remanent spectra, attributed to detrital titanomagnetite (Font et al., 2011). The low MS interval is featured by a bimodal distribution indicating the admixture of a harder (i.e. more coercive) magnetic phase attributed to akaganeite.* ***b,*** *IRM data are treated by the cumulative log-Gaussian function (Kruiver et al., 2001). In most samples, a low coercive (i.e. magnetite/maghemite) phase contribute to more than 90% of the magnetic signal whereas the hard fraction probably corresponding to secondary (pigmentary) hematite, which is a minor presence. The low MS interval is characterized by very low content of magnetite and by admixture of a high coercive magnetic phase, i.e. akaganeite, which does not reach saturation below 1.2 T.*

Concomitant with the decrease in MS values is an admixture of a harder (higher $B_{1/2}$ values) magnetic phase as evident by a bimodal association of IRM parameters (Fig. 4). After unmixing raw IRM curves by using the CLG function (Robertson and France, 1994; Kruiver et al., 2001), two to three magnetic phases (called component) were isolated (Fig. 3b, Table X2).

Components 1 and 2 correspond to low to medium coercive phases with values of mean acquisition field ($B_{1/2}$) varying from 24 to 80 and 57 to 77 mT, respectively (Table X2). These values are in the range of magnetite and maghemite populations commonly found in sedimentary rocks (Kruiver et al., 2001) and at Bidart (Galbrun and Gardin, 2004). Values of remanent coercivity ($B_{1/2}$) of the hard fraction vary between 389 and 1479 mT and are typical of antiferromagnetic behaviour, similarly to hydroxide such as haematite or goethite commonly found in marine rocks (Kruiver et al., 2003). However, the latter are not depicted in our thermomagnetic analyses and microscopic observations.

The decrease in MS values can be explained by reduced detrital titanomagnetite (and accessorily maghemite) content, the main magnetic carrier of the Maastrichtian marls at Bidart (Galbrun and Gardin, 2004; Font et al., 2011), as observed by a characteristic reduction in mass normalized saturation isothermal remanent magnetization (SIRM/Mass) values of component 1+2 (Fig. 3, Table X2). A maximum 90% reduction in component 1+2 remanence is observed in the middle part of the interval (Fig. 3).

Scanning Electron Microscope (SEM) observations coupled to Energy Dispersive Spectra (EDS) show the occurrence of Cl-bearing iron hydroxides with a specular, plate-like morphology and grain sizes <10-40mm (Fig. 5). This mineral was only observed in samples from the low MS interval. EDS spectra show the presence of Fe, O, Cl and Ca. Compositional mapping reveals only Fe and Cl together whereas Ca is associated with the sediment matrix (Fig. 5). Ti-bearing iron oxides (Ti being an indicator of detrital origin) are rare in samples from the low MS interval but exist either as small (<10mm) cubic-like and eroded crystals of magnetite or as severely oxidized ilmenite (Fig. 6).

We infer that the Cl-rich iron hydroxide corresponds to akaganeite, in agreement with our magnetic and SEM-EDS data. Indeed, akaganeite is antiferromagnetic giving an explanation for the high coercivity component (comp. 3) identified in our IRM analyses. Concentration in Cl is estimated by semi-quantitative analysis of EDS spectra (more than twenty analyses) and vary between 0.68 and 4.64 wt%, considering that it corresponds to a minimum value since other elements contained in the matrix also contribute to the calculation. The association Fe-Cl is explained by the hollandite-type structure of akaganeite (Post and Buchwald, 1991). In this arrangement the octahedral sites are occupied by iron cations whereas Cl^- ions partially fill the tunnels. The subeuhedral and plate-like morphologies of the crystals contrast with the eroded aspect of the detrital titanomagnetite and rather argue for an aeolian transport (Fig. 6).

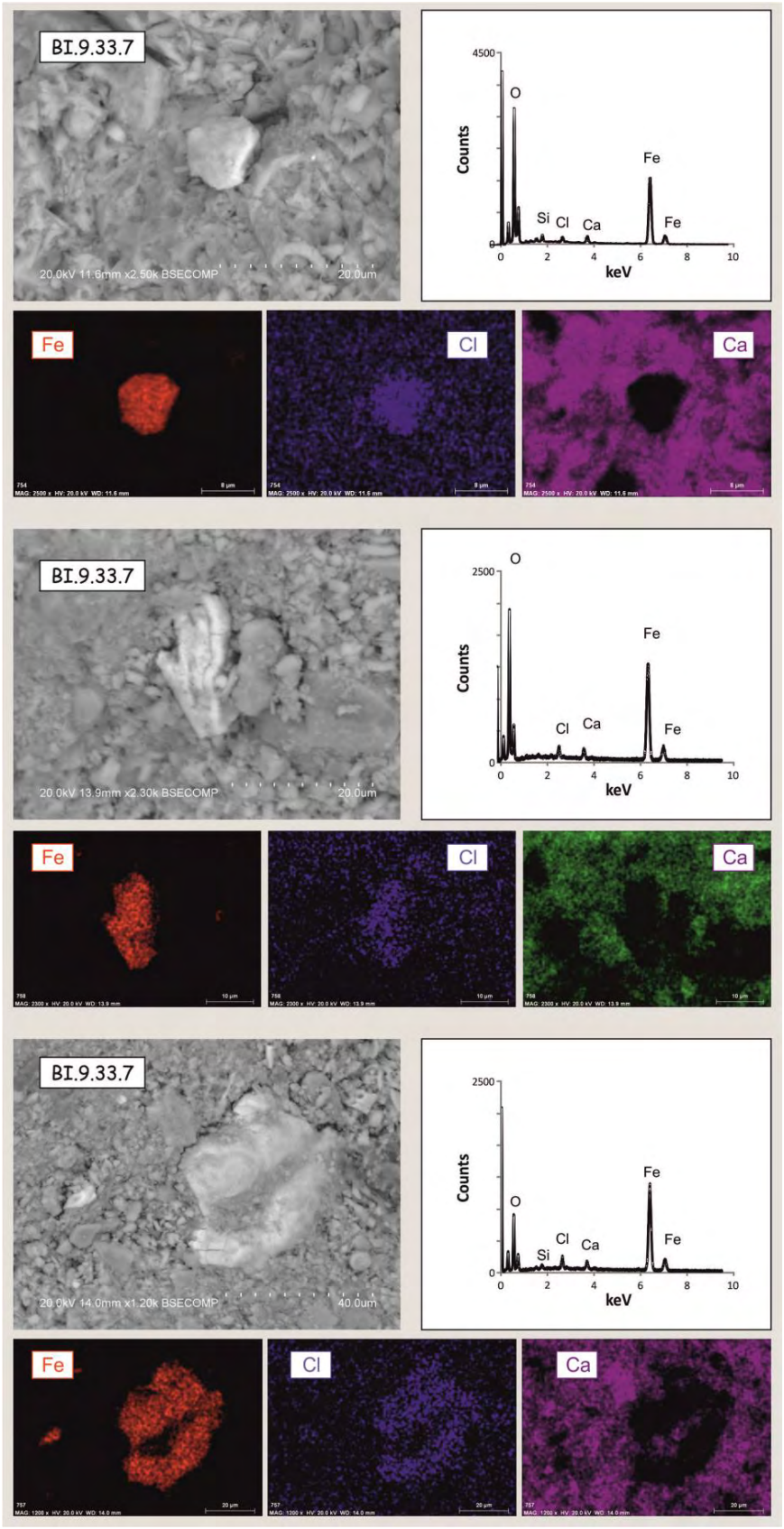

Figure 5. *Scanning Electron Microscopy coupled to Energy Dispersive Spectra (EDS) and Composition Mapping of the Cl-bearing iron hydroxide found in the interval of low MS values at Bidart.*

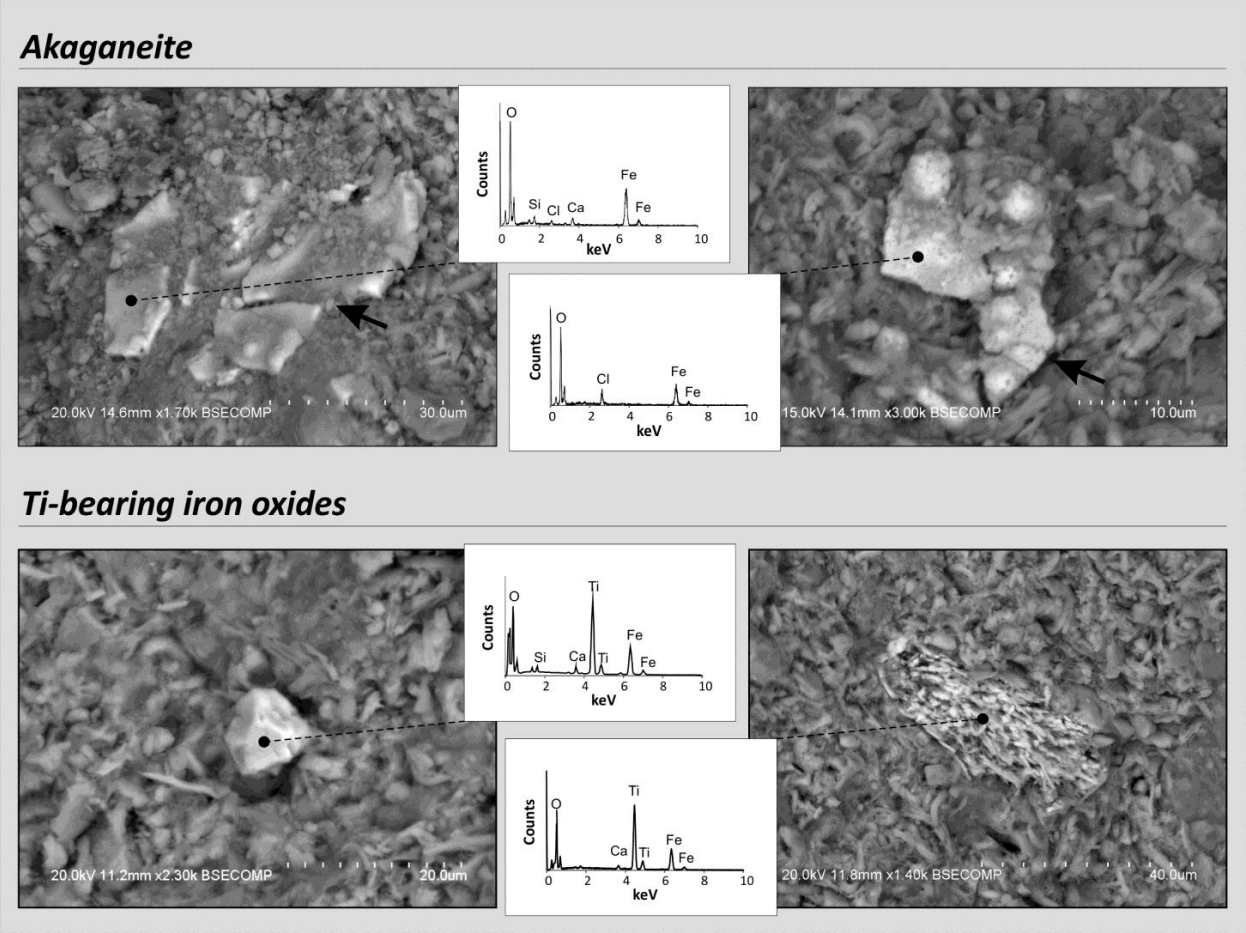

Figure 6. *Additional SEM photographs and EDS spectra of plate-like and semi-hexagonal akaganeite (above) and eroded and severely altered Ti-bearing iron oxides (below).*

Grain-size from micrometer to tens of micrometers is in the range of Quaternary aeolian dust (Maher, 2011). The presence of akaganeite, which is yellow-brown in colour, is also consistent with Diffuse Reflectance Spectra that show significant trends of the low MS interval in the red (CIE_a) and yellow (CIE_b) colours (Fig. 3). It also explains the characteristic yellow-brown colour of the low MS interval at Bidart (Fig. 1, 3).

It is worthwhile to note that the origin of the low MS interval and the appearance of akaganeite, although located in the same stratigraphic interval, are the results of two independent phenomena. Indeed, akaganeite is highly coercive (i.e. very low susceptibility) and extremely rare under SEM observations and below the detection limit of most classical mineralogical investigation (>>0.1%wt). Therefore, it cannot contribute significantly to the magnetic susceptibility after normalization per mass units (Fig. 3).

5. DISCUSSION

5.1. Akaganeite: a new Deccan marker?

The discovery of akaganeite in the low MS interval at Bidart (this study) and at Gubbio (Font et al., 2011) just below the KPB mass extinction and coeval with the main Deccan phase-2 argues for a volcanic origin. The subeuhedral and plate-like morphologies of the newly found akaganeite crystals contrast with the eroded aspect of detrital magnetite and their scarcity

(<0.1%wt) in the sedimentary matrix is compatible with aeolian transport from a distant source. Akaganeite (b-$Fe_2(OH)_3Cl$) is rare in natural conditions but a common product of corrosion of steel or archaeological items in marine environments because its formation requires large concentrations of both dissolved Fe(II) and chloride ions (Reguer et al., 2007; Remazeilles and Refait, 2007,2008). Akaganeite is also described from weathered steel exposed to an acidic atmosphere (Li et al., 2008). Johnston (1977) described akaganeite co-occurring with jarosite near the steaming fumarole vents of the White Island volcano in New Zealand. Akaganeite also precipitates naturally as a pure mineral phase with an average Fe/Cl molar ratio of 6.7 from oxidation of iron sulphide minerals during occasional drying of sulphide sediments from Australian wetlands (Bibi et al., 2011). Naturally occurring akaganeite is also observed in weathered meteorites especially from cold environments such as the Antarctic continent (Bland et al., 1997; Lee and Bland, 2004). Akaganeite from meteorites often contains a small amount of Ni.

Akaganeite crystals found in the Bidart and Gubbio sediments do not have the composition of meteorite-derived akaganeite. Their formation in periodically dried sulphidic coastal wetlands in the vicinity of the Deccan is a possible scenario, but in this hypothesis their transportation to Gubbio (Italy) and Bidart (France) is highly unlikely (Font et al., 2011). However, their formation in relation with Deccan volcanic degassing followed by eolian transport is a possible scenario.

Metal transfer (notably iron but also Na, K, Zn) from degassing lava to the atmosphere as simple chlorides has been observed and predicted by thermochemical modelling. These compounds are highly volatile, especially when the lava is at a high temperature. We infer that akaganeite results from a gaseous reaction between such iron chlorine compounds and volcanic/atmospheric gases, such as water and oxygen. The structural formula of akaganeite (oxyhydroxide and not oxide) pleads for a reaction at a rather low temperature. Indeed, at temperatures higher than 550°C, akaganeite would react to form hematite. At these temperatures, $FeCl_2$ is the most abundant iron species, whereas at temperatures higher than 750°C it is replaced by $Fe(OH)_2$ (Symonds and Reed, 1993). $FeCl_2$ sublimates rapidly (64.4 mg/100 mL) allowing its dissolution in the aqueous and atmospheric medium. Fe^{2+} and Cl^- ions could then react according to the following equation to form akaganeite:

$$2Fe^{2+}_{(aq)} + Cl^-_{(aq)} + 3/2H_2O + 3/4O_2(g) = \beta\text{-}Fe_2(OH)_3Cl_{(s)}.$$

Considering a standard free energy of formation for β-$Fe_2(OH)_3Cl$ (Remazeilles and Refait, 2007) and enthalpies of aqueous Fe(II), Cl(II) and water (Wagman et al., 1982), the computed $\Delta G°_r$ is –280.74 $kJ.mol^{-1}$. According to this reactive pathway, the akaganeite formation is thermodynamically possible.

Delivery of SO_2 and halogens to the atmosphere by active volcanoes is well-known especially for arc volcanism (Pyle and Mather, 2009), but also occurs in continental flood basalt eruptions (Thordarson and Self, 1996; Self et al., 2008a). Glass analyses recently demonstrated that Deccan basalts were responsible for a huge HCl input into the atmosphere (Self et al., 2008a) (4×10^{12} g SO_2 and 1×10^{12} g HCl released into the atmosphere per cubic km of lava) confirming former scenarios (Glasby and Kunzendorf, 1996). The volume of lavas extruded

during Deccan phase-2 is ~80% of the total lava volume, i.e. ca 10^6 km^3 (Self et al., 2006). These figures are fairly consistent with the calculations of Black et al. (2012) for the Siberian traps that are suggested to have released 7 x 10^{12} g S and 3 to 9 x 10^{12} g Cl in the atmosphere. In the latter case, the variability of Cl degassing is due to the possible contribution of contact heating and metamorphism of the Tunguska sediments. The Kilauea volcano in Hawaii sometimes generates additional HCl when lavas flow into the sea (Edmonds and Gerlach, 2006). Using the conservative hypothesis of 1 x 10^{12} g HCl released by Deccan phase-2 for 200,000 yrs, a mean value of 5 Mt Cl and 10 Mt S per year would have been released in the atmosphere (i.e., quantities equivalent to one Pinatubo eruption every year or every two-years for 200,000 years). These calculations assume a rather unrealistic regular volcanic gas production and over a much longer time period than the currently estimated tens of thousands of years to at most 50,000 to 100,000 years (Chenet et al., 2008). Despite these uncertainties it is obvious that Deccan phase-2 corresponds to a severe atmospheric change and was responsible for major environmental hazards due to acid rains over tens of thousands of years, as recently suggested by Ward (2009).

The fate of the acidic gases depends on humidity at the emission site, because of their very high water-solubility. At the time of Deccan phase-2 volcanism, India was a large island in the southern part of the Tethys Ocean located at about 21°S. Climate was relatively warm and humid, but arid close to the Deccan Volcanic Province as a result of "mock aridity" (e.g. volcanically induced conditions and extreme geochemical alkalinity) (Khadkikar et al., 1999; Gertsch et al., 2011; Keller et al., 2012). Therefore, a large proportion of the released gases would have been transported into the high atmosphere (Kaminski et al., 2011) rather than scavenged locally by rains. Deccan volcanism likely occurred as large fissure eruptions with thermal plumes penetrating into the stratosphere due to the high lava volume and high temperatures (Self et al., 2008). A significant percentage of acid gases and halogens are therefore expected to have remained in the lower stratosphere for several years after each eruption (Ward, 2009). This is the likely explanation for environmental changes such as acid rains over a large portion of the Earth, especially the intertropical and peri-Tethys region.

5.2. Low MS interval: consequence of Deccan phase-2 acid rains?

Low magnetic susceptibility values just below the Cretacous-Paleogene boundary may reflect a drastic decrease in titanomagnetite content. Titanomagnetite is generally detrital, which means that it originated from erosion of igneous rocks and/or their pedogenetic products and was transported into basin sediments. Any variations in detrital titanomagnetite content at Bidart can be explained by i) a rapid sea-level rise (e.g., dilution and remoteness to the source), or ii) annihilation of iron oxides at or close to their continental source. The first hypothesis is less probable since the maximum flooding surface is located just above the low MS interval (at the base of the KPB) as attested by bioturbation similar to other KPB sections. The second hypothesis can be tested based on the effect of acid rains as a consequence of the huge Deccan volcanic gas emissions, which could have dissolved the continental magnetite grains before any riverine transfer to the oceanic basin. Rain in equilibrium with present-day atmospheric CO_2 is characterized by a pH of 5.6, whereas acidic volcanic rains have a much lower pH. For instance, the distribution of regional rain pH due to Mount Etna, a major gas emitter, has a pH of 3-4.5 (Calabrese et al., 2011).

Our weathering model indicates that equilibrium between magnetite and the weathering solution is reached between rain events (circa one day). The time required to dissolve 90 percent of the initial magnetite mass is between 31,000 (pH 3.3) and 68,000 yrs (pH 4.3). These values are compatible with the temporal duration of the volcanic emissions based upon magneto-stratigraphic measurements and estimated at less than 100 kyrs (10-20 yrs per flow) (Chenet et al., 2007; Chenet et al., 2008)_ENREF_38. Note that our calculations based on the pH of present-day rainwater (5.6) lead to a dissolution time of several million years, which is much longer than the expected landscape davisian stability and consistent with previous work (White et al., 1994) giving very long residence time for sand-sized grains of magnetite subjected to present-day weathering conditions.

5.3. Conceptual model

A conceptual model for the formation of akaganeite and its aeolian deposition at Bidart and Gubbio infers the formation of akaganeite in the buoyant volcanic plume and transported into the stratosphere by penetrative convection together with huge amounts of aerosols containing dissolved acid species (Fig. 7). It is well known that heat associated with widespread lava flows may generate convection in the atmosphere (Kaminski et al., 2011). These penetrative convections produce a thick well-mixed heated atmospheric layer where buoyancy ensures that volcanic gases get transported to the stratosphere, despite the low explosive nature of tholeiitic volcanism. Subtropical eruptions such as the Deccan are important contributors to global climate because stratospheric aerosols have a long lifetime in the tropical-subtropical stratosphere and can be transported into the mid-latitudes of both hemispheres. For example, in the Soufrière Hills eruption (16.7ºN) in 2006, the aerosol plume reached altitudes up to 20 km (Prata et al., 2007), which is well above the tropical tropopause layer. Two weeks after the eruption of the Nabro volcano (East Africa, 13.5ºN) in 2011, the Cloud Aerosol Lidar and Infrared Pathfinder Satellite Observation (CALIPSO) detected enhanced aerosol backscatter in the lower stratosphere (~18 km) (Vernier et al., 2013). During the 1991 Pinatubo eruption (15ºN) the plume reached a maximum altitude of 39 km (Holasek et al., 1996), whereas the buoyant regions of the volcanic SO_2 and ash cloud are estimated at 25 km and 22 km, respectively (Guo et al., 2004b).

Once injected into the stratosphere the large aerosol particles and small ones being formed by the volcanic gases are rapidly advected around the globe (Robock, 2000). The lifetime of sulphate aerosols is up to 3 years in the stratosphere, but only 3 weeks in the troposphere. Observations after the 1883 Krakatau eruption (6ºS) showed that the aerosol cloud circled the globe in 2 weeks (Robock, 2000). The El Chichón (17ºN) in 1982 and the Pinatubo in 1991 are other examples of volcanic eruptions where aerosol clouds circled the globe within 3 weeks and caused considerable cooling of the lower troposphere in the 2 years after the eruptions (Robock, 2000; Guo et al., 2004a). The effect of the Laki eruption (1783) in Iceland, which extruded about 15 km^3 of lava over 8 months (Thordarson and Self, 2003), is also well documented including climate change and acid rains over most of Europe up to 3000 km from the volcano (Garnier, 2011). Numerical modelling of the Laki eruption confirmed that cooling was mostly due to stratospheric sulphate aerosols (Chenet et al., 2005).

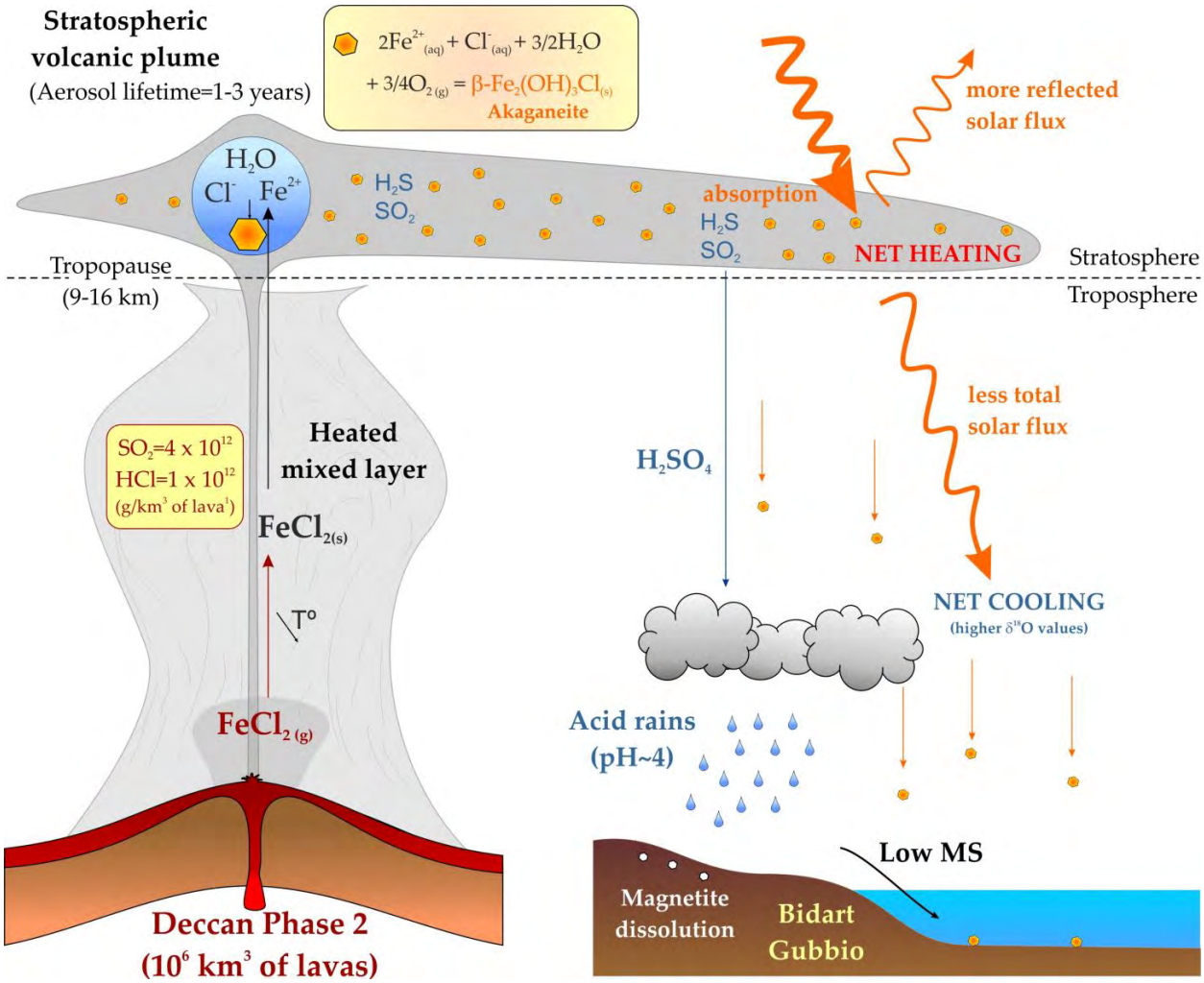

Figure 7. *Conceptual model of the sedimentary marine record of continental magnetite dissolution caused by volcanic acidic rains (modified from Kaminski et al. (2010) and Robock (2000)).*

In comparison, Deccan eruptions were much more intense, with an estimated 1 million km^3 lava extruded (Self et al., 2006) over tens of thousands of years (Chenet et al., 2007). This likely caused acid rains through the intertropical peri-Tethys zone, reaching the North Atlantic and France (Bidart), in particular, about 7000 km from the erupting Deccan basalts. Our model assumes that Deccan volcanism caused acid rain at Bidart (France) and Gubbio (Italy) resulting in weathering and dissolution effect on continental surface. As noted above these assumptions are well supported by historical comparison as well as our numerical weathering model. The subsequent cooling effect results from the huge input of stratospheric aerosols (Self et al., 2006; Self et al., 2008a), as also supported by our C and O isotopic data (Fig. 2).

We conclude that since volcanic plumes of relatively very small volcanic eruptions reached the stratosphere and caused significant acid rain and climate changes over relatively very large areas (~3000 km for the Laki eruption which extruded 15km^3 of lava), then the giant pulsed Deccan eruptions near the end of the Maastrichtian with an estimated 800,000 km^3 lava erupted (Self et al., 2006) (~53 times the Laki eruptions) must have resulted in the most devastating

global environmental changes. A comparison of stratospheric volcanic aerosol output from recent volcanos and its effect on Earth's radiation budget with the output from Deccan eruptions reveals further clues to the magnitude, nature and importance of the enormous global Deccan-related environmental changes and their likely devastating contribution to the end-Cretaceous mass extinction.

6. Conclusion

The magnetic and mineral markers identified in the Bidart section are consistent with a major change in atmospheric conditions linked to Deccan-induced volcanic gas emissions. The low magnetic susceptibility signal is likely to be recognized elsewhere in the Tethys sedimentary record, particularly in shallow and proximal marine environments where terrestrial input is appropriate and provided that wet local climatic conditions prevailed and that the continental surfaces contained significant amounts of magnetite. Presence of akaganeite is expected in the Tethys realm, but with a variable probability depending on the mechanisms of aeolian transport. Moreover, both markers may help unravel the signature of other large igneous provinces (LIPs) emplaced in similar palaeogeographic and palaeoclimatic conditions, such as the Central Atlantic Magmatic Province. These newly discovered markers provide a promising tool to evaluate the environmental effects of LIPs and their possible consequences for the biosphere.

ACKNOWLEDGEMENTS Funding was provided by Pest-OE/CTE/LA0019/2011-IDL, PTDC/CTE_GIX/110205/2010 and PTDC/CTE-GIX/117298/2012 funded by FCT. We thank Jorge Miguel Miranda and Celia Lee for technical and administrative supply, Bernard Peybernès for bibliographic supply and help in the field, Dominique Serça and Céline Mari (Laboratoire d'Aérologie, OMP, Toulouse) and Gilles Berger (IRAP, Toulouse) for helpful discussions. We thank anonymous reviewers for their constructive comments.

REFERENCES

Abramovich, S., Yovel-Corem, S., Almogi-Labin, A., Benjamini, C., 2010. Global climate change and planktic foraminiferal response in the Maastrichtian. Paleoceanography 25.

Appelo, C.A.J., Parkhurst, D.L., 1999. User's guide to PHREEQC version 2 - A computer program for speciation, batch-reaction, one -dimensional transport, and inverse calculations. . Water-Ressources Investigations Rep. U.S. Geological Survey, Denver, Colorado. , 99-4259, .

Bibi, I., Singh, B., Silvester, E., 2011. Akaganeite (beta-FeOOH) precipitation in inland acid sulfate soils of south-western New South Wales (NSW), Australia. Geochim Cosmochim Ac 75, 6429-6438.

Black, B.A., Elkins-Tanton, L.T., Rowe, M.C., Peate, I.U., 2012. Magnitude and consequences of volatile release from the Siberian Traps. Earth Planet Sc Lett 317, 363-373.

Bland, P.A., Kelley, S.P., Berry, F.J., Cadogan, J.M., Pillinger, C.T., 1997. Artificial weathering of the ordinary chondrite Allegan: Implications for the presence of Cl- as a structural component in akaganeite. Am Mineral 82, 1187-1197.

Bonté, P., Delacotte, O., Renard, M., Laj, C., Boclet, D., Jehanno, C., Rocchia, R., 1984. An Iridium Rich Layer at the Cretaceous Tertiary Boundary in the Bidart Section (Southern France). Geophysical Research Letters 11, 473-476.

Brunauer, S., Emmett, P.H., Teller, E., 1938. Adsorption of gases in multimolecular layers. J Am Chem Soc 60, 309-319.

Calabrese, S., Aiuppa, A., Allard, P., Bagnato, E., Bellomo, S., Brusca, L., D'Alessandro, W., Parello, F., 2011. Atmospheric sources and sinks of volcanogenic elements in a basaltic volcano (Etna, Italy). Geochim Cosmochim Ac 75, 7401-7425.

Channell, J.E.T., Hodell, D.A., Singer, B.S., Xuan, C., 2010. Reconciling astrochronological and Ar-40/Ar-39 ages for the Matuyama-Brunhes boundary and late Matuyama Chron. Geochemistry Geophysics Geosystems 11.

Chenet, A.L., Fluteau, F., Courtillot, V., 2005. Modelling massive sulphate aerosol pollution, following the large 1783 Laki basaltic eruption. Earth Planet Sc Lett 236, 721-731.

Chenet, A.L., Fluteau, F., Courtillot, V., Gerard, M., Subbarao, K.V., 2008. Determination of rapid Deccan eruptions across the Cretaceous-Tertiary boundary using paleomagnetic secular variation: Results from a 1200-m-thick section in the Mahabaleshwar escarpment. Journal of Geophysical Research-Solid Earth 113.

Chenet, A.L., Quidelleur, X., Fluteau, F., Courtillot, V., Bajpai, S., 2007. K-40-Ar-40 dating of the Main Deccan large igneous province: Further evidence of KTB age and short duration. Earth Planet Sc Lett 263, 1-15.

Chudaeva, V.A., Urchenko, S.G., Chudaev, O.V., Sugimory, K., Matsuo, M., Kuno, A., 2006. Chemistry of rainwaters in the south Pacific area of Russia. J Geochem Explor 88, 101-105.

Courtillot, V., 2012. Mass Extinctions and Massive Volcanism. J Geol Soc India 79, 107-108.

Edmonds, M., Gerlach, T.M., 2006. The airborne lava-seawater interaction plume at Kilauea Volcano, Hawai'i. Earth Planet Sc Lett 244, 83-96.

Ellwood, B.B., MacDonald, W.D., Wheeler, C., Benoist, S.L., 2003. The K-T boundary in Oman: identified using magnetic susceptibility field measurements with geochemical confirmation. Earth Planet Sc Lett 206, 529-540.

Fabre, S., Berger, G., 2012. How tillite weathering during the snowball Earth aftermath induced cap carbonate deposition. Geology 40, 1027-1030.

Fabre, S., Berger, G., Nedelec, A., 2011. Modeling of continental weathering under high-CO2 atmospheres during Precambrian times. Geochemistry Geophysics Geosystems 12.

Floor, G.H., Calabrese, S., Roman-Ross, G., D'Alessandro, W., Aiuppa, A., 2011. Selenium mobilization in soils due to volcanic derived acid rain: An example from Mt Etna volcano, Sicily. Chemical Geology 289, 235-244.

Font, E., Nedelec, A., Ellwood, B.B., Mirao, J., Silva, P.F., 2011. A new sedimentary benchmark for the Deccan Traps volcanism? Geophysical Research Letters 38.

Gaillardet, J., Dupre, B., Louvat, P., Allegre, C.J., 1999. Global silicate weathering and CO2 consumption rates deduced from the chemistry of large rivers. Chemical Geology 159, 3-30.

Galbrun, B., Gardin, S., 2004. New chronostratigraphy of the Cretaceous-Paleogene boundary interval at Bidart (France). Earth Planet Sc Lett 224, 19-32.

Garnier, E., 2011. Les brouillards du Laki en 1783: volcanisme et crise sanitaire en Europe. Bull.

Acad. Natle Méd. 195, 1043-1055.

Gertsch, B., Keller, G., Adatte, T., Garg, R., Prasad, V., Berner, Z., Fleitmann, D., 2011. Environmental effects of Deccan volcanism across the Cretaceous-Tertiary transition in Meghalaya, India. Earth Planet Sc Lett 310, 272-285.

Glasby, G.P., Kunzendorf, H., 1996. Multiple factors in the origin of the Cretaceous/Tertiary boundary: The role of environmental stress and Deccan Trap volcanism. Geol Rundsch 85, 191-210.

Guo, S., Bluth, G.J.S., Rose, W.I., Watson, I.M., Prata, A.J., 2004a. Re-evaluation of SO2 release of the 15 June 1991 Pinatubo eruption using ultraviolet and infrared satellite sensors. Geochemistry Geophysics Geosystems 5.

Guo, S., Rose, W.I., Bluth, G.J.S., Watson, I.M., 2004b. Particles in the great Pinatubo volcanic cloud of June 1991: The role of ice. Geochemistry Geophysics Geosystems 5.

Holasek, R.E., Self, S., Woods, A.W., 1996. Satellite observations and interpretation of the 1991 Mount Pinatubo eruption plumes. Journal of Geophysical Research-Solid Earth 101, 27635-27655.

Johnston, J.H., 1977. Jarosite and Akaganeite from White Island Volcano, New-Zealand - an X-Ray and Mossbauer Study. Geochim Cosmochim Ac 41, 539-544.

Kaminski, E., Chenet, A.L., Jaupart, C., Courtillot, V., 2011. Rise of volcanic plumes to the stratosphere aided by penetrative convection above large lava flows. Earth Planet Sc Lett 301, 171-178.

Keller, G., Adatte, T., Bhowmick, P.K., H., U., Dave, A., A.N., R., Jaiprakash, B.C., 2012. Nature and timing of extinctions in Cretaceous-Tertiary planktic foraminifera preserved in Deccan intertrappean sediments of th eKrishna–Godavari Basin, India. Earth Planet Sc Lett in press.

Keller, G., Adatte, T., Juez, A.P., Lopez-Oliva, J.G., 2009. New evidence concerning the age and biotic effects of the Chicxulub impact in NE Mexico. J Geol Soc London 166, 393-411.

Keller, G., Bhowmick, P.K., Upadhyay, H., Dave, A., Reddy, A.N., Jaiprakash, B.C., Adatte, T., 2011. Deccan Volcanism Linked to the Cretaceous-Tertiary Boundary Mass Extinction: New Evidence from ONGC Wells in the Krishna-Godavari Basin. J Geol Soc India 78, 399-428.

Keller, G., Li, L., MacLeod, N., 1995. The Cretaceous Tertiary boundary stratotype section at El Kef, Tunisia: How catastrophic was the mass extinction? Palaeogeography Palaeoclimatology Palaeoecology 119, 221-254.

Khadkikar, A.S., Sant, D.A., Gogte, V., Karanth, R.V., 1999. The influence of Deccan volcanism on climate: insights from lacustrine intertrappean deposits, Anjar, western India. Palaeogeography Palaeoclimatology Palaeoecology 147, 141-149.

Kruiver, P.P., Dekkers, M.J., Heslop, D., 2001. Quantification of magnetic coercivity components by the analysis of acquisition curves of isothermal remanent magnetisation. Earth Planet Sc Lett 189, 269-276.

Kruiver, P.P., Langereis, C.G., Dekkers, M.J., Krijgsman, W., 2003. Rock-magnetic properties of multicomponent natural remanent magnetization in alluvial red beds (NE Spain). Geophys J Int 153, 317-332.

Kuiper, K.F., Deino, A., Hilgen, F.J., Krijgsman, W., Renne, P.R., Wijbrans, J.R., 2008. Synchronizing rock clocks of Earth history. Science 320, 500-504.

Lee, M.R., Bland, P.A., 2004. Mechanisms of weathering of meteorites recovered from hot and cold deserts and the formation of phyllosilicates. Geochim Cosmochim Ac 68, 893-916.

Li, L.Q., Keller, G., 1998. Abrupt deep-sea warming at the end of the Cretaceous. Geology 26, 995-998.

Li, Q.X., Wang, Z.Y., Han, W., Han, E.H., 2008. Characterization of the rust formed on weathering steel exposed to Qinghai salt lake atmosphere. Corros Sci 50, 365-371.

Maher, B.A., 2011. The magnetic properties of Quaternary aeolian dusts and sediments, and their palaeoclimatic significance. Aeolian Res 3, 87-144.

Pardo, A., Ortiz, M., Keller, G., 1996. Latest Maastrichtian and Cretaceous-Tertiary Boundary Foraminiferal Turnover and Environmental Changes at Agost, Spain. In :N. Macleod, and G. Keller (Eds). Cretaceous-Tertiary Mass Extinction: Biotic and Environmental Changes. W. W. Norton and Company, New York-London, pp. 139 - 171.

Post, J.E., Buchwald, V.F., 1991. Crystal-Structure Refinement of Akaganeite. Am Mineral 76, 272-277.

Prata, A.J., Carn, S.A., Stohl, A., Kerkmann, J., 2007. Long range transport and fate of a stratospheric volcanic cloud from Soufriere Hills volcano, Montserrat. Atmos Chem Phys 7, 5093-5103.

Pyle, D.M., Mather, T.A., 2009. Halogens in igneous processes and their fluxes to the atmosphere and oceans from volcanic activity: A review. Chemical Geology 263, 110-121.

Reguer, S., Dillmann, P., Mirambet, F., 2007. Buried iron archaeological artefacts: Corrosion mechanisms related to the presence of Cl-containing phases. Corros Sci 49, 2726-2744.

Remazeilles, C., Refait, P., 2007. On the formation of beta-FeOOH (akaganeite) in chloride-containing environments. Corros Sci 49, 844-857.

Remazeilles, C., Refait, P., 2008. Formation, fast oxidation and thermodynamic data of Fe(II) hydroxychlorides. Corros Sci 50, 856-864.

Renne, P.R., Deino, A.L., Hilgen, F.J., Kuiper, K.F., Mark, D.F., Mitchell, W.S., Morgan, L.E., Mundil, R., Smit, J., 2013. Time Scales of Critical Events Around the Cretaceous-Paleogene Boundary. Science 339, 684-687.

Renne, P.R., Mundil, R., Balco, G., Min, K.W., Ludwig, K.R., 2010. Joint determination of K-40 decay constants and Ar-40*/K-40 for the Fish Canyon sanidine standard, and improved accuracy for Ar-40/Ar-39 geochronology. Geochim Cosmochim Ac 74, 5349-5367.

Robertson, D.J., France, D.E., 1994. Discrimination of remanence-carrying minerals in mixtures, using Isothermal Remanent Magnetization acquisition curves. Physics of the Earth and Planetary Interiors 82, 223-234.

Robock, A., 2000. Volcanic eruptions and climate. Reviews of Geophysics 38, 191-219.

Schulte, P., Alegret, L., Arenillas, I., Arz, J.A., Barton, P.J., Bown, P.R., Bralower, T.J., Christeson, G.L., Claeys, P., Cockell, C.S., Collins, G.S., Deutsch, A., Goldin, T.J., Goto, K., Grajales-

Nishimura, J.M., Grieve, R.A.F., Gulick, S.P.S., Johnson, K.R., Kiessling, W., Koeberl, C., Kring, D.A., MacLeod, K.G., Matsui, T., Melosh, J., Montanari, A., Morgan, J.V., Neal, C.R., Nichols, D.J., Norris, R.D., Pierazzo, E., Ravizza, G., Rebolledo-Vieyra, M., Reimold, W.U., Robin, E., Salge, T., Speijer, R.P., Sweet, A.R., Urrutia-Fucugauchi, J., Vajda, V., Whalen, M.T., Willumsen, P.S., 2010. The Chicxulub Asteroid Impact and Mass Extinction at the Cretaceous-Paleogene Boundary. Science 327, 1214-1218.

Self, S., Blake, S., Sharma, K., Widdowson, M., Sephton, S., 2008a. Sulfur and chlorine in Late Cretaceous Deccan magmas and eruptive gas release. Science 319, 1654-1657.

Self, S., Jay, A.E., Widdowson, M., Keszthelyi, L.P., 2008b. Correlation of the Deccan and Rajahmundry Trap lavas: Are these the longest and largest lava flows on Earth? J Volcanol Geoth Res 172, 3-19.

Self, S., Widdowson, M., Thordarson, T., Jay, A.E., 2006. Volatile fluxes during flood basalt eruptions and potential effects on the global environment: A Deccan perspective. Earth Planet Sc Lett 248, 518-532.

Smit, J., 1990. Meteorite Impact, Extinctions and the Cretaceous-Tertiary Boundary. Geol Mijnbouw 69, 187-204.

Stuben, D., Kramar, U., Berner, Z.A., Meudt, M., Keller, G., Abramovich, S., Adatte, T., Hambach, U., Stinnesbeck, W., 2003. Late Maastrichtian paleoclimatic and paleoceanographic changes inferred from Sr/Ca ratio and stable isotopes. Palaeogeography Palaeoclimatology Palaeoecology 199, 107-127.

Sverdrup, H., Warfvinge, P., 1995. Estimating field weathering rates using laboratory kinetics. Rev Mineral 31, 485-541.

Symonds, R.B., Reed, M.H., 1993. Calculation of Multicomponent Chemical-Equilibria in Gas-Solid-Liquid Systems - Calculation Methods, Thermochemical Data, and Applications to Studies of High-Temperature Volcanic Gases with Examples from Mount St-Helens. Am J Sci 293, 758-864.

Thordarson, T., Self, S., 1996. Sulfur, chlorine and fluorine degassing and atmospheric loading by the Roza eruption, Columbia River Basalt Group, Washington, USA. J Volcanol Geoth Res 74, 49-73.

Thordarson, T., Self, S., 2003. Atmospheric and environmental effects of the 1783-1784 Laki eruption: A review and reassessment. J Geophys Res-Atmos 108.

Vernier, J.P., Thomason, L.W., Fairlie, T.D., Minnis, P., Palikonda, R., Bedka, K.M., 2013. Comment on "Large Volcanic Aerosol Load in the Stratosphere Linked to Asian Monsoon Transport". Science 339.

Vonhof, H.B., Smit, J., 1997. High-resolution late Maastrichtian early Danian oceanic Sr-87/Sr-86 record: Implications for Cretaceous-Tertiary boundary events. Geology 25, 347-350.

Wagman, D.D., Evans, W.H., Parker, V.B., Schumm, R.H., Halow, I., Bailey, S.M., Churney, K.L., Nuttall, R.L., 1982. The Nbs Tables of Chemical Thermodynamic Properties - Selected Values for Inorganic and C-1 and C-2 Organic-Substances in Si Units. J Phys Chem Ref Data 11, 1-&.

Ward, P.D., Kennedy, W.J., 1993. Maastrichtian Ammonites from the Biscay Region (France,

Spain). J Paleontol 67, 1-58.

Ward, P.L., 2009. Sulfur dioxide initiates global climate change in four ways. Thin Solid Films 517, 3188-3203.

White, A.F., Peterson, M.L., Hochella, M.F., 1994. Electrochemistry and Dissolution Kinetics of Magnetite and Ilmenite. Geochim Cosmochim Ac 58, 1859-1875.

White, R.V., Saunders, A.D., 2005. Volcanism, impact and mass extinctions: incredible or credible coincidences? Lithos 79, 299-316.

Wilf, P., Johnson, K.R., Huber, B.T., 2003. Correlated terrestrial and marine evidence for global climate chanaes before mass extinction at the Cretaceous-Paleogene boundary. P Natl Acad Sci USA 100, 599-604.

APPENDIX – II

RAW DATA
On CD